LUMINESCENT ASSEMBLIES BASED ON SURFACE ACTIVE TRANSITION METAL COMPLEXES AND SUPRAMOLECULAR HOST-GUEST SYSTEMS

By

SHIVA FARABI

A Thesis submitted to
The University of Birmingham
For the degree of
DOCTOR OF PHILOSOPHY

Dedicated to my loving parents, Soheila and Behrooz Farabi

Abstract

Miniaturisation of devices and components is becoming increasingly important in the field of molecular devices. The design of multicomponent supramolecular systems that undergo photoinduced energy or electron transfer processes has been well recognised in view of its potential for development of nanosized molecular devices for solar energy conversion and components in photonic devices. Consequently research has expanded to the properties of monolayers formed from rather simple organic molecules to biological systems and metal complexes. In the present approach, surface active Ru(II) and Os(II) complexes have been designed. Their attachment to surfaces and their photophysical properties in solution, as powders and as self-assembled monolayers have been investigated. The complexes present relatively high quantum yields and long lifetimes in solution, as powders and in monolayers.

The complexes have been developed further to carry β-cyclodextrin recognition sites in their structure. This new group of molecules opens a window into guest-host chemistry on surfaces, with the view to examining photophysical properties of supramolecular functional surface-active systems. The surface active Ru(II) and Os(II) complexes bearing β-cyclodextrin exhibit formation of emissive monolayers. Later Ir(III) and Ru(II) metalloguests with a specific design to bind to β-cyclodextrin cavity have been synthesised and the photo-induced communication between metals were investigated both in solution and on gold surface.

Finally, we propose a new and efficient method of sensitising Nd(III) NIR emission by non-covalent attachment of a BODIPY dye attached to β-cyclodextrin (BODIPY-CD).

The BODIPY-CD has been proved to be a good sensitizer for neodymium complexes. This is the first time that NIR lanthanides have been sensitised through non-covalent host-guest approach using cyclodextrin. The inclusion of the hydrophobic biphenyl and phenyl tails in the cyclodextrin has been proved by the NMR studies.

Acknowledgements

Firstly I would like to thank Dr. Zoe Pikramenou for giving me the opportunity to join the group, and be involved in an interesting and challenging field of research. Thanks for all the support and guidance all these years.

Thanks to all the members of ZP group, I had the pleasure to work and share funny moments with Lasse, Stephen, Dita, Luca, Dave, Alison, Nikola, Sully, Kim, Sam, Sunil, Amy, Richard and Federica. Thanks for be great friends and for all helps and supports.

Thanks to the staff of the analytical facility, Dr. Neil Spencer for NMR, Mr Pete Ashton and Mr. Nick May for mass spectrometry, Mr. Graham Burns for HPLC, and Dr. Louise Male for X-ray crystallography.

Thanks to the support staff of Haworth, Terry Green, Stuart Arkless, Steve Williams, A. Bilkhu, Pam Marshall, Barbara Satchwell, Helen Vahey, Lynn Blake, Ian Bodfish, Katie Bowden and Norihan Taib.

A really special mention must go to all my friends outside chemistry for sharing great times over last four years with me, Ahmad, Ali, Pilar, Leva, Dawn, Molly, Amelia, Saman, Maryam and Nooshin.

And finally my special thanks to my family, my mom and dad and my sister for their unconditional love and support throughout the years.خیلی وستتون دارم.

Contents

Abbreviations

AIBN	2,2'-Azobisisobutyronitrile
bpy	2,2'-bipyridine
br s	Broad singlet
CD	cyclodextrin
COD	1,5-cyclooctadiene
CV	Cyclic voltammetry
d	doublet
DCM	dichloromethane
DCC	N,N'-Dicyclohexylcarbodiimide
DMAP	4-Dimethylaminopyridine
DMF	N,N'-dimethylformamide
DMSO	dimethylsulfoxide
ECL	Electro-chemiluminescence
EDC	ethyl-(N',N'-dimethylamino)propylcarbodiimide hydrochloride
EtOH	ethanol
EtOAC	Ethyl acetate
Em	emission
Exc	excitation
FTIR	Fourier transform infrared spectroscopy
H_{Glu}	Glucose proton
HOBt	Hydroxybenzotriazole
HSQC	Heteronuclear Single Quantum Correlation
Hz	Hertz
ITO	Indium tin oxide
ISC	Intersystem crossing
J	coupling constant
K	Equilibrium constant
LC	Ligand-centred

m	multiplet
m/z	Mass to charge ratio
MALDI-TOF	Matrix Assisted Laser Desorption Ionisation Time Of Flight
MC	Metal-centred
Me	methyl
MeOH	methanol
NIR	Near infra-red
MLCT	Metal to ligand charge transfer
MS	Mass Spectrometry
NBS	N-bromo succinimide
N-Em	N-Ethylmaleimide
NMR	Nuclear Magnetic Resonance
NMP	N-Methyl-2-pyrrolidone
OMe	Methoxy
p.m.	permethylated
PENDANT	Polarisation ENhancement During Attached Nucleus Testing
Ph	phenyl
Phen	phenanthroline
PMT	Photomultiplier tube
ppm	parts per million
q	quartet
Rf	Retention Factor
s	singlet
SAM	Self-assembled monolayer
STM	Scanning tunnelling microscopy
t	triplet
THF	tetrahydrofuran
TLC	Thin Layer Chromatography
TMS	trimethylsilyl
tpy	2,2';6',2"-terpyridine
UV-vis	Ultra Violet-visible
XPS	X-ray photoelectron spectroscopy

δ	Chemical shift
ε	Extinction coefficient
φ	Quantum Yield
λ	Wavelength
ν	Frequency
τ	Lifetime
*	Solvent peak
↓	Radiative transition
⤋	Nonradiative transition

CHAPTER 1

Introduction

1.1. Photoactive supramolecular devices based on donor-acceptor metal complex systems

The need for smaller components for information processing and storage in electronic devices gave birth to the development of molecular scale devices. Such molecular devices can operate by converting an energetic input and using it for energy or charge propagation, or to create conformational changes that induce molecular motion, leading to an output from the device.[1] This energetic input can be chemical energy or light. The significance of light as a source of energy has been widely recognised and many systems have been developed. Mimicking this model has been the basis of the construction of photochemical molecular devices which absorb light and display energy or electron transfer between different components. Examples include the synthesis of artificial light harvesting arrays, switching units, sensors and photoactive molecular wires.[1-3]

To this end, molecular wire designs that are capable of transferring energy or electrons over long, space-controlled distances have been a major goal in the continuous quest for smaller subunits for electronic devices.

The design of a molecular wire involves three main components, two photoactive units that are connected by a spacer (Scheme 1.1). When the donor unit is excited, energy or electrons are passed to the acceptor unit. Furthermore, the nature of the spacer is very important as it plays two important roles in the molecular wire. Firstly, it dictates the geometry of the system and secondly, it controls the electronic interactions between the terminal units.[4]
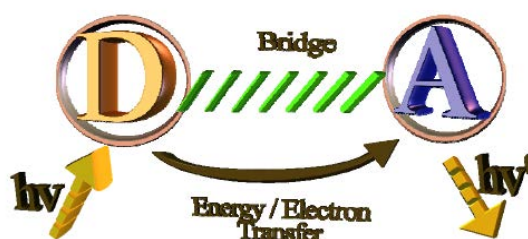
Scheme 1.1 Schematic representation of a photoactive molecular wire.

In an example by Balzani *et al.*[5] organic subunits are used to form molecular wire where an anthryl donor and a napthyl acceptor are linked by a phenylene bridge. Energy transfer has been observed between the two units and was mediated by the conjugated spacer (Scheme 1.2).
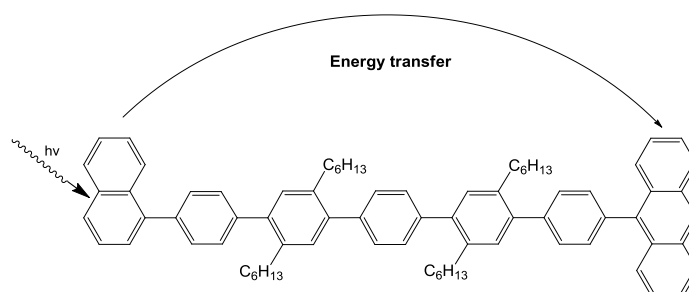
Scheme 1.2 Molecular wire containing photoactive organic subunits.[5]

Multi-electron metal centres, with appropriate redox and photochemical properties in a single supramolecular structure, provide a basis for the development of molecular energy conversion systems and wires.

Among the most popular metal centres for the construction of molecular wires are ruthenium and osmium polypyridyl complexes.[2] The MLCT excited state of osmium(II) complexes lies at a lower level than corresponding ruthenium complexes as they are easier to oxidise than ruthenium(II) complexes, making osmium(II) an ideal energy acceptor from ruthenium(II). Constable and coworkers[6] have investigated energy transfer between ruthenium and osmium terpyridine complexes containing thiophene spacers (Scheme 1.3). In order to lengthen the luminescence of the ruthenium complexes the terpyridine units are functionalised with methylsulfonyl substituents in the 4' position. The complexes with thiophene spacers show energy transfer assisted by the good conductive properties of the thiophenyl group. Energy transfer is estimated to occur over less than 30 ps leading to a rate constant of $\geq 3.3 \times 10^{-10}$ s^{-1}.

n = 0, 1, 2
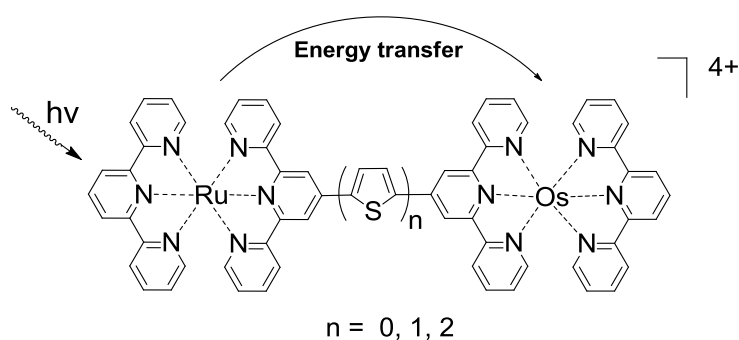
Scheme 1.3 Molecular wires based on ruthenium and osmium terpyridyl units and aromatic spacers.[6]

This thesis describes the synthesis and function of luminescent surface active metal complexes and their employment for the surface assemblies and energy transfer between metal centres through guest-host chemistry on surfaces.

1.2. Ruthenium and osmium polypyridyl complexes and their photophysical properties

Polypyridyl complexes of Group 8 transition metals have been extensively used as donor and acceptor components in molecular wire designs due to their photoactive units. Furthermore, their wide range of energetic and geometrical patterns makes them even more suitable as building blocks in such systems.

Ruthenium and osmium terpyridine and bipyridine complexes received much attention as their structure and energy potentials are well adapted for constructing electron or energy transfer devices. They show intense absorption in the visible region, are luminescent at room temperature, have excited state lifetimes in the range of nanoseconds, and the ability to undergo photo-induced electron and energy transfer processes.[7] Scheme 1.4 shows a representative energy level diagram for plausible light absorption and emission processes in group 8 complexes. Upon irradiation of the ^{1}MLCT energy state, fast intersystem crossing leads to the population of the lower lying ^{3}MLCT level, which can either return to the ground state by emission of light or, if a suitable energy acceptor is present, further transfer its energy to an inter- or intramolecular quencher.[8]
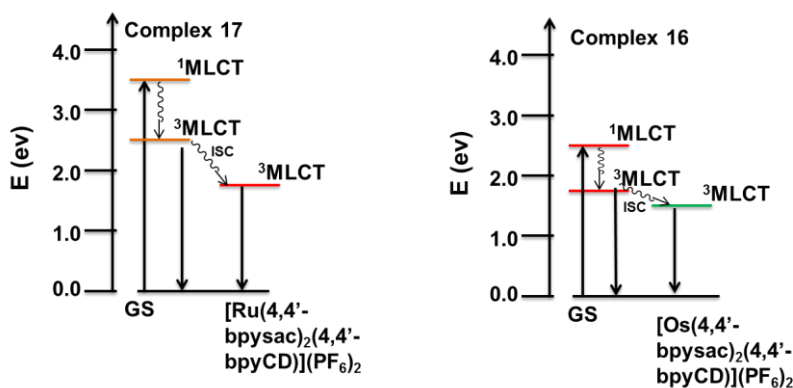
Scheme 1.4 Simplified energy level diagram which indicates plausible energy transfer processes between different metal complexes. Complexes 16 and 17 are introduced in chapter 4 and complexes [Ru(4,4'-bpysac)$_2$(4,4'-bpyCD)](PF$_6$)$_2$ and [Os(4,4'-bpysac)$_2$(4,4'-bpyCD)](PF$_6$)$_2$ are introduced in chapter 3.

A large number of bipyridine and terpyridine based complexes of ruthenium(II)[9-11] and osmium(II)[12-14] have been synthesised and investigated by spectroscopic and electrochemical techniques. One of the most famous examples of ruthenium polypyridine complexes is [Ru(bpy)$_3$]$^{2+}$,[15-19] which has a strong absorption (log ε= 4.16) at 450 nm assigned to the lowest ^{1}MLCT. Excitation to the ^{1}MLCT of [Ru(bpy)$_3$]$^{2+}$ leads to an emission at 600 nm with a quantum yield of 0.028 and a lifetime of 390 ns at room temperature.

Unlike [Ru(bpy)$_3$]$^{2+}$, [Ru(tpy)$_2$]$^{2+}$ does not exhibit luminescence at room temperature. This is surprising, since the absorption coefficient of the ^{1}MLCT band of [Ru(tpy)$_2$]$^{2+}$ is considerably higher than for [Ru(bpy)$_3$]$^{2+}$ based systems (Scheme 1.5). A crystal structure of [Ru(tpy)$_2$]$^{2+}$ shows that the bite angle N-Ru-N is 160°. It is a well-known deactivation effect in organic systems that a decrease in structural freedom cause more energy from the excited state to be given to vibrational and rotational energy and therefore, increases non-radiative deactivation processes.

By introducing electron-withdrawing substitutes at the 4'-position of terpyridine, the energy level of the ^{3}MLCT state can be moved away from the metal centred states and stabilised, allowing room temperature emission to be observed. Several derivatives of ruthenium terpyridine were found to be luminescent at room temperature. For example $[Ru(ttp)_2]^{2+}$ is reported to emit at 640 nm (ethanol, $\tau \sim 5$ ns).[7]
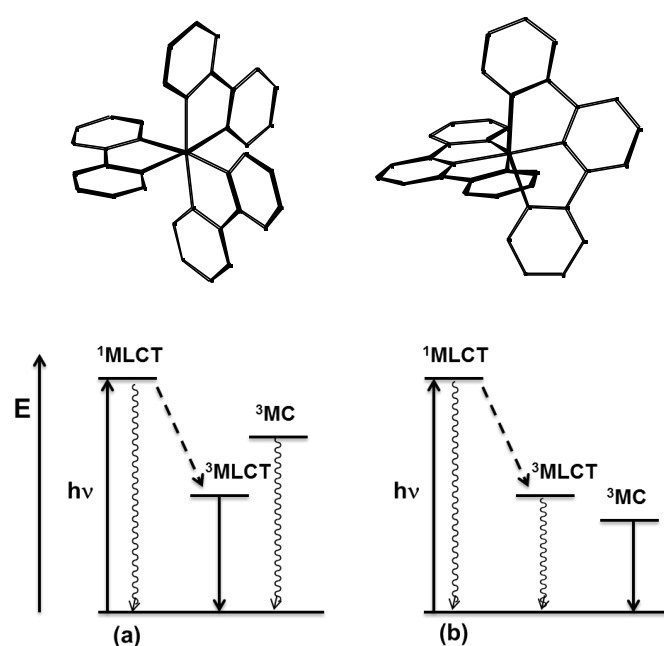
Scheme 1.5 Structure and relative energy levels of (a) $[Ru(bpy)_3]^{2+}$ and (b) $[Ru(tpy)_2]^{2+}$.

Energy can be passed to a suitable triplet acceptor whose triplet state lies lower than that of the ^{3}MLCT. Energy transfer can occur via two major mechanisms. For chromophores that are close in space and have a good orbital overlap the Dexter or exchange mechanism predominates. As its name suggests, this involves through-bond exchange of electrons into holes created on excitation. The alternative to this is the Förster mechanism, which relies on coulombic interactions from the electronic dipole transitions of donor and acceptor. This mechanism requires no overlap

between the two interacting units and operates through space. These two mechanisms can occur simultaneously in energy transfer, making it difficult to compute their relative overall contribution.[4]

1.3. Self-assembled monolayers (SAMs): versatile platforms for molecular devices

The concept of monolayers was presented in early 20th century. Spreading of amphiphiles on water resulted in formation of a film having the thickness of only one molecule[20]. Later, the monolayer structure was transferred from a water-air interface onto a solid substrate with multilayer composition.[21] After the spontaneous monolayer formation being described[22] in 1946, various adsorbate/substrate compositions have been found to form self-assembled monolayers (SAMs). For example, sulfur, alkyltrichlorosilane and fatty acid adsorbate groups have been reported on gold, glass and metal oxide surfaces, respectively (Scheme 1.6).[23,24]
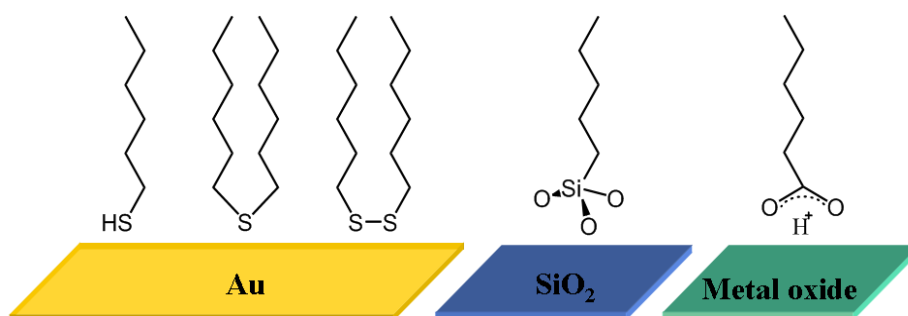
Scheme 1.6 Surface attachment anchors on gold, glass and metal oxides.

Thiol, R–SH, and disulfides, RS–SR, are common functional anchor groups for surfaces. Their popularity lies on the versatility and ease of attachment to the metal surfaces such as gold by simple formation of monolayer.

In addition, the functionalised surfaces are stable across a wide range of temperatures and potentials and when in contact with a wide range of solvents because of the high-bond strength, typically of the order of 100 kJmol^{-1}. Furthermore, formation of the thiol monolayer does not require anhydrous, anaerobic or vacuum conditions, which make it suitable for large scale industrial applications.

There are also other groups such as nitrogen, mainly based on pyridine or analogues that are mainly used for chemical functionalisation of substrates such as metals[47], non-metal oxide semiconductors such as TiO_2,[45] glass[38] and indium tin oxide[33].

Monolayers of thiol based compounds usually form within a few seconds of deposition in solutions containing millimolar concentrations of the thiol. The monolayers are initially highly defective but when left in contact with the deposition solution for longer periods, slowly give a low-defect density surface.[25]

Gold is historically the most studied metal and widely used substrate to form monolayers. Gold surfaces are easy to prepare (physical vapour deposition, sputtering or electro-deposition) and may be obtained as thin films or colloids. Most importantly, gold is a rather inert metal; it does not oxidise below its melting point nor react with atmospheric O_2 or most chemicals. It is also a common substrate in many spectroscopic methods and analytical techniques. Gold has a very high affinity for thiols[26] and deposition is known to displace some other materials from the surface. The gold surface is also known to be stable in a liquid environment for long periods of time, with no proof of toxicity and is therefore suitable for cell studies.

1.4. Surface active transition metal complexes

Over the last decade, scientific interest in the surface adsorption of chemical systems has been growing. Diverse types of systems have been investigated by the scientific community, from simple organic molecules to biological systems, metal complexes and supramolecular systems. Among all examples, coordination compounds draw more attention due to their multiple functions, such as surface immobilisation, light emission and electron transfer with relative synthetic ease. There are two key fields to study monolayers of coordination compounds, these being electrochemical and photochemical properties. Although the behaviour of surface immobilised electrochemically active species is well studied, the behaviour of photoactive species has received considerably less attention. The photophysical properties of a molecule, such as the emission lifetime may change and be monitored upon attachment to a surface. This depends on the properties of the molecule and the film produced, the rigidity of the film, its oxygen sensitivity, and the presence of a surface plasmon.[27]

The photophysical properties of a luminescent compound attached to a metal surface can be complex because of a various possible routes of luminescence quenching or luminescence enhancement arising from the compound itself and properties of the metal substrate.[28] The excited-state quenching is expected for the monolayers on smooth metal surfaces when there is a sufficiently small (<100 Å) [29] distance between the excited state and the surface. In contrast, roughening of the metal surface on the nano-meter length scale can enhance the luminescence intensity due to the excitation and/or emitting electromagnetic fields by the surface

plasmon of the substrate.[29,30] The length and structure of the bridging ligand, the electrode potential and the redox potentials of the electronically excited state, the extent of electronic coupling between luminophore and substrate and the luminescence quantum can also affect the properties of the film.

Amongst transition metal complexes, osmium, ruthenium and iridium polypyridyl complexes became more attractive due to their well-defined optical transitions and their strongly allowed charge transfer bands in the visible region. They can be used for creating light within a film due to their luminescence properties, and their reversible electrochemical properties across different oxidation states.[25] Some of the more recent studies of surface active transition metal complexes have been reviewed in this chapter.

1.4.1. Bipyridine and phenanthroline ruthenium and osmium complexes on surfaces

Some of the examples of monolayers on surfaces based on polypyridyl transition metal complexes were based on Ru(II)/Os(II) tris-bpy and Ru(II)/Os(II) tris-phen cores, where bpy is 2,2'-bipyridine and phen is 1,10-phenanthroline.

Takido *et al.*[31] reported ruthenium complexes based on bipyridine ligands, containing fully conjugated ligands terminated with thiol groups (Scheme 1.7). These surface active complexes were immobilised on gold surfaces and studied by STM. The bipyridine ligands in this case were substituted in the 4,4'-positions, bearing an acetylide linkage between the pyridine ring and the aromatic thiol. The STM studies presented images of single molecules immobilised on Au surfaces.
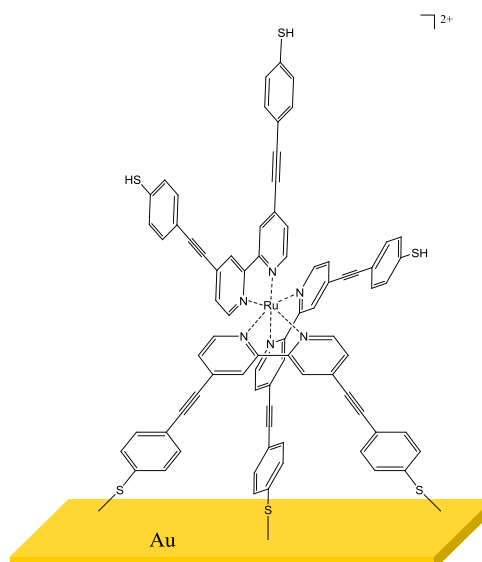
Scheme 1.7 Modified tris-bipyridine Ru(II) complex immobilised on Au surfaces.[31]

Ma, Wang and co-workers[32] have fabricated the thin films containing $Ru(phen)_3Cl_2$ and 12-molybdophosphoric acid $[PMo_{12}O_{40}]^{3-}$ on quartz, silicon and ITO substrates by a layer-by-layer (LBL) method. The LBL films were characterised by X-ray photoelectron spectroscopy, UV-Vis spectroscopy, cyclic voltammetry and atomic force microscopy. The films exhibit bifunctional electrocatalytic activity, which allows the system to be used as an electrocatalyst for both the reduction of IO_3^-, BrO_3^-, ClO_3^- and the oxidation of $C_2O_4^{2-}$.

Forster and co-workers[33] reported formation of a monolayer of $[Ru(dpp)_2Qbpy]^{2+}$ (Scheme 1.8), by adsorption onto clean platinum microelectrodes. The monolayer was studied by cyclic voltammetry, and it was found that three distinct oxidation states, over the potential range of ±1.3 V, were electrochemically accessible. The emission of the metal complex was observed at 600 nm in fluid, solid solution and when it is bound to a platinum electrode surface. In the case of the monolayer, it

appears that radiationless energy transfer to the metal is not deactivating the excited states completely.
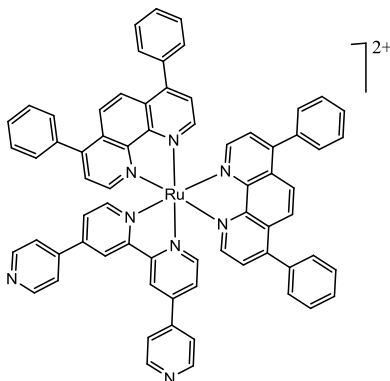
Scheme 1.8 Structure of [Ru(dpp)$_2$Qbpy]$^{2+}$ complex.[33]

Forster and co-workers[34] monitored the time evolution of the surface coverage using in-situ voltammetry in order to study the formation mechanism of monolayers of [Ru(bpy)$_2$Qbpy]$^{2+}$ (Scheme 1.9) on platinum microelectrodes. They have reported that the behaviour of surfactants at the solid/solution interface depends on both the deposition time and bulk concentration of [Ru(bpy)$_2$Qbpy]$^{2+}$. Even at low concentrations of the surface active molecule, formation of the monolayer was limited by the kinetics of surface binding and not by mass transport. To reach the equilibrium surface coverage in micromolar concentrations, time scales of 10-20 hours were needed.
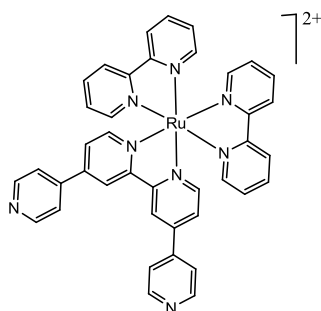
Scheme 1.9 Structure of the [Ru(bpy)$_2$Qbpy]$^{2+}$ complex.[34]

Williams, Unwin, De Cola and co-workers[35], have synthesised luminescent ruthenium trisbipyridine complexes containing one or two thioacetate-alkyl chains on one of the bipyridyl units (Scheme 1.10). The electrochemical and photophysical properties of these complexes, determined in solution and in the solid state, were compared. Deposition on electrode surfaces (gold, platinum and indium tin oxide) was realised by self-assembly and the resulting adsorbed layers were characterised by electrochemistry and fluorescence confocal microscopy. The effect of the number of chains and the chain length in the complexes is highlighted. Emission of the adsorbed complexes was reported to be strongly quenched by the metallic surfaces, while confocal microscopy images showed aggregate formation on nm length scale.
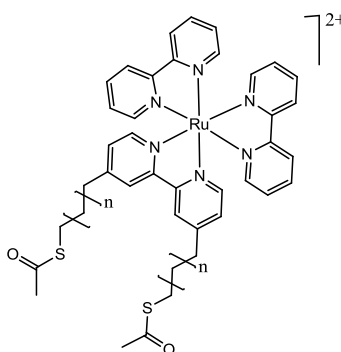
Scheme 1.10 Structure of the ruthenium tri-bipyridine derivative complex, n = 2 and 5.[35]

In other work by Thomas and co-workers[36], a thiol functionalised derivative of ruthenium(II) trisbipyridyl complex [(Ru(bpy)$_3^{2+}$-C$_5$-SH] was attached to gold nanorods (Scheme 1.11) in dodecanethiol using a place-exchange reaction. In this study, both emission quenching and transient absorption studies confirmed the ability of gold nanorods to deactivate excited Ru(bpy)$_3^{2+}$ via an energy transfer pathway. The energy transfer is completed within the laser pulse duration of 100 ps.

Both the size and shape of the gold nanorods influence the quenching of the excited state to proceed via an energy transfer mechanism.
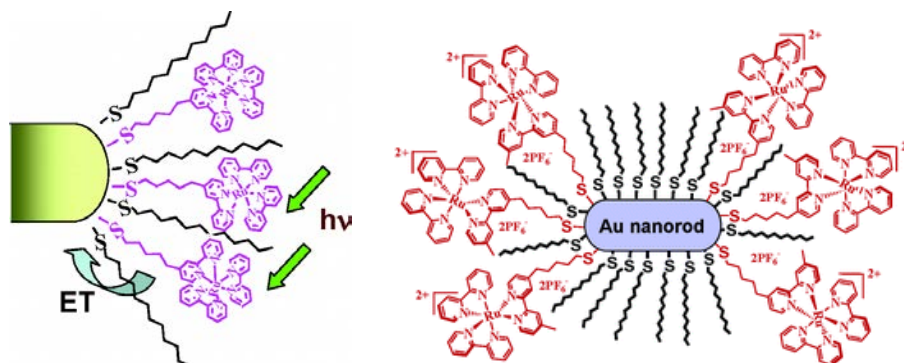
Scheme 1.11 Excited-state interactions between thiol derivative ruthenium(II) trisbipyridine and gold nanorods.[36]

In another report of osmium complexes on surfaces[37], gold surfaces were modified with Os(bpy)$_2$(py)Cl (Scheme 1.12) The modified gold surfaces were characterised by resonance Raman spectroscopy and infrared reflection absorption spectroscopy. Cyclic voltammetry was employed to study the electrochemical properties of the covalently attached osmium complexes to the surface. Very fast electron transfer rates were observed for the Os^{III}/Os^{II} surface redox couple.
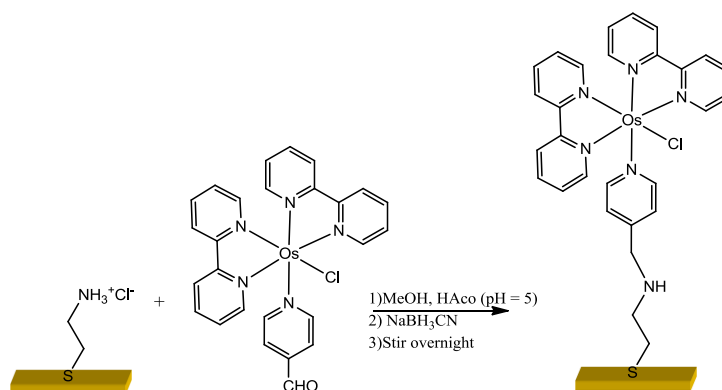
Scheme 1.12 Formation of the monolayer of Os(bpy)$_2$(py)Cl complex on gold surface.[37]

In a study by Van der Boom and co-workers[38], optical detection of NO_2 (1–10 ppm) and NO_x (800–2550 ppm) was demonstrated by a structurally well-defined monolayer of osmium polypyridyl complexes (Scheme 1.13) on glass substrates, of which it is believed is a selective, stable and reversible device. The UV-Vis spectroscopy of the modified substrates was used to detect the NO_2 and NO_x absorption by following the intensity of MLCT bands of the osmium complex.
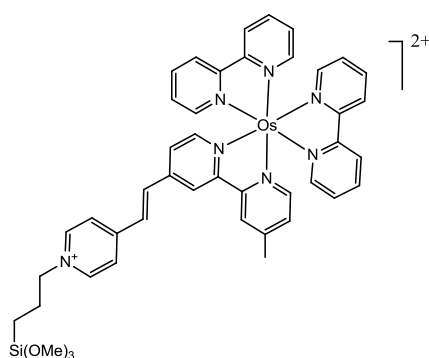
Scheme 1.13 Structure of the osmium tris-bipyridine derivative complex used to attack on glass substrates.[38]

The chemical conditions such as pH may also modulate the electron-transfer rate across luminescent monolayers. Forster[39] reported that the imidazole moiety can be protonated or deprotonated in the $[Ru(bpy)_2PIC](PF_6)_2$ monolayers where PIC is 2-(4-carboxyphenyl)imidazo[4,5-f][1,10]phenanthroline (Scheme 1.14).

Through the carboxy terminus, these materials form luminescent monolayers on fluorine doped tin oxide. The luminescence intensity and the interfacial heterogeneous electron-transfer rate were modified by Ionisation of the imidazo-bridge. As the pH of the supporting electrolyte was increased from 1.7 to 9.3, the heterogeneous electron-transfer rate constant measured to be over potential of +50 mV, decreased from $7.0 \pm 1.1 \times 10^5$ to $0.7 \pm 0.1 \times 10^5$ s^{-1}. A super exchange electron-

transfer process was concluded trough these observations where the (carboxyphenyl)imidazo bridge plays an important mediating role in the redox switching process.
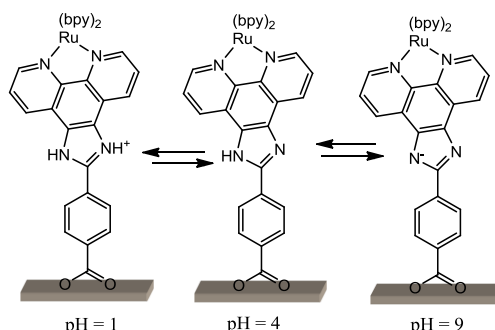
Scheme 1.14 The [Ru(bpy)$_2$PIC](PF$_6$)$_2$ monolayers on fluorine doped tin oxide surfaces in different pH.[39]

In a study by Vanzetti *et al.*[40] a series of silicon chips containing sputtered gold electrodes were first coated with a self-assembled monolyayer of lipoic acid and then were functionalised by using a Ru(bpy)$_3$$^{2+}$ amine derivative (Scheme 1.15). It was believed that the two-step preparation of the emitting layer increased both the compactness of the SAM and the density of ruthenium emitting sites, as evidenced by electrochemiluminescence (ECL) and X-ray photoelectron spectroscopy (XPS) investigations.
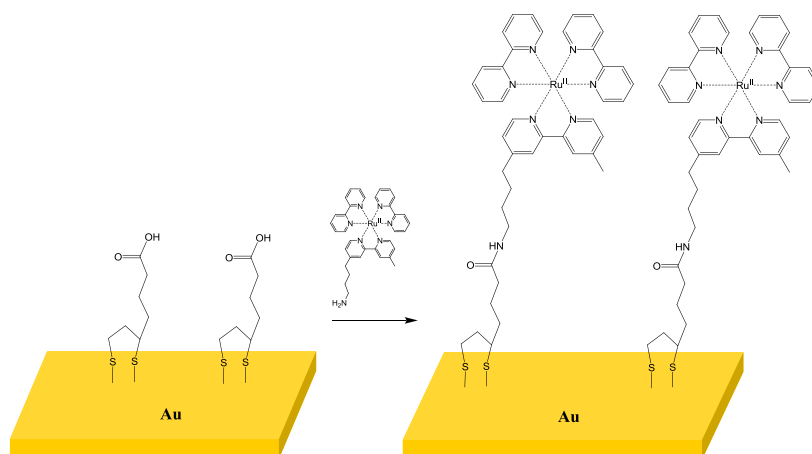
Scheme 1.15 Coupling of a tris-bipyridine ruthenium (II) derivative on a gold surface.[40]

Van der Boom and co-workers[41] demonstrated long-range electron transfer process between two redox-active monolayer-based systems using a metal ion as an optical readout and an electron carrier to determine the active surface area and oxidation state of the system (Scheme 1.16). More specifically, the system is consisted of two glass substrates covalently coated by analogous osmium (1, 2) and ruthenium (3, 4) polypyridyl complexes. The authors showed that the osmium centres of monolayer 1 could be oxidised within minutes from Os^{2+} to Os^{3+} by trace amounts of $FeCl_3$ in acetonitrile to generate monolayer 2 and Fe^{2+}. System 2 showed simultaneous bleaching of the MLCT bands. Washing with water for less than one minute can reset (2→1) the highly robust monolayer. Similarly, the ruthenium-based monolayers (3) could be easily reduced from Ru^{3+} to Ru^{2+} (3→4) by parts per million (ppm) levels of Fe^{2+} in organic solvents. It was concluded that their redox-active monolayer setup successfully demonstrated information transfer by metal ions as electron carriers coupled with optical readout between two interfaces. Through this process one system was able to detect the chemical oxidation state and also dimensions of other indirectly connected interfaces which were placed in the same chemical

environment. Importantly, three metals of the same group have been used as a reporter system, information carrier and signal generator.
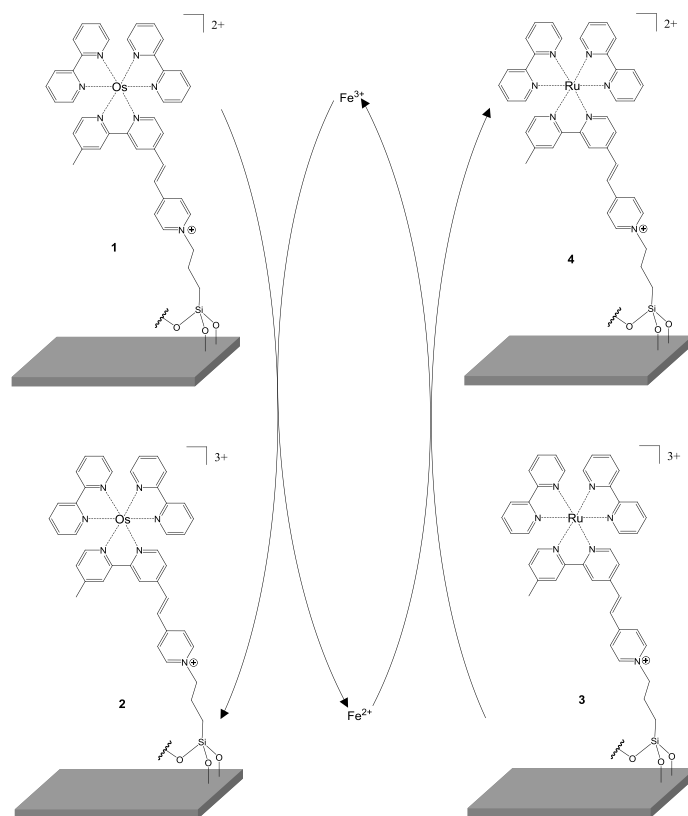
Scheme 1.16 Chemical communication between metal complex (ruthenium and osmium tris-bipyridine derivatives) monolayers on glass substrates.[41]

The co-adsorption of three thiol compounds on gold was studied by Coudret and co-workers[42], yielding a self-assembled monolayer (SAM), the behavior of which was studied by impedance spectroscopy (Scheme 1.17). Two redox active thiols with a good miscibility in a supporting inert component, distinct heterogeneous electron transfer rate constant and non-degenerate first-oxidation redox couples were

chosen. However, in the ternary monolayer, it was found that the slowest process depends on concentration of the other redox site.
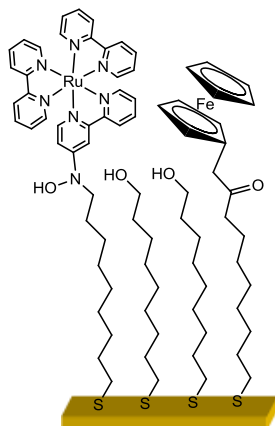
Scheme 1.17 Pictorial representation of a self-assembled monolayer containing ferrocene and ruthenium thiol derivatives on gold surface.[42]

In another study from Van der Boom and co-workers,[43] a hybrid structure consisting of a robust and structurally well-defined polypyridyl osmium complex and a commercially available palladium precursor was constructed, using an iterative two step assembly method (Scheme 1.18). UV-Vis measurements in the transmission mode of the glass bound assemblies showed the characteristic singlet and triplet metal to ligand charge transfer (MLCT) bands of the Os(II) complex. The thickness of the film was also measured by XRR (X-ray-reflectometry) and ellipsometry methods, which showed an exponential increase with the number of deposition cycles, which is in agreement with the optical data.
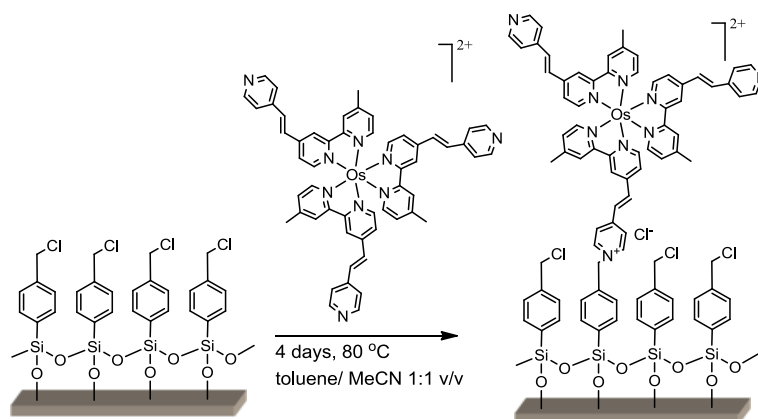
Scheme 1.18 Formation of the osmium tris-bipyridine derivative complex on glass and silica surfaces.[43]

Chemical coupling of the redox-active complex [Os(bpy)$_2$(4-aminomethylpyridine)Cl](PF$_6$) (Scheme 1.19) to gold and carbon-based surfaces was undertaken by the group of Leech.[44] This redox-active complex attached on carbon-based electrodes showed increase in stability and surface coverage compared to gold surfaces, providing a basis for preparation of highly stable redox-active layers on such surfaces.
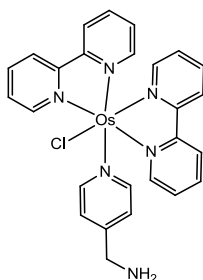
Scheme 1.19 Structure of [Os(bpy)$_2$(4-aminomethylpyridine)Cl](PF$_6$) complex.[44]

Meyer *et al.*[45] demonstrated electrocatalytic water oxidation by [Ru(tpy)(bpz)(OH$_2$)]$^{2+}$ surface-bound complex that functions on conducting as well as semiconducting oxide surfaces (Scheme 1.20). The complex retains the solution properties on the

surface, and provides a basis for sustained, electrocatalytic water oxidation over a wide range of pH values. Their observations reveal that the surface-bound complex retains its chemical properties ($E_{1/2}$ values, pH dependence) and physical properties (UV-Vis spectra), including its ability to catalyze water oxidation. Electrocatalysis also occurs on TiO_2 surfaces, which is extensively used in dye-sensitised solar cells.
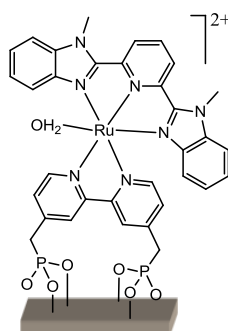
Scheme 1.20 Structure of [Ru(tpy)(bpz)(OH$_2$)]$^{2+}$ complex attached to the semiconducting oxide electrode.[45]

In a more recent study by Gulino and co-workers[46], a [Ru(bpy)$_2$L](PF$_6$)$_2$ (L is 4-p-hydroxyphenyl-6-bromo-2-(2′-pyridyl)quinolone) (Scheme 1.21) molecular monolayer was covalently assembled on engineered silica and Si(100) substrates, with its luminescent behavior exploited. It has been claimed that transferring the photoluminescence molecular property to the solid state, suited for CO optical recognition in air, is yields emission in the visible range. It was also indicated that the Ru-SAM is a solid chromophore which can also be useful for chemical sensors.
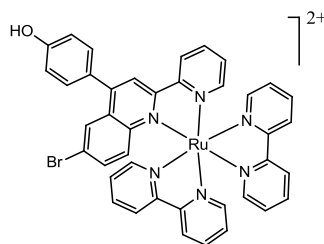
Scheme 1.21 Structure of [Ru(bpy)₂L](PF₆)₂ complex, L is 4-p-hydroxyphenyl-6-bromo-2-(2′-pyridyl)quinolone.[46]

In a recent study by Jonsson's group[47], Os$^{II/III}$ and Co$^{II/III}$ polypyridine complexes adsorbed on Au(111) and Pt(111)-electrode surfaces have been prepared (Scheme 1.22) and characterised by electrochemical scanning tunnelling microscopy (in situ STM). The oxidation states of the complexes were controlled, first by introducing chloride counter atoms and followed by spontaneous attraction of electrons from the complexes. The solvent is found to provide strong dielectric screening of this charge transfer process and thus crucial for achieving the full chemically meaningful charge separated ionic oxidation states.
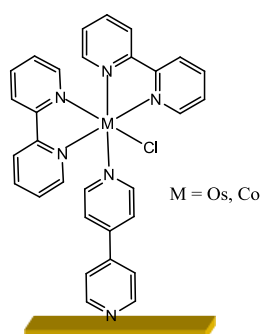
Scheme 1.22 Structure of [M(bpy)₂(4,4'-bipyridine)Cl] (M = Os, Co) complexes attached to Au and Pt surfaces.[47]

In a recent study by Lee and co-workers[48], a new electro-generated chemiluminescence (ECL) sensor based on a self-assembled monolayer of [Ru(bpy)$_2$(aminopropyl imidazole)Cl]$^+$ on a gold-deposited screen printed electrode (SPE) was developed (Scheme 1.23). The amine group of the initial ruthenium complex was coupled to the propionic acid self-assembly monolayer, pre-formed on gold deposited SPE surfaces. The ECL emission of the ruthenium complex occurred at an applied potential of less than +0.7 V, which reduced the oxidation stripping of the ruthenium complex. These modifications meant that the stability of the resulting ruthenium complex SAM-based ECL sensor was greatly enhanced compared to those previously reported.
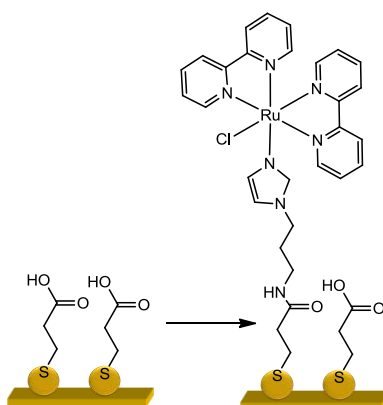
Scheme 1.23 The sensor based on a self-assembled monolayer of [Ru(bpy)$_2$(aminopropyl imidazole)Cl]$^+$ complex on gold deposited SPE surfaces.[48]

Modification of gold electrodes with [Os(2,2-bpy)$_2$PyCH$_2$NHCOPhX] complex, where X = C, S tethered to the surface by two alternative bonds: Au–C and by Au–S (Scheme 1.24), have been reported recently by Calvo *et al.*[49] The amide coupling of the osmium complex and the benzoic acid tethered to the surface was confirmed by various types of vibrational and electron spectroscopy. The resulting modified Au surfaces were characterised by polarisation modulated infrared reflection absorption

spectroscopy (PM-IRRAS), STM, XPS, resonance raman spectroscopy and cyclic voltammetry.
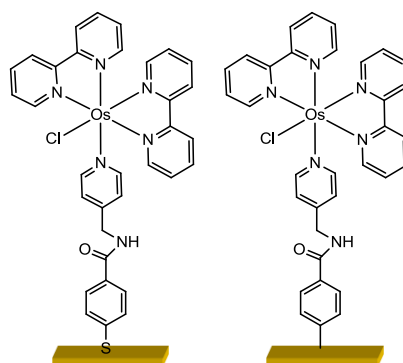
Scheme 1.24 Schematic structure of [Os(2,2-bpy)$_2$PyCH$_2$NHCOPhX] (x = C, S) complex tethered to a gold surface by (a) a S–Au bond and (b) a C–Au bond.[49]

The group of De Cola[50] recently presented luminescent ruthenium complexes containing tripod-type end groups linked to a phenanthroline derivative (Scheme 1.25). One of the compounds was functionalised with thioacetate groups in order to link the metal complex to metallic surfaces. The photophysical and electrochemical behaviour of the complexes were studied in solution and on conductive substrates and, furthermore, self-assembled monolayers were investigated in tunnel junction system using gold or an indium gallium eutectic alloy electrodes, by time-resolved confocal microscopy. The results showed that the complexes formed very stable and well-ordered monolayers because of the tripod system, which can anchor the complex almost perpendicular to the surfaces.
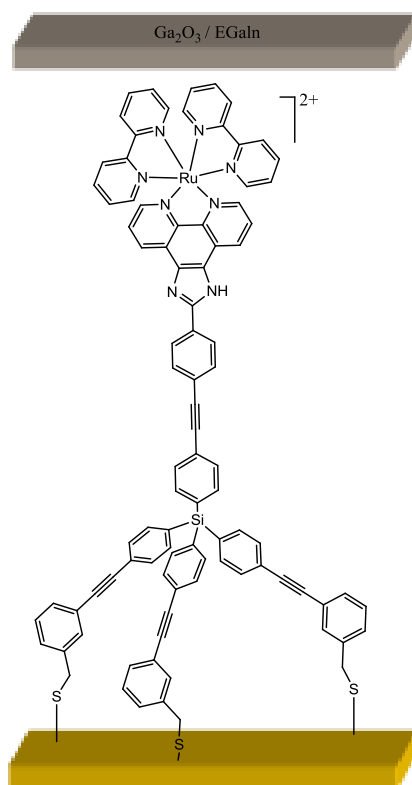
Scheme 1.25 Schematic of the Au–Ru–tripod / Ga$_2$O$_3$ / EGaln tunnel junction.[50]

The group of Ekinci[51] demonstrated functionalised electrodes with nitrogen-containing ligands such as quinolone, pyridine and especially phenanthroline which were used as templates due to their well-known complexation ability. These electrodes were used for the formation of ruthenium-functionalised surfaces (Scheme 1.26). The attachment and the surface concentration of heteroaromatic molecules to glassy carbon (GC) surfaces were confirmed by X-ray photoelectron spectroscopy (XPS). Additionally, XPS verified the chemical transformation of the characterised ligand films to the ruthenium complex films on the surfaces. Voltammetric methods were applied to investigate the electrochemical behavior of these films in acetonitrile solution and to determine the surface coverage of the organometallic films by reversible metal-based Ru^{II}/Ru^{III} oxidation waves.
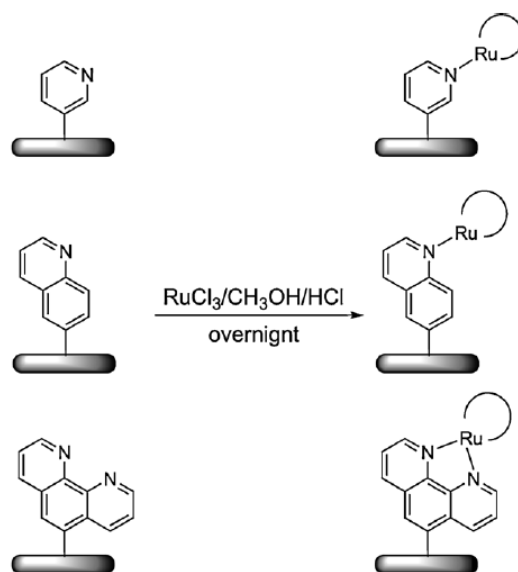
Scheme 1.26 Schematic view of ruthenium monolayers formation on glassy carbon surfaces.[51]

The group of Pikramenou[52] reported a new complex, RuBpySH, bearing two thiol-based anchoring groups for surface attachment (Scheme 1.27). Monolayers of RuBpySH were formed on micro and macro platinum electrodes by spontaneous adsorption from micromolar solutions of the complex in 1:1 v/v water/acetone. These monolayers were able to reversibly switch between the Ru^{II} and the Ru^{III} forms. It was reported that the adsorption of the complex was irreversible in this system, with saturation coverage of $8.1 \pm 0.4 \times 10^{-11}$ mol.cm^{-2}, when the concentration of the complex in the deposition solution was between 0.01- 1.0 mM. Dry monolayers displayed luminescence properties similar to those of powder samples of the complex, indicating that the monolayer of the complex displays more properties of the solid state than solution. Significantly, efficient ECL is generated using tripropylamine as the co-reactant.
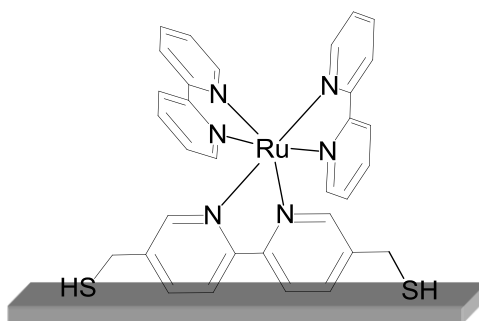
Scheme 1.27 Schematic representation of the RuBpySH monolayer on platinum surface.[52]

1.4.2. Terpyridine ruthenium and osmium complexes on surfaces

Terpyridine monolayers are attractive materials for supramolecular devices due to their ability to bind metals either in a reversible or non-reversible manner[53] producing redox-active complexes.[2,54]

In a study by Constable and co-workers[55], [Ru(tpy)(pytpy)]$^{2+}$ and [Os(tpy)(pytpy)]$^{2+}$ complexes were synthesised, where pytpy is 4'-(4''-pyridyl)-2,2':6',2''-terpyridine, and these were used to prepare monolayers on Pt surfaces (Scheme 1.28). These monolayers were studied by STM experiments and the results revealed that the molecules are ordered in hexagonal arrays. The surface coverage was reported to be Γ = 2.5 x 10^{-11} and 3.3 x 10^{-11} mol·cm^{-2} for the Ru^{II} and Os^{II} complexes respectively. The above mentioned work was later expanded to dinuclear complexes involving both bipyridine and terpyridine moieties.

$M^{II} = Ru(II), Os(II)$

Ru(II) ⇆ Ru(III) + e⁻
Os(II) ⇆ Os(III) + e⁻

Pt
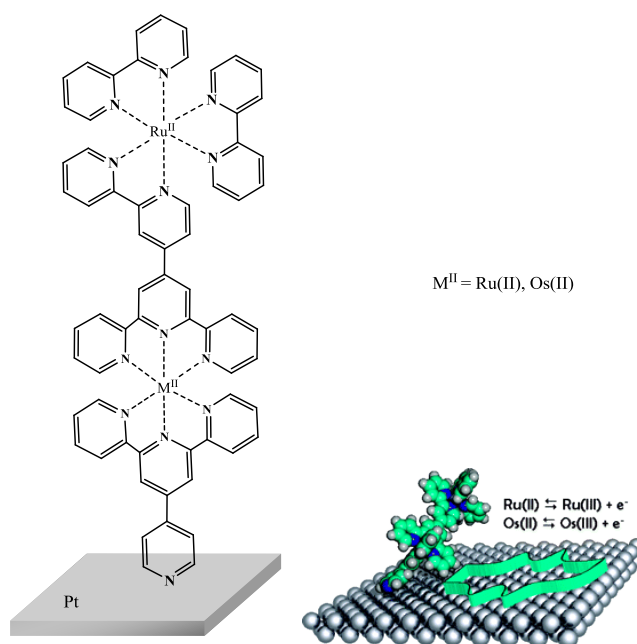
Scheme 1.28 Schematic structure of the dinuclear ruthenium and osmium bis-terpyridine complexes on Pt surface.[55]

Nishihara and co-workers[56] presented a heterometallic molecular wire on a gold surface bearing Co and Ru bis-terpyridine metallocentres (Scheme 1.29). The molecular wire was constructed in a step-wise manner by first inserting a terpyridine bearing a surface active anchor onto a gold surface followed by a coordination step involving CoCl₂. A ruthenium bisterpyridine complex bearing an uncomplexed terpyridine moiety was then introduced to the monolayer. Results from cyclic voltammetry indicated reversible redox reactions of both metallo centres on the gold electrode.
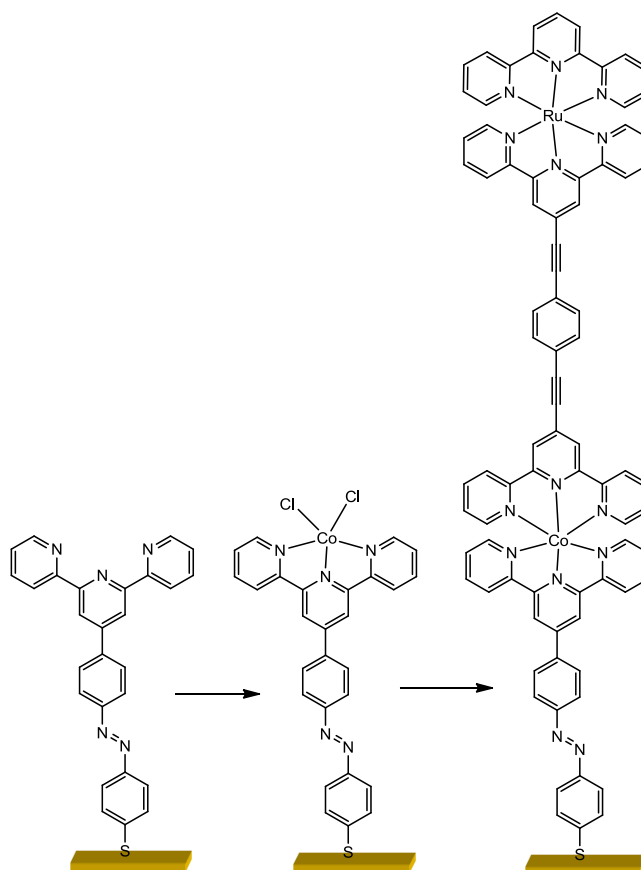
Scheme 1.29 A heterometallic molecular wire of bis-terpyridine osmium (II) and cobalt (III) on a gold electrode.[56]

In a similar approach, Ulstrup *et al.*[57] reported the application of an ionic liquid, 1-butyl-3-methylimidazoliumhexafluorophosphate (BMI), as an electrochemical gate medium for tunnelling spectroscopy at the single-molecule scale. The authors used the Os(II)/Os(III) redox transition of a heteroleptic redox-active Os bisterpyridine complex (OsSac) to achieve tunneling current modulation at room temperature. One terpyridine ligand was functionalised with a 6-acetylthiohexyloxy linker to achieve efficient binding to Au electrode surfaces (Scheme 1.30). The surface redox potential of OsSac was determined by monolayer cyclic voltammetry, and found to be E^0_{surf} =

+0.68 V *vs* saturated calomel electrode (SCE) in good agreement with solution redox potentials of closely related osmium complexes.
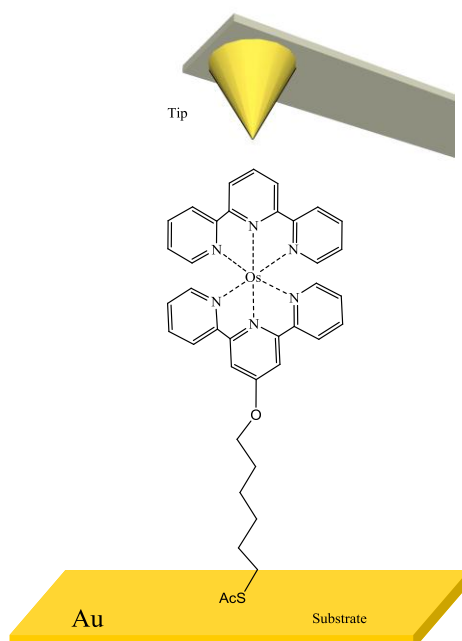
Scheme 1.30 Scanning tunneling microscopy for a surface active Os(II)-terpyridine complex in an ionic liquid.[57]

In a biological approach, Haga *et al.*[58] synthesised a rod-shaped ruthenium complex bearing naphthalene-1,4:5,8-bis(dicarboximide) (ndi) as a DNA intercalating group and an alkylphosphonate moiety as an anchoring group (Scheme 1.31). It was observed that both the π–π* (ndi) transition at 364 and 385 nm and metal-to-ligand charge transfer (MLCT) bands at 491 nm were shifted to longer wavelengths and their intensity was decreased upon addition of calf thymus DNA to aqueous solution of the ruthenium complex suggesting that the Ru(II) complex was intercalated into the double-stranded DNA base pairs. Later, a Ru(II) complex immobilised on a mica surface was prepared, with a DNA intercalator used to captivate a double-stranded DNA in a point-to-point manner on a mica surface.

The combination of the ability of the complex to participate in DNA intercalation and electron transfer by an immobilised rod-shaped Ru(II) complex makes this study a very strong case for the material use of DNA as a wire or scaffold towards molecular electronics or for applications in DNA sensing.
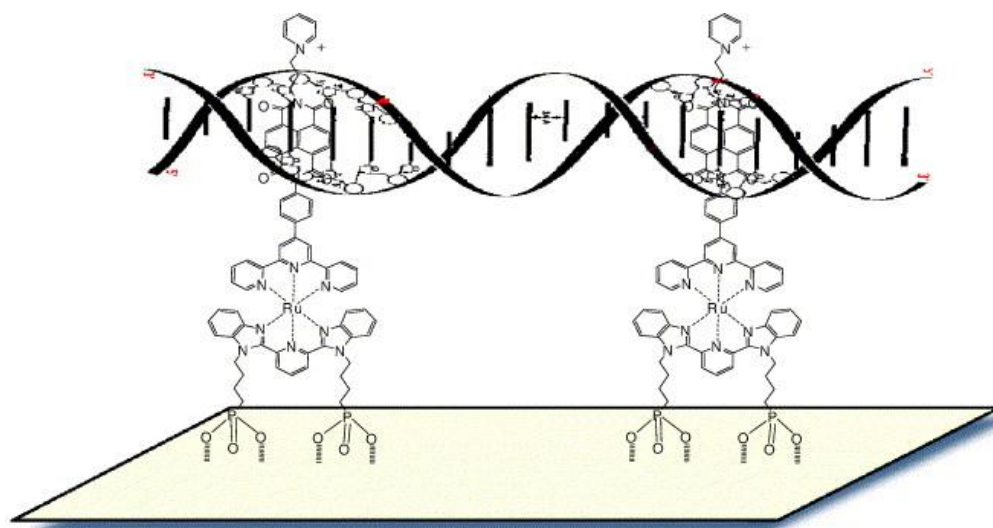
Scheme 1.31 Scheme of DNA captivation by immobilised ruthenium bis-terpyridine derivative complex.[58]

Licciardello and co-workers[59] have reported the stepwise synthesis of polypyridine–ruthenium complexes (Scheme 1.32) by direct coordination reaction at the surface, following the formation of the monolayer by X-ray photoelectron spectroscopy (XPS) and time-of-flight secondary ion mass spectrometry (ToF-SIMS).

Since the synthesis of heteroleptic Ru^{II} terpyridine-type complexes requires relatively severe conditions and the monolayer is unstable under refluxing conditions, it was necessary to perform the reaction in milder conditions, at room temperature during 8 weeks of treatment. The stepwise formation of the monolayer was compared with analogous monolayers prepared via surface anchoring of the pre-synthesised

ruthenium complex. Both methods yielded layers with very similar characterisations, however the direct coordination of Ru(II) terpyridine-functionalised on the surface was found to be more efficient.
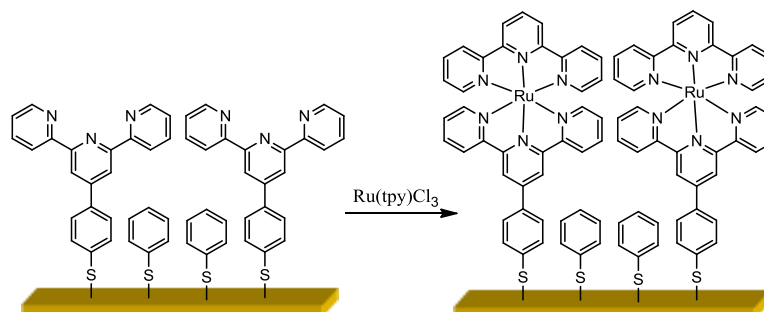
Scheme 1.32 Thiol-terpyridine/thiophenol SAM and step wise formation of ruthenium bis-terpyridine complex on gold surface.[59]

In a study by Dong and co-workers,[60] the formation of a stable monolayer of dithiol-bifunctionalised Ru^{II}-terpyridine onto a gold electrode (Scheme 1.33) was described. Electrochemical techniques were used to study the coverage-dependent behaviour onto gold electrode. The surface charge coverage, stability, and electron transfer kinetics of the monolayer were determined by cyclic voltammetry which suggested the formation of saturated and overlapped edge-on orientation monolayer.
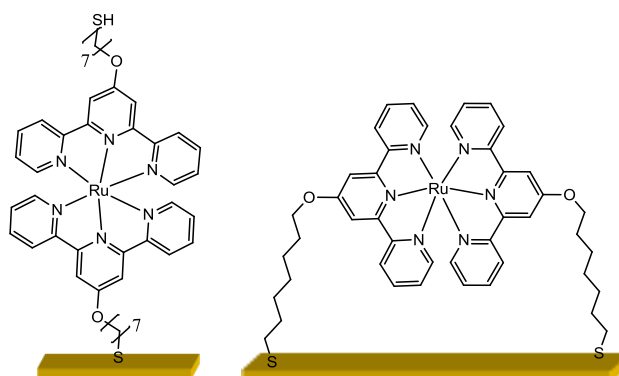
Scheme 1.33 Ru^{II}-terpyridine monolayer onto a gold electrode.[60]

Lee and co-workers[61] recently synthesised a voltage-driven molecular switch based on a thiol-tethered Ru^{II} terpyridine complex (Scheme 1.34). Scanning tunnelling microscopy (STM) was employed to reveal well-defined single Ru^{II} complexes isolated in the highly ordered dielectric monolayer. When a negative sample-bias was applied, the threshold voltage to the high conductance state in the molecular junctions of the Ru^{II} complex was consistent with the electronic energy gap between the Fermi level of the gold substrate and the lowest ligand-centred redox state of the metal complex molecule. As an active redox centre leading to conductance switching in the molecule it was hypothesised that the lowest ligand-centred redox state of Ru^{II} complex trapped an electron injected from the gold substrate. The authors concluded that their single-molecule switch-on mechanism in the solid state could provide guidance in designing complexes that would improve the charge-trapping efficiency of the ligands with different metal substrates.
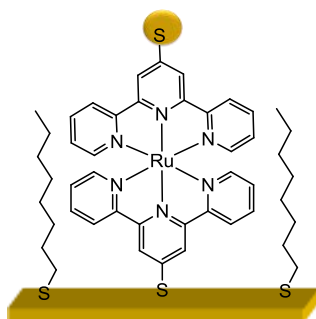
Scheme 1.34 A voltage-driven molecular switch based on thiol-tethered Ru^{II} terpyridine on gold surface.[61]

In a study by Haga *et al.*[62] new tri-nuclear Ru(II) complexes bearing both 1,3,5-tris(2,2':6',2''-terpyridyl)benzene and bis(benzimidazol-2-yl)pyridine with six phosphonate anchors were synthesised and immobilised on an ITO electrode (Scheme 1.35), with the claimed canopied structures proved by AFM measurements.

The immobilised Ru(II) trinuclear complex revealed a one-step three-electron oxidation process for the $Ru^{II/III}$ couple at around +0.9 V *vs.* Ag/AgCl, indicating that the Ru–Ru interaction was small. For the Ru(II) immobilised ITO surface, the electron transfer blocking and the electron mediation of $[Fe(CN)_6]^{4-}$ oxidation through the $Ru^{III} \leftrightarrow Ru^{II}$ catalytic cycle are strongly dependent on the alkyl chain length. The spectro-electrochemistry of the Ru(II) tri-nuclear complex monolayer on the ITO electrode showed a stable electrochromic response under the potential pulse. The present 'canopied' Ru(II) tri-nuclear complexes hold a small cavity that encapsulates tetrathiafulvalene molecules, which were proved by cyclic voltammetry.
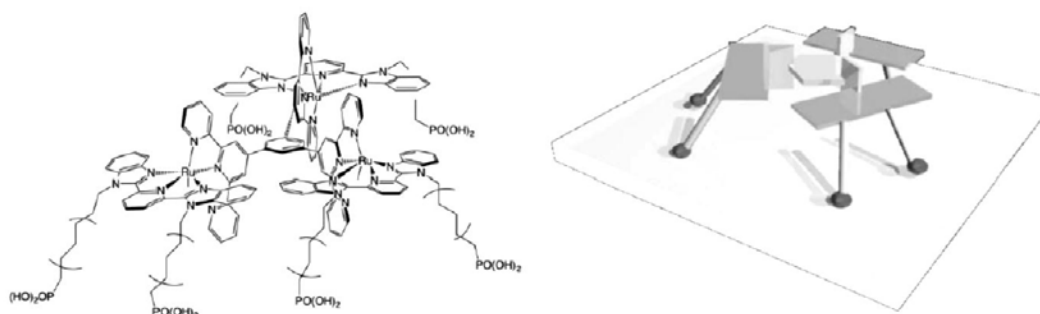
Scheme 1.35 Structure of a ruthenium trinuclear complex and its simplified image for a canopied structure on an ITO electrode.[62]

Ishida and co-workers[63] examined the formation of self-assembled monolayers and multilayers of a redox-active Ru(II) complex (Scheme 1.36) on SiO_2 surfaces by ellipsometry, time of flight secondary mass-ion spectroscopy (TOF-SIMS) and X-ray photoelectron spectroscopy (XPS). In this report, it was claimed that introduction of a Zr adlayer increases the surface molecular density of the Ru(II) complex monolayer compared with direct adsorption of the complex onto a SiO_2 surface. It was also reported that the saturation in film growth was achieved after 6 more layers on the

SiO$_2$ surface which, due to the large tilt angle of the molecular layer, was confirmed by a molecular domain boundary effect.
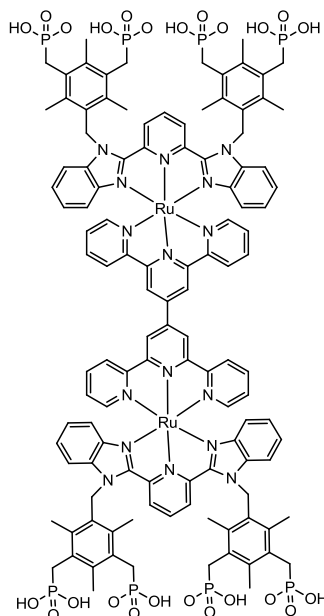
Scheme 1.36 Molecular structure of a bis-terpyridine Ru(II) derivative used to attach onto a SiO$_2$ surface.[63]

In another approach to make nano-wires, Loh *et al.*[64] formed an array of organometallic molecular wires on a gold surface by using the preassembled self-assembled monolayers of pyridine-terminated benzene to build-up a second layer of transition metal complexes (Scheme 1.37). Ru(tpy)(bpy)$^{2+}$ or cyclometalated Pt^{II}(6-phenyl-2,2'-bipyridine) units were attached onto the organic monolayer via the terminal pyridine moieties.

Current-voltage (I-V) studies showed that the electronic coupling between organic wire and the transition metal produced a molecular wire with higher conductance in comparison with the initial organic chain.
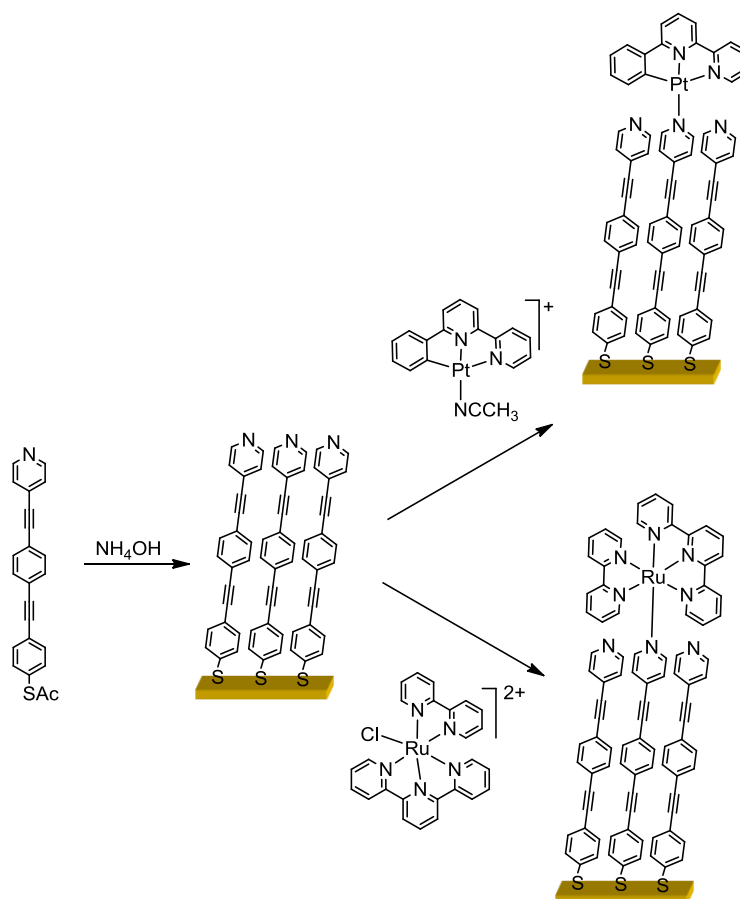
Scheme 1.37 Ru(tpy)(bpy)$^{2+}$ and Pt^{II}(6-phenyl-2,2'-bipyridine) complexes on gold surface.[64]

Draper and co-workers[65] employed a dithiocarbamate (DTC)-anchoring group to generate SAMs of Ru(II) and Os(II) complexes (Scheme 1.38) from the in-situ reaction of piperazine with CS_2 in the presence of a gold substrate. Electrochemical investigation of SAMs of both Ru(II) and Os(II) complexes obtained revealed their ideal surface behavior. Faster electron transfer rate constants in comparison with SAMs of similar compounds were calculated from repeated CVs at increasing scan rates. The surface coverage of the monolayer was reported to be significantly larger than other SAMs of comparable bis-terpyridine complexes. The DTC self-assembly monolayers were exceptionally strong in bearing agents and resisting potentials which can destroy thiol-based SAMs on gold surfaces.
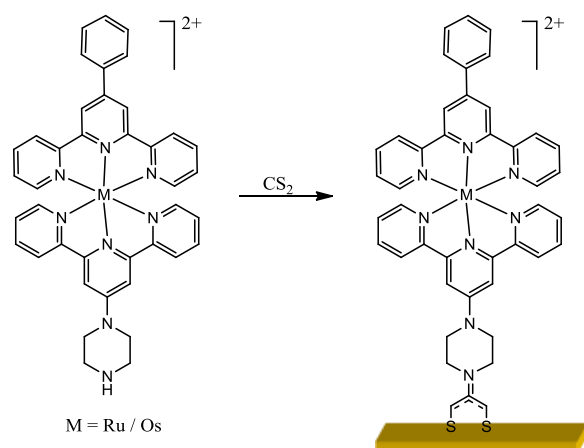
Scheme 1.38 Formation of the monolayers of bis-terpyridine derivative ruthenium and osmium complexes on a gold surface.[65]

Chen, Sasaki and co-workers[66] recently reported a butadiyne-linked diruthenium complex immobilised on a gold surface (Scheme 1.39). The stability of the mixed-valence state $Ru_2^{II,III}$ was found to be even higher on the surface (Kc is 4.47×10^{10} against 1.34×10^9 in solution). The information on the electronic structures of the SAMs in three oxidation states was evidenced by in-situ IR absorption spectroscopy.
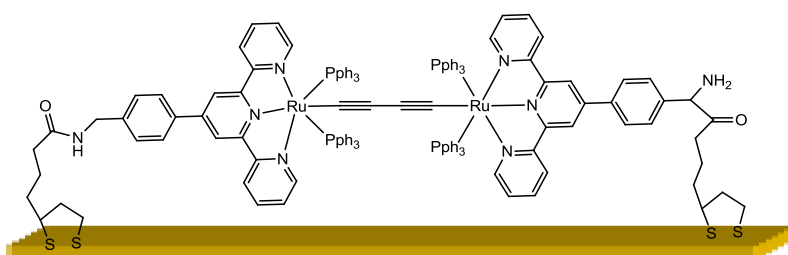
Scheme 1.39 Butadiyne-linked diruthenium complex, immobilised on a gold surface.[66]

Ulstrup *et al.*[67] demonstrated self-assembled molecular monolayers (SAMs) of complexes of $Os^{II/III}$, $Fe^{II/III}$, and $Ru^{II/III}$ with a terpyridine derivative (Scheme 1.40) linked to Au(111)-electrode surfaces. The complexes were prepared in situ by first

linking the tpy ligand to the surface, followed by addition of suitable metal compounds. The metal-tpy SAMs were studied by cyclic voltammetry (CV), and scanning tunnelling microscopy (STM). Sharp CV peaks were observed for the Os and Fe complexes, with interfacial electrochemical electron transfer rate constants of 6-50 s^{-1}. Well-defined but significantly broader peaks (up to 300 mV) observed for the ruthenium complex.
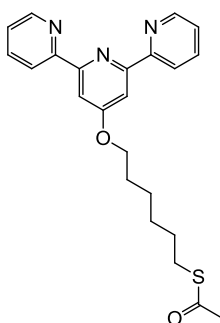
Scheme 1.40 terpyridine derivative ligand which was used by Ulstrup *et al* to attach metal complexes on gold surface.[67]

1.4.3. Other ligands used in ruthenium and osmium complexes on surfaces

Cao *et al.*[68] have used a layer-by-layer method in order to develop a compact and organised monolayer of Ru(II) complex bearing bis(3,5-dimethylpyrazol-1-yl)dithioacetate on gold and silver surfaces (Scheme 1.41), which was confirmed by cyclic voltammetric measurements and AFM imaging. Cyclic voltammetry was also applied to study the two-step process and the ability of the complex to detect nitric

oxide traces. As was evidenced in the paper, the monolayer formed on silver electrodes was more compact, although the complex showed more stable properties on gold.
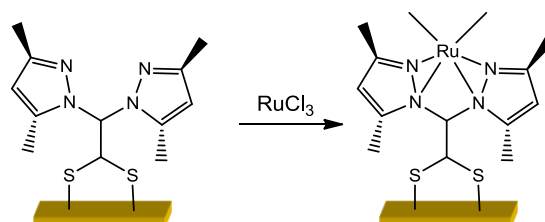
Scheme 1.41 Schematic representation of the monolayer formation of a Ru^{II} complex on surface by a layer-by-layer approach.[68]

Sugimura and co-workers[69] reported a redox active SAM of Ru(III) ions coordinated to ethylenediamine moieties by a vapour phase silane coupling of *N*-(2-aminoethyl)-3-aminopropyltrimethoxysilane (AEAPS) molecules to a Si/SiO$_2$ substrate. This was followed by the complexation of Ru^{III} ions in an aqueous RuCl$_3$ solution (Scheme 1.42). A similar SAM with 3-aminopropyltriethoxysilane was also attempted, but did not form a monolayer of the Ru^{III} complex. This confirms the importance of the chelation ability in immobilising Ru^{III} ions on the surface. The ruthenium-attached AEAPS-SAMs showed reduction and oxidation peaks at −0.1 and +1.0 V vs. Ag/AgCl respectively, corresponding to the Ru^{III}/Ru^{IV} redox reaction.
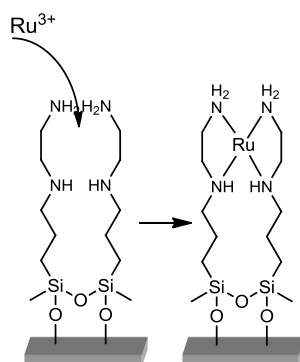
Scheme 1.42 Schematic illustration of the trapping behaviour of Ru^{III} ions on AEAPS-SAM on Si/SiO$_2$ substrate.[69]

In another example of ruthenium complexes on gold electrodes, a general method for accumulation of a dinuclear ruthenium complex on a gold surface was developed.[70] Surface-enhanced Raman scattering (SERS) measurements of the silver electrode confirmed that the base hydrolysis process converted the methyl benzoate group in the SAM into a benzoic acid group. To accumulate the complex on the gold electrode, voltammetric waves of Ru^{III}Ru^{III}/Ru^{II}Ru^{II} redox couple were observed until the gold electrodes were fully covered with the complex (Scheme 1.43). This type of ligand substitution reactions can be a very useful method to assemble other complexes and to design functional electrodes.
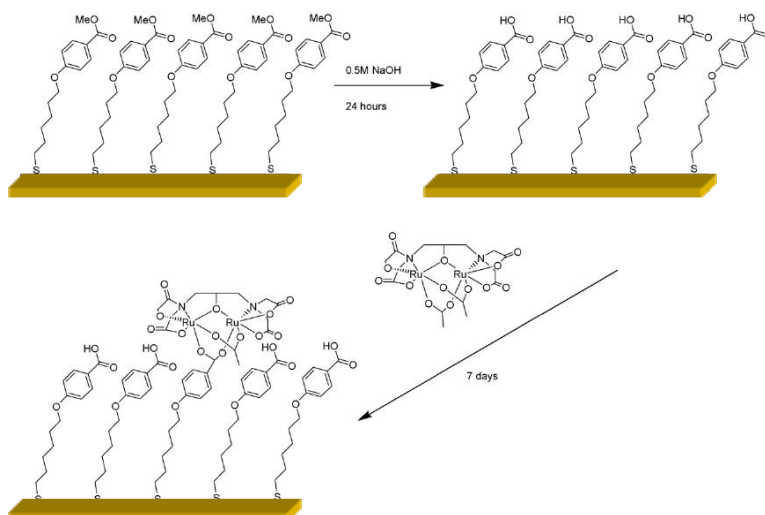
Scheme 1.43 Schematic representation of ligand substitution reaction to accumulate Ru dinuclear complex on gold electrode surface.[70]

Ye and co-workers[71] proposed a new strategy to make patterned SAM surfaces terminated with different kinds of moiety, such as carbon monoxide (CO), nitric oxide (NO) and successive layers of Ru₃ clusters by high yield ligand-exchange reaction (Scheme 1.44). It was proposed that the combined photochemical and electrochemical control is a powerful way to create delicate pattern structures on the SAM surface with various functionalities.
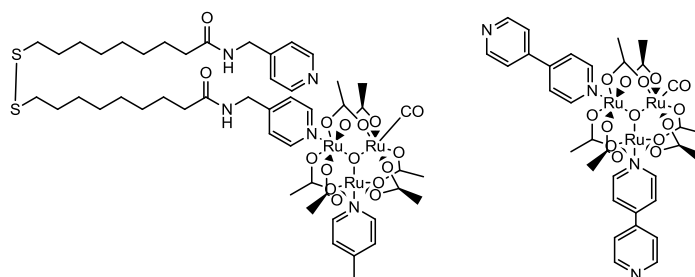
Scheme 1.44 Structure of Ru₃ cluster molecules with sulfur and nitrogen moieties.[71]

In a study from Dong's group[72], 4-(2-(4-pyridinyl)ethynyl)benzenic diazonium salt (PBD) was designed and used to modify a self-assembled substrate. Under UV irradiation and following the decomposition of diazonium group, the ionic bonds between PBD and substrate were converted into covalent bonds (Scheme 1.45). Later, the UV-Vis analysis results indicated that self-assembled multilayer films with axial ligands positioned between ruthenium atoms and pyridine groups were successfully formed. The assemblies were characterised by AFM images, UV-Vis absorption spectra and cyclic voltammograms. Under illumination, the ITO self-assembled films showed an effective photo-induced charge transfer and changed the current density of ITO.
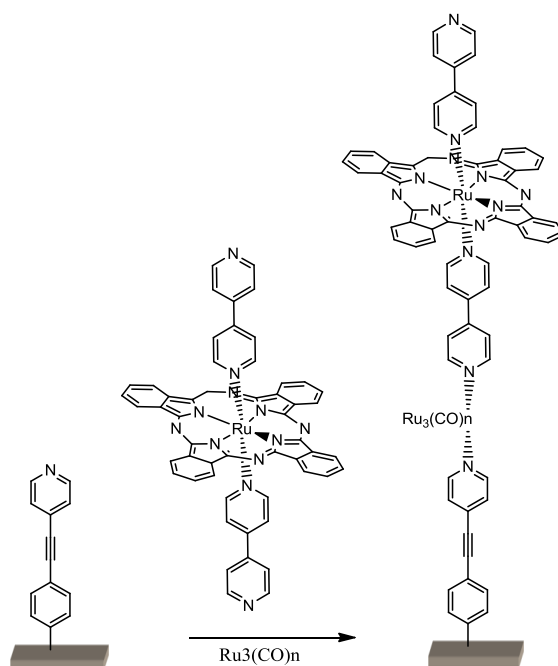
Scheme 1.45 Schematic presentation of attaching the ruthenium (II) complex on an ITO surface via PBD molecules.[72]

Lee, Han and co-workers[73] have reported the formation of SAMs of Ru clusters/di(3-aminopropyl)viologen (DAPV) on an ITO system by surface reaction in a $Ru_3(CO)_{12}$

solution (Scheme 1.46). Emission spectroscopy and time-resolved photoluminescence spectroscopy were recorded to elucidate the photo-induced charge transfer process from ruthenium clusters to DAPV.
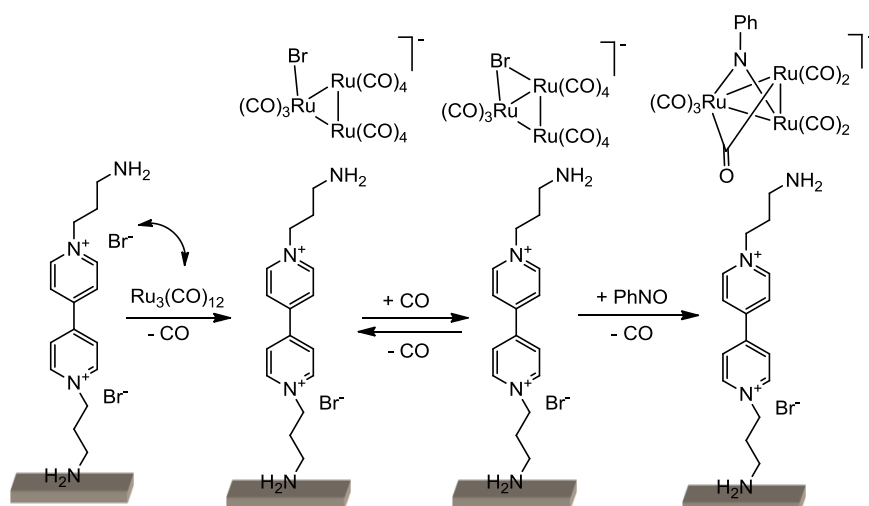
Scheme 1.46 Scheme of the synthesis of Ru clusters on DAPV/ITO and the chemical structure of Ru clusters.[73]

Rigaut and co-workers[74] have presented the charge transport of two series of molecular wires containing redox-active ruthenium centres (Scheme 1.47). The self-assembled monolayers of these molecular wires on Au surfaces were characterised by ellipsometry, X-ray photoelectron spectroscopy (XPS), reflection-absorption infrared spectroscopy (RA-FTIR), and cyclic voltammetry. The weak length and temperature dependence revealed an extremely efficient charge transport through the ruthenium centres.
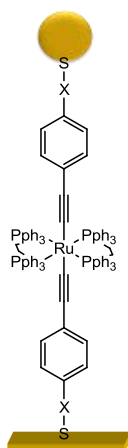
Scheme 1.47 Schematic representation of a molecular junction, The Au-coated tip was brought into contact with a SAM of Ru wires formed on an Au substrate.[74]

Dennany and co-workers[75] reported luminescence quenching of the metallopolymers $[Ru(bpy)_2(PVP)_{10}]^{2+}$ and $[Ru(bpy)_2(PVP)_{10}Os(bpy)_2]^{4+}$ (Scheme 1.48), both in solution and as thin films. It was shown that the solution phase photophysical properties are not fully transferred to thin films of these materials. In particular, surface immobilisation makes the emission intensity less sensitive to quenching by species in solution. Moreover, it is apparent that mixed metal systems such as $[Ru(bpy)_2(PVP)_{10}Os(bpy)_2]^{4+}$ can be created in which the individual luminophores communicate only weakly, opening up new possibilities for multi-analyte sensing. This result contrasts with previous studies of ruthenium- and osmium-containing polypyridyl polymers which show that the osmium centers act as traps for the energy migration through the polymer.
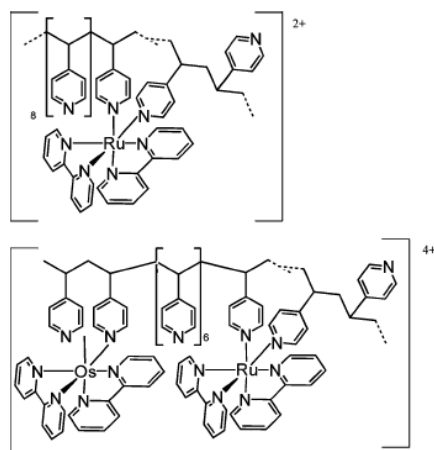
Scheme 1.48 Molecular structure of [Ru(bpy)$_2$(PVP)$_{10}$]$^{2+}$ and [Ru(bpy)$_2$(PVP)$_{10}$Os(bpy)$_2$]$^{4+}$. [75]

1.4.4. Luminescent and sensing surfaces of other metal complexes

Beer *et al.*[76] have reported an anion template which is used to assemble redox active bis-ferrocene functionalised rotaxane self-assembled monolayers (SAMs) on to gold electrode surfaces (Scheme 1.49). The system was shown to be capable of electrochemically recognising chloride anions selectively after template removal. It was shown that the anion binding site resides within the confines of the surface interlocked cavity, as evidenced by different techniques such as SPR, FTIR and ellipsometry.
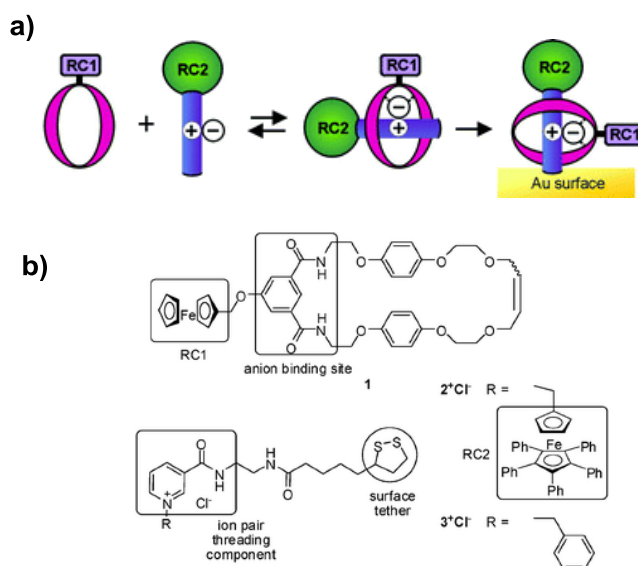
Scheme 1.49 a) Rotaxane SAM formation by surface stoppering b) Redox-active ferrocene-functionalised wheel and axle components.[76]

In a study by Gulino *et al.*[77] the optical detection of parts-per-million (ppm) levels of CO by a structurally well-defined monolayer consisting of bimetallic rhodium complexes on glass substrates were demonstrated (Scheme 1.50). The monolayer of the bimetallic–rhodium complex exhibited excellent selectivity towards CO in the presence of a series of other gases and air. Interestingly, the CO detection range could be controlled and expanded as a function of sensor temperature.
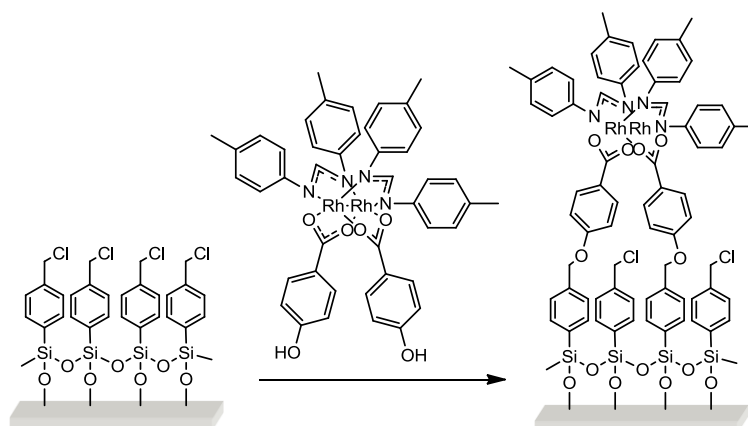
Scheme 1.50 Schematic representation of the formation of the bimetallic–rhodium complex monolayer.[77]

Scandola, Wurthner, Licciardello and co-workers[78] have reported metallo-supramolecular multilayers of a terpyridine-functionalised perylene bisimide ligand. Fe(II) complexes were prepared on gold surfaces via a self-assembling stepwise method involving direct coordination reactions at the sample surface (Scheme 1.51). The formation and growth of the multilayers were demonstrated by TOF-SIMS and UV-Vis spectroscopy. Moreover, AFM measurements on micro-patterned samples suggested that the metal–ligand chains grow approximately perpendicular on the gold surface. In these self-assembled multilayers, the photophysical behavior seems to indicate that the energy absorbed by the multilayer is promptly dissipated to the gold surface by ultrafast (sub-picosecond) processes.
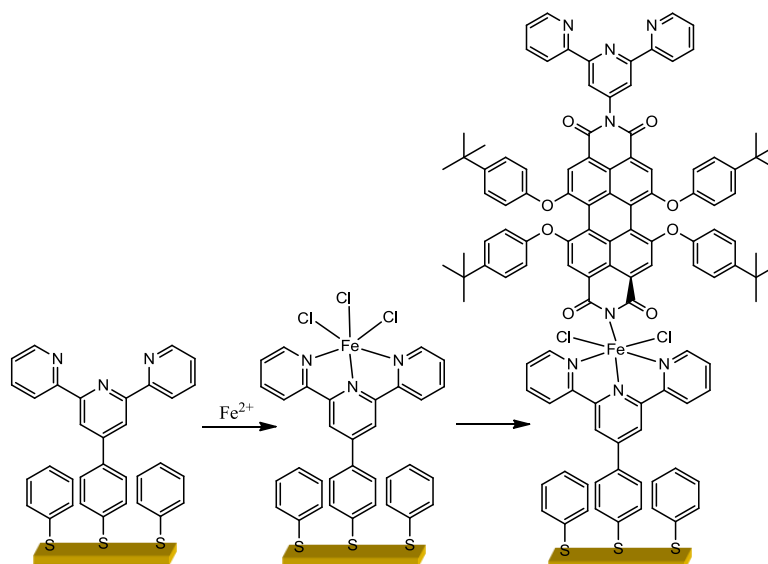
Scheme 1.51 Schematic representation of the step by step formation of the monolayers of bis-terpyridine Fe(II) complex on a gold surface.[78]

In another recent study from Yamashita and co-workers[79], a series of iridium photocatalysts was anchored to mesoporous silica material (Scheme 1.52). At room temperature, the anchored Ir^{III} complex exhibits strong phosphorescence emission at 530 nm due to triplet metal-to-ligand charge transfer (^{3}MLCT) transitions. There is a correlation between the intensity of photoluminescence emission due to the ^{3}MLCT states at room temperature and the photo-induced aerobic oxidation activity. It has been suggested that the mesoporous silica does not only act as a support, but also provides a promising microenvironment that alters the photochemical properties of the metal complexes.
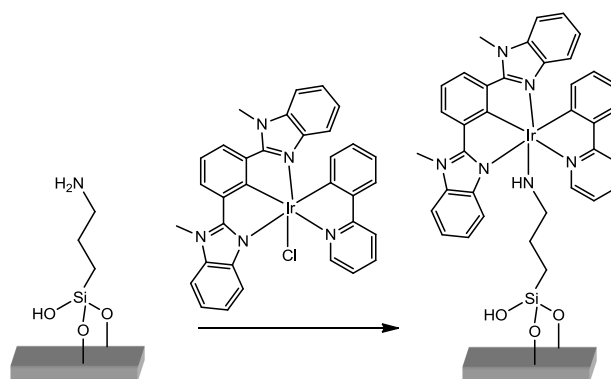
Scheme 1.52 Anchoring of Ir complex to Mesoporous Silica.[79]

Gunnlaugsson and co-workers[80] have demonstrated the formation of an assembly between a sensitising antenna and a Eu^{III} functionalised cyclen complex (Scheme 1.53). The monothiol conjugated cyclen complexes, possessing a coordinatively unsaturated Eu^{III} centre, can be used to develop a luminescent lanthanide-based self-assembled monolayer on a gold surface. The Eu^{III} emission from the gold sample was switched on in the presence of an appropriate sensitising antenna (2). Furthermore, this emission could then be switched off upon addition of a competitive coordinating ligand (3).
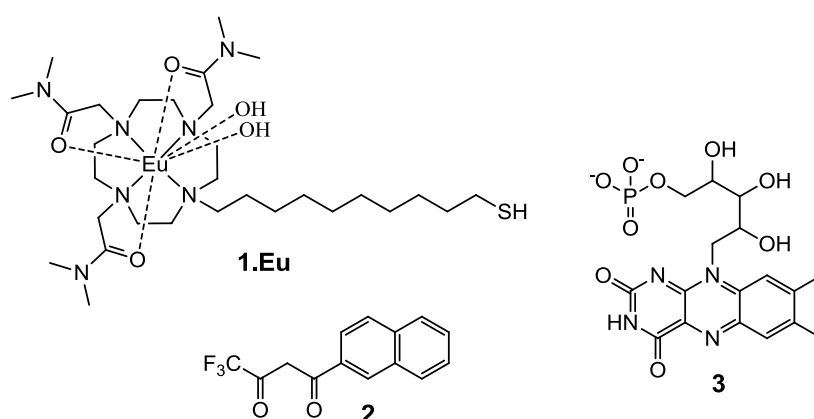
Scheme 1.53 Structures of the Eu complex, antenna and the competitive coordinating ligand.[80]

In another study by Constable and co-workers[81], Langmuir-Blodgett (LB) films of the amphiphilic iridium complex **1** were fabricated by using a EuW10 aqueous solution as a subphase (Scheme 1.54). It was illustrated by AFM and SXR measurements that the **1**/EuW10 LB films have a well-defined layered structure, in contrast with the LB films of **1** prepared on a pure water subphase.

The **1**/EuW10 LB films exhibit a yellow emission due to **1** with partial quenching, while the characteristic emission of EuW10 is not detectable. No energy transfer between Europium and Iridium has been observed in the LB films. Infrared and UV-Vis spectroscopy of the transferred LB films indicate that EuW10 and **1** are incorporated within these LB films.
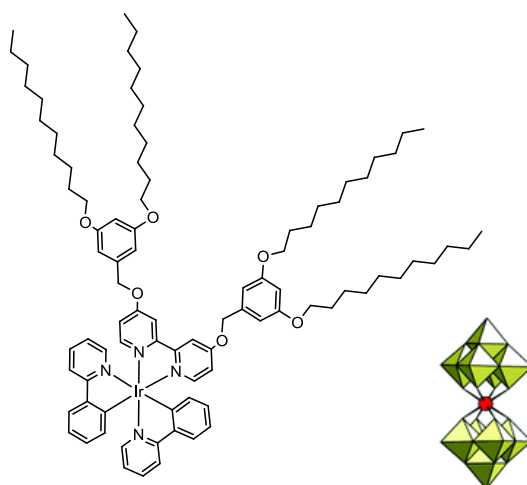
Scheme 1.54 Molecular Structure of 1 and the EuW$_{10}$ Polyanion.[81]

Penzkofer's group[82] demonstrated a thin film of triphenylamine dimer doped with platinum octaethyl-porphine (PtOEP) and *fac*-tris(2-phenylpyridine) iridium (Ir(ppy)$_3$) (Scheme 1.55). Photoluminescence emission measurements at several excitation wavelengths and photoluminescence excitation measurements at relevant emission

wavelengths in a temperature range of 10 K to room temperature were applied to characterise the thin film. Multi-band emissions and excitations were obtained due to multiple component excitations and energy transfers. The host (TPD) to guest (Ir(ppy)$_3$ and PtOEP), as well as the guest (Ir(ppy)$_3$) to guest (PtOEP) energy transfer in the singlet systems and in the excited triplet states was studied. Photoluminescence emission in the wavelength range 390 nm to 730 nm was also reported. It was proposed that lightly increasing the doping level of Ir(ppy)$_3$ and reducing the PtOEP doping level can result in a film with similar emission intensities of TPD, Ir(ppy)$_3$, and PtOEP resulting in an emission spectrum similar to that of white light.
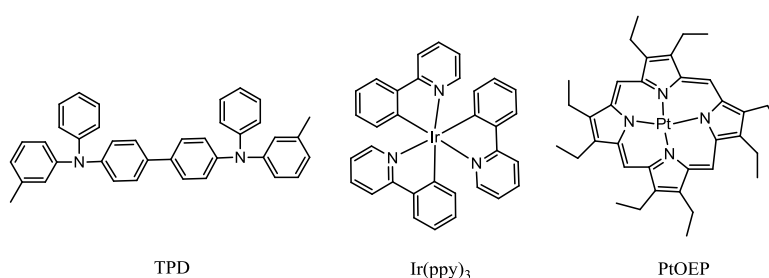
Scheme 1.55 Molecular structure of Ir(ppy)$_3$, PtOEP and TPD.[82]

In a very recent study by Galloni *et al.*[83] tetraferrocenylporphyrins-containing self-assembled mono-layers were prepared using two different strategies, covalent attachment of the monosubstituted metal-free porphyrin using a specific spacer and axial coordination of ZnTFcP to the pre-formed imidazole-containing SAM (Scheme 1.56). The covalent approach yielded an excellent density of porphyrins on the surface, while the second approach provided a simple, cheap and versatile method to functionalise pre-formed mono-layers with metalloporphyrins.

Self-assembled monolayers were characterised using UV-Vis spectroscopy and cyclic voltammetry (CV). Photo-electrochemical properties were also investigated by photocurrent generation (PG) experiments which showed that the asymmetric tetraferrocenylporphyrin constitutes the photo-active material of the photoelectrochemical cell.
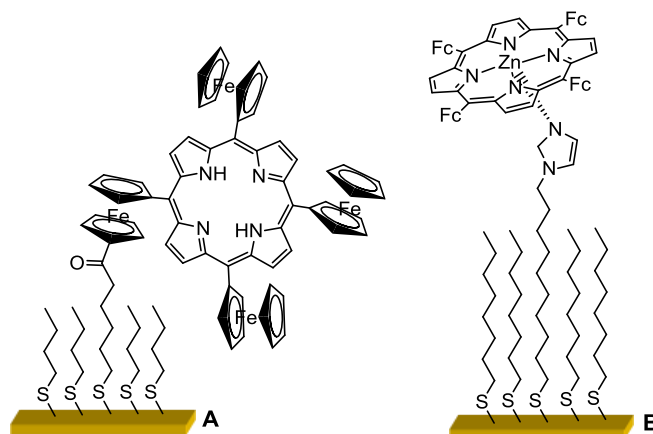
Scheme 1.56 structures of the SAMs prepared with A) monosubstituted-H2TFcP and mixed with BuSH 1 : 5 B) thioacetate of 11-(N-imidazolyl)-1-undecyl—ZnTFcP andmixed with OctSH1:5.[83]

In a study by Ramirez *et al.*[84] a transparent, very smooth, perfectly crystallised high density thin film of Y_2O_3:Eu^{3+}/Tb^{3+} were synthesised by a sol–gel method. The synthesised luminescent thin films showed a strong Eu^{3+} emission centered at 612 nm which increases with increasing temperature. These properties make the thin films great candidates for luminescent applications. Moreover, the luminescence arising from Eu(III) was improved due to an energy transfer process from Tb^{3+} to Eu^{3+}.

Direct excitation to $^5D_3$ and $^5D_4$ energy levels of Tb^{3+} resulted in no emission band, which can be explained by low concentration of active ions. They concluded that the high concentration of donor ions (Eu^{3+}) enhance the energy transfer process.

1.5. Supramolecular self-assembly systems using metallo-cyclodextrin receptor molecules

Cyclodextrins are cyclic oligosaccharides produced from the enzymatic degradation of starch, popular in host/guest chemistry due to their environmentally friendly nature and their facility to undergo a range of functionalisations.[85]

Glucose units arrange themselves in such a way that the cyclodextrin molecules are cone-shaped, with the secondary (2,3) hydroxyl groups on the wider top rim and the primary (6) hydroxyls on the more narrow lower rim (Scheme 1.57). Glycosidic oxygen and hydrogen atoms are contained inside the cavity, which makes it far more hydrophobic than the outside of the molecule. The size of the inner cavity varies with the number of glucose units in the molecule. The three major industrially produced cyclodextrins are α-, β- and γ- consisting of 6, 7 and 8 glucose units respectively. Larger cyclodextrins have been synthesised and isolated but are not widely used in guest/host chemistry.[85]
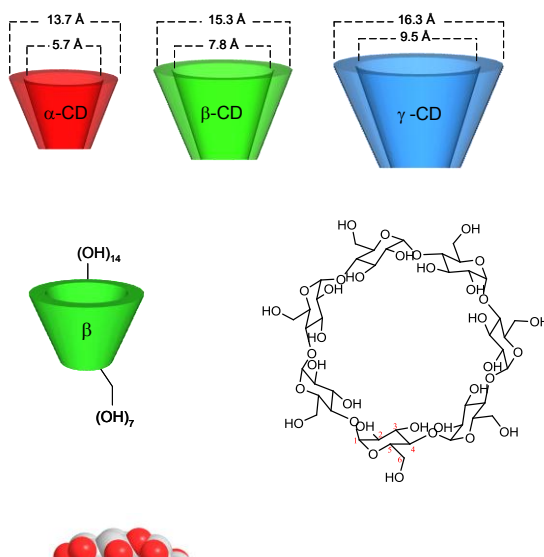
Scheme 1.57 Structure and dimensions of common cyclodextrins.

Cyclodextrins have the ability to form inclusion complexes with a wide range of guest molecules through van der Waals forces, ring strain release on complexation, hydrophobic interactions and the discarding of high-energy water trapped in the cavity. The number of reported inclusion complexes with cyclodextrins in the literature has been increasing dramatically over recent years. Their association properties have been studied extensively and examined for a huge variety of applications. A few important examples of applications of cyclodextrins are their use as stabilisers to protect vitamins and sensitive aromatic compounds from oxidation, hydrolysis and photolysis. Due to their special hydrophilic/hydrophobic character, cyclodextrins are also studied for various transfer processes through cell membranes and they also attractive receptor models for enzyme catalysis reactions.[86]

Our aim is to follow Nature's construction by bringing donor and acceptor units together in close proximity via non-covalent bonds, employing cyclodextrin as a receptor molecule (Scheme 1.58). This approach allows the selective binding of a

guest molecule via non covalent bonds. By appending a redox active, energy donating or accepting metal center to the cyclodextrin, the compounds become ideal candidates in the study of electron or energy transfer in supramolecular chemistry. In aqueous solutions, cyclodextrins are known to form very stable inclusion complexes with hydrophobic guest molecules.
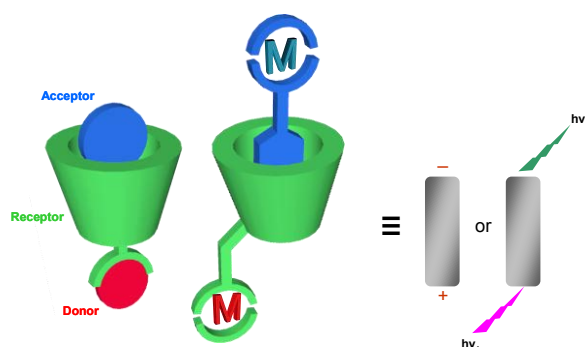
Scheme 1.58 Bringing donor and acceptor units together via non-covalent bonds.

Metallo-cyclodextrins are compounds with versatile properties. The cyclodextrin unit makes them attractive receptor molecules, enabling the sensing and inclusion of hydrophobic guests. The metallo-unit gives the receptor molecule interesting redox and luminescence properties. The combination of both features in one compound makes metallo-cyclodextrins useful building blocks for the development of supramolecular systems and designates them as attractive candidates for possible applications in molecular devices in nanotechnology.[87]

Ruthenium centres were first attached to cyclodextrins by Deschenaux *et al.*[88] 6-monohydroxy permethylated β-cyclodextrin was reacted with succinic anhydride, followed by an ester bond linkage to 6-(bromomethyl)-2,2'-bipyridine (Scheme 1.59). The ruthenium complex was obtained by reacting the ligand with $Ru(bpy)_2Cl_2$ and fully characterised. Its absorption and emission spectroscopic properties as well as

electrochemical behaviour were investigated. Emission quantum yields and lifetimes values were significantly lower than for the parent $[Ru(bpy)_3]^{2+}$ complex which was attributed to the steric restriction around the ruthenium centres. Substitution on the 6-position of the bipyridine is sterically demanding for the formation of an octahedral complex, resulting in a weaker crystal field splitting of the d orbitals on the metal, facilitating non-radiative deactivation of the excited state energy.
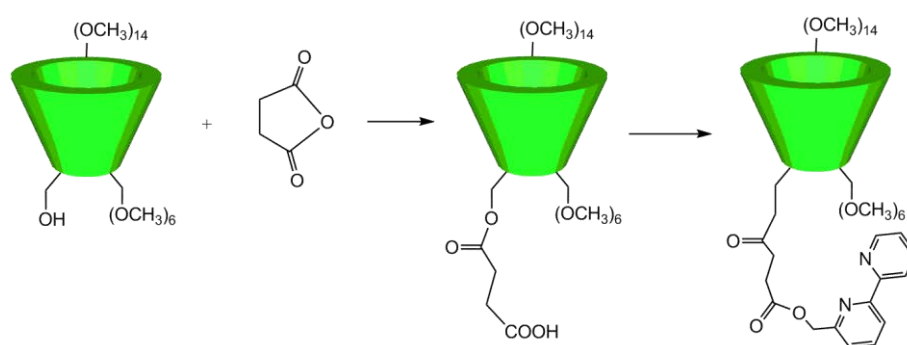
Scheme 1.59 Reaction scheme to form a cyclodextrin substituted bipyridyl ligand [88]

Harriman *et al.*[89] utilised the bi-capped cyclodextrin approach to attach a metal centre to the bottom rim of a cyclodextrin. 2,2'-bipyridine was covalently bonded at the 4,4'-positions to the A/D glucose units of an 6A,6D-diamino-6A,6D-didesoxy - permethylated−α-cyclodextrin. Complexation to the heteroleptic compound (Scheme 1.60) was achieved by reaction with $[Ru(bpy)_2(Me_2CO)_2][BF_4]_2$. Upon addition of a benzoquinone electron acceptor guest, strong quenching of the ruthenium based emission was observed. The data suggested a distinctively linear 1:1 complex formation, indicating the presence of an additional bimolecular, diffusion controlled process dominating at high quencher concentration. An edge-to-edge separation

distance between the benzoquinone and the ruthenium metal centre of 7Å was determined by NMR studies.
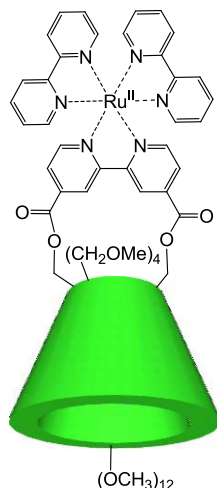
Scheme 1.60 Ruthenium centre attached to the bottom rim of a cyclodextrin.[89]

1.5.1. Host-guest chemistry based on cyclodextrins

Binding properties of native cyclodextrins have been investigated by a wide variety of techniques and more sophisticated architectures have also been examined to develop new materials for sensors and electronic devices.[90] Such systems often require attachment of metal centers to the proximity of the cyclodextrin guest binding site in order to facilitate communication between two or more photo- or electroactive units.[17]

The group of Nolte reported a β-cyclodextrin dimer connected via a bipyridine spacer. This was used to form a Ru[II] trisbipyridyl complex (Scheme 1.61a).[91,92] The

complex exhibited a poor luminescence quantum yield due to steric crowding around the metal center which prevented a perfect octahedral arrangement of the bipyridyl ligands around the metal center. Further optimization of the ligand with a further spacer between the bipyridyl and the cyclodextrin units yielded a highly luminescent compound upon coordination with Ru[II], capable of detecting steroids in aqueous solution, with the presence of dialkyl viologen (Scheme 1.61b).[91,93]

The luminescence of the complex is quenched by dialkyl viologens bound to the cyclodextrins via alkyl groups in non-covalent fashion resulting in an energy transfer process from Ru[II] to the chromophore.[94] Viologen groups can be replaced by an addition of steroids such as ursodeoxycholic acid, litocholic acid and cholesterol which lead to the reappearance of the original luminescence from the ruthenium trisbipyridyl complex.
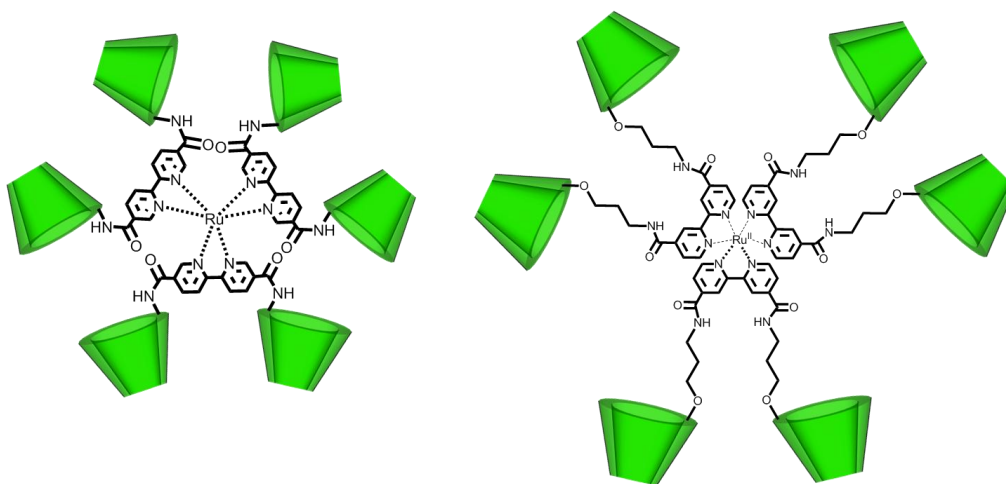
Scheme 1.61 Ruthenium tris-bipyridine complexes bearing cyclodextrin units.[94]

The group of Pikramenou *et al.*[95] have reported a ruthenium tris(bipyridyl) cyclodextrin "wheel" (Scheme 1.62) which acts as either an energy donor or acceptor in the presence of suitable transition metal guest compounds. The supramolecular complexes of the "wheel" with Os^{2+} and Ir^{3+} polypyridine guests assembled via hydrophobic interactions between either cyclodextrin and biphenyl or adamantane moiety allowed directional energy- or electron transfer between photoactive components.
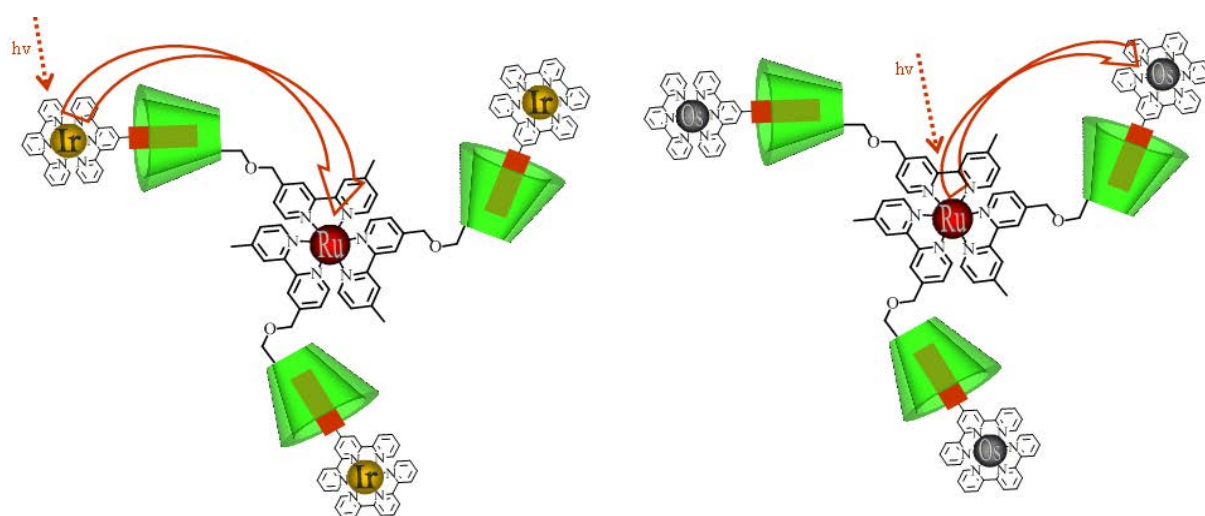
Scheme 1.62 Directional energy transfer of a ruthenium "wheel" and hydrophobic guest molecule.[95]

The system was modified to examine unidirectional energy conversion through three different photoactive units (ruthenium and osmium metals and anthracene).[96] Two-step photoinduced energy transfer was set up with two different cyclodextrins, *α*- and *β*-, which were connected through a ruthenium core (Scheme 1.63). Selective excitation of anthracene, bound to the *α*-cyclodextrin, was found to result in energy transfer to ruthenium and further to the osmium guest bound selectively in the *β*-cyclodextrin cavity, thus demonstrating the directionality of the system.
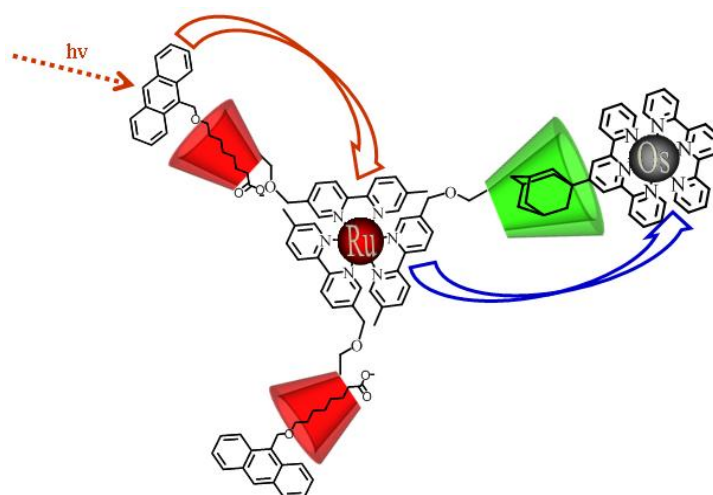
Scheme 1.63 Unidirectional energy transfer in anth·Ru($\alpha_2\beta$)·Os-ada triad.[96]

More recently, the group have reported the preparation of an anthracene *β*-cyclodextrin and ruthenium tris (acetylene bipyridine) cyclodextrin complex[97] and described energy transfer processes taking place from ruthenium metal core to anthracene in a supramolecular complex connected *via* a bisadamantane bridge (Scheme 1.64). Further, unidirectional energy transfer from anthracene to the osmium guest was established.
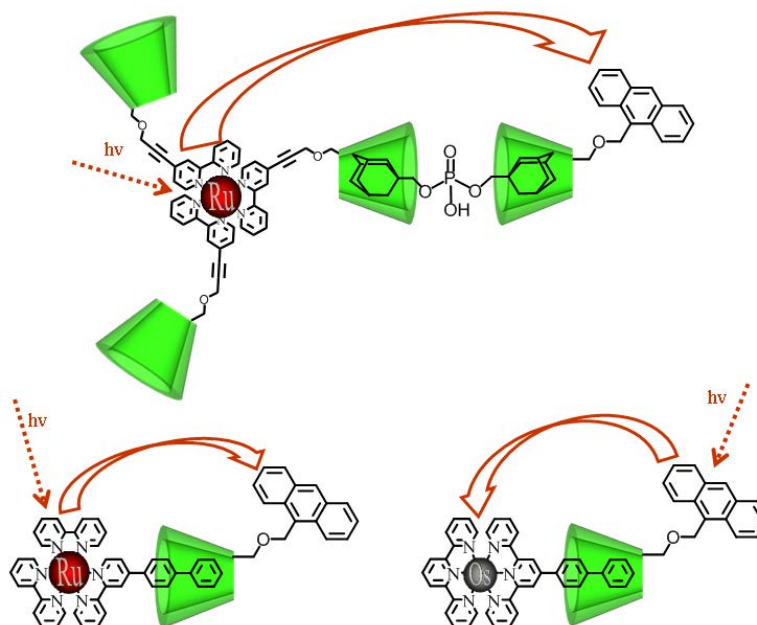
Scheme 1.64 Supramolecular energy transfer systems.[97]

1.5.2. Supramolecular self-assembled monolayer systems using metallo-cyclodextrin receptor molecules

Cyclodextrin monolayers are interesting due to their receptor properties for molecular recognition. One of the early examples of cyclodextrins modified with a surface binding anchor was presented by Stoddart *et al.* (Scheme 1.65).[98] Substitution of the primary hydroxyl groups of a *β*-Cyclodextrin with thiol moieties led to poorly organised monolayers with average 64-75 % surface coverage. However, it was shown that defects in the monolayer could be covered by simultaneous adsorption of ferrocene and pentanethiol. Ferrocene, a known guest for *β*-cyclodextrin, occupies the cyclodextrin cavity while pentanethiol covers defects on the monolayer.
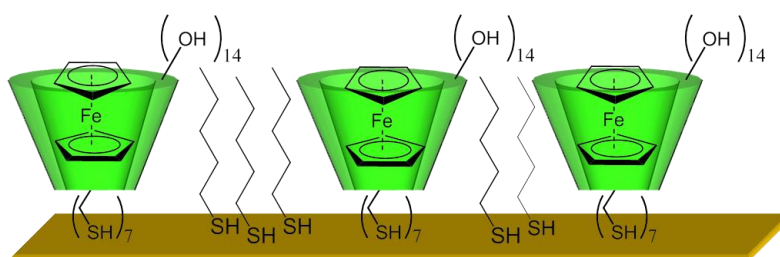
Scheme 1.65 Monolayer of thiolated β-cyclodextrin and pentanethiol.[98]

Willner *et al.*[99] reported molecular switch on a gold electrode based on a ferrocene functionalised *β*-cyclodextrin which, upon irradiation of light, shuttled between an aliphatic chain and an azobenzene unit (Scheme 1.66). The ferrocene cyclodextrin resides preferentially on the azobenzene moiety in the *trans* configuration, but trans-locates to the aliphatic moiety upon irradiation of light due to the photoisomerisation of the azobenzene to its *cis* configuration.
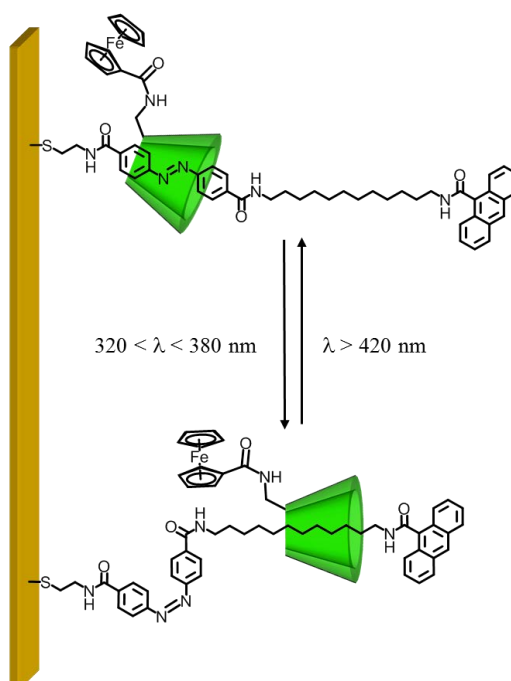
Scheme 1.66 Photoactivated molecular train on a gold surface.[99]

The groups of Forster and Keyes[100,101] reported a γ-cyclodextrin assembled on a platinum surface *via* pyridinium anchors (Scheme 1.67). The cyclodextrin monolayers backfilled with alkanethiols were shown to form host-guest complexes with redox active compounds such as C_{60} and $[Co(biptpy)_2]^{2+}$ and as a result created tunnelling currents between the platinum and mercury electrodes.
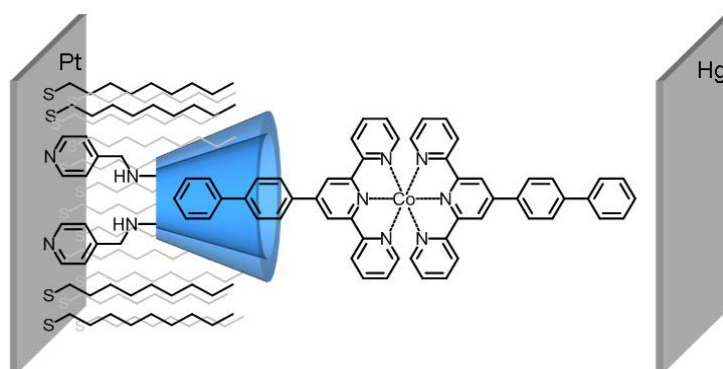
Scheme1.67 A γ-cyclodextrin assembled on a platinum surface *via* pyridinium anchors and $[Co(biptpy)_2]^{2+}$ guest. [100,101]

Harada *et al.*[102] have reported molecular motion imagining of a single rotaxane molecule consisting a *α*-cyclodextrin functionalised with the fluorescent probe rhodamine B and a diaminodiphenylacetylene axle on silica surfaces (Scheme 1.68). Fast rotation of the fluorescent cyclodextrin was observed around the axle by fluorescence microscopy.
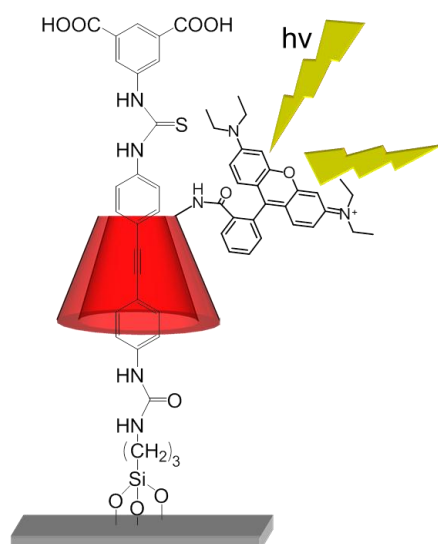
Scheme 1.68 Fluorescent α-cyclodextrin rotaxane molecule on a silica surface.[102]

In a recent study by Pikramenou *et al.*[103] a supramolecular conducting system was constructed using a novel (±)-thioctic acid functionalised β-cyclodextrin host attached to a gold (Au) surface, with an iridium bearing guest molecule functionalised with biphenyl tails to insert into the cyclodextrin cavity (Scheme 1.69). Remote electron transfer between the flat gold surface and the Pt/Ir tip of a scanning tunnelling microscope was investigated by the resulting supramolecular system. The morphology of the surfaces was also studied after successive deposition of host molecules followed by guest molecules. The gold surface functionalised with the supramolecular system showed the formation of 2 nm height features. Spectroscopic analysis of the tunnelling current through this supramolecular layer revealed the relationship between tunnelling distance and the effective barrier height. In conclusion, in the supramolecular system of host–metallo guest, a small increase of conductance was observed, compared to the layer without the guest. This can be

explained by the presence of the Ir-guest, which creates intermediate energy states between the Au substrate and the Pt/Ir tip.
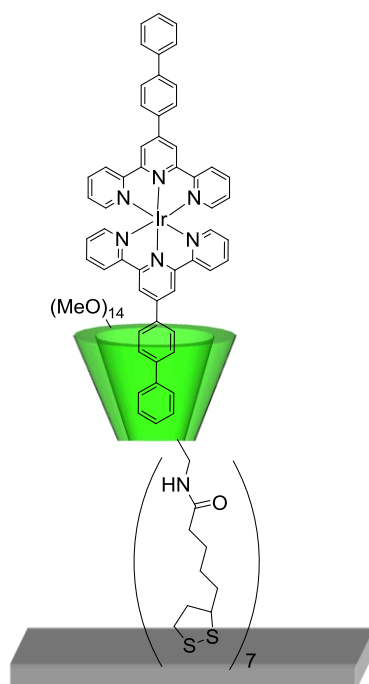
Scheme 1.69 Iridium guest and the (±)-thioctic acid functionalised β-cyclodextrin host on gold surface.[103]

1.6. Thesis outline

This thesis focuses on the design of surface active metal complexes, their attachment on surfaces, and the investigation of their photophysical properties in solution, powder and as self-assembled monolayers. In chapter 3, six novel ruthenium(II) and osmium(II) complexes are synthesised and well characterised. The complexes were attached to the gold surfaces and their photophysical and surface properties investigated by several methods. We introduced a simple method to

prepare very stable monolayers with full coverage of the surface. The monolayers show strong emission with relatively long emission lifetime. Unlike it was expected that the emission of the metal complexes quench in small distances (<100 Å)[29] from the surfaces, we proved that although the metal complexes will experience some quenching but with only 9 Å distance from the surface we are able to record a reasonable high emission lifetimes (about 100 ns). In chapter 4, new biquinoline-pyridine ligands are introduced and photophysical and surface analysis of a surface active ruthenium(II) complex has been studied by different methods such as XPS, Ellipsometry, absorption and emission spectrometry. A biphenyl derivative of the same ligand has been synthesised and its ruthenium(II) and iridium(III) complexes are proposed as strong emitting guests for metallo-cyclodetrins. In chapter 5, surface active ruthenium and osmium complexes bearing two β-cyclodextrins on one of the bipyridine ligands have been synthesised and characterised. The photo-induced communication of these complexes and the metal guests prepared in chapter 4 are investigated in both aqueous solution and on gold surfaces. We were able to see some energy transfer between the metal complexes both in solution and on the surface. Chapter 6 proposes a new and efficient method of sensitizing Nd(III) NIR emission by non-covalent attachment of a BODIPY dye attached to β-cyclodextrin (BODIPY-CD) and we showed that BODIPY-CD is a good sensitizer for NIR lanthanides.

1.7. References

(1)   Balzani, V. *Photochem. Photobiol. Sci.* **2003**, *2*, 459-476.

(2)   Barigelletti, F.; Flamigni, L. *Chem. Soc. Rev.* **2000**, *29*, 1-12.

(3)   Belser, P.; von Zelewsky, A.; Frank, M.; Seel, C.; Vogtle, F.; De Cola, L.; Barigelletti, F.; Balzani, V. *J. Am. Chem. Soc.* **1993**, *115*, 4076-4086 .

(4)   De Cola, L.; Belser, P. *Coord. Chem. Rev.* **1998**, *177*, 301-346.

(5)   Schlicke, B.; De Cola, L.; Belser, P.; Balzani, V. *Coord. Chem. Rev.* **2000**, *208*, 267-275.

(6)   Encinas, S.; Flamigni, L.; Barigelletti, F.; Constable, E. C.; Housecroft, C. E.; Schofield, E. R.; Figgemeier, E.; Fenske, D.; Neuburger, M.; Vos, J. G. *Chem. Eur. J.* **2002**, *8*, 137-150.

(7)   Juris, A.; Balzani, V.; Barigelletti, F.; Campagna, S.; Belser, P.; Zelewsky, A. V. *Coord. Chem. Rev.* **1988**, *84*, 85-277.

(8)   Campagna, S.; FaustoPuntoriero; FrancescoNastasi; Bergamini, G.; Balzani, V. *Photochemistry and Photophysics of Coordination Compounds: Ruthenium*; Springer-Verlag Berlin Heidelberg, 2007.

(9)   Coe, B.; Thompson, D.; Meyer, T. *J. Inorg. Chem.* **1995**, *34*, 3385-3395.

(10)   Constable, E. C.; Cargill Thompson, A.; Tocher, D. A.; Daniels, M. A. M. *New J. Chem.* **1992**, *16*, 855-867.

(11)   Maestri, M.; Armaroli, N.; Balzani, V.; Constable, E. C.; Cargill Thompson, A. *Inorg. Chem.* **1995**, *34*, 2759-2767.

(12)   Amouyal, E.; Mouallem-Bahout, M. *J. Chem. Soc., Dalton Trans.* **1992**, 509-513.

(13)   Belser, P.; Dux, R.; Balzani, V. *Angew. Chem. Int. Ed.* **1995**, *34*, 595-513.

(14)   Klassen, D.; Hudson, C.; Shaddix, E. *Inorg. Chem.* **1975**, *14*, 2733-2736.

(15)   Cook, M.; Lewis, A.; Thompson, A.; Robbins, D. *J. Chem. Soc., Perkin Trans. 2* **1984**, 1293-1298.

(16)   David, E.; Born, R.; Kaganer, E.; Willner, I. *J. Am. Chem. Soc.* **1997**, *119*, 7778-7790.

(17)   Deschenaux, R.; Harding, M. M.; Ruch, T. *J. Chem. Soc., Perkin Trans. 2* **1993**, 1251-1258 .

(18)   Kurimura, Y.; Takato, K.; Tsuchida, E.; Yamada, A. *J. Phys. Chem.* **1982**, *86*, 2432-2437.

(19)   Nagle, J.; Bernstein, J.; Young, R.; Meyer, T. *J. Inorg. Chem.* **1981**, *20*, 1760-1764.

(20)   Langmuir, I. *J. Am. Chem. Soc.* **1917**, *39*, 1848-1906.

(21)   Blodgett, K. B. *J. Am. Chem. Soc.* **1935**, *57*, 1007-1022.

(22)   Bigelow, W. C.; Pickett, D. L.; Zisman, W. A. *J. Colloid Sci.* **1946**, *1*, 513-538.

(23)   Flink, S.; van Veggel, F. C. J. M.; Reinhoudt, D. N. *Adv. Mater.* **2000**, *12*, 1315-1328.

(24)   Flink, S.; van Veggel, F. C. J. M.; Reinhoudt, D. N. *J. Phys. Org. Chem.* **2001**, *14*, 407-415.

(25)   Forster, R. J.; Keyes, T. E. *Coord. Chem. Rev.* **2009**, *253*, 1833–1853.

(26)   Nuzzo, R. G.; Allara, D. L. *J. Am. Chem. Soc.* **1983**, *105*, 4481-4483.

(27)   Forster, R. J.; Keyes, T. E.; Vos, J. G. *Interfacial Supramolecular Assemblies*; Wiley, 2003.

(28)   Richie, B.; Burstein, E. *Phys. Rev. B* **1981**, *24*, 4843.

(29)   Wokuan, A.; Lutz, H.-P.; King, A. P.; Wild, U. P.; Ernst, R. R. *J. Chem. Phys.* **1983**, *79*, 509.

(30) Weitz, D. A.; Garoff, S.; Gersten, J. I.; Nitzan, A. J. *J. Chem. Phys.* **1983**, *78*, 5324.

(31) Otsuki, J.; Kameda, H.; Tomihira, S.; Sakaguchi, H.; Takido, T. *Chem. Lett.* **2002**, 610-611.

(32) Ma, H.; Dong, T.; Wang, G.; Zhang, W.; Wang, F.; Electroanalysis, X. W. *Electroanalysis* **2006**, *18*, 2475-2480.

(33) Brennan, J. L.; Keyes, T. E.; Forster, R. J. *Langmuir* **2006**, *22*, 10754-10761.

(34) Forster, R. J.; Pellegrin, Y.; Leane, D.; Brennan, J. L.; Keyes, T. E. *J. Phys. Chem. C* **2007**, *111*, 2063-2068.

(35) D'Aléoa, A.; Williams, R. M.; Chriquib, Y.; Iyerb, V. M.; Belserb, P.; Vergeerc, F.; Ruizd, V.; Unwin, P. R.; De-Cola, L. *The Open J. Inorg. Chem.* **2007**, *1*, 26-36.

(36) Jebb, M.; Sudeep, P. K.; Pramod, P.; Thomas, K. G.; , P. V. K. *J. Phys. Chem. B* **2007**, *111*, 6839-6844.

(37) Ricci, A.; Rolli, C.; Rothacher, S.; Baraldo, L.; Bonazzola, C.; Calvo, E. J.; Tognalli, N.; Fainstein, A. *J. Solid State Electrochem* **2007**, *11*, 1511–1520.

(38) Gulino, A.; Gupta, T.; Mineoa, P. G.; van der Boom, M. E. *Chem. Commun.* **2007**, 4878–4880.

(39) Forster, R. J.; Pellegrin, Y.; Keyes, T. E. *Electrochem. Commun.* **2007**, *9*, 1899.

(40) Zanarini, S.; Rampazzo, E.; Bich, D.; Canteri, R.; Ciana, L. C.; Marcaccio, M.; Marzocchi, E.; Moltalti, M.; Panciatichi, C.; Pederzolli, C.; Paolucci, F.; Prodi, L.; Vanzetti, L. *J. Phyc. Chem. C* **2008**, *112*, 2949-2957.

(41) Gupta, T.; van der Boom, M. E. *Angew. Chem. Int. Ed.* **2008**, *47*, 2260-2262.

(42) Hortholary, C. d.; Coudret, C. *C. R. Chimie* **2008**, *11*, 702-708.

(43)   Motiei, L.; Altman, M.; Gupta, T.; Lupo, F.; Gulino, A.; Evmenenko, G.; Dutta, P.; van der Boom, M. E. *J. Am. Chem. Soc.* **2008**, *130*, 8913–8915.

(44)   Boland, S.; Foster, K.; Leech, D. *Electrochimica Acta* **2009**, *54*, 1986–1991.

(45)   Chen, Z.; Concepcion, J. J.; Jurss, J. W.; Meyer, T. J. *J. Am. Chem. Soc.* **2009**, *131*, 15580–15581.

(46)   Lupo, F.; Fragala, M. E.; Gupta, T.; Mamo, A.; Aureliano, A.; Bettinelli, M.; Speghini, A.; Gulino, A. *J. Phys. Chem. C* **2010**, *114*, 13459–13464.

(47)   Jonsson, E. O.; Thygesen, K. S.; Ulstrup, J.; , K. W. J. *J. Phys. Chem. B* **2011**, *115*, 9410–9416.

(48)   Kang, C. H.; Choi, Y.-B.; Kim, H.-H.; Choi, H. N.; Lee, W.-Y. *Electroanalysis* **2011**, *23*, 2131 – 2138.

(49)   Ricci, A. M.; Tognalli, N.; Llave, E. d. l.; Vericat, C.; Leo, L. P. M. D.; Williams, F. J.; Scherlis, D.; Salvarezzac, R.; Calvo, E. J. *Phys. Chem. Chem. Phys.* **2011**, *13*, 5336–5345.

(50)   Ramachandra, S.; Schuermann, K. C.; Edafe, F.; Belser, P.; Nijhuis, C. A.; Reus, W. F.; Whitesides, G. M.; De Cola, L. *Inorg. Chem.* **2011**, *50*, 1581–1591.

(51)   Yesildag, A.; Ekinci, D. *Electrochimica Acta* **2010**, *55*, 7000–7009.

(52)   Bertoncello, P.; Kefalas, E. T.; Pikramenou, Z.; Unwin, P. R.; Forster, R. J. *J. Phys. Chem. B* **2006**, *110*, 10063-10069.

(53)   Loiseau, F.; Di Pietro, C.; Serroni, S.; Campagna, S.; Licciardello, A.; Manfredi, A.; Pozzi, G.; Quici, S. *Inorg. Chem.* **2001**, *40*, 6901-6909.

(54)   Balzani, V.; Juris, A.; Venturi, M.; Campagna, S.; Serroni, S. *Chem. Rev.* **1996**, *96*, 759-833.

(55) Figgemeier, E.; Constable, E. C.; Housecroft, C. E.; Zimmermann, Y. C. *Langmuir* **2004**, *20*, 9242-9248.

(56) Ohba, Y.; Kanaizuka, K.; Murata, M.; Nishihara, H. *Macromol. Symp.* **2006**, *235*, 31-38.

(57) Albrecht, T.; Moth-Poulsen, K.; Christensen, J. B.; Hjelm, J.; Bjørnholm, T.; Ulstrup, J. *J. Am. Chem. Soc.* **2006**, *128*, 6647-6656.

(58) Haga, M.-A.; Ohta, M.; Machida, H.; Chikira, M.; N. T. *Thin Solid Films* **2006**, *499*, 201–206.

(59) Tuccitto, N.; Torrisi, V.; Cavazzini, M.; Morotti, T.; Puntoriero, F.; Quici, S.; Campagna, S.; Licciardello, A. *Chem. Phys. Chem* **2007**, *8*, 227-230.

(60) Dong, T.-Y.; Huang, C.; Chen, C.-P.; Lin, M.-C. *J. Organomet. Chem.* **2007**, *692*, 5147–5155.

(61) Seo, K.; Konchenko, A. V.; Lee, J.; Bang, G. S.; Lee, H. *J. Am. Chem. Soc.* **2008**, *130*, 2553-2559.

(62) Terada, K.; Kobayashi, K.; Haga, M.-A. *Dalton Trans.* **2008**, 4846–4854.

(63) Ishida, T.; Terada, K.-i.; Hasegawa, K.; Kuwahata, H.; Kusama, K.; Sato, R.; Nakano, M.; Naitoh, Y.; Haga, M.-A. *Applied Surface Science* **2009**, *225*, 8824–8830.

(64) Ng, Z.; Loh, K. P.; Li, L.; Ho, P.; Bai, P.; Yip, J. H. K. *ACS Nano* **2009**, *3*, 2103–2114.

(65) Murphy, F. A.; Surez, S.; Figgemeier, E.; Schofield, E. R.; Draper, S. M. *Chem. Eur. J.* **2009**, *15*, 5740 – 5748.

(66) Zhang, L.-Y.; Zhang, H.-X.; Ye, S.; Wen, H.-M.; Chen, Z.-N.; Osawa, M.; Uosakic, K.; Sasaki, Y. *Chem. Commun.* **2011**, *47*, 923–925.

(67)   Salvatore, P.; Hansen, A. G.; Moth-Poulsen, K.; Bjørnholm, T.; Nicholsd, R. J.; Ulstrup, J. *Phys. Chem. Chem. Phys.* **2011**, *13*, 14394–14403.

(68)   Díaz-García, A.; Gutiérrez, S.; Ortiz, M.; Sánchez, I.; Cao, R.; Otero, A. *Inorg. Chem. Commun.* **2007**, *10*, 1482–1484.

(69)   Moriguchi, T.; Murase, K.; Sugimura, H. *Colloids and Surfaces A: Physicochem. Eng. Aspects* **2008**, *321*, 94-98.

(70)   Takagi, H.; Mikata, Y.; Ichimura, A.; Yano, T.; Kinoshita, I.; Horic, M.; Collins, T. J.; Gottschaldt, M.; Yano, S. *Electrochimica Acta* **2009**, *54*, 1286–1291.

(71)   Zhang, Y.; Tong, Y.; Abe, M.; Uosaki, K.; Osawa, M.; Sasakiab, Y.; Ye, S. *J. Mater. Chem.* **2009**, *19*, 261–267.

(72)   Zhao, W.; Tong, B.; Pan, Y.; Shen, J.; Zhi, J.; Shi, J.; Dong, Y. *Langmuir* **2009**, *25*, 11796–11801.

(73)   Leea, D. Y.; Leea, M.-S.; Lima, I.; Kangb, S. H.; Nahc, Y.-C.; Leea, W.; Han, S.-H. *Applied Surface Science* **2011**, *257*, 9879– 9884.

(74)   Luo, L.; Benameur, A.; Brignou, P.; Choi, S. H.; Rigaut, S.; Frisbie, C. D. *J. Phys. Chem. C* **2011**, *115*, 19955–19961.

(75)   Dennany, L.; Keyes, T. E.; Forster, R. J. *Analyst* **2008**, *133*, 753–759.

(76)   Bayly, S. R.; Gray, T. M.; Chmielewski, M. J.; Davis, J. J.; Beer, P. D. *Chem. Commun.* **2007**, 2234–2236.

(77)   Gulino, A.; Gupta, T.; Altman, M.; Schiavo, S. L.; Mineo, P. G.; Fragala, I. L.; Evmenenko, G.; Duttad, P.; van der Boom, M. E. *Chem. Commun.* **2008**, 2900–2902.

(78)   Tuccitto, N.; Delfanti, I.; Torrisi, V.; Scandola, F.; Chiorboli, C.; Stepanenko, V.; Wurthner, F.; Licciardello, A. *Phys. Chem. Chem. Phys.* **2009**, *11*, 4033– 4038.

(79) Mori, K.; Tottori, M.; Watanabe, K.; Che, M.; Yamashita, H. *J. Phys. Chem. C* **2011**, *115*, 21358–21362.

(80) Murray, N. S.; Jarvisbc, S. P.; Gunnlaugsson, T. *Chem. Commun.* **2009**, 4959–4961.

(81) Clemente-Leon, M.; Coronado, E.; Lopez-Munoz, A.; Repetto, D.; Konya, T. T.; Yamase, T.; Edwin C. Constable; Housecroft, C. E.; Doyle, K.; Graber, S. *Langmuir* **2010**, *26*, 1316-1324.

(82) Tsuboi, T.; Murayama, H.; Penzkofer, A. *Appl. Phys. B* **2005**, *81*, 93-99.

(83) Vecchi, A.; Gatto, E.; Floris, B.; Conte, V.; Venanzi, M.; Nemykin, V. N.; Galloni, P. *Chem. Commun.* **2012**, *48*, 5145–5147.

(84) Ramirez, A. D. J. M.; Murillo, A. G. A.; Romo, F. D. J. C.; Hernández, M. G. A.; Rosa, E. d. l.; Palmerin, J. M. *J Sol-Gel Sci Technol* **2011**, *58*, 366.

(85) Szejtli *J. Chem. Rev.* **1998**, *98*, 1743-1754.

(86) Alston, D.; Lilley, T.; Stoddart, J. F. *J. Chem. Soc. Chem. Commun.* **1985**, 1602-1604.

(87) Haider, J. M.; Pikramenou, Z. *Chem. Soc. Rev.* **2005**, *34*, 120-132.

(88) Deschenaux, R.; Ruch, T.; Deschenaux, P. F.; Juris, A.; Ziessel, R. *Helv. Chim. Acta* **1995**, *78*, 619-628.

(89) Armspach, D.; Matt, D.; Harriman, A. *Eur. J. Inorg. Chem.* **2000**, 1147-11450.

(90) Harada, A. *Acc. Chem. Res.* **2001**, *34*, 456-464.

(91) Nelissen, H. F. M.; Schut, A. F. J.; Venema, F.; Feiters, M. C.; Nolte, R. J. M. *Chem. Commun.* **2000**, 577-578.

(92) Venema, F.; Nelissen, H. F. M.; Berthault, P.; Birlirakis, N.; Rowan, A. E.; Feiters, M. C.; Nolte, R. J. M. *Chem.-Eur. J.* **1998**, *4*, 2237-2250.

(93)   Nelissen, H. F. M.; Feiters, M. C.; Nolte, R. J. M. *J. Org. Chem.* **2002**, *67*, 5901-5906.

(94)   Nelissen, H. F. M.; Kercher, M.; De Cola, L.; Feiters, M. C.; Nolte, R. J. M. *Chem.-Eur. J.* **2002**, *8*, 5407-5414.

(95)   Haider, J. M.; Williams, R. M.; De Cola, L.; Pikramenou, Z. *Angew. Chem., Int. Ed.* **2003**, *42*, 1830-1833.

(96)   Faiz, J. A.; Williams, R. M.; Silva, M. J. J. P.; De Cola, L.; Pikramenou, Z. *J. Am. Chem. Soc.* **2006**, *128*, 4520-4521.

(97)   Faiz, J. A.; Kyllonen, L. E. P.; Conteras-Carballda, P.; Williams, R. M.; De Cola, L.; Pikramenou, Z. *Dalton Trans.* **2009**, 3980–3987.

(98)   Rojas, M. T.; Koniger, R.; Stoddart, J. F.; Kaifer, A. E. *J. Am. Chem. Soc.* **1995**, *117*, 336-343.

(99)   Willner, I.; Pardo-Yissar, V.; Katz, E.; Ranjit, K. T. *J. Electroanal. Chem.* **2001**, *497*, 172-177.

(100)   Mallon, C. T.; Forster, R. J.; McNally, A.; Campagnoli, E.; Pikramenou, Z.; Keyes, T. E. *Langmuir* **2007**, *23*, 6997-7002.

(101)   Mallon, C. T.; McNally, A.; Keyes, T. E.; Forster, R. J. *J. Am. Chem. Soc.* **2008**, *130*, 10002-10007.

(102)   Nishimura, D.; Takashima, Y.; Aoki, H.; Takahashi, T.; Yamaguchi, H.; Ito, S.; Harada, A. *Angew. Chem., Int. Ed.* **2008**, *47*, 6077-6079.

(103)   Kyllönen, L. E. P.; Chinuswamy, V.; Maffeo, D.; Kefalas, E. T.; Haider, J. M.; Pikramenou, Z.; Mavridis, I. M.; Yannakopoulou, K.; Glezos, N. *J. Phys. Org. Chem.* **2012**, *25*, 198 – 206.

CHAPTER 2

General Experimental

2.1. Materials and Methods

All materials were purchased from Sigma-Aldrich or Fisher unless noted. $RuCl_3 \cdot xH_2O$ was supplied by Alfa Aesar (Johnson-Matthey). Solvents were purchased from Sigma-Aldrich or Fisher. Deuterated solvents were purchased from Goss Scientific or Sigma-Aldrich and used as received. HPLC grade solvents were used in photophysical studies. Water was deionised using an Elga Option 3 water purifier. Dry DMF was prepared by degassing of technical grade DMF under nitrogen further stored over 3 Å molecular sieves. Column chromatography was performed using silica gel 0.035-0.070 nm, 60 A (Acros) and thin layer chromatography (TLC) was performed on silica gel 60 F_{254} (Macherey-Nagel). All reactions were performed under dinitrogen with degassed anhydrous solvents unless indicated, using standard Schlenk and high vacuum techniques.

^1H, ^{13}C and 2D NMR spectra were obtained using Brüker AC 300, AVIII 300 or AVIII 400 spectrometers. FTIR spectra were collected on a Perkin Elmer Spectrum 100

FTIR spectrometer. Electrospray mass spectra were recorded on a Micromass LC-TOF machine. MALDI mass spectrometry was carried out on a Micromass MX MALDI-TOF. Elemental analyses were recorded on a Carlo Erba EA1110 Simultaneous CHN elemental analyser at the University of Birmingham, U.K.

2.2. X-Ray Crystallography

Suitable crystals were selected and datasets were measured on a Bruker SMART 6000 diffractometer ($\lambda_{Cu-K\alpha}$ = 1.5418 Å) for **[Ru(bpy)$_2$(4,4'-bpyhex)](PF$_6$)$_2$** and on a Bruker APEXII CCD diffractometer at the window of a Bruker FR591 rotating anode ($\lambda_{Mo-K\alpha}$ = 0.71073 Å) for **[Os(bpy)$_2$(4,4'-bpyhex)](PF$_6$)$_2$, [Os(bpy)$_2$(4,4'-bpysac)](PF$_6$)$_2$** and **[Ru(bpy)(4,4'-bpyhex)$_2$](PF$_6$)$_2$**. The data collection was driven by SMART[1] and processed by SAINTPLUS[2] for **[Ru(bpy)$_2$(4,4'-bpyhex)](PF$_6$)$_2$**, were driven by COLLECT[3] and were processed by DENZO[4] for **[Os(bpy)$_2$(4,4'-bpyhex)](PF$_6$)$_2$, [Os(bpy)$_2$(4,4'-bpysac)](PF$_6$)$_2$** and **[Ru(bpy)(4,4'-bpyhex)$_2$](PF$_6$)$_2$**. Absorption corrections were applied using SADABS[5] for all compounds. The structures of **[Ru(bpy)$_2$(4,4'-bpyhex)](PF$_6$)$_2$** and **[Os(bpy)$_2$(4,4'-bpyhex)](PF$_6$)$_2$** were solved using ShelXS-97[6] and of **[Os(bpy)$_2$(4,4'-bpysac)](PF$_6$)$_2$** and **[Ru(bpy)(4,4'-bpyhex)$_2$](PF$_6$)$_2$** by SIR92[7] and all structures were refined by a full-matrix least-squares procedure on F^2 in ShelXL-97.[6] All non-hydrogen atoms were refined with anisotropic displacement parameters. All hydrogen atoms were added at calculated positions and refined by use of a riding model with isotropic displacement parameters

based on the equivalent isotropic displacement parameter (U_{eq}) of the parent atom. Figures were produced using OLEX2.[8] The UK National Crystallography Service are acknowledged for X-ray diffraction data collections for compounds **[Os(bpy)$_2$(4,4'-bpysac)](PF$_6$)$_2$**, **[Os(bpy)$_2$(4,4'-bpyhex)](PF$_6$)$_2$** and **[Ru(bpy)(4,4'-bpyhex)$_2$](PF$_6$)$_2$**.

2.3. Photophysical studies

UV-Vis spectroscopy was carried out on a Varian Cary 50 or Cary 5000 spectrophotometer. UV-Vis spectra of solution samples were collected using 1 cm path length quartz cuvettes. UV-Vis spectra of powders were obtained by an integrating sphere attachment in reflectance mode. UV-Vis spectra of gold surfaces were recorded by placing glass slides coated with 30 nm polycrystalline gold at the normal to the plane of the beam source in transmission mode.

Steady-state luminescence experiments were carried out using a PTI fluorescence system. A PTI L-210M using a 75 W xenon arc lamp was employed as the illumination source. The visible detection arm used a Shimadzu R298 PMT in a PTI model 814 analogue/photon-counting multiplier. The visible emission monochromator was equipped with interchangeable 500 nm and 750 nm blazed gratings. Spectra were recorded using PTI Felix fluorescence analysis software. Luminescence spectroscopy was also carried out on an Edinburgh Instruments 7 FLSP920 Steady State, Fluorescence and Phosphorescence Lifetime Spectrometer fitted with an Olympus IX71 inverted microscope. The illumination source uses a 450 W xenon arc

lamp. The detection system used was a Hamamatsu R928 PMT. The emission monochromator is fitted with two interchangeable gratings blazed at 500 nm and 1200 nm. F900 spectrometer analysis software was used to record the data. Emission lifetimes were recorded using 445 and 375 nm picosecond pulsed diode LASERs or 100 W μF920H lamp with a time-correlated single photon counting method using Edinburgh Instruments F900 v6.8 PC Software using the exponential tail fit option. Luminescence imaging was executed with the FLS920 spectrometer, fitted with an Olympus IX71 inverted microscope and a 510 nm dichroic filter. Appropriate long pass filters were used in every experiment.

Luminescence experiments for solution samples were carried out using 1 x 1 cm path length quartz cuvettes with four transparent polished faces. Degassed samples were obtained by bubbling nitrogen through the cuvettes for 10 – 20 minutes. In order to collect the emission spectra of gold surfaces, glass slides coated with 30 nm polycrystalline gold were placed at an angle of 90° from the detector. Powder samples were measured using a solid state attachment angled 45° from detector and lamp.

Quantum yields of solution samples were measured using the optically dilute relative method using the equation below:[9]

$$\Phi_x = \Phi_r \left(\frac{A_r(\lambda_r)}{A_x(\lambda_x)} \right)\left(\frac{I(\lambda_r)}{I(\lambda_x)} \right)\left(\frac{n_x^2}{n_r^2} \right)\left(\frac{D_x}{D_r} \right)$$

Where Φ_x is the quantum yield of the lanthanide complex, Φ_r is the quantum yield of reference, $A(\lambda)$ is the absorbance of samples at excitation wavelength λ, $I(\lambda)$ the relative intensity of exciting light at wavelengths λ, n the refractive index of the

solvent in question and D the integrated area of the emission spectrum for sample and reference (corrected for PMT response). Ruthenium(II) tris-bipyridine chloride in aerated water (Φ = 0.028)[10] was used as standard for quantum yield measurement. Absolute quantum yield of powders and gold surfaces was measured using an integrating sphere attachment on Edinburgh Instruments FLS920.

2.4. Self-assembled Monolayers

Polycrystalline gold with 30nm thickness on 100- 4 inch-silicon wafer, pre-coated with titanium (rms-roughness < 1nm), has been purchased from Georg Albert PVD-Beschichtungen. Planar gold surfaces were cleaned with either cold piraña (H_2SO_4/H_2O_2 70:30) solution for 10 minutes followed by rinsing with Millipore H_2O and HPLC grade ethanol and drying with gentle N_2 (g) flow before use, or with UV-ozone radiation for 1 hour. For ellipsometry experiments, contamination of each surface was recorded immediately after cleaning the substrates and the data used as a background when measuring the thickness of the SAM. All solvents used in surface studies were HPLC grade, except water which was Millipore quality (resistivity 18 mΩ).

The gold substrates were inserted into the 1 mM solution of metal complexes in CH_3CN for 24 hours. The unbound materials were removed by insertion of the substrates in to CH_3CN for short period of time (typically 10 - 15 minutes) and the substrates were dried under nitrogen.

Ellipsometry measurements to determine the apparent thickness of the thin films used were performed using a multi-spectroscopic ellipsometer (Horiba Jobin-Yvon) uvisel operating with DeltaPsi2 v2.0.8 software. The collision between the analyser and the polariser was set to the angle of 70$^\text{o}$ and was maintained the same for all measurements. The light wavelength range of 250-800 nm and ambient temperature, pressure and humidity conditions were applied in all measurements. Film thicknesses are results of an average of minimum three measurements of different locations on the substrate. It was avoided to perform measurements on visibly defective locations of the sample. For each measurement, mathematical calculations of the SAM thickness, based on a three-phase ambient/SAM/Au model, were performed in which the SAM was assumed to be isotropic. Background ellipsometry readings for the clean Au substrate for each sample were used as the respective underlying Au layer. The SAM was modeled using a Classical layer with initial thickness resulted from using a multiguess iterative calculation procedure. The outcome of each iteration process was the number with the lowest χ^2 which is a measure of the agreement between the modeling process and the experimentally obtained data. Lower χ^2 values indicate better agreement between model and data. The average of those results with the lowest χ^2 for each measurement, were used as the final SAM thickness. All errors presented are the standard error of the mean SAM thickness.

X-ray photoelectron spectroscopy (XPS) measurements were performed on a Kratos Axis Ultra-DLD photoelectron spectrometer, utilising monochromatic Al kα radiation (photon energy 1486.6 eV) at a power of 144W (12 mA emission at 12 kV). Charge neutralisation for non-conducting samples was performed using an immersion lens system typically and spectra subsequently calibrated to the Au(4f) peak at 84 eV for

the gold film supports or the C(1s) peaks. Spectra were collected at pass energies of 40 and 160 eV for high resolution and survey scans respectively using the hybrid spectroscopy mode over an area of approximately 400x300 microns. Spectra were processed using CasaXPS software using sensitivity factors supplied by the instrument manufacturer.

2.5. References

(1)   SMART*, program for instrument control and data acquisition* **1997**, *Bruker AXS, Inc. 5465 East Cheryl Parkway, Madison, Wisconsin 53711-5373, USA*.

(2)   SAINTPLUS*, program suite for data processing* **1997**, *Bruker AXS, Inc. 5465 East Cheryl Parkway, Madison, Wisconsin 53711-5373, USA*.

(3)   Hooft, R. W. W. *COLLECT Data Collection Software* **1998**, *Nonius B. V., Delft*.

(4)   Otwinowski, Z.; Minor, W. *Methods in Enzymology* **1997**, *ed. C. W. Carter and R. M. Sweet, Academic Press, New York, 276, 307-326.*

(5)   Sheldrick, G. M. *SADABS* **2007**, *Bruker AXS Inc., Madison, Wisconsin, USA*.

(6)   Sheldrick, G. M. *Acta Cryst.* **2008**, *A64*, 112-122.

(7)   Altomare, A.; Cascarano, G.; Giacovazzo, C.; Guagliardi, A.; Burla, M. C.; Polidori, G.; Camalli, M. *J. Appl. Crystallogr.* **1994**, *27*, 435-388.

(8)   Dolomanov, O. V.; Bourhis, L. J.; Gildea, R. J.; Howard, J. A. K.; Puschmann, H. *J. Appl. Crystallogr.* **2009**, *42*, 339-341.

(9)   Demas, J. N.; Crosby, G. A. *J. Phys. Chem.* **1971**, *75*, 991-1024.

(10)   Nakamaru, K. *Bull. Chem. Soc. Jpn.* **1982**, *55*, 2697.

CHAPTER 3

Bipyridine Ruthenium and Osmium Complexes for Surface Attachment

3.1. Introduction

Crossing over from solution to solid state is one of the essential steps for building molecular based devices. In order to move from disordered solid samples to organised monolayers, it is necessary to assemble the molecules, via covalent or non-covalent interactions, on a substrate and to study their properties at this inter-face. Molecular monolayers and thin films have been the subject of extensive research as reviewed in chapter 1.

Amongst all materials, transition metal photoactive complexes which are able to give strong emission have attaracted particular attentions. Monolayers of such photoactive molecules on metal surfaces have been used to develop molecular devices[1-3], nanowire transitor[4,5] or sensors[6], and are able to mimic natural light harvesting and charge separation[7]. Ruthenium (II) and osmium (II) complexes containing polypyridine ligands are good candidates for such applications because of their rich redox and photophysical properties such as high absorption in the

visible region, luminescent and long-lived excited states (^{3}MLCT) and reversible redox-properties[8].

Although ruthenium (II) and osmium (II) polypyridine complexes are extensively studied for their solution luminescence and redox behaviour, there are only few reports of complexes developed for gold and platinium surfaces. The attachment of thiol-functionalised ruthenium complexes to surfaces such as gold[9-11] and platinum[12,13] have been reported but there is little information on the quality of the packing, the distance between the chromophore (metal center) and the surface, the coverage and the stability of the surface. Furthermore, a good understanding and correlation between the above mentioned parameters, and the influence of the metal surfaces, on the photophysical properties of complexes is lacking. Based on a study of a self-assembled monolayer (SAM) of a fluorescent thiol molecule (BodipyC10SH) on an Au surface, it is predicted that metallic surfaces could quench the emission of attached molecules by energy transfer and/or electron transfer from the luminophore to the surface.[14] On the other hand, studies on fluorescent dyes showed that these surfaces can induce an emission enhancement[15,16].

Here we report the synthesis and photophysical properties of six novel ruthenium and osmium trisbipyridine complexes in which the one or two bipyridine ligands have alkyl chains either in the 4,4'-positions or 3,3'-positions, terminated with protected thiol groups (SAc) (Scheme 3.1). These positions were simply chosen to afford a proper orientation of the complexes in order to attach on the surfaces. Later we found out that the attachment of the aliphatic spacers in the 4,4'-positions provides better photophysical properties of the ruthenium and osmium complexes both in solution and on surface. Based on previous work in the group on surface

active bipyridine ligands it was understood that a surface active bipyridine with longer spacers would help enhance the photophysical properties for the ruthenium bipyridine core attached onto the surface.[12,17] This could be achieved simply by increasing the distance from the surface, using the alkyl chains as spacers, and subsequently decreasing the luminescence quenching induced by the surface. The spacer needs to be long enough to stop the quenching but not too long to allow the attached complex to wobble on the surface and consequently make an unorganised monolayer. We chose a commercially available six member aliphatic chain as the spacer with the length of about 9 Å.
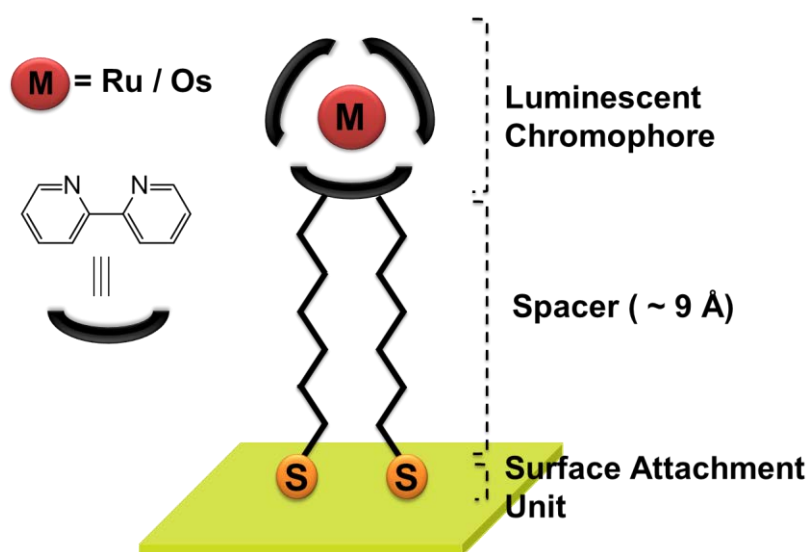
Scheme 3.1 Design of surface-active Ru (II) and Os (II) tris-bipyridine complexes.

We also report ruthenium complexes with two modified ligands in either 3,3'-positions or 4,4'-positions, [Ru(bpy)(3,3'-bpysac)$_2$](PF$_6$)$_2$ and [Ru(bpy)(4,4'-bpysac)$_2$](PF$_6$)$_2$, which carry four long chains with surface binding moieties (Scheme 3.2). It was shown that these complexes have stronger attachments to the gold

surface and consequently introduce better photophysical properties on the surface. The surface properties of the complexes were investigated by different techniques such as X-ray photoelectron spectroscopy, ellipsometry and FTIR spectroscopy. Furthurmore the photophysical properties of these complexes and the corresponding functionalised surfaces have been studied using emission spectroscopy and time resolved confocal microscopy. For the first time we were able to record emission of the osmium tris-bipyridine complexes on the gold surface.

We also synthesised a ruthenium tris-phenanthroline complex in which one of the phenanthroline ligands has long alkyl chains in the 4,7-positions. The photophysical properties of this complex were investigated in acetonitrile solution. The development of photochemical molecular devices with ligands of the 1,10-phenanthroline type (phen) has been investigated extensively and some of their ruthenium complexes have been used as luminescent probes for DNA (DNA sensors).[18,19] Initially the complex [Ru(phen)$_2$(4,7-phenhex)](PF$_6$)$_2$ was synthesised for use as a surface active probe, but as the photophysical properties of the complex was very close to the similar complex with the bipyridine units, no further investigations were carried out. However this complex has the potential to be attached to the nanoparticles and can be used as a sensor in biological systems especially to interact with DNA.
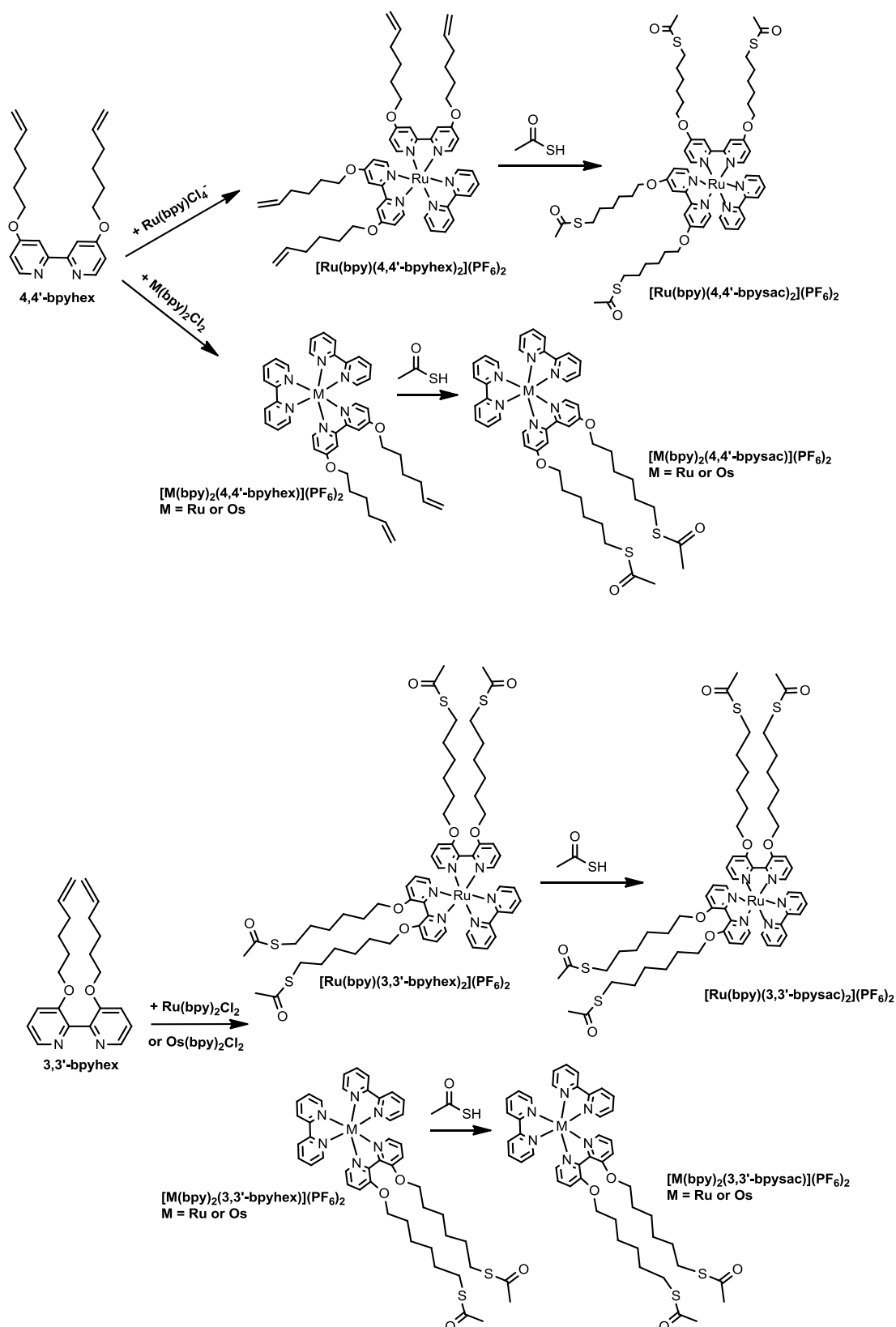
Scheme 3.2 molecular structure of Ru (II) and Os (II) tris-bipyridine complexes discussed in this chapter.

3.2. Results and discussion

3.2.1. Synthesis of modified bipyridine ligands, 3,3'-bpyhex and 4,4'-bpyhex

The scheme 3.3 shows the overall synthetic route of the modified ligands bearing long alkyl subsituents in 3,3'-positions of the bipyridine units.
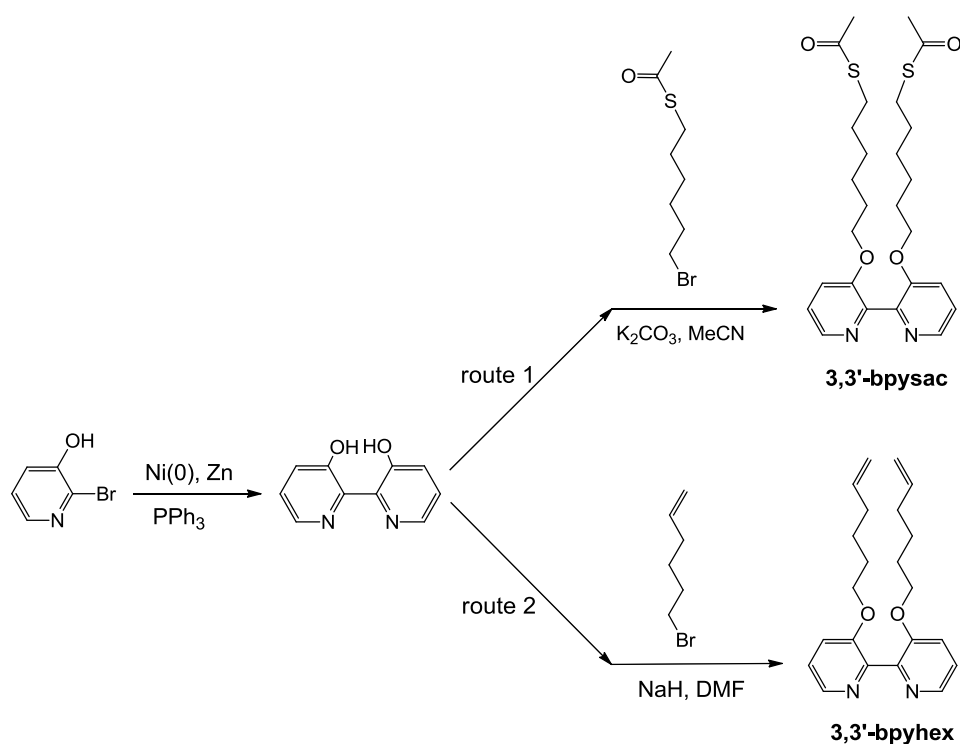
Scheme 3.3 Synthetic routes to 3,3'-bpysac and 3,3'-bpyhex.

The compound 3,3'–dihydroxy-2,2'–bipyridine was synthesised by reacting 2-bromo-3-hydroxy pyridine with $Ni^0/Zn/PPh_3$ (39 % yield).[20] It was characterised by ^1H and ^{13}C NMR spectroscopy and all the data were in agreement with

literature[21,22]. Preparation of dihydroxybipyridines has been examined previously by aryl coupling using the phenol oxidation of 3-hydroxypyridines, which gave very poor yields.[21] Therefore, a reductive organometallic coupling of 2-bromo-3-hydroxypyridines became an attractive way to synthesise this type of compound.[20] As the isolated yield of the product was low due to further reaction of the dihydroxybipyridine, the compound was protected by metal complexation of Ni^0. Thus it was prepared by the reduction of Ni^{II} with Zn in the presence of triphenylphosphine.[23,24] Several attempts were carried out in order to improve the yield and finally modification of the published purification procedure gave us reasonable yield. It was realized that the pH control during acidification has an important role in improving the amount of precipitation.

Initially the synthesis of 3,3'-bpysac as a ligand with long alkyl chains attachments for the preparation of ruthenium and osmium complexes, [Ru(bpy)$_2$(3,3'-bpysac)](PF$_6$)$_2$, [Os(bpy)$_2$(3,3'-bpysac)](PF$_6$)$_2$ was targeted. The compound 3,3'-bpysac was prepared following route 1 in Scheme 3.3 in two steps. In first step, 6-(thioacetoxy)- bromohexane was synthesised in quantitative yield by reacting 6-bromo-hex-1-ene and thioacetic acid in dry toluene[25] and in the final step Williamson ether conditions were employed to obtain the targeted 3,3'-bpysac. In the previous preparation method in our group,[17] the ligand had been synthesised in a small scale and the crude product had been purified with analytical HPLC on reverse phase silica eluting with a H$_2$O/MeOH gradient. However upon moving to a larger scale and using the preparative HPLC, the separation was not successful. Normal column chromatography on silica using DCM/MeOH [gradiant of MeOH from 1% to 10%] as eluent afforded the compound in small yield, 22 mg (8 %) of

3,3'-bpysac as an orange solid. As the yield was low and purification methods were also demanding, the synthetic path was altered by introducing the SAc group after formation of the complexes and synthesis of the 3,3'-bpyhex ligand (Scheme 3.3, route 2).

The 3,3'-bpysac showed characteristic peaks in electrospray mass spectrum corresponding to $[M + H]^+$ (505.1) and $[M + Na]^+$ (527.0). The ligand 3,3'-bpySAc, has been fully characterised by FTIR, ^{1}H NMR and ^{13}C NMR spectroscopy. The FTIR spectrum of the ligand showed a strong band at 1685 cm^{-1} which is characteristic of the stretch of the carbonyl group. In the ^{1}H NMR spectrum, the ether formation was confirmed by H_7 shift from 3.4 ppm in 6-(thioacetoxy)-bromohexane to 3.8 ppm in 3,3'-bpySAc and the hydrogen of the SAc group (H_{14}) which appears as a singlet in 2.1 ppm (Figure 3.1).
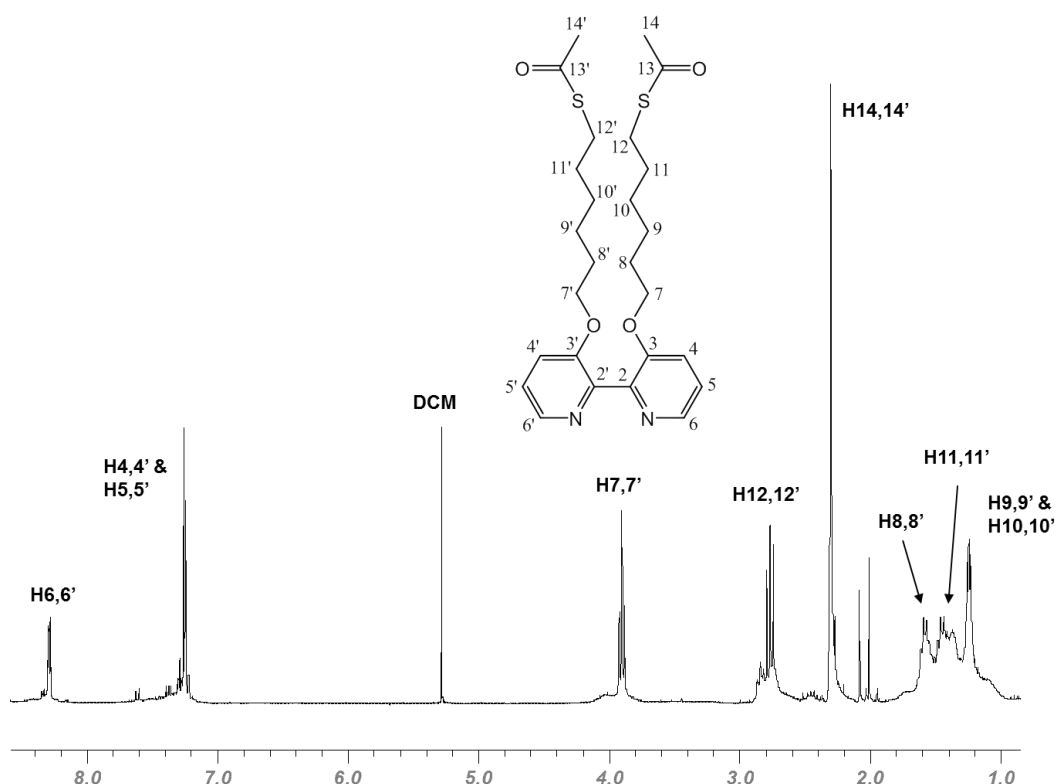
Figure 3.1 300 MHz ^{1}H NMR spectrum of 3,3'-bpysac (CDCl$_3$).

Williamson ether conditions were employed to synthesise 3,3'-bpyhex (Scheme 3.3). In the absence of the sensitive thioacetoxy group (SAc) a stronger base was used which improved the yield to 27% and the time of the reaction was decreased.

The ligand showed characteristic peaks in electrospray mass spectra corresponding to [M + H]$^+$ (353.6) and [M + Na]$^+$ (375.6). The ligand 3,3'-bpyhex has also been fully characterised by FTIR, ^{1}H and ^{13}C NMR spectroscopy. In the ^{1}H NMR spectrum, the signature of the 3,3'-bpyhex ligand is given by the two distinct areas of signals, one for the aromatic peaks arising from the bipyridine unit (integrating for 6 H) and the second one from the aliphatic peaks arising from the alkyl substituents attached on the 3,3' position (integrating for 22 H) (Figure 3.2). The shift for H$_7$ from 3.4 ppm

in 6-(thioacetoxy)- bromohexane to 3.9 ppm in the ligand confirms the ether formation of desired compound. In the ^{13}C NMR spectrum the obvious shift of C_7 from 34.0 ppm in 6-(thioacetoxy)- bromohexane to 72.4 ppm in the ligand again confirms etherification (Figure A3.5). In the aliphatic region, H_{11} and H_{12} which are characteristic for the double bond in 3,3'-bpyhex, are clear in the ^{1}H NMR spectrum. H_{11} appears as a triplet of doublets of doublets at 5.56-5.70 ppm, the triplet is from two hydrogens of H_{10} and two doublets are a result of gem coupling effect of cis and trans hydrogens of H_{12} position. H_{12} is clear as a multiplet at 4.87 ppm.
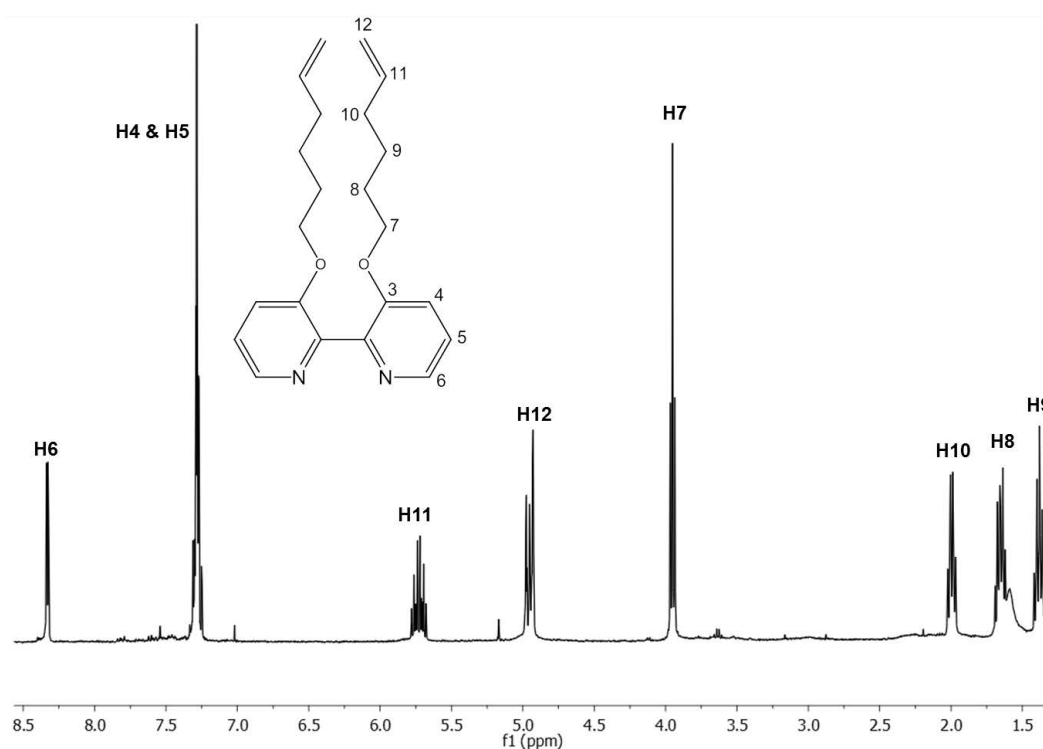
Figure 3.2 300 MHz ^{1}H NMR spectrum of 3,3'-bpyhex (CDCl$_3$).

Similarly, Williamson ether conditions were employed to synthesise the ligand 4,4'-bpyhex. The 4,4'- dihydroxy-2,2'-bipyridine was prepared by ether cleavage of commercially available 4,4'-methoxy-2,2'-bipyridine with 90% yield, and was characterised by ^{1}H NMR and mass spectrometry which were in agreement with the published data.[26]
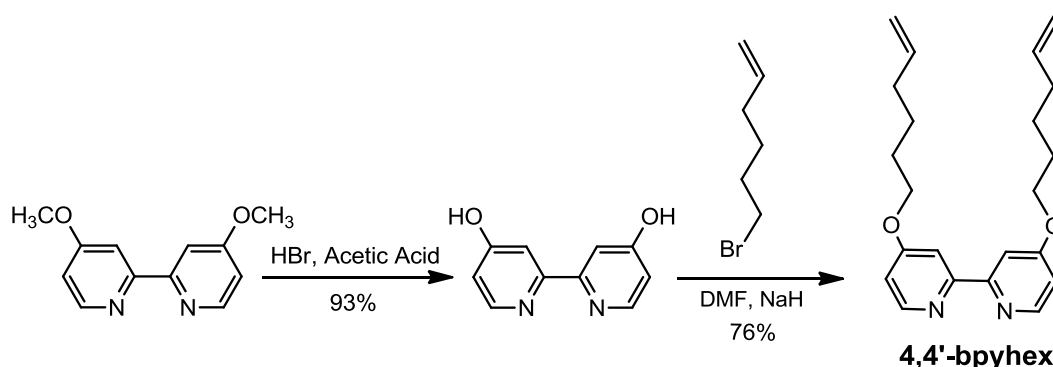
Scheme 3.4 Synthesis of 4,4'-bpyhex and the corresponding metal complexes.

The ^{1}H NMR spectrum of 4,4'-bpyhex shows the typical pattern in the aromatic region of a bipyridine unit substituted at the 4,4'-position, with the aliphatic region displaying signals that are a signature of the attached hexene chain. The shift for H_7 from 3.4 ppm in 6-bromo-1-hexene to 4.3 ppm in the ligand and shift of C_7 from 34.0 ppm in 6-(thioacetoxy)- bromohexane to 67.8 ppm confirms the formation of desired ether compounds (Figure 3.3). The formation of the 4,4'-bpyhex was also confirmed by electrospray mass spectrometry showing the peaks corresponding to $[M+H]^+$ (353.4) and $[M+Na]^+$ (375.4).
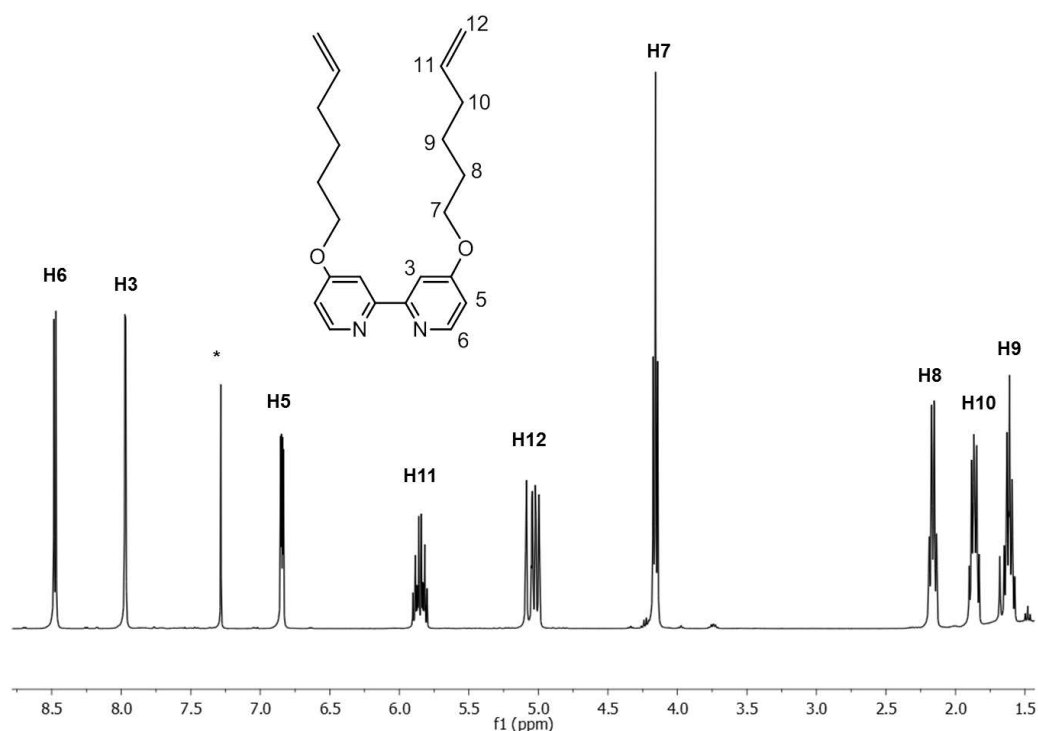
Figure 3.3 300 MHz ^{1}H NMR spectrum of 4,4'-bpyhex (CDCl$_3$).

3.2.2. Synthesis of surface active tris-bipyridine ruthenium (II) and osmium (II) complexes, [M(bpy)$_2$(3,3'-bpysac)]$^{2+}$, [M(bpy)$_2$(4,4'-bpysac)]$^{2+}$, [Ru(bpy)(3,3'-bpysac)$_2$]$^{2+}$ and [Ru(bpy)(4,4'-bpysac)$_2$]$^{2+}$, (M = Ru/ Os)

The first step toward the synthesis of the surface active tris-bipyridine ruthenium (II) complexes is the preparation of Ru(bpy)$_2$Cl$_2$. The complex Ru(bpy)$_2$Cl$_2$ .2H$_2$O was prepared following two different procedures. In an initial attempt a reaction following the procedure of Meyer *et al.* was carried out[27,28] and produced 60%

Ru(bpy)$_2$Cl$_2$.2H$_2$O after washing the precipitate with water and diethyl ether which removed any impurities of Ru(bpy)$_3$Cl$_2$.
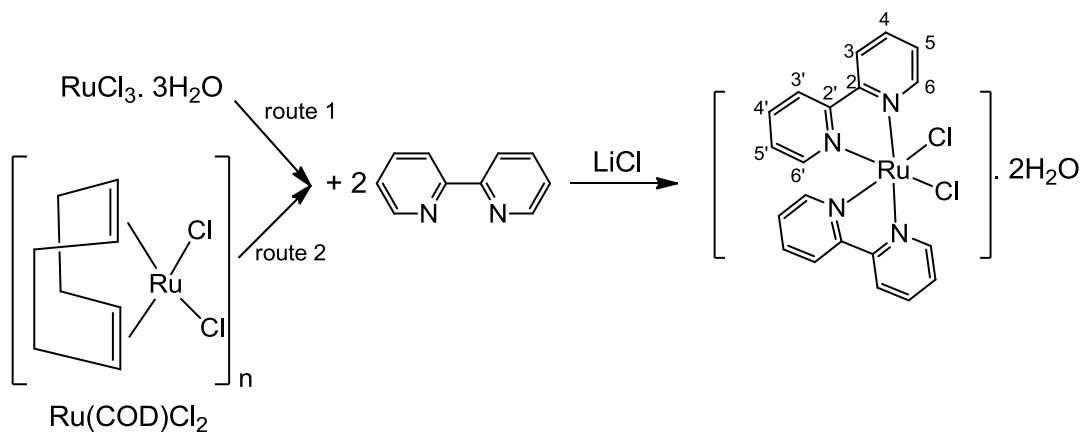
Scheme 3.5 Synthetic routes to Ru(bpy)$_2$Cl$_2$ .2H$_2$O.

The product was identified by its characteristic absorption spectrum which shows MLCT bands at 550 nm and 375 nm and an intense π-π^* band at 300 nm.[27,29]
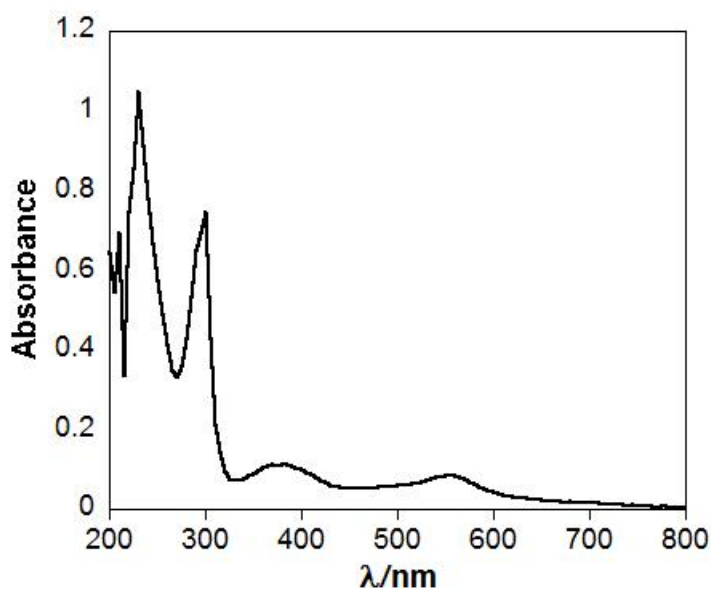
Figure 3.4 Absorption spectrum of Ru(bpy)$_2$Cl$_2$ in DCM.

The preserence of [Ru(bpy)(3,3'-bpyhex)$_2$](PF$_6$)$_2$ which contains two 3,3'-bpyhex ligands in the next step identified the formation of a large amount of impurity of [Ru(bpy)Cl$_4$]$^{2-}$ in the Ru(bpy)$_2$Cl$_2$ prepared by route 1 method. For this reason, a relatively new procedure was adopted which originally was used to synthesise [Ru(phen)$_3$]Cl$_2$.[30] It was followed using polymeric Ru(COD)Cl$_2$ to synthesise the target Ru(bpy)$_2$Cl$_2$ complex.[31] The complex was identified by its characteristic absorption spectrum and characterised by ^{1}H NMR spectrum[32], which was in agreement with literature.
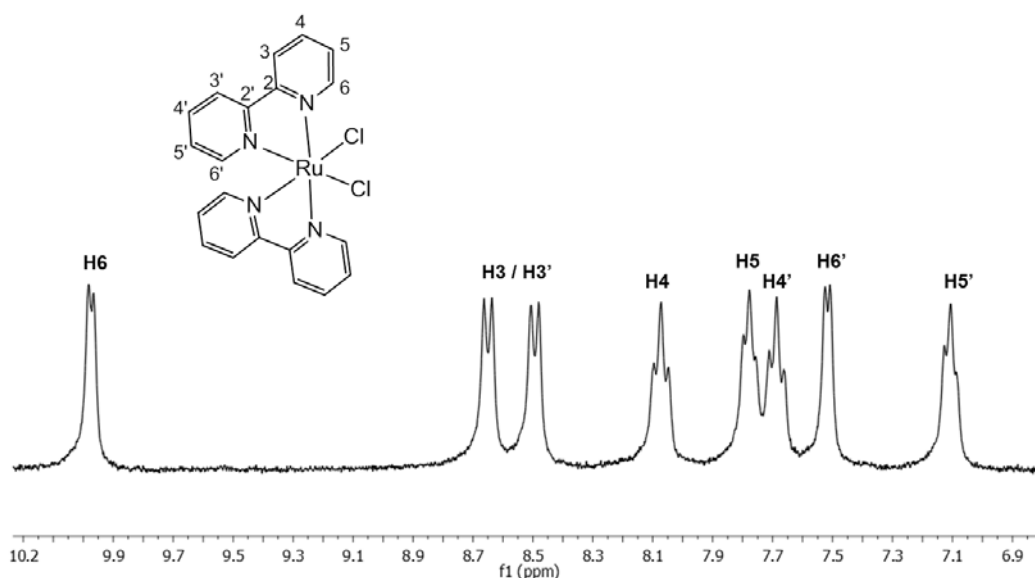
Figure 3.5 300 MHz ^{1}H NMR spectrum of Ru(bpy)$_2$Cl$_2$ (DMSO).

It was discovered that Ru(bpy)$_2$Cl$_2$ can be contaminated by some of the [Ru(bpy)Cl$_4$]$^{2-}$ as the by-product. The [Ru(bpy)Cl$_4$]$^{2-}$ can be also synthesised independently following the published procedure[33] by adding HCl to the solution of the RuCl$_3$.3H$_2$O salt and bipyridine and standing for several days. The resulting

black solid was filtered and used without further purification. The $[Ru(bpy)Cl_4]^{2-}$ is insoluble in most solvents which makes it difficult to characterise. The absorbance spectrum of the partially dissolved complex in MeOH (and 1% DMSO) shows two MLCT bands at 495 and 300 nm and an intense π- π^* band at around 200 nm. There is also a broad band centered at 650 nm which can be assigned to ^{3}MLCT of ruthenium complex.
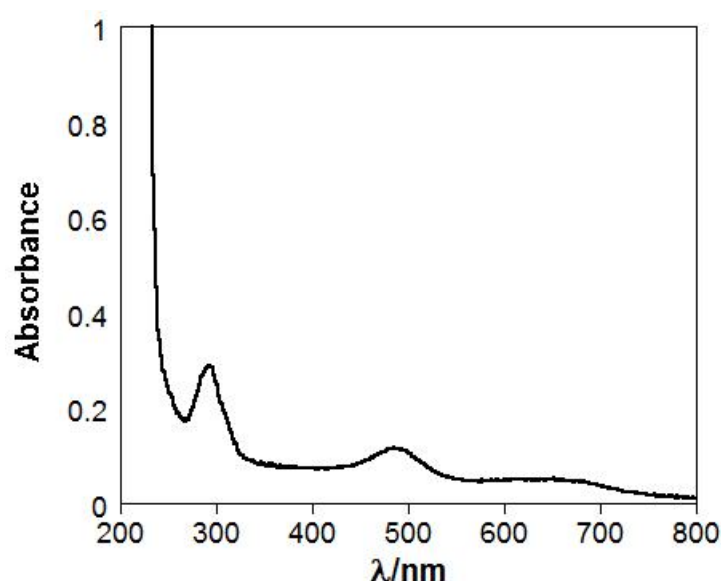
Figure 3.6 Absorption spectrum of Ru(bpy)Cl$_4$$^{2-}$ in MeOH.

Our first approach towards a surface active ruthenium complex involved the reaction of Ru(bpy)$_2$Cl$_2$ with either 3,3'-bpyhex or 4,4'-bpyhex (Scheme 3.6).
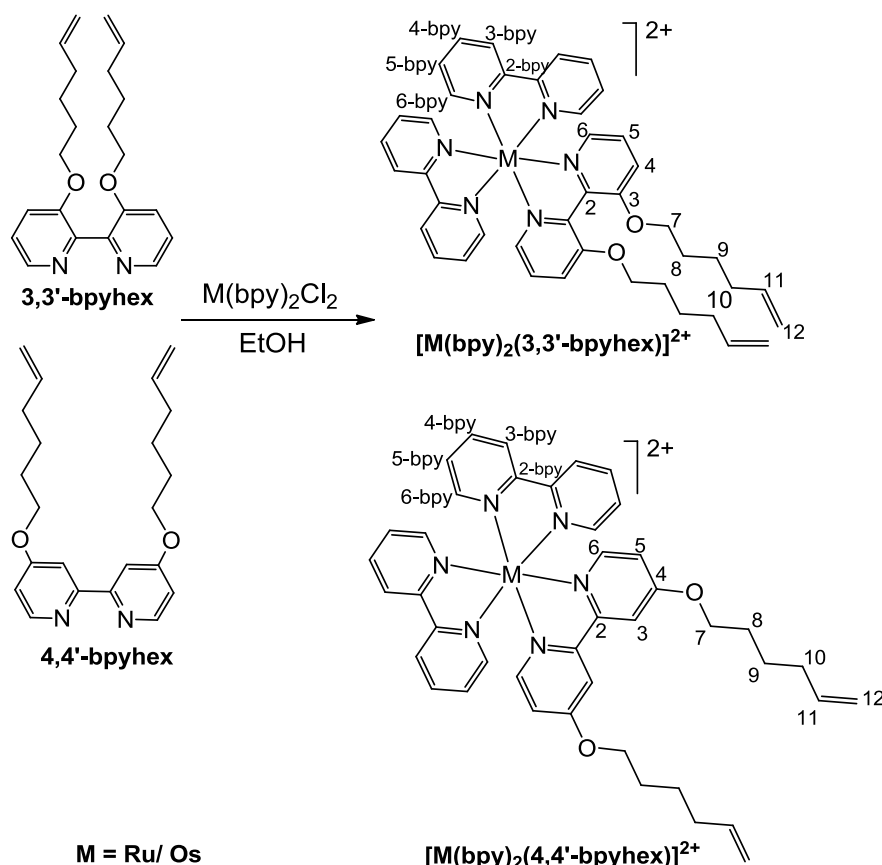
Scheme 3.6 Synthetic route to [M(bpy)$_2$(3,3'-bpyhex)]$^{2+}$ and [M(bpy)$_2$(4,4'-bpyhex)]$^{2+}$

(M = Ru/ Os).

The complex [Ru(bpy)$_2$(3,3'-bpyhex)](PF$_6$)$_2$ was characterised by ^{1}H NMR and ^{13}C NMR spectroscopy, mass spectrometry and FTIR spectroscopy. The electrospray mass spectrum of [Ru(bpy)$_2$(3,3'-bpyhex)](PF$_6$)$_2$ shows a signal at *m/z* 911 which corresponds to {M-[PF$_6$]}$^+$ and 383 for {M-2[PF$_6$]}$^{2+}$. Two-dimensional NMR techniques including COSY and HSQC were employed to allow full assignments of the peaks. In the ^{1}H NMR spectrum, the compound was characterised by two distinct areas of signals, one for the aromatic peaks arising from the bipyridine units (integrating for 22 H) and the second one from the aliphatic peaks arising from the

alkyl substituents of 3,3'-bpyhex (integrating for 22 H). The aromatic region of ^{1}H NMR spectrum contains signals that are assigned to the different ligands by their characteristic multiplicities. The H_{3-bpy} appears as two doublets at 8.49 and 8.51 ppm, which are followed by a multiplet at 8.07 ppm corresponding to H_{4-bpy}. The H_6 of 3,3'-bpyhex ligand shifted from 8.16 ppm in the free ligand to a doublet of doublet at 7.65 ppm in the complex, which shows shielding of the metal and indicates coordination of the third ligand to ruthenium complex (Figure 3.7). Similarly there is also a shift for C_6 in ^{13}C NMR spectrum from 142.2 ppm in free ligand to 122.1 ppm in complex (Figure A3.12). Shifts in the aliphatic region and a change in the multiplicity of H_7 from a triplet in 3.88 ppm in free ligand to a multiple around 4.2 ppm in complex are indicative of the coordination and isomers formed in the octahedral ruthenium complex.
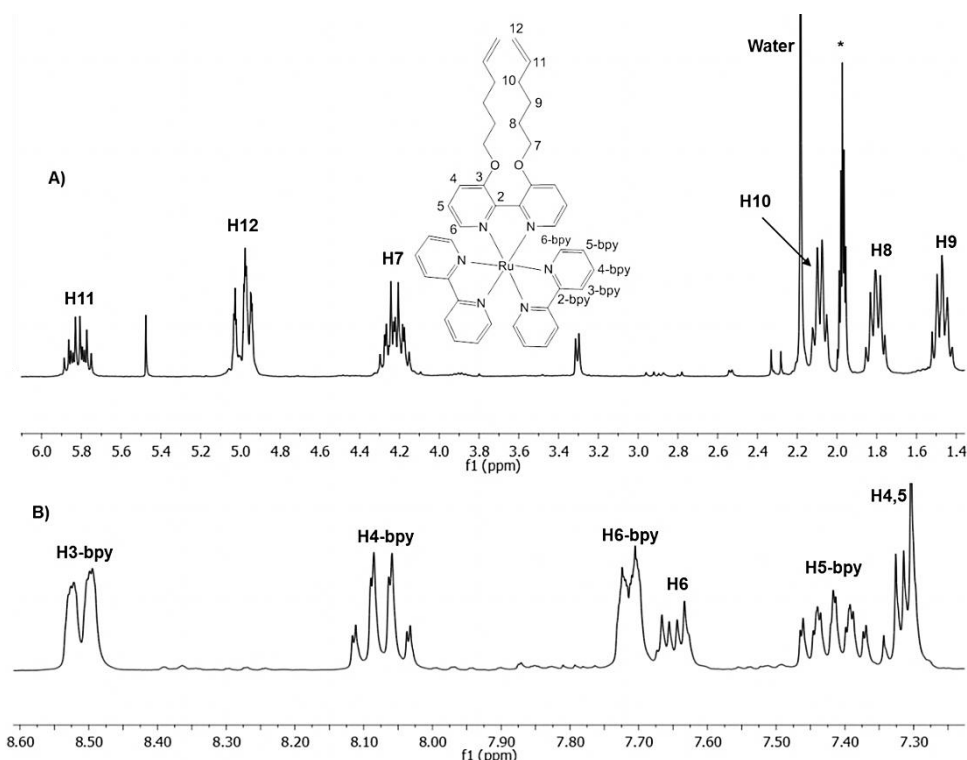
Figure 3.7 300 MHz ^{1}H NMR spectrum of [Ru(bpy)$_2$(3,3'-bpyhex)](PF$_6$)$_2$ A) aliphatic region B) aromatic region (CD$_3$CN).

During the reaction of Ru(bpy)$_2$Cl$_2$ with 3,3'-bpyhex using Ru(bpy)$_2$Cl$_2$ prepared from route 1, [Ru(bpy)(3,3'-bpyhex)$_2$](PF$_6$)$_2$ was also formed which was isolated from the main product by column chromatography on silica using DCM/Isopropanol [98:2] as eluent. The complex was initially characterised by mass spectrometry and UV-Vis spectroscopy, as well as by FTIR spectroscopy, ^{1}H, ^{13}C, HSQC and COSY NMR spectroscopy. The electrospray mass spectrum of [Ru(bpy)(3,3'-bpyhex)$_2$](PF$_6$)$_2$ shows signals at *m/z* 1107.4 which corresponds to {M-[PF$_6$]}$^{+}$ and 481 for {M-2[PF$_6$]}$^{2+}$.

The signals in the ^{1}H NMR spectrum are similar to those of [Ru(bpy)$_2$(3,3'-bpyhex)](PF$_6$)$_2$ with different ratios of integrations for aliphatic and aromatic regions,

arising from the bipyridine and the aliphatic chain in 3,3'-position. The other interesting difference in the ^{1}H NMR spectra of the two complexes comes from the H_6 protons of the bipyridine ligands. In the ^{1}H NMR apectrum of [Ru(bpy)(3,3'-bpyhex)$_2$](PF$_6$)$_2$, H_{6-bpy} appears as in two signals, one signal at 8.35 ppm and another at 7.85 ppm, each corresponding to one hydrogen. The H_6 splits in two peaks in 7.53 and 7.61 ppm. This is attributed to the influence of the symmetry around the octahedral metal. (Figure 3.8)
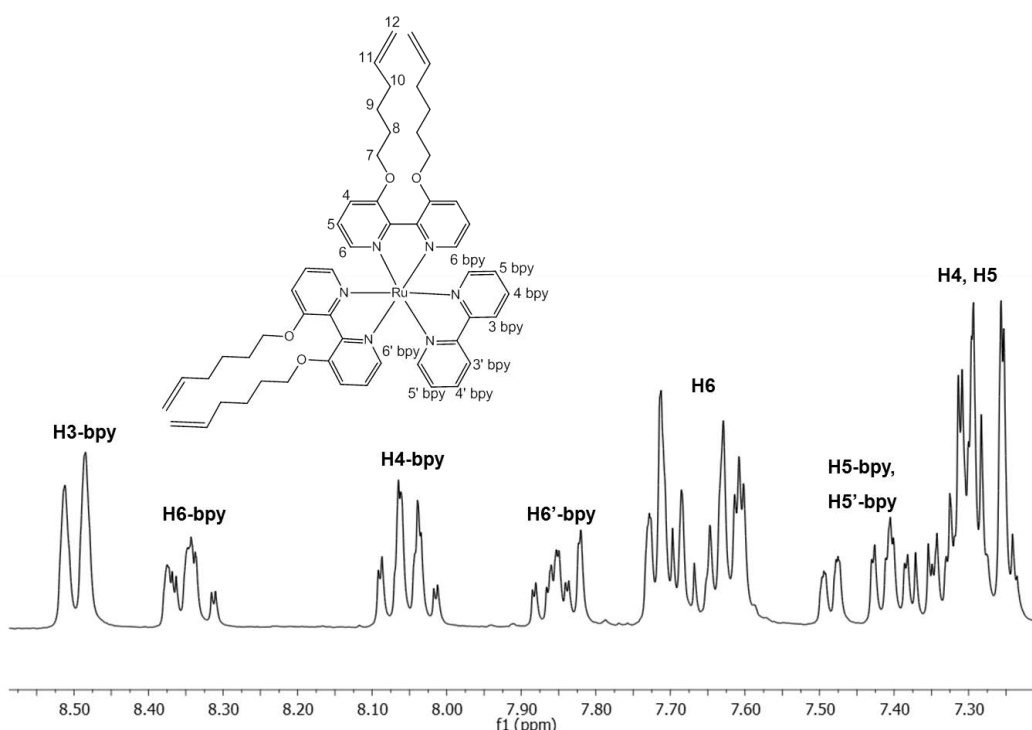
Figure 3.8 300 MHz ^{1}H NMR spectrum of [Ru(bpy)(3,3'-bpyhex)$_2$](PF$_6$)$_2$ (aromatic region) (CD$_3$CN).

Reaction of Ru(bpy)$_2$Cl$_2$ with 4,4'-bpyhex results in the formation of [Ru(bpy)$_2$(4,4'-bpyhex)](PF$_6$)$_2$ complex in 60% yield (Scheme 3.6). The compound was fully characterised by ^{1}H NMR, ^{13}C NMR, mass spectrometry, FTIR spectroscopy and

elemental analysis and two-dimensional NMR techniques including COSY and HSQC were employed to allow full assignments of the peaks.

In the ^{1}H NMR spectrum, the compounds were characterised by two distinct areas of signals, one for the aromatic peaks arising from the bipyridine units (integrating for 22 H) and the second one from the aliphatic peaks arising from the alkyl substitutants of 4,4'-bpyhex (integrating for 22 H). The aromatic region of ^{1}H NMR spectrum contains signals that are assigned to the different ligands by their characteristic multiplicities. Shielding effects of the metal shifts the H_6 signal of 4,4'-bpyhex from 8.45 ppm in the free ligand to a doublets of doublet at 7.39 ppm in the complex, which indicates the coordination to the ruthenium complex (Figure 3.9). Similarly there is also a shift for C_6 in ^{13}C NMR spectrum from 150.1 ppm in free ligand to 152.1 ppm in complex (Figure 3.10). Shifts in the aliphatic region and changes in the multiplicity of H_7 from a triplet in 4.13 ppm in free ligand to around 4.21 ppm in complex are indicative of the coordination and isomers formed in the octahedral ruthenium complex. It was also observed that in ^{1}H NMR spectrum all peaks assigned for the hydrogens of the bipyridine ligand split which is because of the symmetry around the metal centre.

The electrospray mass spectrum of [Ru(bpy)$_2$(4,4'-bpyhex)](PF$_6$)$_2$ shows signals at *m/z* 911.5 which corresponds to {M-[PF$_6$]}$^+$ and 383.2 for {M-2[PF$_6$]}$^{2+}$. The compound was also characterised by its single crystal x-ray structure (Section 3.2.3.1).
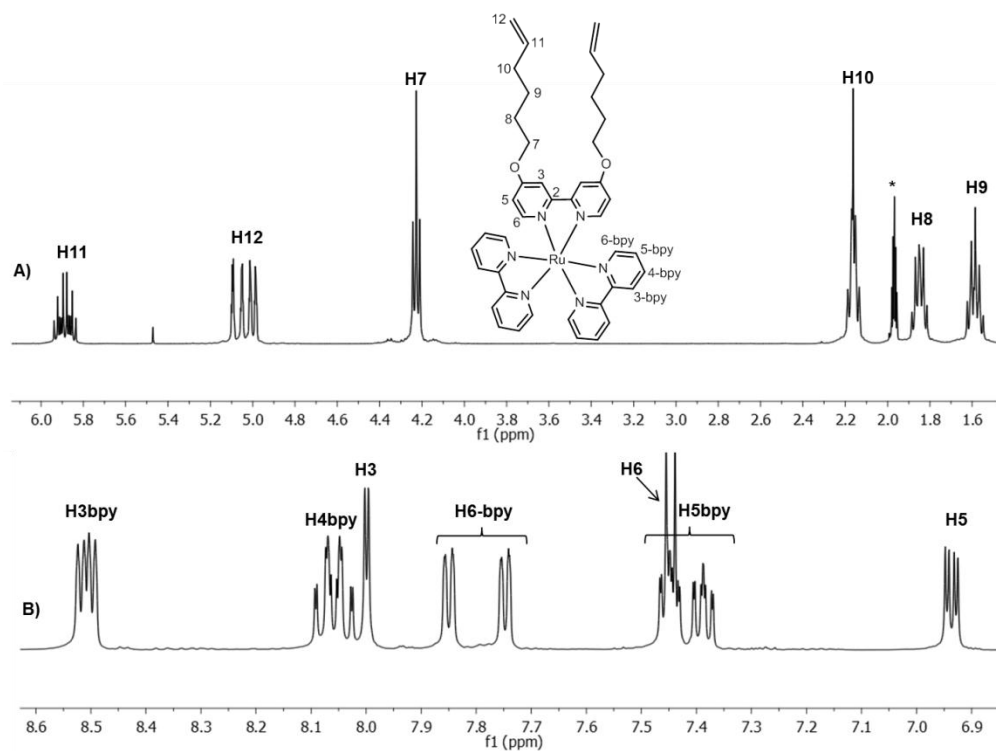
Figure 3.9 400 MHz ^{1}H NMR spectrum of [Ru(bpy)$_2$(4,4'-bpyhex)](PF$_6$)$_2$ A) aliphatic region B) aromatic region (CD$_3$CN).
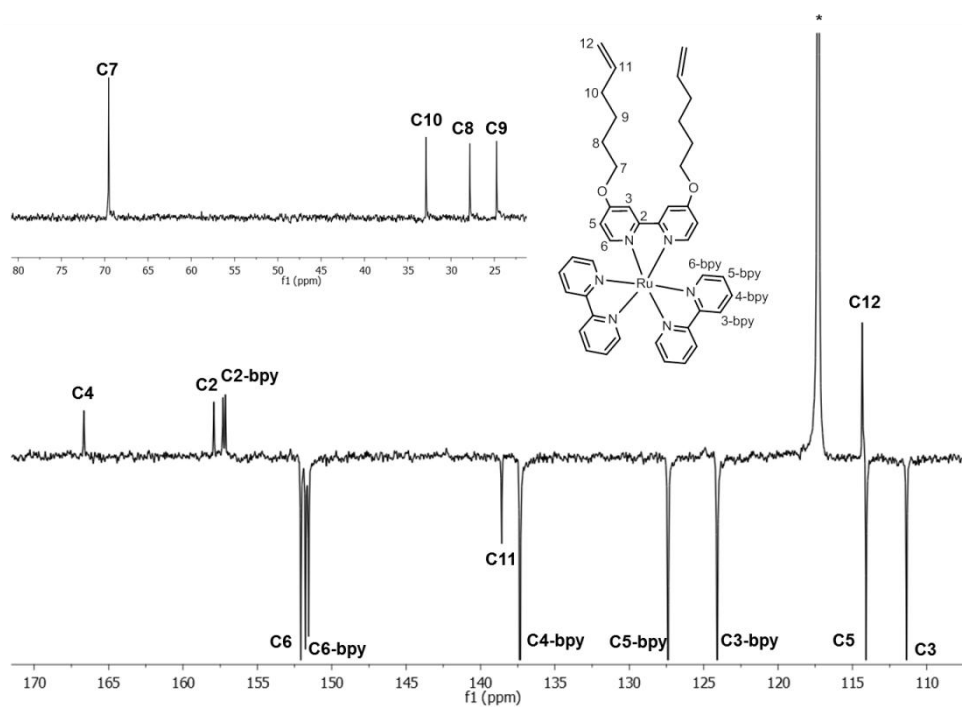
Figure 3.10 100 MHz ^{13}C NMR spectrum of [Ru(bpy)$_2$(4,4'-bpyhex)](PF$_6$)$_2$ (CD$_3$CN).

The reaction of [Ru(bpy)Cl$_4$]$^{2-}$ and two equivalents of 4,4'-bpyhex results in the formation of [Ru(bpy)(4,4'-bpyhex)$_2$](PF$_6$)$_2$ which has two ligands carrying long alkyl substituents in their 4,4'-position. The next section describes the conversion of the double bonds of the substituents to the surface active terminal (SAc) groups to get the complex with four attachment sites which can make a very strong and rigid monolayer of the ruthenium complex on gold surface.
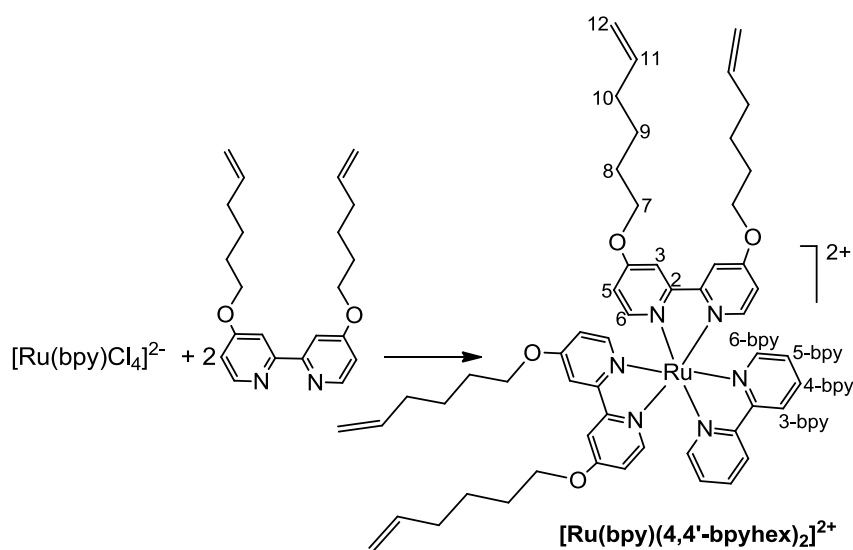
Scheme 3.7 Synthetic route to [Ru(bpy)(4,4'-bpyhex)$_2$](PF$_6$)$_2$.

[Ru(bpy)(4,4'-bpyhex)$_2$](PF$_6$)$_2$ was characterised by ^{1}H, ^{13}C, HSQC and COSY NMR spectroscopy as well as mass spectrometry and FTIR spectroscopy. The electrospray mass spectrum of [Ru(bpy)(4,4'-bpyhex)$_2$](PF$_6$)$_2$ shows signals at *m/z* 1107.6 which corresponds to {M-[PF$_6$]}$^+$ and 481.3 for {M-2[PF$_6$]}$^{2+}$.

The NMR spectrum of [Ru(bpy)(4,4'-bpyhex)$_2$](PF$_6$)$_2$ is similar to that of [Ru(bpy)$_2$(4,4'-bpyhex)](PF$_6$)$_2$, with different ratios of integrations for aliphatic and aromatic regions. The only differences are found in the aromatic region where each

of the H_3, H_5 and H_6 signals of the 4,4'-bpyhex ligand split into two peaks due to the symmetry around the octahedral metal (Figure 3.11).[34] The compound was also characterised by its single crystal x-ray structure (Section 3.2.3.2).
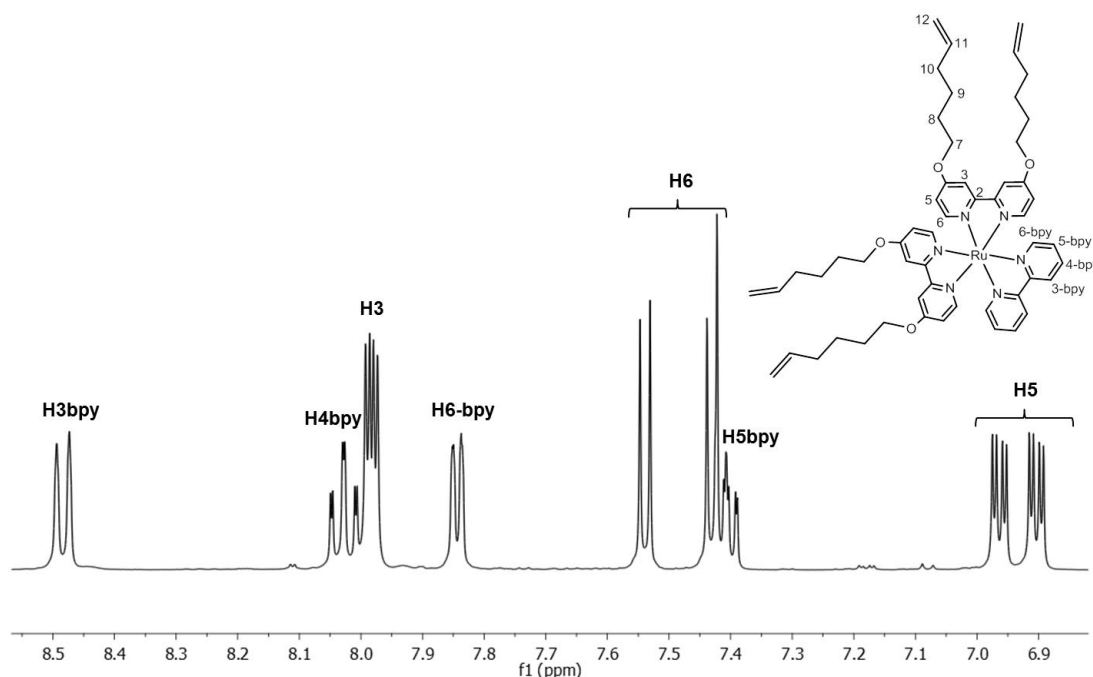
Figure 3.11 400 MHz ^{1}H NMR spectrum (CD$_3$CN) of [Ru(bpy)(4,4'-bpyhex)$_2$](PF$_6$)$_2$ (aromatic region)

Osmium polypyridine complexes are challenging but interesting compounds due to their low lying ^{3}MLCT transition state. The synthesis of new osmium complexes bearing surface active terminals is desirable for attachment onto gold surfaces. Similar to ruthenium complexation, the first step towards synthesis of surface active osmium complexes was the reaction of Os(bpy)$_2$Cl$_2$ with 3,3'-bpyhex. (Scheme 3.8)

Os(bpy)$_2$Cl$_2$ had been prepared following a published procedure[35] and characterised by mass spectrometry showing the peak at 573.8 for [M+H]$^+$ and by UV-Vis

spectroscopy showing the MLCT bands at 565, 470 and 380 nm and an intense π-π^* band at 300 nm.
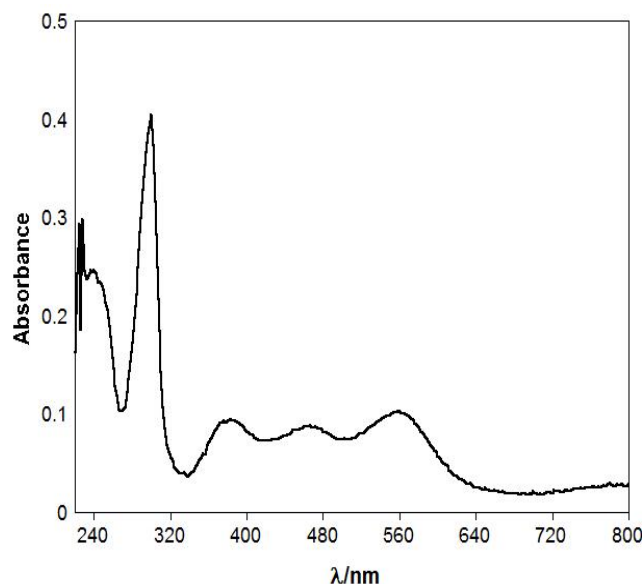
Figure 3.12 Absorption spectrum of Os(bpy)$_2$Cl$_2$ in DCM.

The Os(bpy)$_2$Cl$_2$ was used without further purification and reacted with either 3,3'-bpyhex or 4,4'-bpyhex to get the complexes [Os(bpy)$_2$(3,3'-bpyhex)](PF$_6$)$_2$ or [Os(bpy)$_2$(4,4'-bpyhex)](PF$_6$)$_2$ as dark green solids. The compounds were characterised by ^{1}H NMR, ^{13}C NMR, mass spectrometry and FTIR spectroscopy. Two-dimensional NMR techniques including COSY and HSQC were employed to allow full assignments of the peaks.

The electrospray mass spectrum of [Os(bpy)$_2$(3,3'-bpyhex)](PF$_6$)$_2$ shows signals at *m/z* 1001.2 which corresponds to {M-[PF$_6$]}$^+$ and 428.1 for {M-2[PF$_6$]}$^{2+}$. Comparison of ^{1}H NMR and ^{13}C NMR data from ruthenium and osmium complexes revealed the same pattern for the two compounds. In the case of the osmium complexes,

aromatic protons were slightly shifted up-field compared to the ruthenium complex (Figure 3.13).
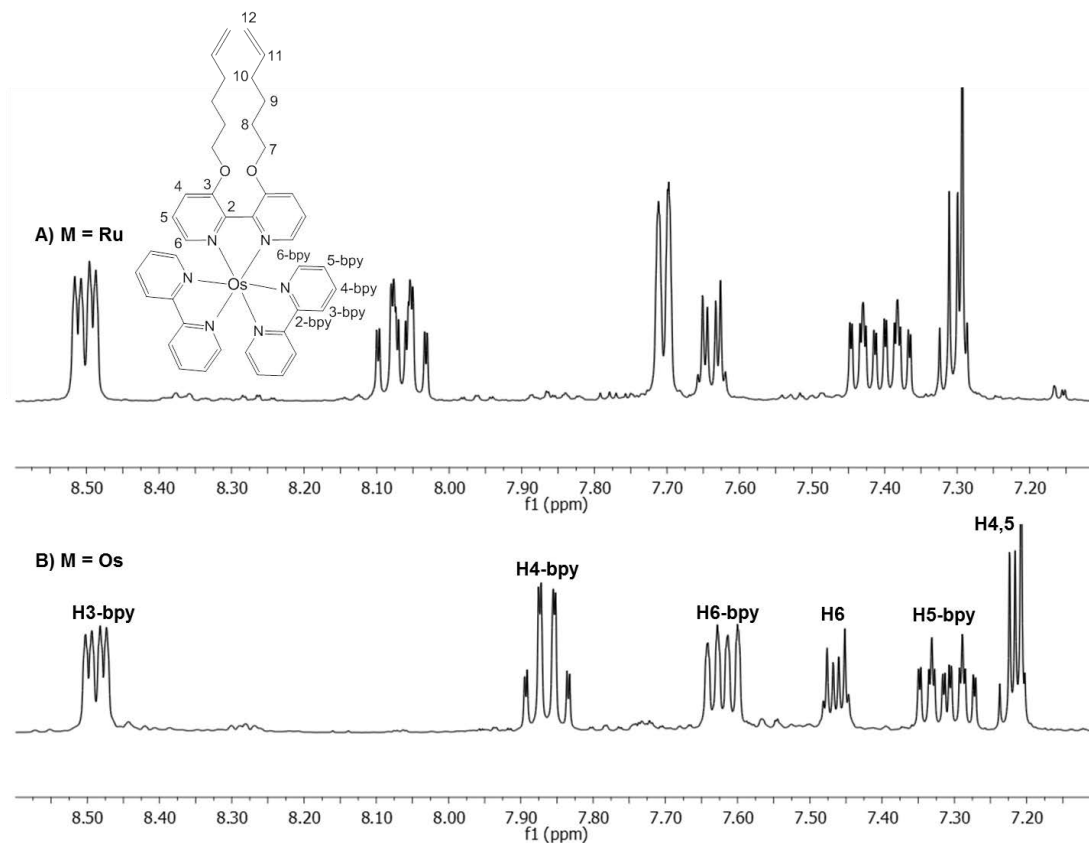
Figure 3.13 300 MHz ^{1}H NMR spectrum of A) [Os(bpy)$_2$(3,3'-bpyhex)](PF$_6$)$_2$ and B) [Os(bpy)$_2$(3,3'-bpyhex)](PF$_6$)$_2$ (aromatic region) (CD$_3$CN).

[Os(bpy)$_2$(4,4'-bpyhex)](PF$_6$)$_2$ was synthesised by reacting Os(bpy)$_2$Cl$_2$ with 4,4'-bpyhex in 40% yield as a dark green solid. The compound was characterised by ^{1}H NMR (Figure 3.14), ^{13}C NMR (Figure 3.15), COSY and HSQC NMR, mass spectrometry and FTIR spectroscopy. The electrospray mass spectrum of [Os(bpy)$_2$(4,4'-bpyhex)](PF$_6$)$_2$ shows signals at *m/z* 1001.5 which corresponds to {M-[PF$_6$]}$^+$ and 428.2 for {M-2[PF$_6$]}$^{2+}$. Comparison of ^{1}H NMR and ^{13}C NMR data

from the ruthenium and osmium complexes revealed the same pattern for the two compounds. The compound was also characterised by its single crystal x-ray structure (Section 3.2.3.3).
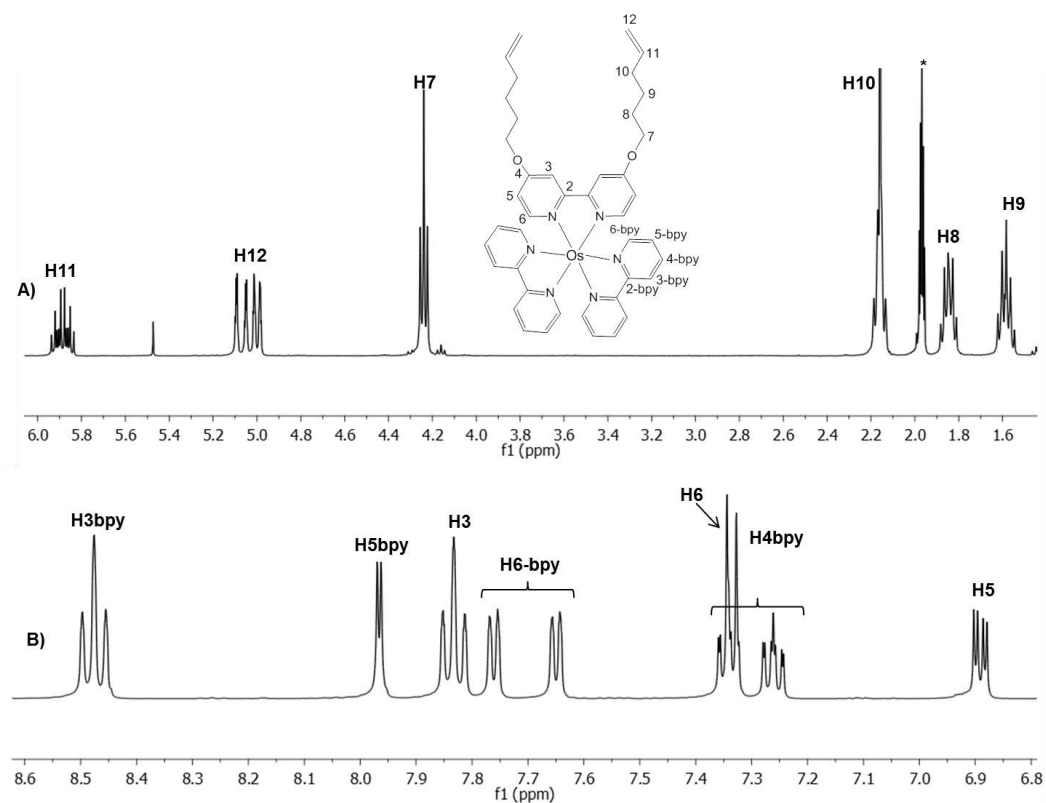
Figure 3.14 400 MHz ^{1}H NMR spectrum of [Os(bpy)$_2$(4,4'-bpyhex)](PF$_6$)$_2$ A) aliphatic region B) aromatic region (CD$_3$CN).
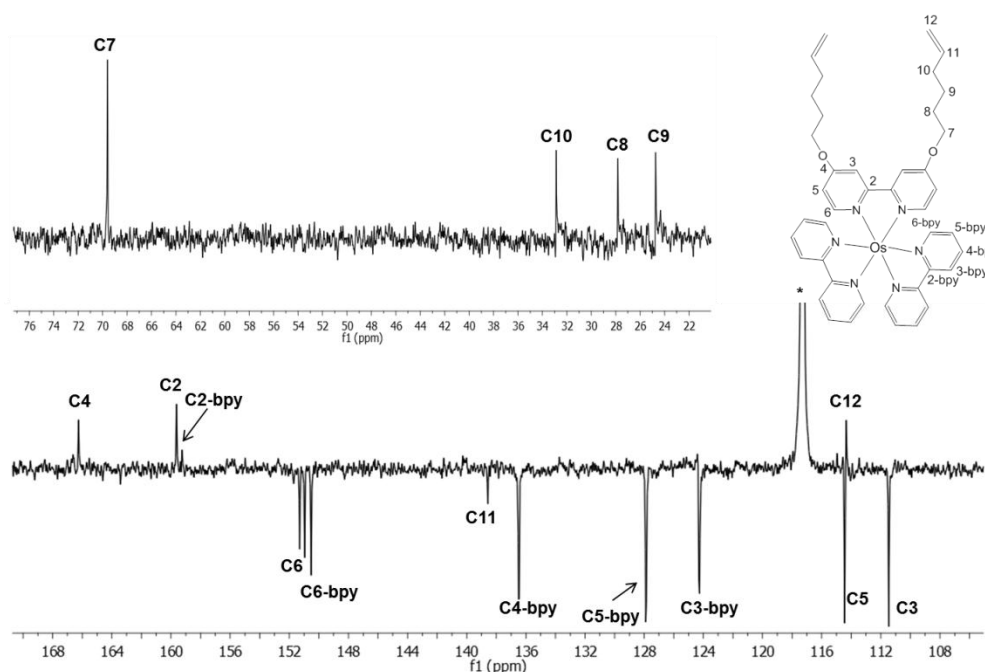
Figure 3.15 100 MHz ^{13}C NMR spectrum of [Os(bpy)$_2$(4,4'-bpyhex)](PF$_6$)$_2$ (CD$_3$CN).

The last step towards a surface active ruthenium complex involved thioesterification of [Ru(bpy)$_2$(3,3'-bpyhex)](PF$_6$)$_2$, [Ru(bpy)(3,3'-bpyhex)$_2$](PF$_6$)$_2$, [Ru(bpy)$_2$(4,4'-bpyhex)](PF$_6$)$_2$, [Ru(bpy)(4,4'-bpyhex)$_2$](PF$_6$)$_2$, [Os(bpy)$_2$(3,3'-bpyhex)](PF$_6$)$_2$ and [Os(bpy)$_2$(4,4'-bpyhex)](PF$_6$)$_2$ by using thioacetic acid under free radical conditions in the presence of AIBN, a radical initiator, in order to open the double bond and attach the SAc group to the terminal olefin.

M = Ru/ Os
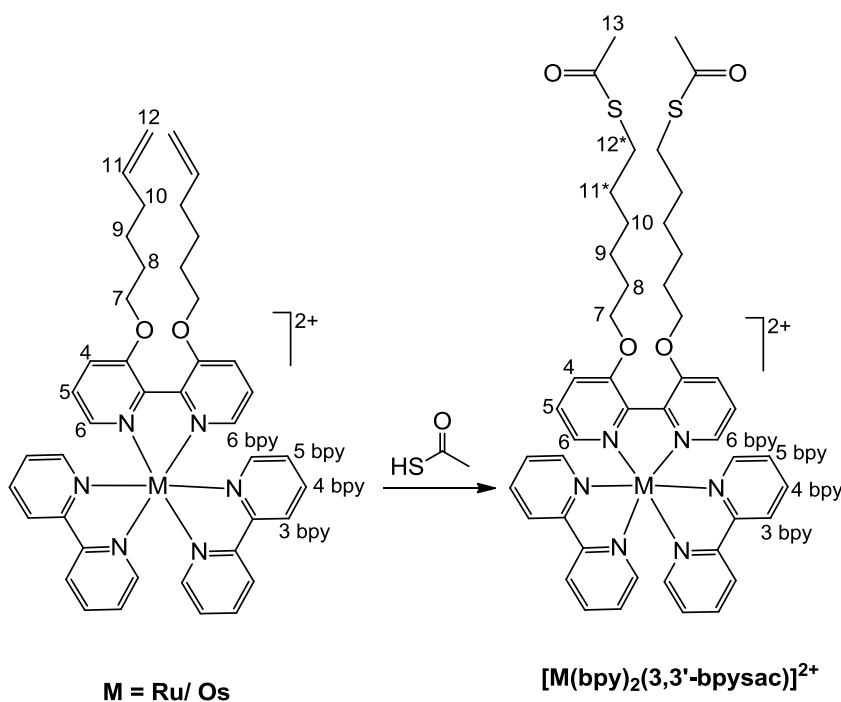
[M(bpy)$_2$(3,3'-bpysac)]$^{2+}$

Scheme 3.8 Synthetic route to [M(bpy)$_2$(3,3'-bpysac)]$^{2+}$.

In first attempt a typical procedure of thioesterification for the simple aliphatic chains was followed, reported for a reaction involving formation of 6-(thioacetoxy)-bromohexane from thioesterification of bromo-hex-1-ene,[25] which was unsuccessful. In the original reference[25] they faced a similar problem when the double bond was close to a pyridine ring and they explained this by interference of the radical pathway of the piperazine ring.

In literature reports different ways of thioesterification have been introduced, such as K-10 clay (a mild acidic montmorillonite) catalysed anti-Markovnikoff method to avoid radical reaction,[36] Michael addition of thioacetic acid on the racemic derivatives,[37] or different conditions and environments for the radical reaction.[38,39] Based on these literature precedents a Michael addition and different canditions for

radical reactions were attempted. It was discovered that by adding the complex dropwise in to an excess amount of the radical initiator and thioacetic acid which are stirred in 60°C for at least 30 minutes before, and also using dry conditions for a longer time, gave the desired compound. The disappearance of the double bond was monitored by ^{1}H NMR spectroscopy during the reaction to optimise thioesterification and the reaction was pushed to completion by adding more thioacetic acid and AIBN after around 18 hours (Figure 3.16).

The identity of all of them final complexes can be confirmed from their ^{1}H NMR spectra, and they were further characterised by ^{13}C NMR, HSQC, COSY, mass spectrometry and FTIR spectroscopy. Full spectroscopic assignments for the final complexes are in the experimental section.
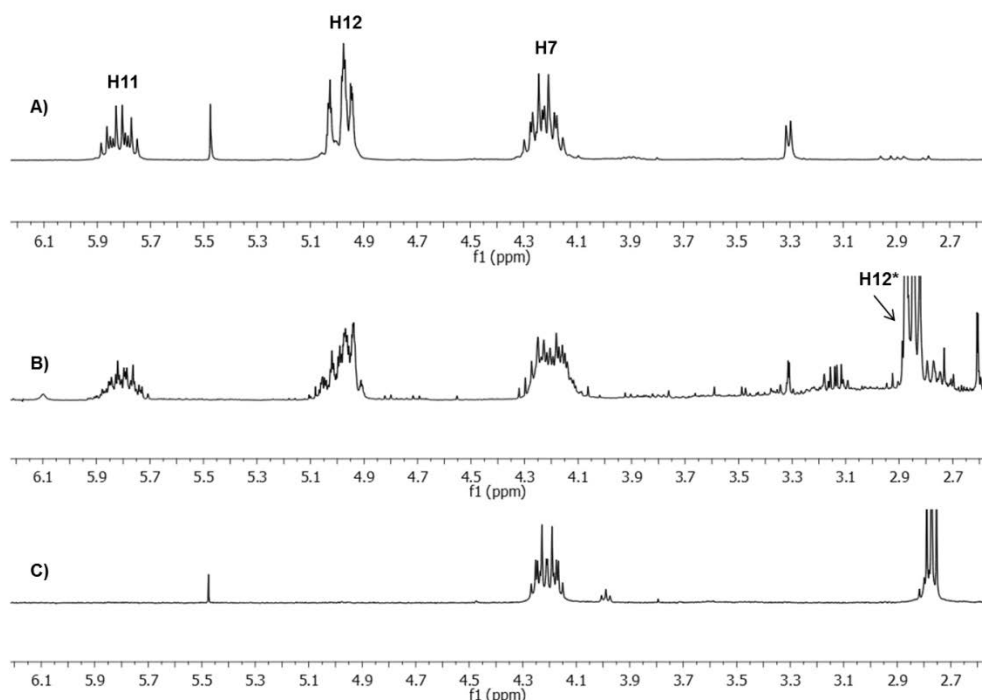
**Figure 3.16 ^{1}H NMR spectrum in the double bond region during the thioesterification A)
before reaction, H$_{11}$ and H$_{12}$ are characteristics of double bond B) 1st reaction, H$_{12*}$ formed as
a result of attaching the SAc group C) thioesterification completed (CD$_3$CN).**

The electrospray mass spectrum of [Ru(bpy)$_2$(3,3'-bpysac)](PF$_6$)$_2$ shows signals at
m/z 1063.1 corresponding to {M-[PF$_6$]}$^+$ and 459.1 for {M-2[PF$_6$]}$^{2+}$. In the ^{1}H NMR
spectrum, the aromatic region of the compound is same as described for
[Ru(bpy)$_2$(3,3'-bpysac)](PF$_6$)$_2$. In the aliphatic region, H$_{11}$ shifts from a triplet of
doublet of doublets at 5.75-5.85 ppm to a multiplet at 1.48-1.57 ppm. H$_{12}$ also shifts
from 4.90-5.08 ppm to 2.72-2.85 ppm, which both confirm the conversion of the
double bond to the thioacetate ester(Figure 3.17). H$_{14}$ (CH$_3$) is clear in the ^{1}H NMR
spectrum (2.30 ppm). Shifts of C$_{11}$ from 151.3 ppm to 29.2 ppm and C$_{12}$ from 114.3
ppm to 28.5 ppm in ^{13}C NMR spectrum are significant and again confirm the
successful esterification process. Furthermore the C$_{13}$ carbonyl carbon atom is clear

in the ^{13}C spectrum at 195.5 ppm. The FTIR spectrum was in agreement with general FTIR assignments for ruthenium tris-bipyridine complexes and strong carbonyl stretching signal at 1681 cm^{-1} can be observed (Figure 3.18).
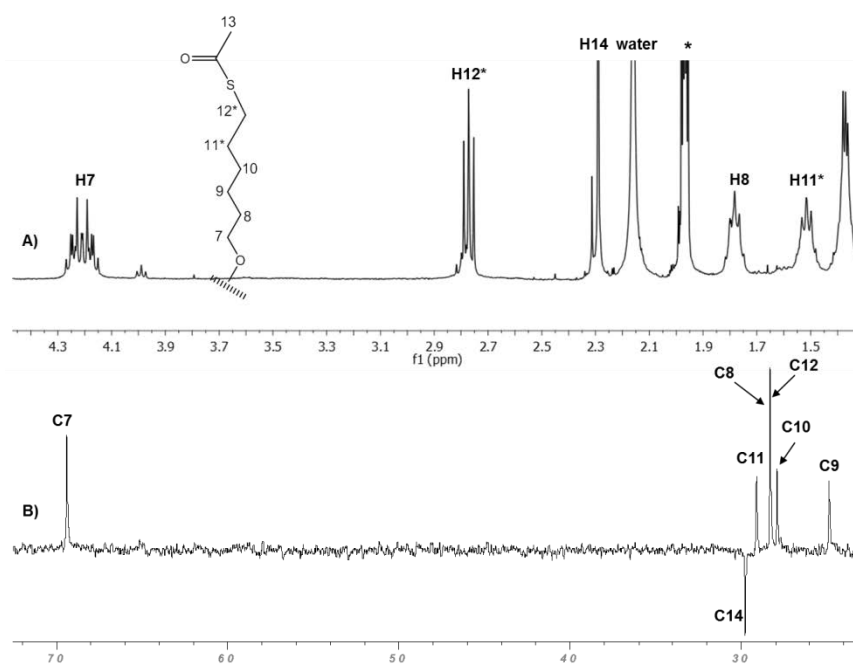
Figure 3.17 A) 400 MHz ^{1}H NMR and B) 100 MHz ^{13}C NMR spectrum of [Ru(bpy)$_2$(3,3'-bpysac)](PF$_6$)$_2$ (aliphatic region) (CD$_3$CN).
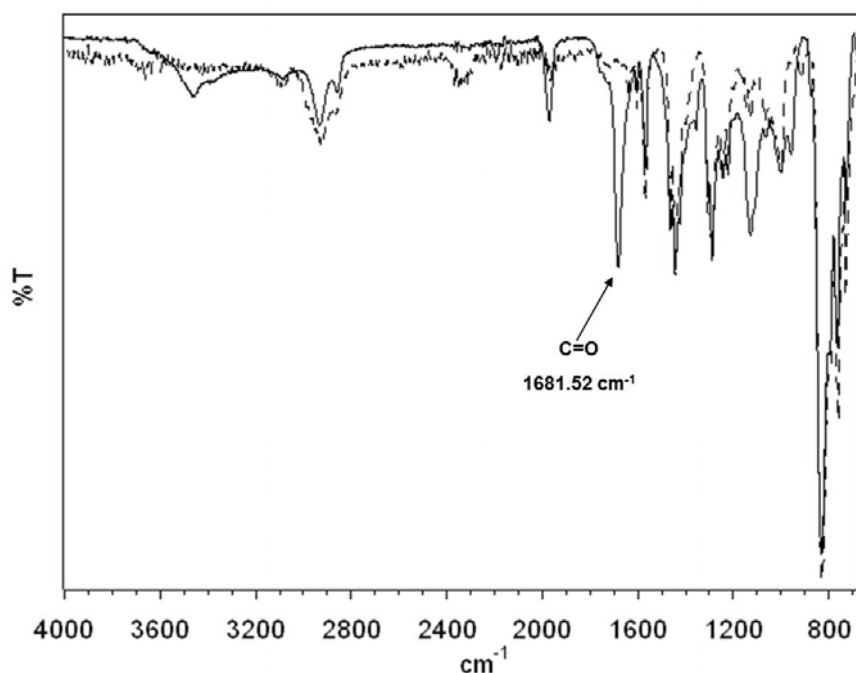
Figure 3.18 FTIR spectrum of [Ru(bpy)$_2$(3,3'-bpyhex)](PF$_6$)$_2$ (dashed line) and [Ru(bpy)$_2$(3,3'-bpysac)](PF$_6$)$_2$ (solid line).

The electrospray mass spectrum of [Ru(bpy)(3,3'-bpysac)$_2$](PF$_6$)$_2$ shows a signal m/z 633.2 for {M-2[PF$_6$]}$^{2+}$. All the signals in the ^{1}H NMR spectrum and ^{13}C NMR are comparable with those of [Ru(bpy)$_2$(3,3'-bpysac)](PF$_6$)$_2$. Similarly to the previous complex, the FTIR spectrum was in agreement with general FTIR assignments for ruthenium tris-bipyridine complexes, and the strong signal of the carbonyl stretch at 1682 cm^{-1} is similar to that of [Ru(bpy)(3,3'-bpyhex)$_2$](PF$_6$)$_2$.

The electrospray mass spectrum of [Ru(bpy)$_2$(4,4'-bpysac)](PF$_6$)$_2$ shows signals at m/z 1063.1, corresponding to {M-[PF$_6$]}$^+$, and 459.1 for {M-2[PF$_6$]}$^{2+}$. In the ^{1}H NMR and ^{13}C NMR spectra, the aliphatic region shows dramatic changes when the conversion is completed, H$_{11}$ shifts from 5.81-5.95 ppm to 1.53-1.61 ppm, H$_{12}$ shifts

from 4.95-5.10 ppm to 2.85 ppm and H_{14} (CH_3) appears at 2.27 ppm. In the ^{13}C NMR spectrum, the C_{11} signal shifts from 138.6 ppm to 30.2 ppm and C_{12} from 114.4 ppm to 29.4 ppm (Figure 3.19). Finally the FTIR spectrum confirms the formation of the final complex by showing the strong carbonyl stretching signal at 1683 cm^{-1}.
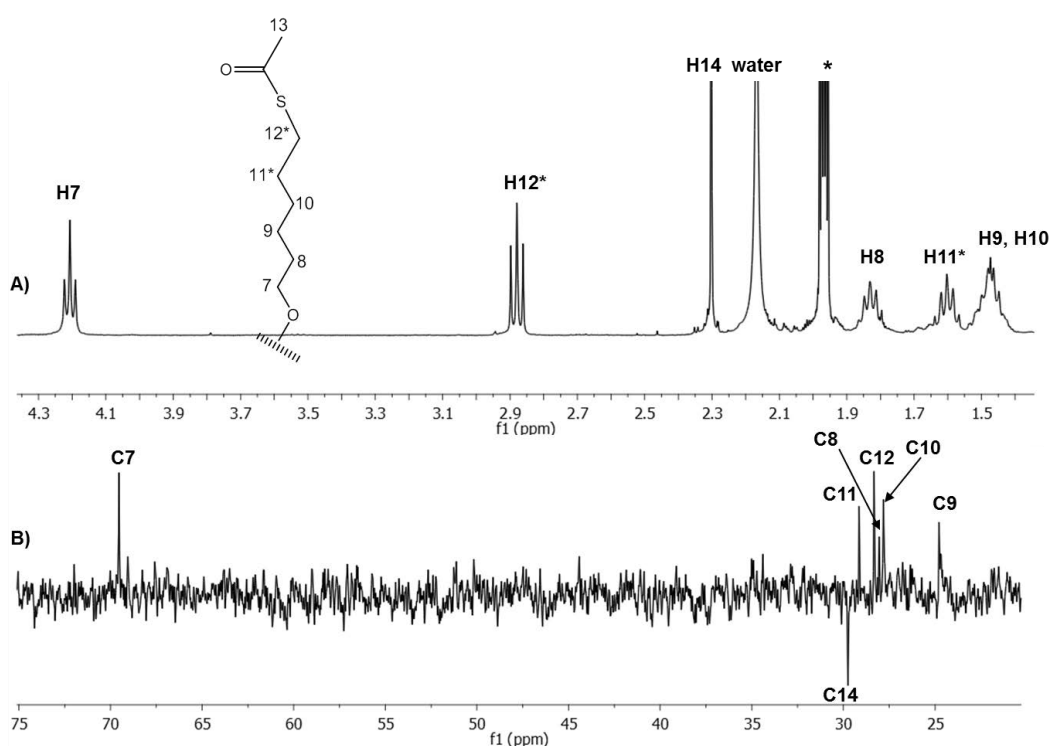
Figure 3.19 A) 400 MHz ^{1}H NMR and B) 100 MHz ^{13}C NMR spectrum of [Ru(bpy)$_2$(4,4'-bpysac)](PF$_6$)$_2$ (aliphatic region) (CD$_3$CN).

The electrospray mass spectrum of [Ru(bpy)(4,4'-bpysac)$_2$](PF$_6$)$_2$ shows signals at *m/z* 1411.5 for {M-[PF$_6$]}$^+$ and 633.3 for {M-2[PF$_6$]}$^{2+}$. Attachment of the SAc group was also confirmed by FTIR spectroscopy.

The electrospray mass spectrum of $[Os(bpy)_2(3,3'-bpysac)](PF_6)_2$ shows signals at *m/z* 1153.3 which corresponds to $\{M-[PF_6]\}^+$ and 504.1 for $\{M-2[PF_6]\}^{2+}$. The new complex was characterised by ^{1}H, ^{13}C, COSY and HSQC NMR spectroscopy, and FTIR spectroscopy. ^{1}H NMR data from the ruthenium and osmium complexes revealed the same pattern for the two compounds. The strong of carbonyl stretching signal at 1681 cm^{-1} can be seen in the FTIR spectrum (Figure 3.20).
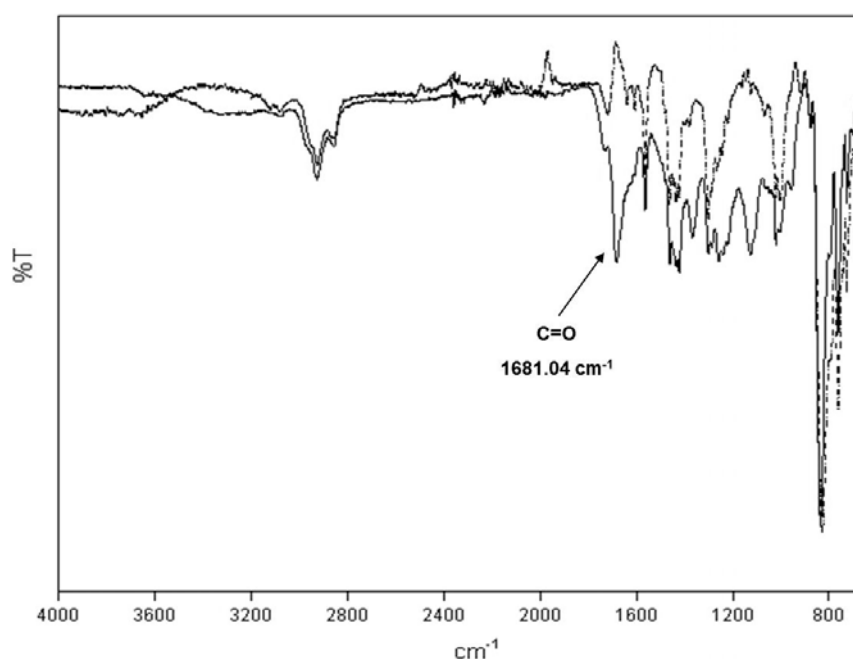
Figure 3.20 FTIR spectrum of $[Os(bpy)_2(3,3'-bpyhex)](PF_6)_2$ (dashed line) and $[Os(bpy)_2(3,3'-bpysac)](PF_6)_2$ (solid line).

The electrospray mass spectrum of $[Os(bpy)_2(4,4'-bpysac)](PF_6)_2$ shows signals at *m/z* 1153.2, corresponding to $\{M-[PF_6]\}^+$, and 504.1 for $\{M-2[PF_6]\}^{2+}$. ^{1}H NMR data from the ruthenium and osmium complexes revealed the same pattern for the two

compounds. The compound was also characterised by its single crystal x-ray structure (Section 3.2.4.4).

3.2.3. Synthesis of ruthenium (II) tris-phenanthroline complex, [Ru(phen)$_2$(4,7-phenhex)]$^{2+}$

A similar approach has been used to synthesis the ligand 4,7-Phenhex, using 4,7-dihydroxy-phenanthroline as the starting material and performing the Williamson ether reaction.
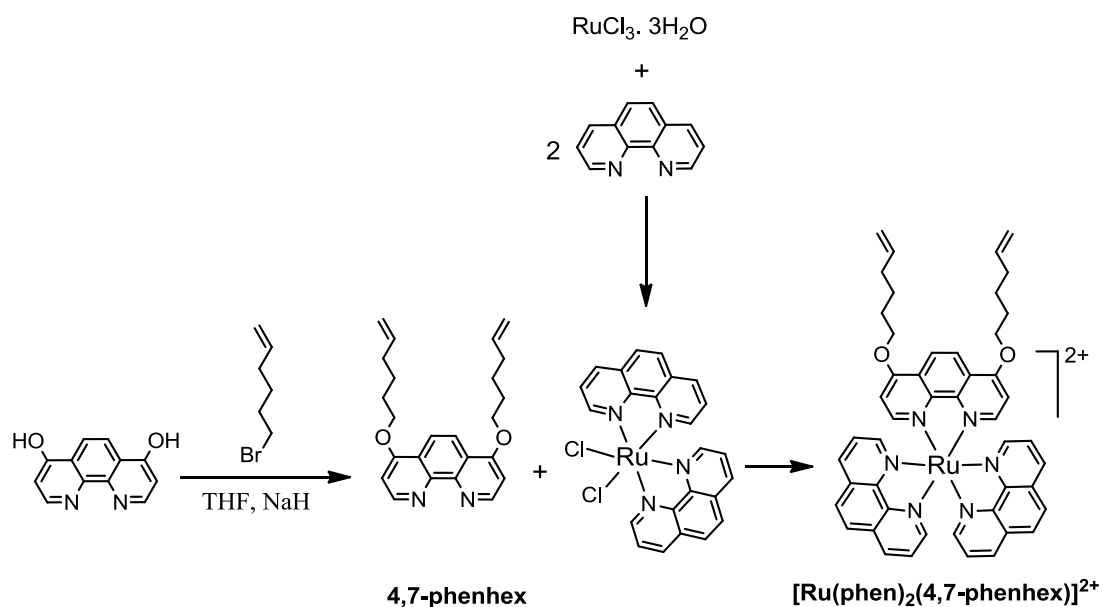
Scheme 3.9 Synthetic route to [Ru(phen)$_2$(4,7-phenhex)]$^{2+}$.

The final ligand was characterised by ^{1}H NMR and ^{13}C NMR spectroscopy to confirm the formation of the ether bond. Electrospray mass spectrometry showed the peaks at 377.2 and 399.2 corresponding to [M+H]$^+$ and [M+Na]$^+$ respectively.

In the ^{1}H NMR spectrum, the 4,7-phenhex ligand is charactrised by the two distinct areas of signals, one for the aromatic peaks arising from the phenanthroline unit (integrating for 6 H) and the second one from the aliphatic peaks arising from the alkyl substituents attached on the 4,7 position (integrating for 22 H). (Figure 3.21)
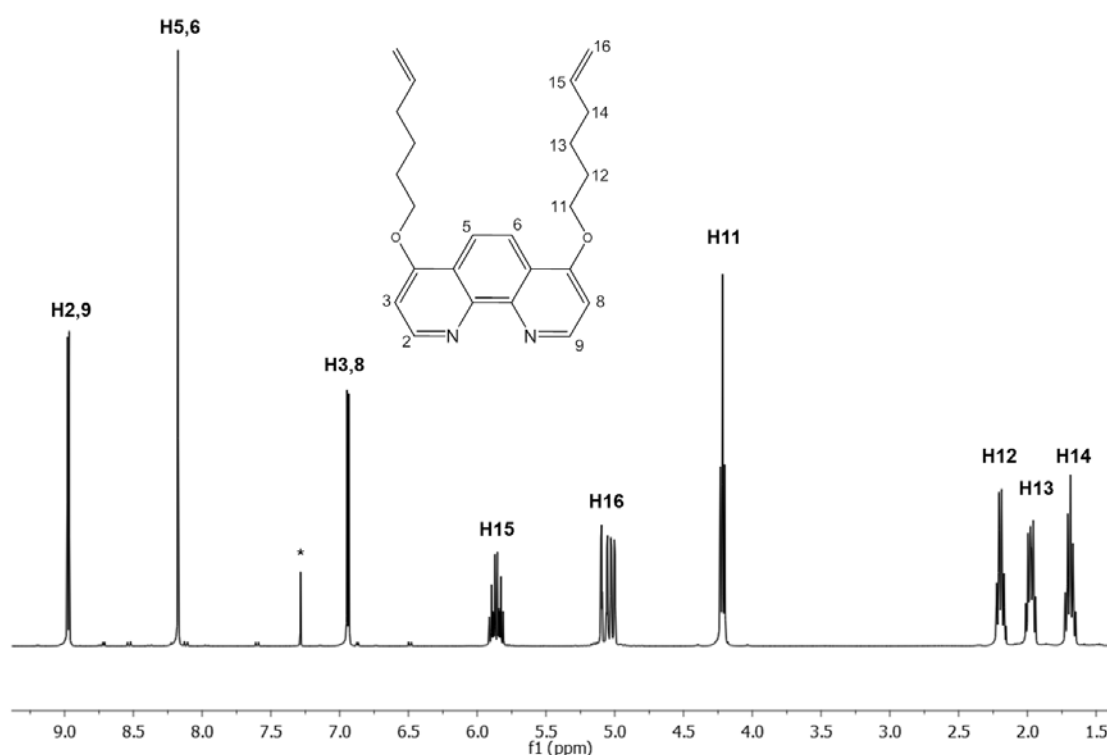
Figure 3.21 300 MHz ^{1}H NMR spectrum of 4,7-phenhex (CDCl$_3$).

Ru(phen)$_2$Cl$_2$ was prepared following the procedure of Meyer *et al.*[27,28] and characterised by electrospray mass spectrometry showing the peak at 581.1 assigned for [Ru(phen)$_2$Cl(OEt) + K]$^+$ (Ru(phen)$_2$Cl$_2$ was dissolved in EtOH) and by

UV-Vis spectroscopy showing MLCT bands at 560 nm and 480 nm and an intense π- π^* band at 280 nm.
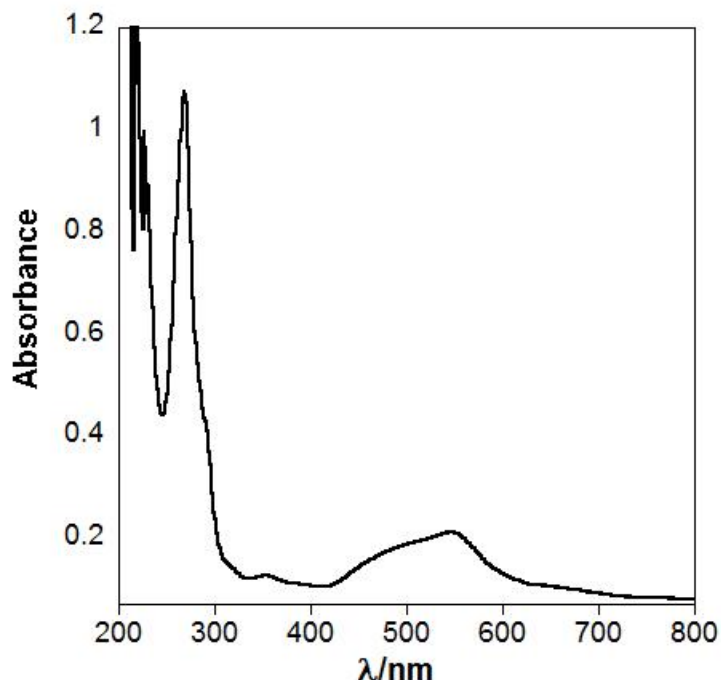
Figure 3.22 Absorption spectrum of Ru(phen)$_2$Cl$_2$ in DCM.

The Ru(phen)$_2$Cl$_2$ was reacted with the 4,7-phenhex ligand, giving the complex [Ru(phen)$_2$(4,7-phenhex)](PF$_6$)$_2$. [Ru(phen)$_2$(4,7-phenhex)](PF$_6$)$_2$ was purified by column chromatography on silica using DCM/ 5% MeOH as eluent. The final compound was characterised by ^{1}H, ^{13}C, COSY and HSQC NMR spectroscopy. The electrospray mass spectrometry of the ligand showed peaks at *m/z* 983.3 and 419.2 assigned for {M-[PF$_6$]}$^+$ and {M-2[PF$_6$]}$^{2+}$ respectively.
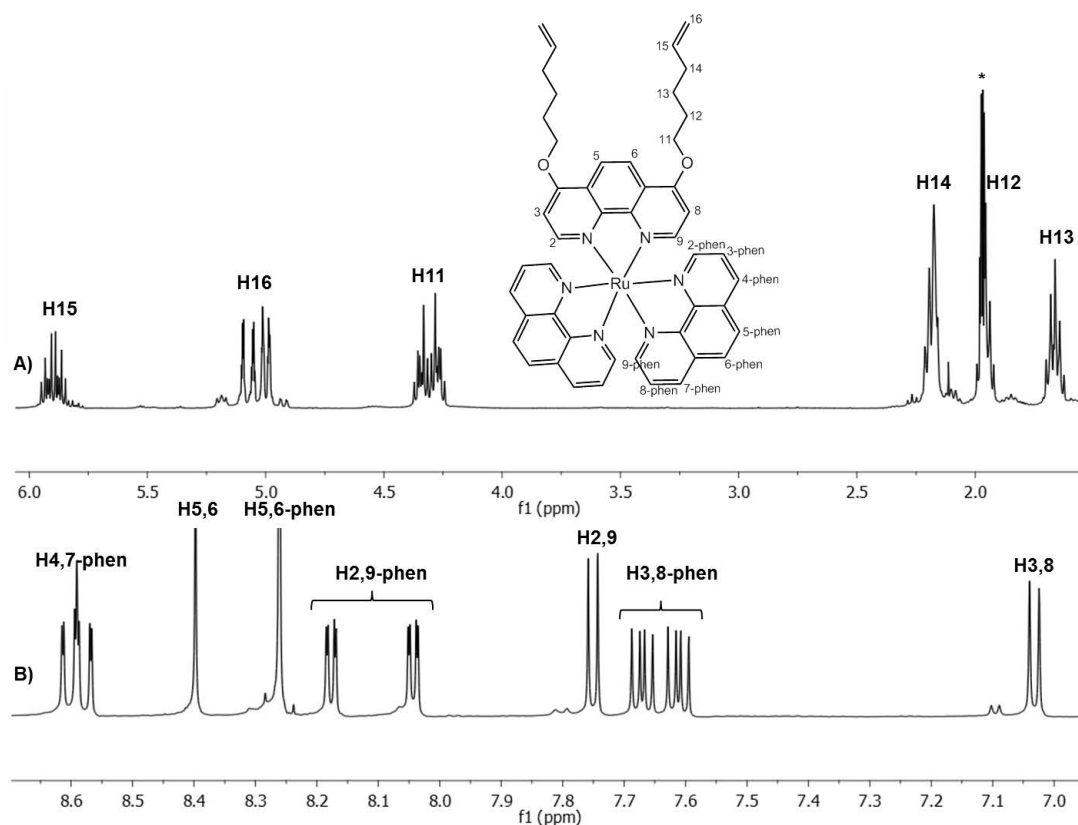
Figure 3.23 400 MHz ^{1}H NMR spectrum of [Ru(phen)$_2$(4,7-phenhex)](PF$_6$)$_2$ A) aliphatic region B) aromatic region (CD$_3$CN).

Initially [Ru(phen)$_2$(4,7-phenhex)](PF$_6$)$_2$ was synthesised for use as a surface active probe as we were expecting that it would show improvement in photophysical properties such as quantum yield and life time in comparison with [Ru(bpy)$_2$(4,4'-bpyhex)](PF$_6$)$_2$. But as the photophysical properties of the complex were very similar to those of [Ru(bpy)$_2$(4,4'-bpyhex)](PF$_6$)$_2$, no further investigations were carried out.

3.2.4. X- ray Crystallography Studies of the ruthenium and osmium complexes

3.2.4.1. X-ray crystallography of [Ru(bpy)$_2$(4,4'-bpyhex)](PF$_6$)$_2$

Suitable single crystals for X-ray analysis were obtained by slow evaporation of acetonitrile: ethanol [50:50] solutions over several weeks at room temperature. The X-ray diffraction crystal structure confirms the predicted structure of the complex.

The Ru-N bond lengths vary from 2.046(9) Å to 2.106(9) Å, with an average length of 2.076 Å. This relates well to [Ru(bpy)$_3$](PF$_6$)$_2$ which is reported to have bond lengths between 2.061-2.100 Å, with the average being 2.08 Å. The bond angles also compare favourably with [Ru(bpy)$_3$](PF$_6$)$_2$.[40] The bite angle of the 4,4'-bpyhex chelating unit is 77.6(4)^o which has a decrease compared to 78.7^o for [Ru(bpy)$_3$](PF$_6$)$_2$. The angle between adjacent vertices of the octahedron is 96.4(4)^o and 87.9(4)^o (compared to 96.2^o and 89.2^o for [Ru(bpy)$_3$](PF$_6$)$_2$) and the angle between opposite vertices is 173.4(4)^o (compared to 173.0^o for [Ru(bpy)$_3$](PF$_6$)$_2$). On the aliphatic chains, the groups C(31)-C(35) and C(31')-C(35'), and C(37)-C(42) and C(37')-C(42') are disordered over two positions, with 50% occupancy in for each position.

Details of crystal data and data collection parameters for [Ru(bpy)$_2$(4,4'-bpyhex)](PF$_6$)$_2$ are listed in table 3.1 and tables A3.1 – A3.5. Looking at the packing

of the complex in the unit cell, there is no evidence of intermolecular interactions such as $\pi-\pi$ stacking or hydrogen bonding.
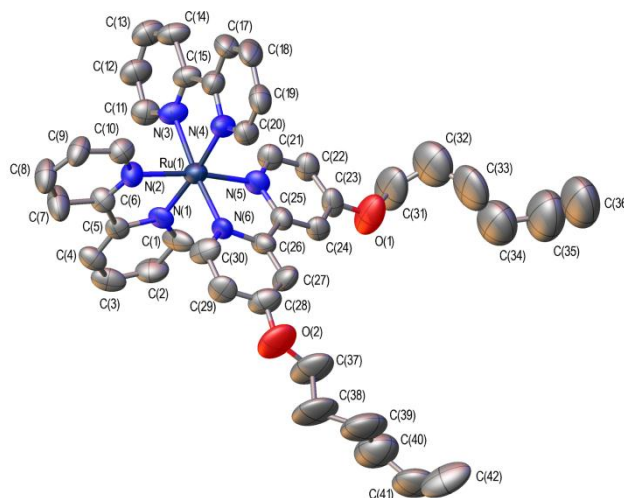
Figure 3.24 Single crystal structure of [Ru(bpy)$_2$(4,4'-bpyhex)](PF$_6$)$_2$ with ellipsoids drawn at the 50 % probability level. The groups C(31)-C(35) and C(31')-C(35'), and C(37)-C(42) and C(37')-C(42') are disordered over two positions. One of the positions of the disordered groups, the PF$_6$ anions and all hydrogen atoms have been omitted for clarity.

3.2.3.2. X-ray crystallography of [Ru(bpy)(4,4'-bpyhex)$_2$](PF$_6$)$_2$

Suitable single crystals for X-ray analysis were obtained by slow evaporation of acetonitrile: ethanol [50:50] solutions over several weeks at room temperature. The X-ray diffraction crystal structure confirms the predicted structure of the complex.
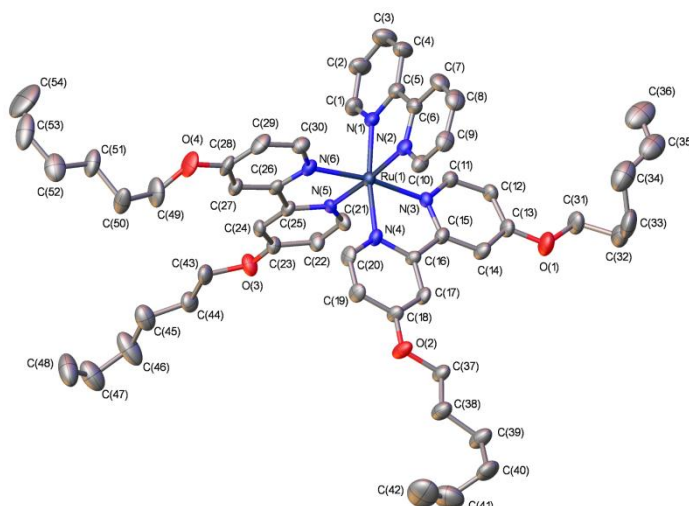
Figure 3.25 Single crystal structure of [Ru(bpy)(4,4'-bpyhex)$_2$](PF$_6$)$_2$ with ellipsoids drawn at the 50 % probability level. The groups C(31)-C(36) and C(31')-C(36'), C(40)-C(42) and C(40')-C(42'), C(47)-C(48) and C(47')-C(48'), and C(50)-C(54) and C(50')-C(54') are disordered over two positions. The minor positions of the disordered groups, the PF$_6$ anions and all hydrogen atoms have been omitted for clarity.

The crystal was a non-merohedral twin with the two domains related by 180° about the reciprocal axis (0 0 1). The refined percentage ratio of the twin domains was 50:50. Several groups are disordered over two positions. The refined percentage occupancy ratio of the disordered group C(31)-C(36) and C(31')-C(36') is 83:17 respectively. The refined percentage occupancy ratio of the disordered group C(40)-C(42) and C(40')-C(42') is 65:35 respectively. The refined percentage occupancy ratio of the disordered group C(47)-C(48) and C(47')-C(48') is 64:36 respectively. The percentage occupancy ratio of the disordered group C(50)-C(54) and C(50')-C(54') has been set at 50:50. The hydrogen atoms were fixed as riding models.

The Ru-N bond lengths are in range of 2.044(6) Å to 2.072(5) Å, (average length of 2.063 Å) which is shorter than the value which is reported for [Ru(bpy)$_3$]$^{2+}$ (bond

lengths between 2.061-2.100 Å, with the average being 2.08 Å).[40] The bite angles of two 4,4'-bpyhex chelating units are 78.4(2)º and 77.8(2)º, which both show some decrease in comparison with the parent $[Ru(bpy)_3](PF_6)_2$ with bite angle of 78.7º. The torsion angle of pyridine rings of the 4,4'-bpyhex ligands, is decreased to 2.2(6)º in comparison with the 8.0º torsion angle for $[Ru(bpy)_3](PF_6)_2$. This can explain the increase of the emission life time and quantum yield of this complex in solid form and monolayer. In addition, there is no evidence of intermolecular interactions such as $\pi-\pi$ stacking or hydrogen bonding in the crystal structure of the molecule.

Details of crystal data and data collection parameters for $[Ru(bpy)(4,4'-bpyhex)_2](PF_6)_2$ are listed in table 3.1 and tables A3.6- A3.10.

Table 3.1 Crystal data and structure refinement for [Ru(bpy)₂(4,4'-bpyhex)](PF₆)₂ and [Ru(bpy)(4,4'-bpyhex)₂](PF₆)₂

Identification code	[Ru(bpy)₂(4,4'-bpyhex)](PF₆)₂		[Ru(bpy)(4,4'-bpyhex)₂](PF₆)₂	
Empirical formula	$C_{42}H_{44}N_6O_2Ru, 2(PF_6)$		$C_{54}H_{64}N_6O_4Ru, 2(PF_6)$	
Formula weight	1055.84		1252.12	
Temperature	120(2) K		120(2) K	
Wavelength	1.54178		0.71073 Å	
Crystal system	Orthorhombic		Triclinic	
Space group	P na2(1)		P -1	
Unit cell dimensions	a=19.0018(9)Å	α=90(0)°	a = 9.6068(3) Å	α=71.8720(10)°
	b = 25.9396(10)Å	β= 90(0)°	b = 14.6996(3) Å	β= 80.0800(10)°
	c = 8.6996(4)Å	γ= 90(0)°	c = 21.8407(6) Å	γ= 72.4410(10)°
Volume	4288.0(3) Å³		2784.11(13) Å³	
Z	4		2	
Density (calculated)	1.635 Mg/m³		1.494 Mg/m³	
Absorption coefficient	4.542 mm⁻¹		0.430 mm⁻¹	
F(000)	2144.0		1288	
Crystal size	0.27 x 0.20 x 0.03 mm³		0.20 x 0.05 x 0.01 mm³	
θ range for data collection	6.55 to 66.60°		3.01 to 25.03°	
Absorption correction	Semi-empirical from equivalents		Semi-empirical from equivalents	
Index ranges	-22<=h<=17, -30<=k<=30, -7<=l<=10		-11<=h<=11, -16<=k<=17, 0<=l<=25	
Reflections collected	21883		9817	
Independent reflections	5912 [R(int) = 0.0398]		9817 [R(int) = 0.0000]	
Completeness to θ[°]	θ= 66.60° - 98.4 %		θ= 25.03° - 99.6 %	
Max. and min. transmission	0.8758 and 0.3735		0.9957 and 0.9189	
Refinement method	Refinement method		Full-matrix least-squares on F²	
Data/ restraints/ parameters	5912 / 891 / 686		9817 / 1197 / 861	
Goodness-of-fit on F²	1.121		1.236	
Final R indices [I>2σ(I)]	R1 = 0.0967, wR2 = 0.2514		R1 = 0.0778, wR2 = 0.1616	
R indices (all data)	R1 = 0.1014, wR2 = 0.2556		R1 = 0.0906, wR2 = 0.1727	
Absolute structure parameter	0.40(3)			
Largest diff. peak and hole	2.348 and -0.905 e.Å⁻³		1.042 and -0.865 e.Å⁻³	

3.2.4.3. X-ray crystallography of [Os(bpy)₂(4,4'-bpyhex)](PF₆)₂ and [Os(bpy)₂(4,4'-bpysac)](PF₆)₂

Suitable single crystals for X-ray analysis were obtained by slow evaporation of acetonitrile: ethanol [50:50] solutions over several weeks at room temperature. The X-ray crystal structure confirms the predicted structure of the complexes. For [Os(bpy)₂(4,4'-bpyhex)](PF₆)₂, the structure has been refined as a racemic twin with the ratio of enantiomers being 73(3):27(3).
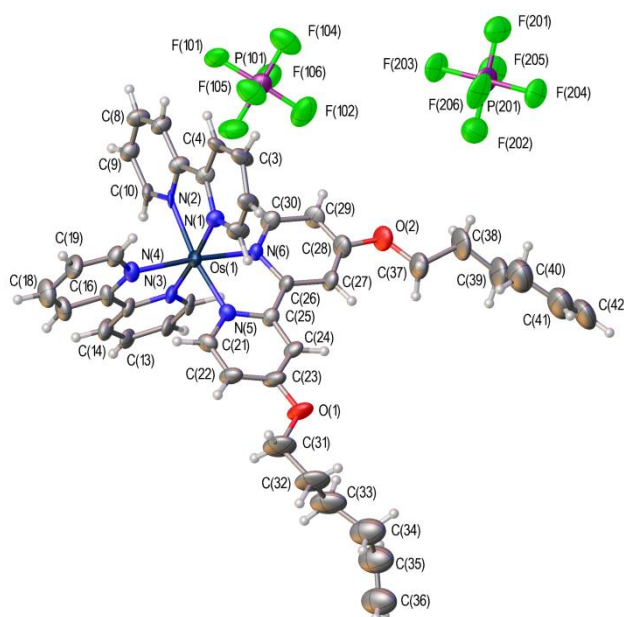
Figure 3.26 Single crystal structure of [Os(bpy)₂(4,4'-bpyhex)](PF₆)₂ with ellipsoids drawn at the 50 % probability level and hydrogen atoms shown as spheres of arbitrary radius.
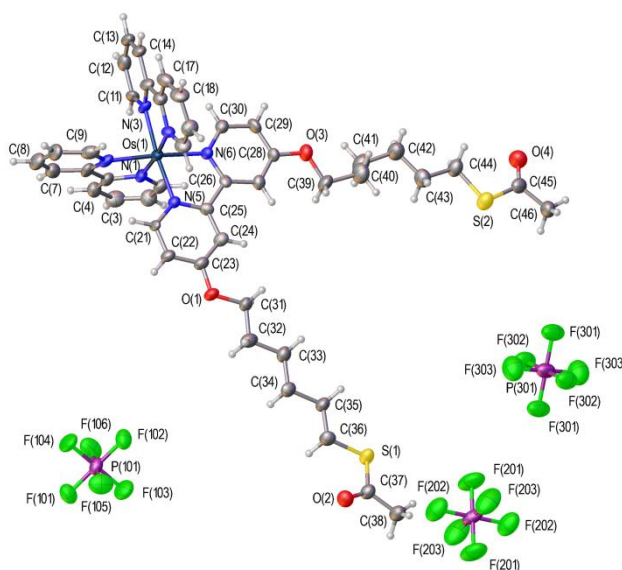
Figure 3.27 Single crystal structure of [Os(bpy)₂(4,4'-bpysac)](PF₆)₂ with ellipsoids drawn at the 50 % probability level and hydrogen atoms shown as spheres of arbitrary radius. The phosphorus atoms P201 and P301 lie on inversion centres such that these PF₆ anions are both present at 50% occupancy.

The Os-N bond lengths for [Os(bpy)$_2$(4,4'-bpyhex)](PF$_6$)$_2$ vary from 2.022(17) Å to 2.087(18) Å, with an average length of 2.060 Å, and for [Os(bpy)$_2$(4,4'-bpysac)](PF$_6$)$_2$ are between 2.039(8) Å and 2.074(8) Å, and average of 2.060 Å. Both results relate well to [Os(bpy)$_3$]$^{2+}$ which is reported to have average Os-N bond lengths of 2.062 Å.[41] It was anticipated that some decrease in bond lengths by coordinating the 4,4'-subtituted bipyridine ligands would be observed as it has been previously reported that the average bond length of [Os(4,4'-OMe-bpy)$_3$]$^{2+}$ is 2.052 Å.[42] The bite angle of the chelating unit is 76.1(7)° for [Os(bpy)$_2$(4,4'-bpyhex)](PF$_6$)$_2$ and 77.4(3)° for the [Os(bpy)$_2$(4,4'-bpysac)](PF$_6$)$_2$, which both have a decrease compared to 77.9° for [Os(bpy)$_3$](PF$_6$)$_2$ and closer to the 77.3° for [Os(4,4'-OMe-bpy)$_3$](PF$_6$)$_2$. The angles between adjacent vertices of the octahedron are 96.2(7)°

and 86.7(7)° (compared to 96.2° and 89.2° for [Ru(bpy)$_3$](PF$_6$)$_2$) and the angle between opposite vertices is 170.4(6)° (compared to 173.0° for [Ru(bpy)$_3$](PF$_6$)$_2$). Comparison of the data from [Os(bpy)$_2$(4,4'-bpyhex)](PF$_6$)$_2$ and [Os(bpy)$_2$(4,4'-bpysac)](PF$_6$)$_2$ shows that the [Os(bpy)$_2$(4,4'-bpysac)](PF$_6$)$_2$ is closer to an octahedral structure, which could be due to the removal of the disorders arising from the double bond in [Os(bpy)$_2$(4,4'-bpyhex)](PF$_6$)$_2$. Also the torsion between the pyridine rings, decreased from 7.8(2)° for [Os(bpy)$_2$(4,4'-bpyhex)](PF$_6$)$_2$ to 1.5(4)° for [Os(bpy)$_2$(4,4'-bpysac)](PF$_6$)$_2$.

The [Os(bpy)$_2$(4,4'-bpysac)](PF$_6$)$_2$ also contains two PF$_6$$^-$ anions in total per osmium complex. The phosphorus atoms P(201) and P(301) lie on inversion centres such that these anions are both present at 50% occupancy.

Looking at the packing of both complexes in the unit cell, there is no evidence of intermolecular interactions such as $\pi-\pi$ stacking or hydrogen bonding.

Details of crystal data and data collection parameters for [Os(bpy)$_2$(4,4'-bpyhex)](PF$_6$)$_2$ and [Os(bpy)$_2$(4,4'-bpysac)](PF$_6$)$_2$ are listed in Table 3.2 and tables A3.11-A3.15 and tables A3.16-A3.20.

Table 3.2 Crystal data and structure refinement for [Os(bpy)$_2$(4,4'-bpyhex)](PF$_6$)$_2$ and [Os(bpy)$_2$(4,4'-bpysac)](PF$_6$)$_2$

Identification code	[Os(bpy)$_2$(4,4'-bpyhex)](PF$_6$)$_2$		[Os(bpy)$_2$(4,4'-bpysac)](PF$_6$)$_2$	
Empirical formula	C$_{42}$H$_{44}$N$_6$O$_2$Os, 2(PF$_6$)		C$_{46}$H$_{52}$N$_6$O$_4$OsS$_2$, 2(PF$_6$)	
Formula weight	1144.97		1297.20	
Temperature	120(2) K		120(2) K	
Wavelength	0.71073 Å		0.71073 Å	
Crystal system	Orthorhombic		Triclinic	
Space group	P na2(1)		P -1	
Unit cell dimensions	a=19.1814(7) Å	α=90(0)°	a=9.1777(4)Å	α=94.085(2)°
	b = 26.0337(9)Å	β= 90(0)°	b=12.4650(5)Å	β= 98.027(2)°
	c = 8.7167(3)Å	γ= 90(0)°	c=23.0868(9)Å	γ= 103.685(2)°
Volume	4352.8(3) Å^3		2526.04(18) Å^3	
Z	4		2	
Density (calculated)	1.747 Mg/m^3		1.705 Mg/m^3	
Absorption coefficient	3.100 mm^{-1}		2.764 mm^{-1}	
F(000)	2272		1296	
Crystal size	0.08 x 0.06 x 0.03 mm^3		0.10 x 0.01 x 0.01 mm^3	
θ range for data collection	3.01 to 25.02°		2.97 to 25.03°	
Index ranges	-22<=h<=22, -30<=k<=29,10<=l<=10		-10<=h<=10, -14<=k<=14, -27<=l<=27	
Reflections collected	19870		27795	
Independent reflections	7474 [R(int) = 0.0537]		8840 [R(int) = 0.0727]	
Completeness to θ [°]	θ = 25.02° - 99.7%		θ = 25.03° - 99.1%	
Absorption correction	Semi-empirical from equivalents		Semi-empirical from equivalents	
Max. and min. transmission	0.911 and 0.800		0.9729 and 0.7696	
Refinement method	Full-matrix least-squares on F^2		Full-matrix least-squares on F^2	
Data / restraints / parameters	7474 / 644 / 587		8840 / 0 / 663	
Goodness-of-fit on F^2	1.264		1.199	
Final R indices [I>2σ (I)]	R1 = 0.1045, wR2 = 0.2314		R1 = 0.0754, wR2 = 0.1338	
R indices (all data)	R1 = 0.1211, wR2 = 0.2405		R1 = 0.1097, wR2 = 0.1508	
Absolute structure parameter	0.27(3)			
Largest diff. peak and hole	4.384 and -4.911 e.Å^{-3}		1.166 and -0.767 e.Å^{-3}	

3.2.5. Surface monolayers of ruthenium and osmium complexes on planar gold

Surface monolayers of modified ruthenium and osmium tris-bipyridine complexes bearing a thioacetate (SAc) moiety as a gold attachment anchor (Scheme 3.10) have been investigated on planar gold surfaces.

In order to characterise the attached compounds on the surfaces, FTIR spectroscopy and XPS have been used. Also ellipsometry has been applied to measure the thickness of the monolayers on the gold surface.

In all above experiments, polycrystalline gold with 30 nm thickness on 0.01 inch-silicon wafer, pre-coated with titanium (rms-roughness < 1 nm) has been used, which has been cleaned with either Piranha solution for 10 min or UVO (UV-Ozone) for 1 hour before usage.

In section 3.2.5 photophysical properties of ruthenium and osmium complexes on the gold surface have been studied, using glass slides coated with 30 nm polycrystalline gold.
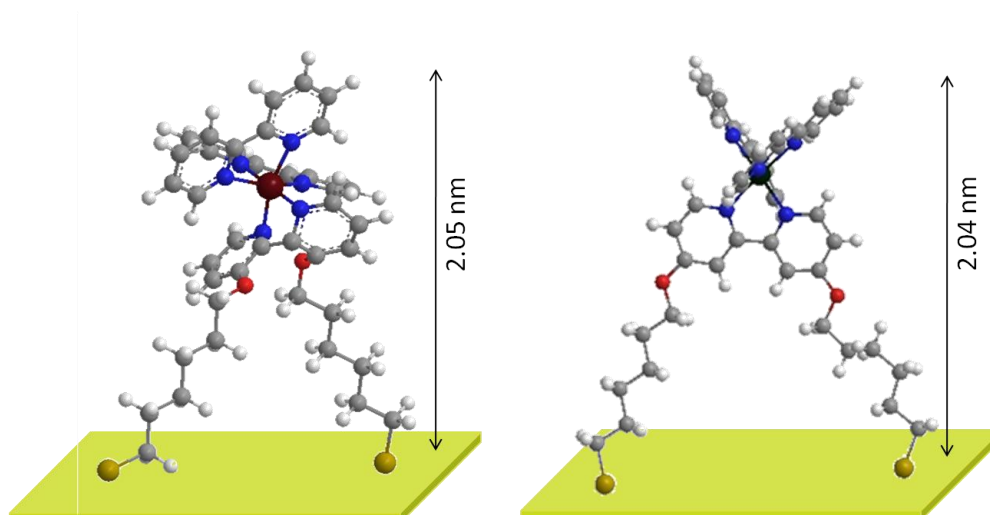
Scheme 3.10 Schematic representation of surface monolayers (M = Ru /Os),

right [Ru(bpy)$_2$(3,3'-bpysac)](PF$_6$)$_2$and left [Os(bpy)$_2$(4,4'-bpysac)](PF$_6$)$_2$.

3.2.5.1. Ellipsometry Study of Surface assemblies of metal complexes

Ellipsometry was used to investigate the formation of the surface monolayer of [Ru(bpy)$_2$(3,3'-bpysac)](PF$_6$)$_2$ on a planar gold surface as a function of time. After measuring the thickness of the surface at different times, it was decided to leave the surface for 24 hours to achieve maximum loading while still remaining a monolayer (Figure 3.38). The attachment of the complex was a monolayer as shown by Chem3D calculations. After 24 hours the total thickness of the surface was 2.06 ± 0.096 nm which is very close to the estimated length (~ 2.05 nm) of the molecule from Chem3D modelling. The Au-S (~ 2.36 Å) bond is also considered in this estimation.
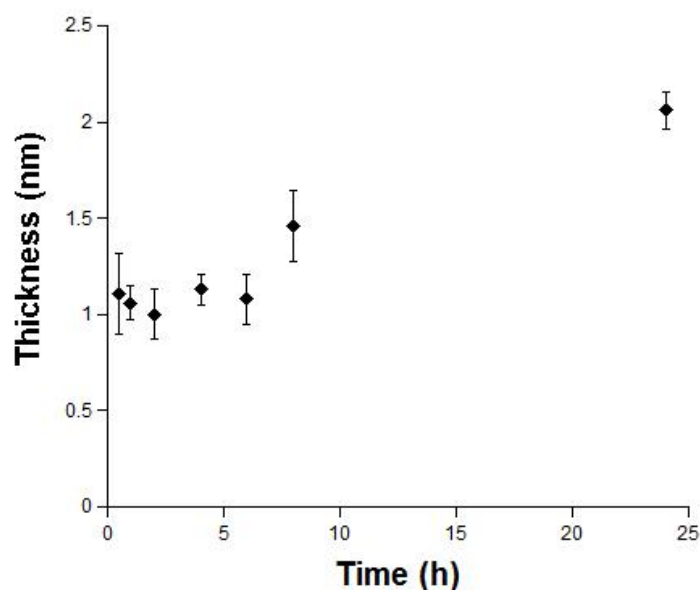
Figure 3.28 Formation of [Ru(bpy)$_2$(3,3'-bpysac)](PF$_6$)$_2$ monolayer in different deposition times from 1mM acetonitrile solution.

A similar experiment has been carried out using [Ru(bpy)(3,3'-bpysac)$_2$](PF$_6$)$_2$, to investigate the formation of the surface monolayer on a planar gold surface as a function of time (Figure 3.29). The [Ru(bpy)(3,3'-bpysac)$_2$](PF$_6$)$_2$ has the advantage of having a stronger intraction with surface via its four gold attachment anchors. In this case the thickness of the surface was monitored for 24 hours, during which time the thickness growth curve gave clearer trend. The thickness after 24 hours deposition time was measured to be 1.87 ± 0.109 nm which is very close to the estimated length (~ 1.90 nm) of a monolayer of such a molecule by Chem3D modelling.
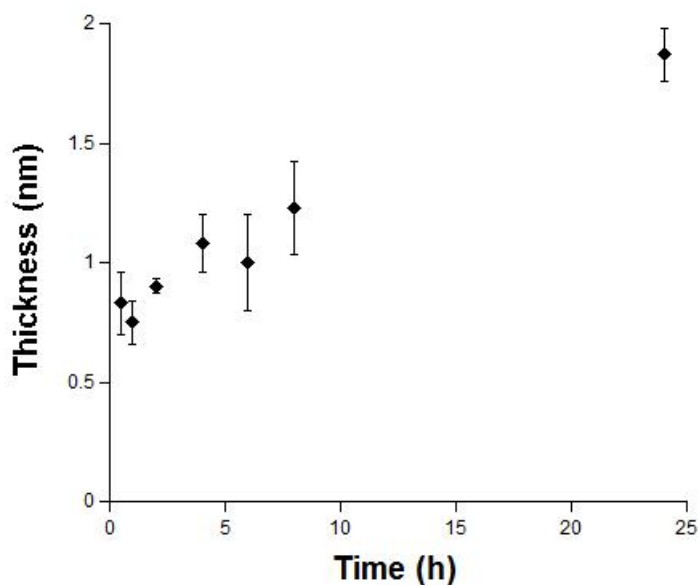
Figure 3.29 Formation of [Ru(bpy)(3,3'-bpysac)$_2$](PF$_6$)$_2$ monolayer in different deposition times from 1mM acetonitrile solution.

Based on these ellipsometric experiments, for the rest of the surface monolayers, the thickness was measured after 24 hours deposition of the gold substrate using a 1 mM acetonitrile solution of the metal complex. Ellipsometry data corresponding to the monolayer thickness of all complexes are very close to the calculated length of the monolayer of such molecules from Chem3D modelling. The ellipsometry data and the estimated lengths of the metal complexes are summarised in the table 3.3.

Table 3.3 The estimated and ellipsometric length of surface bound metal complexes

Metal complex	~ Estimated length of molecule (nm)	Measured thickness of layer (nm)
[Ru(bpy)$_2$(3,3'-bpysac)](PF$_6$)$_2$	2.05	2.06 ± 0.10
[Ru(bpy)(3,3'-bpysac)$_2$](PF$_6$)$_2$	1.91	1.87 ± 0.11
[Ru(bpy)$_2$(4,4'-bpysac)](PF$_6$)$_2$	2.04	1.94 ± 0.16
[Ru(bpy)(4,4'-bpysac)$_2$](PF$_6$)$_2$	1.90	2.00 ± 0.18
[Os(bpy)$_2$(3,3'-bpysac)](PF$_6$)$_2$	2.05	2.35 ± 0.07
[Os(bpy)$_2$(4,4'-bpysac)](PF$_6$)$_2$	2.04	1.79 ± 0.31
[Ru(bpy)$_2$(4,4'-bpyhex)](PF$_6$)$_2$		0.42 ± 0.04

As a control experiment, a planar gold surface was deposited in a solution of 1 mM [Ru(bpy)$_2$(4,4'-bpyhex)](PF$_6$)$_2$ (with no gold anchor) for 24 hours. The surface thickness has been measured under the same conditions resulting in a surface thickness of 0.42 ± 0.04. This confirms the need of the SAc groups for attachment of the metal complexes to the gold surface.

3.2.5.2. X-ray photoelectron spectroscopy (XPS) Study of Surface assemblies of metal complexes

X-ray photoelectron spectroscopy is a useful method for the study of SAMs for several purposes such as elemental analysis, determination of the connection among some atoms or the presence of certain functional groups. The observed binding energies in the XPS spectrum depend on the electron density of a specific atom, which varying primarily with the nature of the element considered and

secondarily with the nature of the atoms directly attached to it (especially their electronegativity).[43] With XPS, qualitative analyses of SAMs are usually possible, but quantitative analyses are normally restricted to specific cases due to their experimental uncertainties (e.g. in the case of inhomogeneous SAM while the matter-dependent attenuation length of photoelectrons is typically not known with certainty).[44]

The XPS spectra (wide spectrum and the C 1s + Ru 3d region) of [Ru(bpy)(4,4'-bpysac)$_2$](PF$_6$)$_2$ film is shown in figure 3.30 as a representative of all films of ruthenium complexes. The XPS spectra of [Ru(bpy)$_2$(3,3'-bpysac)](PF$_6$)$_2$, [Ru(bpy)(4,4'-bpysac)$_2$](PF$_6$)$_2$, [Ru(bpy)$_2$(4,4'-bpysac)](PF$_6$)$_2$ are presented in appendix (A3.59 – A3.61). All spectra show the presence of carbon, sulfur, and oxygen in addition to the underlying gold substrate.
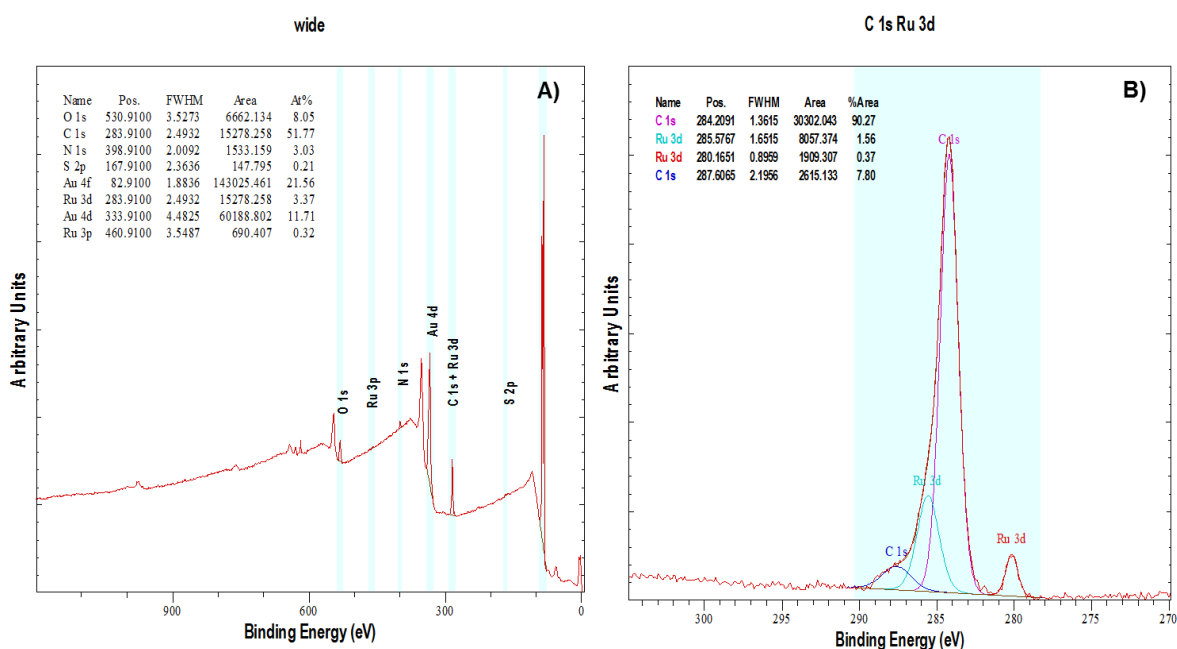
Figure 3.30 A) Full XPS spectrum of [Ru(bpy)(4,4'-bpysac)$_2$](PF$_6$)$_2$ monolayer on planar gold surface, B) The narrow scan spectra of the C 1s, Ru 3d region.

The $3p_{3/2}$, $3d_{3/2}$ and $3d_{5/2}$ signals of metallic ruthenium are clearly observed at 460.91, 285.58 and 280.16 eV respectively, referenced to Au $4f_{7/2}$ at 83.9 eV with full widths at half-maximum (fwhm) of 4.1 eV.[45,46] The spectrum of [Ru(bpy)(4,4'-bpysac)$_2$](PF$_6$)$_2$ also exhibits the characteristic C 1s and O 1s peaks at 284.21 and 531.19 eV.[47] Unfortunately, the Ru 3d peaks are close to the binding energy of C 1s peaks which are masked by the C 1s signals for the carbon support and heteroaromatic rings. However, the pronounced asymmetry of these peaks give a broad shoulder on the low binding energy side of the spectrum at 280.16 eV, which is attributed to the Ru $3d_{5/2}$ peak.[48,49] In addition to the N 1s signal at 399.24 eV, the C 1s, and O 1s peaks also can all be observed which provides a strong evidence for the presence of heteroaromatic molecules, bipyridines, on the surface. Finally the C: N: Ru peak area ratios (after peak-fitting and adjustment with the atomic sensitivity factors) were in good agreement with the theoretical ratios predicted by the molecular structure. The XPS data that were observed for each ruthenium complex monolayer are included in Table 3.4.

Table 3.4 X-Ray photoelectron spectroscopic analysis of ruthenium surfaces

	Binding energy (eV)			
	O 1s	C 1s	N 1s	Ru 3d
[Ru(bpy)$_2$(3,3'-bpysac)](PF$_6$)$_2$	531.56	284.16	399.31	285.66 280.25
[Ru(bpy)(3,3'-bpysac)$_2$](PF$_6$)$_2$	531.18	283.96	399.15	284.94 279.98
[Ru(bpy)$_2$(4,4'-bpysac)](PF$_6$)$_2$	531.11	284.08	399.29	285.56 280.21
[Ru(bpy)(4,4'-bpysac)$_2$](PF$_6$)$_2$	531.19	284.21	399.24	285.58 280.16

In the case of the monolayers of the osmium complexes, XPS analysis of the various osmium complex monolayers showed the $4f_{7/2}$ and $4f_{5/2}$ signals of osmium at around 50.7 eV and 53.4 eV respectively, referenced to Au $4f_{7/2}$ at 83.9 eV with full widths at half-maximum (fwhm) of 4.1 eV. The XPS spectrum of the $[Os(bpy)_2(4,4'-bpysac)](PF_6)_2$ film has been shown in Figure 3.32. The XPS spectra of $[Os(bpy)_2(3,3'-bpysac)](PF_6)_2$ are presented in appendix (A3.62).
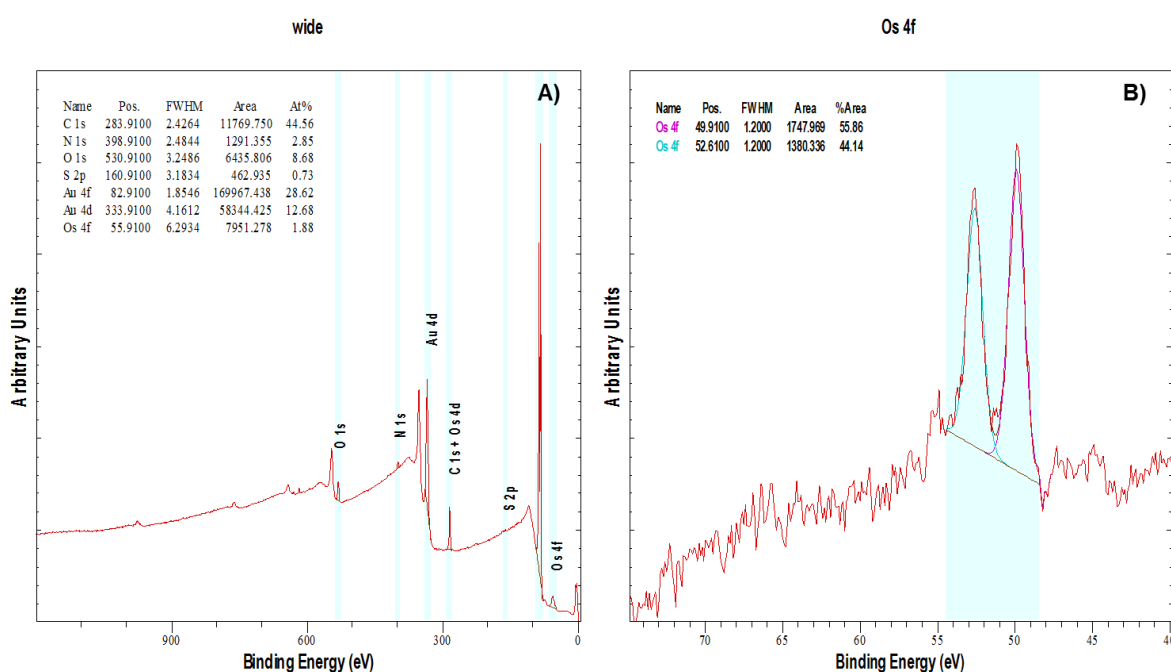
Figure 3.31 A) Full XPS spectrum of $[Os(bpy)_2(4,4'-bpysac)](PF_6)_2$ monolayer on planar gold surface B) The narrow scan spectra of the Os 4f region.

The XPS spectrum of $[Os(bpy)_2(4,4'-bpysac)](PF_6)_2$ exhibits the characteristic peaks of the Os $4f_{7/2}$ (49.91 eV), Os $4f_{5/2}$ (52.61 eV), C 1s (284.12 eV), N 1s (399.41 eV) and O 1s (530.57 eV). The Os 4d peaks are masked by the C 1s signals of the carbon. However a broad shoulder on the low binding energy side at 277.46 eV, is attributed to the Os $4d_{5/2}$ peak which can be measured. Similar peaks for

polypyridine osmium complexes have been reported before by other groups.[50] And finally the C: N: Os peak area ratios (after peak-fitting and adjustment with the atomic sensitivity factors) were in good agreement with the theoretical ratios predicted by the molecular structure.

Table 3.5 X-Ray photoelectron spectroscopic analysis of osmium surfaces

	Binding energy (eV)				
	O 1s	C 1s	N 1s	Os 4f	Os 4d
[Os(bpy)$_2$(3,3'-bpysac)](PF$_6$)$_2$	530.35	283.78	399.10	49.54 52.45	287.95
[Os(bpy)$_2$(4,4'-bpysac)](PF$_6$)$_2$	530.57	284.12	399.41	49.91 52.61	277.46 291.69

A more detailed analysis is needed for the S 2p region to understand the binding of the complexes to the gold surface. An examination of the S 2p region of an XPS spectrum of SAMs on gold is precisely informative for two reasons. Firstly, the existence of unbound sulfur associated with either the formation of a multilayer or the incomplete attachment of the adsorbates can be confirmed. We assigned the photoelectron peaks with binding energies of around 162 and 163 eV to the doublet S 2p$_{3/2}$ -S 2p$_{1/2}$, respectively, for sulfur bound to gold. The unbound sulfur can be confirmed by the observation of a signal at around 164 eV.[51-53] Secondly, the potential oxidation of sulphur atoms can be evaluated by peaks at around 167 eV. The narrow scans of the S 2p signals of all complexes are shown in figure 3.32.

It has previously been found that acetyl-protected thiols provide an excellent method to avoid problems of isolating and using the oxidatively unstable thiols.[53] Acetyl protected thiols can be deacylated completely within 10 min using aqueous NH_4OH. Experiments have also been carried out showing that SAM formation is possible without deprotection by base (in this case thioacetate will be eliminated in the process of monolayer formation, to form the gold thiolate). However thioacetyl-containing adsorbates in higher concentrations, relative to thiols, do require initial base deprotection to achieve monolayer coverage.[53] It was also reported that, in the cases of base-promoted adsorptions or direct adsorption of the thioacetyl-terminated systems, the XPS results confirmed that the SAMs were similar in their composition to the SAMs produced from the free thiols [53], which is similar to what we also observed.
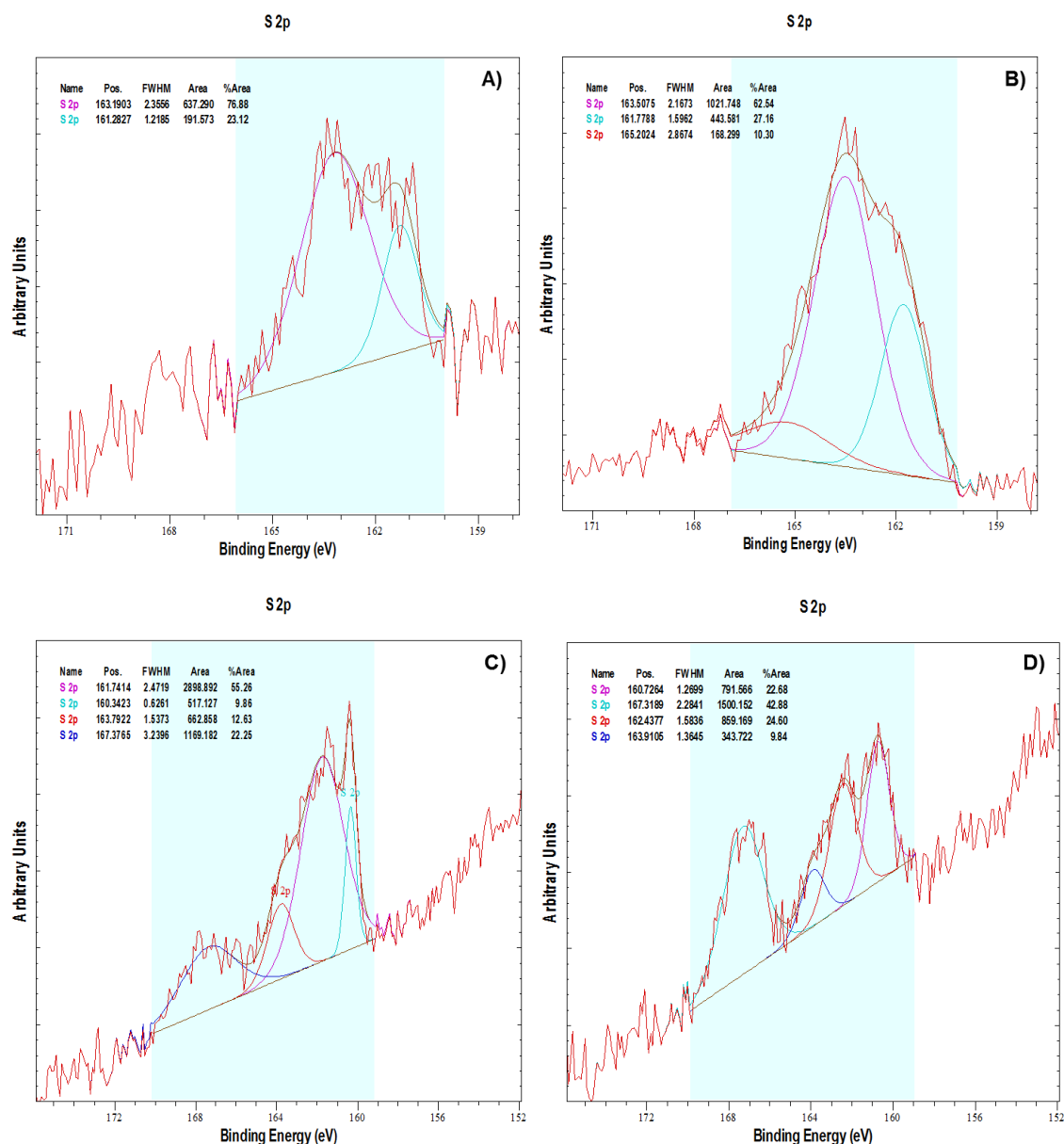
Figure 3.32 The narrow scan spectra of the S 2p region of A) [Ru(bpy)$_2$(3,3'-bpysac)](PF$_6$)$_2$ B) [Ru(bpy)(3,3'-bpysac)$_2$](PF$_6$)$_2$ C) [Ru(bpy)$_2$(4,4'-bpysac)](PF$_6$)$_2$ D) [Ru(bpy)(4,4'-bpysac)$_2$](PF$_6$)$_2$.

In figure 3.32 the monolayers of [Ru(bpy)$_2$(3,3'-bpysac)](PF$_6$)$_2$ and [Ru(bpy)(3,3'-bpysac)$_2$](PF$_6$)$_2$ are formed by using the thioacetates without deprotection using base. Looking at the S 2p region of these two monolayers, we can see that all of the sulfur atoms are bound to the surface of gold, and thioacetate has been completely

removed. However in case of the $[Ru(bpy)(3,3'-bpysac)_2](PF_6)_2$, it seems that a small peak corresponding to the unbound sulfur species is also present.

During the formation of the $[Ru(bpy)_2(4,4'-bpysac)](PF_6)_2$ and $[Ru(bpy)(4,4'-bpysac)_2](PF_6)_2$ monolayers, when base (NH_4OH) was used to deprotect the thioacetate group, no peak for unbound sulphur atoms can be seen, which confirms that the use of base is more promising for removing all thioacetate groups. However this will also cause the sulphur to oxidise which can be evaluated by relatively large peaks at around 167 eV.

The monolayer formation of $[Os(bpy)_2(3,3'-bpysac)](PF_6)_2$ and $[Os(bpy)_2(4,4'-bpysac)](PF_6)_2$ needs base (as we also disscuss in surface IR analysis), but again peaks for both sulphate and sulfonate can be observed, indication some oxidation.

Surface coverage of ruthenium and osmium compexes on gold substrates has been estimated to be a full surface coverage of gold substrates, which confirms the formation of the packed and full monolayers. This can be calculated from the peak ratio of Ru: Au or Os: Au, using the atomic radius of the Au atoms and the estimated foot print of the complexes from chem-3D.

3.2.5.3. FTIR Study of surface assemblies of metal complexes

The deposition of ruthenium and osmium complexes on the gold surface has been confirmed by mid-IR range FTIR spectroscopy, using the ATR (Attenuated Total Reflectance) attachment and running 50-100 scans due to the weak intensity of the

peaks. Silica plates coated with a 30 nm gold layer were used to prepare the surface monolayer. The monolayer side of the surface was placed faced down on the ATR attachment and fixed to ensure that the gap between the surface and the spectrometer is at a minimum, and the spectrum of the monolayer was obtained.

The IR spectra of monolayers of ruthenium and osmium complexes on the gold surface are very similar to the spectra of their powders. They are characterised by bands at 2915 and 1553 cm^{-1} that can be assigned to the C-H stretching and scissoring vibrations of the alkyl chains, and a band at 2990 cm^{-1} can be assigned to the C-H stretching of the aromatic rings. Further bands at 1450,1424,and 1411 cm^{-1} can be assigned to the C=C, C=N ring stretching and the band at 1116 cm^{-1} can be assigned to the C-O-C asymmetric stretching.

The bands at 760 cm^{-1} and 710 cm^{-1} for out of plane C-H bending of aromatic rings, are presented very weakly and with a 10 cm^{-1} shift to higher wave number. The low intensity of the peaks in this region can be attributed to the high background of blank gold which does not allow the peaks to be seen easily. The ruthenium complex in nutrelised upon attachment to the gold surface and as the result, the band at 851 cm^{-1} assigned to the PF_6^- counter ions disappeared in monolayer unlike the powder form where it has a strong intensity.
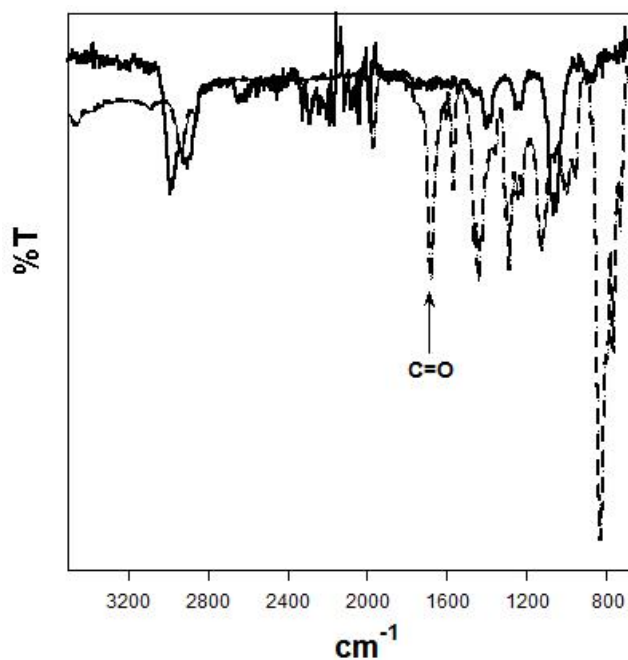
Figure 3.33 FTIR spectrum of a monolayer of [Ru(bpy)$_2$(3,3'-bpysac)](PF$_6$)$_2$ on a gold surface (solid line) and powder (dashed line).

Another characteristic peak for C=O stretching in SAc group which is present in the powder FTIR spectrum is at around 1681 cm^{-1}. This disappeared in monolayer spectrum, which confirms the leaving of the acetyl protection group while attaching to the gold surface.
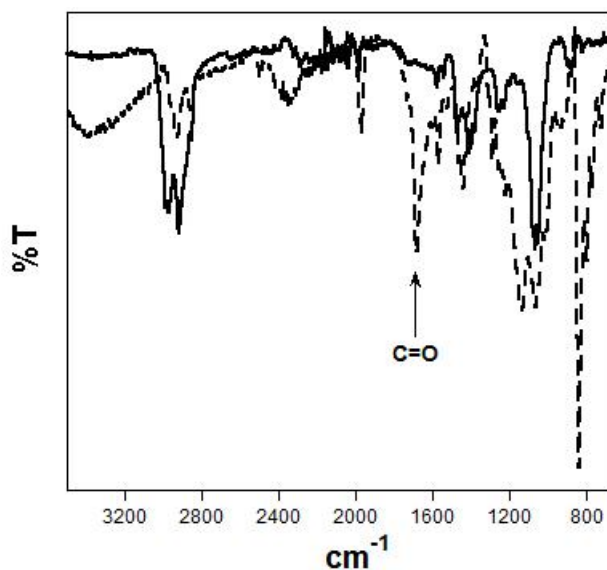
Figure 3.34 FTIR spectrum of a monolayer of [Ru(bpy)(3,3'-bpysac)$_2$](PF$_6$)$_2$ on a gold surface (solid line) and powder (dashed line).

In case of the osmium complexes, a very small peak assigned to C=O stretching can be observed, which indicates that the acetyl group has not been removed completely. In that case, de-protection of thiol group was assisted by the addition of a small amount of ammonia solution into the acetonitrile solution of the osmium complex and shaking for 10 min, which allowed removal of all acetyl groups. Deposition onto the gold surface of such a solution of the osmium complex will show no C=O stretching band in FTIR spectrum at around 1681 cm^{-1}. Stretching vibration of C-S band should appear in range of 700-600 cm^{-1}, but the weakness of absorption and variability of position make this band of little value.
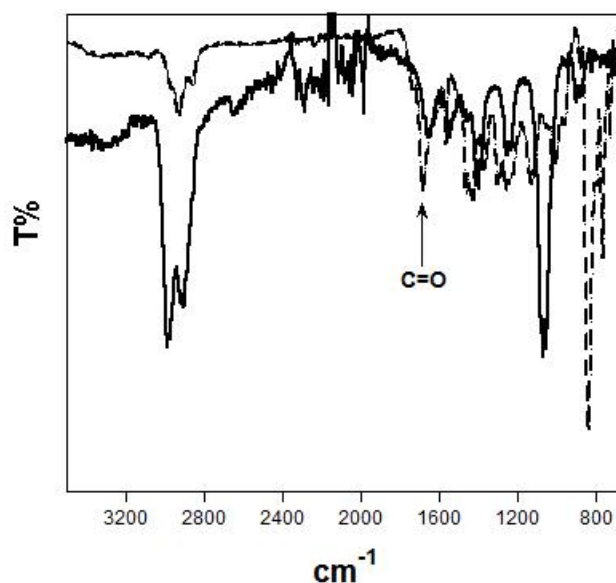
Figure 3.35 FTIR spectrum of a monolayer of [Os(bpy)$_2$(3,3'-bpysac)](PF$_6$)$_2$ on a gold surface (solid line) and powder (dashed line).

3.2.6. Photophysical properties of the complexes in solution, and as powders and monolayers

3.2.6.1. Ruthenium tris-bipyridine complexes

The photophysical properties of all ruthenium complexes were investigated in acetonitrile solution, in powder form and as a monolayer on a gold surface. Acetonitrile solutions of [Ru(bpy)$_2$(3,3'-bpysac)](PF$_6$)$_2$ and [Ru(bpy)(3,3'-bpysac)$_2$](PF$_6$)$_2$ exhibit absorption spectra in which the visible region is dominated by a broad band at around 454 nm ([1]MLCT) and two further absorptions in the UV

region, at 292 nm (LC) and 247 nm ([1]MLCT) which are typical for ruthenium tris-bipyridyl complexes. There is also a weak [3]MC band present at 360 nm. The $[Ru(bpy)_2(3,3'-bpysac)](PF_6)_2$ and $[Ru(bpy)(3,3'-bpysac)_2](PF_6)_2$ powders display a very similar absorption spectrum to that in acetonitrile solution, with more discrete [1]MLCT bands. The absorption spectrum of $[Ru(bpy)(3,3'-bpysac)_2](PF_6)_2$ as a powder exhibits two [1]MLCT bands at 440 and 470 nm, arising from two different ligands (Figure 3.36). The absorption and emission spectra of the $[Ru(bpy)_2(3,3'-bpysac)](PF_6)_2$ and $[Ru(bpy)(3,3'-bpysac)_2](PF_6)_2$ monolayers on gold surfaces are very weak and can't be recorded.
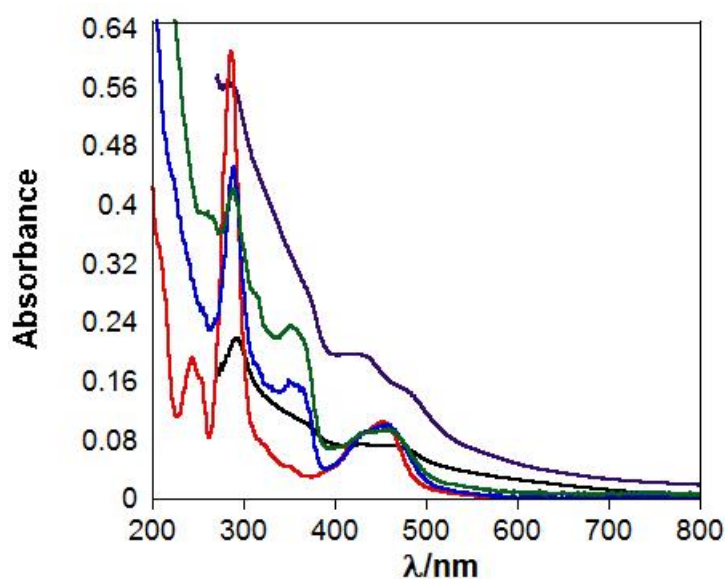
Figure 3.36 Absorption spectra of $[Ru(bpy)_3]Cl_2$ (C = 7.1 × 10^{-6} M, red), $[Ru(bpy)_2(3,3'-bpysac)](PF_6)_2$ (C = 1.1 × 10^{-5} M, blue), $[Ru(bpy)(3,3'-bpysac)_2](PF_6)_2$ (C = 2.1 × 10^{-5} M, green) in acetonitrile and $[Ru(bpy)_2(3,3'-bpysac)](PF_6)_2$ powder (black) and $[Ru(bpy)(3,3'-bpysac)_2](PF_6)_2$ powder (purple).

Acetonitrile solutions of [Ru(bpy)$_2$(3,3'-bpysac)](PF$_6$)$_2$ and [Ru(bpy)(3,3'-bpysac)$_2$](PF$_6$)$_2$ display weak luminescence from the ^{3}MLCT excited states, at 625 nm for [Ru(bpy)$_2$(3,3'-bpysac)](PF$_6$)$_2$ and 610 nm for [Ru(bpy)(3,3'-bpysac)$_2$](PF$_6$)$_2$, when excited at around 455 nm (^{1}MLCT) at room temperature (Figure 3.37). The ^{3}MLCT band of [Ru(bpy)$_2$(3,3'-bpysac)](PF$_6$)$_2$ is red-shifted by 5 nm in comparison with Ru(bpy)$_3$Cl$_2$ in water which has a quantum yield of 0.028.[8,54] The ^{3}MLCT band of [Ru(bpy)(3,3'-bpysac)$_2$](PF$_6$)$_2$ is 10 nm blue-shifted in comparison with Ru(bpy)$_3$Cl$_2$ in water. This can be due to the orientation of the aliphatic substituents around the ruthenium complex.
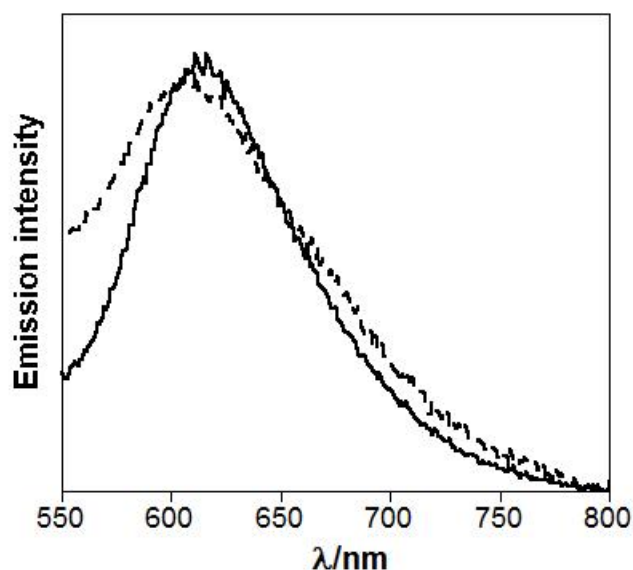
Figure 3.37 Emission spectrum of [Ru(bpy)$_2$(3,3'-bpysac)](PF$_6$)$_2$ (C = 1.1 × 10^{-5} M, solid line) in acetonitrile, λ_{exc} = 451 nm and [Ru(bpy)(3,3'-bpysac)$_2$](PF$_6$)$_2$ (C = 2.1 × 10^{-5} M, dashed line) in acetonitrile, λ_{exc} = 458 nm.

The measured quantum yields of these ruthenium complexes were surprisingly low in comparison to that of Ru(bpy)$_3$Cl$_2$. This is the result of geometric distortion of the

complexes symmetry due to the substitution at the 3,3'- positions of the bipyridine ligand, as previously reported.[8,54,55] For instance the photophysical properties of the ruthenium complex of 3,3'-dimethyl-2,2'-bipyridine (3-dmbpy) were studied by Nakamaru[54] and showed a 66-80 % drop in quantum yield in comparison with the parent $[Ru(bpy)_3]^{2+}$ complex. This has been justified by the expected twisting of the bipyridine unit due to substitution on this 3,3'-position, and hence the formation of a non-coplanar conformation. The photophysical properties of the ruthenium complexes of the bipyridine ligand with substituents in 3,3'-positions are summarised in table 3.7.

It is expected that the substitution in the 4,4'-positions of the bipyridine should give better photophysical properties to the ruthenium and osmium complexes. Hou *et al.* have previously studied ruthenium (II) complexes bearing different substitutions in the 4,4'-positions of the bipyridine.[56] The properties of the substituents were varied from electron-donating (OCH_3, NH_2) to electron-withdrawing (CO_2Et, $COOH$, NO_2) but in all cases the maximum in the MLCT band and the emission energy shifted to lower energy, compared with the $Ru(bpy)_3Cl_2$ complex. The complexes bearing electron withdrawing substituents were reported to have higher luminescence quantum yields and longer excited-state lifetimes than those bearing electron-donating ones, at room temperature.

These observations were explained by considering the MLCT nature of the excited state. When the substituents are electron-accepting groups, the π^* ligand-centred orbital is more stabilized than the π (t_{2g}) metal-centred orbital. While when the substituents are electron-donating groups, the MLCT excited state energy

decreases as a consequence of the larger destabilisation of the metal π (t_{2g}) orbital compared with the ligand-centred π^* orbital.

The absorption spectra of the [Ru(bpy)$_2$(4,4'-bpysac)](PF$_6$)$_2$ and [Ru(bpy)(4,4'-bpysac)$_2$](PF$_6$)$_2$ complexes in acetonitrile solution display features which are typical of ruthenium (II) complexes with ethynyl-substituted bipyridyl ligands. These namely consist of ^{1}MLCT absorptions at 460 nm, and two further ligand centred absorptions with maxima at 288 nm and 257 nm. In both complexes, the ^{1}MLCT absorptions are red-shifted in comparison with the parent complex Ru(bpy)$_3$Cl$_2$. In the case of the [Ru(bpy)(4,4'-bpysac)$_2$](PF$_6$)$_2$ all the bands are even more red shifted, and the ^{1}MLCT absorption appears at 468 nm. Figure 3.38 shows the UV-Vis absorption spectra of [Ru(bpy)$_2$(4,4'-bpysac)](PF$_6$)$_2$ and [Ru(bpy)(4,4'-bpysac)$_2$](PF$_6$)$_2$ and the parent complex Ru(bpy)$_3$Cl$_2$.
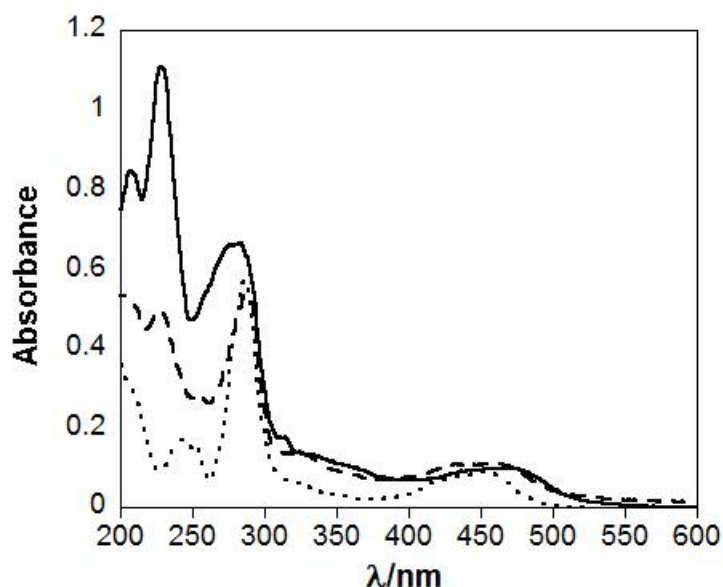
Figure 3.38 Absorption spectra of Ru(bpy)$_3$Cl$_2$ (C = 7.1 × 10^{-6} M, dotted line), [Ru(bpy)$_2$(4,4'-bpysac)](PF$_6$)$_2$ (C = 7.4 × 10^{-6} M, dashed line) and [Ru(bpy)(4,4'-bpysac)$_2$](PF$_6$)$_2$ (C = 1.3 × 10^{-5} M, solid line) in acetonitrile.

The UV-Vis spectra of surface monolayers of these ruthenium complexes have been compared to that of them in powder form and in acetonitrile solution. As the boro-float glass used in this study does not exhibit absorbance at wavelengths over the range 250-800 nm, the absorbance recorded by UV-Vis spectroscopy can be attributed to electronic transitions of the surface films deposited on it.

The ^{1}MLCT band of [Ru(bpy)$_2$(4,4'-bpysac)](PF$_6$)$_2$ in acetonitrile solution appears at 460 nm. This is significantly red-shifted in the powder spectrum, and appears at 490 nm, whereas it appears even further red-shifted in [Ru(bpy)$_2$(4,4'-bpysac)](PF$_6$)$_2$ monolayer, at 510 nm. Similar shifts can be seen with the MC band which apears at 330 nm in solution, 340 nm in the powder spectrum and at 360 nm in the monolayer spectrum. The intense LC band at 290 nm remains in same position in all spectra. Another LC band which usually appears at around 250 nm cannot be observed due to the strong absorption of the glass substrate which has been used in this study (Figure 3.39).
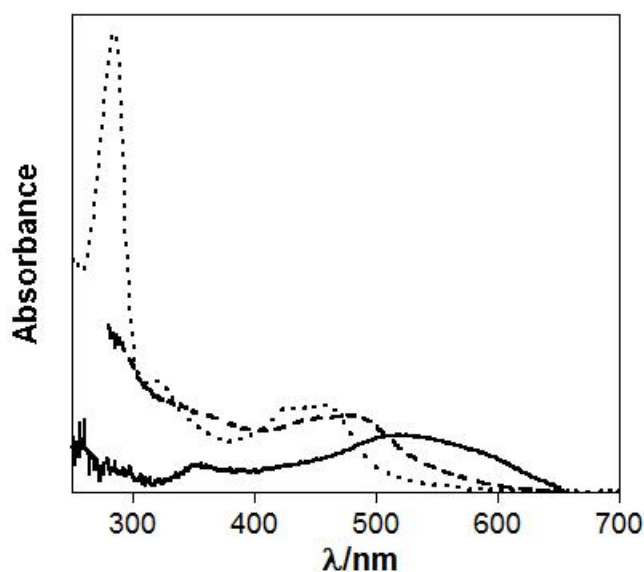
Figure 3.39 UV-Vis spectrum of [Ru(bpy)$_2$(4,4'-bpysac)](PF$_6$)$_2$ in acetonitrile solution (dotted line), reflectance spectrum of powder (dashed line) and transmittance spectrum of monolayer (solid line). Not in same y scale.

Similarly for the complex [Ru(bpy)(4,4'-bpysac)$_2$](PF$_6$)$_2$, the [1]MLCT absorption band in acetonitrile solution appears at 468 nm, but is red-shifted to 490 nm in the powder spectrum and further red-shifted to 495 nm for the monolayer. In both the monolayer and powder spectra, the [1]MLCT band splits into two components. The MC band appeared at 330 nm in solution; at 340 nm in the powder spectrum and at 360 nm in the monolayer spectrum. The intense LC band at 290 nm remains in same position in all three spectra (Figure 3.40). The observed shifts can be explained by the immobilisation of the complexes in powder and monolayer forms, which makes a different environment around the luminescent centre. Immobilisation of the complexes also deactivates high energy vibrational modes which have effect on position and intensity of the peaks. In addition, in the powder and monolayer spectra, the [3]MLCT absorption band of the ruthenium complexes can be seen, at

580 nm. The ^{3}MLCT band of Ru(bpy)$_3$Cl$_2$ has been reported before in the absorption spectrum at 550 nm in an ethanol–methanol glass at 77 K.[57]
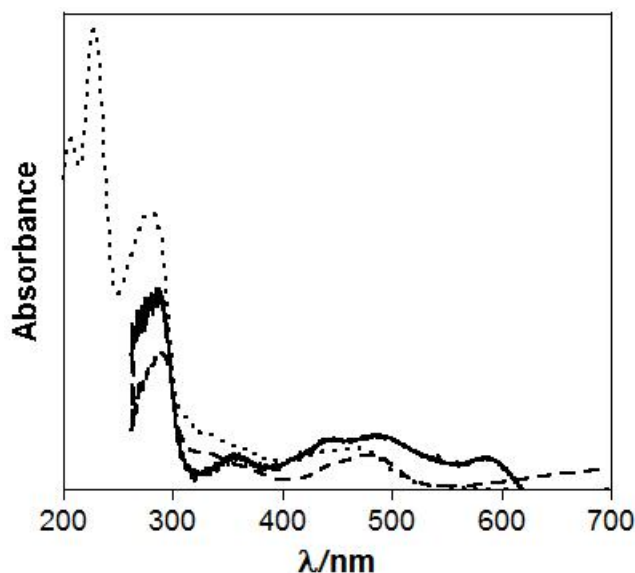
Figure 3.40 UV-Vis spectrum of [Ru(bpy)(4,4'-bpysac)$_2$](PF$_6$)$_2$ in acetonitrile solution (dotted line), reflectance spectrum of powder (dashed line) and transmittance spectrum of monolayer (solid line). Not in the same y scale.

The red shift in the MLCT bands of ruthenium (II) complexes upon attachment to gold surfaces, has been observed before by Dong *et al*.[58] Similar effects have been also reported by Gulino *et al*, who observed a 7 nm red shift for the ligand-centred π−π* transition of the monolayer of the ruthenium polypyridine complex.[59]

Excitation of the ^{1}MLCT state leads to emission from the lowest triplet state (^{3}MLCT) with a maximum at 633 nm for [Ru(bpy)$_2$(4,4'-bpysac)](PF$_6$)$_2$ and 657 nm for [Ru(bpy)(4,4'-bpysac)$_2$](PF$_6$)$_2$ in acetonitrile solution (Figure 3.41). These ruthenium complexes show significantly red-shifted MLCT states, in comparison to Ru(bpy)$_3$Cl$_2$. The emission of the ruthenium complexes have relative high quantum

yields and long life times (up to 4.9% quantum yield and 685 ns life time for [Ru(bpy)$_2$(4,4'-bpysac)](PF$_6$)$_2$, and 2.4% quantum yield and 409 ns life time for [Ru(bpy)(4,4'-bpysac)$_2$](PF$_6$)$_2$ in deaerated acetonitrile) but still exhibit decreased life times and quantum yields in comparision to Ru(bpy)$_3$Cl$_2$. Both absorption and emission spectra of [Ru(bpy)(4,4'-bpysac)$_2$](PF$_6$)$_2$ are more red-shifted than [Ru(bpy)$_2$(4,4'-bpysac)](PF$_6$)$_2$ spectra in comparision to Ru(bpy)$_3$Cl$_2$ due to having four aliphatic substituents around the ruthenium centre. Although carrying four aliphatic substituents and surface active moieties makes [Ru(bpy)(4,4'-bpysac)$_2$](PF$_6$)$_2$ less symmetric but improves its attachment to the surface which leads in better photophysical properties on the surface.
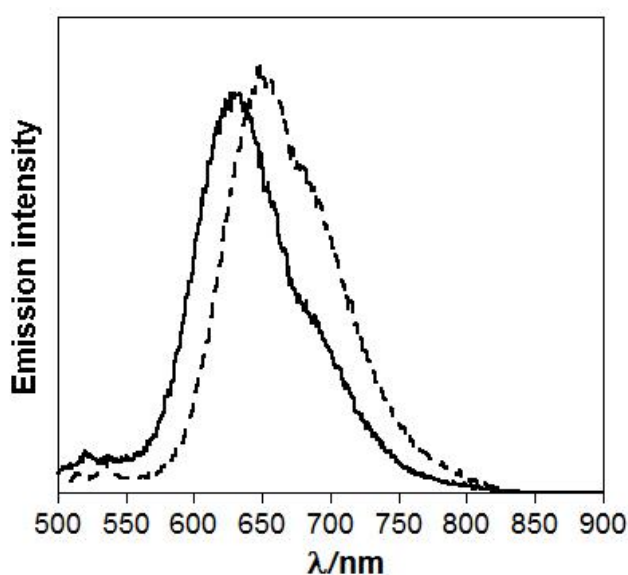
Figure 3.41 Emission spectra of [Ru(bpy)$_2$(4,4'-bpysac)](PF$_6$)$_2$, λ_{exc} = 460 nm (C = 7.4 × 10^{-6} M, solid line) and [Ru(bpy)(4,4'-bpysac)$_2$](PF$_6$)$_2$, λ_{exc} = 468 nm (C = 1.3 × 10^{-5} M, dashed line) in acetonitrile.

The emission spectra of the powder samples and the monolayers of the surface active ruthenium complexes were also recorded. The molecular immobilisation in the solid state reduces the deactivation routes involving high energy vibrational modes in both the powder and the monolayer sample and makes a different envornment around the metal complex. The later effect, results in a blue shift in the emission maxima of the $[Ru(bpy)_2(4,4'-bpysac)](PF_6)_2$, at 620 nm, which is 13 nm shifted to the higher energy in comparison with the one in acetonitrile solution. The dry monolayer of $[Ru(bpy)_2(4,4'-bpysac)](PF_6)_2$ displays an emission with maximum at 610 nm which is 10 nm more blue shifted from the powder sample (Figure 3.42), confirming that the surface attachment immobilises the complex even more. The quantum yield of the powder form of $[Ru(bpy)_2(4,4'-bpysac)](PF_6)_2$ was measured to be 0.05, which is similar to the deaerated quantum yield in solution, suggesting that oxygen quenching does not have much effect in the powder form. The emission spectra of $[Ru(bpy)_2(4,4'-bpysac)](PF_6)_2$ in acetonitrile solution, as a powder and a monolayer are shown in figure 3.42. The emission lifetime of the complex in deareated acetonitrile solution is 685 ns, this is decreased to 545 ns (94 %) in the powder sample. The powder sample shows a bi-exponential lifetime decay containing a small fraction (6%) of a faster component with lifetime of 70 ns which is caused by self-quenching process in the solid sample. The lifetime of the luminescence from the monolayer drops significantly to 90 ns (93 %) which indicates that a huge quenching occurs by electron transfer from excited state of the ruthenium (II) complex to the gold. A short component of 7 ns (7 %) is also included in this decay. The time-resolved emission of a dry monolayer of $[Ru(bpy)_2(4,4'-bpysac)](PF_6)_2$ is shown in figure 3.43.
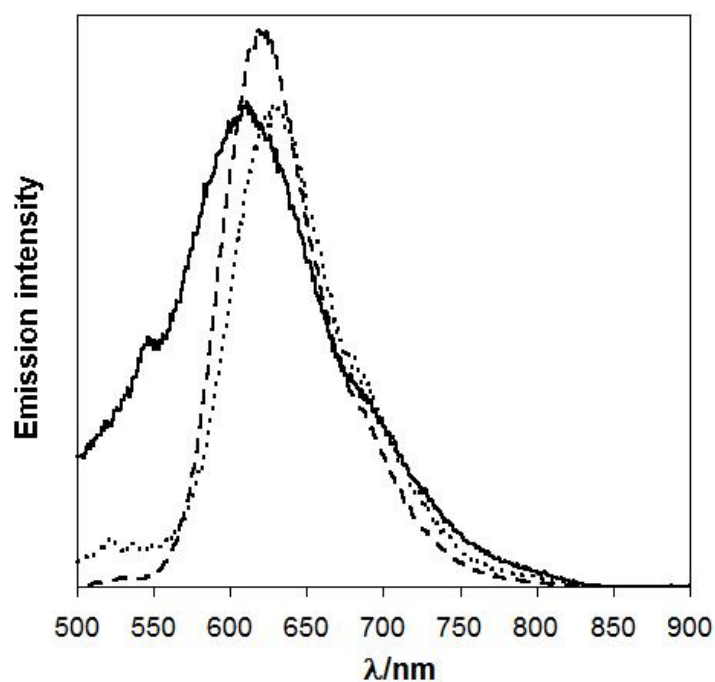
Figure 3.42 Transmittance emission spectra of a dry monolayer of [Ru(bpy)$_2$(4,4'-bpysac)](PF$_6$)$_2$ on a gold surface (solid line), in acetonitrile solution (dotted line) and reflectance spectrum of powder (dashed line) - λ_{ex} = 450 nm.
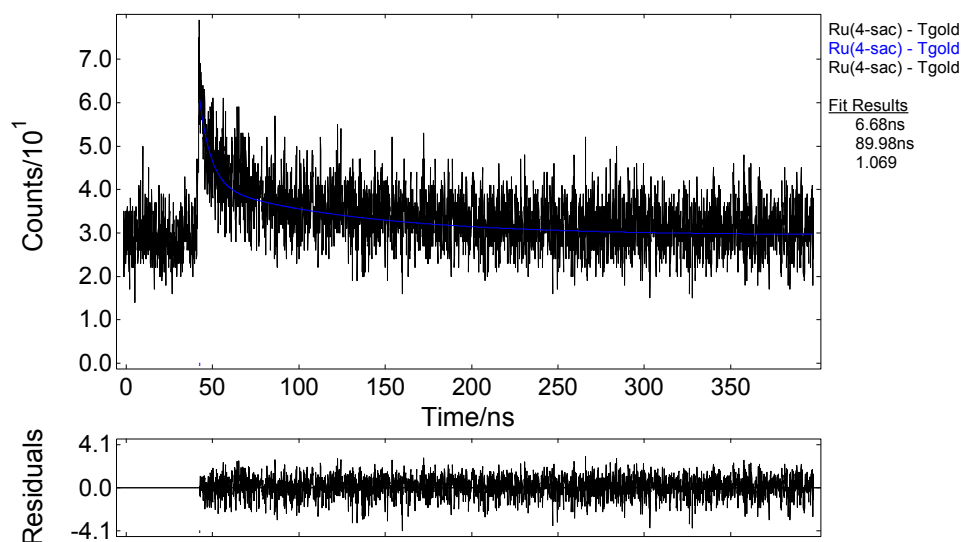
Figure 3.43 Time-resolved emission of [Ru(bpy)$_2$(4,4'-bpysac)](PF$_6$)$_2$ on gold surface recorded at 610 nm. Lifetime detected to be 90 ns (93 %) and 7 ns (7 %) - λ_{exc} = 445 nm.

Luminescence images of the gold surfaces modified with [Ru(bpy)$_2$(4,4'-bpysac)](PF$_6$)$_2$ were also obtained (Figure 3.44 A). Non-ordered islands of concentrated areas of the complex were obsereved on the surface, which can be seen as bright spots in the luminescence images. Similar effect have been also reported by De Cola *et al*.[60]

In order to ascertain whether the luminescence image arise from attached [Ru(bpy)$_2$(4,4'-bpysac)](PF$_6$)$_2$ complex on the surface or not, the emission spectrum of the surface was monitored at different spots, which is shown in figure 3.44 B. The emission spectrum shows a peak for the ^{3}MLCT emission band at 610 nm for the attached complex on the surface.
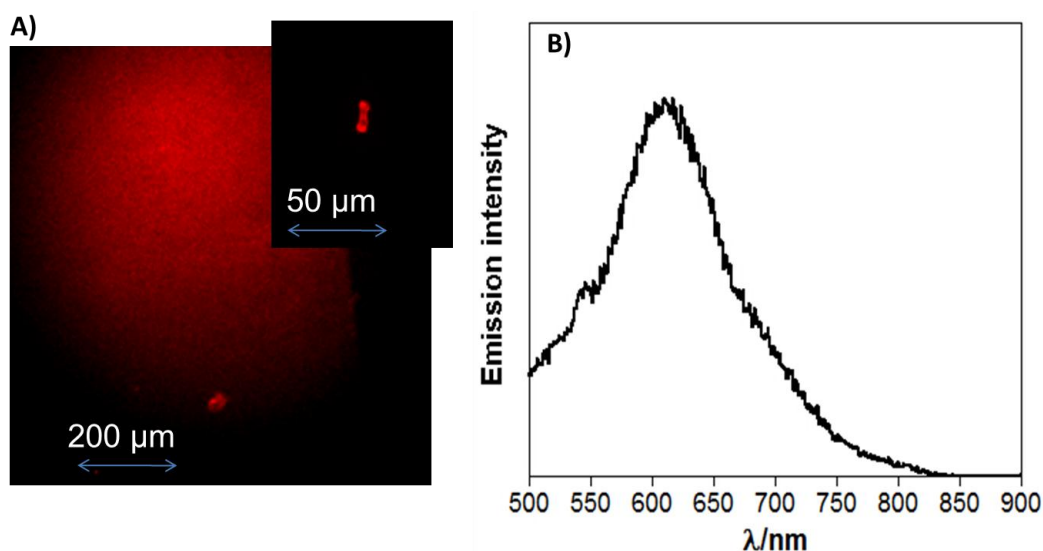
Figure 3.44 A) Fluorescence microscopy images of [Ru(bpy)$_2$(4,4'-bpysac)](PF$_6$)$_2$ on a gold surface. B) Emission spectrum of the image - λ$_{exc}$ = 450.

Upon attachment of [Ru(bpy)(4,4'-bpysac)$_2$](PF$_6$)$_2$ to a planar gold surface, strong emission was observed with a maximum at 615 nm. This is blue-shifted in relation to the acetonitrile solution and the powder sample (Figure 3.45). The lifetime of the luminescence in deareated acetonitrile solution of [Ru(bpy)(4,4'-bpysac)$_2$](PF$_6$)$_2$ is 409 ns. The luminescence of the powder is bi-exponential containing a longer component of 376 ns (93 %) and some short component of 74 ns (7 %) caused by self-quenching of the powder. The lifetime of the monolayer is a bi-exponential containing mainly a long component of 212 ns (88 %) which is shorter than that of the powder, confirming that some quenching is occurring on the gold surface, and a shorter component of 30 ns (12 %) (Figure 3.46). The luminescence lifetime of the monolayer of [Ru(bpy)(4,4'-bpysac)$_2$](PF$_6$)$_2$ shows that there is much less electron transfer quenching from the excited state of the ruthenium (II) complex to the gold surface, in comparison to the [Ru(bpy)$_2$(4,4'-bpysac)](PF$_6$)$_2$ monolayer. Also the emission of the [Ru(bpy)(4,4'-bpysac)$_2$](PF$_6$)$_2$ monolayer is much stronger than the [Ru(bpy)$_2$(4,4'-bpysac)](PF$_6$)$_2$ monolayer. These are due to the four surface attachment anchors which results in to very strong attachment to the gold surface.
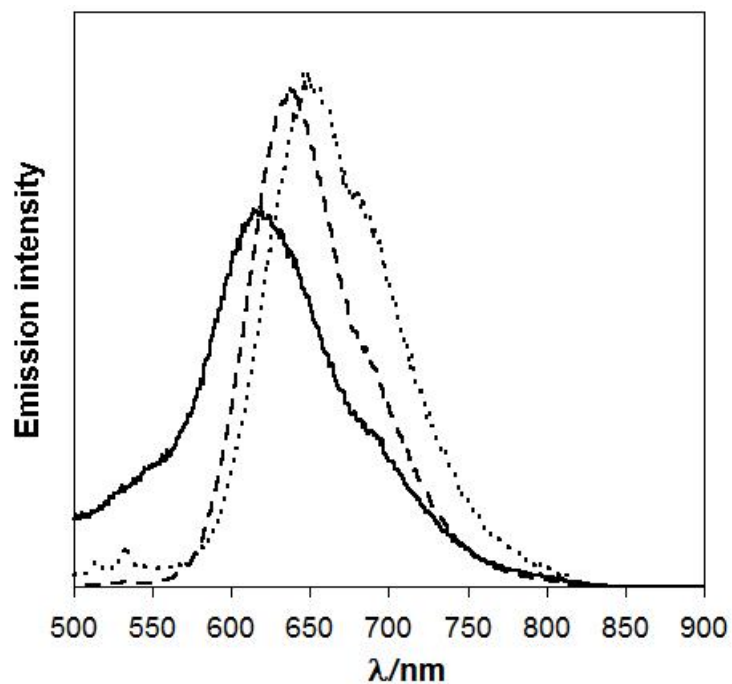
Figure 3.45 Emission spectra of a dry monolayer of [Ru(bpy)(4,4'-bpysac)$_2$](PF$_6$)$_2$ on a gold surface (solid line), in acetonitrile solution (dotted line), and as a powder (dashed line). λ_{ex} = 458 nm.
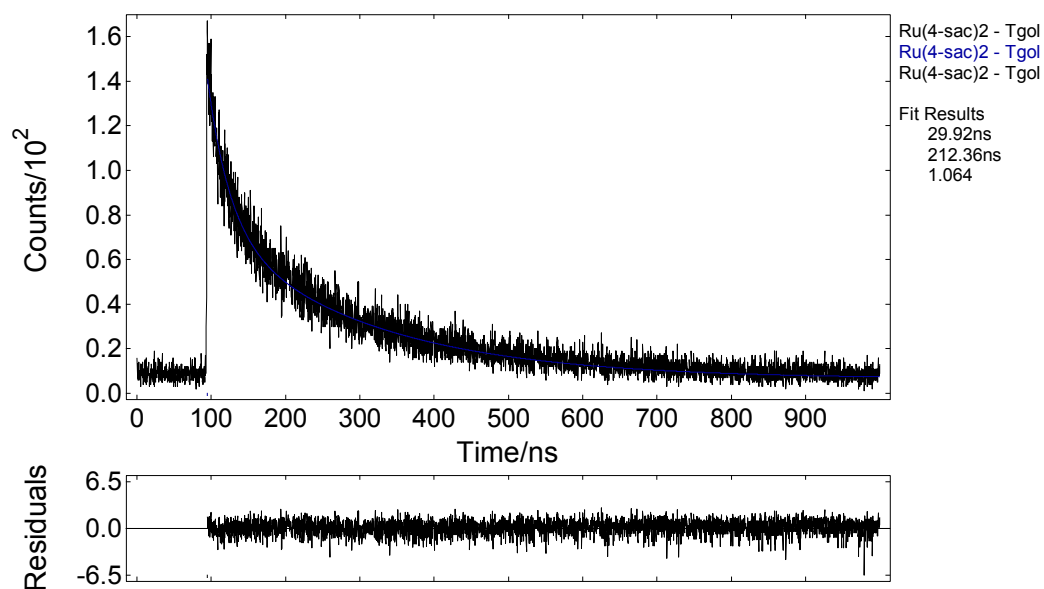
Figure 3.46 Time-resolved emission of of [Ru(bpy)(4,4'-bpysac)$_2$](PF$_6$)$_2$ on a gold surface recorded at 615 nm. Life time detected to be 212 ns (88 %) and 30 ns (12 %) - λ_{exc} = 450 nm.

Luminescence images of the gold surfaces modified with [Ru(bpy)(4,4'-bpysac)$_2$](PF$_6$)$_2$ were also obtained (Figure 3.47 A). Non-ordered islands of concentrated areas of the complex were observed on the surface, which can be seen as bright spots in the luminescence images. In order to ascertain whether the luminescence arises conclusively [Ru(bpy)(4,4'-bpysac)$_2$](PF$_6$)$_2$ or not, an emission spectrum of the surface was taken at different spots, an example of which is shown in figure 3.47 B. The emission spectrum shows a peak for the [3]MLCT emission band of attached complex on the surface at 615 nm.
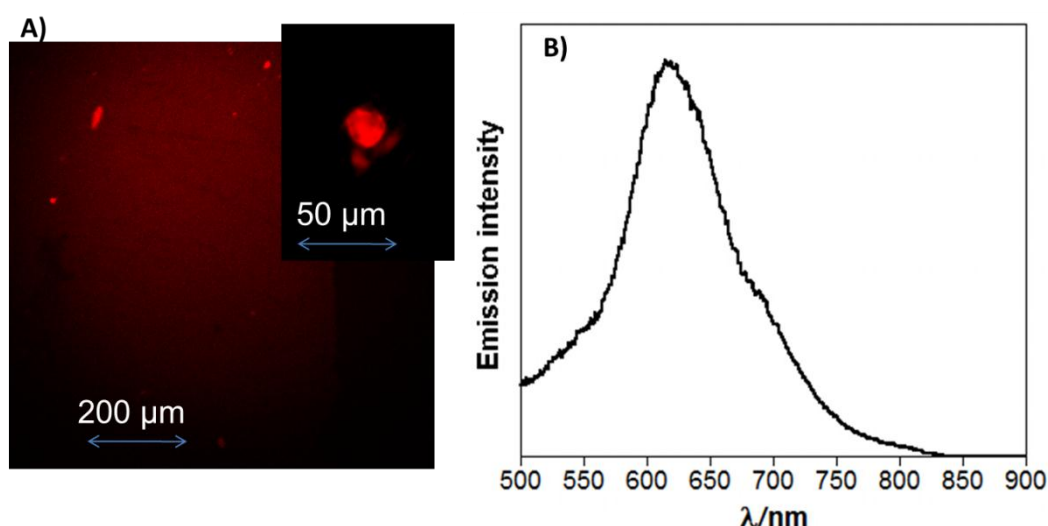
Figure 3.47 A) Fluorescence microscopy images of [Ru(bpy)(4,4'-bpysac)$_2$](PF$_6$)$_2$ on a gold surface. B) Emission spectrum of the image - λ_{exc} = 458.

As mentioned above, the [Ru(bpy)$_2$(4,4'-bpysac)](PF$_6$)$_2$ and [Ru(bpy)(4,4'-bpysac)$_2$](PF$_6$)$_2$ monolayers show some quenching of the emission in comparison with the solution and powder samples. However comparing the results of these monolayers with previously published reports from our group on ruthenium tris-

bipyridine complexes carrying two thiols but no aliphatic substituents as spacer,[12] reveals that the spacer has a significant role in decreasing the quenching process. We can conclude that in future we need a longer spacer to completely prevent the quenching. The maxima of the absorption and emission spectra, the emission quantum yields, as well as results from time-resolved emission of the ruthenium complexes of the bipyridine ligand with substituents in the 4,4'-positions are summarised in Table 3.6.

Table 3.6 Photopysical properties of tris-bipyridine Ru^{II} complexes in acetonitrile

	Ru(bpy)$_3$ Cl$_2$ in water	[Ru(bpy)$_2$ (4,4'- bpysac)] (PF$_6$)$_2$	[Ru(bpy) (4,4'- bpysac)$_2$] (PF$_6$)$_2$	[Ru(bpy)$_2$(4- OMebpy)]$^{2+}$	[Ru(bpy)$_2$ (3,3'- bpysac)](PF$_6$)$_2$	[Ru(bpy) (3,3'- bpysac)$_2$](PF$_6$)$_2$	[Ru(bpy)$_2$(3 -dmbpy)]$^{2+}$
λ_{max} (^{1}MLCT) nm, Solution	452 [54]	460	468	464 [61]	454	458	453
ε (^{1}MLCT)	14000 [54]	13547	7648	9010	9434	4786	12600
λ_{max} (^{1}MLCT) nm, Powder	435, 470 (sh)	490	445, 490 (sh)		430, 460 (sh)	440, 470 (sh)	
λ_{max} (^{1}MLCT) nm, Surface		510	445, 495				
λ_{max} (^{3}MLCT) nm, Solution	610	633	657	605 [56]	625	610	630
φ (^{3}MLCT), aerated	2.8 × 10^{-2} [54]	1.1× 10^{-2}	7.0 × 10^{-3}		6.8 × 10^{-4}	2.6 × 10^{-3}	(3.1±0.2) × 10^{-4}
φ (^{3}MLCT), deaerated	4.2 × 10^{-2} [54]	4.9× 10^{-2}	2.4 × 10^{-2}	1.9 × 10^{-2} [56]	7.0 × 10^{-4}	2.8 × 10^{-3}	(3.6±0.3) × 10^{-4}
τ (^{3}MLCT) ns, aerated	390 [54]	127	100		13	6	
τ(^{3}MLCT) ns, deaerated	650 [54]	685	409	176 [56]	13		
λ_{max} (^{3}MLCT) nm, Powder	600	620	640		603	612	
φ (^{3}MLCT), Powder		5 × 10^{-2}	3 × 10^{-2}				
τ (^{3}MLCT) ns, Powder		545 (94 %) 70 (6 %)	376 (93 %) 74 (7 %)				
λ_{max} (^{3}MLCT) nm, Surface		610	615				
φ (^{3}MLCT), Surface			2.6 × 10^{-2}				
τ (^{3}MLCT) ns, Surface		90 (93 %) 7 (7 %)	212 (88 %) 30 (12 %)				

3.2.6.2. Ruthenium tris-phenanthroline complex

The luminescence properties of the parent complex $[Ru(phen)_3]Cl_2$ have been reported in several papers.[54,62-65] In aqueous solution, the complex exhibits absorption bands at 447 nm (ε = 18100), 420, 262 and 222 nm. The maximum of the emission band appears at 604 nm, with a quantum yield of 0.032 at room temperature.[54]

The absorption spectrum of the $[Ru(phen)_2(4,7\text{-}phenhex)](PF_6)_2$ complex in acetonitrile solution is dominated by a broad band at 458 nm (^{1}MLCT) and at 420 nm in the visible region, and two further absorptions in the UV region, at 290 nm (LC) and 220 nm (^{1}MLCT). The ^{1}MLCT band is significantly red shifted in comparison to $[Ru(phen)2]Cl3$ (Figure 3.48).
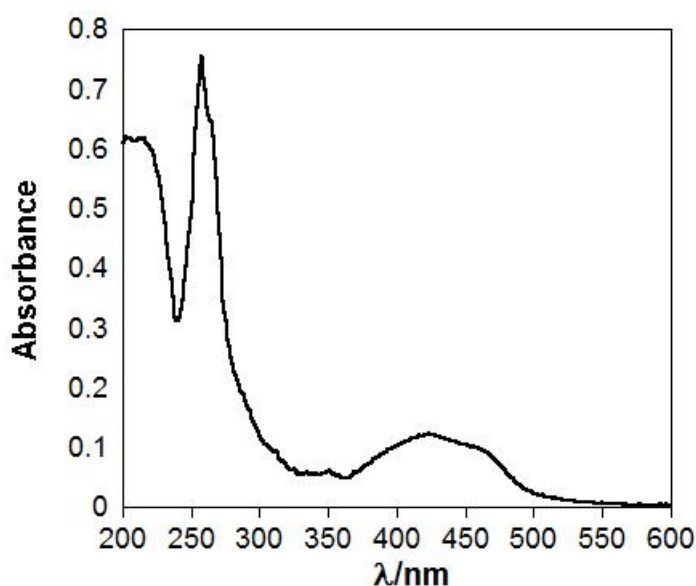
Figure 3.48 Absorption spectrum of [Ru(phen)$_2$(4,7-phenhex)](PF$_6$)$_2$ in acetonitrile (C = 1.2 × 10^{-5} M).

Excitation into the ^{1}MLCT band leads to emission from the lowest triplet state (^{3}MLCT) with a maximum at 630 nm (Figure 3.49). This has a 26 nm bathochromic shift with respect to [Ru(phen)$_3$]Cl$_2$. The photophysical properties of [Ru(phen)$_2$(4,7-phenhex)](PF$_6$)$_2$ are summarised in table 3.7.
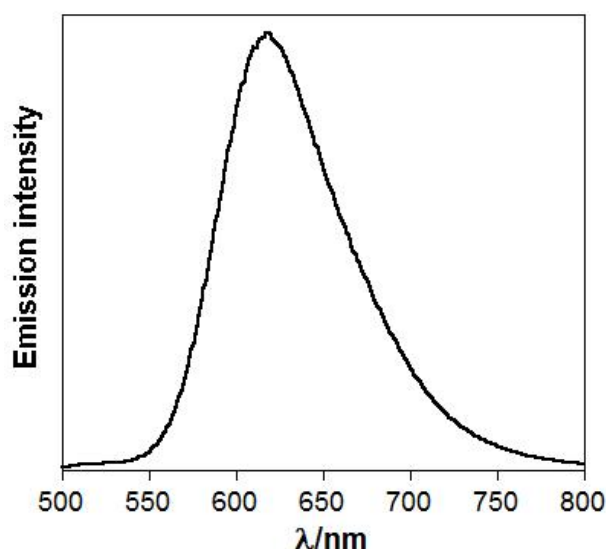
Figure 3.49 Emission spectrum of [Ru(phen)$_2$(4,7-phenhex)](PF$_6$)$_2$, λ_{exc} = 460 nm in acetonitrile (C = 1.2 × 10^{-5} M).

Table 3.7 Photopysical properties of [Ru(phen)$_2$(4,7-phenhex)](PF$_6$)$_2$ and the parent complex [Ru(phen)$_3$]Cl$_2$.

	Ru(phen)$_3$Cl$_2$	[Ru(phen)$_2$(4,7-phenhex)](PF$_6$)$_2$
λ_{max} (^{1}MLCT) nm	447	458
ε (^{1}MLCT)	18100	10186
λ_{max} (^{3}MLCT) nm	604	630
φ (^{3}MLCT), aerated	3.2 × 10^{-2}	6 × 10^{-3}
φ (^{3}MLCT), deaerated	5.8 × 10^{-2}	9.5 × 10^{-2}
τ (^{3}MLCT) ns, aerated	459 [62]	100

3.2.6.3. Osmium tris-bipyridine complexes

The absorption spectrum of the acetonitrile solution of [Os(bpy)$_2$(4,4'-bpysac)](PF$_6$)$_2$ exhibits a broad band at 650 nm (^{3}MLCT), at 490 nm with a shoulder at 470 nm for the ^{1}MLCT, and two further absorptions in the UV region at 290 nm (LC) and 247 nm (^{1}MLCT). The absorption spectrum of [Os(bpy)$_3$]$^{2+}$ has been reported previously, with bands at 480 nm, 430 nm ,375 nm and two bands in UV region around 290 and 250 nm.[66-68]

The absorption spectrum of a monolayer of the [Os(bpy)$_2$(4,4'-bpysac)](PF$_6$)$_2$ complex adsorbed on a gold surface displays a broad ^{3}MLCT band at 690 nm, the ^{1}MLCT band at 510 nm, the ^{3}MC band at 380 nm, and a LC band in the UV region at 295 nm. The LC band at 250 nm cannot be observed due to the high absorption of the glass substrate in this region (Figure 3.50).

The ^{3}MLCT, ^{1}MLCT and ^{3}MC bands all undergo a bathochromic shift in the powder and monolayer spectra, in comparison with the spectrum of the acetonitrile solution, while the ligand centred band, LC, does not shift. However the intensity of this peak in UV-Vis spectrum of [Os(bpy)$_2$(4,4'-bpysac)](PF$_6$)$_2$ monolayer is very weak.
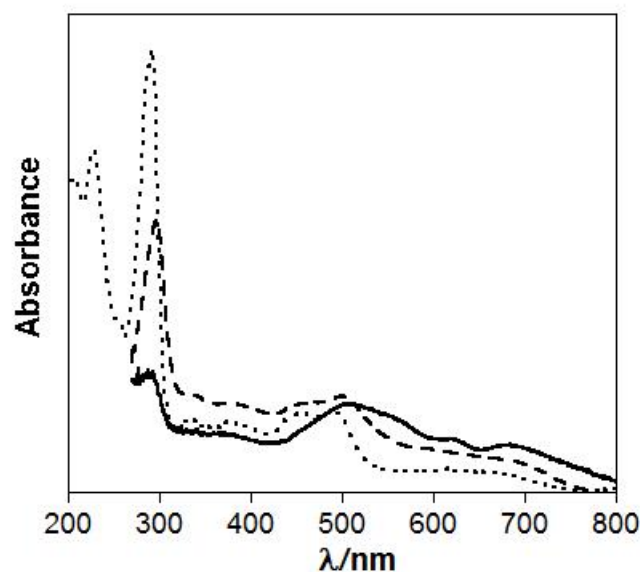
Figure 3.50 UV-Vis spectrum of [Os(bpy)$_2$(4,4'-bpysac)](PF$_6$)$_2$ in acetonitrile solution (7.6 × 10^{-6} M, dotted line), reflectance spectrum of powder (dashed line) and transmittance spectrum of monolayer (solid line). Not in same y scale.

Similarly, the absorption spectrum of a acetonitrile solution of [Os(bpy)$_2$(3,3'-bpysac)](PF$_6$)$_2$ displays a broad band at 650 nm (^{3}MLCT), 478 nm with a shoulder at 435 nm, and two further absorptions in the UV region at 295 nm (^{1}LC) and 247 nm (^{1}MLCT) (Figure 3.51). A ^{3}MC band at 365 nm is also observed. Shifts for the metal character peaks (^{3}MLCT, ^{1}MLCT, ^{3}MC) can be seen for [Os(bpy)$_2$(3,3'-bpysac)](PF$_6$)$_2$ as a monolayer and a powder, as has been shown in figure 3.51. Similarly, the intensity of the LC band at 295 nm is very weak.
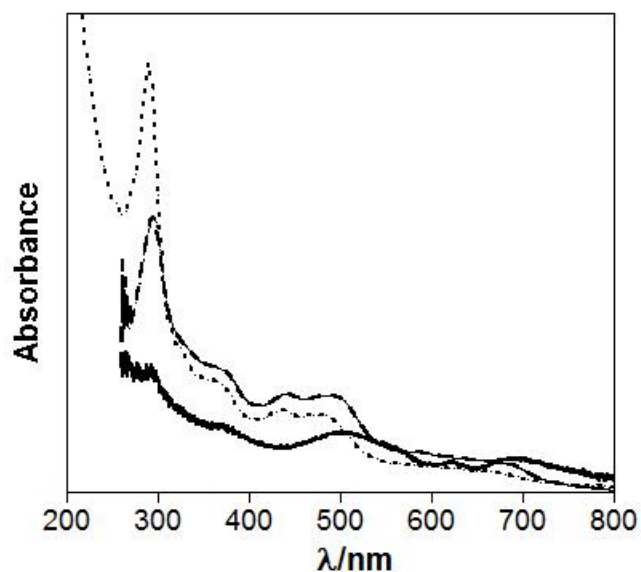
Figure 3.51 UV-Vis spectrum of [Os(bpy)$_2$(3,3'-bpysac)](PF$_6$)$_2$ in acetonitrile solution (C = 1.2 ×

10^{-5} M, dotted line), reflectance spectrum of the powder (dashed line) and transmittance

spectrum of the monolayer (solid line). Not in same y scale.

An acetonitrile solution of [Os(bpy)$_2$(3,3'-bpysac)](PF$_6$)$_2$ displays some luminescence

from the ^{3}MLCT band at 747 nm, when excited at 478 nm at room temperature

(Figure 3.52). The typical emission wavelength of [Os(bpy)$_3$]Cl$_2$ in acetonitrile is 723

nm.[67] The quantum yield of [Os(bpy)$_2$(3,3'-bpysac)](PF$_6$)$_2$ was measured to be 2.54

× 10^{-3} (in acetonitrile). As a monolayer on gold and as powder, [Os(bpy)$_2$(3,3'-

bpysac)](PF$_6$)$_2$ exhibits weak emission at 717 nm.
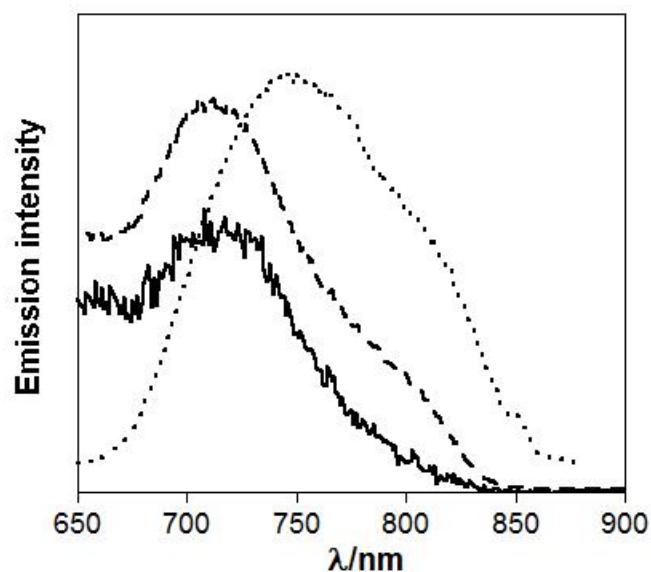
Figure 3.52 Emission spectra, subtracted from the background, of a dry monolayer of

[Os(bpy)$_2$(3,3'-bpysac)](PF$_6$)$_2$ on a gold surface (solid line), in acetonitrile solution (dotted line)

and powder (dashed line) - λ_{ex} = 478 nm. Not in same y scale.

In the case of [Os(bpy)$_2$(4,4'-bpysac)](PF$_6$)$_2$, acetonitrile solutions displayed luminescence from the [3]MLCT band at 760 nm, when excited at 490 nm at room temperature (Figure 3.53). The emission maximum of the powder [Os(bpy)$_2$(4,4'-bpysac)](PF$_6$)$_2$, is the same as that of the solution (760 nm), while upon forming the monolayer the emission maximum is significantly blue-shifted to 730 nm. Due to the weak emission of the osmium complexes on the surface, emission spectra need to be subtracted from the background. The osmium complex has a very short life time (expected for the osmium complexes) in all forms and is not affected by oxygen or quenching by the gold surface.
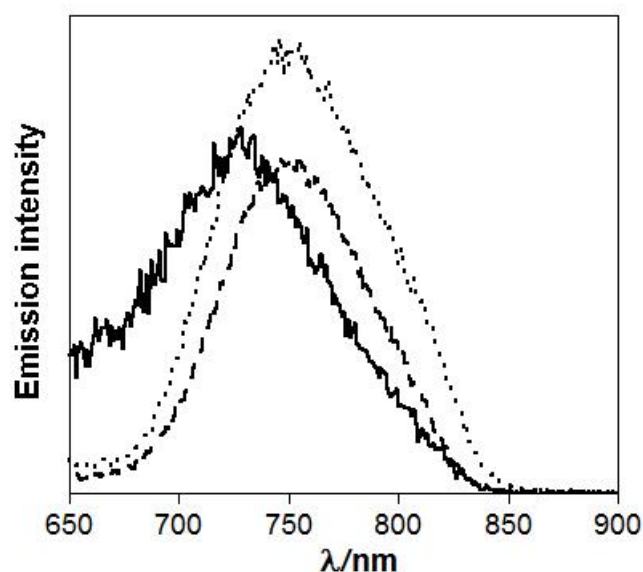
Figure 3.53 Emission spectra, subtracted from the background, of a dry monolayer of [Os(bpy)$_2$(4,4'-bpysac)](PF$_6$)$_2$ on a gold surface (solid line), in acetonitrile solution (dotted line) and powder (dashed line) - λ_{ex} = 490 nm. Not in same y scale.

Luminescence images of the surface modified [Os(bpy)$_2$(4,4'-bpysac)](PF$_6$)$_2$ were also obtained (Figure 3.54). The osmium complex forms some non-ordered islands on the surface (similar to the ruthenium complexes) which can be seen as the bright spots in the luminescence images, where the complex is more concentrated. The emission signal of the surface is very weak and can not be recored by the microscope on different spots. While comparison of the image with the image of the bare gold concludes that the fluorescent image is arrsing from the attached osmium complex on the surface. The photophysical properties of the surface active osmium complexes are summarised in Table 3.8.
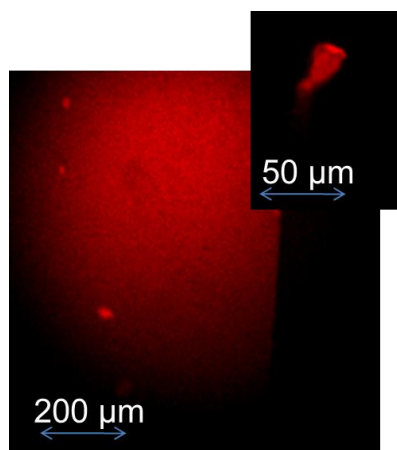
Figure 3.54 Fluorescence microscopy images of [Os(bpy)$_2$(4,4'-bpysac)](PF$_6$)$_2$ on a gold surface.

Table 3.8 Photopysical properties of Os^{II} complexes

	[Os(bpy)$_3$]Cl$_2$	[Os(bpy)$_2$(3,3'-bpysac)](PF$_6$)$_2$	[Os(bpy)$_2$(4,4'-bpysac)](PF$_6$)$_2$	[Os(4-OMebpy)$_3$](PF$_6$)$_2$
λ$_{max}$ (^{1}MLCT) nm, Solution	480	478	490	516
ε (^{1}MLCT)	11100 [61]	6387	13178	6800 [61]
λ$_{max}$ (^{1}MLCT) nm, Powder		485	496	
λ$_{max}$ (^{1}MLCT) nm, Surface		500	510	
λ$_{max}$ (^{3}MLCT) nm, Solution	723	747	760	
φ (^{3}MLCT), aerated		5.8 × 10^{-3}	1.6 × 10^{-3}	
φ (^{3}MLCT), deaerated	5 × 10^{-3} [69]	8.2 × 10^{-3}	2 × 10^{-3}	
τ (^{3}MLCT) ns, aerated		38	21	
τ (^{3}MLCT) ns, deaerated		55	21	
λ$_{max}$ (^{3}MLCT) nm, Powder		717	760	
φ (^{3}MLCT), Powder		5 × 10^{-3}	2 × 10^{-3}	
τ (^{3}MLCT) ns, Powder			19	
λ$_{max}$ (^{3}MLCT) nm, Surface		717	730	

3.3. Conclusions

New surface-active ruthenium(II) and osmium(II) bipyridine complexes, bearing two long chains in either the 3,3'- positions or 4,4'-positions, and one ruthenium(II) phenanthroline complex with the 4,7-substituted phenanthroline ligand, have been synthesised and fully characterised by NMR, mass spectrometry, FTIR spectroscopy and elemental analysis.

The photophysical properties of the complexes in solution, as powders and as monolayers on a gold surface have been studied. The acetonitrile solutions of the 3,3'-substituted bipyridine complexes display weak luminescence from the ^{3}MLCT band, when excited at room temperature, with a red shift in emission spectrum with respect to $[Ru(bpy)_3]Cl_2$. Twisting effects caused by substitution on the 3,3'-position of the bipyridine decrease the quantum yield and lifetime of the complex. However, the complexes with substitutions on the 4,4'-position of the bipyridine display very good photophysical properties, with relatively high quantum yields and life times.

The monolayers of the different ruthenium (II) and osmium (II) tris-bipyridine complexes have been studied by ellipsometry, FTIR spectroscopy and XPS. Based on ellipsometric experiments, after 24 hours deposition of the gold substrate in the 1 mM acetonitrile solution of the metal complex, formation of the monolayer is completed. Ellipsometry data corresponding to the monolayer thickness of all complexes were very close to the calculated length of the monolayer of such molecules from Chem3D modelling. The XPS results showed that the ratio of the metals and other elements were in good agreement with the theoretical ratios

predicted by the molecular structure, confirming the formation of the well structured monolayer. Additionally the XPS results as well as FTIR data revealed that there is no need of the addition of the base in order to deprotect the thioacetate group in ruthenium complxes. However it was needed to use some NH_4OH to reduce the thioacetate groups in osmium complexes in order to efficiently attach them to the gold surface. Surface coverage of ruthenium and osmium compexes on gold substrates was estimated from the peak ratio of Ru: Au or Os: Au in XPS spectra, using the atomic radius of the Au atoms and the estimated foot print of the complexes from chem-3D. All calculated results showed almost full surface coverage of gold substrates, which confirmed the formation of the packed and full monolayers.

The monolayers also exhibit strong luminescence properties, especially with the $[Ru(bpy)(4,4'\text{-bpysac})_2](PF_6)_2$ complex. The $[Ru(bpy)_2(4,4'\text{-bpysac})](PF_6)_2$ and $[Ru(bpy)(4,4'\text{-bpysac})_2](PF_6)_2$ monolayers show some quenching of the emission in comparison with the solution and powder samples. However comparing the results of these monolayers with previously published report in our group on a ruthenium tris-bipyridine complex carring two thiols but no aliphatic spacers[12] reveals that the spacer has a significant role in decreasing the quenching process. We can conclude that in future we need a longer spacer to completely stop the quenching. The emission of the osmium complex monolayers was reported for the first time.

3.4. Experimental

3.4.1. Synthesis

6-(thioacetoxy)bromohexane (Br-SAc)[25]
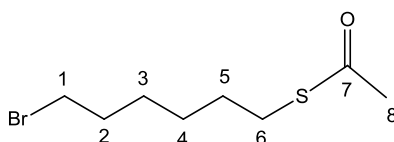
To a solution of 6-Bromo-hex-1-ene (1.092 g, 6.70 mmol) and thioacetic acid (1.04 g, 13.70 mmol) in dry toluene (15 mL), was added AIBN (25 mg) and the solution was heated to reflux for 30 min, cooled and 1 M aqueous sodium bicarbonate solution (5 cm^3) was added. The mixture was extracted with ethyl acetate (60 mL) and the organic phase was washed with aqueous sodium bicarbonate solution (1M, 3 × 20 mL) and brine (30 cm^3), dried over Na_2SO_4. Evaporation of the solvent yielded 6-(thioacetoxy)bromohexane as a yellow oil. (1.576 g, 98% yield)

^{1}H NMR (300 MHz, CDCl$_3$): δ = 3.39 (t, J = 6.8, 2H, H$_1$), 2.86 (t, J = 7.5, 2H, H$_6$), 2.33 (s, 3H, H$_8$), 1.85 (tt, J = 6.8, 6.8, 2H, H$_5$), 1.63-1.53 (tt, J = 6.8, 7.5, 2H, H$_2$), 1.47-1.34 (m, 4H, H$_3$, H$_4$).

^{13}C NMR (75 MHz, CDCl$_3$): δ = 194.3 (C$_7$), 34.0 (C$_1$), 32.9 (C$_8$), 30.9 (C$_5$), 29.7 (C$_6$), 29.2 (C$_2$), 28.2 (C$_4$), 27.9 (C$_3$).

ESI-MS(+): m/z 238.0 [M$^+$].

3,3'-Dihydroxy-2,2'-bipyridiyl (3,3'-bpyOH)[20]
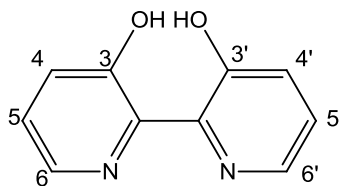
To a solution of $NiCl_2.6H_2O$ (4.06 g, 17.2 mmol) in DMF (75 ml) was added PPh_3 (17.92 g, 69.0 mmol) and Nitrogen gas passed through the solution. The solution was heated to 50°C. Zn powder (3.10g, 47.7 mmol) was suspended in the solution and stirred for 1 h at 50°C during which the color turned to red-brown. 2-bromo-3-hydroxypyridine (3.00 g, 17.2 mmol) was added and the suspention was stirred for another 2 h at 50°C. The warm mixture was filtered and the solid was washed with $CHCl_3$. The aqueous phases were combined and HCl (0.1 N) was added until pH=4. Further purification was achieved by passing through several columns on silica using $CHCl_3$ as eluent (R_f: silica gel, $CHCl_3$ = 0.37). (0.63 g, 38.93% yield).

^{1}H NMR (300 MHz, CDCl3): δ = 14.68 (s, 2 H, H_{OH}), 8.05 (dd, 2 H, J= 4.8, 1.47 $H_{6,6'}$), 7.40 (dd, 2 H, J=8.3, 1.47 $H_{4,4'}$) 7.30 (dd, 2 H, J= 8.3, 4.8 $H_{5,5'}$).

^{13}C-NMR (75 MHz, $CDCl_3$): δ = 156.2 ($C_{3,3'}$), 139.8 ($C_{2,2'}$), 136.0 ($C_{6,6'}$), 125.9 ($C_{4,4'}$), 124.9 ($C_{5,5'}$).

ES-MS(+): *m/z* 188.06 [M].

3,3'-bpysac
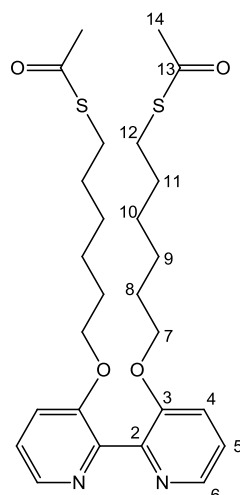
A suspention of 3,3'-dihydroxy-2,2'-bipyridine (100 mg, 0.53 mmol) and potassium carbonate (4.26 g, 30.82 mmol) was heated to reflux in dry acetonitrile (80 mL) for 30 min. 6-(Thioacetoxy)bromohexane (935 mg, 3.19 mmol) was added dropwise and the reaction mixture was brought to reflux for 90 h. After cooling down to room temperature the reaction mixture was filtered and the solvent was removed in vacuum to yield an orange-brown oil. The crude was purified by column chromatography on silica using DCM/MeOH [MeOH gradient 1 to 10 %] as eluent to yield 21.75 mg (8.25%) of 3,3'-bpysac as a brown solid.

R_f (silica gel, CH_2Cl_2/MeOH [95:5]) = 0.47.

^{1}H NMR (300 MHz, CDCl$_3$): δ = 8.30 (dd, 2 H, J = 4.2, 1.8 H$_6$), 7.25-7.21 (m, 4 H, H$_5$, H$_4$), 3.82 (t, 4 H, J = 6.4, H$_7$), 2.69 (t, 4 H, J = 7.5, H$_{12}$), 2.32 (s, 6 H, H$_{14}$), 1.64-1.58 (m, 4 H, H$_8$), 1.52-1.45 (m, 4 H, H$_{11}$), 1.28-1.26 (m, 8 H, H$_9$, H$_{10}$).

^{13}C-NMR (75 MHz, CDCl$_3$): δ = 195.7 (C$_{13}$), 153.5 (C$_3$), 147.3 (C$_2$), 141.2 (C$_6$), 123.6 (C$_5$), 119.1 (C$_4$), 68.4 (C$_7$), 30.5 (C$_{14}$), 29.3 (C$_{11}$), 28.8 (C$_{12}$), 28.7 (C$_8$), 28.3 (C$_{10}$), 25.3 (C$_9$).

ES-MS(+): *m/z* 505.1 [M+H]⁺, 527.0 [M+Na]⁺.

IR (cm⁻¹): 2930, 2857, 1685 (C=O), 1571, 1429, 1353, 1277, 1200, 1131, 1116, 952.

3,3'-bpyhex
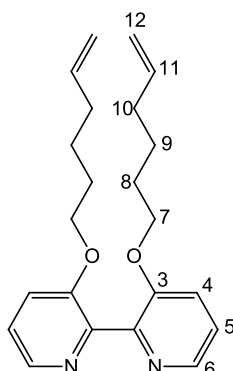
A solution of 3,3'-dihydroxy-2,2'-bipyridine (100 mg, 0.53 mmol) and sodium hydride (740 mg, 30.82 mmol) was heated in 60 C in dry DMF (50 mL) for 30 min. 6-bromo-1-hexene (524 mg, 3.18 mmol) was added drop wise and the reaction mixture was brought to reflux for 4 h. After cooling down to room temperature, NaH was quenched by adding 75 ml ice-cold ethanol in ice bath. The solvent was removed and the organic phase was extracted by water-dicholoromethane mixture. The organic layer was separated and dried over MgSO₄. The solvent was removed to yield an orange-brown oil. The crude was purified by column chromatography on silica (2% MeOH in DCM, R_f = 0.68) to yield 3,3'-bpyhex (50 mg, 27% yield) as orange solid.

¹H NMR (300 MHz, CDCl3/MeOH): δ = 8.16 (dd, 2 H, *J* = 4.2, 1.8 H₆), 7.29-7.24 (m, 4 H, H₅, H₄), 5.56-5.70 (tdd, 2 H, J=16.8, 10.6, 6.9 H₁₁), 4.85-4.90 (m, 4 H, H₁₂),

3.88 (t, 4 H, J = 6.4, H_7), 1.86-1.93 (dt, 4 H, J=7.5, 6.9 H_{10}), 1.52-1.61 (tt,4 H, J=6.4, 7.5 H_8), 1.23-1.33 (tt, 4 H, J=7.5, 7.5 H_9).

^{13}C-NMR (100 MHz, $CDCl_3$): δ = 157.8 (C_3), 150.2 (C_2), 144.3 (C_{11}), 142.2 (C_6), 128.3 (C_5), 123.6 (C_4), 118.4 (C_{12}), 72.4 (C_7), 37.0 (C_{10}), 32.2 (C_8), 28.9 (C_9).

ES-MS(+): m/z 353.6 [M+H]$^+$, 375.6 [M+Na]$^+$.

IR (cm^{-1}): 2971, 2901, 1586, 1444, 1383, 1277, 1066, 1057, 907.

Anal. Calc. for $C_{22}H_{28}O_2N_2$ $(C_6H_{14})_{0.33}$: C 75.61, H 8.64, N 7.35. Found C 75.93, H 8.55, N 7.64.

4,4'-dihydroxy-2,2'-bipyridine (4,4'-bpyOH)[26]
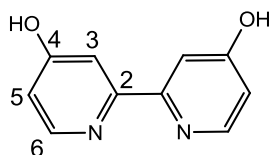
To a solution of 4,4'-dimethoxy-2,2'-bipyridine (1.00 g, 4.61 mmol) in 60 mL of glacial acetic acid, the aqueous HBr solution (48%) (8 mL, 47 mmol) was added. The mixture was heated to reflux overnight under N_2 (g). The mixture was allowed to cool and the solvent was removed *in vacuo* to render a white solid. The residue was dissolved in minimum amount of water and neutralised by adding aqueous ammonium hydroxide. The white solid (0.80 g, 4.19 mmol, 91 % yield) was filtered and dried, and used in the next step without further purification.

^{1}H NMR (300 MHz, DMSO): δ_H = 11.21 (s, 1H, OH), 8.24 (s, 2H, H_6), 7.45 (s, 2H, H_3), 6.54 (s, 2H, H_5).

EI-MS(+): *m/z* 188.1 [M]$^+$, 160.1 [M-N$_2$]$^+$, 94.0 [c-C$_5$H$_3$N-OH]$^+$.

IR (cm^{-1}): 3192, 3147, 2462, 1843, 1616, 1582, 1560, 1491, 1455, 1302, 1268, 1192.

4,4'-bpyhex
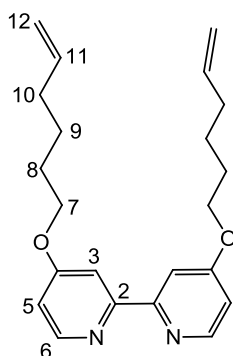
A solution of 4,4'-dihydroxy-2,2'-bipyridine (4,4'-bpyOH) (700 mg, 3.72 mmol) in dry DMF was heated at 60°C for 30 min until it is partially dissolved. Sodium hydride (1.5 g, 62.5 mmol, 60% in mineral oil) was added and kept stirring for another 30 min, which after that time 6-bromo-1-hexene (3.7g, 22.5 mmol) was added and the mixture was heated at 60°C for 16 hours. After cooling down to room temperature, the excess of NaH was quenched by adding 75 ml ice-cold ethanol. The solvent was removed and the organic phase was extracted by water-dicholoromethane mixture. The organic layer was separated and dried over MgSO4. The solvent was removed to yield orange-brown oil. The crude was recrystallized from ethanol to give desired product as a white solid (650 mg, 50% yield).

^{1}H NMR (400 MHz, CDCl3): δ = 8.45 (d, 2 H, J = 5.6, H_6), 7.94 (d, 2 H, J = 2.5, H_3), 6.85 (dd, 2 H, J = 2.5, 5.6, H_5), 5.75-5.90 (tdd, 2 H, J=17.2, 10.3, 6.6 H_{11}), 4.95-5.10 (m, 4 H, H_{12}), 4.13 (t, 4 H, J = 6.4, H_7), 2.10-2.17 (dt, 4 H, J=7.5, 6.9 H_{10}), 1.79-1.90 (tt,4 H, J=6.4, 7.5 H_8), 1.55-1.65 (tt, 4 H, J=7.5, 7.5 H_9).

^{13}C-NMR (100 MHz, CDCl$_3$): δ = 166.1 (C_2), 157.9 (C_4), 150.1 (C_6), 138.3 (C_{11}), 114.9 (C_{12}), 111.3 (C_5), 106.7 (C_3), 67.8 (C_7), 33.3 (C_{10}), 29.4 (C_8), 25.2 (C_9).

ES-MS(+): m/z 353.2 [M+H]$^+$, 375.2 [M+Na]$^+$.

IR (cm^{-1}): 2952, 2921, 1576, 1558, 1456, 1297, 1245, 1003.

Anal. Calc. for $C_{22}H_{28}O_2N_2$ $(C_6H_{14})_{0.2}$: C 75.37, H 8.40, N 7.58. Found C 75.25, H 8.66, N 7.22.

4,7-phenhex
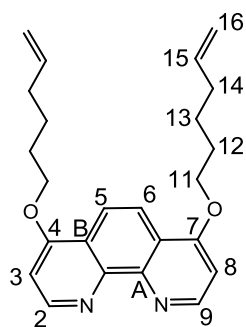
A solution of 4,7-dihydroxy-1,10-phenanthroline (1.00 g, 4.71 mmol) and sodium hydride (2 g, 83.3 mmol, 60% in mineral oil) in dry DMF was heated at 60°C for 30 min. The 6-bromo-1-hexene (4.0 g, 24.3 mmol) was added and the suspention was heated at 60 ^{o}C overnight. After cooling down to room temperature, the excess of

NaH was quenched by adding ice-cold ethanol. The solvent was removed and the organic phase was extracted by water-dicholoromethane. The organic layer was separated and dried over MgSO4 and the solvent was removed to yield orange-brown oil. The crude was recrystallized from ethanol to give desired product as a white solid (1.15 g, 65% yield).

^{1}H NMR (400 MHz, CDCl3): δ = 8.97 (d, 2 H, J = 5.2, $H_{2,9}$), 8.18 (s, 2 H, $H_{5,6}$), 6.94 (d, 2 H, J = 5.2, $H_{3,8}$), 5.81-5.91 (tdd, 2 H, J=20.4, 8.3, 6.4 H_{15}), 5.00-5.10 (m, 4 H, H_{16}), 4.22 (t, 4 H, J = 6.3, H_{11}), 2.16-2.23 (dt, 4 H, J=7.3, 6.3 H_{12}), 1.94-2.01 (tt,4 H, J=6.3, 7.5 H_{13}), 1.65-1.73 (tt, 4 H, J=7.5, 8.3 H_{14}).

^{13}C-NMR (100 MHz, CDCl$_3$): δ = 161.6 (C_A), 151.1 ($C_{2,9}$), 147.0 ($C_{4,7}$),138.3 (C_{15}), 121.0 (C_B) , 118.9 ($C_{5,6}$), 115.0 (C_{16}), 103.3 ($C_{3,8}$), 68.4 (C_{11}), 33.4 (C_{12}), 28.4 (C_{13}), 25.4 (C_{14}).

ES-MS(+): *m/z* 377.2 [M+H]$^+$, 399.2 [M+Na]$^+$.

IR (cm^{-1}): 2945, 2884, 1615, 1587, 1567, 1504, 1426, 1294, 1229, 1025.

Anal. Calc. for $C_{24}H_{28}O_2N_2$ $(H_2O)_{0.25}$: C 75.65, H 7.54, N 7.36. Found C 75.98, H 7.64, N 7.52.

cis-Bis(2,2′-bipyridine)dichlororuthenium(II) (Ru(bpy)$_2$Cl$_2$ .2H$_2$O)
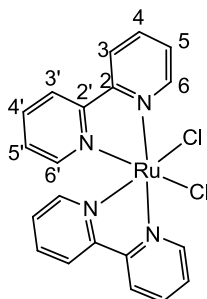
Ru(bpy)$_2$Cl$_2$ was synthesised following two different procedures:

Procedure 1[28]

Ruthenium (III) chloride trihydrate 40% (630 mg, 1 mmol), 2,2′-bipyridine (300 mg, 2 mmol), and LiCl (280 mg, 7 mmol) were dissolved in dry N,N-dimethylformamide (3 mL) and the solution was heated to reflux for 8 h. After cooling to room temperature, it was poured into rapidly stirred acetone (5 mL) and the combined suspentions were allowed to stand overnight at -4 ^{o}C. The resultant dark purple microcrystalline material was collected by filtration, washed with water (3 × 2 mL) and ether (3 × 2 mL). (309 mg, 60% yield).

Procedure 2 [31]

A relatively new procedure was followed to synthesise the target Ru(bpy)Cl$_2$ complex using polymeric Ru(COD)Cl$_2$ in refluxing 2-methoxyethanol, adapting a published procedure for [Ru(Phen)$_3$]Cl$_2$.

A suspension of dichloro(1,5-cyclooctadiene)ruthenium(II) polymer (20 mg, 0.07 mmol) and lithium chloride (120 mg, 2.83 mmol) was heated to reflux in 2-methoxyethanol (5 mL). Nitrogen gas was passed through the mixture. 2,2′-

bipyridine (22 mg, 0.14 mmol) in 2-methoxyethanol was added dropwise and the solution was maintained to reflux. After 160 min, the dark purple solution was cooled to room temperature under nitrogen. The solvent was evaporated, the residue was taken up in DCM and filtered, and the solvent was removed. The dark purple solid was washed several times with water and ether to yield 20 mg (52%).

R_f (silica gel, $CH_3CN/ H_2O/ KNO_3$ (sat.) [95: 4: 1]) = 0.32.

^{1}H NMR (300 MHz, DMSO): δ_H = 9.97 (d, 2H, J = 4.7, H_6), 8.64 / 8.49 (d, 2H, J = 7.8, H_3,$H_{3'}$), 8.07 (m, 2H, H_4), 7.77 (m, 2H, H_5), 7.68 (m, 2H, $H_{4'}$), 7.51 (d, 2H, J = 4.6, $H_{6'}$), 7.10 (m, 2H, $H_{5'}$).

^{13}C NMR (100 MHz, DMSO): δ = 160.15 (C_2), 158.2 ($C_{2'}$), 153.1 (C_6), 151.9 ($C_{6'}$), 134.5 (C_4), 133.3 ($C_{4'}$), 125.24 (C_5), 125.2 ($C_{5'}$), 122.8 (C_3), 122.4 ($C_{3'}$).

TOF ES-MS(+): m/z 481.1 [Ru(bpy)$_2$(OMe)Cl+H]$^{+.}$, 449.0 [M-Cl]$^+$.

UV-VIS (DCM) λ_{max} / nm: 555, 377, 300.

IR (cm^{-1}): 3067, 1933, 1601, 1443, 1418, 1308, 1266, 1155.

[Ru(bpy)$_2$(3,3'-bpyhex)](PF$_6$)$_2$
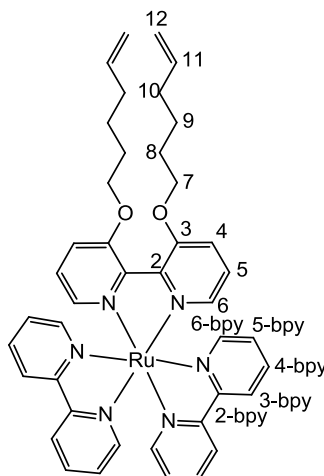
Ru(bpy)$_2$Cl$_2$·2H$_2$O (26 mg, 0.05 mmol) and 3,3'-bpyhex (30 mg, 0.085 mmol) were heated to reflux for 22 hr, under nitrogen in ethanol (5 mL). The solution was set aside to cool to room temperature, and then concentrated under vacuum to 2 ml. A saturated aqueous solution of ammonium hexafluorophosphate was added and a red precipitation was formed. It was cooled at 0 ^{o}C for 30 min to promote precipitation and the solid was collected by filtration and washed with water and ether. The crude is a mixture of two complexes, [Ru(bpy)$_2$(3,3'-bpyhex)](PF$_6$)$_2$ and [Ru(bpy)(3,3'-bpyhex)$_2$](PF$_6$)$_2$which were separated by column chromatography on silica using DCM/isopropanol [95:5] as eluent to yield [Ru(bpy)$_2$(3,3'-bpyhex)](PF$_6$)$_2$ (24mg, 45.5%).

R$_f$ (silica gel, CH$_2$Cl$_2$/isopropanol [95:5]) = 0.32.

^{1}H NMR (300 MHz, CD$_3$CN) : δ = 8.49, 8.51 (dd, *J* = 8.1, 1.3 4H, H$_{3\text{-bpy}}$), 8.07 (m, *J* = 8.1, 1.3 4H, H$_{4\text{-bpy}}$), 7.72 (m, 4H, H$_{6\text{-bpy}}$), 7.65 (dd, *J* = 6.4, 3.1 2H, H$_6$), 7.47-7.36 (m, 4H, H$_{5\text{-bpy}}$), 7.35 (m, 4H, H$_{4,5}$), 5.75-5.85 (tdd, 2H, *J* =17.0, 10.2, 6.9 H$_{11}$), 4.90-

5.08 (m, 4H, H_{12}), 4.12-4.3 (m, 4 H, H_7), 2.03-2.15 (dt, 4 H, J = 7.8, 6.9 H_{10}), 1.73-1.88 (tt,4 H, J = 7.6, 6.9 H_8), 1.41-1.58 (tt, 4 H, J=7.5, 7.5 H_9).

^{13}C NMR (100 MHz, CD$_3$CN): δ = 157.1 ($C_{2\text{-bpy}}$), 156.2 (C_2), 151.8 ($C_{6\text{-bpy}}$), 151.3 (C_{11}), 146.2 (C_3), 143.0 (C_4), 137.6 ($C_{4\text{-bpy}}$), 127.4 ($C_{5\text{-bpy}}$), 127.0 (C_5), 124.1 ($C_{3\text{-bpy}}$), 122.1 (C_6), 114.3 (C_{12}), 69.3 (C_7), 32.8 (C_{10}), 28.0 (C_8), 24.7 (C_9).

ES MS(+) (MeOH): m/z 911 {M - [PF$_6$]}$^+$, 383 {M - 2[PF$_6$]}$^{2+}$.

IR (cm^{-1}): 2926, 1604, 1568, 1464, 1444, 1424, 1289, 1127.

UV-Vis (MeCN) λ_{max} in nm: 454, 435(sh), 360, 292, 247.

Emission (MeCN): λ_{max} = 625 nm.

Anal. Calc. for C$_{42}$H$_{44}$O$_2$N$_6$F$_{12}$P$_2$Ru: C 47.72, H 4.20, N 7.95. Found C 48.00, H 7.80, N 4.14.

[Ru(bpy)$_2$(3,3'-bpysac)](PF$_6$)$_2$
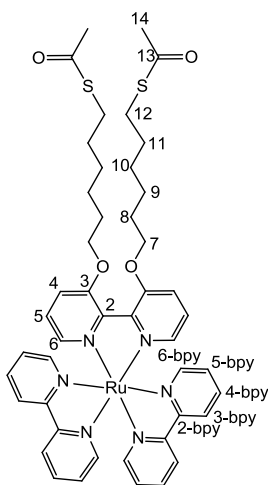
A solution of 50 mg (0.660 mmol) fresh thioacetic acid and 20 mg (0.115 mmol) AIBN in 2ml dry THF was heated at 60 °C and degassed under nitrogen for 30 minutes. [Ru(bpy)$_2$(3,3'-bpyhex)](PF$_6$)$_2$, 35 mg (0.033 mmol), was solved in 4 ml dry THF and was added dropwise. The reaction remained at 60 °C for 15 hrs. The transformation of the double bond was followed by ^{1}H NMR to monitor its disappearance. During the reaction, further addition of the AIBN and thioacetic acid, pushed the reaction to the full conversion of the double bond. The solution was cooled to room temperature and the excess thioacetic acid was neutralized by addition of aqueous solution of saturated NaHCO$_3$. The THF was evaporated and the organic phase was extracted by DCM. The solvent was removed and the residue was washed several times with to yield 35.6 mg (89 %) of [Ru(bpy)$_2$(3,3'-bpysac)](PF$_6$)$_2$as a red solid.

^{1}H NMR (400 MHz, CD$_3$CN): δ = 8.48, 8.50 (dd, J = 8.1, 2.7, 4H, H$_{3\text{-bpy}}$), 8.06 (m, J = 8.1, 1.3 4H, H$_{4\text{-bpy}}$), 7.69 (m, 4H, H$_{6\text{-bpy}}$), 7.63 (m, 2H, H$_6$), 7.46-7.36 (m, 4H, H$_{5\text{-bpy}}$), 7.34-7.27 (m, 4H, H$_{4,5}$), 4.13-4.28 (m, 4 H, H$_7$), 2.72-2.85 (m, 4H, H$_{12}$), 2.30 (m, 6H, H$_{14}$), 1.75-1.82 (m, 4 H, H$_8$), 1.48-1.57 (m,4 H, H$_{11}$), 1.33-1.41 (m, 8 H, H$_{9,\,10}$).

^{13}C NMR (100 MHz, CD$_3$CN): δ = 195.5 (C$_{13}$), 157.2 (C$_{2\text{-bpy}}$), 156.2 (C$_2$), 151.6 (C$_{6\text{-bpy}}$), 146.4 (C$_3$), 142.9 (C$_4$), 137.6 (C$_{4\text{-bpy}}$), 127.3 (C$_{5\text{-bpy}}$), 127.0 (C$_5$), 124.1 (C$_{3\text{-bpy}}$), 122.1 (C$_6$), 69.4 (C$_7$), 39.9 (C$_{14}$), 29.2 (C$_{11}$), 28.5 (C$_{12}$), 28.4 (C$_8$), 28.0 (C$_{10,10'}$), 25.0 (C$_9$).

ES MS(+) (MeCN): m/z 1063.1 {M - [PF$_6$]}$^+$, 459.1 {M - 2[PF$_6$]}$^{2+}$.

IR (cm^{-1}): 2933, 1681 (C=O), 1567, 1463, 1443, 1424, 1288, 1127.

UV-Vis (MeCN) λ$_{max}$ in nm: 454, 435(sh), 360, 292, 247.

Emission (MeCN): λ_{max} = 625 nm.

[Ru(bpy)(3,3'-bpyhex)$_2$](PF$_6$)$_2$
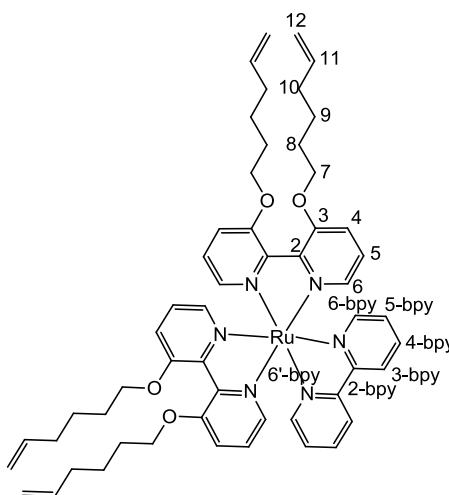
[Ru(bpy)(3,3'-bpyhex)$_2$](PF$_6$)$_2$ was formed as byproduct in the synthetic procedure of

[Ru(bpy)$_2$(3,3'-bpyhex)](PF$_6$)$_2$ and was isolated during the purification process. (23

mg, 37% yield)

R$_f$ (silica gel, CH$_2$Cl$_2$/isopropanol [95:5]) = 0.53.

^{1}H NMR (300 MHz, CD$_3$CN): δ = 8.50 (d, J = 8.1, 2H, H$_{3\text{-bpy}}$), 8.35 (m, 1H, H$_{6\text{-bpy}}$),

8.06 (m, J = 8.1, 1.3, 2H, H$_{4\text{-bpy}}$), 7.85 (m, 1H, H$_{6'\text{-bpy}}$), 7.59-7.73 (m, 4H, H$_6$), 7.49-

7.38 (m, 2H, H$_{5\text{-bpy}}$), 7.37-7.24 (m, 8H, H$_{4,5}$), 5.72-5.89 (tdd, 4H, J =17.2, 10.5, 6.9

H$_{11}$), 4.91-5.06 (m, 8H, H$_{12}$), 4.10-4.29 (m, 8H, H$_7$), 2.03-2.12 (dt, 8H, J = 7.3, 6.9

H$_{10}$), 1.74-1.85 (tt, 8H, J = 7.3, 6.9 H$_8$), 1.42-1.53 (tt, 8H, J=7.3, 7.3 H$_9$).

^{13}C NMR (100 MHz, CD$_3$CN): δ = 157.2 (C$_{2\text{-bpy}}$), 155.8 (C$_2$), 151.4 (C$_{6\text{-bpy}}$), 147.0

(C$_{11}$), 146.2 (C$_3$), 142.8 (C$_4$), 137.3 (C$_{4\text{-bpy}}$), 127.2 (C$_{5\text{-bpy}}$), 126.7 (C$_5$), 123.7 (C$_{3\text{-bpy}}$),

121.7 (C$_6$), 114.1 (C$_{12}$), 69.1 (C$_7$), 32.6 (C$_{10}$), 27.8 (C$_8$), 24.5 (C$_9$).

ES MS(+) (MeOH): *m/z* 1107.4 {M - [PF$_6$]}$^+$, 481 {M - 2[PF$_6$]}$^{2+}$.

IR (cm^{-1}): 2925, 1568, 1464, 1444, 1423, 1289, 1127.

UV-Vis (MeCN) λ_{max} in nm: 458, 435(sh), 360, 292, 247.

Emission (MeCN): λ_{max} = 610 nm.

Anal. Calc. for C$_{54}$H$_{64}$O$_4$N$_6$F$_{12}$P$_2$Ru (NH$_4$PF$_6$)$_{0.35}$: C 49.8, H 5.05, N 6.80. Found C 49.67, H 5.43, N 6.89.

[Ru(bpy)(3,3'-bpysac)$_2$](PF$_6$)$_2$
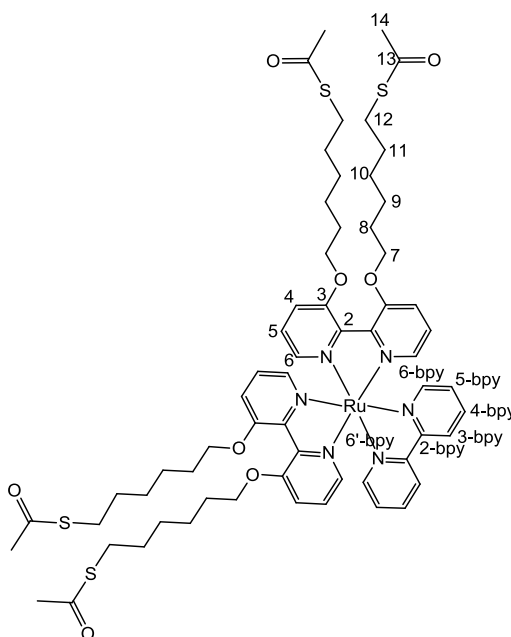
Following the similar procedure of [Ru(bpy)$_2$(3,3'-bpysac)](PF$_6$)$_2$, 35 mg (0.028 mmol) [Ru(bpy)(3,3'-bpyhex)$_2$](PF$_6$)$_2$ in 4 ml dry THF was reacted with 100 mg (1.32 mmol) fresh thioacetic acid and 30 mg (0.172 mmol) AIBN in 2ml dry THF to get

[Ru(bpy)(3,3'-bpysac)$_2$](PF$_6$)$_2$ (37.2 mg, 85.5%) as a red solid. The conversion of the double bond was followed by ^{1}H NMR during the reaction.

^{1}H NMR (400 MHz, CD$_3$CN): δ = 8.38 (dd, J = 8.2, 1.3, 2H, H$_{3\text{-bpy}}$), 8.22 (m, 1H, H$_{6\text{-bpy}}$), 7.93 (m, J = 8.1, 1.3, 2H, H$_{4\text{-bpy}}$), 7.73 (m, 1H, H$_{6\text{-bpy}}$), 7.62-7.49 (m, 4H, H$_6$), 7.37-7.28 (m, 2H, H$_{5\text{-bpy}}$), 7.26-7.12 (m, 8H, H$_{4,5}$), 4.19-4.00 (m, 8H, H$_7$), 2.74-2.61 (m, 8H, H$_{12}$), 2.21 (m, 12H, H$_{14}$), 1.69-1.63 (m, 8H, H$_8$), 1.49-1.36 (m, 8H, H$_{11}$), 1.27-1.21 (m, 16H, H$_{9,\,10}$).

^{13}C NMR (100 MHz, CD$_3$CN): δ = 192.06 (C$_{13}$), 157.0 (C$_{2\text{-bpy}}$), 156.1 (C$_2$), 151.5 (C$_{6\text{-bpy}}$), 146.4 (C$_3$), 142.8 (C$_4$), 137.5 (C$_{4\text{-bpy}}$), 127.1 (C$_{5\text{-bpy}}$), 126.8 (C$_5$), 124.0 (C$_{3\text{-bpy}}$), 121.9 (C$_6$), 69.4 (C$_7$), 29.8 (C$_{14}$), 29.1 (C$_{11}$), 28.4 (C$_{12}$), 28.3 (C$_8$), 27.9 (C$_{10}$), 24.8 (C$_9$).

ES MS(+) (MeCN): m/z 1063.1 {M - [PF$_6$]}$^+$, 459.1 {M - 2[PF$_6$]}$^{2+}$.

IR (cm^{-1}): 2926, 1682 (C=O), 1568, 1460, 1442, 1424, 1288, 1127.

UV-Vis (MeCN) λ$_{max}$ in nm: 458, 435(sh), 360, 292, 247.

Emission (MeCN): λ$_{max}$ = 610 nm.

[Ru(bpy)₂(4,4'-bpyhex)](PF₆)₂
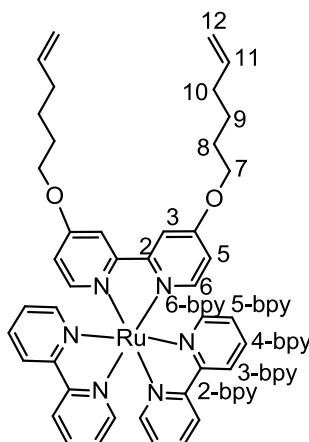
Ru(bpy)₂Cl₂·2H₂O (160 mg, 0.31 mmol) and 4,4'-bpyhex (170 mg, 0.48 mmol) were heated to reflux for 20 hr, under dinitrogen in ethanol (15 mL). The solution was set aside to cool to room temperature, and then concentrated under vacuum to 5 ml. A saturated aqueous solution of ammonium hexafluorophosphate (130 mg, 0.81 mmol in 5 ml water) was added to form a red precipitation. It was cooled at 0 °C for 30 min to promote precipitation and the solid was collected by filtration and washed with water and ether. The [Ru(bpy)₂(4,4'-bpyhex)](PF₆)₂ was purified by column chromatography on silica (1% methanol in DCM, R_f = 0.15) to yield [Ru(bpy)₂(4,4'-bpyhex)](PF₆)₂ as red solid (140 mg, 45.5%).

^{1}H NMR (400 MHz, CD₃CN) : δ = 8.49, 8.50 (dd, J = 8.0, 3.2, 4H, H$_{3\text{-bpy}}$), 8.05 (m, J = 8.0, 1.5 4H, H$_{4\text{-bpy}}$), 8.01 (d, J = 2.6, 2H, H$_3$), 7.83 (d, J =5.2, 2H, H$_{6\text{-bpy}}$), 7.74 (d, J =5.2, 2H, H$_{6'\text{-bpy}}$), 7.43 (m, 4H, H$_{5\text{-bpy}}$), 7.37 (d, 2H, J = 6.4, H$_6$), 6.92 (dd, J = 6.4, 2.5, 2H, H$_5$), 5.81-5.95 (tdd, 2H, J =17.1, 10.3, 6.6 H$_{11}$), 4.95-5.10 (m, 4H, H$_{12}$), 4.21 (t, 4 H, J= 6.5, H$_7$), 2.09-2.17 (dt, 4 H, J = 7.8, 6.5 H$_{10}$), 1.77-1.85 (tt,4 H, J = 7.6, 6.9 H$_8$), 1.51-1.61 (tt, 4 H, J=7.5, 7.5 H$_9$).

^{13}C NMR (100 MHz, CD$_3$CN): δ = 166.4 (C$_2$), 157.6 (C$_4$), 157.0/156.8 (C$_{2\text{-bpy}}$), 152.1 (C$_6$), 151.8/151.6 (C$_{6\text{-bpy}}$), 138.6 (C$_{11}$), 137.4 (C$_{4\text{-bpy}}$), 127.4 (C$_{5\text{-bpy}}$), 124.1 (C$_{3\text{-bpy}}$), 114.4 (C$_{12}$), 114.1 (C$_5$), 111.4 (C$_3$), 69.2 (C$_7$), 32.6 (C$_{10}$), 27.5 (C$_8$), 24.4 (C$_9$).

ES MS(+) (MeOH): *m/z* 911.1 {M - [PF$_6$]}$^+$, 383.2 {M - 2[PF$_6$]}$^{2+}$.

UV-Vis (MeCN) λ$_{max}$/nm: 460, 435(sh), 325, 288, 257, 227.

Emission (MeCN, λ$_{ex}$ = 460 nm): λ$_{max}$/nm = 633 nm.

IR (cm^{-1}): 3082, 2934, 1612, 1491, 1464, 1446, 1337, 1313, 1219, 1028, 823.

Anal. Calc. for C$_{42}$H$_{44}$O$_2$N$_6$F$_{12}$P$_2$Ru: C 47.72, H 4.20, N 7.95. Found C 47.96, H 7.68, N 4.19.

[Ru(bpy)$_2$(4,4'-bpysac)](PF$_6$)$_2$
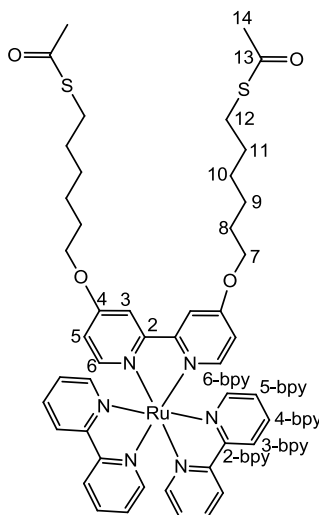
Following the similar procedure of [Ru(bpy)$_2$(3,3'-bpysac)](PF$_6$)$_2$, 35 mg (0.033 mmol) [Ru(bpy)$_2$(4,4'-bpyhex)](PF$_6$)$_2$ in 4 ml dry THF was reacted with 50 mg (0.660 mmol) fresh thioacetic acid and 20 mg (0.115 mmol) AIBN in 2ml dry THF to get

[Ru(bpy)$_2$(4,4'-bpysac)](PF$_6$)$_2$ (37.2 mg, 85.5%) as a red solid. The conversion of the double bond was followed by ^{1}H NMR during the reaction. Reaction quenched by adding NaHCO$_3$. The solvent was removed and the organic phase was extracted by water-DCM. The organic layer was separated and dried over MgSO$_4$. Solvent removed and residue was stirred in hexane for few hours to remove excess of AIBN and thioacetic acid (yield 35.6 mg, 89.3%).

^{1}H NMR (400 MHz, CD$_3$CN) : δ = 8.50, 8.49 (dd, J = 8.0, 4.6, 4H, H$_{3\text{-bpy}}$), 8.03 (m, J = 8.0, 1.5 4H, H$_{4\text{-bpy}}$), 7.97 (d, J = 2.5, 2H, H$_3$), 7.81 (d, J =5.5, 2H, H$_{6\text{-bpy}}$), 7.71 (d, J =5.5, 2H, H$_{6'\text{-bpy}}$), 7.43 (m, 4H, H$_{5\text{-bpy}}$), 7.39 (d, 2H, J = 6.5, H$_6$), 6.90 (dd, J = 6.5, 2.5, 2H, H$_5$), 4.18 (t, 4 H, J= 6.5, H$_7$), 2.85 (t, 4H, J= 7.3, H$_{12}$), 2.27 (s, 6H, H$_{14}$), 1.84-1.76 (m, 4H, H$_8$), 1.61-1.53 (m, 4 H, H$_{11}$), 1.52-1.38 (m,8 H, J = H$_9$/H$_{10}$).

^{13}C NMR (100 MHz, CD$_3$CN): δ = 166.4 (C$_2$), 157.6 (C$_4$), 157.0/156.8 (C$_{2\text{-bpy}}$), 153.0(C$_6$), 152.7/152.5 (C$_{6\text{-bpy}}$), 138.3 (C$_{4\text{-bpy}}$), 128.4 (C$_{5\text{-bpy}}$), 125.1 (C$_{3\text{-bpy}}$), 115.1 (C$_5$), 112.4 (C$_3$), 70.6 (C$_7$), 30.8 (C$_{14}$), 30.2 (C$_{11}$), 29.4 (C$_{12}$), 29.1 (C$_8$), 28.9/25.8 (C$_9$/C$_{10}$).

ES MS(+) : m/z 1063.2 {M - [PF$_6$]}$^+$, 459.2 {M - 2[PF$_6$]}$^{2+}$.

UV-Vis (MeCN) λ$_{max}$ /nm: 460, 435(sh), 325, 288, 257, 227.

Emission (MeCN, λ$_{ex}$ = 460 nm): λ$_{max}$ /nm = 633 nm.

IR (cm^{-1}): 2930, 2857, 1683 (C=O), 1556, 1491, 1464, 1444, 1396, 1339, 1278, 1222, 1120.

Anal. Calc. for C$_{46}$H$_{52}$O$_4$N$_6$S$_2$F$_{12}$P$_2$Ru: C 45.64, H 4.34, N 6.95. Found C 45.51, H 4.16, N 7.14.

[Ru(bpy)Cl$_4$]$^{2-}$ [33]

In a flask, 1.03 g (4.23 mmol) RuCl$_3$.2H$_2$O and 0.75 g (4.84 mmol) 2,2'-bipyridine and 5 ml HCl (1N) was added. The flask was stirred for 30 min to help dissolving the solids. The flask was sealed and kept in room temperature for 10 days, after that time the product was isolated by filtration and washed with water and dried for several hour *in vacua* to get 1.53 g, 3.81 mmol of H$_2$RubpyCl$_4$ (90% yield).

ES MS(+) : *m*/*z* 449.3 [Na$_2$Ru(bpy)Cl$_3$OH + Na]$^+$, 480.9 [K$_2$Ru(bpy)Cl$_3$OH + Na]$^+$, 490.3 [K$_2$Ru(bpy)Cl$_3$(OMe) + NH$_4$]$^+$.

UV-Vis (MeCN) λ$_{max}$ /nm: 650, 495, 300, 200.

IR (cm^{-1}): 3076, 1601, 1468, 1447, 1311, 1245, 1038, 762.

[Ru(bpy)(4,4'-bpyhex)$_2$](PF$_6$)$_2$
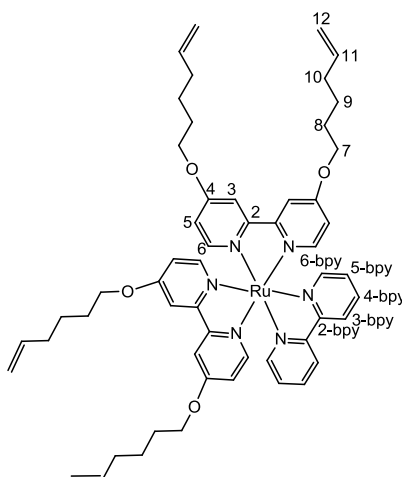
Ru(bpy)Cl$_4$$^{2-}$ (300 mg, 0.075 mmol) and 4,4'-bpyhex (66.4 mg, 0.188 mmol) were heated to reflux for 20 hr, under dinitrogen in ethanol (5 mL). The solution was set

aside to cool to room temperature, and then concentrated under vacuum to 3 ml. A saturated aqueous solution of ammonium hexafluorophosphate (61 mg, 0.37 mmol in 2 ml water) was added and a red precipitate was formed. It was cooled at 0 ^{o}C for 30 min to promote precipitation and the solid was collected by filtration and washed with water, and ether. Crude product was separated by column chromatography on silica (1% methanol in DCM) to yield [Ru(bpy)(4,4'-bpyhex)$_2$](PF$_6$)$_2$ as a red solid (65 mg, 70%).

^{1}H NMR (400 MHz, CD$_3$CN): δ = 8.49 (d, J = 8.0, 2H, H$_{3\text{-bpy}}$), 8.02 (m, J = 8.0, 1.5, 2H, H$_{4\text{-bpy}}$), 7.99 (d, J = 2.6, 2H, H$_3$), 7.97 (d, J = 2.6, 2H, H$_{3'}$), 7.85 (d, J = 5.2, 2H, H$_{6\text{-bpy}}$), 7.54 (d, J = 6.5, 2H, H$_6$), 7.43 (d, J = 6.5, 2H, H$_{6'}$), 7.40 (m, 2H, H$_{5\text{-bpy}}$), 6.97 (dd, J = 6.4, 2.5, 2H, H$_5$), 6.89 (dd, J = 6.4, 2.5, 2H, H$_{5'}$), 5.83-5.95 (m, 4H, J =17.2, 10.5, 6.9 H$_{11}$), 4.93-5.11 (m, 8H, H$_{12}$), 4.23((2×t), J = 6.4, 8H, H$_7$), 2.11-2.21 (m, 8H, H$_{10}$), 1.80-1.90 (m, 8H, H$_8$), 1.54-1.64 (m, 8H, H$_9$).

^{13}C NMR (100 MHz, CD$_3$CN): δ = 166.3 (C$_2$), 158.1/158 (C$_{2\text{-bpy}}$), 157.4 (C$_4$), 152.1/151.9 (C$_6$), 151.6 (C$_{6\text{-bpy}}$), 138.5 (C$_{11}$), 136.7 (C$_{4\text{-bpy}}$), 127.1 (C$_{5\text{-bpy}}$), 123.8 (C$_{3\text{-bpy}}$), 115.2 (C$_{12}$), 114.2 (C$_5$), 111.1/111.0 (C$_3$), 69.4 (C$_7$), 32.8 (C$_{10}$), 27.7 (C$_8$), 24.6 (C$_9$).

ES MS(+): m/z 1107.4 {M - [PF$_6$]}$^+$, 481 {M - 2[PF$_6$]}$^{2+}$.

IR (cm^{-1}): 2935, 1610, 1556, 1490, 1467, 1444, 1217, 1001, 823.

UV-Vis (MeCN) λ$_{max}$ in nm: 468, 440(sh), 325, 288, 275, 227.

Emission (MeCN): λ$_{max}$ = 657 nm.

Anal. Calc. for $C_{54}H_{64}O_4N_6F_{12}P_2Ru$ (H_2O): C 51.01, H 5.24, N 6.61. Found C 50.99, H 5.23, N 6.93.

[Ru(bpy)(4,4'-bpysac)₂](PF₆)₂
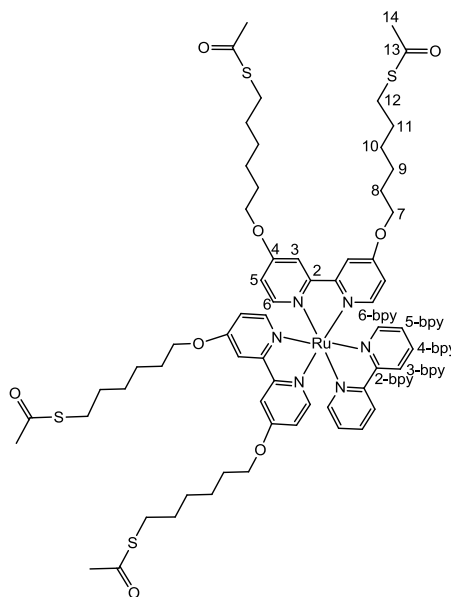
Following the similar procedure of [Ru(bpy)₂(3,3'-bpysac)](PF₆)₂, 65 mg (0.052 mmol) [Ru(bpy)(4,4'-bpyhex)₂](PF₆)₂ in 8 ml dry THF was reacted with 186 mg (2.45 mmol) fresh thioacetic acid and 55.8 mg (0.320 mmol) AIBN in 4 ml dry THF to get [Ru(bpy)(4,4'-bpysac)₂](PF₆)₂ (69.2 mg, 85.5%) as a red solid. The conversion of the double bond was followed by ^{1}H NMR during the reaction.

^{1}H NMR (400 MHz, CD₃CN): δ = 8.37 (d, J = 8.0, 2H, H₃-bpy), 7.91 (m, J = 8.0, 1.5, 2H, H₄-bpy), 7.89 (d, J = 2.6, 2H, H₃), 7.87 (d, J = 2.6, 2H, H₃'), 7.71 (d, J = 5.5, 2H, H₆-bpy), 7.42 (d, J = 6.3, 2H, H₆), 7.31 (d, J = 6.5, 2H, H₆'), 7.29 (m, 2H, H₅-bpy), 6.85 (dd, J = 6.7, 2.7, 2H, H₅), 6.79 (dd, J = 6.7, 2.7, 2H, H₅'), 4.09 ((2×t), J = 6.4, 8H,

H$_7$), 2.77 (dt, J = 7.3, 2.7, 8H, H$_{12}$), 2.19/2.20 (s, 12H, H$_{14}$/H$_{14'}$), 1.75-1.69 (m, 8H, H$_8$), 1.54-1.45 (m, 8H, H$_{11}$), 1.42-1.31 (m, 16H, H$_{9, 10}$).

^{13}C NMR (100 MHz, CD$_3$CN): δ = 175.5/174.4 (C$_{13}$,C$_{13'}$), 165.3 (C$_2$), 157.9 (C$_{2\text{-bpy}}$), 157.4 (C$_4$), 151.6/151.5 (C$_6$), 151.3 (C$_{6\text{-bpy}}$), 136.0 (C$_{4\text{-bpy}}$), 127.1 (C$_{5\text{-bpy}}$), 123.5 (C$_{3\text{-bpy}}$), 114.0 (C$_5$), 111.2 (C$_3$), 69.6 (C$_7$), 29.9 (C$_{14}$), 29.3 (C$_{11}$), 28.4 (C$_{12}$), 28.2 (C$_8$), 27.9 (C$_{10}$), 24.9 (C$_9$).

ES MS(+): m/z 1063.1 {M - [PF$_6$]}$^+$, 459.1 {M - 2[PF$_6$]}$^{2+}$.

IR (cm^{-1}): 2932.70, 1681.59 (C=O), 1556, 1490, 1466, 1445, 1218, 1027, 826.

UV-Vis (MeCN) λ$_{max}$ in nm: 468, 440(sh), 325, 288, 275, 227.

Emission (MeCN): λ$_{max}$ = 657 nm.

Anal. Calc. for C$_{62}$H$_{80}$O$_8$N$_6$S$_4$F$_{12}$P$_2$Ru (thioacetic acid C$_4$H$_4$O$_2$S$_2$): C 46.47, H 4.97, N 4.93. Found C 46.49, H 4.63, N 4.87.

Ru(phen)$_2$Cl$_2$
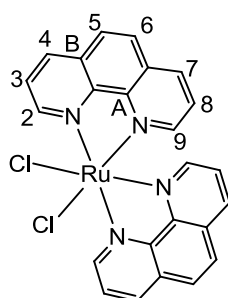
The RuCl$_3$.2H$_2$O 40% (630 mg, 1 mmol), 1,10-phenanthroline (360 mg, 2 mmol), and LiCl (280 mg, 7 mmol) were dissolved in dry N,N-dimethylformamide (3 mL)

and the solution was heated to reflux for 8 h. After cooling to room temperature, it was poured into rapidly stirred acetone (5 mL) and the combined phases were allowed to stand overnight at -4 $^{\circ}$C. The resultant dark purple microcrystalline material was collected by filtration, washed with water and ether (293 mg, 55% yield).

^{1}H NMR (300 MHz, DMSO): δ_H = 9.92 (d, 2H, J = 4.7, H_2), 9.70 (d, 2H, J = 4.7, H_9), 8.97 (d, 2H, J = 8.0, H_4), 8.88 (d, 2H, J = 8.0, H_7), 8.33 (m, 4H, $H_{5,6}$), 8.23 (m, 2H, H_3), 8.11 (m, 2H, H_8).

^{13}C NMR (100 MHz, DMSO): δ = 154.5 (C_2), 151.6 (C_9), 147.3/145.7 (C_A), 138.7 (C_4), 138.3 (C_7), 130.2/130.0 (C_B), 127.5 (C_3), 127.2 (C_8), 125.5 (C_5), 125.4 (C_6).

TOF ES-MS(+): m/z 581.1 [Ru(bpy)$_2$(OEt)Cl + K]$^+$.

UV-VIS (DCM) λ_{max} / nm: 560, 480, 280, 200.

IR (cm^{-1}): 3109, 3055, 1562, 1510, 1426, 1401, 1219, 1196, 1094, 1013.

[Ru(phen)$_2$(4,7-phenhex)](PF$_6$)$_2$
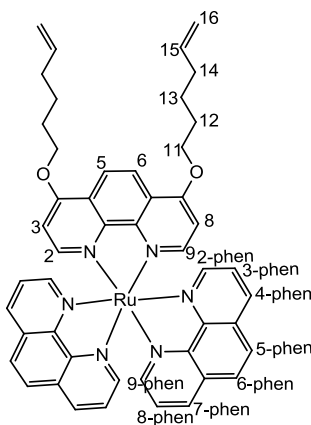
Ru(phen)$_2$Cl$_2$ (200 mg, 0.38 mmol) and 4,7-phenhex (215 mg, 0.57 mmol) were heated to reflux for 20 hr, under nitrogen in ethanol (20 mL). The solution was set aside to cool to room temperature, and then concentrated under vacuum to 5 ml. A saturated aqueous solution of ammonium hexafluorophosphate was added and a red precipitation was formed. It was cooled at 0 ^{o}C for 30 min to promote precipitation and the solid was collected by filtration and washed with water and ether. The crude was purified by column chromatography on silica using DCM/MeOH [95:5] as eluent to yield 170 mg, 40% [Ru(phen)$_2$(4,7-phenhex)](PF$_6$)$_2$.

^{1}H NMR (300 MHz, CD$_3$CN) : δ = 8.59 (m, J = 7.8, 1.2, 4H, H$_{4,7\text{-phen}}$), 8.40 (s, 2H, H$_{5,6}$), 8.26 (s, 4H, H$_{5,6\text{-phen}}$), 8.18/8.04 (dd, J = 5.3, 1.2, 4H, H$_{2,9\text{-phen}}$), 7.75 (d, J = 6.2, 2H, H$_{2,9}$), 7.67/7.61 (dd, J = 7.8, 5.3, 4H, H$_{3,8\text{-phen}}$), 7.03 (d, J = 6.2, 2H, H$_{3,8}$), 5.95-5.84 (tdd, 2H, J =20.3, 10.4, 6.7 H$_{15}$), 5.10-4.98 (m, 4H, H$_{16}$), 4.37-4.24 (m, 4 H, H$_{11}$), 2.17 (m, 4H, H$_{14}$), 1.99-1.92 (m, 4H, H$_{12}$), 1.70-1.62 (m, 4H, H$_{13}$).

^{13}C NMR (100 MHz, CD$_3$CN): δ = 153.6 (C$_{2,9}$), 153.1/152.7 (C$_{2,9\text{-phen}}$), 138.6 (C$_{15}$), 136.3 (C$_{4,7\text{-phen}}$), 128.0 (C$_{5,6\text{-phen}}$), 125.7 (C$_{3,8\text{-phen}}$), 120.9 (C$_{5,6}$), 114.4 (C$_{16}$), 106.8 (C$_{3,8}$), 70.1 (C$_{11}$), 32.9 (C$_{14}$), 27.8 (C$_{12}$), 24.9 (C$_{13}$).

ES MS(+) (MeOH): m/z 983.3 {M - [PF$_6$]}$^+$, 419.2 {M - 2[PF$_6$]}$^{2+}$.

IR (cm^{-1}): 2918, 2852, 1576, 1504, 1427, 1416, 1298, 1227, 824.

UV-Vis (MeCN) λ$_{max}$ in nm: 458, 420(sh), 290, 220.

Emission (MeCN): λ$_{max}$ = 630 nm.

Os(bpy)₂Cl₂ [35]
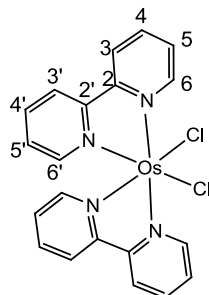
In a typical preparation 100 mg $(NH_4)OsCl_6$ and 2,2'-bipyridine (75 mg, 0.48 mmol) in 5 ml ethylene glycol were heated to reflux for 45 min under N_2. Since the crude reaction mixture contained both cis-Os(bpy)₂Cl₂ and [cis-Os(bpy)₂Cl₂]⁺, an equal volume of saturated aqueous sodium dithionite was added to the cooled reaction mixture in order to reduce excess Os^{III} to Os^{II}. The purple-black precipitate that had formed was isolated by filtration, washed with water to remove $[Os(bpy)_3]^{2+}$ and other ionic products, and washed with large volumes of ether (85% yield).

ES MS(+) (MeOH): *m/z* 573.8 $[M + H]^+$.

UV-Vis (MeCN) λ_{max} in nm: 565, 470, 380, 300.

[Os(bpy)₂(3,3'-bpyhex)](PF₆)₂
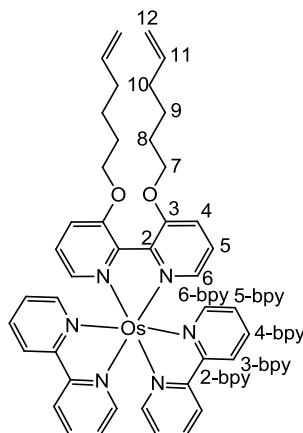
Os(bpy)$_2$Cl$_2$ (40.4 mg, 0.06 mmol) and 3,3'-bpyhex (40 mg, 0.114 mmol) were heated to reflux for 24 hr, under nitrogen in a solvent mixture ethanol-water (3.5:2 mL). Following cooling of the solution at room temperature, a saturated aqueous solution of ammonium hexafluorophosphate (48.9 mg, 0.3 mmol in 1 ml water) was added. It was cooled at 0 °C for 30 min to promote precipitation and the solid was collected by filtration and washed with water (2 × 5 mL), and ether (5 mL). Further purification was achieved by column chromatography on silica using DCM/methanol [96:4] as eluent to yield 32 mg (45.8%) [Os(bpy)$_2$(3,3'-bpyhex)](PF$_6$)$_2$ as a green powder.

R$_f$ (silica gel, CH$_2$Cl$_2$/methanol [85:15]) = 0.47.

^{1}H NMR (400 MHz, CD$_3$CN): δ = 8.49, 8.48 (dd, J = 8.1, 3.5, 4H, H$_{3\text{-bpy}}$), 7.85 (m, J = 8.1, 1.5, 4H, H$_{4\text{-bpy}}$), 7.61 (dd, J = 5.2, 11.0, 4H, H$_{6\text{-bpy}}$), 7.46 (dd, J = 6.4, 3.5, 2H, H$_{-6}$), 7.36-7.27 (m, 4H, H$_{5\text{-bpy}}$), 7.29 (m, 4H, H$_{4,5}$), 5.87-5.77 (tdd, 2H, J =17.1, 10.3, 6.7 H$_{11}$), 4.94-5.03 (m, 4H, H$_{12}$), 4.16-4.30 (m, 4 H, H$_7$), 2.03-2.15 (dt, 4 H, J = 7.0, 7.5 H$_{10}$), 1.73-1.88 (tt,4 H, J = 7.0, 7.5 H$_8$), 1.41-1.58 (tt, 4 H, J=7.5, 7.5 H$_9$).

^{13}C NMR (100 MHz, CD$_3$CN): δ = 158.8 (C$_{2\text{-bpy}}$), 156.3 (C$_2$), 150.7 (C$_{6\text{-bpy}}$), 150.2 (C$_{11}$), 148.0 (C$_3$), 142.1 (C$_4$), 138.2 (C$_{4\text{-bpy}}$), 136.7 (C$_{5\text{-bpy}}$), 127.6 (C$_5$), 124.0 (C$_{3\text{-bpy}}$), 121.4 (C$_6$), 114.0 (C$_{12}$), 69.2 (C$_7$), 32.6 (C$_{10}$), 27.7 (C$_8$), 24.4 (C$_9$).

ES MS(+) (MeOH): *m/z* 1001.2 {M - [PF$_6$]}$^+$, 428.1 {M - 2[PF$_6$]}$^{2+.}$

IR (cm^{-1}): 2924, 1563, 1463, 1436, 1422, 1302.

UV-Vis (MeCN) λ$_{max}$ in nm: 650, 480, 435(sh), 365, 295, 247.

Emission (MeCN): λ$_{max}$ = 747 nm.

[Os(bpy)$_2$(3,3'-bpysac)](PF$_6$)$_2$
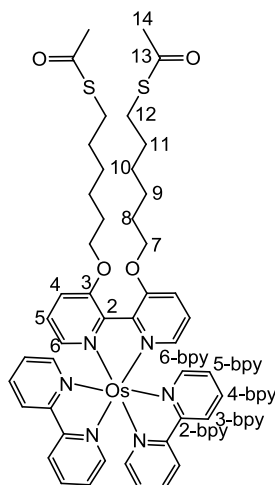
Following the similar procedure of [Ru(bpy)$_2$(3,3'-bpysac)](PF$_6$)$_2$, 30 mg (0.032 mmol) [Os(bpy)$_2$(3,3'-bpyhex)](PF$_6$)$_2$ in 4 ml dry THF was reacted with 50 mg (0.66 mmol) fresh thioacetic acid and 20 mg (0.115 mmol) AIBN in 2 ml dry THF to get [Os(bpy)$_2$(3,3'-bpysac)](PF$_6$)$_2$ 35.6 mg (89.3%) as a green solid. The conversion of the double bond was followed by ^{1}H NMR during the reaction.

^{1}H NMR (400 MHz, CD$_3$CN): δ = 8.49, 8.48 (dd, J = 8.1, 2.2, 4H, H$_{3\text{-bpy}}$), 7.85 (m, J = 8.1, 1.6, 4H, H$_{4\text{-bpy}}$), 7.61 (dd, J = 5.1, 11.0, 4H, H$_{6\text{-bpy}}$), 7.46 (dd, J = 6.5, 3.8, 2H, H$_6$), 7.35-7.26 (m, 4H, H$_{5\text{-bpy}}$), 7.21 (m, 4H, H$_{4,5}$), 4.16-4.26 (m, 4 H, H$_7$), 2.77 (t, J = 7.2, 4H, H$_{12}$), 2.28 (s, 6H, H$_{14}$), 1.69-1.63 (m, 4H, H$_8$), 1.49-1.36 (m, 4H, H$_{11}$), 1.27-1.21 (m, 8H, H$_{9, 10}$).

^{13}C NMR (100 MHz, CD$_3$CN): δ = 195.5 (C$_{13}$), 159.1 (C$_{2\text{-bpy}}$), 156.5 (C$_2$), 150.9 (C$_{6\text{-bpy}}$), 148.2 (C$_3$), 142.3 (C$_4$), 136.9 (C$_{4\text{-bpy}}$), 127.8 (C$_{5\text{-bpy}}$), 127.5 (C$_5$), 124.3 (C$_{3\text{-bpy}}$), 121.6 (C$_6$), 69.5 (C$_7$), 29.8 (C$_{14}$), 29.1 (C$_{11}$), 28.3 (C$_{12}$), 28.1 (C$_8$), 27.9 (C$_{10}$), 24.8 (C$_9$).

ES MS(+) (MeOH): m/z 1153.3 {M - [PF$_6$]}$^+$, 504.1 {M - 2[PF$_6$]}$^{2+.}$

IR (cm^{-1}): 2925, 1681 (C=O), 1563, 1461, 1434, 1421, 1301, 1126.

UV-Vis (MeCN) λ$_{max}$ in nm: 650, 480, 435(sh), 365, 295, 247.

Emission (MeCN): λ$_{max}$ = 747 nm.

Anal. Calc. for C$_{46}$H$_{52}$O$_4$N$_6$S$_2$F$_{12}$P$_2$Os (NH$_4$PF$_6$)$_{0.35}$: C 40.62, H 3.97, N 6.57. Found C 40.47, H 4.23, N 6.43.

[Os(bpy)$_2$(4,4'-bpyhex)](PF$_6$)$_2$
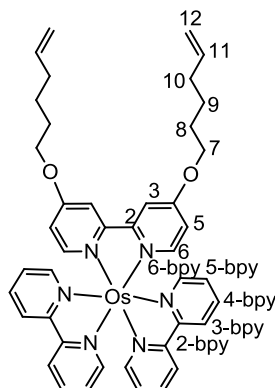
Os(bpy)$_2$Cl$_2$ (100 mg, 0.150 mmol) and 4,4'-bpyhex (100 mg, 0.281 mmol) were heated to reflux for 24 hr, under nitrogen in ethanol (10 mL). Following cooling of the solution at room temperature, a saturated aqueous solution of ammonium hexafluorophosphate was added. It was cooled at 0 ^{o}C for 30 min to promote precipitation and the brown precipitate was collected by filtration, washed with water and ether. Further purification was achieved by column chromatography on silica (4% methanol in DCM) to get 87 mg, 0.076 mmol of [Os(bpy)$_2$(4,4'-bpyhex)](PF$_6$)$_2$ as a dark green solid (51% yield).

^{1}H NMR (400 MHz, CD$_3$CN) : δ = 8.48 (m, J = 8.2, 4H, H$_{3\text{-bpy}}$), 7.96 (d, J = 2.6 4H, H$_{5\text{-bpy}}$), 7.83 (m, 2H, H$_3$), 7.76/7.65 (d, J =5.6, 4H, H$_{6\text{-bpy}}$), 7.34 (d, 2H, J = 6.7, H$_6$), 7.34/7.26 (m, J =8.2, 1.3, 4H, H$_{4\text{-bpy}}$), 6.90 (dd, J = 6.7, 2.7, 2H, H$_5$), 5.94-5.84 (tdd, 2H, J =18.0, 10.1, 6.5 H$_{11}$), 4.10-4.98 (m, 4H, H$_{12}$), 4.22 (t, 4 H, J= 6.5, H$_7$), 2.19-2.13 (m, 4 H, H$_{10}$), 1.88-1.81 (m,4 H, H$_8$), 1.62-1.51 (m, 4 H, H$_9$).

^{13}C NMR (100 MHz, CD$_3$CN): δ = 166.2 (C$_4$), 159.6 (C$_2$), 159.7 (C$_{2\text{-bpy}}$), 151.3 (C$_6$), 151.0/150.5 (C$_{6\text{-bpy}}$), 138.6 (C$_{11}$), 136.5 (C$_{4\text{-bpy}}$), 127.9 (C$_{5\text{-bpy}}$), 124.3 (C$_{3\text{-bpy}}$), 114.4 (C$_5$), 114.3 (C$_{12}$), 111.5 (C$_3$), 69.6 (C$_7$), 32.9 (C$_{10}$), 27.8 (C$_8$), 24.7 (C$_9$).

ES MS(+) (MeOH): *m/z* 1001.2 {M - [PF$_6$]}$^+$, 428.1 {M - 2[PF$_6$]}$^{2+}$.

IR (cm^{-1}): 2926, 1552, 1485, 1462, 1447, 1423, 1218, 1022, 1006.

UV-Vis (MeCN) λ$_{max}$ in nm: 650, 490, 470(sh), 290, 247.

Emission (MeCN): λ$_{max}$ = 760 nm.

[Os(bpy)$_2$(4,4'-bpysac)](PF$_6$)$_2$
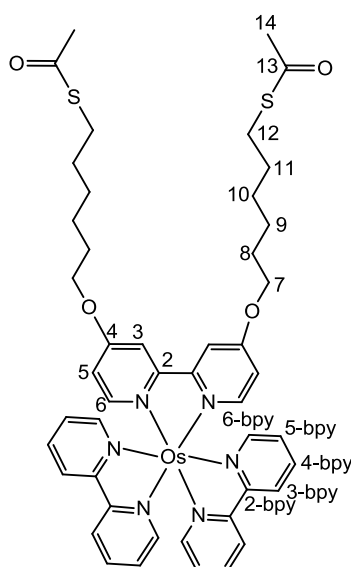
Following the similar procedure of [Ru(bpy)$_2$(3,3'-bpysac)](PF$_6$)$_2$, 30 mg (0.032 mmol) [Os(bpy)$_2$(4,4'-bpyhex)](PF$_6$)$_2$ in 4 ml dry THF was reacted with 50 mg (0.66 mmol) fresh thioacetic acid and 20 mg (0.115 mmol) AIBN in 2 ml dry THF to get [Os(bpy)$_2$(4,4'-bpysac)](PF$_6$)$_2$ 35.6 mg (89.3%) as a green solid. The conversion of the double bond was followed by ^{1}H NMR during the reaction.

^{1}H NMR (400 MHz, CD$_3$CN) : δ = 8.48 (m, *J* = 8.0, 4H, H$_{3-bpy}$), 7.96 (d, *J* = 2.8 4H, H$_{5-bpy}$), 7.83 (m, 2H, H$_3$), 7.76/7.65 (d, *J* =5.6, 4H, H$_{6-bpy}$), 7.34 (d, 2H, *J* = 6.7, H$_6$),

7.34/7.26 (m, J =8.0, 1.3, 4H, $H_{4\text{-bpy}}$), 6.90 (dd, J = 6.7, 2.7, 2H, H_5), 4.23 (t, 4 H, J= 6.5, H_7), 2.88 (m, 4H, H_{12}), 2.30 (s, 6H, H_{14}), 1.85-1.78 (m, 4H, H_8), 1.65-1.57 (m, 4 H, H_{11}), 1.53-1.38 (m, 8H, J = H_9/H_{10}).

^{13}C NMR (100 MHz, CD$_3$CN): δ = 165.9 (C_4), 159.3 (C_2), 158.9 ($C_{2\text{-bpy}}$), 150.9 (C_6), 150.2/150.6 ($C_{6\text{-bpy}}$), 136.1 ($C_{4\text{-bpy}}$), 127.6 ($C_{5\text{-bpy}}$), 124.0 ($C_{3\text{-bpy}}$), 114.2 (C_5), 111.2 (C_3), 69.4 (C_7), 29.5 (C_{14}), 28.9 (C_{11}), 28.1 (C_{12}), 27.8 (C_8), 27.6 (C_{10}), 24.6 (C_9).

ES MS(+): m/z 1153.2 {M - [PF$_6$]}$^+$, 504.1 {M - 2[PF$_6$]}$^{2+.}$

IR (cm^{-1}): 2932, 1680 (C=O), 1551, 1462, 1446, 1422, 1218, 1005, 824.

UV-Vis (MeCN) λ_{max} in nm: 650, 490, 470(sh), 290, 247.

Emission (MeCN): λ_{max} = 760 nm.

Anal. Calc. for $C_{46}H_{52}O_4N_6S_2F_{12}P_2Os$: C 42.59, H 4.04, N 6.48. Found C 42.73, H 4.22, N 6.41.

3.5. References

(1)   Bakker, B. H.; Goes, M.; Hoebe, N.; van Ramesdonk, H. J.; Ver-hoeven, J. W.; Werts, M. H. V.; Hofstraat, J. W. *Coord. Chem. Rev.* **2000**, *208*, 3-16.

(2)   Bignozzi, C. A.; Argazzi, R.; Kleverlaan, C. *J. Chem. Soc. Rev.* **2000**, *29*, 87-96.

(3)   Gust, D.; Moore, T. A.; Moore, A. L. *Accounts Chem. Res.* **2001**, 40-48.

(4)   Li, C.; Fan, W.; Straus, D. A.; Lei, B.; Asano, S.; Zhang, D. H.; Han, J.; Meyyappan, M.; Zhou, C. W. *J. Am. Chem. Soc.* **2004**, *126*, 7750-7751.

(5)   Li, C.; Fan, W. D.; Lei, B.; Zhang, D. H.; Han, S.; Tang, T.; Liu, X. L.; Liu, Z. Q.; Asano, S.; Meyyappan, M.; Han, J.; Zhou, C. W. *Appl. Phys. Lett.* **2004**, *84*, 1949-1951.

(6)   Zimmerman, R.; Basabe-Desmonts, L.; van der Baan, F.; Rein-houdt, D. N.; Crego-Calama, M. *J. Mater. Chem.* **2005**, *15*, 2772-2777.

(7)   Nierengarten, J. F.; Armaroli, N.; Accorsi, G.; Rio, Y.; Eckert, J. F. *Chem. Eur. J.* **2003**, *9*, 36-41.

(8)   Juris, A.; Balzani, V.; Barigelletti, F.; Campagna, S.; Belser, P.; Zelewsky, A. V. *Coord. Chem. Rev.* **1988**, *84*, 85-277.

(9)   Faiz, J.; Philipp opoulos, A. I.; Kontos, A. G.; Falaras, P.; Pikramenou, Z. *Adv. Func. Mat.* **2007**, *17*, 54-58.

(10)   Smalley, J. F.; Finklea, H. O.; Chidsey, C. E. D.; Linford, M. R.; Creager, S. E.; Ferraris, J. P.; Chalfant, K.; Zawodzinsk, T.; Feld-berg, S. W.; Newton, M. D. *J. Am. Chem. Soc.* **2003**, *125*, 2004-2013.

(11)   Smalley, J. F.; Newton, M. D.; Feldberg, S. W. *J. Electroanal. Chem.* **2006**, *589*, 1-6.

(12)   Bertoncello, P.; Kefalas, E. T.; Pikramenou, Z.; Unwin, P. R.; Forster, R. J. *J. Phys. Chem. B* **2006**, *110*, 10063-10069.

(13)   Silva, M. J. J. P.; Bertoncello, P.; Daskalakis, N. N.; Spencer, N.; Kariuki, B. M.; Unwin, P. R.; Pikramenou, Z. *Supramol. Chem.* **2007**, *19*, 115-127.

(14)   Shepherd, J. L.; Kell, A.; Chung, E.; Sinclar, C. W.; Workentin, M. S.; Bizzotto, D. *J. Am. Chem. Soc.* **2004**, *126*, 8329-8335.

(15)   Zhang, J.; Lakowicz, J. R. *J. Phys. Chem. B* **2005**, *109*, 8701-8706.

(16)   Zhang, J.; Malicka, J.; Gryczynski, I.; Lakowicz, J. R. *J. Phys. Chem. B* **2005**, *109*, 7643.

(17)   Kefalas, E. *PhD, University of Birmingham* **2008**.

(18)   Mesmaeker, A. K.; Orellana, G.; Barton, J. K.; Turro, N. J. *Photochem. Photobiol.* **1990**, *52*, 461–472 .

(19)   Mongelli, M. T.; Heinecke, J.; Mayfield, S.; Okyere, B.; Winkel, B. S. J.; Brewer, K. J. *J. Inorg. Biochem.* **2006**, *100*, 1983–1987.

(20)   Naumann, C.; Langhals, H. *Synthesis* **1990**, *4*, 279-281.

(21)   Langhals, H.; Pust, S. *Chem. Ber.* **1986**, *118*, 4674-4681.

(22)   Mongin, F.; Trecourt, F.; Mongin, O.; Queguiner, G. *Tetrahedron* **2002**, *58*, 309-314.

(23)   Kende, A. S.; Liebeskind, L. S.; Braitsch, D. M. *Tetrahedron letters* **1957**, 3375-3377.

(24)   Tieco, M.; Testaferri, L.; Tingoly, M.; Chiannelli, D.; Montanucci, M. *Synthesis* **1984**, 736-738.

(25)   Pearson, A. J.; Hwang, J.-J. *J. Org. Chem.* **2000**, *65*, 3466-3472.

(26)   Hong, Y.-R.; Gorman, C. B. *J. Org. Chem.* **2003**, *68*, 9019-9025.

(27)   Lay, P. A.; Sargeson, A. M.; Taube, H. *Inorg. Synth.* **1986**, 291.

(28)   Sulivan, B. P.; Salmon, D. J.; Meyer, T. *J. Inorg. Chem.* **1978**, *17*, 3334-3341.

(29)   Fergusson, J. E.; Harris, G. M. *J. Chem. Soc. A* **1966**, 1296-1302.

(30)   Walker, G. W.; Nocera, D. G. *Inorg. Synth.* **2004**, *34*, 66.

(31)   Faiz, J. A. *PhD, University of Birmingham* **2005**.

(32)   Birchall, J. D.; O' Donoghue, T. D.; Wood, J. R. *Inorganic Chimica Acta* **1979**, *37*, L461-L463.

(33)   Krause, R. A. *Inorganica Chimica Acta* **1977**, *22*, 209-213.

(34)   Rau, S.; Ruben, M.; Büttner, T.; Temme, C.; Dautz, S.; Görls, H.; Rudolph, M.; Walther, D.; Brodkorb, A.; Duati, M.; O'Connor, C.; Vos, J. G. *J. Chem. Soc., Dalton Trans.* **2000**, 3649–3657.

(35)   Kober, E. M.; Caspar, J. V.; Sullivan, B. P.; Meyer, T. J. *J. Inorg. Chem.* **1988**, *27*, 4587-4598.

(36)   Mattos, M. C. S.; Bernini, R. B. *J. Braz. Chem. Soc.* **2007**, *18*, 1068-1072.

(37)   Inguimbert, N.; Coric, P.; Poras, H.; Meudal, H.; Teffort, F.; Fournie-Zaluski, M. C.; Roques, B. P. *J. Med. Chem.* **2002**, *45*, 1477-1486.

(38)   Buskas, T.; Soderberg, E.; Konradsson, P.; Fraser-Reid, B. *J. Org. Chem.* **2000**, *65*, 958-963.

(39)   Nicolaou, K. C.; Cho, S. Y.; Hughes, R.; Winssinger, N.; Smethurst, C.; Labischinski, H.; Endermann, R. *Chem. Eur. J.* **2001**, *7*, 3798-3823.

(40)   Rillema, D. P.; Jones, D. S.; Levy, H. A. *J. Chem. Soc. Chem. Commun.* **1979**, 849-851.

(41)   Richter, M. M.; Scott, B.; Brewer, K. J.; Willett, R. D. *Acta Cryst.* **1991**, *C47*, 2443-2444.

(42)   Shklover, V.; Zakeeruddin, S. M.; Nesper, R.; Fraser, D.; Gratzel, M. *Inotganica Chimica Acta* **1998**, *274*, 64-72.

(43)   Be´thencourt, M. I.; Srisombat, L.-o.; Chinwangso, P.; Lee, T. R. *Langmuir* **2009**, *25*, 1265-1271.

(44)   Fadley, C. S.; Baird, R. J.; Siekhaus, W. J.; Novakov, T.; Bergstrom, S. A. *J. Electron Spectrosc. Relat. Phenom.* **1974**, *4*, 93.

(45)   Bemdtseon, A. *J. Phys. Statues Solidi B* **1979**, *93*, K103-K105.

(46)   Yesildaˇg, A.; Ekinci, D. *Electrochimica Acta* **2010**, *55*, 7000-7009.

(47)   Chen, P.; McCreery, R. L. *Anal. Chem.* **1996**, *68*, 3958-3965.

(48)   Panziera, N.; Pertici, P.; Fratoddi, I.; La, G. A.; Russo, M. V. *J. Organomet. Chem.* **2006**, *691*, 2648.

(49)   Patrocinio, A. O. T.; Paniago, E. B.; Paniago, R. M.; Iha, N. Y. M. *Appl. Surf. Sci.* **2008**, *254*, 18741871-.

(50)   Zhou, M.; Laux, J. M.; Edwards, K. D.; Hemminger, J. C.; Hong, B. *Chem. Commun.* **1997**, 1977-1978.

(51)   Gelius, U.; Heden, P. F.; Hedman, J.; Lindberg, B. J.; Bernt, J.; Manne, R.; Nordberg, R.; Nordling, C.; Siegbahn, K. *Phys. Scr.* **1970**, 70-80.

(52)   Lu, H. B.; Campbell, C. T.; Castner, D. G. *Langmuir* **2000**, *16*, 1711.

(53)   Tour, J. M.; Jones, L.; Pearson, D. L.; Lamba, J. J. S.; Burgin, T. P.; Whitesides, G. M.; AUara, D. L.; Parikh, A. N.; Atre, S. V. *J. Am. Chem. Soc.* **1995**, *117*, 9529-9534.

(54)   Nakamaru, K. *Bull. Chem. Soc. Jpn.* **1982**, *55*, 2697-2705.

(55) Xie, P.-H.; Hou, Y.-J.; Zhang, B.-W.; Cao, Y.; Wu, F.; Tian, W.-J.; Shen, J.-C. *J. chem. Soc., Dalton Trans.* **1999**, 4217-4221.

(56) Hou, Y.; Xie, P.; Wu, K.; Wang, J.; Zhang, B.; Cao, Y. *Solar Energy Materials & Solar Cells* **2001**, *70*, 131–139.

(57) Klassen, D. M.; Crosby, G. A. *J. Chem. Phys.* **1968**, *48*, 1853-1865.

(58) Zhao, W.; Tong, B.; Pan, Y.; Shen, J.; Zhi, J.; Shi, J.; Dong, Y. *Langmuir* **2009**, *25*, 11796–11801.

(59) Lupo, F.; Fragala`, M. E.; Gupta, T.; Mamo, A.; Aureliano, A.; Bettinelli, M.; Speghini, A.; Gulino, A. *J. Phys. Chem. C* **2010**, *114*, 13459–13464 .

(60) D'Aléo, A.; Williams, R. M.; Chriqui, Y.; Iyer, V. M.; Belser, P.; Vergeer, F.; Ruiz, V.; Unwin, P. R.; De Cola, L. *Open Inorg. Chem. J.* **2007**, *1*, 26-36.

(61) Nazeeruddin, M. K.; Zakeeruddin, S. M.; Kalyanasundaram, K. *J. Phys. Chem. C* **1993**, *97*, 9607-9612.

(62) Baggott, J. E.; Gregory, G. K.; Pilling, M. J.; Anderson, S.; Seddon, K. R.; Turp, J. E. *chem. Soc., faraday trans.* **1983**, *79*, 195.

(63) Hauenstein-Jr, B. L.; Dressick, W. J.; Buell, S. L.; Demas, J. N.; DeGraff, B. A. *J. Am. Chem. Soc.* **1983**, *105*, 4251-4255.

(64) Kobayashi, H.; Kaizu, Y. *Coord. Chem. Rev.* **1985**, *64*, 540.

(65) Lin, C. T.; Boettcher, W.; Chou, M.; Creutz, C.; Sutin, N. *J. Am. Chem. Soc.* **1985**, *107*, 1138-1141.

(66) Creutz, C.; Chou, M.; Netzel, T. L.; Okumura, M.; Sutin, N. *J. Am. Chem. Soc.* **1980**, *102*, 1309-1319.

(67) Kalyanasundaram, K.; Nazeeruddin, M. K. *Chemical Physics letters* **1989**, *158*, 45-50.

(68)   Richter, M. M.; Brewer, K. *J. Inorganic Chimica Acta* **1991**, *180*, 125-131.

(69)   Johnson, S. R.; Westmoreland, T. D.; Caspar, J. V.; Barqawi, K. R.; Meyer,

T. J. *Inorg.Chem.* **1988**, *27*, 3195-3200.

CHAPTER 4

Surface Active Metal Complexes of New Tridentate Ligands

4.1. Introduction

As was mentioned in the introduction, ruthenium polypyridine complexes have attracted a lot of attention in order to develop molecular devices[1-3], nanowire transistors[4,5], sensors[6] and photovoltaic systems. In this context, $[Ru(bpy)_3]^{2+}$ derivatives have been widely used due to the favorable properties of their lowest excited triplet metal-to-ligand charge transfer (^{3}MLCT) state, including room temperature ^{3}MLCT emission lifetimes of up to 1 μs, high emission quantum yields, and strong oxidizing and reducing properties.[7] However, in most cases, different optical isomers are formed, which prevents the desired vertical electron transfer and complicates kinetic analyses.[8]

Unlike $[Ru(bpy)_3]^{2+}$, $[Ru(tpy)_2]^{2+}$ yields rod-like donor-photosensitizer-acceptor assemblies when substituted at the 4′-position of the 2,2′;6′,2″-terpyridine (tpy) ligands. However $[Ru(tpy)_2]^{2+}$ does not exhibit luminescence at room temperature and has a short excited state lifetime (τ = 0.25 ns).[9] The short lifetime arises due to deactivation via short-lived metal-centered (^{3}MC) states that are thermally populated from the ^{3}MLCT state.[7,9] Several strategies to prolong the excited state lifetime of bis-

tridentate Ru(II) complexes have been introduced recently, including modification of tpy ligands to increase the energy gap between the ^{3}MLCT and ^{3}MC states.[9] However, this approach often results in a substantial decrease in ^{3}MLCT energy that makes these chromophores less useful in photosensitizer applications. An alternative strategy is to increase the ligand field, and thus the energy of the ^{3}MC states, by making the complex more octahedral.[10] Following this strategy, Hammarström *et al.*[11,12] reported a Ru^{II}-bistridentate complex with a much longer excited state lifetime (τ = 15 ns in CH$_3$CN) than that of [Ru(tpy)$_2$]$^{2+}$ without any substantial decrease in excited state energy. Later the group introduced a new, near octahedral bis-tridentate Ru^{II} complex[10] involving only six-membered chelates, based on the 2,6-bis(8′-quinolinyl)pyridine ligand (bqp). The structure drew even more attention as it leaves the 4-positions of the central pyridines available for the preparation of linear donor-chromophore-acceptor assemblies for vertical electron migration. It was claimed that because of the strong ligand field, the ^{3}MLCT state lifetime of this complex at room temperature is dramatically increased and is even longer than the 1 μs observed for the [Ru(bpy)$_3$]$^{2+}$. The group of Johansson developed a range of functionalised 2,6-bis-(quinolin-8-yl)-pyridyl (bqp) ligands[13] prepared via a Pd-catalysed coupling strategy and a one-step ring-forming process, generating the central pyridine ring.[14-18] Later, Hammarström *et al.* reported a series of complexes based on the bqp ligand with electron donating and/or accepting substituents in the 4-position of the pyridine,[19] improving photophysical properties of the complexes further, reporting ^{3}MLCT state lifetime of 5.5 μs for the homoleptic complex based on bqpCO$_2$Et. Borg *et al.*[20] investigated the potential energy of the first excited triplet state of the

$[Ru(bqp)_2]^{2+}$ complexes by means of density functional theory, to give a better understanding of the photophysical properties of the new series of Ru(II) complexes.

In this chapter, we report the synthesis of new derivatives of the bqp ligand in order to make a surface active ruthenium(II) complex that exhibits a long luminescence lifetime. Several routes for the synthesis of a bqp ligand bearing two surface active thioacetic acid moieties were attempted. The photophysical and surface properties of the resulting ruthenium(II) complexes were investigated. Another derivative of the bqp ligand bearing a biphenyl group was also prepared and Ru(II) and Ir(III) complexes of the ligand were synthesised, exhibiting very promising photophysical properties. These complexes are used later (Chapter 5) as metallo-guests for photo-induced communication in solution and on surfaces.

4.2. Results and discussion

4.2.1. Synthesis of surface active bqp ligands and corresponding Ru(II) complex

In order to synthesise the surface active bqp derivative ligand, our initial strategy was based on the Suzuki-Miyaura cross coupling reaction following procedures which were previously developed by Buchwald[21] and Hammarström.[10]

Our first attempt was the synthesis of the non-substituted bqp ligand (**1**), reacting quinoline-8-boronic acid and 2,6-dibromopyridine, with Pd(dba)$_2$ and 2-dicyclohexylphosphino-2′,6′-dimethoxybiphenyl (**P′**) as catalysts in toluene at 110 °C, which gave the ligand **1** in a 79 % isolated yield (Scheme 4.1).[10] The compound was characterised by ^{1}H NMR spectroscopy (Figure A4.1) and mass spectrometry which were in agreement with previously published data.
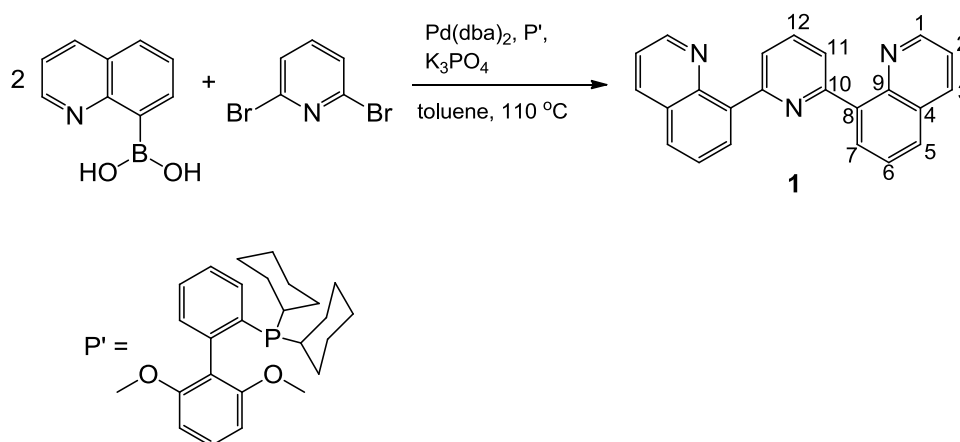
Scheme 4.1 Pd-Catalysed coupling of quinoline-8-boronic acid and 2,6-bromopyridine.

We attempted to prepare some other bqp derivatives through this strategy, however as quinoline-8-boronic acid is an expensive starting material, and owing to the fact that there is not a wide range of appropriate dihalopyridine derivatives which are commercially available, we switched to a one-step ring-forming process, generating the central pyridine ring in situ (Scheme 4.2). In this later method we also targeted the introduction of 4-aryl-substituents on the central pyridine ring since such substituents often have a profound effect on the photophysical properties of corresponding bisterpyridine Ru(II) complexes by increasing the quantum yield of the

luminescence,[9,22,23] and this is also a well-known strategy to increase the donor (D)-acceptor (A) distance in D-chromophore-A triads.[24]
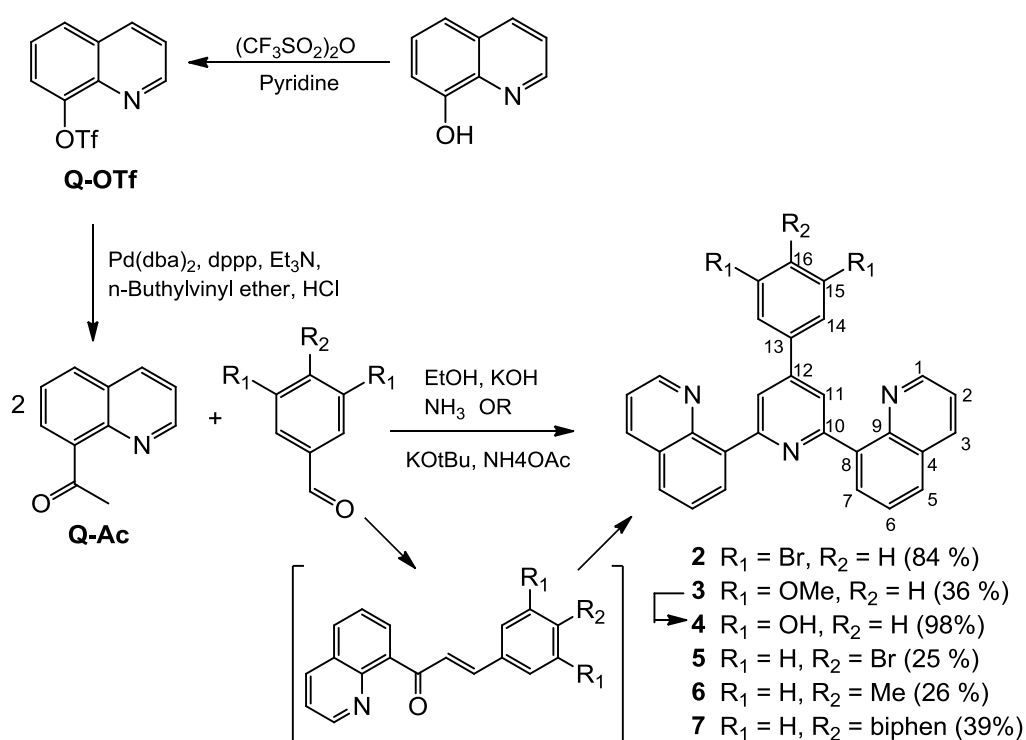
Scheme 4.2 Synthetic route for **synthesis of 4-aryl-substituted and 3,5- aryl-substituted bqp.**

Hanan and co-workers recently reported a simple one-step procedure for the preparation of a variety of 4′-aryl substituted tpy ligands.[17] Later, Johansson's group adopted the procedure to gain access to 4-aryl-substituted 2,6-bis-(quinolin-8-yl)pyridyl ligands.[13] We were also interested in the same procedure to synthesise a variety of different bqp ligands. In order to achieve this, we first prepared 8-acetylquinoline (**Q-Ac**). 8-acetylquinoline is not commercially available, and is synthesised in a two-step reaction as shown in scheme 4.2. The 8-triflate-quinoline

(**Q-OTf**) was prepared following a previously published procedure using 8-hydroxy-quinolone and trifluoromethane sulfonic anhydride $(CF_3SO_2)_2O$.[25] **Q-Ac** was synthesised by a palladium-catalysed Heck coupling reaction involving n-butyl vinyl ether as a partner with high yield.[26] Following the synthesis by ^1H NMR reveals a large shift of H_7 from 7.65 in **Q-OTf** to 7.86 in **Q-Ac** (Figure A4.2 and A4.4), confirming the formation of the **Q-Ac**. The routes of both compounds were also confirmed by mass spectrometry. ^1H NMR and ^{13}C NMR spectra were in agreement with the published data.

The reaction of 3,5-bromobenzaldehyde with two equivalents of **Q-Ac** in a basic aqueous ethanolic solution of ammonia at 40 °C afforded **2** (Scheme 4.2), which precipitated from solution after 18 hours. The desired compound has a very low solubility in acetone and can be purified by washing with cold acetone until it affords an off-white solid in high yield. The intermediate enone precipitates as a pale yellow solid during the reaction. **2** was fully characterised by ^1H NMR, ^{13}C NMR, mass spectrometry and FTIR spectroscopy, as well as two-dimensional NMR techniques including COSY and HSQC to allow a complete assignment of the peaks. In the ^1H NMR spectrum, the singlet peak at 8.20 ppm for H_{11} is very characteristic, indicating the formation of the pyridine ring. Additionally, the dramatic shift for H_7 from 7.65 ppm in **Q-Ac** to 8.25 ppm in the final ligand confirms the formation of desired compound (Figure 4.1). In the ^{13}C NMR spectrum, the peak at 123.6 ppm for C_{11} and the obvious shift of C_7 from 129.5 ppm in **Q-Ac** to 133.8 ppm in the ligand again confirms the ring formation (Figure A4.6). The electrospray mass spectrum of **2** shows signals at *m/z* 567.8 which corresponds to $[M+H]^+$, 589.8 for $[M+Na]^+$ and 605.8 for $[M+K]^+$.
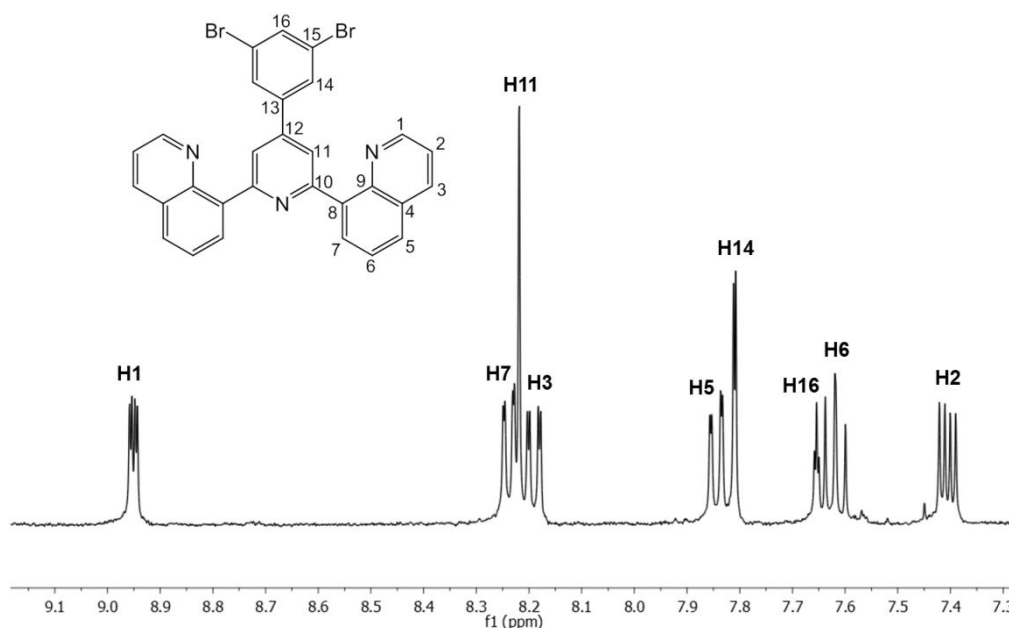
Figure 4.1 400 MHz ^{1}H NMR spectrum (CDCl$_3$) of 2.

In order to synthesise the surface active bqp ligand, Pd(0)-catalysed Sonogashira cross-coupling conditions were used. Initially, we examined a synthetic strategy which provides the direct attachment of **10** to **2** (Scheme 4.3). **10** was synthesised by peptide coupling conditions in the presence of 1-ethyl-3-(3-dimethylaminopropyl)-carbodiimide (EDC), N-ethylmorpholine (N-Em) and hydroxybenzotriazole (HOBt).

Dicyclohexylcarbodiimide (DCC) is commonly used to prepare amides. However, the by-product formed from DCC is nearly insoluble in most organic solvents and precipitates from the reaction mixture as the reaction progresses. Ethyl-(N',N'-dimethylamino)propylcarbodiimide hydrochloride (EDC) on the other hand produces by-products which are water soluble, allowing the by-product and any excess reagent to be removed easily by aqueous extraction.
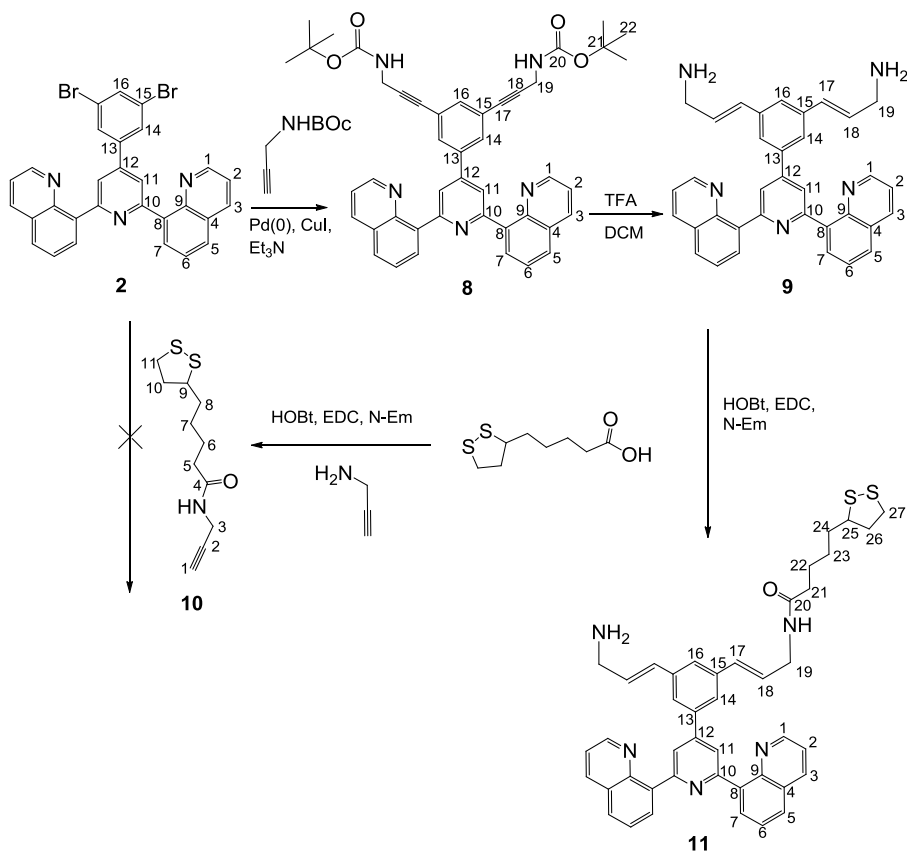
Scheme 4.3 Synthetic route for the dithiol substituted bqp ligand, 11.

10 was fully characterised by ^{1}H NMR, ^{13}C NMR and mass spectrometry. In the ^{1}H NMR spectrum, the down-field shift of H_3 from a singlet at 3.39 ppm in propargylamine to a doublet of doublets at 4.07 ppm confirms the amide coupling (Figure A4.8).

Although several attempts were made to directly attach the **10** to **2** by Sonogashira coupling, none of the results indicated product formation. This could be due to the sensitivity of the sulfur groups in the thioctic acid which prevent the coupling. The procedure was modified to first attach the protected propargylamine (N-Boc-propargylamine), using Pd(PPh$_3$)$_4$ and CuI in a mixture of triethylamine and DMF.

Similar reactions have been performed before for terpyridine ligands.[27,28] The desired product was isolated and purified by column chromatography on deactivated silica by Et$_3$N and EtOAc/ petroleum ether (4:5) mixture as eluent. Further down-field shift of H$_{19}$ to a doublet at 4.13 ppm indicates that the coupling was successful (Figure A4.10). The ligand **8** was also characterised by electrospray mass spectrometry showing signal at *m/z* 732.2 assigned to [M+NH$_4$]$^+$.

The removal of the protecting groups was achieved by treatment with trifluoroacetic acid (TFA) and DCM (50:50) mixture for 5 hours at room temperature. The deprotection process was followed by TLC and ^{1}H NMR spectroscopy. However, the careful analysis of the mass spectrum results revealed that the acetylene bonds are converted to vinylic groups. Different ratios of TFA/DCM were used but results were similar. **9** was characterised by electrospray mass spectrometry, ^{1}H NMR, ^{13}C NMR and FTIR spectroscopy. The removal of the protecting group is evidenced by the disappearance of the large singlet peak of the Boc group (H$_{22}$) at 1.47 ppm, and a shift for H$_{19}$ from a doublet at 4.13 ppm in the protected form to a singlet at 3.67 ppm in the free amine ligand, as well as a large up-field shift of protons in the amine group from 4.95 ppm in the Boc protected form (NH) to 2.09 ppm in the free amine (NH$_2$) (Figure A4.14). A shift for C$_{19}$ from 30.9 ppm to 32.1 ppm is also evident in the ^{13}C NMR spectrum (Figure A4.15).

The last step in the synthesis of the surface active bqp ligand involved the peptide coupling of **9** with thioctic acid, using conditions analogous to those described previously. The peptide coupling resulted in the substitution of only one amine group. This can be attributed to the short distance between the amine groups. The resulting ligand (**11**) showed characteristic peaks in the electrospray mass spectrum

corresponding to $[M+Na]^+$ (730.1) and $[M+K]^+$ (746.1). The ligand is also fully characterised by FTIR, ^1H and ^{13}C NMR spectroscopy. In the ^1H NMR spectrum, the formation of the ligand **11** is evidenced by the distinct areas of signals, one for the aromatic peaks arising from the bqp unit (integrating for 17 H) and the second one from the aliphatic peaks arising from the substituents attached at the 3,5-positions (integrating for 22 H) (Figure 4.2). The shift for H_{19} from a singlet at 3.67 ppm in **9** to a doublet at 4.20 ppm in the final ligand confirms the amide coupling. The amine protons are also largely shifted from 2.09 ppm to 6.75 ppm. In the ^{13}C NMR spectrum two peaks for C_{19} are observed. One is attributed to the substituted leg which is shifted from 32.1 ppm in the free amine ligand to 36.5 ppm, and another which remains unchanged confirming the substitution of just one of the positions. In the aliphatic region, the characteristic signals of the thioctic acid are clear by ^1H NMR. In the FTIR spectrum, a strong signal of carbonyl stretching at 1655 cm^{-1} is also observed.
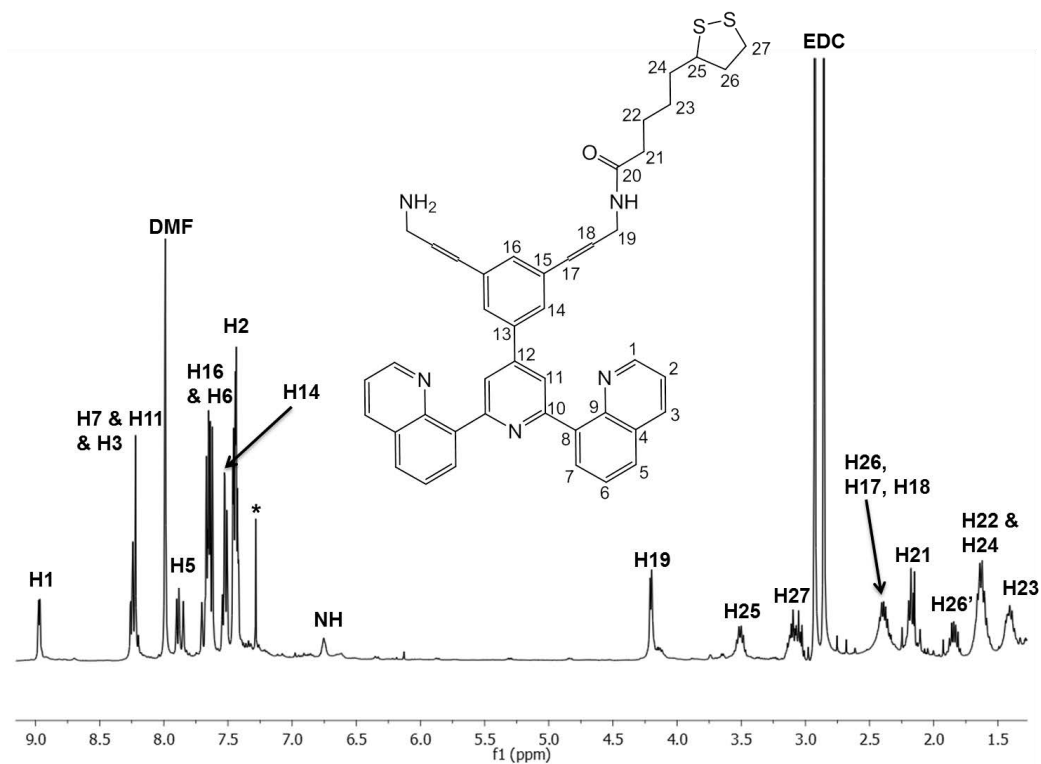
Figure 4.2 400 MHz ^{1}H NMR spectrum (CDCl$_3$) of 11.
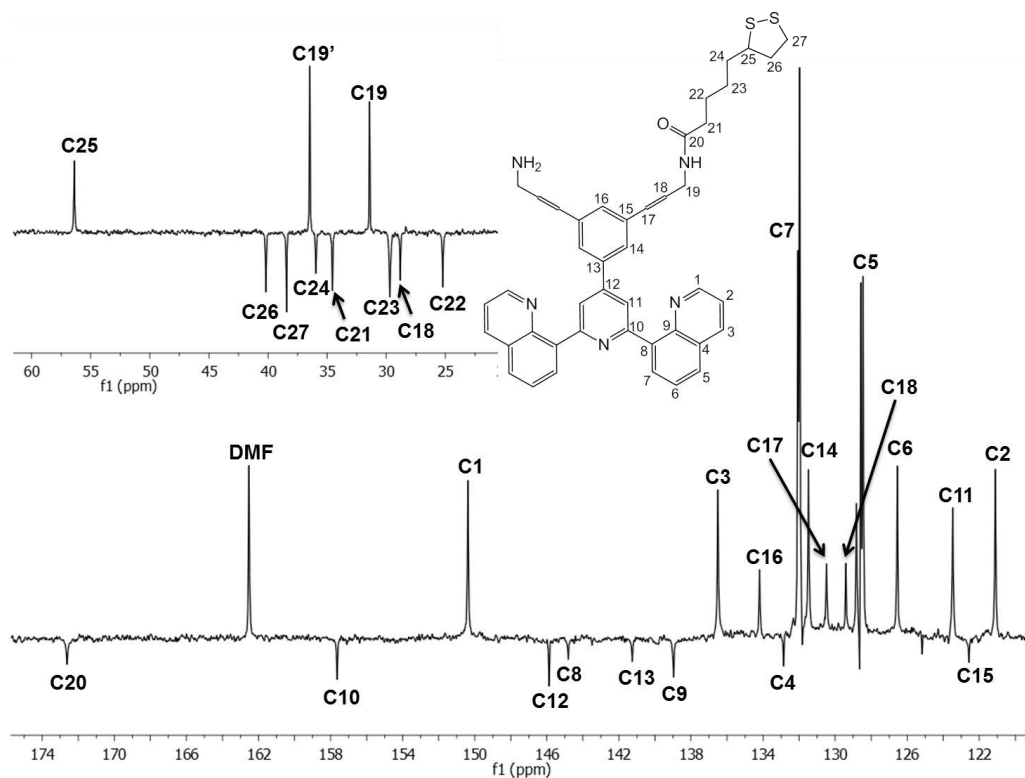
Figure 4.3 400 MHz ^{13}C NMR spectrum (CDCl$_3$) of 11.

Another strategy for the synthesis of a surface active bqp ligand has been introduced in scheme 4.4. In this method we use a the Williamson-ether approach, instead of the Pd(0) catalysed Sonogashira coupling, to attach the substituents to the bqp unit. In order to achieve this, **3** was synthesised by the procedure shown in scheme 4.2. The one step ring formation reaction resulted in the intermediate enone as a pale yellow solid only. The intermediate was isolated and the mass spectrum showed the expected peak at *m/z* 342.1 [M+Na]$^+$ and 661.1 [2M+Na]$^+$. The second peak in mass spectrum shows that the intermediates combine together, most likely causing the failure of the ring formation. The ^{1}H NMR signals from the vinylic protons are at 7.8 ppm. In order to decrease the conjugation of the intermediates, the reaction was repeated in more dilute and basic conditions. These conditions also resulted in a failure to isolate the expected product. Thus harsher conditions including higher temperature and longer reaction time were employed to attempt to form the ring system.

Constable and co-workers reported similar derivatives of tpy ligand bearing methoxy groups in 3,5-positions of the phenyl ring, formed through the ring formation mechanism, followed by an ether cleavage to afford hydroxyl moieties in the 3,5-positions.[29,30] We adopted this synthetic route to prepare **3** and the subsequently **4**. By this method, the reaction of 8-acetylquinoline with 3,5-dimethoxybenzaldehyde proceeded smoothly in a sequential one-pot process involving treatment with KOtBu in THF followed by ammonium acetate to give 36% yield of the dimethoxy compound (**3**).

3 was fully characterised by ^{1}H NMR, ^{13}C NMR, mass spectrometry and FTIR spectroscopy, as well as two-dimensional NMR techniques including COSY and

HSQC to allow full assignment of the peaks. The electrospray mass spectrum of **3** shows a signal at *m/z* 470.1 which corresponds to $[M+H]^+$. In the ^{1}H NMR spectrum, the ring formation is evidenced by the characteristic singlet peak of H_{11} at 8.30 ppm. Additionally, the down-field shift of H_7 from 7.65 ppm in **Q-Ac** to 8.31 ppm in the final ligand confirms the formation of desired compound (Figure 4.4). In the ^{13}C NMR spectrum, the peak at 123.9 ppm for C_{11} and the shift of C_7 from 129.5 ppm in **Q-Ac** to 131.5 ppm in the ligand again confirms the ring formation (Figure A4.18).
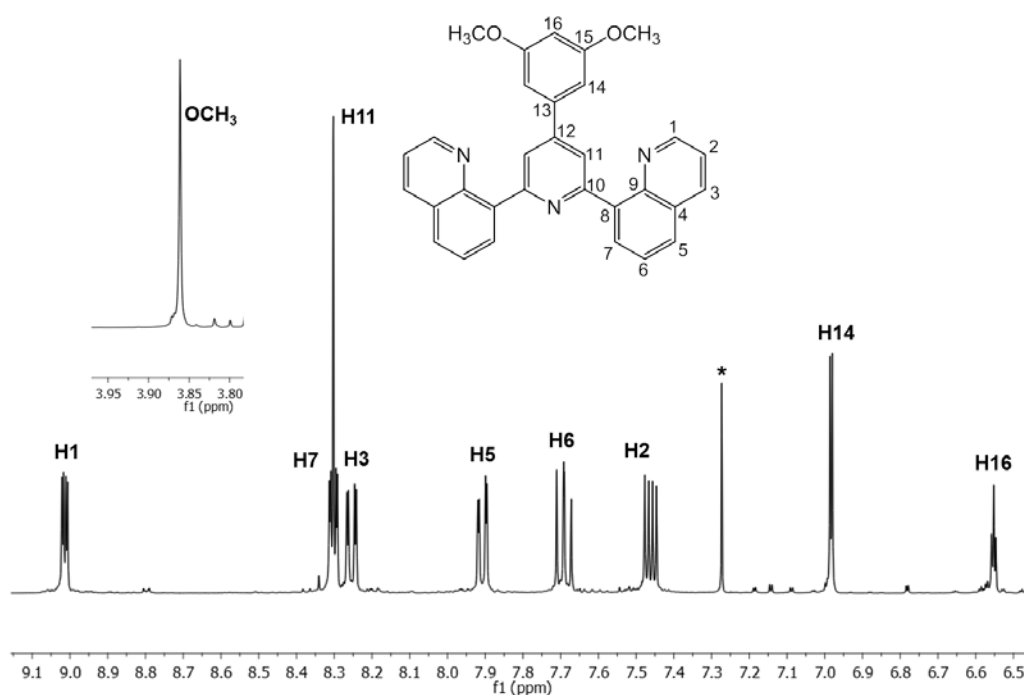
Figure 4.4 400 MHz ^{1}H NMR spectrum (CDCl₃) of 3.
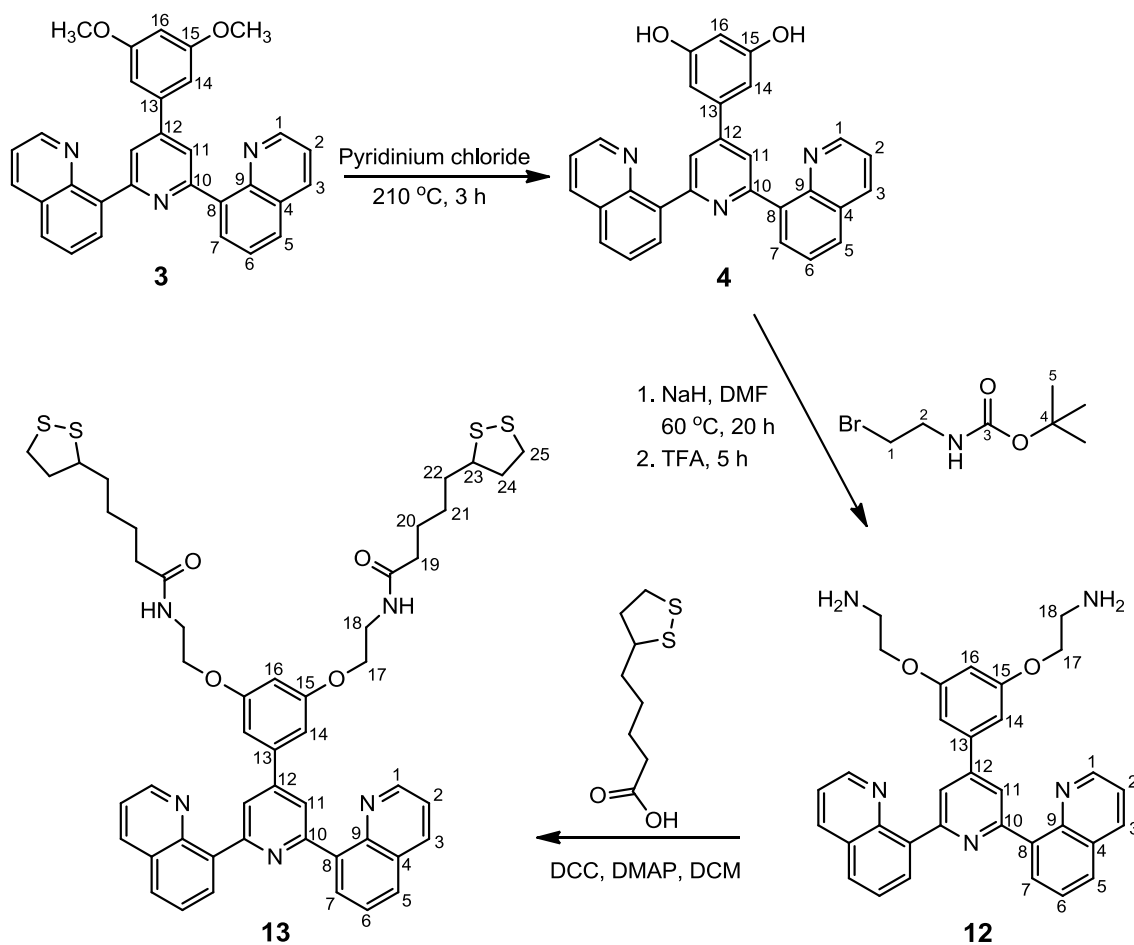
Scheme 4.4 Synthetic route for the bis-dithiol substituted bqp ligand, 13.

Deprotection by heating with pyridinium chloride afforded the ligand **4** in quantitative yield (Scheme 4.4). A similar procedure was previously used for ether cleavage of terpyridine and bipyridine ligands.[29-32] The ^{1}H NMR spectrum of **4** shows a typical pattern in the aromatic region for a bqp unit substituted at the 3,5-positions of the phenyl rings, with a broad peak indicative of hydroxy protons at 9.75 ppm (Figure 4.5). The peaks at 3.86 ppm for protons in the methoxy groups are also removed. The formation of **4** was also confirmed by electrospray mass spectrometry showing a peak corresponding to [M+H]$^+$ (442.1).
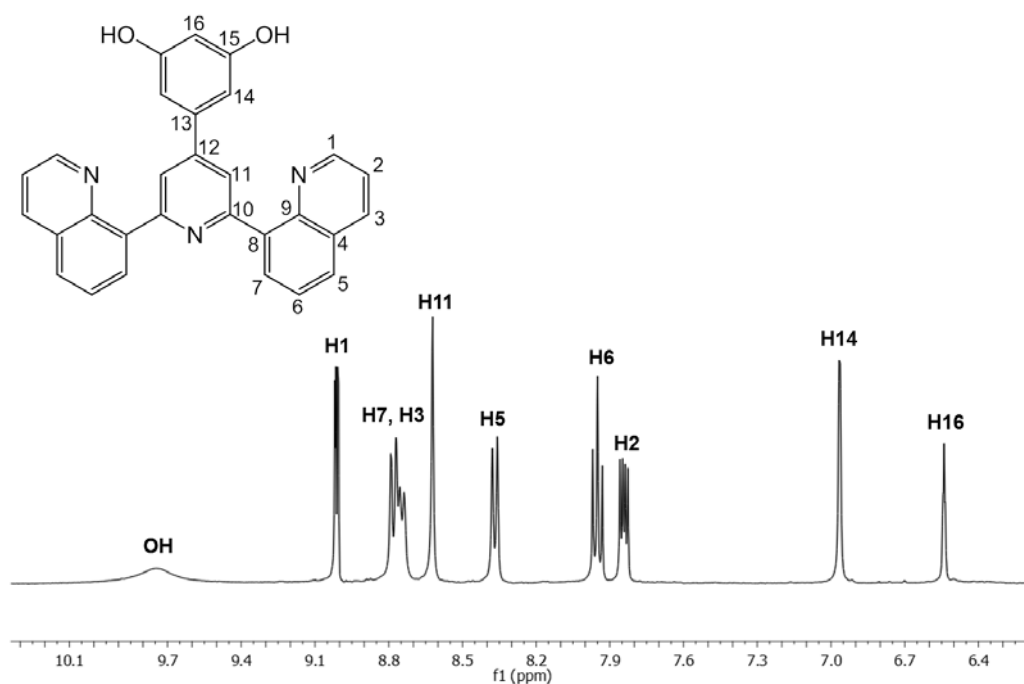
Figure 4.5 400 MHz ¹H NMR spectrum (CDCl₃) of 4.

Williamson ether conditions were employed using sodium hydride as a base with the Boc protecting group removed in situ to afford **12** in a 20 % yield (Scheme 4.4). The ligand showed a characteristic peak in the electrospray mass spectrum at *m/z* 566.0 corresponding to [M+K]$^+$ and a peak at *m/z* 527.9 corresponding to [M+H]$^+$ in the TOF-MALDI mass spectrum. The NH$_2$ protons in the ¹H NMR appear at 1.75 ppm, which confirms the success of deprotection process (the NH proton in Br(CH$_2$)$_2$NHBOc is at 5.08 ppm). Also, the signals of H$_{17}$ and H$_{18}$ are shifted in comparison with the corresponding resonances in Br(CH$_2$)$_2$NHBOc which further confirms the formation of the product (Figure A4.22).

The final step in the synthesis was achieved by functionalising the above-mentioned **12** by reaction with thioctic acid, utilizing the EDC method to afford **13** in a 25 %

yield. The pure product was obtained following column chromatography on silica with 1% MeOH in DCM (v/v) as eluent. Similar reactions have been performed previously for terpyridine ligands where DCC and DMAP are used as coupling reagents.[33] Using the modified preparation with EDC as a coupling regent, the peptide coupling resulted in substitution at both amine groups. The resulting **13** ligand was characterised by electrospray mass spectrometry, with a characteristic peak at *m/z* 899.5 corresponding to $[M]^+$. The ligand was also been also characterised by ^{1}H NMR spectroscopy. In the ^{1}H NMR spectrum, the signature of the **13** ligand is evidenced by two distinct areas of signals, with aromatic peaks arising from the bqp unit (integrating for 17 H), and the aliphatic peaks arising from the two 'substituents' attached at the 3,5-positions (integrating for 34 H) (Figure 4.6). The amine protons are shifted from 1.75 ppm in **12** to 5.50 ppm in the final ligand. Both signals assigned to H_{17} and H_{18} are shifted down-field when the peptide has formed. In the aliphatic region, the characteristic signals of the thioctic acid are also evident.
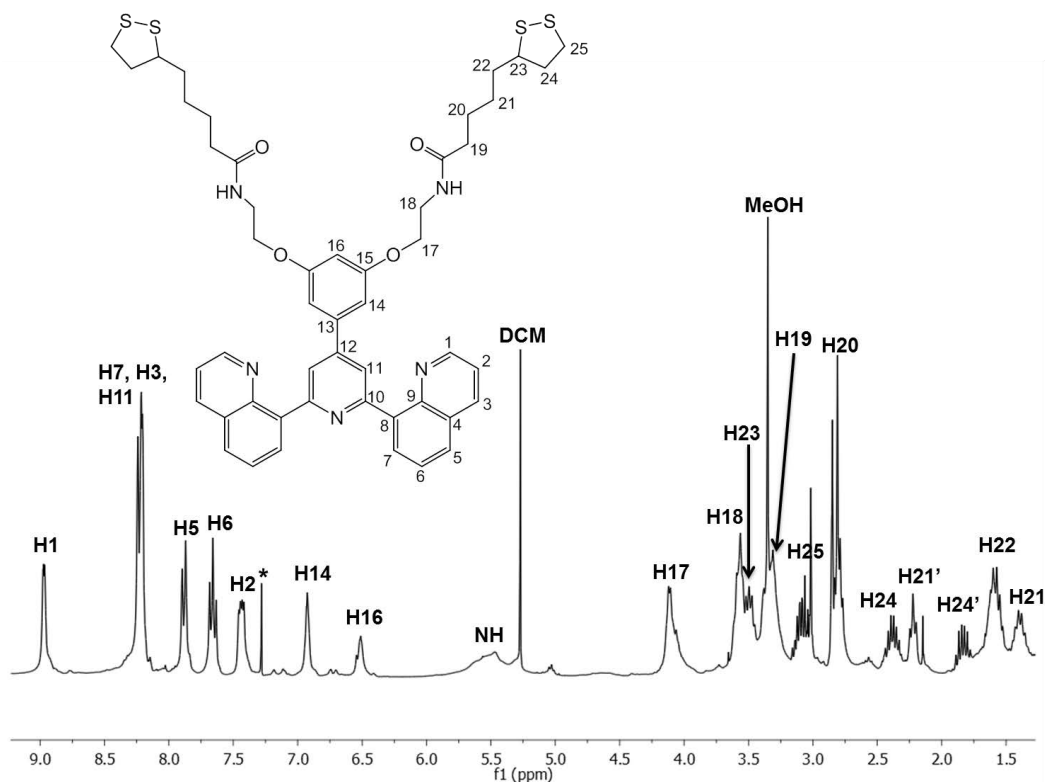
Figure 4.6 300 MHz ^{1}H NMR spectrum (CDCl$_3$) of 13.

The synthesis of the surface active bqp-based ruthenium(II) complex (Scheme 4.5) was performed using a stepwise procedure.
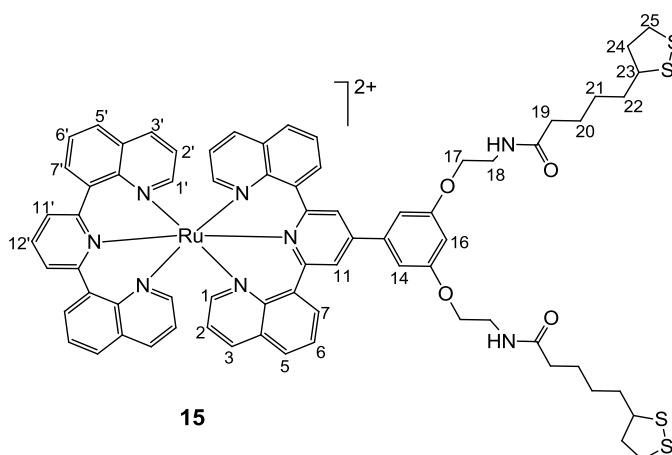
Scheme 4.5 structure the surface active bqp-based ruthenium(II) complex, 15.

In the first step, Ru(**1**)Cl$_3$ was prepared by heating RuCl$_3$. 3H$_2$O and one equivalent of bqp ligand in a sealed tube for 24 h under microwave conditions. Ru(**1**)Cl$_3$ was characterised by electrospray mass spectrometry, showing peaks at *m/z* 505.0 assigned for [Ru(**1**)Cl$_2$]$^+$, 539.0 for [M]$^+$ and 562.9 corresponding to [M+Na]$^+$. Further reflux of Ru(**1**)Cl$_3$ and **13** in EtOH, with a few drops of N-ethylmorpholine (NMP) in the microwave resulted in the desired Ru(II) complex, which was isolated as the PF$_6^-$ salt. **15** was initially identified by mass spectrometry showing a characteristic signal at 669.4 corresponding to {M-2[PF$_6$]}$^{2+}$. The complex was further characterised by ^{1}H NMR (Figure A4.23), FTIR, UV-Vis and emission spectroscopy.

We were also interested in attaching the cyclodextrin unit to the bqp ligand (Scheme 4.6).
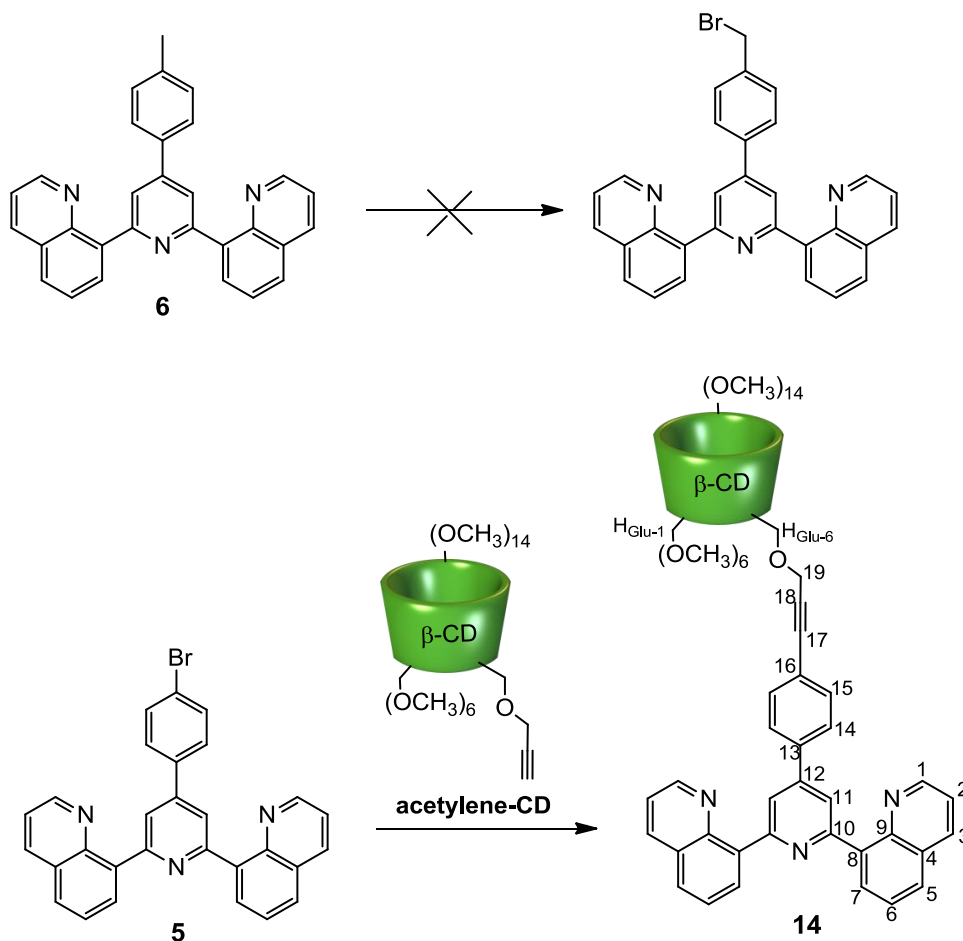
Scheme 4.6 Synthetic route for the cyclodextrin substituted bqp ligand, 14.

To achieve this, we initially attempted the synthesis of **6** as described in scheme 4.2.[13] The analogous reaction using 4-methylbenzaldehyde and **Q-Ac** led to a 26 % isolated yield of **6**. The reaction was optimised by increasing the temperature to 60 °C and also by the addition of CHCl$_3$ to improve the solubility of the intermediate enone. However, careful analysis of the reaction mixture revealed a mixture of two cyclized products, the desired 2,6-bis(quinolin-8-yl)-4-(p-tolyl)pyridyl ligand and the isomer 2,4-bis(quinolin-8-yl)-6-(p-tolyl)pyridine, as well as some unreacted intermediates. The purification of the desired product by column chromatography was

unsuccessful. It was later found that all the impurities, including the undesired isomer, precipitate at a pH of around 5. Utilising this observation, purification was achieved by dissolving the crude mixture in acetic acid and adjusting the pH with an aqueous ammonia solution to pH = 5, up on which all the impurities precipitated as a brown sticky solid. The solution was separated and the pH was brought to 7 to precipitate the product. The compound **6** was fully characterised by ^{1}H NMR, ^{13}C NMR, mass spectrometry and FTIR spectroscopy. Two-dimensional NMR techniques including COSY and HSQC were employed to obtain complete assignment of the peaks. The aromatic region of the ^{1}H NMR spectrum contains signals that are assigned to the different protons by their characteristic multiplicities. The peak at 8.30 ppm for H_{11} and the shift for H_7 from 7.65 ppm in **Q-Ac** to 8.28 ppm confirms the ring formation and the formation of the desired isomer (Figure A4.24). The electrospray mass spectrum of **6** shows two signals, the first at *m/z* 424.1 which corresponds to [M+H]$^+$, and the second one at 446.1 for [M+Na]$^+$.

Bromination of 4-Me-tpy has been previously reported by refluxing in CCl$_4$, using N-bromosuccinimide (NBS) and dibenzoyl peroxide.[34-37] A similar reaction based on these findings was attempted to brominate **6**, but the purification of the crude product with careful chromatography was unsuccessful.

5[13] was synthesised following the reaction described in scheme 4.2, reaction of 4-bromobenzaldehyde with two equivalents of **Q-Ac** in a basic aqueous ethanolic solution of ammonia to afford **5** in a 25 % isolated yield. The electrospray mass spectrum of **5** shows a signal at *m/z* 487.9 which corresponds to [M+H]$^+$. The ^{1}H NMR (Figure A4.28) and ^{13}C NMR (Figure A4.29) spectra are in agreement with published data.

Sonogashira coupling conditions were used to attach the acetylene-cyclodextrin (Chapter 6) to **5**, using Pd(PPh$_3$), CuI and Et$_3$N in DMF. Purification of the product was achieved by size exclusion column chromatography using biobeads SX3 and DCM as the eluent. In the ^{1}H NMR spectrum (Figure 4.7), the aromatic region shows the expected signals for bqp unit. The anomeric protons on the cyclodextrin appear as the multiplet at 5.00-5.23 ppm, with the overlap arising from the non-equivalence of the glucose units in the asymmetrically substituted cyclodextrin. The change in signal pattern from the starting material also confirms that the cyclodextrin has been substituted. The remainder of the cyclodextrin protons appear in the multiplet between 3.01 and 4.01 ppm. The doublet of doublets at 4.07 ppm corresponds to the diastereotopic proton of the 6-position in one of the sugar units in the cyclodextrin. From the ^{1}H NMR spectrum there is still some unreacted acetylene-cyclodextrin present in the product.
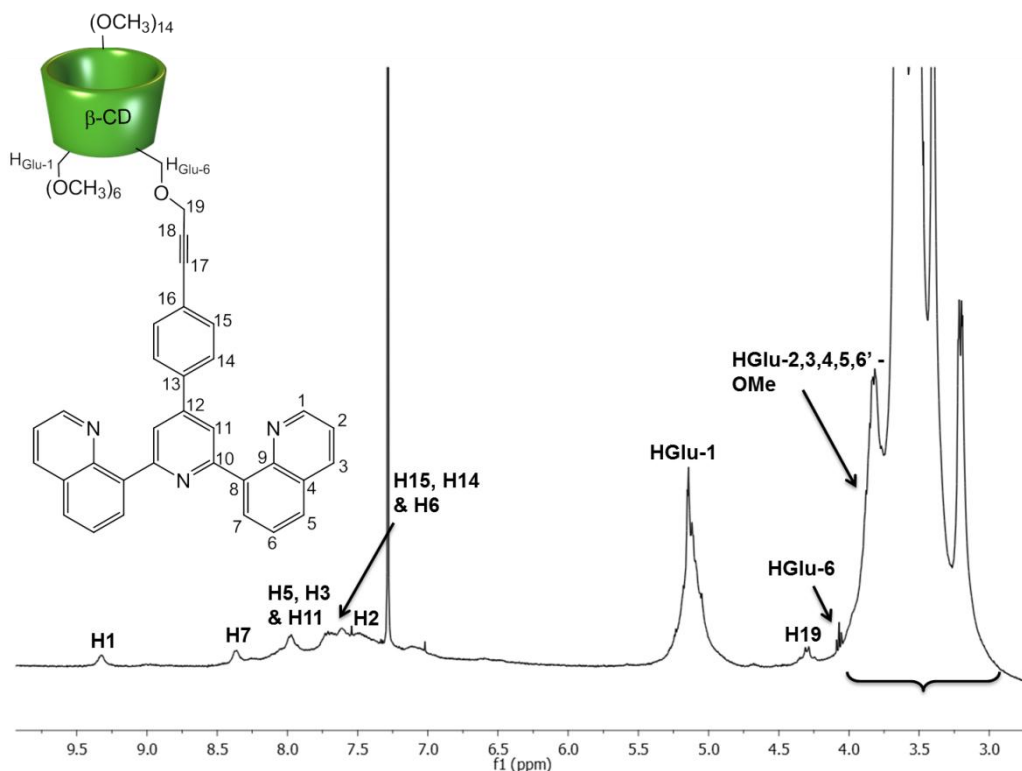
Figure 4.7 300 MHz ^{1}H NMR spectrum (CDCl$_3$) of 14.

4.2.2. Synthesis of biphenyl substituted bqp ligand and corresponding Ru(II) and Ir(III) complexes

The bqp derivative bearing a biphenyl moiety, **7**, was synthesised to act as guest as shown in scheme 4.7. The reaction was performed using two equivalents of **Q-Ac** with 4-biphenylcarboxaldehyde in the presence of KOtBu and NH$_4$OAc. Synthesis of an analogous terpyridine ligand has been reported previously in our group.[38]
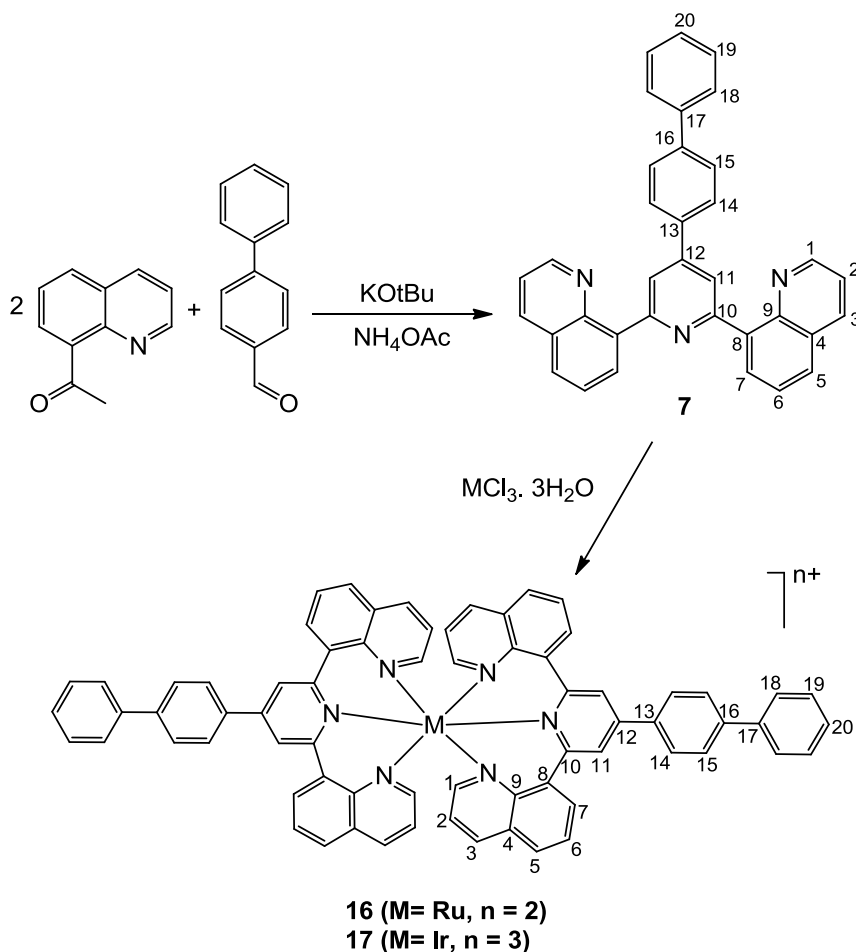
Scheme 4.7 Synthetic route for 16 and 17 complexes.

The ligand was purified by dissolving in acetic acid, followed by adjusting pH to 5 with NH$_4$OH upon which the enone intermediates and other impurities precipitated out. Separation of the solution at this pH and neutralising with further ammonia solution resulted in the isolation of the pure ligand. **7** was characterised by ^{1}H, ^{13}C, HSQC and COSY NMR spctroscopy, as well as mass spectrometry. Evidence of the central pyridine ring formation is confirmed by a singlet peak at 8.41 ppm assigned to H$_{11}$ in the ^{1}H NMR spectrum (Figure 4.8). The shift of H$_7$ from 7.65 ppm in **Q-Ac** to 8.33 also indicates the final product. In the ^{13}C NMR spectrum (Figure 4.9), the C$_{11}$ peak is

observed at 123.7 ppm. Electrospray mass spectrometry showed two peaks at *m/z* 486.2 and 508.2 which were assigned to [M+H]$^+$ and [M+Na]$^+$ respectively.
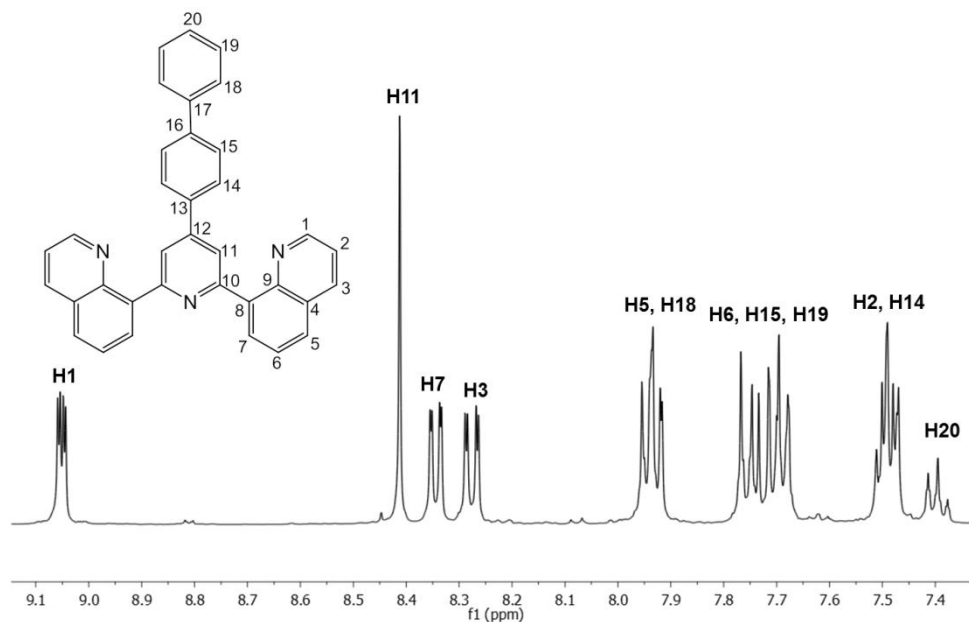
Figure 4.8 400 MHz ^{1}H NMR spectrum (CDCl$_3$) of 7.
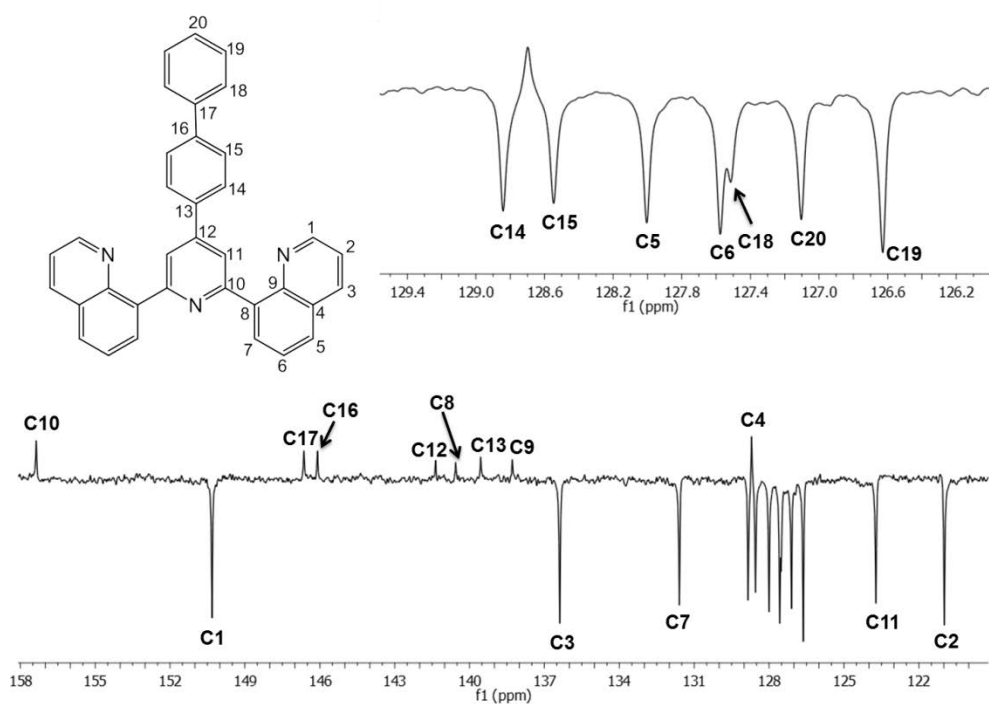
Figure 4.9 100 MHz ^{13}C NMR spectrum (CDCl$_3$) of 7.

The ruthenium (II) complex **16** was prepared via a two-step reaction. The first step involved the reaction of $RuCl_3 \cdot 3H_2O$ and one equivalent of **7** in refluxing EtOH to afford $Ru(7)Cl_3$. The second step involved the addition of $Ru(7)Cl_3$ and **7** with N-ethylmorpholine as a reductant in refluxing EtOH under microwave conditions. The complex was isolated as the hexafluorophosphate salt. The product was confirmed by its characteristic mass spectrum, which shows a peak at *m/z* 536.2 corresponding to $\{M-2[PF_6]\}^{2+}$. The complex was also identified by ^1H and ^{13}C NMR spectroscopy. In the ^1H NMR spectrum, the peaks of some of the aromatic protons are merged and are observed as a multiplet (Figure 4.10).
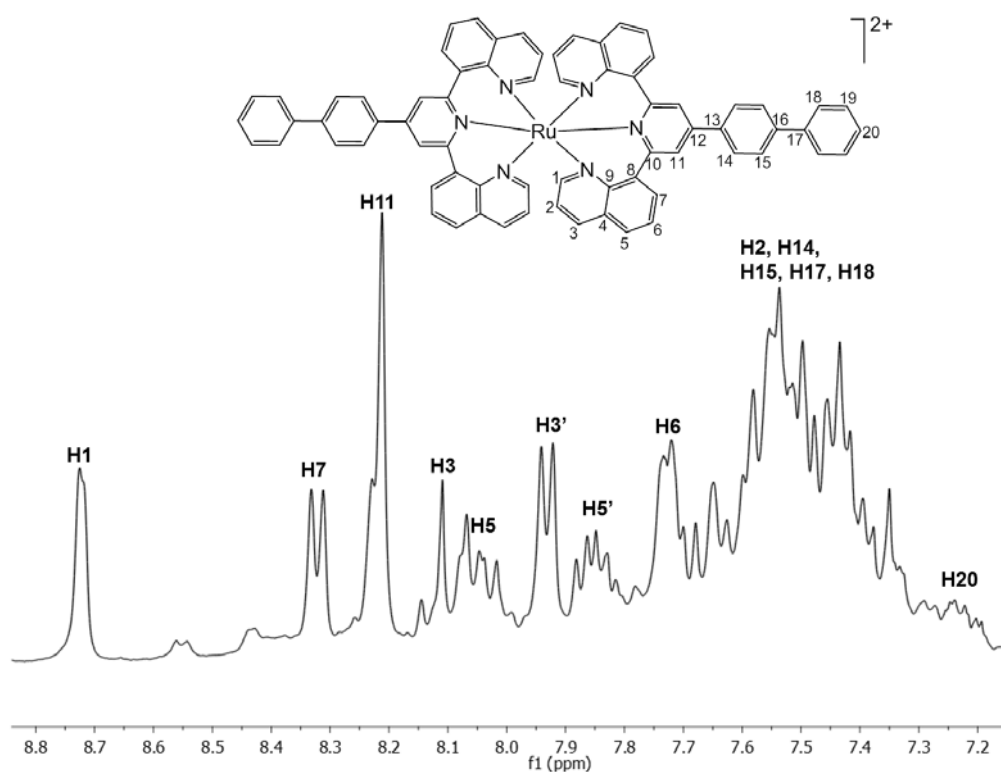
Figure 4.10 300 MHz ^1H NMR spectrum (CDCl$_3$) of 16.

The iridium complex **17** was also synthesised using microwave conditions. In order to achieve **17**, a reaction was carried out for 1 hour at 250 ^{o}C in a sealed tube charged with IrCl$_3$. 3H$_2$O, two equivalents of **7**, ethylene glycol and a few drops of NMP and the final complex was separated as the PF$_6^-$ salt. The ^{1}H NMR spectrum of the complex shows a very broad multiplet in the aromatic region arising from the aromatic protons in the **7** ligands. The TLC showed only one spot confirming the purity of the compound. The electrospray mass spectrum indicates a characteristic signal at *m/z* 652.3 corresponding to {M-2[PF$_6$]}$^{2+}$.

4.2.3. Self-assembled monolayer of 15 on planar gold surfaces

The self-assembled monolayer of **15** has been investigated on planar gold surfaces (Scheme 4.8). Ellipsometry was used to measure the thickness of the monolayers on the gold surface and XPS spectroscopy has also been used in order to characterise the attached complex on the surface.

In all above experiments, polycrystalline gold with 30 nm thickness on 0.01 inch-silicon wafer, pre-coated with titanium (rms-roughness < 1 nm) was used, which was cleaned by UVO (UV-Ozone) for 1 hour before use.

We discussed in chapter 3 that the thickness of the metal monolayers reached saturation after around 24 hours deposition time. As a result, the thickness of the monolayer was measured to be 1.90 ± 0.10 nm after 24 hours of deposition to the

gold substrate in 1 mM acetonitrile solution of the metal complex, which is very close to the calculated length of the molecule (2.54 nm) by Chem3D modelling.
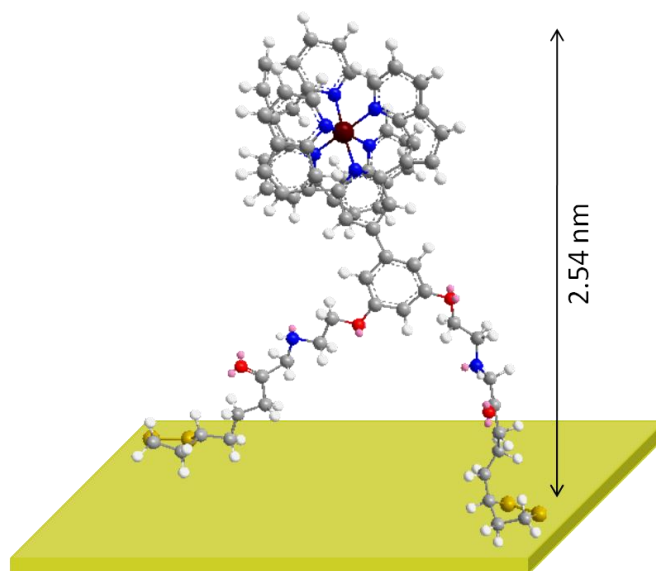
Scheme 4.8 Schematic representation of self-assembled monolayer of 15.

The XPS spectra (wide spectrum and the C1s + Ru 3d region) of the **15** film has been shown in Figure 4.11. The spectra show the presence of carbon, sulfur, nitrogen, ruthenium and oxygen in addition to the underlying gold substrate.
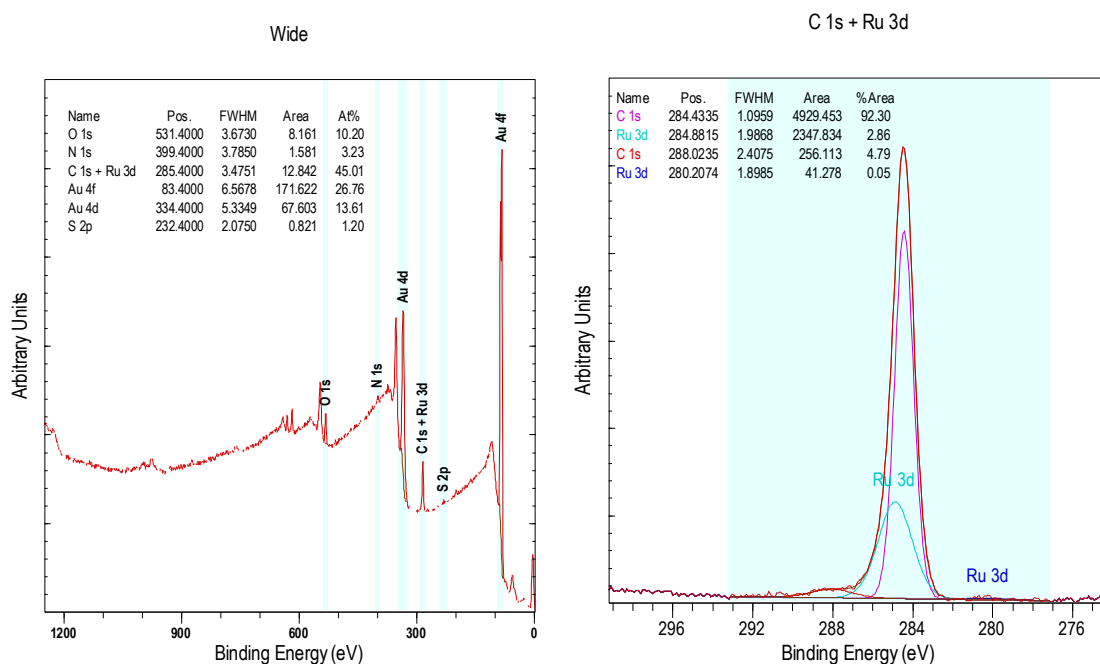
Figure 4.11 A) Full XPS spectrum of 15 monolayer on planar gold surface, B) The narrow scan spectra of the C 1s, Ru 3d region.

The Ru 3d peaks are close to the binding energy of C 1s peaks, and are masked by the C 1s signals of heteroaromatic rings. However, the Ru 3d$_{5/2}$ peak is observed as a broad shoulder on the low binding energy side of the spectrum at 280.21 eV. The 3d$_{3/2}$ orbital of metallic ruthenium is assigned at 284.88 eV referenced to Au 4f$_{7/2}$ at 83.9 eV with full widths at half-maximum (fwhm) of 4.1 eV.[39,40] In addition to the N1s signal at 399.24 eV the C1s and O1s peaks are also observed at 284.43 and 532.40 eV respectively, which provides strong evidence for the presence of heteroaromatic molecules on the surface. Finally, the C:N:Ru peak area ratios (after peak-fitting and adjustment with the atomic sensitivity factors) were in good agreement with the theoretical ratios predicted by the molecular structure.

4.2.4. Photophysical properties of 15

Ru(II) terpyridine complexes have well known photophysical properties. In general, the UV-Vis spectra of Ru(II) terpyridine complexes exhibit low wavelength ligand-centred bands arising from π-π^* and n-π^* transitions, with the spin-allowed ^{1}MLCT in the visible region. Similarly, $[Ru(bqp)_2]^{2+}$ complexes display a broad absorption band between 400 and 600 nm, attributed to the lowest ^{1}MLCT transitions. π-π^* transitions are observed in the UV region, with a strong band around 230 nm, and somewhat weaker ones around 270-280 nm and 315-360 nm.[10,19]

The photophysical properties of **15** were investigated both in solution and as a powder. An acetonitrile solution of the complex demonstrated absorption spectra typical of ruthenium Ru(II) bqp complexes, with the visible region dominated by a broad band around 490 nm and a shoulder at 580 nm, assigned to the ^{1}MLCT transition, as well as a strong band in the UV region around 300 nm (Figure 4.12). The powder absorption spectrum shows a similar pattern with a 5 nm red shift for the ^{1}MLCT band and further red shifts for the ligand centred peaks compared to what was observed in solution. In addition, the shoulders are much more distinct in the powder absorption spectrum.
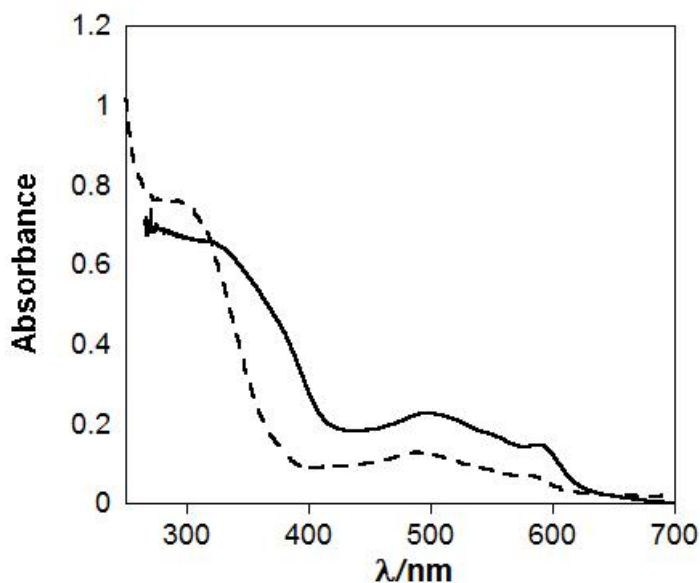
Figure 4.12 Absorption spectra of 15 in acetonitrile (dashed line) and powder (solid line).

Hammarström and co-workers reported that the optimised geometry of $[Ru(bqp)_2]^{2+}$ complexes suggests a more octahedral coordination than is observed in $[Ru(tpy)_2]^{2+}$, with N1-Ru-N3 bite angles of 179.6°,[10] as compared to the experimental value of 158.4° in $[Ru(tpy)_2]^{2+}$.[41] As a result of the larger bite angle of the bqp ligands, the geometry around the ruthenium center is very close to octahedral, and so in sharp contrast to $[Ru(tpy)_2]^{2+}$ complexes, these compounds show strong emission at room temperature, with a maximum at 700 nm.[19] Improved emission quantum yields and long excited-state lifetimes have been reported for this series of complexes. The excited-state lifetime of $[Ru(bqp)_2]^{2+}$ was reported to be 3.0 µs which is one of the longest [3]MLCT lifetimes at room temperature reported for any ruthenium(II) polypyridyl complex.[10] Even longer lifetimes were reported for Ru(II) complexes bearing substituted bqp ligands.[19]

Acetonitrile solutions of **15** display red luminescence from the ^{3}MLCT band, centred at 690 nm, upon excitation at 490 nm (Figure 4.13). The excitation spectrum closely matches the absorption spectrum of the complex. Surprisingly, the quantum yield of the ruthenium complex was very low ($\varphi_{aerated}$ = 6.5 × 10^{-2} %). This is speculated to be a result of the extra phenyl group at the 4-position of the central pyridine ring in the bqp ligand, and vibrations caused by the substituents in 3,5-position of the phenyl ring. However, the excited-state lifetime of the complex ($\tau_{aerated}$ = 329 ns) is higher than tris-bipyridine ruthenium complexes. The powder emission is much stronger, with the maximum at 700 nm. This is likely due to decreasing vibrational effects of the substituents and lack of movement in the powder sample. The powder also presents a relatively long excited-state lifetime of τ = 445 ns. The emission of the monolayer of **15** is very weak and thus cannot be recorded.
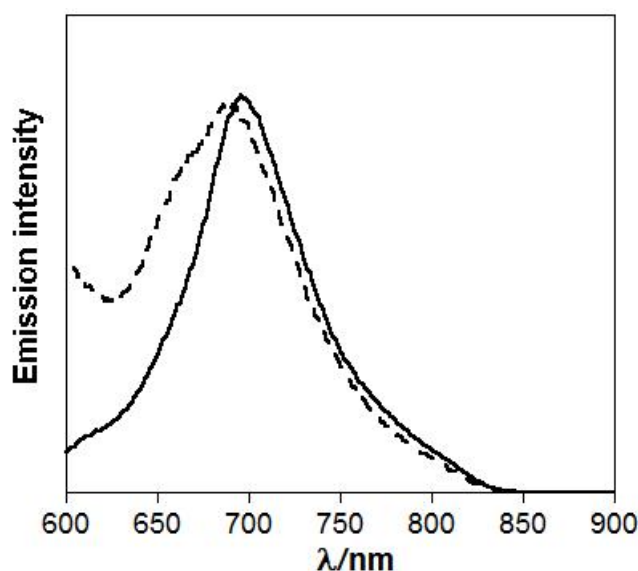
Figure 4.13 Emission spectra of 15 in acetonitrile (dashed line) and as a powder (solid line), λ_{exc} = 490 nm.

The photophysical properties of the ruthenium complex are summarised in Table 4.1.

Table 4.1 Photopysical properties of the surface active Ru^{II} complex (15).

	$[Ru(bqp)_2]^{2+}$	15
λ_{max} (^{1}MLCT) nm, Solution	491 [10,19]	490
λ_{max} (^{1}MLCT) nm, Powder		495
λ_{max} (^{3}MLCT) nm, Solution	700 [10]	690
φ (^{3}MLCT), aerated		6.5×10^{-4}
φ (^{3}MLCT), deaerated	2.0×10^{-2} [10]	
τ (^{3}MLCT), aerated		329 ns
τ(^{3}MLCT), deaerated	3 μs [10]	
λ_{max} (^{3}MLCT) nm, Powder		700
τ (^{3}MLCT) ns, Powder		445 ns

4.2.5. Photophysical properties of 16 and 17

Complexes **16** and **17** have been used as metallo-guests for cyclodextrins in chapter 5. The photophysical properties of these complexes have been investigated in acetonitrile solutions and as powders. The UV-Vis spectrum of **16** in acetonitrile shows characteristic $[Ru(bqp)_2]^{2+}$ peaks (Figure 4.14). In the high-energy region, strong absorption bands from ligand based $\pi{-}\pi^*$ transitions dominate (210, 298 nm)

with the ^{1}MLCT found at 495 nm. The absorption bands of the powder sample are red-shifted and presented at 310, 500 nm with a shoulder at 600 nm attributed to $\pi-\pi^*$ transitions and the ^{1}MLCT absorption.
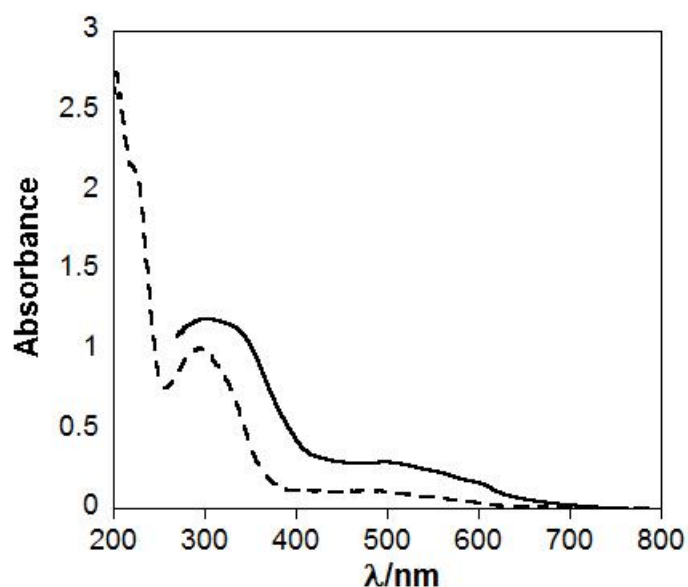
Figure 4.14 Absorption spectra of 16 in acetonitrile (dashed line) and powder (solid line).

Excitation of the complex in acetonitrile at room temperature at 495 nm led to luminescence at 700 nm (Figure 4.15), with a quantum yield of $\varphi_{aerated}$ = 4.7 × 10^{-2} % and $\varphi_{deaerated}$ = 0.2 %. Excited state lifetimes of $\tau_{aerated}$ = 246 ns and $\tau_{deaerated}$ = 1.4 µs were observed. The huge difference between the aerated and deaerated lifetimes indicates that the ^{3}MLCT is strongly quenched by oxygen. The emission spectrum of the powder sample is largely blue-shifted and is observed at 640 nm (τ = 201 ns).
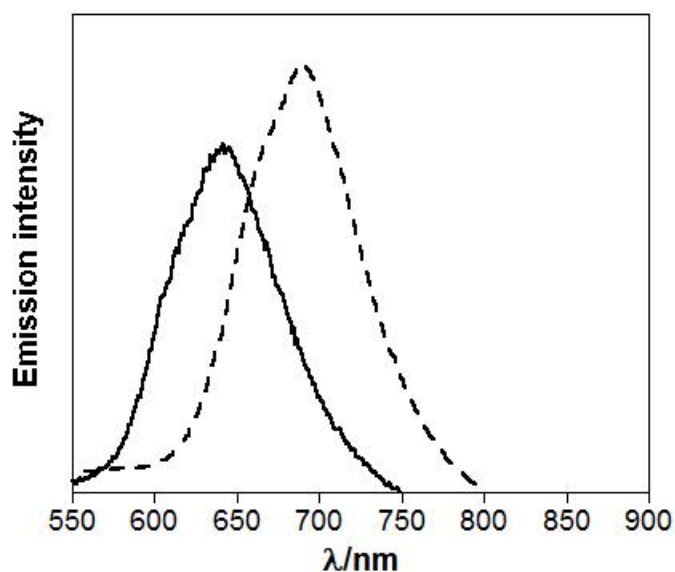
Figure 4.15 Emission spectra of 16 in acetonitrile solution (dashed line) and as a powder (solid line), λ_{exc} = 495 nm.

The UV-Vis absorption spectrum of **17** was recorded in acetonitrile and contains a strong π-π^* absorption band at 230 nm as well as a charge transfer band at λ = 340 nm. The nature of this charge transfer band has been disputed for Ir(III) complexes in the literature and it is believed that it is a metal to ligand charge transfer band (MLCT) with a strong ligand-centred character (Figure 4.16). Similar to what was observed for the ruthenium complex, the peak at 340 nm is red-shifted by 5 nm in the powder absorption spectrum.
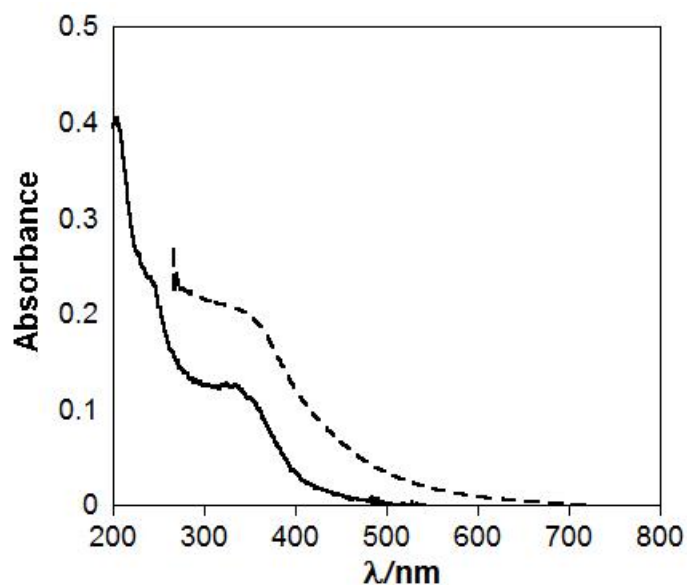
Figure 4.16 Absorption spectra of 17 in acetonitrile solution (dashed line) and powder (solid line).

The Ir(III) complex **17** was highly luminescent at 560 nm when excited at 370 nm in acetonitrile solution, with a quantum yield of $\varphi_{aerated}$ = 0.8 % and $\varphi_{deaerated}$ = 2.8 % (Figure 4.17). **17** displays a long excited state lifetime of $\tau_{aerated}$ = 4 μs and $\tau_{deaerated}$ = 16 μs. The huge difference between aerated and deaerated lifetimes indicates that the ^{3}MLCT is strongly quenched by oxygen. The lifetime of **17** is much higher than similar iridium(III)-terpyridine compounds.[42,43] The powder spectrum displays an unexpected red-shift for the emission maximum and emits at 620 nm (τ = 2.1 μs).
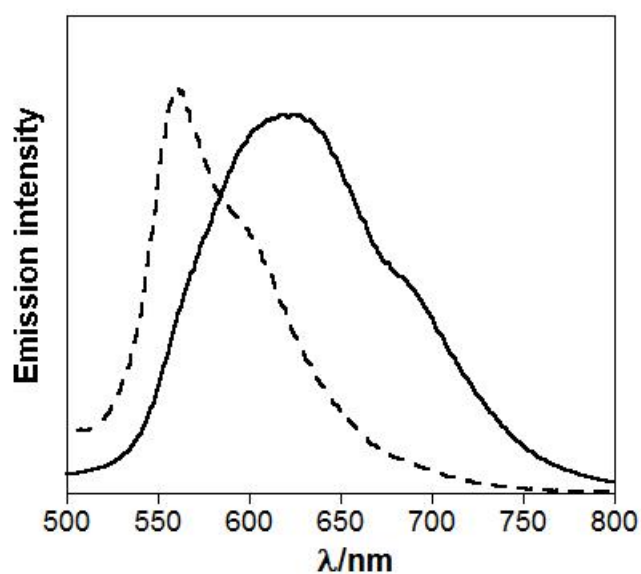
Figure 4.17 Emission spectra of 17 in acetonitrile solution (dashed line) and as a powder (solid line), λ_{exc} = 370 nm.

The photophysical properties of the biphenyl substituted ruthenium and iridium complexes are summarised in Table 4.2.

Table 4.2 Photopysical properties of Ru^{II} and Ir^{III} complexes of the biphenyl substituted bqp ligand.

	$[Ru(bqp)_2]^{2+}$	16	17
λ_{max} (^{1}MLCT) nm, Solution	491 [10,19]	495	340
λ_{max} (^{1}MLCT) nm, Powder		500	345
λ_{max} (^{3}MLCT) nm, Solution	700 [10]	700	560
φ (^{3}MLCT), aerated		4.7×10^{-4}	8×10^{-3}
φ (^{3}MLCT), deaerated	2×10^{-2} [10]	2×10^{-3}	2.8×10^{-2}
τ (^{3}MLCT), aerated		246 ns	4 μs
τ(^{3}MLCT), deaerated	3 μs [10]	1.4 μs	16 μs
λ_{max} (^{3}MLCT) nm, Powder		640	620
τ (^{3}MLCT) ns, Powder		201 ns	2.1 μs

4.3. Conclusion

A new series of derivatives of the bqp ligand have been synthesised and fully characterised. Two strategies for the synthesis of the surface active bqp ligands have been developed, resulting to the synthesis of a surface-bound Ru(II) complex. The monolayer of this complex on planar gold surface has been studied. The complex has the advantage of bearing thioctic acid moieties which have two sulfurs to attach to the gold surface. This makes the monolayer of the complex very stable. Photophysical properties of this complex have been reported in both solution and as a powder. The attached complex on the surface has a very weak absorption and

emission which is impossible to record. The complex is solution shows the characteristic absorption and emission of $[Ru(bqp)_2]^{2+}$ derivatives with a reasonably high excited state lifetime.

The bqp ligand bearing biphenyl groups has been also prepared and Ru(II) and Ir(III) complexes of such ligands has been synthesised in order to be used as metallic guests for cyclodextrin cavities. These complexes show very good photophysical properties with relatively high quantum yields and lifetimes. These complexes have been used later in chapter 5 as the metallo-guests in order to transfer the energy to the metallo-hosts and eventually to the gold surfaces.

4.4. Experimental

8-triflate quinoline (Q-OTf) [25]
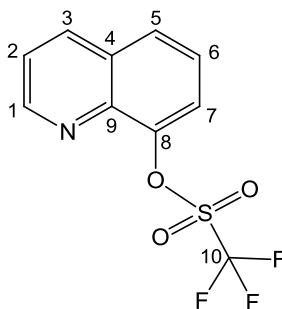
To a solution of 8-hydroxyquinoline (4.70 g, 32.1 mmol) in of pyridine (18 mL) at 0 $^{\circ}$C was slowly added trifluoro-methanesulfonic anhydride (6 mL, 10.0 g, 35.4 mmol). The resulting solution was stirred at 0 $^{\circ}$C for 5 min and then allowed to warm to room temperature and stirred at this temperature for 24 h. The resulting solution was poured into water (100 mL) and extracted with diethyl ether. The ether extract was washed sequentially with water (100 mL), 10% aqueous hydrochloric acid solution (2×30 mL), water (100 mL), and a concentrated sodium chloride solution (100 mL), dried (MgSO$_4$), and concentrated to yield brown oil. Chromatography (flash column, hexane-EtOAc 20:1) afforded **Q-OTf** as a white solid. (7.5 g, 27.1 mmol, 84%)

^{1}H NMR (CDCl$_3$, 300 MHz): δ = 9.08 (dd, 1 H, J = 4.2, 1.8, H$_1$), 8.25 (dd, 1 H, J = 8.1, 1.8, H$_3$), 7.88 (dd, 1 H, J = 7.9, 1.6, H$_5$), 7.65 (dd, 1 H, J = 7.9, 1.6, H$_7$), 7.61 (d, 1 H, J = 7.9, H$_6$), 7.55 (dd, 1 H, J = 8.1, 4.2, H$_2$).

^{13}C NMR (CDCl$_3$, 100 MHz): δ = 151.7 (C$_1$), 146.0 (C$_8$), 141.0 (C$_9$), 135.8 (C$_3$), 129.8 (C$_4$), 128.3 (C$_6$), 125.9 (C$_5$), 122.7 (C$_7$), 121.0 (C$_2$), 120.5 (C$_{10}$).

ES MS(+): m/z 277.9 [M+H]$^+$, 299.8 [M+Na]$^+$.

IR (cm^{-1}): 3077.00, 1496.80, 1432.15, 1420.85, 1395.87, 1200.41, 1132.90, 1067.37, 1019.84, 1040.11.

8-acetylquinoline (Q-Ac) [26]
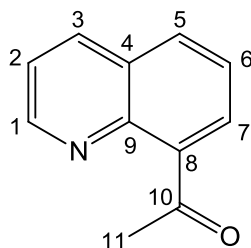
A solution of Pd(dba)$_2$ (1.06 g, 1.84 mmol), dppp (0.83 g, 2.01 mmol), 8-triflatequinoline (10.00 g, 36.10 mmol) and Et$_3$N (10.85 g, 107.21 mmol) in DMF (100 mL) was stirred at room temperature under nitrogen for 30 min. n-Butyl vinyl ether (18.04 g, 180.04 mmol) in DMF (80 mL) was added and stirred at 80 ^{o}C for 24 h, cooled to room temperature, and aqueous HCl (1 M, 361 mL) was added. After 24 h stirring, the reaction mixture was neutralised with aqueous NaOH (1 M) and extracted with diethyl ether (3 × 100 mL). The combined ethereal phases were dried (MgSO$_4$) and concentrated. The crude product was purified by flash chromatography (silica, Hexane/EtOAc 7:3) to give 8-acetylquinoline (5.25 g, 30.68 mmol, 85%) as orange oil.

^{1}H NMR (CDCl$_3$, 300 MHz): δ = 8.90 (dd, 1 H, J = 4.2, 1.8, H$_1$), 8.12 (dd, 1 H, J = 8.1, 1.8, H$_3$), 7.86 (m, 2 H, H$_5$, H$_7$), 7.50 (t, 1 H, J = 8.1, H$_6$), 7.37 (dd, 1 H, J = 8.1, 4.2, H$_2$), 2.87 (s, 3 H, H$_{11}$).

^{13}C NMR (CDCl$_3$, 100 MHz): δ = 203.9 (C$_{10}$), 150.5 (C$_1$), 145.6 (C$_8$), 139.7 (C$_9$), 136.3 (C$_3$), 131.3 (C$_5$), 129.5 (C$_7$), 129.3 (C$_4$), 126.0 (C$_2$), 121.4 (C$_6$), 32.7 (C$_{11}$).

ES MS(+): *m/z* 172.0 [M+H]$^+$, 194.0 [M+Na]$^+$.

8,8'-(4-(3,5-dimethoxyphenyl)pyridine-2,6-diyl)diquinoline (3)
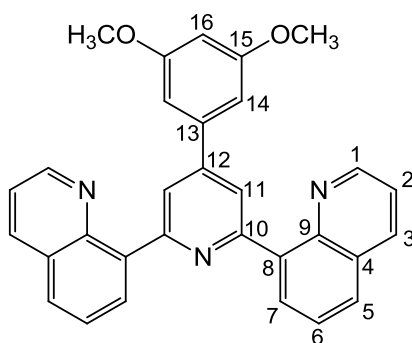
8-Acetylquinoline (3.5 g, 20.50 mmol) was added dropwise to a solution of KO$_t$Bu (3.68 g, 32.91 mmol) in THF (130 mL) and the mixture was stirred at room temperature for 30 min to give a pale yellow suspension. A solution of 3,5-dimethoxybenzaldehyde (1.8 g, 10.71 mmol) in THF (15 mL) was added, whereupon the reaction mixture immediately became clear and bright orange. After stirring for 18 hours at room temperature, a suspension of dried NH$_4$OAc (18 g) in EtOH (210 mL) was added and the reaction mixture was heated to reflux for 8 h. It was cooled to room temperature, poured onto ice and after 2 h water (500 mL) was added resulting in a brown precipitate, which was collected by filtration. The collected solid was dissolved in acetic acid and the pH was adjusted with a solution of NH$_4$OH (1 M). In around pH = 5 some sticky brown solid formed which were separated and the remaining solution was neutralized to pH = 7 when the final product participate as a bright yellow solid. Yield: 1.81 g (36 %)

^{1}H NMR (CDCl$_3$, 400 MHz): δ = 9.01 (dd, 2 H, J = 4.2, 1.8, H$_1$), 8.31 (dd, 2 H, J = 7.3, 1.4, H$_7$), 8.30 (s, 2 H, H$_{11}$), 8.26 (dd, 2 H, J = 8.3, 1.8, H$_3$), 7.91 (dd, 2 H, J = 8.3, 1.4, H$_5$), 7.69 (dd, 2 H, J = 8.3, 7.3, H$_6$), 7.46 (dd, 2 H, J = 8.3, 4.2, H$_2$), 6.99 (d, 2 H, J = 2.3, H$_{14}$), 6.56 (t, 1 H, J = 2.3, H$_{16}$), 3.86 (s, 6 H, H$_{OMe}$).

^{13}C NMR (CDCl$_3$, 100 MHz): δ = 150.3 (C$_1$), 136.4 (C$_3$), 131.5 (C$_7$), 128.5 (C$_5$), 126.6 (C$_6$), 123.9 (C$_{11}$), 121.0 (C$_2$), 105.8 (C$_{14}$), 100.6 (C$_{16}$), 55.4 (C$_{OMe}$).

ES MS(+): m/z 470.1 [M+H]$^+$.

IR (cm^{-1}): 3064.44, 2992.59, 2966.02, 2939.53, 1664.49, 1589.56, 1575.09, 1498.17, 1459.66, 1425.19, 1277.34, 1210.49, 1169.32.

5-(2,6-di(quinolin-8-yl)pyridin-4-yl)benzene-1,3-diol (4)
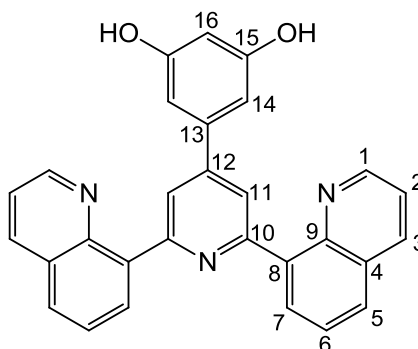
Concentrated hydrochloric acid (13.8 mL) and pyridine (12.5 mL) were heated under nitrogen at 210 ^{o}C for approximately 2 h with continuous removal of water until the solution reached a constant internal temperature of 210 ^{o}C. After cooling to 150 ^{o}C, **3** (1.1 g, 2.34 mmol) was added and the mixture was heated at 210 ^{o}C for 3 h. It was cooled to 100 ^{o}C, whereupon warm water (60 mL) was added. The dark brown

precipitate that formed was collected by filtration and dried under vacuo (Yield: quantitative).

^{1}H NMR (CDCl$_3$, 400 MHz): δ = 9.75 (s, 2 H, OH), 9.01 (dd, 2 H, J = 4.2, 1.8, H$_1$), 8.78 (dd, 2 H, J = 7.3, 1.4, H$_7$), 8.75 (dd, 2 H, J = 8.3, 1.8, H$_3$), 8.62 (s, 2 H, H$_{11}$), 8.37 (dd, 2 H, J = 8.3, 1.4, H$_5$), 7.95 (dd, 2 H, J = 8.3, 7.3, H$_6$), 7.85 (dd, 2 H, J = 8.3, 4.2, H$_2$), 6.97 (d, 2 H, J = 2.3, H$_{14}$), 6.53 (t, 1 H, J = 2.3, H$_{16}$).

ES MS(+): m/z 442.1 [M+H]$^+$.

IR (cm^{-1}): 3061.30 (br), 1594.11, 1504.96, 1416.45, 1362.98, 1305.36, 1270.67, 1150.46, 1007.70.

Br(CH$_2$)$_2$NHBOc
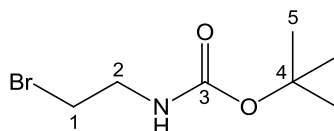
Triethylamine (21 mL) was added to a solution of 2-bromoethanamine hydrobromide (3 g, 14.7 mmol) in MeOH (60 mL). The white suspension was cooled in an ice bath to which di-tert-butyl dicarbonate (6.5 g, 29.4 mmol) dissolved in MeOH (30 mL) was added dropwise over 15 minutes. The resulting mixture was stirred at room temperature overnight. The mixture was concentrated in vacuo and dissolved in DCM. The organic phase was separated and washed with water and the combined DCM extracts were dried (Na$_2$SO$_4$) and the solvent removed in vacuo. The crude product was purified by flash chromatography (silica, DCM) to get the desired product as clear oil. 89 % yield (2.92 g, 13.1 mmol).

^{1}H NMR (CDCl$_3$, 300 MHz): δ = 5.08 (s, 1 H, NH), 3.49 (t, 2 H, J = 5.2, H$_2$), 3.43 (t, 2 H, J = 5.2, H$_1$), 1.42 (s, 9 H, H$_5$).

^{13}C NMR (CDCl$_3$, 100 MHz): δ = 155.6 (C$_3$), 79.7 (C$_4$), 42.3 (C$_2$), 32.6 (C$_1$), 28.2 (C$_5$).

ES MS(+): m/z 224.2 [M+H]$^+$, 246.2 [M+Na]$^+$.

IR (cm^{-1}): 3337.04, 1683.89, 1525.56, 1454.82, 1365.33, 1249.28, 1166.14, 1052.22.

2,2'-((5-(2,6-di(quinolin-8-yl)pyridin-4-yl)-1,3-phenylene)bis(oxy))diethanamine (12)
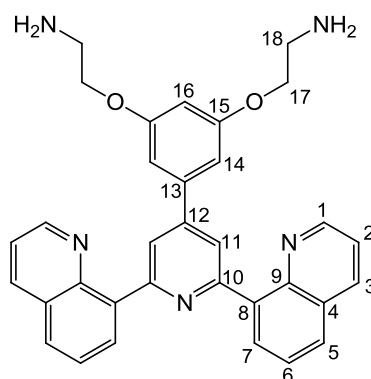
A solution of **4** (1.00 g, 2.26 mmol) in dry DMF (70 mL) was stirred at room temperature for 30 min until it dissolved. Sodium hydride (1.00 g, 41.66 mmol, 60% in mineral oil) was added and kept stirring for another 1 h, whereupon Br(CH$_2$)$_2$NHBOc (3.9g, 18.40 mmol) in 30 mL dry DMF was added and the mixture was heated to 60 °C for 20 hours under nitrogen. After cooling down to room temperature, the excess of NaH was quenched upon addition of 70 mL ice-cold ethanol. The solvent was removed and the organic phase was extracted by water-DCM mixture. The organic layer was separated and dried over MgSO$_4$. The solvent was removed to yield brown solid. The crude was dissolved in 20 mL trifluoroacetic acid and stirred at room

temperature for 5 h. the solvent was removed and the pH was adjust by addition of a solution of NaOH (1 M). The organic phase was extracted by DCM, dried over $MgSO_4$ and solvent was removed. The crude product was purified by column chromatography on silica using DCM/MeOH (98:2) as eluent to yield 240 mg (0.45 mmol, 20 %) of the product as orange solid.

^{1}H NMR (CDCl$_3$, 400 MHz): δ = 8.95 (dd, 2 H, J = 4.2, 1.8, H$_1$), 8.35-8.12 (m, 6 H, H$_7$, H$_3$, H$_{11}$), 7.88 (dd, 2 H, J = 8.3, 1.4, H$_5$), 7.67 (m, 2 H, H$_6$), 7.43 (m, 2 H, H$_2$), 6.92 (m, 2 H, H$_{14}$), 6.50 (m, 1 H, H$_{16}$), 3.59 (m, 4 H, H$_{17}$), 3.37 (m, 4 H, H$_{18}$), 1.75 (br s, 4 H, NH$_2$).

ES MS(+): *m/z* 566.0 [M+K]$^+$.

MALDI-TOF: *m/z* 527.9 [M+H]$^+$.

N,N'-(((5-(2,6-di(quinolin-8-yl)pyridin-4-yl)-1,3-phenylene)bis(oxy))bis(ethane-2,1-diyl))bis(5-(1,2-dithiolan-3-yl)pentanamide) (13)
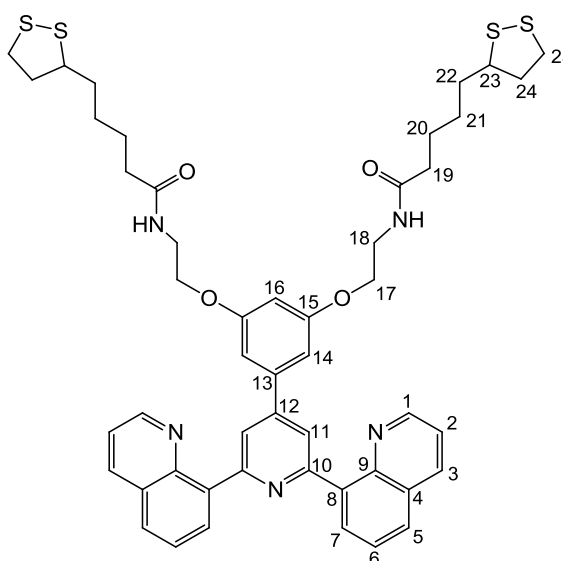
Thioctic acid (0.32 g, 1.5 mmol) and **12** (0.23 g, 0.44 mmol) were dissolved in dry DCM (20 mL). EDC (0.14 g, 0.88 mmol) and a catalytic amount of DMAP were added and the solution stirred at room temperature overnight, during which time a cream precipitate appeared. The mixture was filtered, washed with dry DCM and the solvent evaporated. The crude product was purified by column chromatography on silica eluting with 1% methanol in DCM to yield **13** (0.10 g, 0.11 mmol, 25%) as a brown solid.

^{1}H NMR (CDCl$_3$, 400 MHz): δ = 8.97 (dd, 2 H, J = 4.2, 1.8, H$_1$), 8.30-8.16 (m, 6 H, H$_7$, H$_3$, H$_{11}$), 7.88 (dd, 2 H, J = 8.3, 1.4, H$_5$), 7.66 (dd, 2 H, J = 8.3, 7.3, H$_6$), 7.43 (m, 2 H, H$_2$), 6.93 (t, 2 H, J = 2.3, H$_{14}$), 6.51 (t, 1 H, J = 2.3, H$_{16}$), 5.50 (s, 2 H, NH), 4.12 (m, 4 H, H$_{17}$), 3.56 (m, 4 H, H$_{18}$), 3.50 (m, 2 H, H$_{23}$), 3.32 (m, 4 H, H$_{19}$), 3.06 (m, 4 H, H$_{25}$), 2.82 (m, 4 H, H$_{20}$), 2.39/1.83 (2 × (m, 2 H, H$_{24}$)), 2.22/1.40 (2 × (m, 2 H, H$_{21}$)), 1.57 (m, 4 H, H$_{22}$).

ES MS(+): m/z 899.5 [M]$^+$, 916.5 [M+NH$_4$]$^+$.

8,8'-(4-(3,5-dibromophenyl)pyridine-2,6-diyl)diquinoline (2)
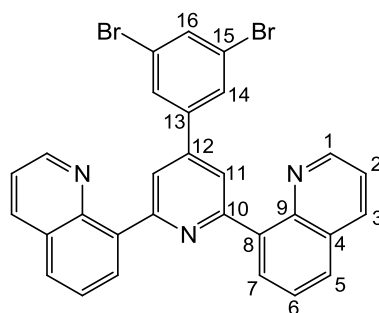
8-Acetylquinoline (3.00 g, 17.54 mmol) and 3,5-dibromobenzaldehyde (2.30 g, 8.76 mmol) were dissolved in EtOH (11 mL). A solution of potassium hydroxide (0.97 g,

17.32 mmol) in aqueous ammonia (10.8 mL, 28%) was added. The reaction mixture was warmed at 40 °C overnight. The solid was filtered off and washed several times with cold acetone to afford **2** as an off-white powder (0.70 g, 84 %).

^{1}H NMR (CDCl$_3$, 400 MHz): δ = 8.95 (dd, 2 H, J = 4.2, 1.8, H$_1$), 8.23 (dd, 2 H, J = 7.3, 1.4, H$_7$), 8.20 (s, 2 H, H$_{11}$), 8.18 (dd, 2 H, J = 8.3, 1.8, H$_3$), 7.84 (dd, 2 H, J = 8.3, 1.4, H$_5$), 7.81 (d, 2 H, J = 2.3, H$_{14}$), 7.65 (t, 1 H, J = 2.3, H$_{16}$), 7.62 (dd, 2 H, J = 8.3, 7.3, H$_6$), 7.40 (dd, 2 H, J = 8.3, 4.2, H$_2$).

^{13}C NMR (CDCl$_3$, 100 MHz): δ = 150.4 (C$_1$), 146.0 (C$_{12}$), 136.4 (C$_3$), 133.8 (C$_7$), 131.6 (C$_{16}$), 129.3 (C$_{14}$), 128.8 (C$_5$), 126.6 (C$_6$), 123.6 (C$_{11}$), 121.1 (C$_2$).

ES MS(+): *m/z* 567.8 [M+H]$^+$, 589.8 [M+Na]$^+$, 605.8 [M+K]$^+$.

MALDI-TOF: *m/z* 568.2 [M+H]$^+$.

IR (cm^{-1}): 3065.44, 3005.10, 2995.72, 1582.16, 1567.80, 1545.76, 1410.68, 1327.10, 1169.70, 1103.23, 1060.25.

5-(1,2-dithiolan-3-yl)-N-(prop-2-yn-1-yl)pentanamide (10)
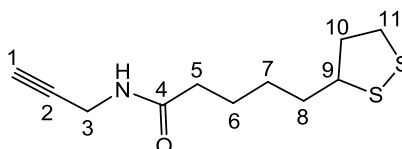
A solution of thioctic acid (0.41 g, 2.0 mmol) and HOBt (0.30 g, 2.2 mmol) in dry DMF (3 mL) was cooled to 0-5 °C, upon which EDC (0.41 g, 2.2 mmol) was added and stirred, maintaining this temperature until the EDC had dissolved (ca. 1 hour). The solution was allowed to warm to room temperature and stirred for a further hour. A

solution of N-EM (0.25 g, 2.2 mmol), and propargylamine (0.74 g, 1.3 mmol) in dry DMF (1 mL) was added to the reaction mixture was stirred overnight. Concentrated and extracted from DCM/ water mixture. Organic phase was separated, dried over MgSO$_4$ and concentrated. The crude product was purified by column chromatography on silica using DCM/MeOH (98:2) as eluent to yield 268 mg (1.1 mmol, 85 %) of the product as yellow solid.

^{1}H NMR (CDCl$_3$, 400 MHz): δ = 5.82 (s, 1 H, NH), 4.07 (dd, 2 H, J = 2.6, 2.6, H$_3$), 3.59 (m, 1 H, H$_9$), 3.22-3.093 (m, 2 H, H$_{11}$), 2.51-2.43 (m, 1 H, H$_{10}$), 2.38 (t, 2 H, J = J = 7.3, H$_5$), 2.24 (m, 1 H, H$_1$), 1.97-1.88 (m, 1 H, H$_{10'}$), 1.78-1.66 (m, 4 H, H$_6$ &H$_8$), 1.58-1.43 (m, 2 H, H$_7$).

^{13}C NMR (CDCl$_3$, 100 MHz): δ = 179.3 (C$_4$), 71.7 (C$_1$), 59.3 (C$_9$), 40.2 (C$_{10}$), 38.5 (C$_{11}$), 34.6 (C$_8$), 33.8 (C$_5$), 29.2 (C$_3$), 28.8 (C$_7$), 25.2 (C$_2$), 24.4 (C$_6$).

EI MS(+): m/z 243.1 [M]$^+$.

di-tert-butyl((5-(2,6-di(quinolin-8-yl)pyridin-4-yl)-1,3-phenylene)bis(prop-2-yne-3,1-diyl))dicarbamate (8)
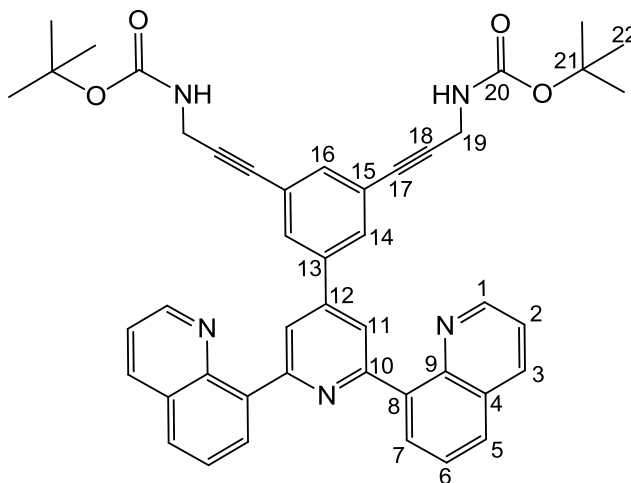
A mixture of **2** (1.07 g, 1.87 mmol), tetrakis(triphenylphosphine)-palladium(0) (25 mg, 0.02 mmol), and CuI (5 mg, 0.03 mmol) in dry THF (10 mL) and triethylamine (8 mL) was deaerated with N_2. N-Boc-propagylamine (1.5 g, 9.37 mmol) was added, and the mixture was heated at 80 °C for 5 h under nitrogen. More $Pd(PPh_3)_4$, CuI and N-Boc-propagylamine were added and continued to heat at 80 °C for further 18 h. The cooled solution was filtered, and the filtrate was evaporated and redissolved in DCM. The solution was washed with water, dried, and concentrated. Purification on silica gel (eluent: petroleum ether/ EtOAC /Et_3N, 5:4:1) gave the title compound as brown solid (1.57 g, 2.19 mmol, 76%).

^{1}H NMR (CDCl$_3$, 400 MHz): δ = 9.02 (dd, 2 H, J = 4.2, 1.8, H_1), 8.30 (dd, 2 H, J = 7.3, 1.4, H_7), 8.28 (s, 2 H, H_{11}), 8.24 (dd, 2 H, J = 8.3, 1.8, H_3), 7.90 (dd, 2 H, J = 8.3, 1.4, H_5), 7.78 (t, 1 H, J = 2.3, H_{16}), 7.69 (dd, 2 H, J = 8.3, 7.3, H_6), 7.65 / 7.54 (2 × (dd, 1 H, J = 1.4, 2.3, H_{14})), 7.45 (m, 2 H, H_2), 4.95 (br s, 2 H, NH), 4.13 (d, 4 H, J = 4.7, H_{19}), 1.45 (s, 18 H, H_{22}).

^{13}C NMR (CDCl$_3$, 100 MHz): δ = 150.8 (C_{20}), 150.4 (C_1), 140.8 (C_{12}), 136.4 (C_3), 136.3 (C_8), 135.9 (C_{13}), 134.2 (C_9), 132.1-131.9 (C_7), 131.6/130.6 (C_{16}), 131.2/129.5 (C_{14}), 129.9 (C_4), 128.7-128.4 (C_5), 126.6 (C_6), 126.1 (C_{17}), 123.6 (C_{11}), 121.6 (C_{18}), 121.0 (C_2), 30.9 (C_{17}), 68.1 (C_{21}), 30.9 (C_{19}), 28.4 (C_{22}).

ES MS(+): m/z 732.2 [M+NH$_4$]$^+$.

3,3'-(5-(2,6-di(quinolin-8-yl)pyridin-4-yl)-1,3-phenylene)bis(prop-2-en-1-amine) (9)
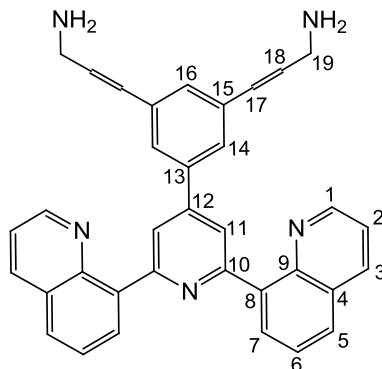
8 was dissolved in DCM/ TFA (50:50), stirred for 5 h at room temperature, and concentrated. The residue was dissolved in dichloromethane, washed with saturated $NaHCO_3$, dried, and concentrated to give **9** as red solid.

^1H NMR (CDCl$_3$, 300 MHz): δ = 9.03 (dd, 2 H, J = 4.2, 1.8, H$_1$), 8.31 (dd, 2 H, J = 7.3, 1.4, H$_7$), 8.28 (s, 2 H, H$_{11}$), 8.26 (dd, 2 H, J = 8.3, 1.8, H$_3$), 7.90 (dd, 2 H, J = 8.3, 1.4, H$_5$), 7.78 (t, 1 H, J = 2.3, H$_{16}$), 7.72 (dd, 2 H, J = 8.3, 7.3, H$_6$), 7.67 / 7.56 (2 × (dd, 1 H, J = 1.4, 2.3, H$_{14}$)), 7.49 (m, 2 H, H$_2$), 3.67 (s, 4 H, H$_{19}$), 2.63 (s, 2 H, H$_{17}$), 2.19 (s, 2 H, H$_{18}$), 2.09 (br s, 4 H, NH$_2$).

^{13}C NMR (CDCl$_3$, 100 MHz): δ = 157.7 (C$_{10}$), 150.4 (C$_1$), 146.8 (C$_{12}$), 146.0 (C$_8$), 138.6 (C$_9$), 136.5 (C$_3$), 134.1 (C$_{16}$), 132.1-131.9 (C$_7$), 131.6 (C$_{14}$), 130.3 (C$_{17}$), 129.4 (C$_{18}$), 128.7-128.4 (C$_5$), 126.6 (C$_6$), 123.6 (C$_{11}$), 121.0 (C$_2$), 32.1 (C$_{19}$).

ES MS(+): *m/z* 542.1 [M+Na]$^+$.

IR (cm^{-1}): 3384.49, 3069.20, 1673.61, 1493.77, 1438.35, 1202.84, 1177.60, 1125.58.

N-(3-(3-(3-aminoprop-1-en-1-yl)-5-(2,6-di(quinolin-8-yl)pyridin-4-yl)phenyl)allyl)-5-(1,2-dithiolan-3-yl)pentanamide (11)
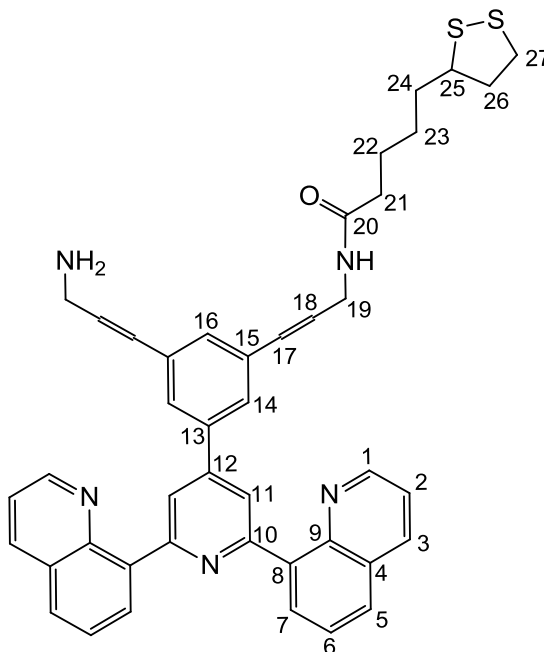
A solution of thioctic acid (0.30 g, 1.4 mmol) and HOBt (0.19 g, 1.4 mmol) in dry DMF (5 mL) was cooled to 0-5 °C, upon which EDC (0.28 g, 1.4 mmol) was added and stirred, maintaining this temperature until the EDC had dissolved (ca. 1 hour). The solution was allowed to warm to room temperature and stirred for a further hour. A solution of N-EM (0.17 g, 1.4 mmol), and **9** (0.25 g, 0.5 mmol) in dry DMF (2 mL) was added to the reaction mixture was stirred overnight. Concentrated and extracted from DCM/ water mixture. Organic phase was separated, dried over MgSO$_4$ and concentrated to yield 0.11 g (1.1 mmol, 24 %) of the product (still containing a small amount of HOBt and EDC) as a brown solid.

^{1}H NMR (CDCl$_3$, 400 MHz): δ = 8.97 (dd, 2 H, *J* = 4.2, 1.8, H$_1$), 8.26 (dd, 2 H, *J* = 7.3, 1.4, H$_7$), 8.24 (s, 2 H, H$_{11}$), 8.22 (dd, 2 H, *J* = 8.3, 1.8, H$_3$), 7.88 (dd, 2 H, *J* = 8.3, 1.4, H$_5$), 7.71 (t, 1 H, *J* = 2.3, H$_{16}$), 7.76 (dd, 2 H, *J* = 8.3, 7.3, H$_6$), 7.52 (dd, 2 H, *J* = 1.4,

2.3, H$_{14}$), 7.44 (m, 2 H, H$_2$), 6.75 (br s, 4 H, NH$_2$), 4.20 (d, 4 H, J = 4.9, H$_{19}$), 3.50 (m, 1 H, H$_{25}$), 3.14-3.01 (m, 2 H, H$_{27}$), 2.43-2.33 (m, 1 H, H$_{26}$), 2.18 (t, 2 H, J = 7.5, H$_{21}$), 1.88-1.79 (m, 1 H, H$_{10'}$), 1.70-1.55 (m, 4 H, H$_{22}$ &H$_{24}$), 1.46-1.34 (m, 2 H, H$_{23}$).

^{13}C NMR (CDCl$_3$, 100 MHz): δ = 172.6 (C$_{20}$), 157.6 (C$_{10}$), 150.4 (C$_1$), 145.9 (C$_{12}$), 144.8 (C$_8$), 141.3 (C$_{13}$), 139.0 (C$_9$), 136.5 (C$_3$), 134.2 (C$_{16}$), 131.8 (C$_4$), 132.1-131.9 (C$_7$), 131.5 (C$_{14}$), 130.5 (C$_{17}$), 129.4 (C$_{18}$), 128.8-128.4 (C$_5$), 126.5 (C$_6$), 123.5 (C$_{11}$), 122.6 (C$_{15}$), 121.1 (C$_2$), 56.4 (C$_{25}$), 40.2 (C$_{26}$), 38.4 (C$_{27}$), 36.5 (C$_{19'}$), 35.9 (C$_{24}$), 34.5 (C$_{21}$), 31.4 (C$_{19}$), 29.7 (C$_{23}$), 28.8 (C$_{18}$), 25.2 (C$_{22}$).

MALDI-TOF: m/z 1. 037 [M+Na]$^+$, 746.1 [M+K]$^+$.

IR (cm^{-1}): 3263.41, 3100.01, 2924.91, 1654.62, 1542.73, 1497.22, 1435.79, 1362.68, 1259.67, 1175.59, 1026.58.

8,8'-(4-(p-tolyl)pyridine-2,6-diyl)diquinoline (6)[13]
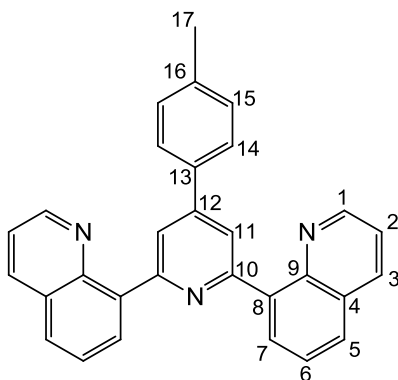
8-Acetylquinoline (3.20 g, 18.71 mmol) and 4-methylbenzaldehyde (1.12 g, 9.33 mmol) were dissolved in EtOH (30 mL). A solution of potassium hydroxide (1.05 g, 18.75 mmol) in aqueous ammonia (23 mL, 28%) was added. The reaction mixture

was warmed at 60 °C overnight. The crude product was extracted between water and DCM. The organic phase was collected, dried over MgSO$_4$ and concentrated. The crude was dissolved in acetic acid and the pH was adjusted with a solution of NH$_4$OH (1 M). In around pH = 5 some brown oil formed which was separated and the remaining solution was neutralized to pH = 7 when the final product participate as an off-white solid. Yield: 1.02 g (26 %)

^{1}H NMR (CDCl$_3$, 400 MHz): δ = 9.03 (dd, 2 H, J = 4.2, 1.8, H$_1$), 8.30 (s, 2 H, H$_{11}$), 8.28 (dd, 2 H, J = 7.3, 1.4, H$_7$), 8.25 (dd, 2 H, J = 8.3, 1.8, H$_3$), 7.92 (dd, 2 H, J = 8.3, 1.4, H$_5$), 7.75 (d, 2 H, J = 8.1, H$_{15}$), 7.70 (dd, 2 H, J = 8.3, 7.3, H$_6$), 7.47 (dd, 2 H, J = 8.3, 4.2, H$_2$), 7.32 (d, 2 H, J = 8.1, H$_{14}$), 2.44 (s, 3 H, H$_{17}$).

^{13}C NMR (CDCl$_3$, 100 MHz): δ = 157.3 (C$_{10}$), 150.3 (C$_1$), 146.1 (C$_{12}$), 143.7 (C$_8$), 139.6 (C$_{13}$), 138.5 (C$_9$), 136.3 (C$_3$), 131.5 (C$_7$), 129.6 (C$_{14}$), 128.7 (C$_4$), 128.4 (C$_5$), 127.4 (C$_{15}$), 126.6 (C$_6$), 123.6 (C$_{11}$), 120.9 (C$_2$), 30.9 (C$_{17}$).

ES MS(+): m/z 424.1 [M+H]$^+$, 446.2 [M+Na]$^+$.

IR (cm^{-1}): 3032.83, 1612.03, 1591.65, 1541.15, 1497.91, 1380.67, 1269.61, 1185.88.

8,8'-(4-(4-bromophenyl)pyridine-2,6-diyl)diquinoline (5)[13]
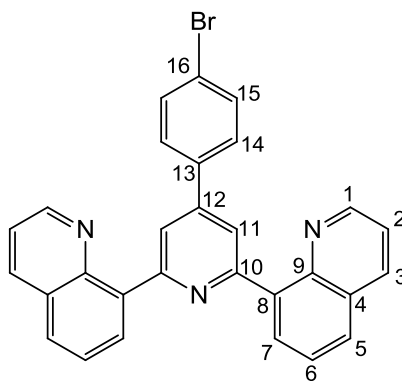
8-Acetylquinoline (2.60 g, 14.7 mmol) and 4-bromobenzaldehyde (1.40 g, 7.3 mmol) were dissolved in EtOH (9.5 mL). A solution of potassium hydroxide (0.85 g, 15.2 mmol) in aqueous ammonia (9.35 mL, 28%) was added. The reaction mixture was warmed at 40 °C overnight. The solid was filtered off and washed with cold acetone to afford **5** as an off-white powder (0.90 g, 25 %).

^{1}H NMR (CDCl$_3$, 400 MHz): δ = 9.03 (dd, 2 H, J = 4.2, 1.8, H$_1$), 8.34 (s, 2 H, H$_{11}$), 8.32 (dd, 2 H, J = 7.3, 1.4, H$_7$), 8.27 (dd, 2 H, J = 8.3, 1.8, H$_3$), 7.93 (dd, 2 H, J = 8.3, 1.4, H$_5$), 7.73 (d, 2 H, J = 8.6, H$_{15}$), 7.71 (dd, 2 H, J = 8.3, 7.3, H$_6$), 7.65 (d, 2 H, J = 8.6, H$_{14}$), 7.48 (dd, 2 H, J = 8.3, 4.2, H$_2$).

^{13}C NMR (CDCl$_3$, 100 MHz): δ = 157.5 (C$_{10}$), 150.3 (C$_1$), 140.1 (C$_{12}$), 140.0 (C$_8$), 139.3 (C$_{13}$), 138.3 (C$_9$), 136.4 (C$_3$), 132.0 (C$_{14}$), 131.6 (C$_7$), 129.2 (C$_{15}$), 128.7 (C$_4$), 128.6 (C$_5$), 126.6 (C$_6$), 123.6 (C$_{11}$), 121.0 (C$_2$).

ES MS(+): m/z 487.9 [M+H]$^+$.

IR (cm^{-1}): 3044.59, 1614.38, 1592.99, 1570.54, 1545.59, 1498.61, 1431.73, 1379.08, 1310.01, 1133.44.

8,8'-(4-(4-(3-methoxycyclodextrin-prop-1-yn-1-yl)phenyl)pyridine-2,6-diyl)diquinoline (14)
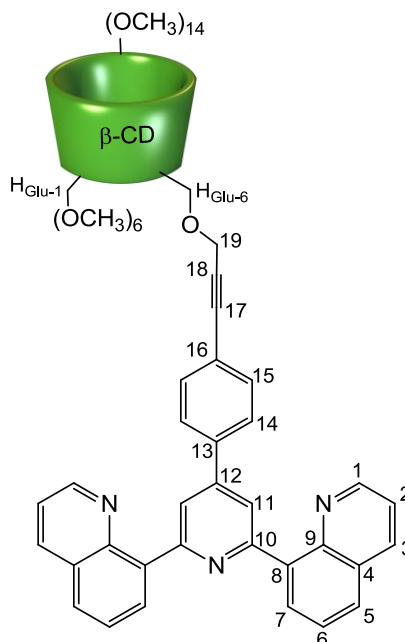
A mixture of **5** (0.49 g, 1.00 mmol), Pd(PPh$_3$)$_4$ (75 mg, 0.06 mmol), and CuI (10 mg, 0.06 mmol) in dry THF (10 mL) and triethylamine (4 mL) was deaerated with nitrogen. Propargyl-p.m.β-CD (0.50 g, 0.34 mmol) was added, and the mixture was heated at 80 °C for 5 h under nitrogen. More Pd(PPh$_3$)$_4$, CuI and propargyl-p.m.β-CD were added and continued to heat at 80 °C for further 18 h. The cooled solution was filtered, and the filtrate was evaporated and redissolved in DCM. The solution was washed with water, dried, and concentrated. The compound was purified through size exclusion column chromatography (Biobeads SX3, DCM) yielding 0.38 g of title compound as brown solid, 60 % yield.

^{1}H NMR (CDCl$_3$, 400 MHz): δ = 9.33 (m, 2 H, H$_1$), 8.37 (m, 2 H, H$_7$), 7.98 (m, 6 H, H$_3$, H$_{11}$, H$_5$), 7.81-7.55 (m, 6 H, H$_{15}$, H$_{14}$, H$_6$), 7.49 (dd, 2 H, J = 8.3, 4.2, H$_2$), 5.23-5.00

(m, 7 H, H_{Glu-1}), 4.30 (d, J = 9.4, 2 H, H_{19}), 4.07 (dd, J = 6.4, 1 H, H_{Glu-6}), 4.01-3.01 (m, 101H).

IR (cm^{-1}): 2926.68, 1594.94, 1454.94, 1366.36, 1193.38, 1138.39, 1087.97, 1021.81, 969.41.

8,8'-(4-([1,1'-biphenyl]-4-yl)pyridine-2,6-diyl)diquinoline (7)
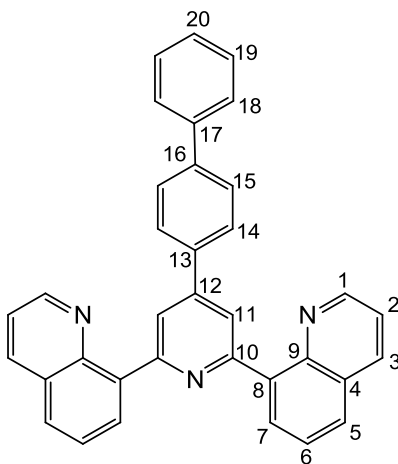
8-Acetylquinoline (2.00 g, 11.7 mmol) was added drop-wise to a solution of KOtBu (2.11 g, 18.9 mmol) in THF (70 mL) and the mixture was stirred at room temperature for 30 min to give a pale yellow suspension. A solution of biphenyl-4-carbaldehyde (1.12 g, 6.1 mmol) in THF (15 mL) was added, whereupon the reaction mixture immediately became clear and dark orange. After stirring for 18 hours at room temperature, a suspension of dried NH_4OAc (11 g) in EtOH (80 mL) was added and the reaction mixture was heated to reflux for 24 h. It was cooled to room temperature, poured onto ice and after 2 h water (500 mL) was added resulting in a brown precipitate, which was collected by filtration. The collected solid was dissolved in acetic acid and the pH was adjusted with a solution of NH_4OH (1 M). In around pH =

5 some sticky brown solid formed which were separated and the remaining solution was neutralized to pH = 7 when the final product participate as a bright yellow solid. Yield: 1.1 g (39 %)

^{1}H NMR (CDCl$_3$, 400 MHz): δ = 9.05 (dd, 2 H, J = 4.2, 1.8, H$_1$), 8.41 (s, 2 H, H$_{11}$), 8.33 (dd, 2 H, J = 7.3, 1.4, H$_7$), 8.27 (dd, 2 H, J = 8.3, 1.8, H$_3$), 7.92 (m, 4 H, H$_5$ & H$_{18}$), 7.77-7.62 (m, 6 H, H$_6$ & H$_{15}$ & H$_{19}$), 7.47 (m, 4 H, H$_2$ & H$_{14}$), 7.40 (t, 1 H, J = 7.3, H$_{20}$).

^{13}C NMR (CDCl$_3$, 100 MHz): δ = 157.4 (C$_{10}$), 150.3 (C$_1$), 146.6 (C$_{17}$), 146.1 (C$_{16}$), 141.4 (C$_{12}$), 140.5 (C$_8$), 139.5 (C$_{13}$), 138.3 (C$_9$), 136.4 (C$_3$), 131.6 (C$_7$), 128.8 (C$_{14}$), 128.7 (C$_4$), 128.5 (C$_{15}$), 128.0 (C$_5$), 127.6 (C$_6$), 127.5 (C$_{18}$), 127.1 (C$_{20}$), 126.6 (C$_{19}$), 123.7 (C$_{11}$), 121.0 (C$_2$).

ES MS(+): m/z 486.2 [M+H]$^+$, 508.2 [M+Na]$^+$.

IR (cm^{-1}): 3047.21, 1611.88, 1591.18, 1566.23, 1538.05, 1497.81, 1488.80, 1380.82, 1308.50, 1269.39, 1131.10.

Anal. Calc. for C$_{35}$H$_{23}$N$_3$ (C$_2$H$_4$O$_2$)$_{0.3}$: C 84.90, H 4.85, N 8.35. Found C 84.67, H 4.63, N 8.49.

2,6-bis(quinolin-8-yl)pyridine (1)
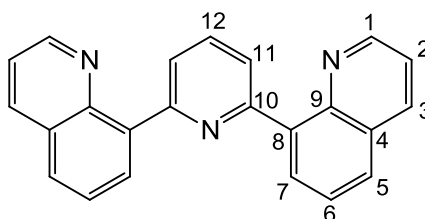
An oven-dried flask was charged with 8-quinolineboronic acid (1.20 g, 6.93 mmol), 2,6-dibromo-pyridine (0.77 g, 3.25 mmol), Pd(dba)$_2$ (0.39 g, 0.07 mmol), 2-dicyclohexylphosphino-2′,6′-dimethoxybiphenyl (0.56 g, 0.13 mmol) and grinded K$_3$PO$_4$ (6.60 g, 31.0 mmol). The flask was evacuated and charged with N$_2$. Dry toluene (25 mL) was added via a syringe and the resulting suspension was stirred at 100° C for 15 h. The mixture was allowed to cool to room temperature, diluted with CH$_2$Cl$_2$ (50 mL) and filtered. The solvent was removed and the remaining solid purified by column chromatography using silica gel and 2.5% MeOH/CH$_2$Cl$_2$ as eluent to give bqp as an off-white solid (0.85 g, 79 %).

^{1}H NMR (CDCl$_3$, 400 MHz): δ = 8.93 (dd, 2 H, J = 4.2, 1.8, H$_1$), 8.20 (dd, 2 H, J = 7.3, 1.5, H$_7$), 8.15 (dd, 2 H, J = 8.3, 1.8, H$_3$), 8.04 (d, 2 H, J = 7.7, H$_{11}$), 7.88 (t, 1 H, J = 7.7, H$_{12}$), 7.81 (dd, 2 H, J = 7.3, 1.5, H$_5$), 7.59 (dd, 2 H, J = 8.3, 7.3, H$_6$), 7.38 (dd, 2 H, J = 8.3, 4.2, H$_2$).

ES MS(+): m/z 334 [M+H]$^+$.

IR (cm^{-1}): 3037.47, 1613.37, 1591.18, 1561.11, 1496.85, 1446.40, 1381.90, 1365.51, 1317.65, 1272.43, 1137.77.

Ru(1)Cl$_3$
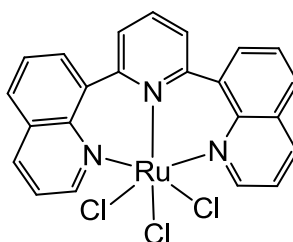
1 (70 mg, 0.21 mmol) and RuCl$_3$·3H$_2$O (57 mg, 0.22 mmol) were suspended in EtOH (4 mL) in a sealed tube and heated at 100 °C for 24 h. The precipitate was filtered off, washed thoroughly with EtOH and Et$_2$O, and finally dried in vacuo at 50°C to yield Ru(**1**)Cl$_3$ (65 mg). Ru(**1**)Cl$_3$ was used without any further purification.

ES MS(+): *m/z* 505.0 [Ru(bqp)Cl$_2$]$^+$, 539.0 [M]$^+$, 562.9 [M+Na]$^+$.

IR (cm^{-1}): 3053.72, 2008.43, 1591.87, 1569.10, 1505.66, 1442.06, 1378.13, 1272.89, 1221.99, 1138.62.

Ru(14)Cl$_3$
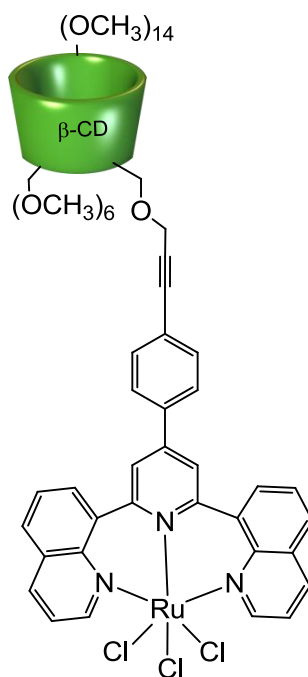
14 (150 mg, 0.08 mmol) and RuCl$_3$·3H$_2$O (21 mg, 0.08 mmol) were suspended in EtOH (4 mL) in a sealed tube and heated at 100 °C for 24 h. The precipitate was filtered off, washed thoroughly with EtOH and Et$_2$O, and finally dried in vacuo at 50°C to yield Ru(**14**)Cl$_3$ (110 mg). Ru(**14**)Cl$_3$ was used without any further purification.

ES MS(+): *m/z* 998.4 [Ru(4-CD-bqp)Cl]$^{2+}$.

IR (cm^{-1}): 2928.38, 1952.72, 1572.57, 1441.19, 1371.20, 1049.97.

15

13 (100 mg, 0.11 mmol), Ru(**1**)Cl$_3$ (60 mg) and 5 drops of N-ethylmorpholine were suspended in EtOH (10 mL) in a sealed tube and heated for 24 h at 100 °C. After filtration of the crude reaction mixture, H$_2$O and EtOAc were added. The aqueous layer was washed once with EtOAc, separated and NH$_4$PF$_6$ and DCM were added. The organic layer was concentrated under reduced pressure to give the final complex as a dark red solid (38 mg, 0.023 mmol, 21 %).

^{1}H NMR (CDCl$_3$, 400 MHz): δ = 8.83 (dd, 2 H, *J* = 4.2, 1.8, H$_{1'}$), 8.76 (m, 2 H, H$_1$), 8.66/8.37 (2× (d, 1 H, *J* = 8.3, H$_{3'}$), 8.58 (dd, 2 H, *J* = 7.3, 1.5, H$_{7'}$), 8.52 (m, 2 H, H$_7$), 8.43 (dd, 2 H, *J* = 8.3, 1.8, H$_3$), 8.28 (s, 2 H, H$_{11}$), 8.19 (dd, 2 H, *J* = 7.3, 1.5, H$_{5'}$), 8.13-8.04 (m, 4 H, H$_5$, H$_{11'}$), 7.89 (t, 1 H, *J* = 7.7, H$_{12'}$), 7.84 (t, 2 H, *J* = 7.3, H$_{6'}$), 7.76-7.55 (m, 6 H, H$_6$, H$_2$, H$_{2'}$), 7.07 (m, 2 H, H$_{14}$), 6.92 (m, 1 H, H$_{16}$), 5.03 (s, 2 H, NH),

4.18-3.93 (m, 8 H, H_{17}, H_{18}), 3.62-3.07 (m, 10 H, H_{23}, H_{19}, H_{25}), 2.83-2.69 (m, 10 H, H_{20}) 1.37-1.00 (m, 16 H, H_{21}, H_{22}, H_{24}).

ES MS(+): *m/z* 669.4 $\{M-2[PF_6]\}^{2+}$.

MALDI-TOF: *m/z* 670.2 $[\{M-2[PF_6]\}^{2+}$.

IR (cm^{-1}): 2953.38, 1670.09, 1594.39, 1502.36, 1445.81, 1367.32, 1266.78, 1168.63, 1065.91.

16
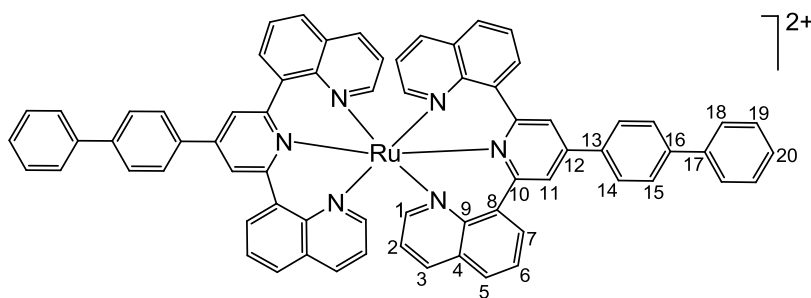
7 (70 mg, 0.14 mmol) and $RuCl_3 \cdot 3H_2O$ (36 mg, 0.14 mmol) were suspended in EtOH (4 mL) in a sealed tube and heated at 100 °C for 24 h. The precipitate was filtered off, washed thoroughly with EtOH and Et_2O, and finally dried in vacuo at 50°C to yield Ru(**7**)Cl_3 (100 mg). Ru(**7**)Cl_3, **7** (70 mg, 0.14 mmol) and few drops of N-ethylmorpholine were suspended in EtOH (10 mL) in a sealed tube and heated for 24 h at 100 °C. After filtration of the crude reaction mixture, H_2O and EtOAc were added. The aqueous layer was washed once with EtOAc, separated and NH_4PF_6 and DCM were added. The organic layer was concentrated under reduced pressure to give the final complex as a dark red solid (63 mg, 0.046 mmol, 33 %).

^{1}H NMR (CDCl$_3$, 400 MHz): δ = 8.73 (d, 4 H, J = 1.8, H$_1$), 8.32 (d, 4 H, J = 7.3, H$_7$), 8.21 (s, 4 H, H$_{11}$), 8.10/ 7.93 (2× (d, 2 H, J = 8.3, H$_3$)), 8.04/ 7.85 (2× (m, 2 H, H$_5$)), 7.73 (m, 4 H, H$_6$), 7.68-7.31 (m, 20 H, H$_2$, H$_{14}$, H$_{15}$,H$_{17}$& H$_{18}$), 7.24 (m, 2 H, H$_{20}$).

^{13}C NMR (CDCl$_3$, 100 MHz): δ = 153.8 (C$_{10}$), 150.0 (C$_1$), 146.6 (C$_{17}$), 144.3 (C$_{16}$), 142.0 (C$_{12}$), 139.3 (C$_{13}$), 138.1/137.6 (C$_3$), 133.5 (C$_7$), 131.7 (C$_{14}$), 130.7 (C$_{15}$), 128.9 (C$_5$), 127.8-126.8 (C$_6$, C$_{18}$, C$_{19}$, C$_{20}$), 126.7 (C$_{11}$), 121.8 (C$_2$).

ES MS(+): m/z 536.2 {M-2[PF$_6$]}$^{2+}$.

IR (cm^{-1}): 3055.45, 1598.40, 1571.69, 1536.03, 1408.89, 1367.69, 1272.24, 1195.30, 1077.27.

Anal. Calc. for C$_{70}$H$_4$N$_6$F$_{12}$P$_2$Ru (C$_5$H$_5$N): C 62.45, H 3.57, N 6.80. Found C 462.31, H 3.57, N 6.61.

17
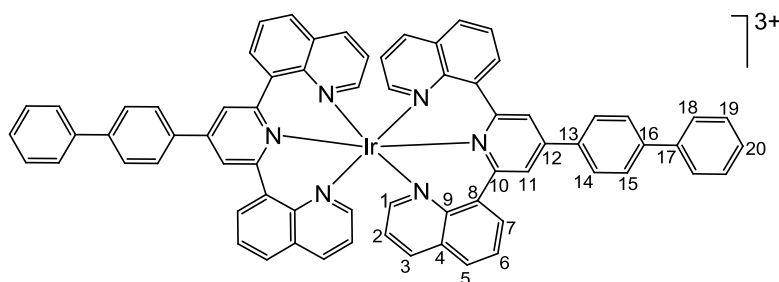
7 (140 mg, 0.29 mmol), IrCl$_3$ (42 mg, 0.14 mmol) and 10 drops of N-ethylmorpholine were suspended in ethylene glycol (7 mL) in a sealed tube and heated at 250 °C for 1 h. After filtration (of the crude reaction mixture, H$_2$O and EtOAc were added. The aqueous layer was washed once with EtOAc, separated and NH$_4$PF$_6$ and DCM were

added. The organic layer was concentrated under reduced pressure to give the final complex as bright orange solid (35 mg, 0.022 mmol, 16 %).

^{1}H NMR (CDCl$_3$, 400 MHz): δ = 8.45-7.19 (m, H$_{aromatic}$)

ES MS(+): *m/z* 652.3 {M-2[PF$_6$]}$^{2+}$.

MALDI-TOF: *m/z* 1163.3 {M-3[PF$_6$]}.

IR (cm^{-1}): 2933.60, 1599.85, 1488.46, 1418.27, 1250.55, 1201.54, 1071.65, 1041.87, 1006.95.

References

(1) Bakker, B. H.; Goes, M.; Hoebe, N.; van Ramesdonk, H. J.; Ver-hoeven, J. W.; Werts, M. H. V.; Hofstraat, J. W. *Coord. Chem. Rev.* **2000**, *208*, 3-16.

(2) Bignozzi, C. A.; Argazzi, R.; Kleverlaan, C. *J. Chem. Soc. Rev.* **2000**, *29*, 87-96.

(3) Gust, D.; Moore, T. A.; Moore, A. L. *Accounts Chem. Res.* **2001**, 40-48.

(4) Li, C.; Fan, W.; Straus, D. A.; Lei, B.; Asano, S.; Zhang, D. H.; Han, J.; Meyyappan, M.; Zhou, C. W. *J. Am. Chem. Soc.* **2004**, *126*, 7750-7751.

(5) Li, C.; Fan, W. D.; Lei, B.; Zhang, D. H.; Han, S.; Tang, T.; Liu, X. L.; Liu, Z. Q.; Asano, S.; Meyyappan, M.; Han, J.; Zhou, C. W. *Appl. Phys. Lett.* **2004**, *84*, 1949-1951.

(6) Zimmerman, R.; Basabe-Desmonts, L.; van der Baan, F.; Rein-houdt, D. N.; Crego-Calama, M. *J. Mater. Chem.* **2005**, *15*, 2772-2777.

(7) Juris, A.; Balzani, V.; Barigelletti, F.; Campagna, S.; Belser, P.; von Zelewsky, A. *Coord. Chem. Rev.* **1988**, *84*, 85-277.

(8) Keene, F. R. *Coord. Chem. Rev.* **1997**, *166*, 121-159.

(9) Medlycott, E. A.; Hanan, G. S. *Chem. Soc. Rev.* **2005**, *34*, 133-142.

(10) Abrahamsson, M.; Jager, M.; Tomas Osterman; Lars Eriksson; Petter Persson; Hans-Christian Becker; Olof Johansson; Hammarström, L. *J. Am. Chem. Soc.* **2006**, *128*, 12616 -12617.

(11) Abrahamsson, M.; Wolpher, H.; Johansson, O.; Larsson, J.; Kritikos, M.; Eriksson, L.; Norrby, P. O.; Bergquist, J.; Sun, L.; Åkermark, B.; Hammarstro¨m, L. *Inorg. Chem.* **2005**, *44*, 3215 -3225.

(12) Wolpher, H.; Johansson, O.; Abrahamsson, M.; Kritikos, M.; Sun, L.; Åkermark, B. *Inorg. Chem. Commun.* **2004**, *7*, 337-340.

(13) Jäger, M.; Lars Eriksson; Jonas Bergquist; Johansson, O. *J. Org. Chem.* **2007**, *72*, 10227-10230.

(14) Hwang, S.-H.; Moorefield, C. N.; Wang, P.; Fronczek, F. R.; Courtney, B. H.; Newkome, G. R. *Dalton Trans.* **2006**, 3518 -3522.

(15) Smith, C. B.; Raston, C. L.; Sobolev, A. N. *Green Chem.* **2005**, *7*, 650 -654.

(16) Vaduvescu, S.; Potvin, P. G. *Inorg. Chem.* **2002**, *41*, 4081-4083.

(17) Wang, J.; Hanan, G. S. *Synlett* **2005**, 1251 -1254.

(18) Winter, A.; Van den Berg, A. M. J.; Hoogenboom, R.; Kickelbick, G.; Schubert, U. S. *Synthesis* **2006**, 2873 -2878.

(19) Abrahamsson, M.; Jager, M.; Kumar, R. J.; Osterman, T.; Persson, P.; Becker, H.-C.; Johansson, O.; Hammarstrom, L. *J. Am. Chem. Soc.* **2008**, *130*, 15533–15542.

(20) Borg, O. A.; Godinho, S. S. M. C.; Lundqvist, M. J.; Lunell, S.; Persson, P. *J. Phys. Chem. A.* **2008**, *112*, 4470–4476.

(21) Barder, T. E.; Walker, S. D.; Martinelli, J. R.; Buchwald, S. L. *J. Am. Chem. Soc.* **2005**, *127*, 4685 -4696.

(22) Medlycott, E. A.; Hanan, G. S. *Coord. Chem. Rev.* **2006**, *250*, 1763 -1782.

(23) Sauvage, J.-P.; Collin, J.-P.; Chambron, J.-C.; Guillerez, S.; Coudret, C.; Balzani, V.; Barigelletti, F.; De Cola, L.; Flamigni, L. *Chem. Rev.* **1994**, *94*, 993-1019.

(24) Baranoff, E.; Collin, J.-P.; Flamigni, L.; Sauvage, J.-P. *Chem. Soc. Rev.* **2004**, *33*, 147-155.

(25)   Echavarren, A. M.; Stille, J. K. *J. Am. Chem. SOC.* **1987**, *109*, 5478-5486.

(26)   Legros, J.-Y.; Primault, G.; Fiaud, J.-C. *Tetrahedron* **2001**, *57*, 2507-2514.

(27)   Peuralahti, J.; Hakala, H.; Mukkala, V.-M.; Loman, K.; Hurskainen, P.; Mulari, O.; Hovinen, J. *Bioconjugate Chem.* **2002**, *13*, 870−875.

(28)   Poupart, S.; Boudou, C.; Peixoto, P.; Massonneau, M.; Renard, P.-Y.; Romieu, A. *Org. Biomol. C hem.* **2006**, *4*, 4165-4177.

(29)   Constable, E. C.; Handel, R. W.; Housecroft, C. E.; Morales, A. F.; Flamigni, L.; Barigelletti, F. *Dalton Trans.* **2003**, 1220-1222.

(30)   Constable, E. C.; Handel, R. W.; Housecroft, C. E.; Morales, A. F. n.; Ventura, B.; Flamigni, L.; Barigelletti, F. *Chem. Eur. J.* **2005**, *11*, 4024 − 4034.

(31)   Constable, E. C.; Morrisa, D.; Carr, S. *New J. Chem.* **1998**, *22*, 287-294.

(32)   Dietrich-Buchecker, C. O.; Sauvage, J. P.; Kintzinger, J. P.; Maltese, P.; Pascard, C.; Guilhem, J. *New J. Chem.* **1992**, *16*, 931 - 942.

(33)   Andres, P. R.; Lunkwitz, R.; Pabst, G. R.; Böhn, K.; Wouters, D.; Schmatloch, S.; Schubert, U. S. *Eur. J. Org. Chem.* **2003**, 3769 - 3776.

(34)   Collin, J.-P.; Guillerez, S.; Sauvage, J.-P.; Barigelletti, F.; Cola, L. D.; Flamigni, L.; Balzani, V. *Inorg. Chem.* **1991**, *30*, 4230-4238

(35)   Haider, J. M.; Chavarot, M.; Weidner, S.; Sadler, I.; Williams, R. M.; Cola, L. D.; Pikramenou, Z. *Inorg. Chem.* **2001**, *40*, 3912-3921.

(36)   Jiang, Q.; Zhu, J.; Zhang, Y.; Xiao, N.; Guo, Z. *Biometals* **2009**, *22*, 297-305.

(37)   Tang, B.; Yu, F.; Li, P.; Tong, L.; Duan, X.; Xie, T.; Wang, X. *J. AM. CHEM. SOC.* **2009**, *131*, 3016-3023.

(38)   Alcock, N. W.; Barker, P. R.; Haider, J. M.; Hannon, M. J.; Painting, C. L.; Pikramenou, Z.; Plummer, E. A.; Rissanen, K.; Saarenketo, P. *J. Chem. Soc ., Dalton Trans.,* **2000**, 1447-1461.

(39)   Bemdtseon, A. *J. Phys. Statues Solidi B* **1979**, *93*, K103.

(40)   Yesildaˇg, A.; Ekinci, D. *Electrochimica Acta* **2010**, *55*, 7000-7009.

(41)   Lashgari, K.; Kritikos, M.; Norrestam, R.; Norrby, T. *Acta Crystallogr.* **1999**, *C55*, 64-67.

(42)   Collin, J.-P.; Dixon, I. M.; Sauvage, J.-P.; Williams, J. A. G.; Barigelletti, F.; Flamigni, L. *J. Am. Chem. Soc.* **1999**, *121*, 5009-5016.

(43)   Flamigni, L.; Ventura, B.; Barigelletti, F.; Baranoff, E.; Collin, J.-P.; Sauvage, J.-P. *Eur. J. Inorg. Chem.* **2005**, 1312-1318.

CHAPTER 5

Surface Active Metallocyclodextrin Complexes and the Host-Guest Interactions on the Surface

5.1. Introduction

We investigated the properties of the modified ruthenium and osmium complexes attached to the gold surfaces and reported very good photophysical properties of the monolayers (Chapter 3). Furthermore we are interested in investigating the interactions of host-guest systems and their photophysical properties such as energy transfer, when these components are immobilised on surfaces.

In order to develope molecular energy-conversion systems and wires in macromolecular systems, employment of multi-electronic metal centres in one single supramolecular structure is necessary.[1-7] The procedures for covalent linkage of metallic building blocks are usually complex reactions and also result in poor yields.[1,2] In contrast, control of photoinduced processes are simply possible in non-covalently assembled systems and various photoactive components.[3,4,6]

In order to achieve this, cyclodextrins were employed as receptors and different metalloguests were designed so that two or more metal centres could be brought together in a self-assembled, non-covalent fashion.[3,4,6] In these systems, simple addition of both host and guest components in aqueous solutions brings the donor and acceptor units together in one supramolecular structure. Photoinduced energy or

electron transfer is expected to occur via non-covalent bonds between the two units. In this way, back electron transfer is also limited since there is no direct linkage via covalent bonds. The host-guest interactions are well understood in our group and there are several reports of the photo-induced processes of such supramolecular systems which have been reviewed in more detail in the introduction chapter.[3,4,6,8] Based on these studies we are now interested in studying photo-induced processes between metal units assembled on the gold surfaces through non-covalent interactions.
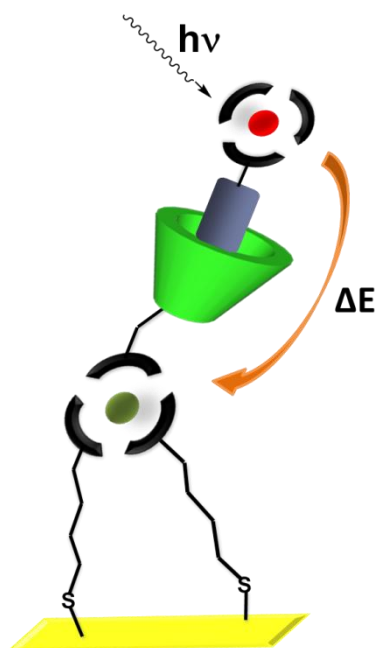
Scheme 5.1 Supramolecular assembly, employing cyclodextrins and metalloguests.

As a result, the focus of the project turned to the synthesis of 2,2'-bipyridine ligands, bearing two cyclodextrin groups in either the 5,5'-positions or the 4,4'-positions. These new ligands have the advantages of having two cyclodextrin receptor units on

a single ligand and a symmetric design which will prevent the formation of the *fac-* and *mer-* geometric isomers that occur with complexes of asymmetrically substituted bipyridines. The ruthenium and osmium complexes of such ligands were synthesised and the photophysical and surface properties of their monolayers were investigated.

Here we have studied the participation of the complexes **16** and **17**, bearing hydrophobic biphenyl tails that ensure high binding constants in the cyclodextrin cavity, in a non-covalent energy transfer process to Ru(II) and Os(II) metallo-cyclodextrin hosts. Later we investigated the communication and energy transfer process between metal centres when immobilised on gold surface.

5.2. Results and discussion

5.2.1. Synthesis of the ruthenium and osmium complexes

The desired metal complexes to attach to the gold surface contain two bipyridine ligands with the spacer and surface active ends (4,4'-bpysac), and one bipyridine ligand with two cyclodextrin attached in either 5,5'-position (5,5'-bpyCD) or 4,4'-position (4,4'-bpyCD) (Scheme 5.2).
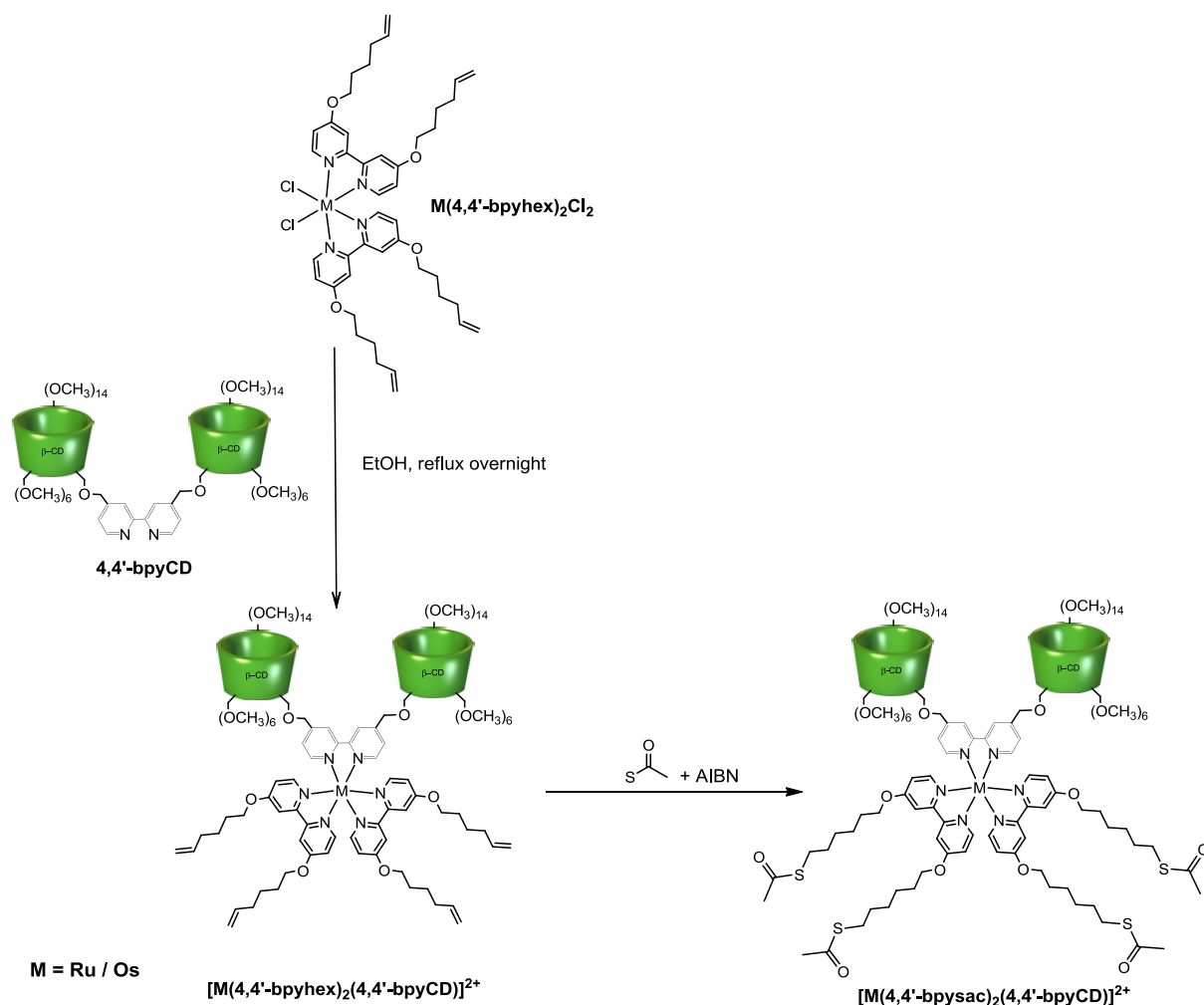
Scheme 5.2 Synthesis route of [M(4,4'-bpysac)$_2$(4,4'-bpyCD)]$^{2+}$, M = Ru/ Os.

In order to attach the cyclodextrin units to the bipyridine molecules we need to selectively functionalise the β-cyclodextrin at one hydroxyl position and so it is necessary to protect the remaining twenty groups. The most frequently used strategy for this goal is protection of one hydroxyl group with a labile protecting group, followed by protection of the remaining groups with an orthogonal protecting group and subsequent removal the first protecting group. This was accomplished following the method of Chen and Bradshaw,[9] in which the cyclodextrin is selectively

protected at one hydroxyl group with *tert*-butyl-dimethyl-silylchloride and imidazole in DMF. When a constant mixture of unreacted cyclodextrin, mono-silylated and other higher silylated products is present, the remaining hydroxyl groups are deprotonated with sodium hydride and methylated with methyl iodide. The silyl protecting group is then removed using ammonium fluoride, and the product isolated in 30% yield after column chromatography on silica (Scheme 5.3).
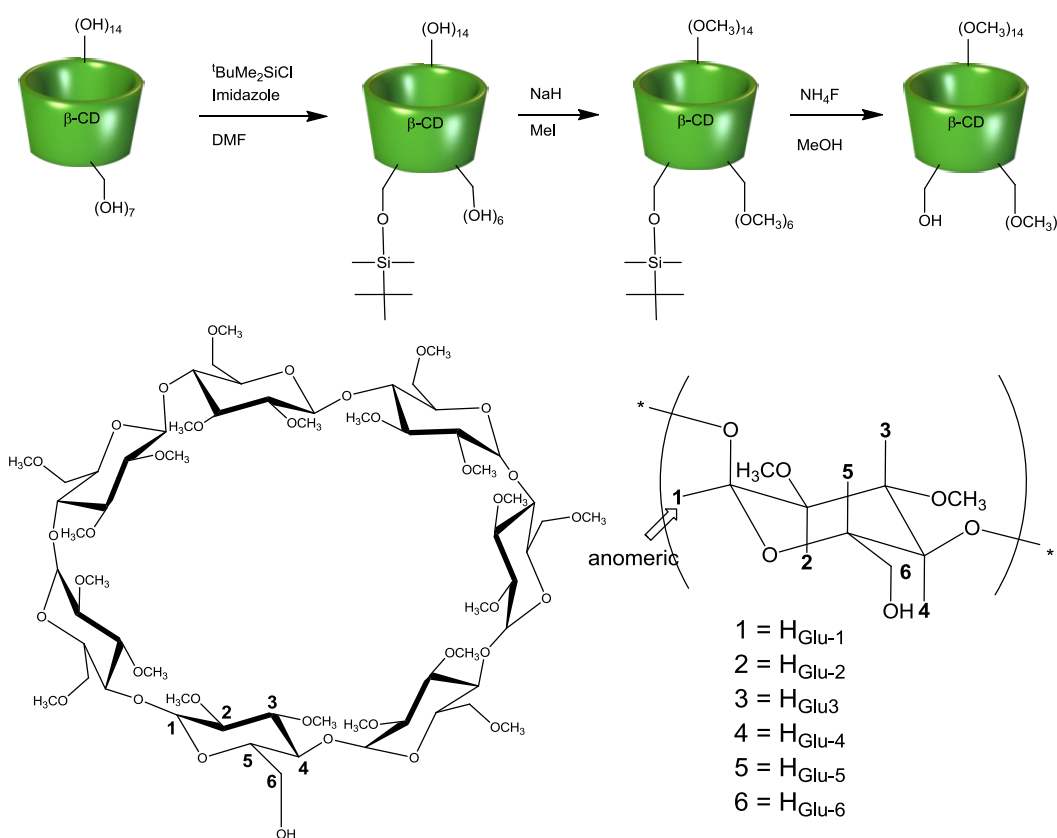
Scheme 5.3 Synthetic route to monohydroxy permethylated β-cyclodextrin.

The product was characterised by NMR and mass spectrometry. The ^{1}H NMR spectrum shows a characteristic multiplet for the anomeric protons around 5 ppm,

which agrees with the published data and spectra recorded previously. The ^{13}C NMR spectrum of the product also agrees with the published data.[9] This shows a CH_2 peak at 61.7 ppm that corresponds to the C_{Glu-6} for the remaining hydroxyl group and the rest of the C_{Glu-6} carbon signals appearing between 71.2 ppm and 71.6 ppm. Other NMR spectral features include the anomeric carbon atom signal at 98.9 ppm. The three sets of methoxy carbons resonate between 58.2-58.7 ppm (3-OMe), 58.9-59.1 (6-OMe) and 61.0-61.6 ppm (2-OMe). The MALDI-TOF spectrum of monohydroxy permethylated β-cyclodextrin shows a peak at m/z = 1437.8, corresponding to the singly charged sodium adduct.

The 5,5'-bpyCD ligand has previously been synthesised in our group.[10] In order to prepare the desired ligand, bromoalkyl-bipyridine has been employed as a building block towards our synthetic assemblies. Synthesis of bromoalkyl bipyridines has previously been achieved by radical halogenation, using NBS in carbon tetrachloride.[11] A route to 5,5'-bis(bromomethyl)-2,2'-bipyridine is shown in Scheme 5.4.
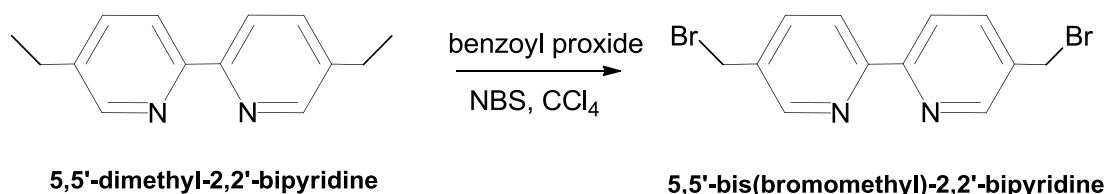
Scheme 5.4 Synthesis of 5,5'-bis(bromomethyl)-2,2'-bipyridine.

The product characterisation agreed with data published in the literature.[11] TLC was employed to monitor the reaction and time of reaction was optimised to 60 min, to avoid the formation of side products which are common in radical reactions (Scheme 5.5). If reaction time was prolonged for more than 60 min, a second spot appeared on the TLC plate, corresponding to the tribromo side product. This side product can easily be identified by ^{1}H NMR spectroscopy from the characteristic signal at 6.72 ppm that corresponds to the H_7 protons.
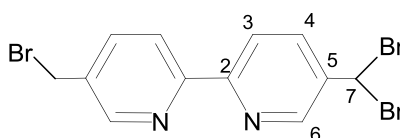
Scheme 5.5 Common side product for prolonged reaction time.

Later 5,5'-bis(bromomethyl)-2,2'-bipyridine has been used to synthesise 5,5'-bpyCD ligand using Williamson ether synthesis conditions. Deprotection of the remaining hydroxyl group of β-CD-OH is achieved using sodium hydride in THF and the resulting anion is reacted with 5,5'-bis(bromomethyl)-2,2'-bipyridine (Scheme 5.6).
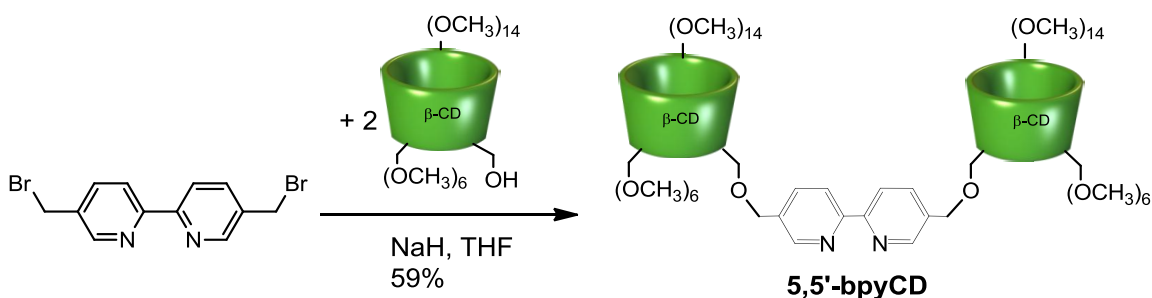
Scheme 5.6 Synthetic route to 5,5'-bpyCD.

The ligand 5,5'-bpyCD was initially characterised by ^{1}H NMR (Figure 5.1) and mass spectrometry and was further characterised by ^{13}C, HSQC and COSY NMR spectroscopy, and all data were in agreement with the literature.[10] Substitution of the cyclodextrin is confirmed by the disappearance of the bromo-methyl signal at 4.56 ppm and the appearance of a signal at 4.61 ppm with an AB coupling pattern that integrates to four protons (two for each side), which exists as the $H_{7,7'}$ protons. The aromatic region shows the expected signals for bipyridines substituted on the 5,5'-positions, a singlet at 8.55 ppm which represents $H_{6,6'}$, followed by a doublet at 8.28 ppm for $H_{3,3'}$ and a broad doublet at 7.76 ppm of $H_{4,4'}$. The anomeric positions on the cyclodextrins appear as the multiplet at 5.02-5.16 ppm (14 protons), the overlap arising from the non-equivalence of the glucose units in the asymmetrically substituted cyclodextrin. The change in signal pattern (all doublets overlap) from the starting material also confirms that the cyclodextrin has been substituted. The remainder of the cyclodextrin protons appear in the multiplet between 3.87 and 3.10 ppm. The multiplet centred at 4.01 corresponds to one of the diastereotopic protons of the 6-position on the cyclodextrin.
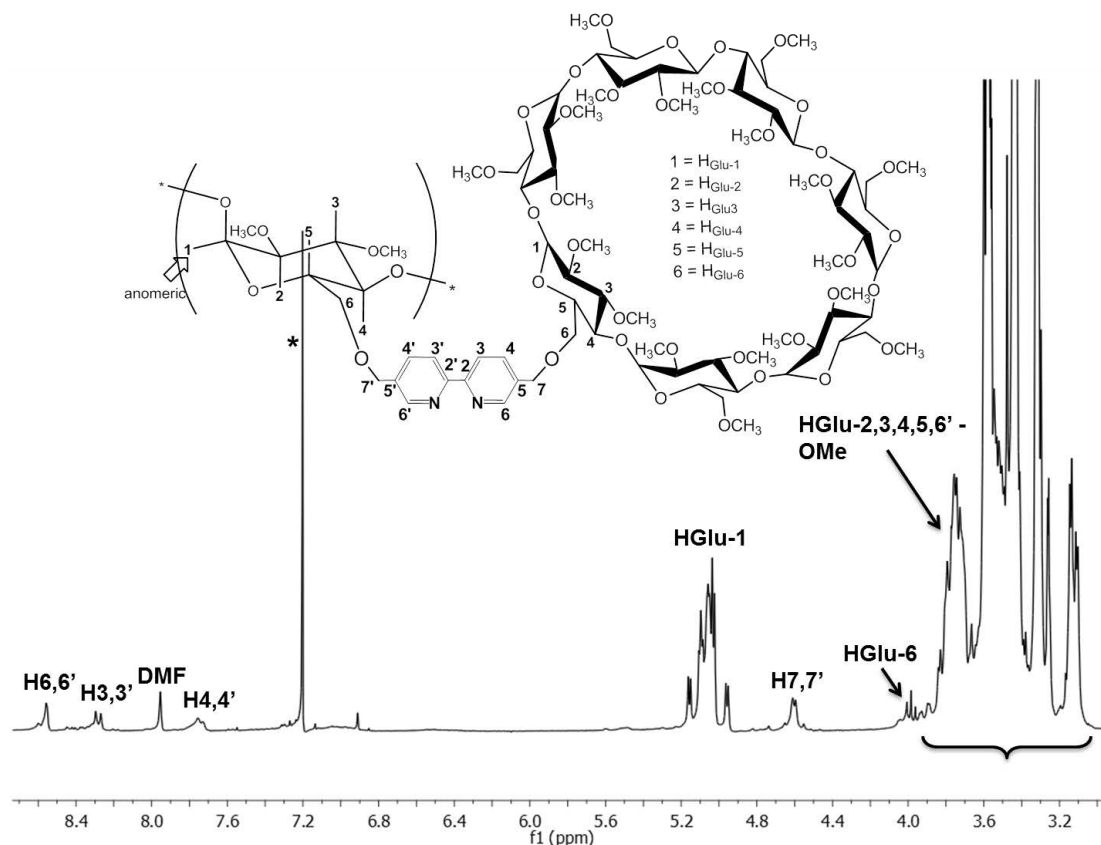
Figure 5.1 300 MHz ^{1}H NMR (CDCl$_3$) of 5,5'-bpyCD.

It was discussed in chapter 3 that the substitution in the 4,4'-positions of the bipyridine ligands enhance the photophysical properties of the ruthenium and osmium complexes. As the result, the 4,4'-bpyCD is potentially the better ligand to improve the photophysical properties of the complexes.

The radical halogenation of the 4,4'-dimethyl-2,2'-bipyridine resulted in a mixture which is very difficult to purify the desired fraction. A more straightforward method of halogenation of bipyridines is shown in scheme 5.7.[12,13] The 4,4'-dimethyl-2,2'-bipyridine is deprotonated with LDA to give a reactive lithium salt, which is trapped using TMS chloride. The deprotected silylated bipyridine serves as an 'anion equivalent' and can react with a brominating or chlorinating agents. We used

Cl$_3$CCCl$_3$ and CsF to get 4,4'-dichloromethyl-2,2'-bipyridine as the required ligand. It is interesting to note that it proves impossible to trap the lithiated species directly with common brominating and chlorinating agents.[12,14]
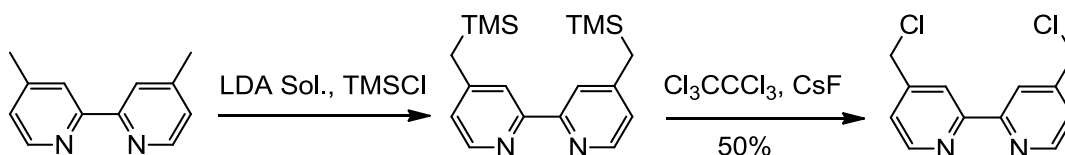
Scheme 5.7 Synthetic route to 4,4'-dichloromethyl-2,2'-bipyridine.

The 4,4'-dichloromethyl-2,2'-bipyridine was characterised by ^{1}H NMR spectroscopy, which agreed with published literature.[12] The aromatic region of the ^{1}H NMR spectrum showed three signals, a doublet at 8.65 corresponding to the H$_{6,6'}$, a singlet at 8.41 arising from H$_{3,3'}$ and a doublet at 7.34 from H$_{5,5'}$. In the aliphatic region, the signal of the H$_{7,7'}$ of the methyl group in the starting material shifts from 2.40 ppm to 2.16 ppm arising from methylene group in silylated bipyridine, and also contains a singlet at 0 ppm corresponding to the nine protons of the TMS group. The methylene signal shifts to 4.60 ppm when the chlorination is completed. Some side products of 4-dichloromethyl-4'-chloromethyl-2,2'-bipyridine also forms which can be easily detected with ^{1}H NMR by its singlet peak at 6.74 ppm for H$_7$.[12]

We applied Williamson ether synthesis conditions to synthesise the final 4,4'-bpyCD ligand, using 4,4'-dichloromethyl-2,2'-bipyridine and β-CD-OH (Scheme 5.8). The product requires careful purification as some mono-substituted fractions can also form during the reaction. Purification was achieved by size exclusion column chromatography, on biobeads S-X3 and DCM as the solvent. Bio-Beads S-X beads

are a series of porous and cross-linked polystyrene polymers used in organic solvents in order to gel permeation separations of hydrophobic materials. Applications of these non-aqueous spherical beads are same as aqueous gels, except that they swell organic solvents during the separation.
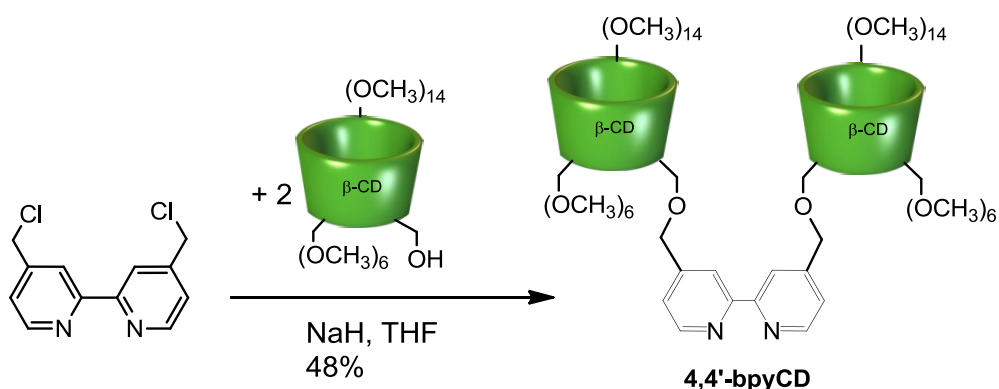
Scheme 5.8 Synthetic route to 4,4'-bpyCD.

The ligand 4,4'-bpyCD was characterised by ^{1}H, ^{13}C, HSQC and COSY NMR spectroscopy and mass spectrometry. In the ^{1}H NMR spectrum, the disappearance of the bromo-methyl signal at 4.60 ppm and the appearance of a signal at 4.68 ppm which integrates to four protons (two for each side) as the $H_{7,7'}$ protons, confirms the substitution by the cyclodextrins (Figure 5.2). In the aromatic region, the pattern signals of 4,4'-substituted bipyridines can be observed, a doublet at 8.57 ppm which represents $H_{6,6'}$ followed by a singlet at 8.30 ppm for $H_{3,3'}$ and a broad doublet at 7.36 ppm of $H_{5,5'}$. The signals for the anomeric positions on the cyclodextrins are overlapping because of the non-equivalence of the glucose units in the asymmetrically substituted cyclodextrin, and appear as a multiplet at 5.10 ppm (14

protons). The remainder of the cyclodextrin protons appear in the multiplet between 3.10 and 3.80 ppm. Additionally the multiplet at 4.11 ppm corresponds to one of the diastereotopic protons of the 6-position on the cyclodextrin.
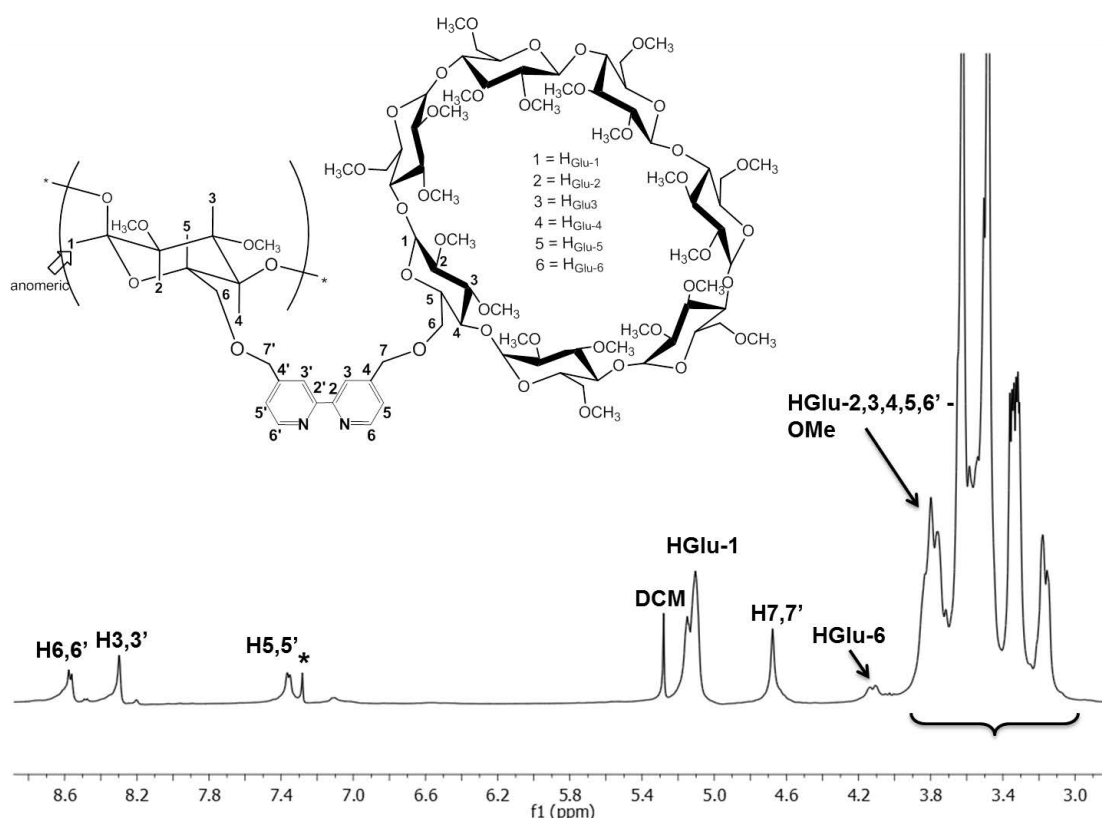
Figure 5.2 300 MHz ^{1}H NMR (CDCl$_3$) of 4,4'-bpyCD.

Evidence of substitution of 4,4'-bpyCD is also confirmed by the ^{13}C NMR spectrum (Figure 5.3). Five signals can be observed in the aromatic section between 119 and 156 ppm, corresponding to two quaternary and three CH signals. The anomeric carbon atoms appear as a broad singlet at 98.9 ppm. Other peaks of interest include three sets of signals for the methoxy substituents between 61.6 and 58.4, ppm and the C$_{7,7'}$ methylene atoms resonate at 28.8 ppm. The MALDI-TOF spectrum of 4,4'-

bpyCD shows a peak at *m/z* = 3033 corresponding to the sodium adduct of the product.
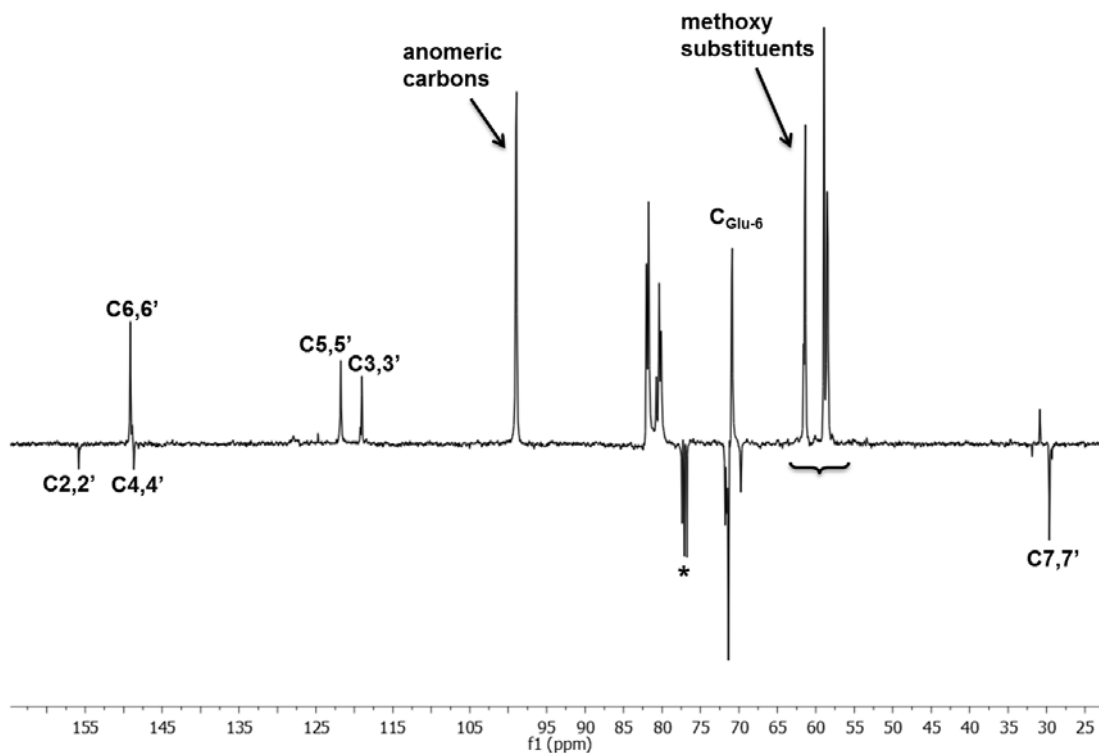
Figure 5.3 100 MHz ^{13}C NMR (CDCl$_3$) of 4,4'-bpyCD.

In order to synthesise the ruthenium-cyclodextrin complexes, the first approach was synthesis of the Ru(4,4'-bpyhex)$_2$Cl$_2$. This was achieved following the general procedure for synthesis of Ru(bpy)$_2$Cl$_2$,[15] reacting the RuCl$_3$.6H$_2$O with two equivalents of 4,4'-bpyhex in DMF in the presence of excess LiCl (Scheme 5.9).
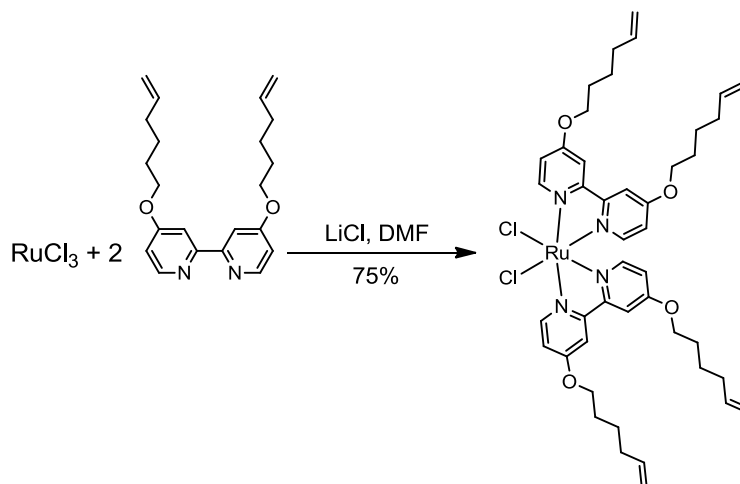
Scheme 5.9 Synthesis route of Ru(4,4'-bpyhex)₂Cl₂.

The Ru(4,4'-bpyhex)$_2$Cl$_2$ was initially characterised by its UV-Vis absorption spectrum which showed two MLCT bands, one centred at 550 nm attributed to π_{Ru} to $\pi^*_{4,4'\text{-bpyhex}}$ transition and another at 370 nm attributed to π_{Ru} to $\pi^*_{Cl^-}$ transition, and an intense $\pi-\pi^*$ band at 280 nm (Figure 5.4). The π_{Ru} to $\pi^*_{4,4'\text{-bpyhex}}$ MLCT band is in fact a broad band split into two bands. This can be explained by the low symmetry around the ruthenium centre and also indicates that the environments around two 4,4'-bpyhex ligands are slightly different (figure A5.8)

The desired compound was also confirmed by ^{1}H NMR and mass spectrometry. The MALDI-TOF spectrum shows a peak at *m/z* = 877.7 corresponding to the Ru(4,4'-bpyhex)$_2$Cl$_2$ molecular mass and the electrospray mass spectrometry shows a peak at *m/z* = 869.1 arising from Ru(4,4'-bpyhex)$_2$(OMe)$_2$.
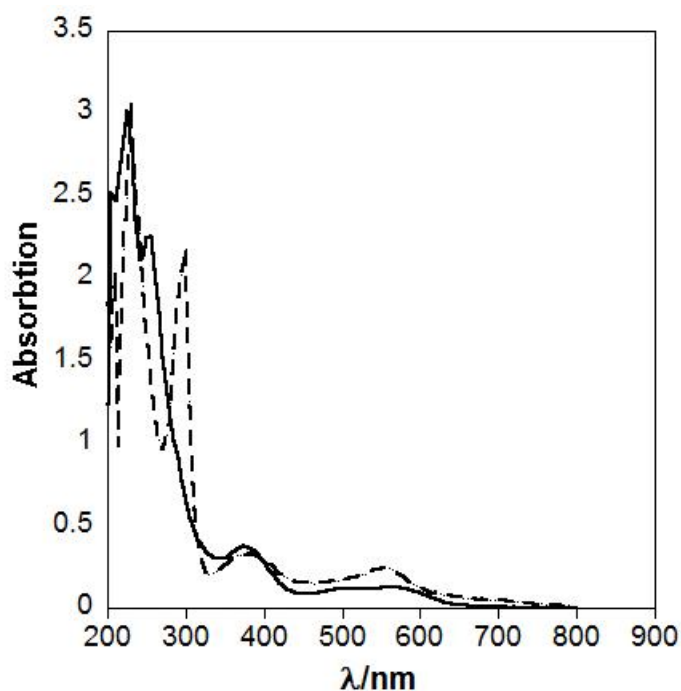
Figure 5.4 Absorption spectrum of Ru(4,4'-bpyhex)$_2$Cl$_2$ (solid line) and Ru(bpy)$_2$Cl$_2$ (dashed line) in DCM.

Reaction of Ru(4,4'-bpyhex)$_2$Cl$_2$ with either 5,5'-bpyCD or 4,4'-bpyCD results to the products [Ru(4,4'-bpyhex)$_2$(5,5'-bpyCD)](PF$_6$)$_2$ or [Ru(4,4'-bpyhex)$_2$(4,4'-bpyCD)](PF$_6$)$_2$ respectively. Both complexes were isolated as their PF$_6^-$ salt and purified through size exclusion columns, sephadex LH20 in chloroform. Sephadex LH20 is made from hydroxypropylated dextran beads that have been cross-linked to yield a polysaccharide network and can be used for gel permeation separations in both water and organic solvents.

Both complexes were characterised by mass spectrometry, ^{1}H NMR spectroscopy and photophysical studies. The ^{1}H NMR spectra of the complexes are less straightforward to analyse as the aromatic peaks, as well as other signals, are very

broad which makes any change in multiplicity or shift hard to identify. This arises from the existence of two big cyclodextrin groups in the structure of the complexes. Complexation of the CD ligands is evident due to the shift of the $H_{6,6'}$ of 4,4'-bpyCD or 5,5'-bpyCD from 8.6 ppm in free ligand to 7.7 ppm in the complex, and also the shifts of H_6 (8.7 ppm) and $H_{6'}$ (9.5 ppm) of Ru(4,4'-bpyhex)$_2$Cl$_2$ to 8.6 ppm in the ^{1}H NMR spectrum of the final complex. All aliphatic protons, attributed to the protons of the cyclodextrin core and protons of the aliphatic chains in 4,4'-bpyhex ligand are shifted up-field (Figure 5.5). Additionally the ratio of integrals of the aromatic area to the cyclodextrin region confirms that the complex has formed with two cyclodextrins around the ruthenium core and no ligand dissociation has taken place.
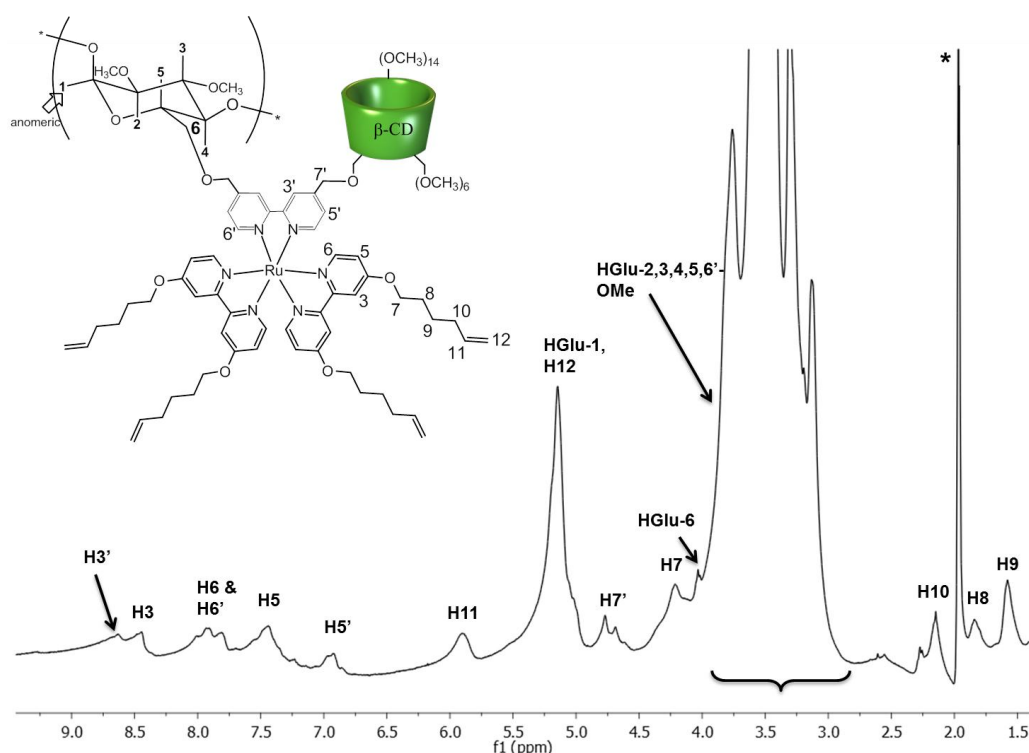
Figure 5.5 400 MHz ^{1}H NMR spectrum (CD$_3$CN) of [Ru(4,4'-bpyhex)$_2$(4,4'-bpyCD)](PF$_6$)$_2$.

Figure 5.6 400 MHz ^{1}H NMR spectrum (CD$_3$CN) of [Ru(4,4'-bpyhex)$_2$(5,5'-bpyCD)](PF$_6$)$_2$.

In order to achieve surface active ruthenium complexes, the [Ru(4,4'-bpyhex)$_2$(4,4'-bpyCD)](PF$_6$)$_2$ was reacted with thioacetic acid and AIBN following the general procedure of transferring the double bond to the SAc group (see chapter 3), and formation of the resulting product [Ru(4,4'-bpysac)$_2$(4,4'-bpyCD)](PF$_6$)$_2$ was confirmed by mass spectrometry.

In order to synthesise the analogous osmium complex, the first step was the synthesis of Os(4,4'-bpyhex)$_2$Cl$_2$ following the general procedure for Os(bpy)$_2$Cl$_2$ synthesis[16]. This is the reaction of (NH$_4$)OsCl$_6$ and two equivalents of 4,4'-bpyhex in ethylene glycol (Scheme 5.10).
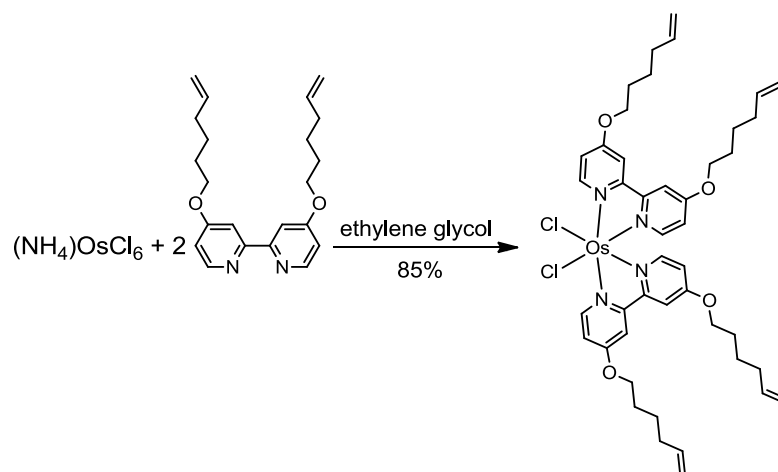
Scheme 5.10 Synthesis route of Os(4,4'-bpyhex)₂Cl₂.

The resulting compound Os(4,4'-bpyhex)$_2$Cl$_2$ was characterised by ^{1}H NMR, ^{13}C NMR spectroscopy and mass spectrometry. The electrospray mass spectrum of Os(4,4'-bpyhex)$_2$Cl$_2$ shows a peak at 966.3 assigned to [M]$^+$.
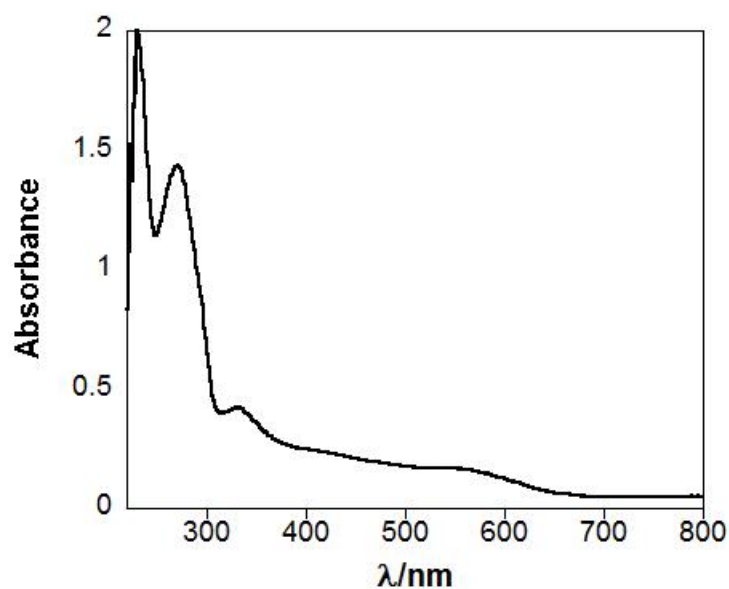
Figure 5.7 Absorption spectrum of Os(4,4'-bpyhex)₂Cl₂ in DCM.

Os(4,4'-bpyhex)$_2$Cl$_2$ and 4,4'-bpyCD were suspended in EtOH (4 mL) in a sealed tube and heated at 100 °C for 20 hours in the microwave to yields the [Os(4,4'-bpyhex)$_2$(4,4'-bpyCD)](PF$_6$)$_2$. The complex was isolated as the hexafluorophosphate salt and purified by size exclusion chromatography, using sephadex LH20 in chloroform. The complex was characterised by mass spectrometry and ^{1}H NMR spectroscopy and photophysical studies were performed. The bulky cyclodextrins cause broadening of the peaks in ^{1}H NMR spectrum which makes it difficult to analyse any changes in multiplicity or identify the shifts. However, complexation is evident due to the shift of the H$_{6,6'}$ protons of 4,4'-bpyCD from 8.6 ppm in the free ligand, to 7.7 ppm in the complex. Upfield shifts of all the aliphatic protons are attributed to the protons of the cyclodextrin core and protons of the aliphatic chains in 4,4'-bpyhex ligand (Figure 5.8).
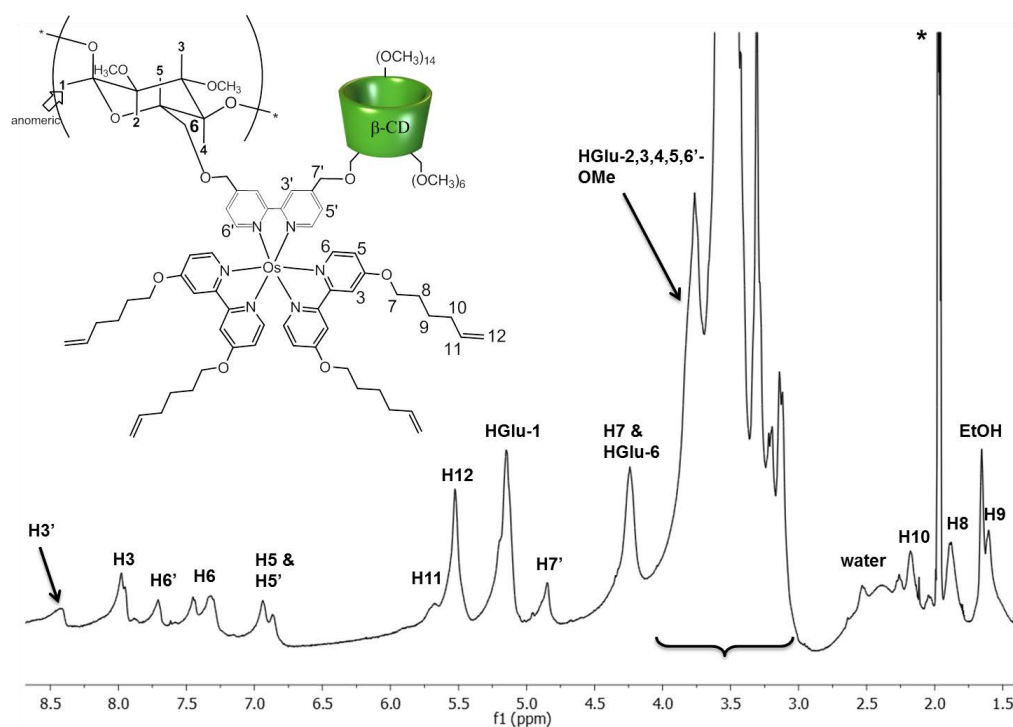
Figure 5.8 400 MHz ^{1}H NMR (CD$_3$CN) of [Os(4,4'-bpyhex)$_2$(4,4'-bpyCD)](PF$_6$)$_2$.

Finally the olefin terminal groups were converted to surface active SAc groups by a free radical reaction with thioacetic acid, using AIBN as the initiator. The disappearance of the double bond was monitored by ^{1}H NMR spectroscopy.

5.2.2. Photophysical properties of the ruthenium and osmium complexes in solution

The photophysical properties of both ruthenium complexes were investigated in solution (water/acetonitrile 90:10) and in powder form. The solution of [Ru(4,4'-bpysac)$_2$(4,4'-bpyCD)](PF$_6$)$_2$ exhibits an absorption spectrum in which the visible region is dominated by a broad band at 490 nm ([1]MLCT) and two further absorptions in the UV region, at 220 nm and 285 nm (LC), which are typical for ruthenium tris-bipyridyl complexes. The [1]MLCT band is red-shifted in the powder spectrum and appears at 495 nm. In comparison with [Ru(bpy)(4,4'-bpysac)$_2$](PF$_6$)$_2$, the most similar compound with no cyclodextrin (chapter 3), the [1]MLCT bands of the solution and powder spectra are red-shifted.

Similarly, the absorption spectrum of the [Ru(4,4'-bpyhex)$_2$(5,5'-bpyCD)](PF$_6$)$_2$ in water/acetonitrile (90:10) solution displays features which are typical of ruthenium (II) complexes. These consist of [1]MLCT absorptions at 467 nm, and two further ligand centred absorptions with maximum at 290 nm and 280 nm. The [1]MLCT absorption is red-shifted in comparison with parent [Ru(bpy)$_3$]Cl$_2$ (Figure 5.9). The [1]MLCT band in

the powder spectrum appears at 475 nm which is red-shifted in comparison with the solution spectrum.
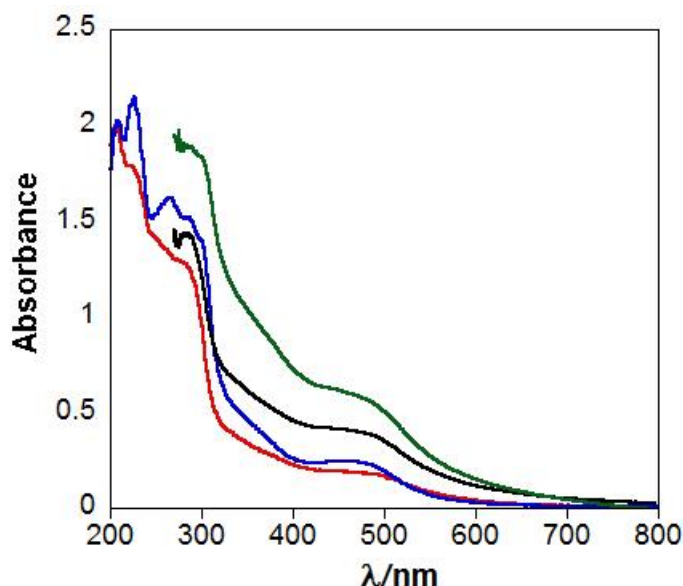
Figure 5.9 Absorption spectra of [Ru(4,4'-bpysac)$_2$(4,4'-bpyCD)](PF$_6$)$_2$ (C = 1.0 × 10^{-5} M, red) and [Ru(4,4'-bpysac)$_2$(5,5'-bpyCD)](PF$_6$)$_2$ (C = 1.2 × 10^{-5} M, blue) in MeCN/Water (10:90), [Ru(4,4'-bpysac)$_2$(4,4'-bpyCD)](PF$_6$)$_2$ powder (black) and [Ru(4,4'-bpysac)$_2$(5,5'-bpyCD)](PF$_6$)$_2$ (green) powder.

[Ru(4,4'-bpysac)$_2$(4,4'-bpyCD)](PF$_6$)$_2$ in a water/acetonitrile (90:10) solution displays luminescence (φ = 3.5 × 10^{-3}) from the ^{3}MLCT state at 660 nm, when excited at 490 nm at room temperature (Figure 5.10). Although the quantum yield of this emission (3.5 × 10^{-3}) is much lower than the parent complex [Ru(bpy)(4,4'-bpysac)$_2$](PF$_6$)$_2$, the lifetime is relatively high (295 ns) in comparison with aerated acetonitrile solution of [Ru(bpy)(4,4'-bpysac)$_2$](PF$_6$)$_2$ and increases to 383 ns in deaerated solution, suggesting that bulky cyclodextrins partially protect the ruthenium centre from oxygen quenching.

The emission spectra of the powder samples were also recorded. The emission maximum of the [Ru(4,4'-bpysac)$_2$(4,4'-bpyCD)](PF$_6$)$_2$, at 654 nm, was observed which is 6 nm shifted to the higher energy in comparison with the one in water/acetonitrile (90:10) solution.

The excitation spectra of both water/acetonitrile (90:10) solution and powder recorded for [Ru(4,4'-bpyhex)$_2$(4,4'-bpyCD)](PF$_6$)$_2$, monitoring the ^{3}MLCT band at 660 nm, is present in Figure 5.10. The excitation profile of solution shows bands with λ_{max} = 490, 370, 330 and 285 nm, corresponding to the ^{1}MLCT, ^{3}MC and ^{1}LC bands in the absorption spectra of the complex. Small red-shifts can be observed for ^{1}MLCT band of the powder compared to the solution absorption spectrum.
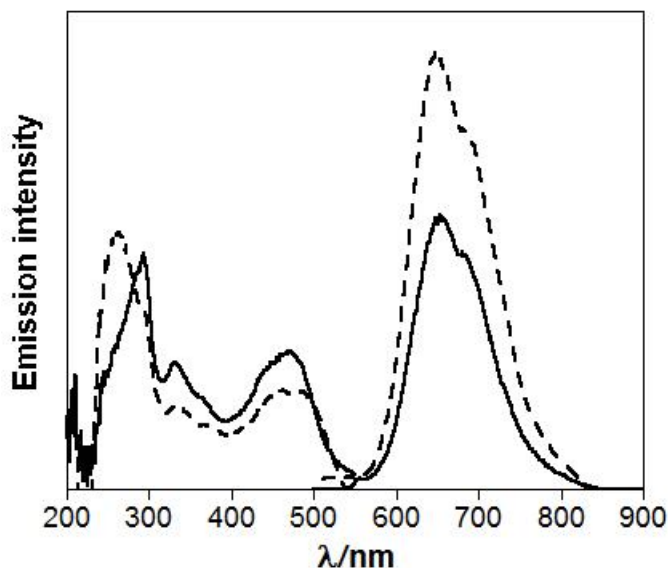
Figure 5.10 Emission and excitation spectra of [Ru(4,4'-bpyhex)$_2$(4,4'-bpyCD)](PF$_6$)$_2$ in MeCN/Water (10:90) (C = 1.0 × 10^{-5} M, solid line) and the powder (dashed line) , λ_{ex} = 490 nm and λ_{em} = 660 nm.

In the case of [Ru(4,4'-bpyhex)$_2$(5,5'-bpyCD)](PF$_6$)$_2$, excitation into the ^{1}MLCT state leads to emission ($\varphi = 2.8 \times 10^{-3}$) from the lowest triplet state (^{3}MLCT) with a maximum at 655 nm in water/acetonitrile (90:10) solution. The ruthenium complex shows significantly red-shifted MLCT states, in comparison to [Ru(bpy)$_3$]Cl$_2$. The excitation spectrum of [Ru(4,4'-bpyhex)$_2$(5,5'-bpyCD)](PF$_6$)$_2$ complex was recorded in water/acetonitrile (90:10), monitoring the ^{3}MLCT band at 655 nm (Figure 5.11). The excitation profile shows bands with λ_{max} = 467, 360, 340 and 310 nm, corresponding to the ^{1}MLCT, ^{3}MC and ^{1}LC bands in the absorption spectra of the complex.

The powder emission spectrum is very weak. This makes this complex a poor candidate for surface studies and as a result no further investigation on photophysical characterisation of powder and monolayer samples of this complex were performed.
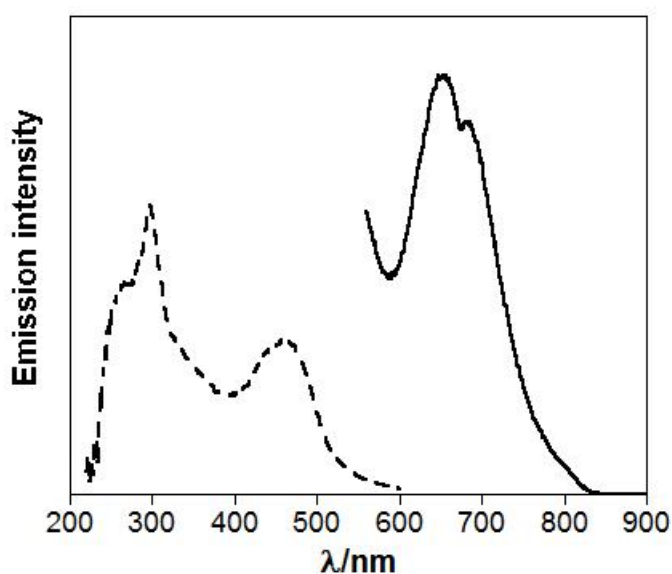
Figure 5.11 Emission spectrum (solid line) and excitation spectrum (dashed line) of [Ru(4,4'-bpyhex)$_2$(5,5'-bpyCD)](PF$_6$)$_2$ in MeCN/Water (10:90), C = 1.2 × 10^{-5} M, λ_{ex} = 467 nm and λ_{em} = 655 nm.

The absorption spectrum of [Os(4,4'-bpyhex)$_2$(4,4'-bpyCD)](PF$_6$)$_2$ in water/acetonitrile (90:10) displays a broad band at 650 nm (^{3}MLCT), a band at 508 nm with a shoulder at 485 nm (^{1}MLCT), and two further absorptions in the UV region at 230 nm and 295 nm (^{1}LC) (Figure 5.12). A ^{3}MC band at 370 nm is also observed. Comparison of the UV-Vis spectrum of [Os(4,4'-bpyhex)$_2$(4,4'-bpyCD)](PF$_6$)$_2$ with the [Os(bpy)$_2$(4,4'-bpysac)](PF$_6$)$_2$, the most similar compound with no cyclodextrin (Chapter 3), reveals a significant red-shift for the ^{1}MLCT bands of the solution and powder spectra.
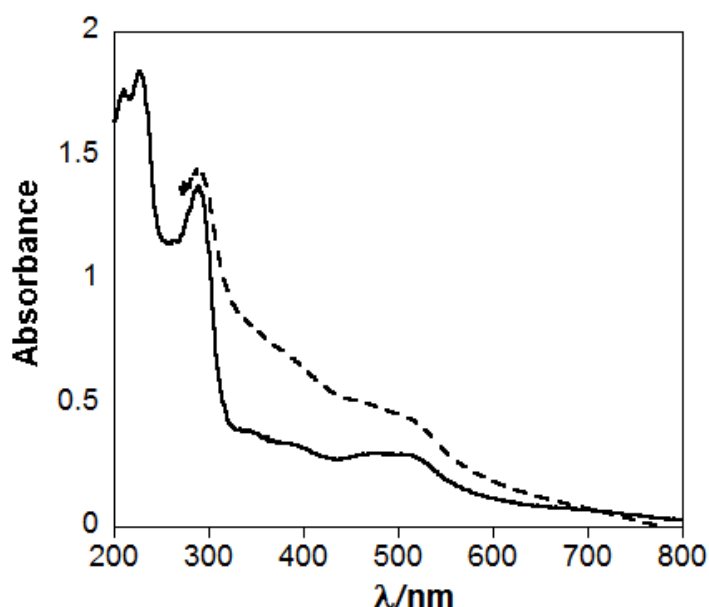
Figure 5.12 Absorption spectrum of [Os(4,4'-bpyhex)$_2$(4,4'-bpyCD)](PF$_6$)$_2$ in MeCN/Water (10:90) (C = 1.2 × 10^{-5} M, solid line) and powder (dashed line).

The solution of [Os(4,4'-bpyhex)$_2$(4,4'-bpyCD)](PF$_6$)$_2$ exhibits some luminescence from the ^{3}MLCT band at 795 nm, when excited at 508 nm at room temperature (Figure 5.13). this is significantly red-shifted in comparison with [Os(bpy)$_3$]Cl$_2$ (723

nm)[17] and the parent complex [Os(bpy)$_2$(4,4'-bpysac)](PF$_6$)$_2$ in acetonitrile. The emission wavelength is almost in the near-infrared region, so the visible detection arm on the emission instrument is not able to collect the full emission spectrum. The visible detection system has the limit at 850 nm. Detection of the emission by the NIR detection arm was also unsuccessful because of high scatterings in that region and weak emission. The powder emission was observed with a maximum at 795 nm. This is blue-shifted in relation to the water/acetonitrile (90:10) solution.

The excitation spectrum of [Os(4,4'-bpyhex)$_2$(4,4'-bpyCD)](PF$_6$)$_2$ complex was recorded in water/acetonitrile (90:10), whilst collecting emission in the ^{3}MLCT band at 795 nm (Figure 5.13). The excitation profile shows bands with λ_{max} = 650, 508, 485, 400 and 350 nm, corresponding to the ^{1}MLCT, ^{3}MC and ^{1}LC bands in the absorption spectrum of the complex.
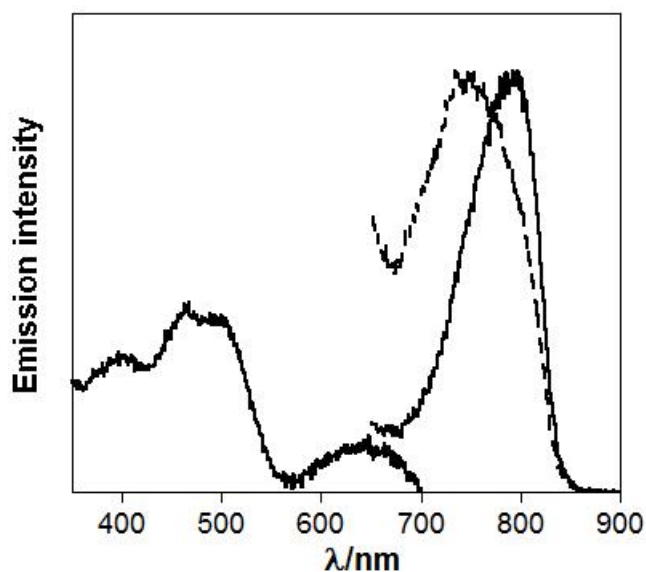
Figure 5.13 Emission and excitation spectra of [Os(4,4'-bpyhex)$_2$(4,4'-bpyCD)](PF$_6$)$_2$ in MeCN/Water (10:90) (C = 1.2 × 10^{-5} M, solid line) and the powder (dashed line), λ_{ex} = 508 nm and λ_{em} = 795 nm.

The maximum of the absorption and emission spectra, the emission quantum yields, as well as results from time-resolved emission of the ruthenium and osmium cyclodetrxin complexes are summarised in Table 5.1. The results for [Ru(bpy)(4,4'-bpysac)$_2$](PF$_6$)$_2$ and [Os(bpy)$_2$(4,4'-bpysac)](PF$_6$)$_2$ are presented for comparison.

Table 5.1 Photopysical properties of Ru^{II} and Os^{II} complexes

	[Ru(bpy)(4,4'-bpysac)$_2$](PF$_6$)$_2$	[Ru(4,4'-bpysac)$_2$(4,4'-bpyCD)](PF$_6$)$_2$	[Ru(4,4'-bpyhex)$_2$(5,5'-bpyCD)](PF$_6$)$_2$	[Os(bpy)$_2$(4,4'-bpysac)](PF$_6$)$_2$	[Os(4,4'-bpyhex)$_2$(4,4'-bpyCD)](PF$_6$)$_2$
λ_{max} (^{1}MLCT) nm, Solution	468	490	467	490	508
ε (^{1}MLCT)	7648	10351	9606	13178	16530
λ_{max} (^{1}MLCT) nm, Powder	445, 490	495	475	496	510
λ_{max} (^{1}MLCT) nm, Surface	445, 495	495		510	490
λ_{max} (^{3}MLCT) nm, Solution	657	660	655	760	795
φ (^{3}MLCT), aerated	7.0×10^{-3}	1.1×10^{-3}	0.8×10^{-3}	1.6×10^{-3}	0.5×10^{-3}
φ (^{3}MLCT), deaerated	2.4×10^{-2}	3.5×10^{-3}	2.8×10^{-3}	2×10^{-3}	2.0×10^{-3}
τ (^{3}MLCT) ns, aerated	100	295	270	21	11
τ (^{3}MLCT) ns, deaerated	409	383	429	21	11
λ_{max} (^{3}MLCT) nm, Powder	640	654		760	780
τ (^{3}MLCT) ns, Powder	358	96		19	
λ_{max} (^{3}MLCT) nm, Surface	615	640		730	
τ (^{3}MLCT) ns, Surface	143	448		21	

5.2.3. [Ru(4,4'-bpysac)$_2$(4,4'-bpyCD)](PF$_6$)$_2$ + 17 host-guest assemblies in solutions and on the gold surfaces

A. An energy transfer study of an iridium(III)-based guest and a ruthenium(II) host centre

A solution of [Ru(4,4'-bpysac)$_2$(4,4'-bpyCD)](PF$_6$)$_2$ and complex **17** (chapter 4) (in 1 ml (90:10) water/ acetonitrile) was prepared by mixing 50 μL of [Ru(4,4'-bpysac)$_2$(4,4'-bpyCD)](PF$_6$)$_2$ (1.0 $\times$ 10^{-4} M in acetonitrile) with 50 μL of complex **17** (3.4 $\times$ 10^{-5} M in acetonitrile). The final concentration was 1.0 $\times$ 10^{-5} M of [Ru(4,4'-bpysac)$_2$(4,4'-bpyCD)](PF$_6$)$_2$ and 3.4 $\times$ 10^{-6} M of complex **17** to give a ratio of 1:3. Two further solutions of 1ml of either [Ru(4,4'-bpysac)$_2$(4,4'-bpyCD)](PF$_6$)$_2$ (1.0 $\times$10^{-5} M) or complex **17** (3.4 $\times$10^{-6} M) were also made for comparison.

To monitor the luminescence of the iridium guest, an excess of the ruthenium complex was used for two reasons: firstly to ensure binding of most of the guests in the cyclodextrin cups. Secondly, using an excess of the host complex also helps to simulate the surface environment where partially filled cyclodextrin cups are more likely to occur. A pictorial description of the excited-state energies of the photoactive metal components is presented in scheme 5.11. The interaction between [Ru(4,4'-bpysac)$_2$(4,4'-bpyCD)](PF$_6$)$_2$ and the metallo-guest **17** was investigated by absorption and steady state emission spectroscopy in water/acetonitrile (90:10) solutions. The photophysical properties of **17** were reported in chapter 4.
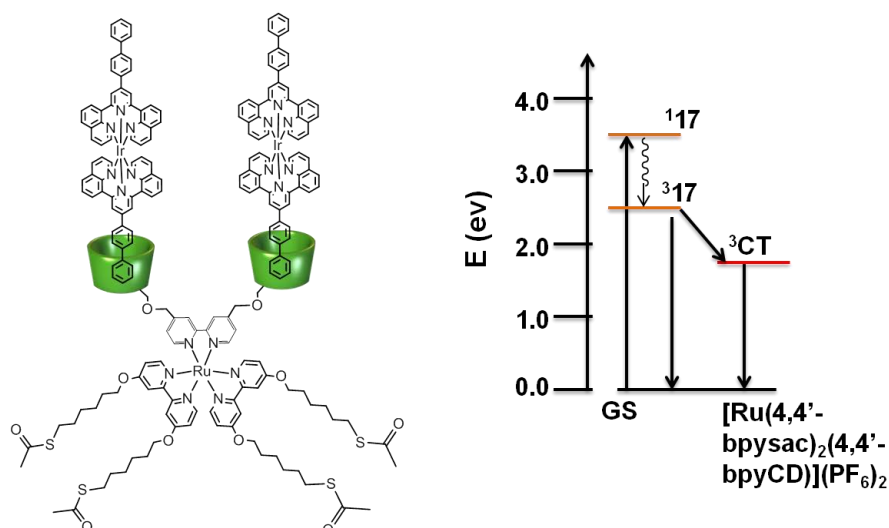
Scheme 5.11 Schematic representation of excited-state energies of the photoactive metal components.

The UV-Vis spectrum of the solution of the mixture of [Ru(4,4'-bpysac)$_2$(4,4'-bpyCD)](PF$_6$)$_2$/ **17** (1.0 × 10^{-5} M: 3.4 × 10^{-6} M) shows peaks at 490 nm, 342 nm and two further absorptions in the UV region, at 285 nm and 220 nm. These peaks are attributed to the ^{1}MLCT band of the complex **17** which appears at 342 nm and to the ^{1}MLCT and LC bands of [Ru(4,4'-bpysac)$_2$(4,4'-bpyCD)](PF$_6$)$_2$, which appear at 490, 285 and 220 nm. The band of **17** at 342 nm is 2 nm red shifted from plain **17** which indicates insertion of the biphenyl in to the cavity.
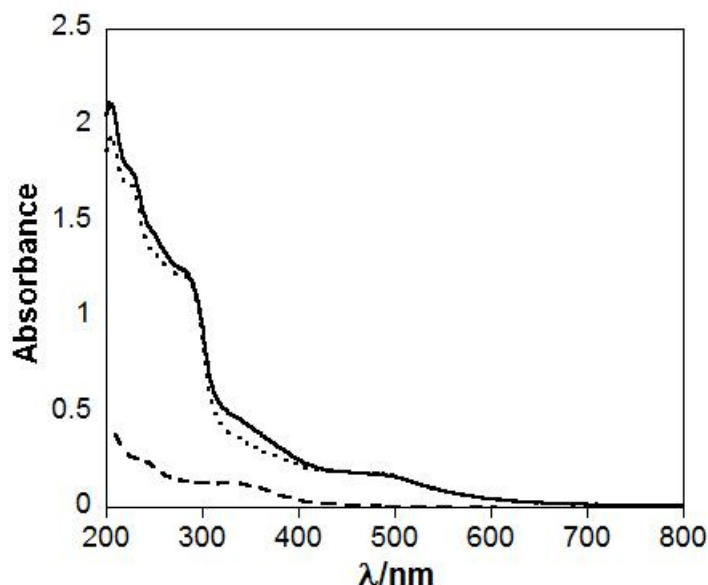
Figure 5.14 UV-Vis spectra of [Ru(4,4'-bpysac)$_2$(4,4'-bpyCD)](PF$_6$)$_2$ (C = 1.0 ×10^{-5} M, dotted line), 17 (C = 3.4×10^{-6} M, dashed line) and the solution of the mixture of [Ru(4,4'-bpysac)$_2$(4,4'-bpyCD)](PF$_6$)$_2$/ 17 (1.0 × 10^{-5} M: 3.4 × 10^{-6} M, solid line), all solutions are in MeCN/Water (10:90).

Upon excitation into the MLCT band of the iridium unit at 350 nm, excited state energy transfer to the ^{3}MLCT level of ruthenium is expected to take place. The emission intensity of the metal centres upon excitation at 350 nm was monitored and a 70 % decrease of the emission intensity from **17** was observed (Figure 5.15). The emission of the **17** is much stronger than that of the [Ru(4,4'-bpysac)$_2$(4,4'-bpyCD)](PF$_6$)$_2$ complex and covers the ruthenium emission region, therefore it is difficult to monitor the increase of the emission intensity of the ruthenium complex. The excitation spectrum of the solution of the mixture of [Ru(4,4'-bpysac)$_2$(4,4'-bpyCD)](PF$_6$)$_2$/ **17** (1.0 × 10^{-5} M: 3.4 × 10^{-6} M) shows a huge peak at 342 nm which is attributed to the absorption of complex **17** confirming the energy transfer process and

indicates that the emission signals are arising mainly from the ^{3}MLCT band of iridium complex (Figure 5.16).
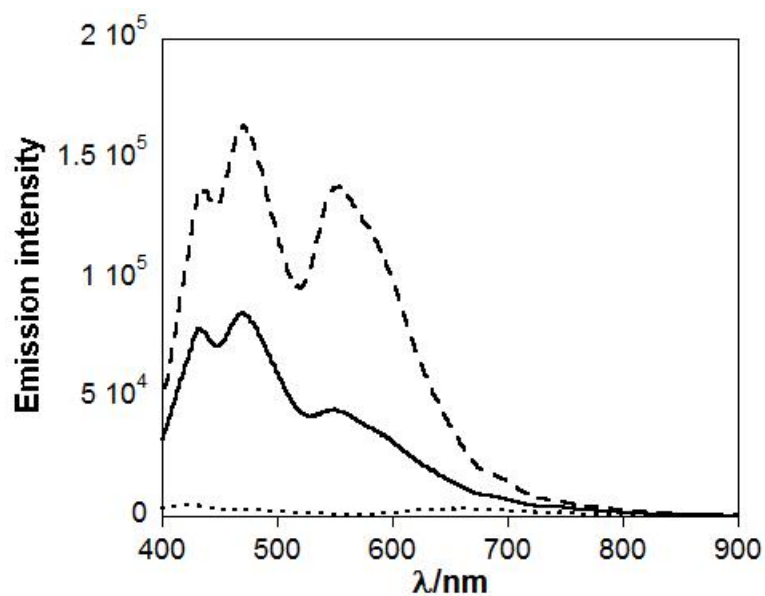
Figure 5.15 Emission spectra of [Ru(4,4'-bpysac)$_2$(4,4'-bpyCD)](PF$_6$)$_2$ (C = 1.0 ×10^{-5} M, dotted line), 17 (C = 3.4 ×10^{-6} M, dashed line) and the solution of the mixture of [Ru(4,4'-bpysac)$_2$(4,4'-bpyCD)](PF$_6$)$_2$/ 17 (1.0 × 10^{-5} M: 3.4 × 10^{-6} M, solid line), all solutions are in MeCN/Water (10:90), λ_{ex} = 350 nm.
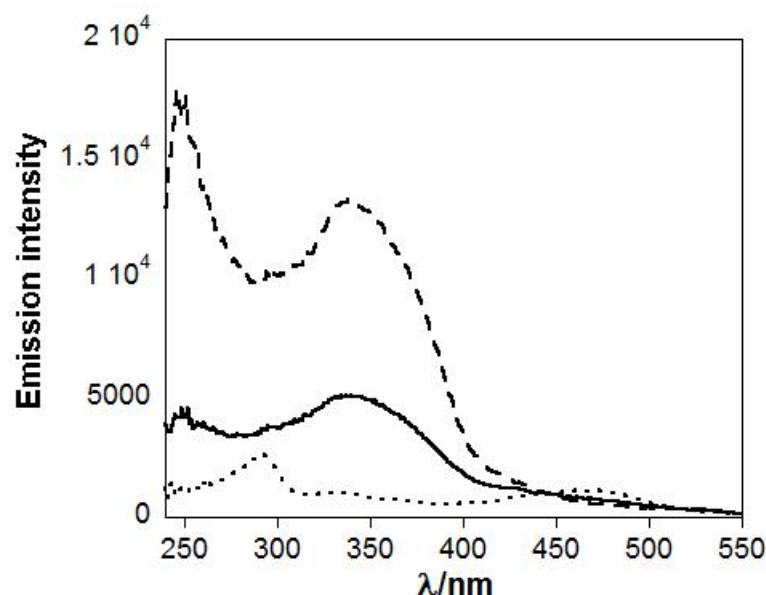
Figure 5.16 Excitation spectra of [Ru(4,4'-bpysac)$_2$(4,4'-bpyCD)](PF$_6$)$_2$ (C = 1.0 $\times 10^{-5}$ M, dotted line), 17 (C = 3.4$\times 10^{-6}$ M, dashed line) and the solution of the mixture of [Ru(4,4'-bpysac)$_2$(4,4'-bpyCD)](PF$_6$)$_2$/ 17 (1.0 $\times$ 10^{-5} M: 3.4 $\times$ 10^{-6} M, solid line), all solutions are in MeCN/Water (10:90), λ_{em} = 660 nm.

Monitoring of the iridium luminescence decay at 550 nm upon excitation at 340 nm showed bi-exponential lifetime, a long component with lifetime of 15 μs (73%) which corresponds to the lifetimes of the free **17** complex, and a faster component with a lifetime of 900 ns (27%). The presence of an electron-transfer process as the prevailing pathway is excluded because monitoring of the emission of the ruthenium centre at 660 nm does not show any change in the ruthenium luminescence lifetime. The ruthenium–iridium photo-induced interaction through non-covalent bonds is attributed to energy transfer from the iridium guest to the ruthenium core.

Inspired by these results we investigated the energy transfer via non-covalent interactions between metal centres when the complexes are immobilised on the surface. Transparent gold surfaces (30 nm gold coated on glass) were used in this

study, and the films were prepared by inserting a gold substrate into a solution of 1 mM [Ru(4,4'-bpysac)$_2$(4,4'-bpyCD)](PF$_6$)$_2$ for 24 hours followed by insertion into a solution of 1mM **17** in water 12 hours. The absorption, emission and excitation spectra of each surface before and after inclusion of the iridium guest were recorded and the energy transfer between the iridium and ruthenium metal centres was studied.

The absorption spectrum of the surface of [Ru(4,4'-bpysac)$_2$(4,4'-bpyCD)](PF$_6$)$_2$/ **17** displays the [1]MLCT band of the iridium complex at 360 nm (Figure 5.17).
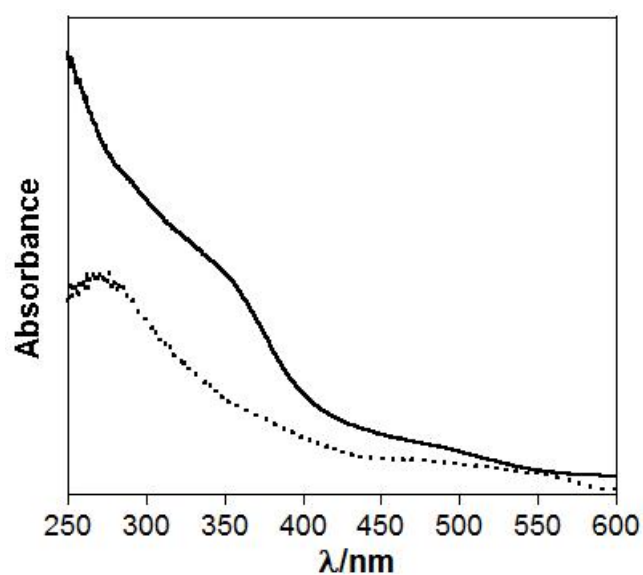
Figure 5.17 UV-Vis spectra of gold surface coated by [Ru(4,4'-bpysac)$_2$(4,4'-bpyCD)](PF$_6$)$_2$ (dotted line) and by [Ru(4,4'-bpysac)$_2$(4,4'-bpyCD)](PF$_6$)$_2$/ 17 (solid line).

Emission spectrum of the monolayer of the [Ru(4,4'-bpysac)$_2$(4,4'-bpyCD)](PF$_6$)$_2$ on the gold surface shows weak emission at 630 nm upon excitation at 490 nm ([1]MLCT)

with a lifetime of 448 ns. This Ru-based emission is blue-shifted compared with the emission of the acetonitrile solution of the free compound (Figure 5.18).
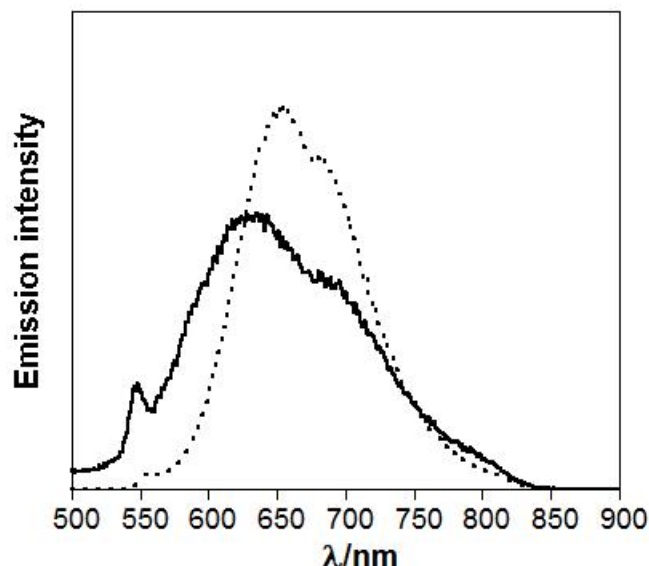
Figure 5.18 Emission spectra of [Ru(4,4'-bpysac)$_2$(4,4'-bpyCD)](PF$_6$)$_2$ on surface (solid line) and in MeCN solution (dotted line), λ_{ex} = 490 nm.

The monolayer of [Ru(4,4'-bpysac)$_2$(4,4'-bpyCD)](PF$_6$)$_2$ alone shows no emission upon excitation at 360 nm whereas the film of [Ru(4,4'-bpysac)$_2$(4,4'-bpyCD)](PF$_6$)$_2$/ **17** shows a very strong emission at 600 nm (τ = 993 ns) (Figure 5.19). The excitation spectrum of the film of [Ru(4,4'-bpysac)$_2$(4,4'-bpyCD)](PF$_6$)$_2$/ **17** shows peaks at 360 nm attributed to the **17** complex and 280 nm attributed to the LC band of [Ru(4,4'-bpysac)$_2$(4,4'-bpyCD)](PF$_6$)$_2$ indicating that emission signal emanated from both excitation of the MLCT band of the iridium guest and LC band of [Ru(4,4'-bpysac)$_2$(4,4'-bpyCD)](PF$_6$)$_2$ complex (Figure 5.20).
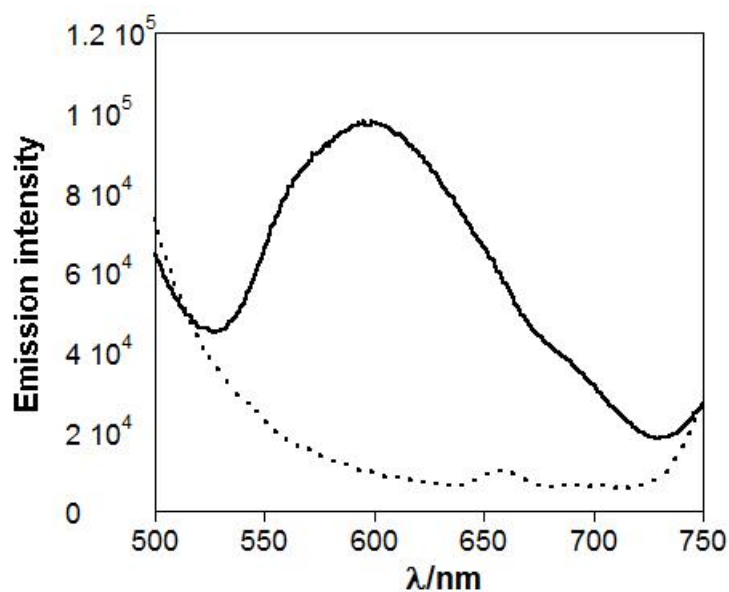
Figure 5.19 Emission spectra of [Ru(4,4'-bpysac)₂(4,4'-bpyCD)](PF₆)₂ on surface (dotted line)

and [Ru(4,4'-bpysac)₂(4,4'-bpyCD)](PF₆)₂/ 17 on surface (solid line) λ_{ex} = 350 nm.
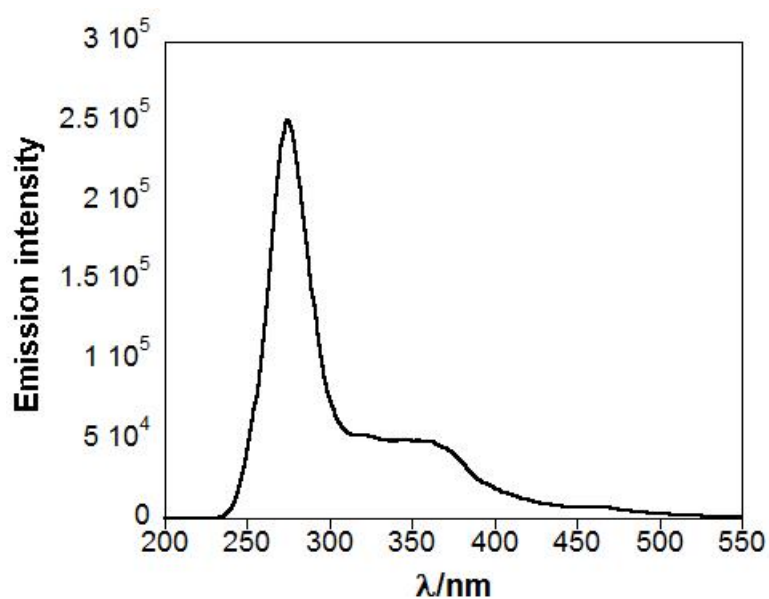
Figure 5.20 Excitation spectra of the surface coated by [Ru(4,4'-bpysac)₂(4,4'-bpyCD)](PF₆)₂/ 17,

λ_{em} = 620 nm.

B. Surface studies (Ellipsometry and XPS)

The supramolecular wire assembly of [Ru(4,4'-bpysac)$_2$(4,4'-bpyCD)](PF$_6$)$_2$ and **17** was examined by ellipsometry and XPS on planar gold substrate. The first component in the wire, [Ru(4,4'-bpysac)$_2$(4,4'-bpyCD)](PF$_6$)$_2$, was deposited over 24 hours to form a monolayer, using a 1 mM [Ru(4,4'-bpysac)$_2$(4,4'-bpyCD)](PF$_6$)$_2$ solution in acetonitrile and the unbound material was washed off in acetonitrile solution. The ellipsometric data indicates a monolayer thickness of 3.49 ± 0.26 nm which is in close agreement with the Chem 3D estimation (~ 3.5 nm) (Figure 5.21, red column). Addition of **17** on the [Ru(4,4'-bpysac)$_2$(4,4'-bpyCD)](PF$_6$)$_2$ monolayer was performed with a 12 hour deposition time, using an aqueous 1 mM **17** solution. The surface was washed with water and dried under nitrogen. Ellipsometry data measured the substrate thickness as 6.20 ± 0.33 nm (Figure 5.21, purple column).

The supramolecular binding of **17** to the [Ru(4,4'-bpysac)$_2$(4,4'-bpyCD)](PF$_6$)$_2$ monolayer was demonstrated in a control experiment. When a substrate bearing the two component supramolecular wire was inserted to acetonitrile solution it was shown that only [Ru(4,4'-bpysac)$_2$(4,4'-bpyCD)](PF$_6$)$_2$ monolayer was present within the experimental error and the supramolecular attachment was removed. Another control experiment was performed to demonstrate the supramolecular nature of the wire architecture. Freshly cleaned substrate gold substrate was immersed in a 1 mM aqueous solution of **17** for 12 hours, after which a thickness of 0.19 ± 0.08 nm was observed which confirms the necessity of metallo-cyclodextrin host to form the wire and that the **17** alone does not bind to the gold surface.
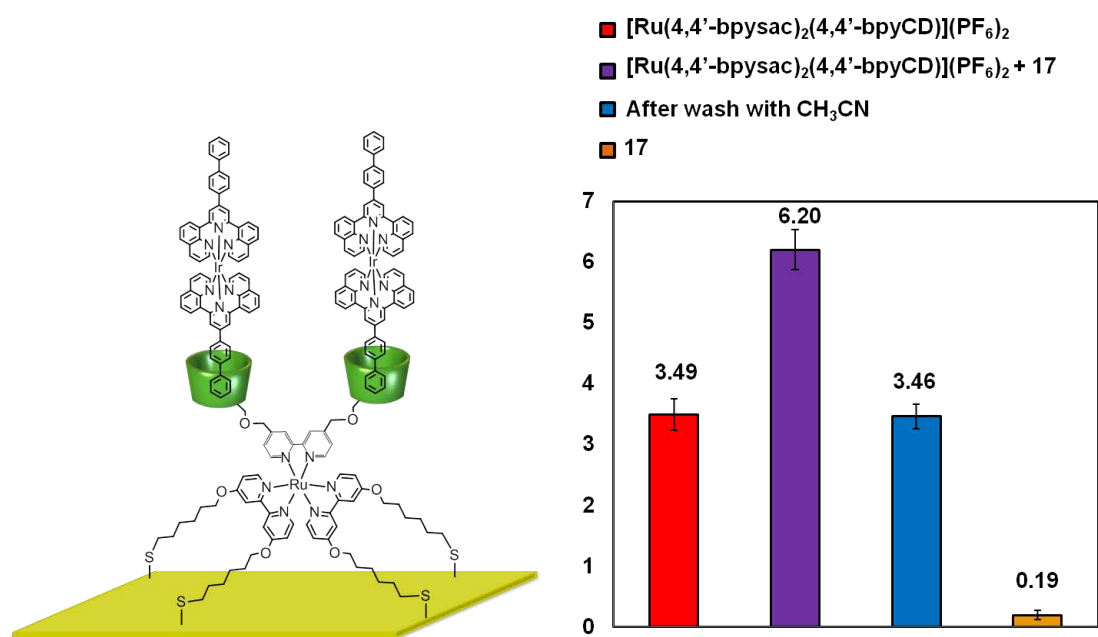
Figure 5.21 Ellipsometry data from wire assembly of [Ru(4,4'-bpysac)₂(4,4'-bpyCD)](PF₆)₂/ 17.

The XPS data of the gold substrate of both components displays peaks for both the ruthenium and iridium metals, confirming formation of the supramolecular assembly. The ratio of the Ru 3d: Ir 4f peaks [1.57: 0.38] suggests that the concentration of the ruthenium host is around 4 times more than the iridium guest (Figure 5.22).

Name	Pos.	FWHM	Area	At%
O 1s	529.9100	4.3272	18076.221	20.00
C 1s + Ru 3d	283.9100	3.3239	17177.430	53.33
N 1s	398.9100	3.5533	1398.396	2.53
F 1s	685.9100	2.3524	1837.573	1.59
Na 1s	1068.9100	3.4502	14133.184	7.24
Au 4f	82.9100	1.8997	67172.374	9.28
S 2p	167.9100	1.7097	195.147	0.25
Ir 4f	60.9100	8.9269	4819.414	0.83
Au 4d	333.9100	4.4511	27756.658	4.95
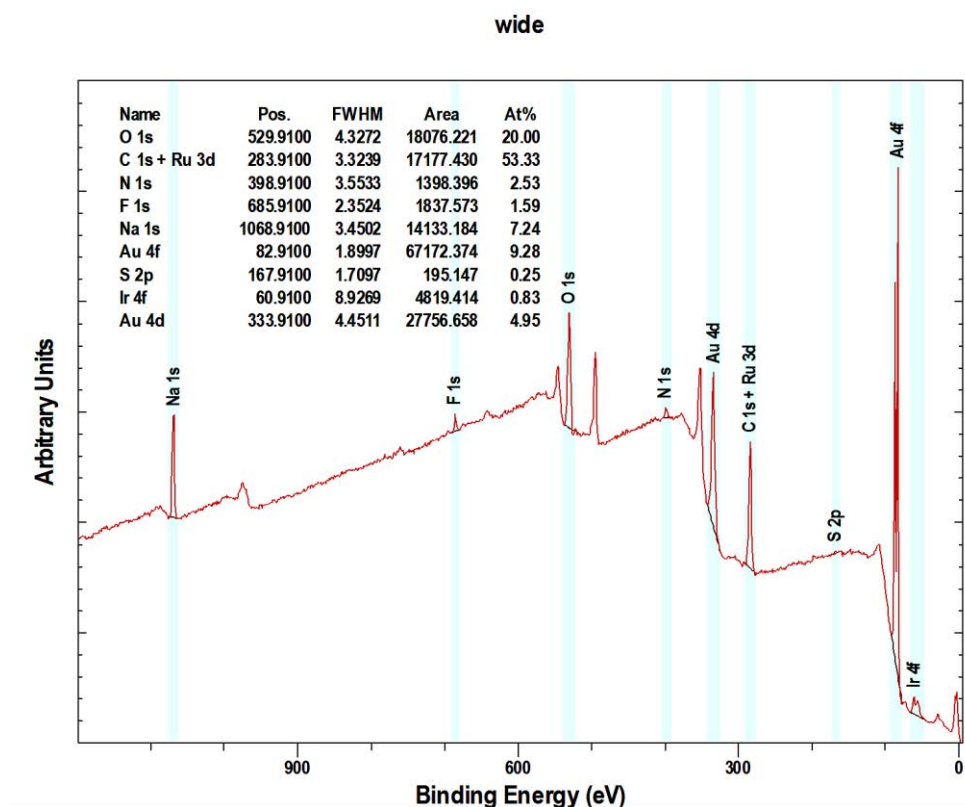
Figure 5.22 wide XPS spectrum from wire assembly of [Ru(4,4'-bpysac)$_2$(4,4'-bpyCD)](PF$_6$)$_2$/ 17 on planar gold surface.

The high resolution scans of C 1s + Ru 3d and Ir 4f regions of the gold substrate before and after iridium complex insertion are shown in figure 5.23. The 3d$_{3/2}$ and 3d$_{5/2}$ orbitals of metallic ruthenium in the [Ru(4,4'-bpysac)$_2$(4,4'-bpyCD)](PF$_6$)$_2$ monolayer are clearly observed at 285.4 and 279.8 eV respectively, referenced to Au 4f$_{7/2}$ at 83.9 eV with full widths at half-maximum (fwhm) of 4.1 eV.[18,19] These peaks are slightly shifted in the gold substrate of both components and are present at 285.3 and 281.4 eV. A small peak assigned to the Ir 4d orbital can also be observed at 291.8 eV in the gold surface of the Ru-Ir film. The 4f$_{7/2}$ and 4f$_{5/2}$ peaks of metallic iridium can be easily observed at 61.3 and 64.2 which are in agreement with the

NIST X-ray photoelectron spectroscopy database and also previously published papers.[20]
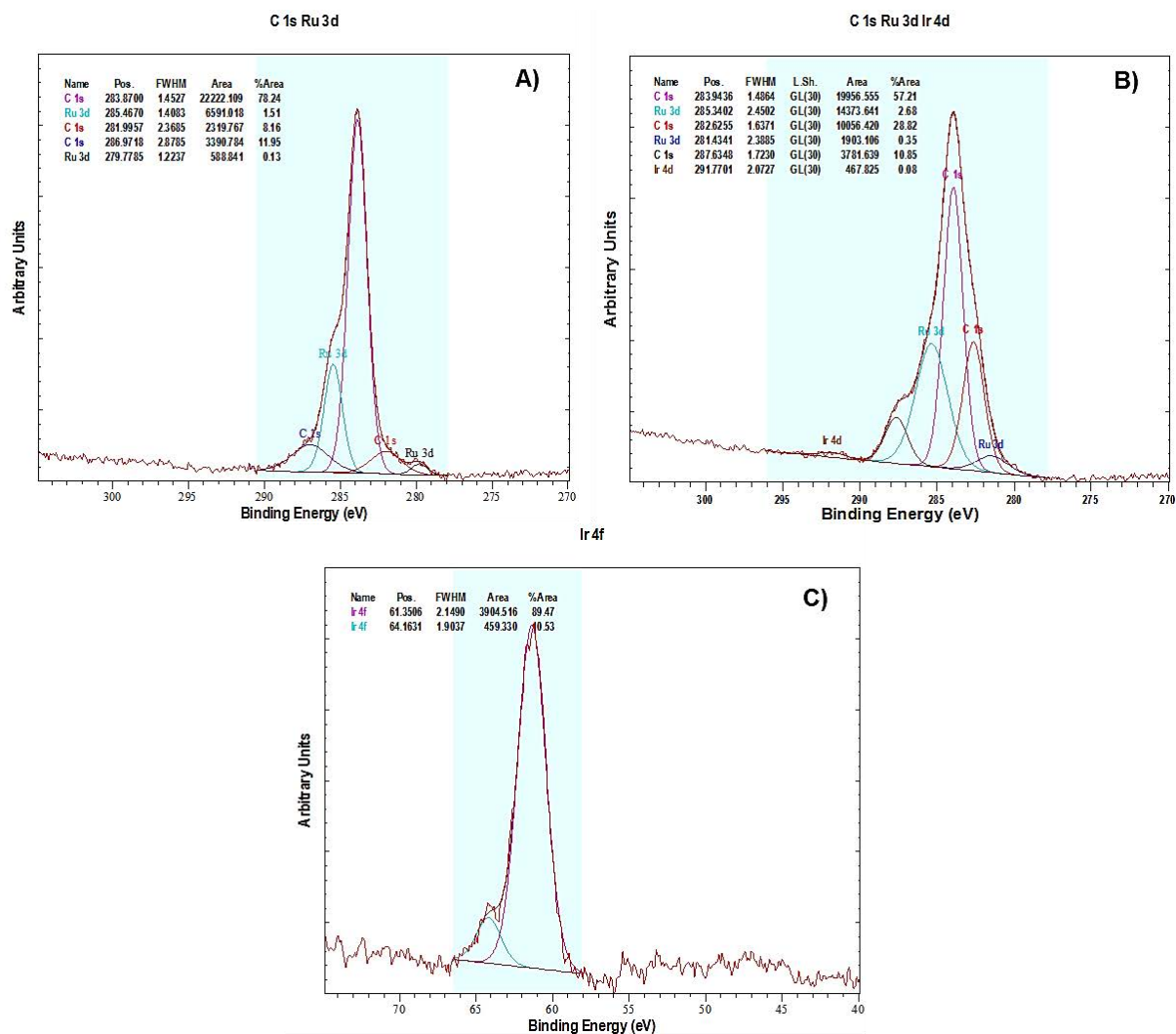
Figure 5.23 High resolution XPS scans of A) The C 1s, Ru 3d region of [Ru(4,4'-bpysac)$_2$(4,4'-bpyCD)](PF$_6$)$_2$ on surface B) The C 1s, Ru 3d, Ir 4d region of [Ru(4,4'-bpysac)$_2$(4,4'-bpyCD)](PF$_6$)$_2$/ 17 on surface C) The Ir 4f region of [Ru(4,4'-bpysac)$_2$(4,4'-bpyCD)](PF$_6$)$_2$/ 17 on planar gold surface.

5.2.4. [Os(4,4'-bpysac)$_2$(4,4'-bpyCD)](PF$_6$)$_2$ + 16 host-guest assemblies in solutions and on the gold surfaces

A. Energy transfer study of ruthenium(II)-based guest and osmium(II) centre

The interaction between [Os(4,4'-bpysac)$_2$(4,4'-bpyCD)](PF$_6$)$_2$ and **16** was investigated by absorption and steady state emission spectroscopy using 1.2×10^{-5} M solution of [Os(4,4'-bpysac)$_2$(4,4'-bpyCD)](PF$_6$)$_2$, 8.0×10^{-7} M solution of **16** and the solution of the mixture of [Os(4,4'-bpysac)$_2$(4,4'-bpyCD)](PF$_6$)$_2$/ **16** (1.2×10^{-5} M: 8.0×10^{-7} M) in 1 ml of water/acetonitrile (90:10). The photophysical properties of complex **16** have been reported in chapter 4. The excess of the osmium complex was used to ensure binding of most of the ruthenium guests in the cyclodextrin cups and simulate the similar environment to gold surface where is more likely to have partially filled cyclodextrin cups and so a lower concentration of the guest complex. A schematic description of the excited-state energies of the photoactive metal components is presented in scheme 5.12.
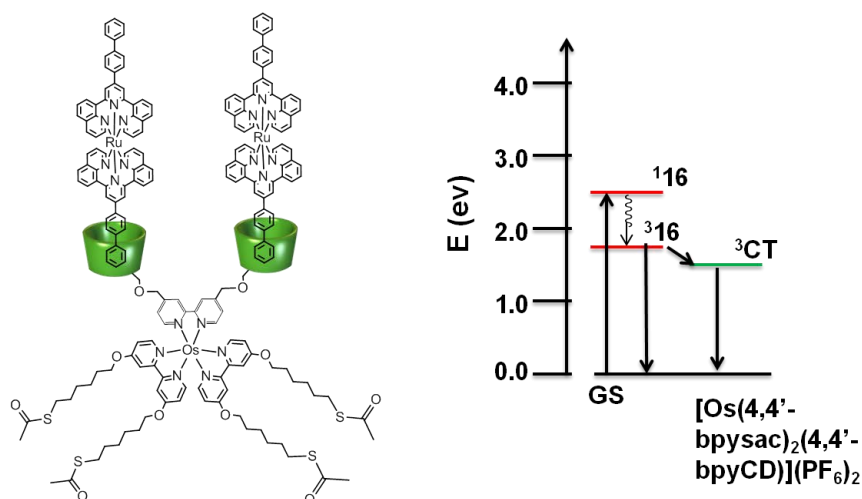
Scheme 5.12 schematic presentation of Energy transfer process between [Os(4,4'-bpysac)$_2$(4,4'-bpyCD)](PF$_6$)$_2$ and 16.

A small red shift of the [1]MLCT band of the **16** in the solution of the mixture of [Os(4,4'-bpysac)$_2$(4,4'-bpyCD)](PF$_6$)$_2$/ **16** (1.2 × 10^{-5} M: 8.0 × 10^{-7} M) indicates the inclusion of the biphenyl tail in to the cyclodextrin cavity (Figure 5.24).
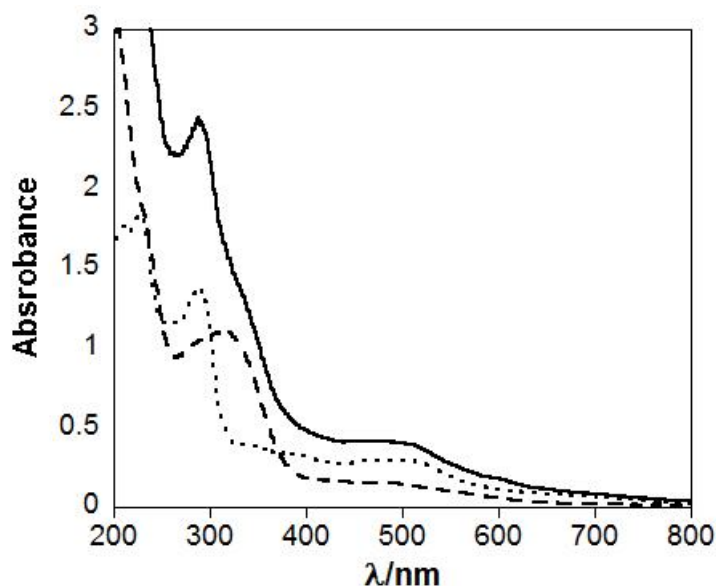
Figure 5.24 UV-Vis spectra of [Os(4,4'-bpysac)$_2$(4,4'-bpyCD)](PF$_6$)$_2$ (C = 1.2×10^{-5} M, dotted line), 16 (C = 8.0×10^{-7} M, dashed line) and the solution of the mixture of [Os(4,4'-bpysac)$_2$(4,4'-bpyCD)](PF$_6$)$_2$/ 16 (1.16 × 10^{-5} M: 0.08 × 10^{-5} M, solid line), all solutions are in MeCN/Water (10:90).

Upon excitation into the ^{1}MLCT band of the ruthenium complex at 490 nm, excited state energy transfer to the ^{3}MLCT level of the osmium complex, in addition to the emission arising directly from the osmium centre, is expected to take place. The emission intensity of the metal centres upon excitation at 490 nm was monitored and showed an 80% decrease of the emission intensity of **16** (Figure 5.25). The emission of the [Os(4,4'-bpysac)$_2$(4,4'-bpyCD)](PF$_6$)$_2$ is very weak and is impossible to monitor.
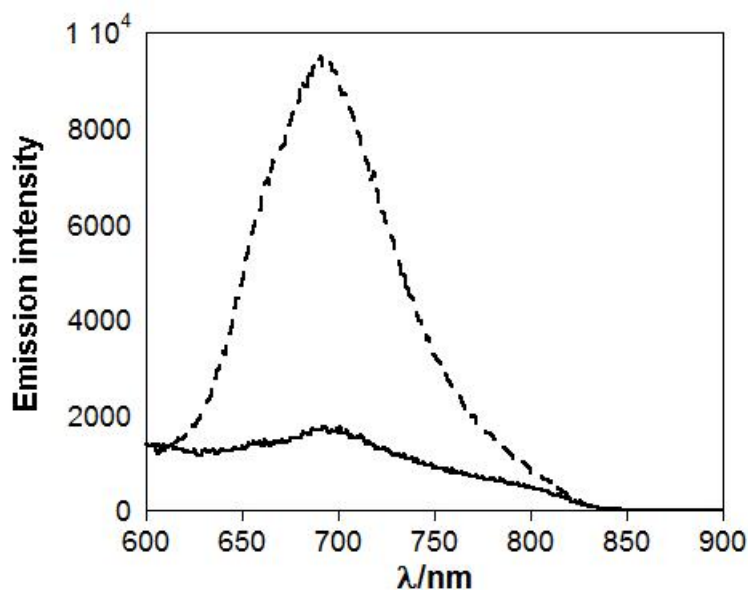
Figure 5.25 Emission spectra of 16 (C = 8.0 $\times 10^{-7}$ M, dashed line) and the solution of the mixture of [Os(4,4'-bpysac)$_2$(4,4'-bpyCD)](PF$_6$)$_2$/ 16 (1.2 × 10^{-5} M: 8.0 × 10^{-7} M, solid line), all solutions are in MeCN/Water (10:90), λ_{ex} = 490 nm.

Monitoring of the ruthenium luminescence lifetime (at 690 nm) upon excitation at 490 nm showed the presence of a fast component with a lifetime of τ = 121 ns which decreased by 65%. In this case we can conclude that the osmium–ruthenium photo-induced communication through non-covalent bonds is attributed to energy transfer from the ruthenium guest to the osmium core. The excitation spectra of [Os(4,4'-bpysac)$_2$(4,4'-bpyCD)](PF$_6$)$_2$ and **16** are very similar and as the result the excitation spectrum cannot give any additional information about the energy transfer process.

In order to investigate the energy transfer when complexes are attached to gold surfaces, transparent gold films (30 nm gold coated on glass) were used. The absorption, emission and excitation spectra of the surface before and after binding of the ruthenium guest were collected and the energy transfer between ruthenium and

osmium complexes was studied. The absorption spectrum of the surface of [Os(4,4'-bpysac)$_2$(4,4'-bpyCD)](PF$_6$)$_2$/ **16** shows two peaks at 460 and 650 nm attributed to the ^{1}MLCT and ^{3}MLCT bands of the ruthenium metallo-guest.
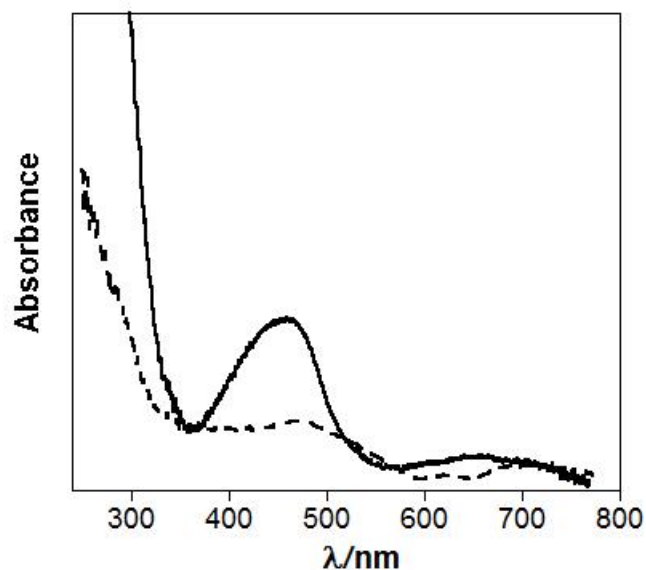
Figure 5.26 UV-Vis spectra of gold surface coated by [Os(4,4'-bpysac)$_2$(4,4'-bpyCD)](PF$_6$)$_2$ (dotted line) and by [Os(4,4'-bpysac)$_2$(4,4'-bpyCD)](PF$_6$)$_2$/ 16 (solid line).

The gold substrate of [Os(4,4'-bpysac)$_2$(4,4'-bpyCD)](PF$_6$)$_2$ alone shows no emission upon excitation at 490 nm while the surface of [Os(4,4'-bpysac)$_2$(4,4'-bpyCD)](PF$_6$)$_2$/ **16** shows some emission at 710 nm as a result of the energy transfer from the ruthenium to the osmium complex (Figure 5.27).
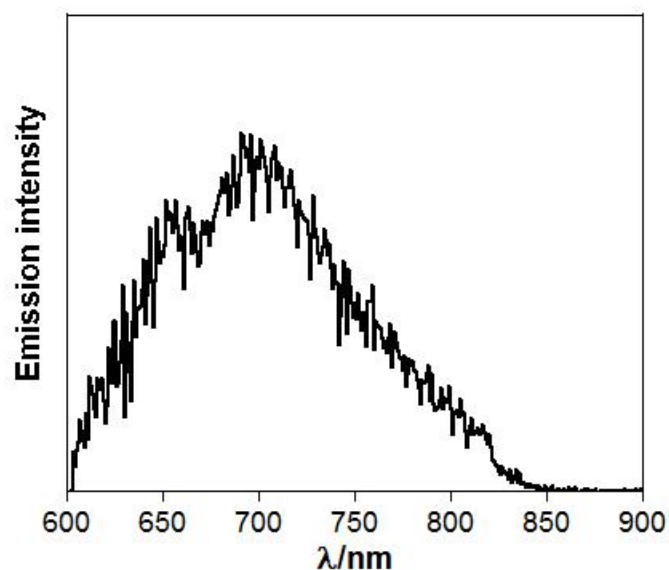
Figure 5.27 Emission spectrum of gold surface coated by [Os(4,4'-bpysac)$_2$(4,4'-bpyCD)](PF$_6$)$_2$/

16.

B. Surface studies (Ellipsometry and XPS)

The supramolecular wire assembly of [Os(4,4'-bpysac)$_2$(4,4'-bpyCD)](PF$_6$)$_2$ and **16** was examined by ellipsometry and XPS on planar gold substrate. First the monolayer of the [Os(4,4'-bpysac)$_2$(4,4'-bpyCD)](PF$_6$)$_2$ was formed by deposition of the gold surface from a 1 mM acetonitrile solution of [Ru(4,4'-bpysac)$_2$(4,4'-bpyCD)](PF$_6$)$_2$ for 24 hours and the unbound material was washed off with acetonitrile solution. The ellipsometric data was recorded indicating a thickness of 4.10 ± 0.16 nm which is in close agreement to the Chem 3D estimation (~ 3.5 nm) (Figure 5.28, green column). Addition of **16** to the [Os(4,4'-bpysac)$_2$(4,4'-bpyCD)](PF$_6$)$_2$ monolayer was performed within 12 hour deposition time from an aqueous 1 mM **16** solution. The washings

were performed with water followed by drying the substrate under nitrogen and the thickness measured at 6.71 ± 0.21 nm (Figure 5.28, purple column).

The supramolecular binding of **16** on the $[Os(4,4'\text{-bpysac})_2(4,4'\text{-bpyCD})](PF_6)_2$ monolayer was demonstrated by ellipsometry with two control experiments. First, a substrate bearing the two component supramolecular wire was inserted to acetonitrile solution which removes the **16** guest and ellipsometric data of $[Os(4,4'\text{-bpysac})_2(4,4'\text{-bpyCD})](PF_6)_2$ monolayer only was measured within the experimental error. Second, a clean gold substrate was immersed in 1 mM aqueous solution of the **16** for 12 hours when a thickness of 0.31 ± 0.22 nm was observed by ellipsometry which confirms the need of metallo-cyclodextrin host to form the wire.
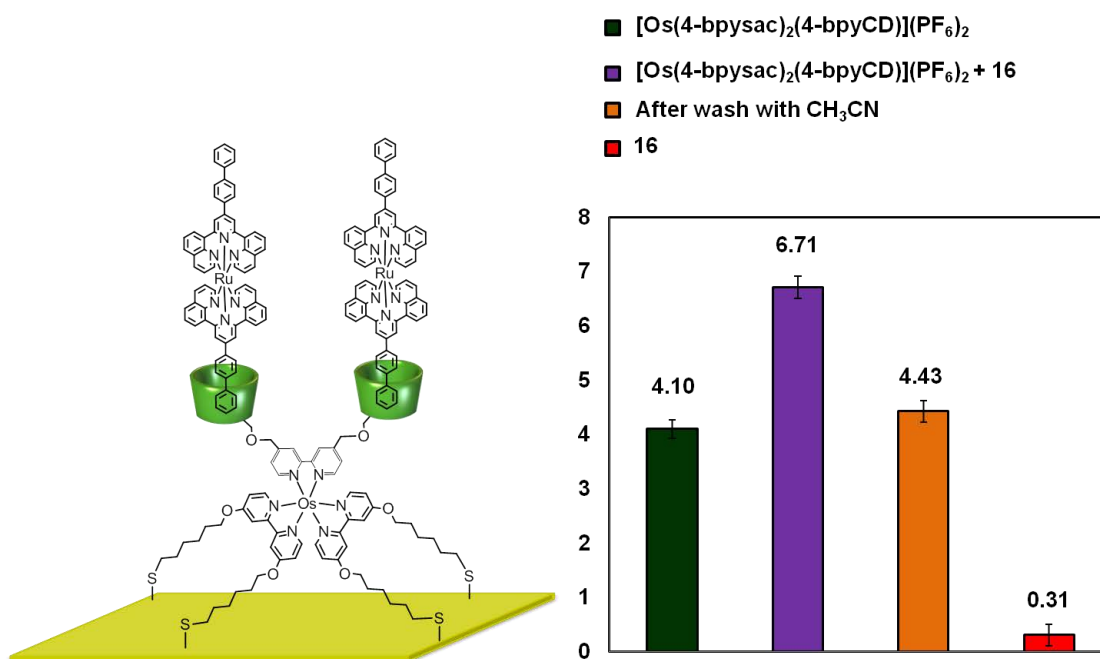
Figure 5.28 Ellipsometry data from wire assembly of [Os(4,4'-bpysac)₂(4,4'-bpyCD)](PF₆)₂/ 16 on planar gold surface.

The XPS data of the monolayer containing both components on the gold surface show peaks for Ru 3d and Os 4f with the ratio of 1.22: 1.58 which suggests that the concentration of the osmium host is around 1.3 times more than the ruthenium guest (Figure 5.29).

wide

Name	Pos.	FWHM	Area	At%
O 1s	531.9100	2.7110	7482.317	9.44
C 1s + Ru 3d + Os 4d	283.9100	3.2457	12944.208	45.83
N 1s	398.9100	2.7970	1269.550	2.62
Au 4f	82.9100	1.8907	152110.566	23.96
S 2p	162.9100	4.0368	2759.676	4.07
Au 4d	333.9100	4.3983	60167.510	12.23
Os 4f	55.9100	6.0273	8379.897	1.85
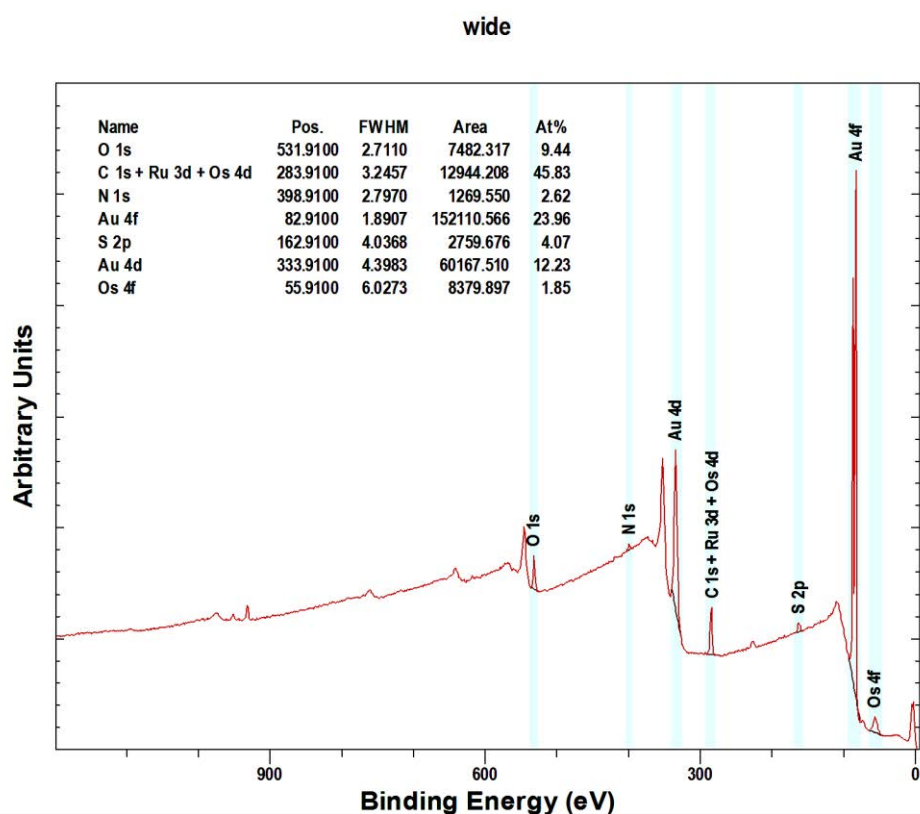
Figure 5.29 wide XPS spectrum from wire assembly of [Os(4,4'-bpysac)$_2$(4,4'-bpyCD)](PF$_6$)$_2$/ 16 on planar gold surface.

The high resolution scans of C 1s + Ru 3d + Os 4d and Os 4f regions of the gold substrate before and after insertion of the ruthenium complex are shown in figure 5.30. The 4f$_{7/2}$ and 4f$_{5/2}$ of metallic osmium peaks of the [Os(4,4'-bpysac)$_2$(4,4'-

bpyCD)](PF$_6$)$_2$ monolayer are clearly observed at 52.9 and 55.1 eV respectively, referenced to Au 4f$_{7/2}$ at 83.9 eV full widths at half-maximum (fwhm) of 4.1 eV. There is a small peak at 50.9 eV in this spectrum which can be attributed to a small amount of unbound osmium complex. The 4f$_{7/2}$ and 4f$_{5/2}$ peaks of osmium complex shift to 50.2 and 53.1 eV respectively, upon addition of the guest **16**. In the 275-295 eV region, the Os 4d peak appears at 288.1 eV in [Os(4,4'-bpysac)$_2$(4,4'-bpyCD)](PF$_6$)$_2$ monolayer and at 287.8 eV in the film of both components on the gold film. In addition the 3d$_{3/2}$ of metallic ruthenium peak of **16** can be observed at 285.7 eV in the gold surface of both complexes.
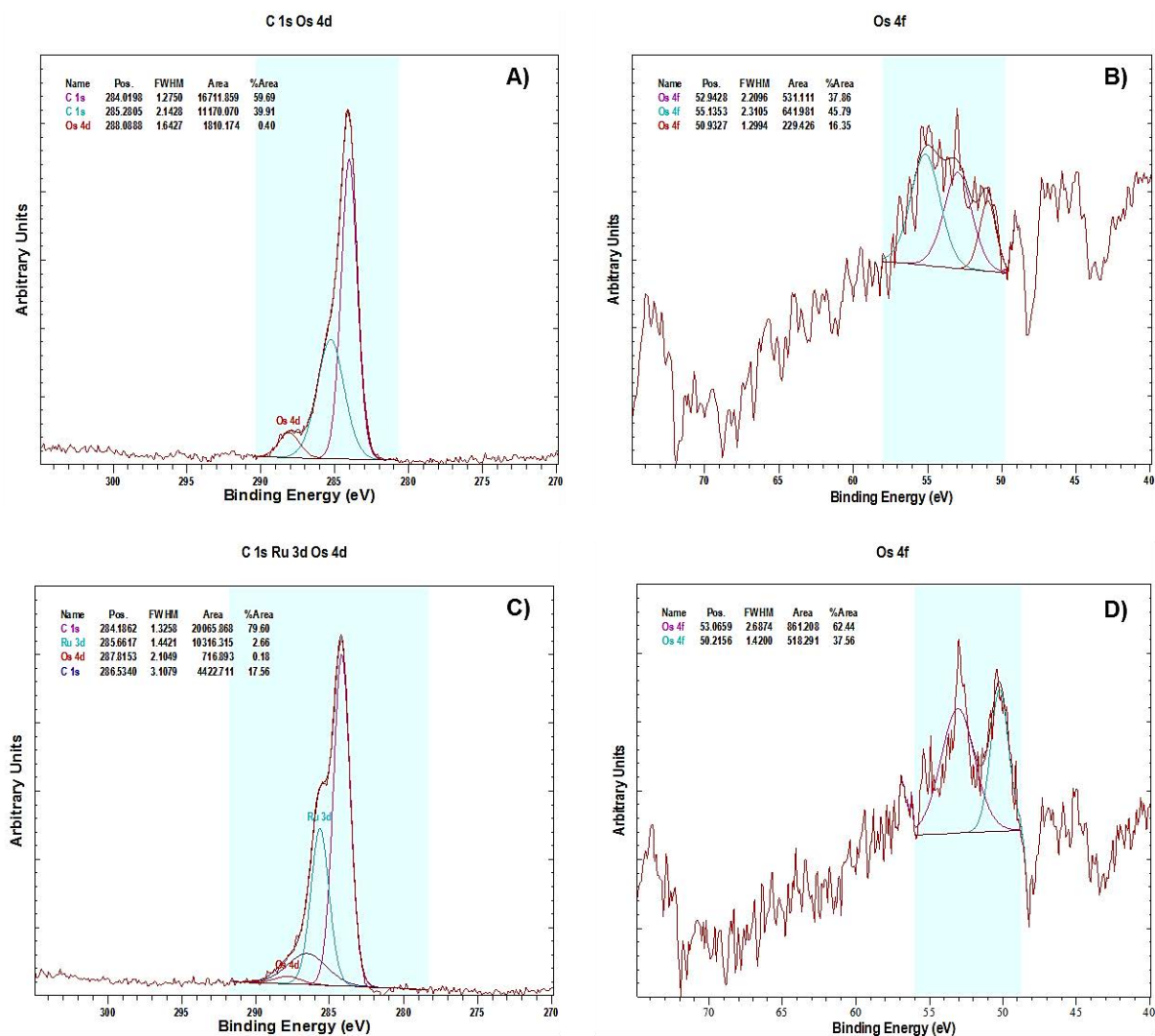
Figure 5.30 High resolution XPS scans of A) The C 1s, Os 4d region of [Os(4,4'-bpysac)$_2$(4,4'-bpyCD)](PF$_6$)$_2$ on gold surface B) The Os 4f region of [Os(4,4'-bpysac)$_2$(4,4'-bpyCD)](PF$_6$)$_2$ on gold surface C) The C 1s, Ru 3d, Os 4d region of [Os(4,4'-bpysac)$_2$(4,4'-bpyCD)](PF$_6$)$_2$/ 16 film on gold surface D) The Os 4f region of [Os(4,4'-bpysac)$_2$(4,4'-bpyCD)](PF$_6$)$_2$/ 16 film on planar gold surface.

5.3. Conclusions

New bipyridine ligands bearing two cyclodextrins in either the 5,5'-positions or the 4,4'-positions and their surface-active ruthenium(II) and osmium(II) complexes were synthesised and fully characterised by NMR, mass spectrometry and FTIR spectroscopy.

The photophysical properties of the complexes in solution have been studied. The acetonitrile solutions of the ruthenium complexes display luminescence from the ^{3}MLCT band, when excited at room temperature, with a red shift in their emission spectrum with respect to $[Ru(bpy)_3]Cl_2$. The osmium complex displays weak emission at room temperature with a large red shift in emission spectrum with respect to $[Os(bpy)_3]Cl_2$.

The multi-metal assemblies of Ru(II) – Ir(III) and Os(II) – Ru(II) were built in both solution and on the surface, using **16** and **17** as metallic guests, and the energy transfer between the metal centres were investigated by luminescence studies. The photoinduced energy transfer between metal centres via the supramolecular assembly of host-guest units in cyclodextrin cavities, in water and on the surface has been demonstrated by emission spectrometry. XPS analysis of the assemblies on the gold substrates confirms the relative concentrations of both metals on the surface.

5.4. Experimental

5.4.1 Preparation of the Self-assembled monolayers

The wire assemblies using either [Ru(4,4'-bpysac)$_2$(4,4'-bpyCD)](PF$_6$)$_2$ or [Os(4,4'-bpysac)$_2$(4,4'-bpyCD)](PF$_6$)$_2$ as hosts, and either **17** or **16** as guests, on planar gold substrates were prepared by insertion of the substrates into 1 mM of the acetonitrile solutions of the hosts for 24 hours. The unbound material was washed off by dipping the substrate in to acetonitrile solution for short period of time (typically 10-15 seconds) and the substrate was dried under nitrogen. Addition of the second component of the wire was performed with an aqueous 1 mM solution of the guest complex over 12 hour deposition time followed by washing with water and drying under nitrogen. The supramolecular wire was disassembled in the ellipsometry experiment by insertion of the substrate in to acetonitrile for short period of time (about 5-10 minutes) and dried under nitrogen.

5.4.2 Synthesis

6-Mono-hydroxy permethylated β-cyclodextrin (β-CD–OH) [9]
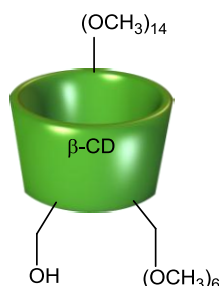
β-Cyclodextrin (8.03 g, 7.08 mmol) and imidazole (1.07 g, 15.8 mmol) were dissolved in DMF (150 cm^3) in a 3-necked 1 litre flask equipped with nitrogen inlet and mechanical stirrer. *Tert*-butyl dimethylsilyl chloride (2.22 g, 14.7 mmol) in DMF (45 cm^3) was added dropwise over 30 min. After 2 h TLC (BuOH/EtOH/water 5:4:3) showed three spots with R$_f$ 0.4, 0.6 and 0.8 corresponding to β-cyclodextrin, monosilylated β-cyclodextrin and higher silylated products respectively. The mixture was cooled to 0 °C, sodium hydride (21 g, 60 % dispersion, 501 mmol) was added portionwise and stirred at 0 °C for 1 h. After stirring at room temperature for 2 h the mixture was cooled to 0 °C and methyl iodide (139.9 g, 979.9 mmol) was added dropwise over 30 min. After stirring at 0 °C for 1 h the mixture was warmed to room temperature and stirred for 24 h, after which time TLC (ethyl acetate/methanol 9:1) showed that full methylation had occurred. The mixture was cooled to 0 °C and methanol (40 cm^3) was added. The mixture was poured into ice-water (750 cm^3) and the aqueous phase was extracted with chloroform (6 × 250 cm^3). The organic phase was washed with 3 % aqueous solution of sodium thiosulfate (200 cm^3) and water

(200 cm^3) and dried over MgSO$_4$. After evaporating the solvent and drying under vacuum at 80 °C for 8 h the dark orange residue was dissolved in methanol (400 cm^3) and heated to reflux with ammonium fluoride (4.82 g, 130.14 mmol) for 24 h. After this time TLC (ethyl acetate/methanol 9:1) revealed that the protecting group had been removed as permethylated β-cyclodextrin was the fastest running spot. The solvent was evaporated and the residue taken up in ethyl acetate, filtered through celite and the solvent evaporated. The light yellow residue was purified on a Biotage prepacked silica column eluting with 4.8 % methanol in ethyl acetate to yield 6-monohydroxy permethylated β-cyclodextrin (2.05 g, 21 %) as a white solid. Characterization of the compound by NMR spectroscopy and mass spectrometry agrees with the previously published data. Selective data are given below.

^{1}H NMR (300 MHz, CDCl$_3$): d = 5.22 (d, J = 4.0, 1H, H$_{Glu-1}$), 5.17-5.15 (m, 2H, H$_{Glu-1}$), 5.09 (d, J = 3.4, 3H, H H$_{Glu-1}$), 5.02 (d, J = 3.6, 1H, H H$_{Glu-1}$), 3.94-3.17 (m, 103H, H H$_{Glu-2-6}$, 2,3,6-OMe).

^{13}C NMR (75 MHz, CDCl$_3$): d = 99.0, 98.8, 82.4, 82.0, 81.9, 81.8, 81.8, 81.7, 81.6, 81.5, 81.1, 80.7, 80.7, 80.6, 80.0, 79.8, 78.6, 71.8, 71.7, 71.6, 71.5, 71.4, 71.2, 71.0, 70.9, 61.7, 61.6, 61.5, 61.3, 61.0, 59.1, 59.0, 58.9, 58.7, 58.6, 58.5, 58.3, 58.2.

MALDI-MS, (2,5-dihydroxybenzoic acid) *m/z* : 1437.8 [M+Na]$^+$.

5,5'-Bis(bromomethyl)-2,2'-bipyridine (5,5'-Brbpy)[11]
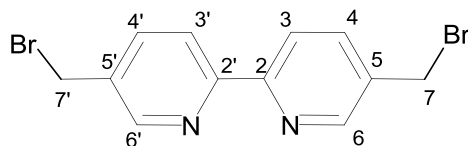
A solution of 5,5'-dimethyl-2,2'-bipyridine (1.14 g, 6.18 mmol), NBS (5.8 g, 32.6 mmol) and catalytic amount of benzoyl peroxide in 100 mL of dry CCl_4, was brought to reflux under N_2 for 60 min and the precipitated succinimide was removed immediately from the hot mixture by filtration. The precipitate was then washed with CCl_4 (40 mL) and the combined CCl_4 phases were evaporated. The remaining solid was dissolved in DCM (100 mL) and extracted with 0.5 M $Na_2S_2O_3$ solution. The combined $Na_2S_2O_3$ fractions extracted with DCM and the combined DCM layers were dried over Na_2SO_4. Finally the crude product was recrystallized from hot DCM yielding 0.6 g (28.5 % yield) of a white solid. Characterization of the compound by NMR spectroscopy agreed with the previously published data.

^{1}H NMR (300 MHz, CDCl$_3$): δ = 8.70 (d, 2 H, J = 2.2, H$_{6,6'}$), 8.42 (d, 2 H, J = 8.2, H$_{3,3'}$), 7.88 (dd, 2 H, ^3J = 8.2, ^4J = 2.2, H$_{4,4'}$), 4.56 (s, 4 H, H$_{7,7'}$).

ES MS(+) (DCM): *m/z* 343.2 [M+H]$^+$, 365.1 [M+Na]$^+$.

IR (cm^{-1}): 3015.95, 2924.81, 1594.04, 1552.22, 1467.54, 1381.77, 1253.17, 1203.45, 1026.45.

Bis[6-mono-permethylated β-cyclodextrin]-5,5'-methyl-bipyridyl (5,5'-bpyCD)[10]
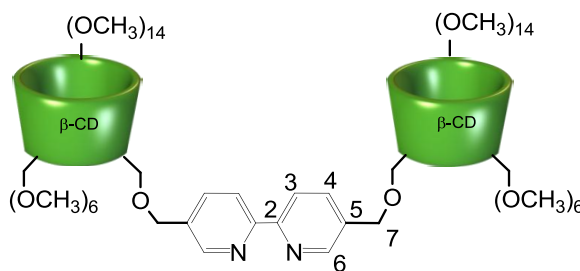
Mono-6-hydroxy-permethylated-β-cyclodextrin   and   5,5'-bis(bromomethyl)-2,2'-bipyridine   were independently dried under vacuum for 2 hours. Mono-6-hydroxy permethylated β-cyclodextrin (1.0 mg, 0.71 mmol) was dissolved in freshly distilled tetrahydrofuran (15 mL). NaH (3 g, 60% suspension in oil, 4.3 mmol) was added and a white precipitate was formed. A solution of 5,5'-bis(bromomethyl)-2,2'-bipyridine (81 mg, 0.24 mmol) in tetrahydrofuran (6 mL) was added. The mixture was left to reflux for 24 h, quenched with brine and the solvent was evaporated. The residue was treated with brine (30 mL) and extracted with dichloromethane (3 × 50 mL). The combined organic phases were dried over Na_2SO_4, filtered and the solvent was evaporated. The compound was purified by size exclusion column chromatography (Biobeads SX3, DCM) yielding 419 mg as pale yellow solid, 58 % yield.

^{1}H NMR (300 MHz, $CDCl_3$): d = 8.55 (s, 2H, $H_{6,6'}$), 8.28 (d, J = 8.0, 2H, $H_{3,3'}$), 7.76 (d, J = 8.0 2H, $H_{4,4'}$), 5.16-5.02 (m, 14H, H_{Glu-1}), 4.61 (m, 4H, $H_{7,7'}$), 4.01 (m, 2 H, 1H, H_{Glu-6}), 3.87 − 3.10 (m, $H_{Glu-2,3,4,5,6}$, OCH_3).

^{13}C-NMR (100 MHz, $CDCl_3$): δ =   151.0, 148.5, 136.5, 125.5, 120.6, 98.9, 82.4-80.2 (m), 71.4-70.9 (m), 61.7-58.5 (m), 29.7.

MALDI-TOF: *m/z* 3033 [M+Na]$^+$.

IR (cm^{-1}): 2928.45, 2830.58, 1453.82, 1366.51, 1138.32, 1088.13, 1019.68, 968.86.

4,4'-Bis(chloromethyl)-2,2'-bipyridine (4,4'-Clbpy)[12]
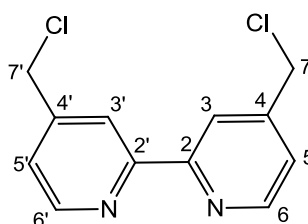
4,4'-Dimethyl-2,2'-bipyridine (1.0 g, 5.4 mmol) dissolved in dry THF (20 mL) was transferred dropwise via cannula into a lithium-diisopropylamide (LDA) solution (7 mL, 12 mmol, 1.8 M in THF/Hexane/Heptane) in 8 ml of THF at -78 °C. The flask and cannula were rinsed with THF (2 × 2 mL). The brown mixture was stirred at -78 °C for 20 min, was warmed to -10 °C for 25 min, and then was cooled to -78 °C before addition of TMSCl (1.8 mL, 14.1 mmol). As soon as the brown reaction mixture became pale yellow-green in color (5-10 s after TMSCl addition), the reaction was quenched with EtOH (3 mL). Saturated aqueous NaHCO$_3$ was added to the cold reaction mixture, which was then allowed to warm to the room temperature. The product was extracted into EtOAc. Combined organic fractions were washed with brine and were dried over Na$_2$SO$_4$. Filtration and concentration afforded the **4,4'-Bis[(trimethylsilyl)methyl]-2,2'-bipyridine**, as a slightly off-white crystalline solid which was used without any further purification (1.6 g, 97%).

To 4,4'-bis[(trimethylsilyl)methyl]-2,2'-bipyridine (1.6 g, 4.9 mmol) and Cl_3CCCl_3 (4.6 g, 19.4 mmol) in THF (40 mL) at -78 °C, CsF (3.0 g, 19.4 mmol) was added, warmed to room temperature and stirred for 2 hours (until TLC indicated that all TMS starting material and intermediates were consumed).

The reaction mixture was poured into a separation funnel containing EtOAc and H_2O. The aqueous layer was extracted with EtOAc and combined organic fractions were washed with H_2O, were shaken with brine and then were dried over Na_2SO_4, filtered and concentrated. The crude was purified by silica column chromatography using Hexane: EtOAc (80:20) as the eluent to give pure product as a white solid (0.58 g, 47%).

^1H NMR (CDCl3, 300 MHz): δ = 8.65 (d, 2 H, J = 4.5, $H_{6,6'}$), 8.41 (s, 2 H, $H_{3,3'}$), 7.34 (d, 2 H, J = 4.5, $H_{5,5'}$), 4.60 (s, 4 H, $H_{7,7'}$).

^{13}C NMR (CDCl3, 75 MHz): δ = 156.1, 149.7, 147.0, 122.8, 120.4, 44.3.

ES MS(+) (DCM): m/z 253.2 $[M+H]^+$, 275.2 $[M+Na]^+$.

IR (cm^{-1}): 3003.53, 2925.49, 1593.13, 1555.50, 1458.35, 1375.10, 1260.11, 1217.11, 1068.26.

Bis[6-mono-permethylated β-cyclodextrin]-4,4'-methyl-bipyridyl (4,4'-bpyCD)
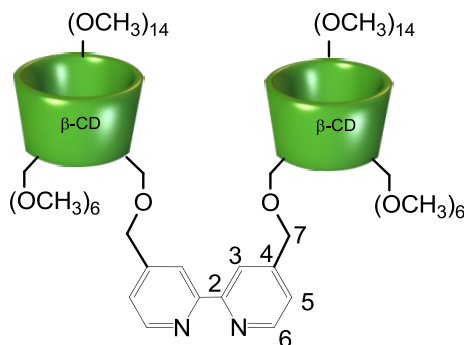
Mono-6-hydroxy-permethylated-β-cyclodextrin and 4,4'-bis(chloromethyl)-2,2'-bipyridine were independently dried under vacuum for 2 hours. Mono-6-hydroxy-permethylated-β-cyclodextrin (1.4 g, 1.0 mmol) was dissolved in freshly distilled THF (20 mL) and NaH (4 g, 60% suspension in oil, 6.0 mmol) was added. After 20 minutes stirring at room temperature, a solution of 4,4'-bis(chloromethyl)-2,2'-bipyridine (86 mg, 0.34 mmol) in THF (10 mL) was added. The mixture was left to reflux for 24 hours, quenched with brine and the solvent was evaporated. The residue was treated with brine (50 mL) and extracted with dichloromethane (3 × 50 mL). The combined organic phases were dried over Na_2SO_4, filtered and the solvent was evaporated. The compound was purified by size exclusion column chromatography (Biobeads SX3, DCM) yielding 614 mg as pale yellow solid, 60 % yield.

^{1}H NMR (300 MHz, CDCl$_3$): d = 8.56 (d, J = 4.6, 2H, H$_{6,6'}$), 8.30 (s, 2H, H$_{3,3'}$), 7.36 (d, J = 4.6, 2H, H$_{5,5'}$), 5.25-5.05 (m, 14H, H$_{Glu-1}$), 4.68 (m, 4H, H$_{7,7'}$), 4.11 (m, 2 H, 1H, H$_{Glu-6}$), 3.80-3.10 (m, H$_{Glu-2,3,4,5,6}$, OCH$_3$).

^{13}C-NMR (100 MHz, CDCl$_3$): δ = 155.9, 149.1, 148.4, 121.8, 119.0, 98.9, 82.0-80.1 (m), 71.8-69.7 (m), 61.6-58.4 (m), 28.8.

MALDI-TOF: *m/z* 3033 [M+Na]$^+$.

IR (cm^{-1}): 2926.66, 2831.53, 1457.55, 1368.00, 1139.08, 1088.53, 1021.30, 969.47.

Anal. Calc. for $C_{136}H_{228}O_{70}N_2$: C 54.47, H 7.49, N 1.23. Found C 54.23, H 7.64, N 0.93.

Ru(4,4'-bpyhex)$_2$Cl$_2$
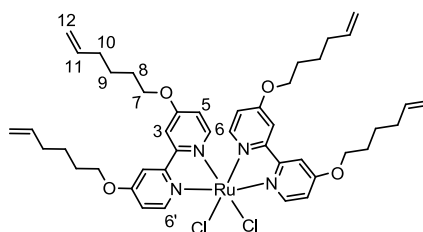
Ruthenium (III) chloride (78 mg, 0.37 mmol), 4,4'-bpyhex (264 mg, 0.75 mmol), and LiCl (100 mg, 2.62 mmol) were dissolved in dry N,N-dimethylformamide (4 mL) and heated to reflux for 8 h. After it cooled to room temperature, 20 ml of water was added and the resultant dark purple solid was collected by filtration and was washed with further portions of water and ether. The crude was purified by column chromatography on silica, using first acetonitrile to elute [Ru(4,4'-bpyhex)$_3$]Cl$_2$ impurities, and then changing to methanol to elute the Ru(4,4'-bpyhex)$_2$Cl$_2$ as the desired product. Yield 85 g (26%).

^{1}H NMR (300 MHz, DMSO): δ_H = 9.25 (dd, 2H, *J* = 4.3, 6.8 H$_6$), 8.64 (d, 2H, *J* = 6.8, H$_{6'}$), 7.94 (m, 4H, H$_3$), 7.22 (m, 4H, H$_5$), 5.93-6.10 (m, 4H, H$_{11}$), 5.22-5.09 (m, 8H, H$_{12}$), 4.37 (m, 8H, H$_7$), 2.24-2.36 (m, 8H, H$_{10}$), 1.95-2.05 (m, 8H, H$_8$), 1.66-1.78 (m, 8H, H$_9$).

MALDI-TOF: *m/z* 877.7 [M]$^+$.

ES MS(+) (MeOH): *m/z* 869.1 [Ru(4,4'-bpyhex)$_2$(OMe)$_2$].

UV-Vis (DCM) λ_{max} in nm: 560, 540, 370, 280.

[Ru(4,4'-bpyhex)$_2$(5,5'-bpyCD)](PF$_6$)$_2$
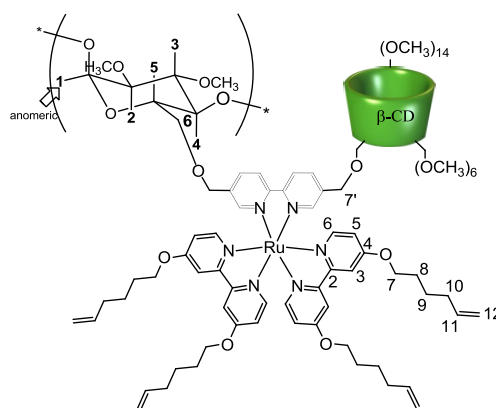
Ru(4,4'-bpyhex)$_2$Cl$_2$ (50 mg, 0.057 mmol) and 5,5'-bpyCD (260 mg, 0.087 mmol) were heated to reflux for 22 hr, under nitrogen in ethanol (10 mL). The solution was set aside to cool to room temperature and concentrated under vacuum to 2 ml. A saturated aqueous solution of ammonium hexafluorophosphate was added and the crude product was extracted with DCM. The product was purified by size exclusion column, sephadex LH20 in chloroform to yield 94 mg (40.1 %).

^{1}H NMR (300 MHz, CD$_3$CN) : δ = 8.46 (m, 4H, H$_3$), 8.13 (m, *J* = 8.4, 2H, H$_{3'}$), 7.97 (m, 2H, H$_{6'}$), 7.70-7.90 (m, 4H, H$_6$), 7.54-7.35 (m, 2H, H$_{4'}$), 6.97-6.76 (m, 4H, H$_5$), 5.78-5.98 (m, 4H, H$_{11}$), 5.39-5.60 (m, 8H, H$_{12}$), 4.93-5.26 (m, 14H, H$_{Glu-1}$), 4.82 (m, 4

H, H$_{7'}$), 4.09-4.30 (m, 8H, H$_7$), 4.02 (m, 2H, H$_{Glu-6}$), 2.93-3.91 (m, 206H, H$_{Glu-2,3,4,5,6}$, OMe), 2.12-2.32 (m, 8H, H$_{10}$), 1.80-1.93 (m, 8H, H$_8$), 1.45-1.69 (m, 8H, H$_9$).

MALDI-TOF: *m/z* 4106 [M]$^+$.

IR (cm^{-1}): 2929.61, 2852.01, 1613.04, 1446.44, 1315.95, 1261.96, 1138.75, 1089.07, 1023.04, 969.75.

UV-Vis (MeCN/ water 10:90) λ_{max} (nm): 467, 350, 290, 280.

Excitation (MeCN/ water 10:90) λ_{max} (nm): 467, 360, 340, 310.

Emission (MeCN/ water 10:90) λ_{max} (nm): 655 nm.

[Ru(4,4'-bpyhex)$_2$(4,4'-bpyCD)](PF$_6$)$_2$
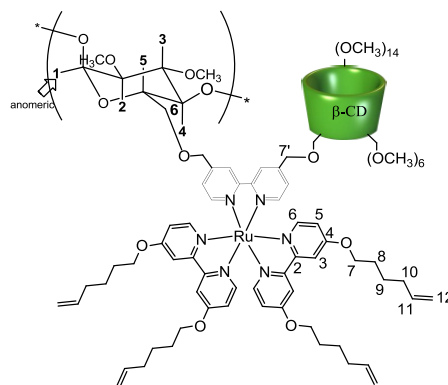
Ru(4,4'-bpyhex)$_2$Cl$_2$ (70 mg, 0.080 mmol) and 4,4'-bpyCD (364 mg, 0.122 mmol) were heated to reflux for 22 hours, under N$_2$ in ethanol (10 mL). The solution was set aside to cool to room temperature and concentrated under vacuum to 2 ml. A saturated aqueous solution of ammonium hexafluorophosphate was added and the crude product was extracted with DCM. The product was purified by size exclusion column, sephadex LH20 in chloroform to yield 125 mg (38 %).

^{1}H NMR (400 MHz, CD$_3$CN) : δ = 8.63 (m, 2H, H$_{3'}$), 8.44 (m, 4H, H$_3$), 7.74-8.02 (m, 6H, H$_6$ & H$_{6'}$), 7.59-7.31 (m, 4H, H$_5$), 6.92 (m, 2H, H$_{5'}$), 5.91 (m, 4H, H$_{11}$), 4.97-5.41 (m, 22H, H$_{12}$ & H$_{Glu-1}$), 4.72 (m, 4H, H$_{7'}$), 4.21 (m, 8H, H$_7$), 4.02 (m, 2H, H$_{Glu-6}$), 2.92-3.97 (m, 206H, H$_{Glu-2,3,4,5,6}$, OMe), 2.13 (m, 8H, H$_{10}$), 1.84 (m, 8H, H$_8$), 1.58 (m, 8H, H$_9$).

ES MS(+) (MeCN): m/z 1909.1 {M - 2[PF$_6$]}$^{2+}$.

IR (cm^{-1}): 2921.07, 2851.01, 1611.63, 1446.64, 1318.72, 1103.69, 1022.09, 971.19.

UV-Vis (MeCN/ water 10:90) λ$_{max}$ (nm): 480, 340, 285, 220.

Excitation (MeCN/ water 10:90) λ$_{max}$ (nm): 480, 370, 330, 290.

Emission (MeCN/ water 10:90) λ_{max} (nm): 660 nm.

[Ru(4,4'-bpysac)$_2$(4,4'-bpyCD)](PF$_6$)$_2$
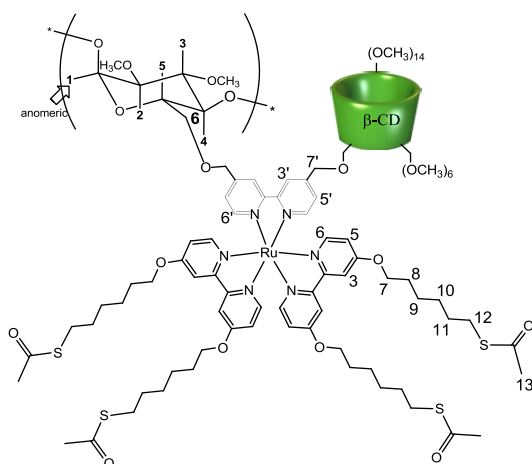
A solution of 100 mg (0.132 mmol) fresh thioacetic acid and 40 mg (0.230 mmol) AIBN in 5ml dry THF was heated at 60 °C and degassed under nitrogen for 30 minutes. 125 mg (0.030 mmol) of Ru(4,4'-bpyhex)$_2$(4,4'-bpyCD) was dissolved in 4 ml dry THF and was added dropwise. The reaction remained at 60 °C for 15 hrs after that time more AIBN and thioacetic acid was added. The solution was cooled to room temperature and excess thioacetic acid was neutralized by aqueous solution of saturated NaHCO$_3$. The THF was evaporated and the organic phase was extracted by DCM. The solvent was removed and the residue was washed several times with to yield 120 mg (90 %) of Ru(4,4'-bpysac)$_2$(4,4'-bpyCD) as a dark red solid.

^{1}H NMR (400 MHz, CD$_3$CN) : δ = 8.43 (m, 4H, H$_3$), 8.14 (m, 2H, H$_{3'}$), 7.77-7.92 (m, 6H, H$_6$ & H$_{6'}$), 7.46-7.28 (m, 4H, H$_5$), 6.92 (m, 2H, H$_{5'}$), 4.92-5.29 (m, 14H, H$_{Glu-1}$),

4.72 (m, 4H, $H_{7'}$), 4.17 (m, 8H, H_7), 4.02 (m, 2H, H_{Glu-6}), 2.98-3.91 (m, 206H, $H_{Glu-2,3,4,5,6}$, OMe), 2.88 (m, 8H, H_{12}), 2.30 (m, 12H, H_{13}), 2.15 (m, 8H, H_8), 1.81 (m, 8H, H_{11}), 1.55 (m, 16H, H_9 & H_{10}).

MALDI-TOF: *m/z* 4406 $[M]^+$.

IR (cm^{-1}): 2928.06, 2851.52, 1687.39(C=O), 1612.74, 1445.74, 1316.66, 1136.56, 1104.18, 1022.16, 969.49.

UV-Vis (MeCN/ water 10:90) λ_{max} (nm): 480, 340, 285, 220.

Excitation (MeCN/ water 10:90) λ_{max} (nm): 480, 370, 330, 290.

Emission (MeCN/ water 10:90) λ_{max} (nm): 660 nm.

Os(4,4'-bpyhex)$_2$Cl$_2$
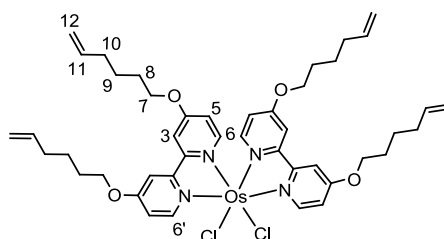
In a typical preparation 158 mg (NH$_4$)OsCl$_6$ (0.375 mmol) and 4,4'-bpyhex (264 mg, 0.75 mmol) in 5 ml ethylene glycol were heated to reflux for 45 min under N$_2$. The mixture was cooled to room temperature and an equal volume of saturated aqueous sodium dithionite was added in order to reduce excess Os^{III} to Os^{II}. The purple-black

precipitate that had formed was isolated by filtration, washed with water and washed with large volumes of ether (290 mg, 80% yield).

ES MS(+) (MeOH): *m/z* 966.3 [M]$^{+}$.

UV-Vis (MeCN/ water 10:90) λ_{max} (nm): 560, 415, 330, 280, 220.

[Os(4,4'-bpyhex)$_2$(4,4'-bpyCD)](PF$_6$)$_2$
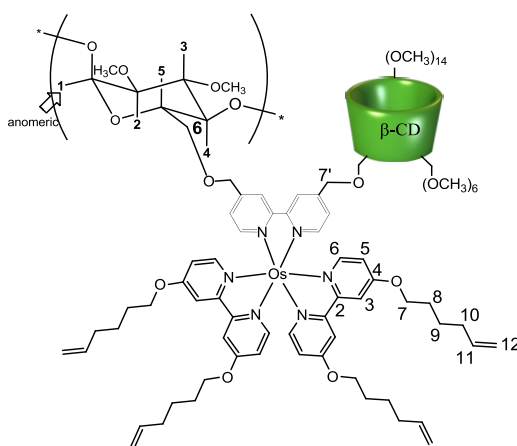
Os(4,4'-bpyhex)$_2$Cl$_2$ (50 mg, 0.052 mmol) and 4,4'-bpyCD (235 mg, 0.078 mmol) were heated in EtOH (5 ml) to 100 $^{\circ}$C for 20 hours in microwave. The solution was set aside to cool to room temperature and concentrated under vacuum to 2 ml. A saturated aqueous solution of ammonium hexafluorophosphate was added and the crude product was extracted with DCM. The product was purified by size exclusion column, sephadex LH20 in chloroform to yield 23 mg (30 %).

^{1}H NMR (400 MHz, CD$_3$CN) : δ = 8.44 (m, 2H, H$_{3'}$), 7.98 (m, 4H, H$_3$), 7.71 (m, 2H, H$_{6'}$), 7.26-7.55 (m, 4H, H$_6$), 6.82-7.05 (m, 6H, H$_5$ & H$_{5'}$), 5.68 (m, 4H, H$_{11}$), 5.52 (m,

8H, H$_{12}$), 5.14 (m, 14H, H$_{Glu-1}$), 4.84 (m, 4H, H$_{7'}$), 4.23 (m, 10H, H$_7$ & H$_{Glu-6}$), 2.92-4.02 (m, 206H, H$_{Glu-2,3,4,5,6}$, OMe), 2.18 (m, 8H, H$_{10}$), 1.87 (m, 8H, H$_8$), 1.60 (m, 8H, H$_9$).

MALDI-TOF: *m/z* 4661 [M+ 2(senapinic acid) + NH$_4$]$^+$.

IR (cm^{-1}): 2928.16, 2832.13, 1614.55, 1445.78, 1314.84, 1139.40, 1088.50, 1025.71, 968.91.

UV-Vis (MeCN/ water 10:90) λ$_{max}$ (nm): 650, 508, 485 (sh), 370, 295, 230.

Excitation (MeCN/ water 10:90) λ$_{max}$ (nm): 650, 508, 485, 400, 350.

Emission (MeCN/ water 10:90) λ$_{max}$ (nm): 795 nm.

[Os(4,4'-bpysac)$_2$(4,4'-bpyCD)](PF$_6$)$_2$
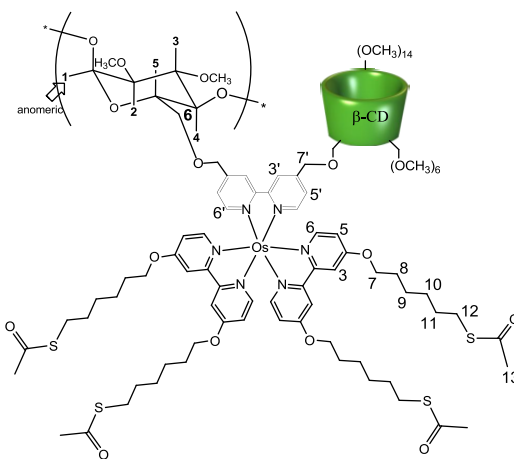
A solution of 100 mg (0.132 mmol) fresh thioacetic acid and 40 mg (0.230 mmol) AIBN in 5ml dry THF was heated at 60 °C and degassed under nitrogen for 30 minutes. 125 mg (0.030 mmol) of [Os(4,4'-bpyhex)$_2$(4,4'-bpyCD)](PF$_6$)$_2$ was

dissolved in 4 ml dry THF and was added dropwise. The reaction remained at 60 $^\circ$C for 15 hrs after that time more AIBN and thioacetic acid was added. The solution was cooled to room temperature and excess thioacetic acid was neutralized by aqueous solution of saturated $NaHCO_3$. The THF was evaporated and the organic phase was extracted by DCM. The solvent was removed and the residue was washed several times with to yield 120 mg (90 %) of $[Os(4,4'-bpysac)_2(4,4'-bpyCD)](PF_6)_2$ as a dark brown solid.

^{1}H NMR (400 MHz, CD_3CN) : δ = 8.37 (m, 4H, $H_{3'}$), 7.91 (m, 2H, H_3), 7.63 (m, 2H, $H_{6'}$), 7.24 (m, 4H, H_6), 6.75-6.92 (m, 6H, H_5 & $H_{5'}$), 5.10 (m, 14H, H_{Glu-1}), 4.81 (m, 4H, $H_{7'}$), 4.18 (m, 8H, H_7), 4.09 (m, 2H, H_{Glu-6}), 2.93-3.87 (m, 206H, $H_{Glu-2,3,4,5,6}$, OMe), 2.68 (m, 8H, H_{12}), 2.48 (m, 12H, H_{13}), 2.15 (m, 8H, H_{10}), 1.85 (m, 8H, H_{11}), 1.59 (m, 16H, H_9 & H_{10}).

IR (cm^{-1}): 2927.71, 2858.32, 1691.30(C=O), 1613.98, 1445.77, 1205.23, 1148.66, 1106.00, 1028.78, 969.47.

UV-Vis (MeCN/ water 10:90) λ_{max} (nm): 650, 508, 485 (sh), 370, 295, 230.

Excitation (MeCN/ water 10:90) λ_{max} (nm): 650, 508, 485, 400, 350.

Emission (MeCN/ water 10:90) λ_{max} (nm): 795 nm.

5.5. References

(1) Cavazzini, M.; Quici, S.; Scalera, C.; Puntoriero, F.; Ganga, G. L.; Campagna, S. *Inorg. Chem.* **2009**, *48*, 8578–8592.

(2) Constable, E. C.; Handel, R. W.; Housecroft, C. E.; Morales, A. F. n.; Ventura, B.; Flamigni, L.; Barigelletti, F. *Chem. Eur. J.* **2005**, *11*, 4024 – 4034.

(3) Faiz, J. A.; Kyllonen, L. E. P.; Contreras-Carballada, P.; Williams, R. e. M.; Cola, L. D.; Pikramenou, Z. *Dalton Trans.* **2009**, 3980–3987.

(4) Faiz, J. A.; Williams, R. M.; Silva, M. J. J. P.; Cola, L. D.; Pikramenou, Z. *J. Am. Chem. Soc.* **2006**, *128*, 4520-4521.

(5) Frampton, M. J.; Anderson, H. L. *Angew. Chem. Int. Ed.* **2007**, *46*, 1028 - 1064.

(6) Haider, J. M.; Williams, R. M.; Cola, L. D.; Pikramenou, Z. *Angew. Chem. Int. Ed.* **2003**, *42*, 1830 – 1833.

(7) He, B.; Wenger, O. S. *Inorg. Chem.* **2012**, *51*, 4335− 4342.

(8) Silva, M. J. J. P.; Haider, J. M.; Heck, R.; Chavarot, M.; Marsura, A.; Pikramenou, Z. *Supramolecular Chemistry* **2003**, *15*, 563–571.

(9) Chen, Z.; Bradshaw, J. S.; Lee, M. L. *Tetrahedron Lett.* **1996**, *37*, 6831-6834.

(10) Kefalas, E. *PhD, University of Birmingham* **2008**.

(11) Schubert, U. S.; Eschbaumer, C.; Hochwimmer, G. *Synthesis* **1999**, 779-782.

(12) Fraser, C. L.; Anastasi, N. R.; Lamba, J. J. S. *J. Org. Chem.* **1997**, *62*, 9314.

(13) Lecourt, T.; Mallet, J. M.; Sinay, P. *Eur. J. Org. Chem.* **2003**, 4553.

(14) Schubert, U. S.; Eschbaumer, C.; Hochwimmer, G. *Tetrahedron Lett.* **1998**, *39*, 8643.

(15) Sulivan, B. P.; Salmon, D. J.; Meyer, T. *J. Inorg. Chem.* **1978**, *17*, 3334-3341.

(16) Kober, E. M.; Caspar, J. V.; Sullivan, B. P.; Meyer, T. J. *J. Inorg. Chem.* **1988**, *27*, 4587-4598.

(17) Kalyanasundaram, K.; Nazeeruddin, M. K. *Chemical Physics letters* **1989**, *158*, 45-50.

(18) Bemdtseon, A. *J. Phys. Statues Solidi B* **1979**, *93*, K103.

(19) Yesildăg, A.; Ekinci, D. *Electrochimica Acta* **2010**, *55*, 7000-7009.

(20) Razgon, A.; Anstey, M. R.; Yakelis, N. A.; Bergman, R. G.; Sukenik, C. N. *Inorganica Chimica Acta* **2011**, *375*, 305–307.

CHAPTER

6

BODIPY-CD, an Efficient Non-Covalent Sensitizer for Neodymium Near-Infrared Emission

6.1. Introduction

The development of efficient sensitisation for lanthanides (Scheme 6.1) is important in many fields such as laser systems, optical amplification, biological imaging and sensing. This is due the long-lived excited states (µs to ms) and line-like emission in the visible and near-infrared regions of the lanthanides which allow them to participate in unique applications.
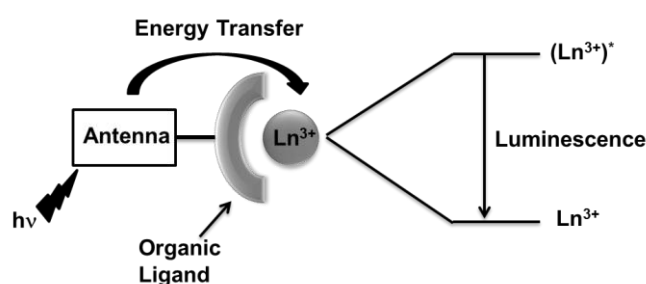
Scheme 6.1 Schematic presentation of lanthanide sensitisation.

The NIR-emitting lanthanides are especially popular in biological applications, since biological samples absorb strongly at the UV and visible wavelengths and hence

restrict the spectroscopic methods of detection to the near infra-red (NIR) region. In addition such relatively low energy excitation wavelengths are generally less damaging to biological material.

However, the optical spectroscopy applications of lanthanide ions suffer from forbidden f–f transitions, which make direct excitation impractical and the emission of lanthanide ions is usually realised by an indirect process called sensitisation, in which energy from an excited state of a sensitizer is transferred to the excited states of the lanthanide ion which emits as it relaxes to its ground state. Due to this effect, a good-absorbing sensitizer with the correct energy level has a significantly important role in the process.

During last two decades, numerous chromophores including terphenyl ligands[1], calix[4]arenes[2-4], β-diketonates[5], 1,4,7,10-tetraazacyclododecane[6], porphyrins[7-10], pyrazolones[11], 8-hydroxyquinoline[12-16], tropolonates[17], imidophosphinates[18], pyrazoylborates[19], and phthalocyanines[20], have been synthesised and their sensitisation capability for NIR emission of lanthanides has been examined. However, these probes exhibit low emission efficiency and require short wavelength excitation.

In recent years there are several reports of sensing the NIR lanthanides with the transition metal complexes, more specifically ruthenium and osmium. Such complexes are strongly-absorbing chromophores in the visible region and have relatively long-lived metal-to-ligand charge-transfer (MLCT) excited states, which increase the efficiency of the sensitisation process.[21-26]

One of candidates could be BODIPY dyes, good-absorbing probes in the visible region with high emission efficiency and long wavelength sensitisation. BODIPY, abbreviated from 4,4-difluoro-4-bora-3a,4a-diaza-s-indacene (Scheme 6.2), describes a family of boron dipyrromethene compounds. The BODIPY dyes were first discovered by Treibs and Kreuzer[27] in 1968 and have been developed significantly due to their outstanding properties including high extinction coefficients, large quantum yields and high stability[27-29], which makes them attractive for diverse applications such as artificial light and biological labelling capability.
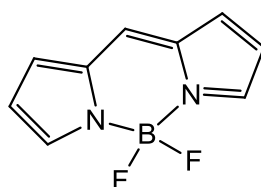
Scheme 6.2 Molecular structure of BODIPY building block.

There are few reports about the sensitisation of NIR emission of lanthanide ions with this family of chromophores. The first report is from Bünzli *et al.*[30], in which a BODIPY unit was attached to a tripyridyl group (Boditerpy) (Scheme 6.3) and, the characteristic NIR emission of three lanthanide ions (Nd^{3+}, Yb^{3+} and Er^{3+}), under UV and visible light excitation, was observed. The NIR emission efficiencies of Yb^{3+} and Nd^{3+} complexes were 0.31% and 0.0016%, respectively and the emission of the Er^{3+} complex was very weak.
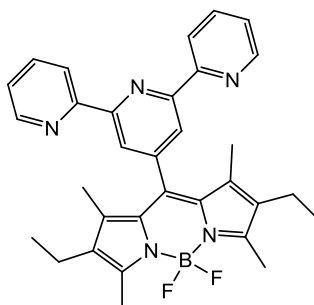
Scheme 6.3 Molecular structure of Boditerpy.[30]

In a recent work by He *et al.*[31] a new BODIPY modified 8-hydroxylquinoline ligand (8-HOQ-BODIPY) (Scheme 6.4) was synthesised for the sensitisation of near-infrared emission of lanthanide (III) ions. The ligand exhibits strong absorption at 506 nm and fluorescence at 510 nm in organic solvents with quantum yields ranging from 0.45 in dichloromethane to 0.015 in ethanol. Upon excitation at 522 nm, they observed a weak emission from the neodymium (III) and erbium (III) complexes at 1060 and 1500 nm, respectively, whereas strong emission at 976 and 1003 nm was seen for the ytterbium (III) complex. Their results demonstrate that the BODIPY dyes have the potential of a new class of sensitizers for efficient sensitisation of lanthanide-induced NIR emission and so efficient application in non-destructive medical diagnosis.
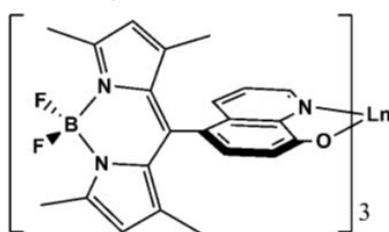
Scheme 6.4 Structure of the (8-HOQ-BODIPY) ligand and its lanthanide complexes.[31]

Inspired by these studies, we devised a route to attach a new BODIPY dye to a modified cyclodextrin (propargyl-p.m.β-CD)[32] in collaboration with Professor Ziessel's group (BODIPY-CD) (Scheme 6.5). This compound is an attractive luminescent receptor molecule with a cyclodextrin cup available for recognition. The photophysical properties of the BODIPY- CD were examined.

Here we have studied the participation of BODIPY-CD in a non-covalent energy transfer process to Nd(III) complexes as near-infrared emitting metallo-guests. This is the first time that such studies have been taken place for non-covalent near infra-red sensitisation of lanthanides through BODIPY sensitizers. $Nd(biphen)_3$ and $Nd(tpop)_3$ prepared by Davis[33] were employed to play the role of energy acceptors for the BODIPY centre. These complexes could act as guests for cyclodextrin due to their hydrophobic biphenyl and phenyl tails that ensure high binding constants in the cyclodextrin cavity. Cyclodextrin receptors are known as valuable supramolecular components and good materials to accommodate a variety of hydrophobic guests in aqueous media.[34]
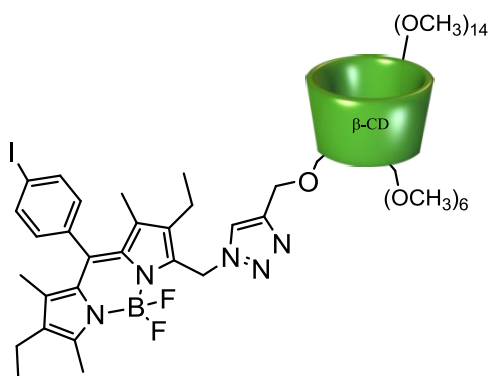
Scheme 6.5 Molecular structure of the BODIPY-CD.

6.2. Results and discussion

6.2.1. Synthesis of propargyl-p.m.β-CD

A permethylated cyclodextrin bearing one propargyl unit was synthesised using the Williamson ether coupling between monohydroxy permethylated β-cyclodextrin and propargyl bromide (Scheme 6.6) [32]. This reaction was carried out in DMF to afford propargyl-p.m.β-CD in 56 % yield after chromatography.
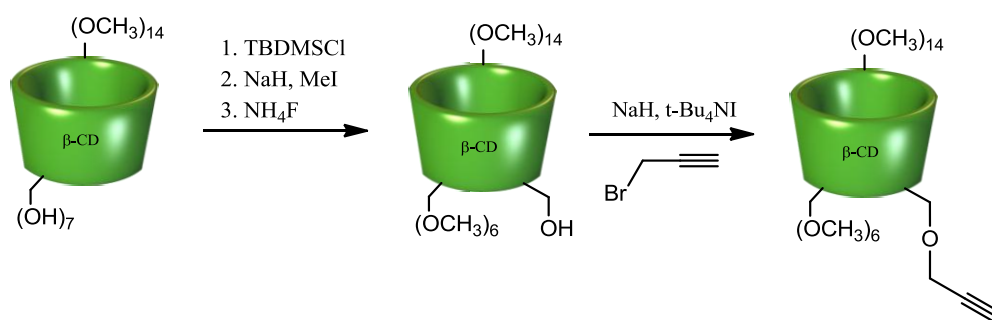
Scheme 6.6 Synthesis of propargyl-p.m.β-CD from monohydroxy permethylated β-cyclodextrin.

The target product propargyl-p.m.β-CD was characterised by mass spectrometry, and ^{1}H NMR and ^{13}C NMR spectroscopy studies. The electrospray mass spectrum shows a signal at m/z = 1476.5, corresponding to the singly charged sodium adduct. The ^{1}H NMR spectrum of propargyl-p.m.β-CD (Figure 6.1) shows a triplet at 2.4 ppm that corresponds to the acetylene proton (H_3), while a ABX system centred at

4.2 ppm represents the methylene protons (H_1) of the propargyl group. These couple in an AB pattern due to their diastereotopicity, and are further coupled with the acetylene proton *via* long range interaction mediated by the propargyl group.
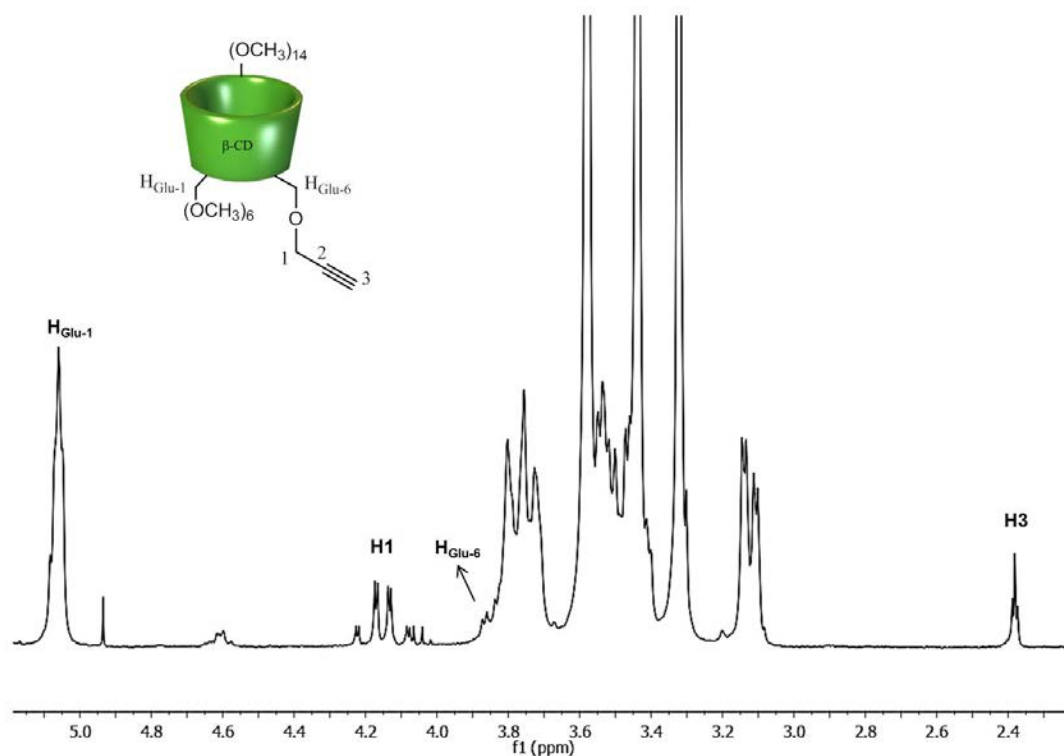
Figure 6.1 400 MHz ^{1}H NMR spectrum of mono-6-propargyl permethylated β-cyclodextrin.

Analysis of the ^{13}C NMR spectrum of propargyl-p.m.β-CD shows that the acetylene carbon atoms of C_3 and C_2 resonate at 80.0 ppm and 74.5 ppm respectively. C_{g-6} of the substituted cyclodextrin appears at 68.9 ppm and the methylene group (C_1) at approximately 59 ppm (Figure A6.1).

6.2.2. Photophysical properties of BODIPY-CD and Nd (III) guest

The absorption spectrum of BODIPY-CD displays absorption bands at 518 nm due to the $S_0 \rightarrow S_1$ transition of the BODIPY dye and at 390 nm, attributed to $S_0 \rightarrow S_2$ transition. There is also an intense band at 220 nm attributed to π - π^* transition of the aromatic modules.[35] A solution of BODIPY-CD in water/acetonitrile (90:10) showed luminescence at room temperature at 540 nm (Φ=0.25) upon excitation at 485 nm (Figure 6.2).
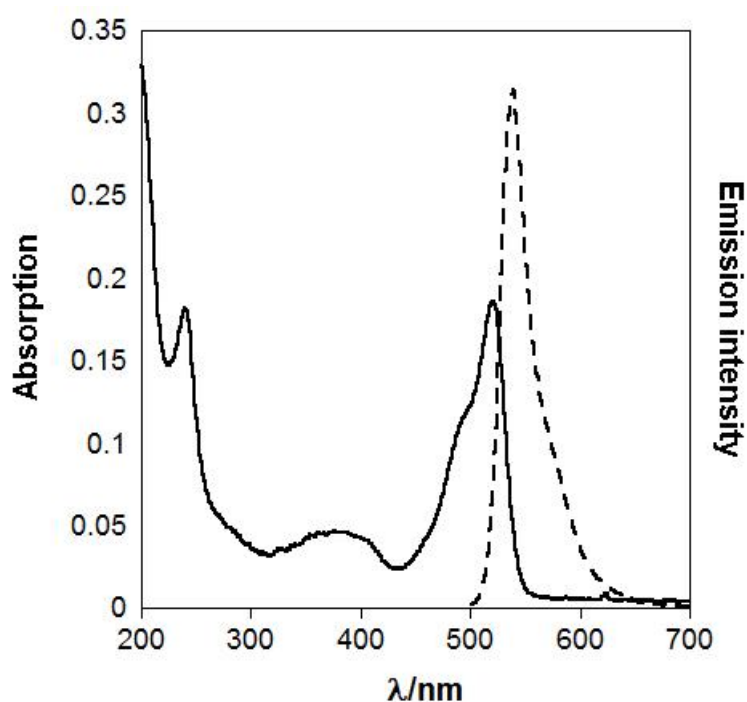
Figure 6.2 Absorption (solid line) and emission spectra (dashed line) of BODIPY-CD (C = 3.3 × 10^{-6} M) in water/MeCN (90:10), λ_{exc} = 485 nm.

The Nd(biphen)$_3$ and Nd(tpop)$_3$ complexes were synthesised by Dr. Davis in our group and used in this study.[33]
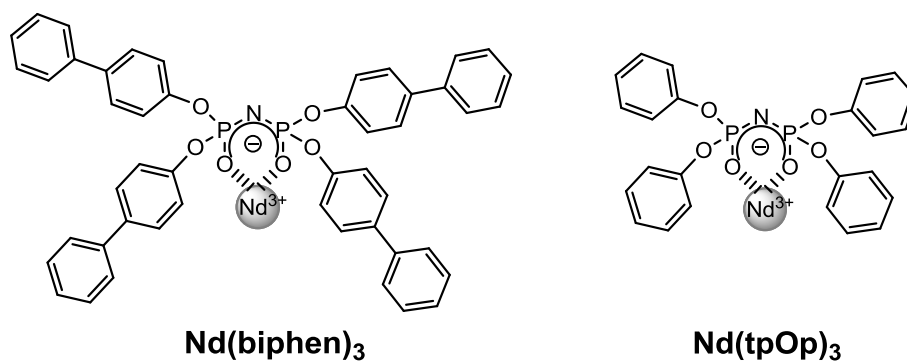
Scheme 6.7 Molecular structure of the Nd(biphen)$_3$ and Nd(tpOp)$_3$.

The UV-vis absorption spectrum of Nd(biphen)$_3$ in water/acetonitrile (90:10) exhibits an unstructured ligand-based band centred at around 255 nm assigned as π - π^* transitions of biphenyl moieties (Figure 6.3).
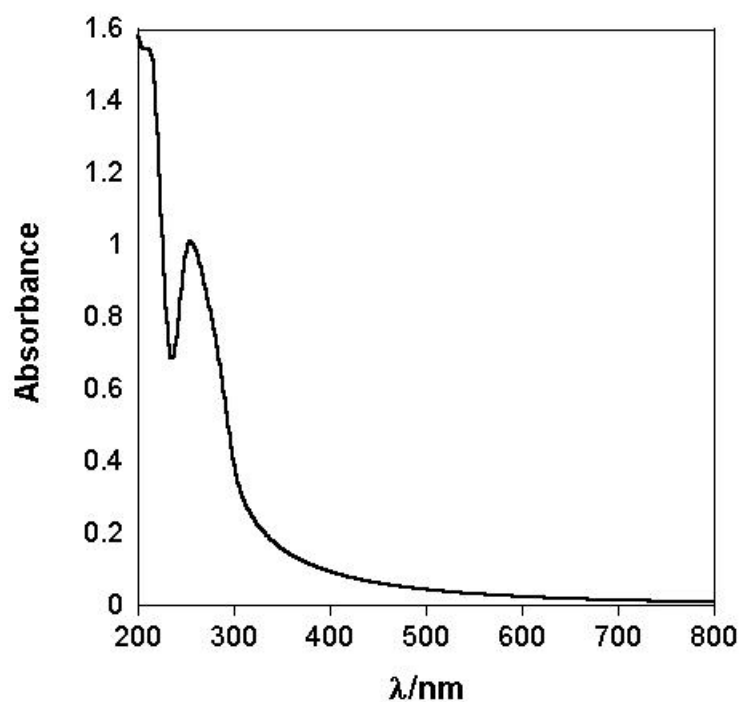
Figure 6.3 UV-Vis spectrum of Nd(biphen)$_3$ (C = 3.2 × 10^{-5} M) in MeCN/Water (10:90).

Excitation of Nd(biphen)$_3$ in water/acetonitrile (90:10) solution at 255 nm yields the characteristic near infra-red emission at 890, 1055 and 1325 nm assigned to the $^4F_{3/2}$ -> ^4I_J (J = 9/2, 11/2 and 13/2) transitions of Nd^{3+} as shown in Figure 6.4.
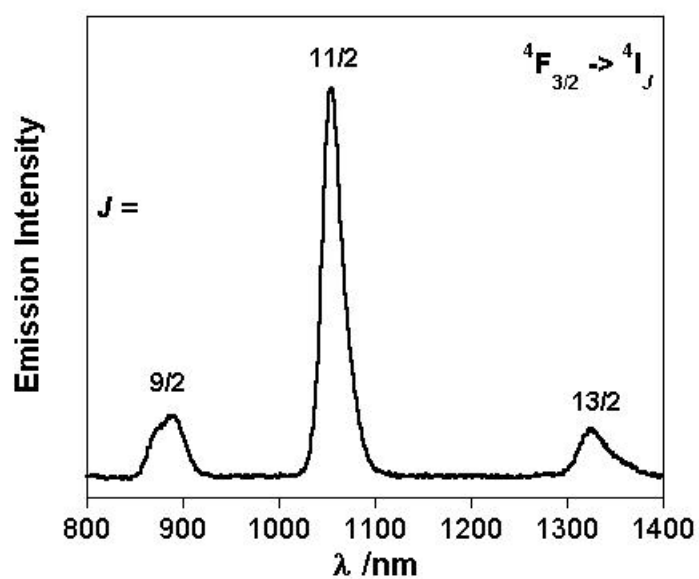
Figure 6.4 Emission spectrum of Nd(biphen)$_3$ in MeCN/Water (10:90) , λ_{exc} = 255 nm.

The UV-Vis absorption spectrum of Nd(tpOp)$_3$ in water/acetonitrile (90:10) exhibits a ligand-based band that is centred at 263 nm attributed to π - π^* transitions of phenoxide moieties (Figure 6.5).
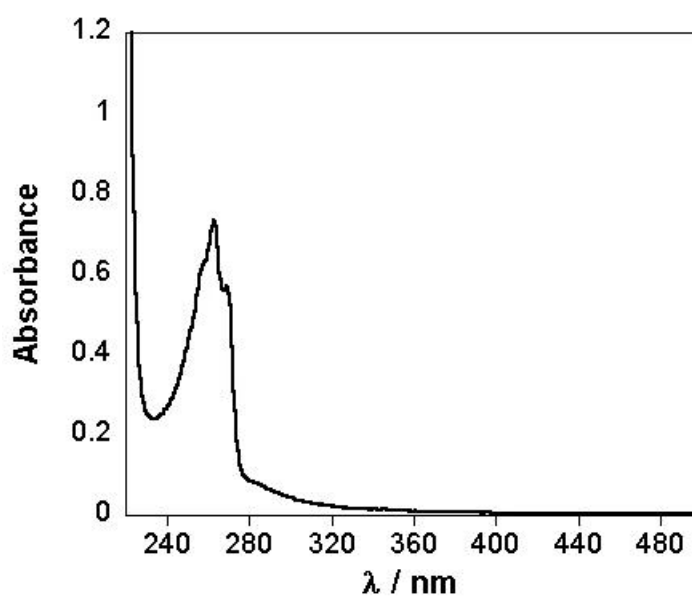
Figure 6.5 UV-Vis spectra of Nd(tpOp)$_3$ (C = 8 × 10^{-5} M) in MeCN/Water (10:90).

The Nd(tpOp)$_3$ spectrum shows emission upon excitation of the tpOp antenna chromophore at 263 nm. At room temperature sensitized emission is observed with three bands with peak maxima at 887, 1058 and 1328 nm. These are assigned to the luminescent transitions of $^4F_{3/2}$ -> ^4I_J (J = 9/2, 11/2, 13/2) respectively, characteristics of the Nd(III) ion (Figure 6.6).
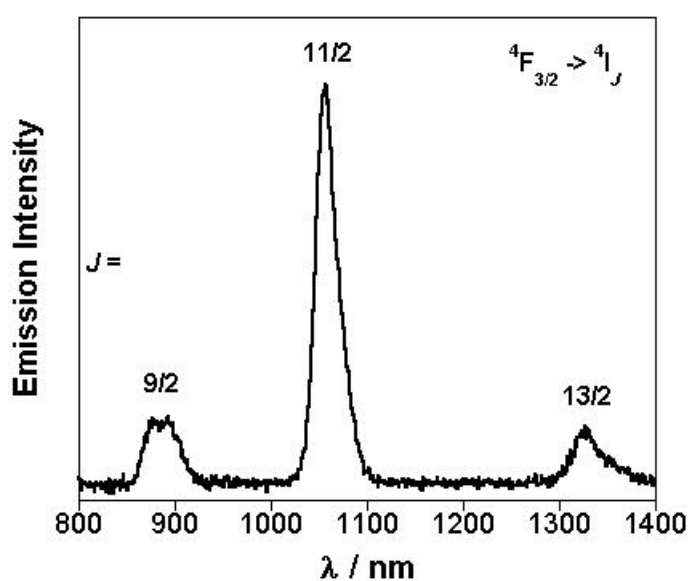
Figure 6.6 Emission spectrum of Nd(tpOp)$_3$ in MeCN/Water (10:90), λ_{exc} = 255 nm.

6.2.3. Photoinduced communication between BODIPY-cyclodextrin and Nd (III) guests

The interaction between BODIPY-CD and the neodymium metalloguests was investigated by absorption and steady state emission spectroscopy in water/acetonitrile (90:10) solutions of BODIPY-CD and excess of Nd(biphen)$_3$ or Nd(tpOp)$_3$.

A solution of BODIPY-CD and Nd(III) complex (in 1 ml water/ acetonitrile (90:10)) was prepared by mixing 50 μL of BODIPY-CD (8 $\times 10^{-5}$ M in acetonitrile) with 50 μL of Nd(III) complex (64 $\times 10^{-5}$ M in acetonitrile). The final concentration was 4×10^{-6} M of BODIPY-CD and 32×10^{-6} M of Nd(III) complex. Two further solutions of 1ml of either BODIPY-CD (4×10^{-6} M) or Nd(III) complex (32×10^{-6} M) were also made for comparison.
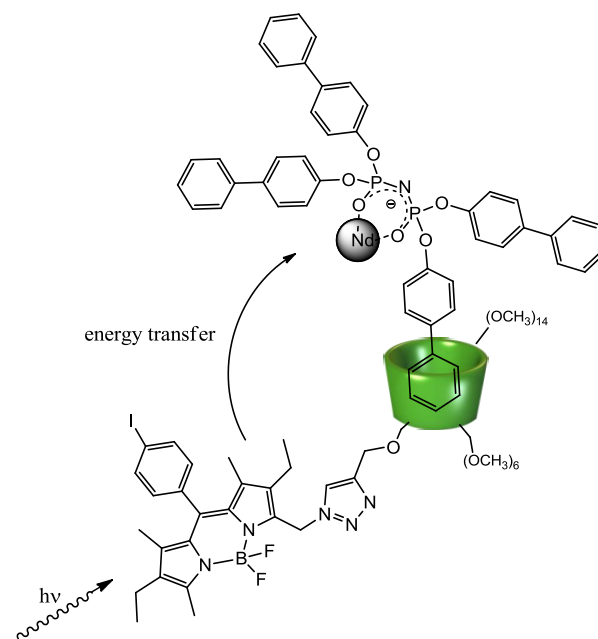
Scheme 6.8 The interaction between BODIPY-CD and Nd(biphen)$_3$.

The solution of the mixture of BODIPY-CD/ Nd(biphen)$_3$ complex (4 × 10^{-6} M: 32 × 10^{-6} M) shows peaks at 207 nm, 260 nm (Figure 6.7A), at 524 and two shoulders at 410 nm and 490 nm (Figure 6.7B). These peaks are attributed to the biphenyl absorption of the Nd(biphen) complex which appears at 207 nm and 260 nm and to the BODIPY chromophore absorptions which appear at 410, 490 and 524 nm. Although it seems that the λ_{max} of Nd(biphen)$_3$ and BOSIPY-CD shift, further investigations revealed that these are not real and just an art effect resulting from the sum of two spectra. As we have excess of Nd(III) complex, not all the biphenyls are inserted in the cyclodextrin cavity and so no shift of λ_{max} is expected.
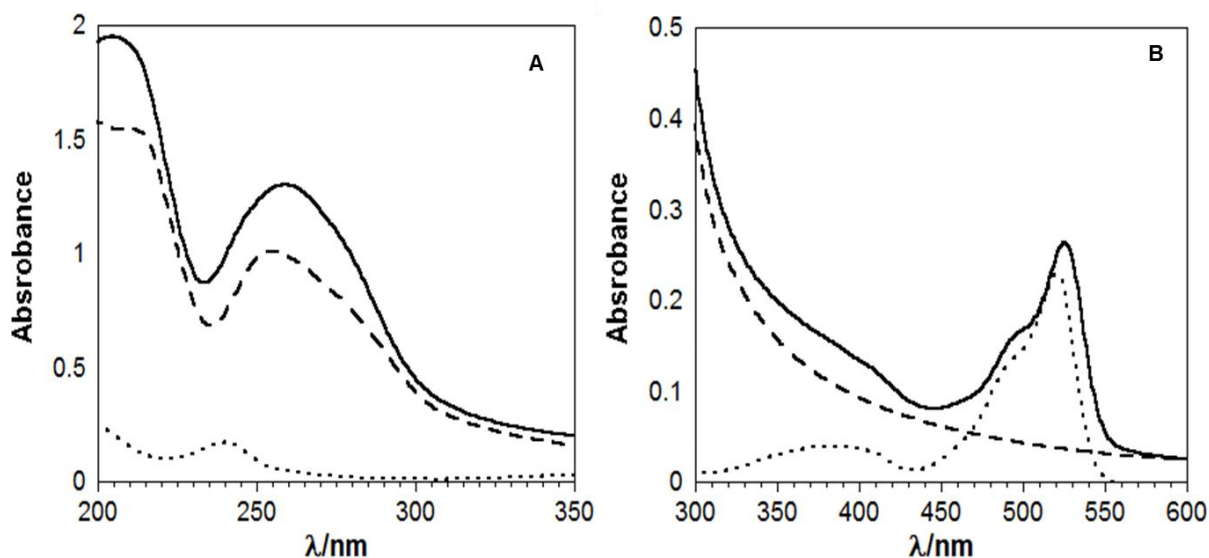
Figure 6.7 (A and B) UV-Vis spectra of BODIPY-CD (C = 4 × 10^{-6} M, dotted line), Nd(biphen)$_3$ (C = 32 × 10^{-6} M, dashed line) and solution of BODIPY-CD/ Nd(biphen)$_3$ (C $_{BODIPY-CD}$ = 4 × 10^{-6} M, C $_{Nd(biphen)3}$ = 32 × 10^{-6} M, solid line), all solutions are in MeCN/Water (10:90).

It is expected that in case of the interaction between BODIPY-CD and Nd(III) complexes, excitation of the BODIPY unit results to an energy transfer to the $^4F_{3/2}$ of Nd(III) complexes and hence to the increase of the NIR emission. Upon excitation at 485 nm the emission intensities of BODIPY-CD (λ_{em} = 540 nm) and Nd(biphen)$_3$ (λ_{em} = 890, 1055, 1325 nm) in all three solutions were monitored. The emission intensity of the mixture of BODIPY-CD / Nd(biphen)$_3$ complex (4× 10^{-6} M : 32 × 10^{-6} M) in the visible region showed a 55% decrease in comparison with the solution of BODIPY-CD (Figure 6.8 A). In the NIR region (Figure 6.8 B) characteristic emission signals of neodymium appeared in the solution of the mixture of BODIPY-CD / Nd(biphen)$_3$ complex (4× 10^{-6} M : 32 × 10^{-6} M). These are purely arising from the energy transfer process as the Nd(biphen)$_3$ solution in absence of BODIPY-CD in same concentration and conditions does not show any emission upon excitation at 485 nm.

This was also confirmed by excitation spectroscopy. The excitation spectrum of the solution of the mixture of BODIPY-CD / Nd(biphen)$_3$ complex (4× 10^{-6} M : 32 × 10^{-6} M) shows a peak at 520 nm which is attributed to the absorption of BODIPY confirming the energy transfer process and indicates that the emission signals are arising from BODIPY unit only.
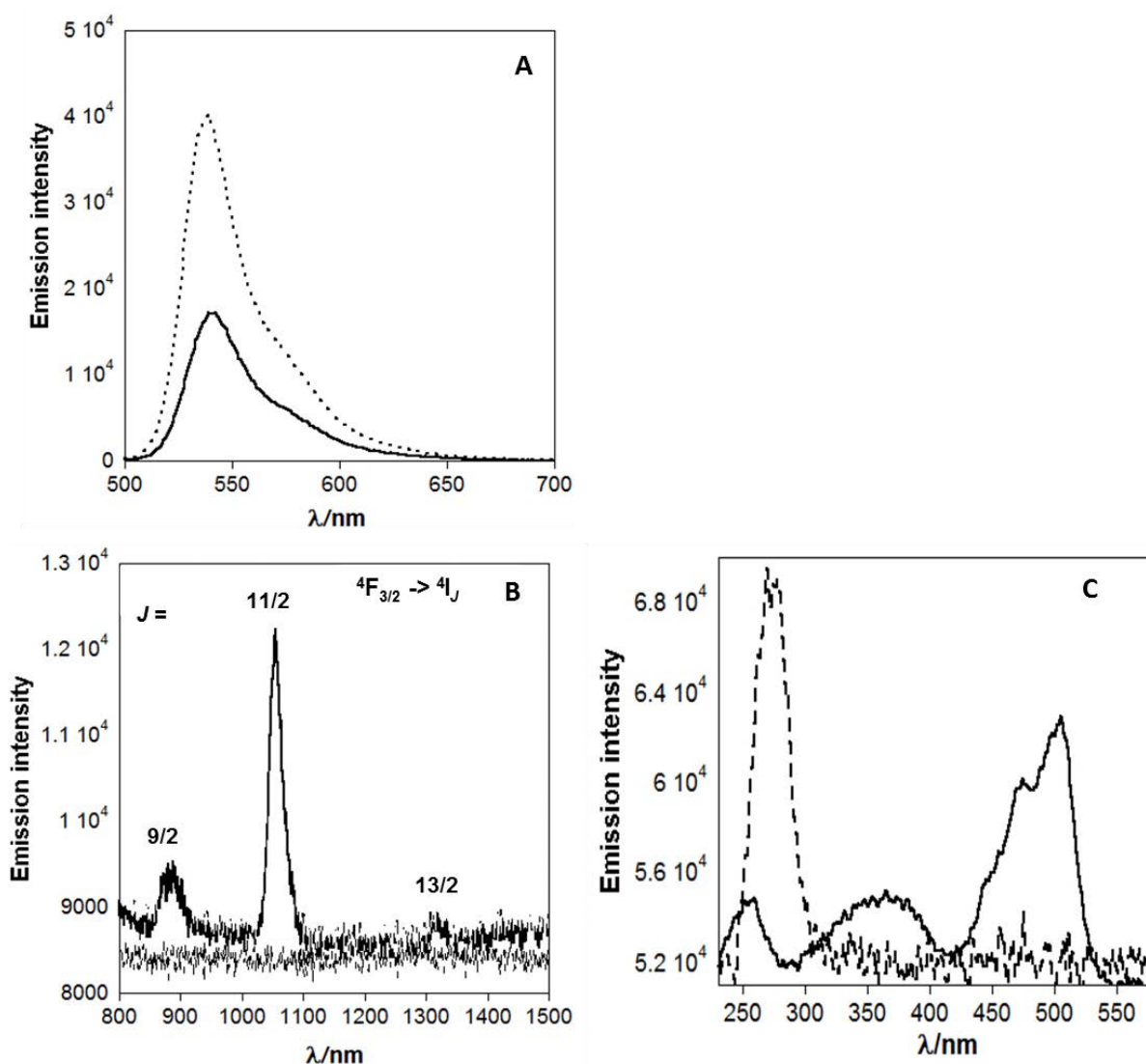
Figure 6.8 A) Visible region and B) NIR region of emission spectra of BODIPY-CD (C = 4 × 10^{-6} M, dotted line), Nd(biphen)$_3$ (C = 32 × 10^{-6} M, dashed line) and the solution of BODIPY-CD/ Nd(biphen)$_3$ (C $_{BODIPY-CD}$ = 4 × 10^{-6} M, C $_{Nd(biphen)3}$ = 32 × 10^{-6} M, solid line), λ_{ex} = 485 nm C) Excitation spectra of Nd(biphen)$_3$ (dashed line) and solution of both components (solid line), λ_{em} = 1055 nm - All solutions are in MeCN/Water (10:90).

Similarly three solutions of either BODIPY-CD (C = 4 ×10^{-5} M) or Nd(tpOp)$_3$ complex (C = 32 ×10^{-5} M) and a solution of the mixture of BODIPY-CD / Nd(tpOp)$_3$ complex (4× 10^{-6} M : 32 × 10^{-6} M) in 1 ml water/acetonitrile (90:10) were prepared and the

362

interaction between BODIPY-CD and Nd(tpOp)$_3$ was investigated by absorption and steady state emission spectroscopy.
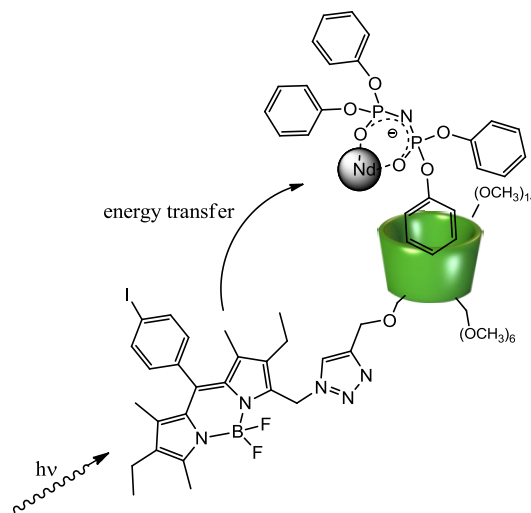
Scheme 6.9 The interaction between BODIPY-CD and Nd(tpOp)$_3$.

The solution of the mixture of BODIPY-CD / Nd(tpOp)$_3$ complex (4× 10^{-6} M : 32 × 10^{-6} M) shows peaks at 205, 240, 263 nm (Figure 6.9A), at 523 and two shoulders at 410 nm and 490 nm (Figure 6.9B). These peaks are attributed to the phenyl absorption of the Nd(tpOp) complex which appears at 205 nm and 263 nm and to the BODIPY chromophore absorption which appears at 410, 490 and 523 nm. Although it seems that the λ_{max} of Nd(tpOp)$_3$ and BOSIPY-CD shift, further investigations revealed that these are not real and just an art effect resulting from the sum of two spectra. As we have excess of Nd(III) complex, not all the phenyls are inserted in the cyclodextrin cavity and so no shift of λ_{max} is expected.
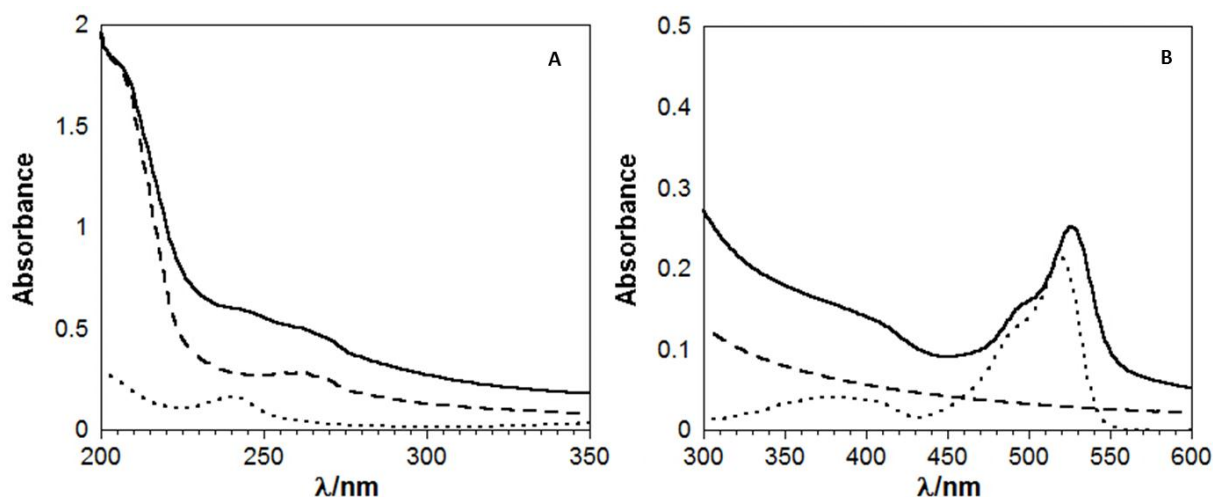
Figure 6.9 (A and B) UV-Vis spectra of BODIPY-CD (C = 4 × 10^{-6} M, dotted line), Nd(tpOp)$_3$ (C = 32 × 10^{-6} M, dashed line) and solution of BODIPY-CD/ Nd(tpOp)$_3$ (C$_{BODIPY-CD}$ = 4 × 10^{-6} M, C$_{Nd(tpOp)3}$ = 32 × 10^{-6} M, solid line), all solutions are in MeCN/Water (10:90).

In a similar approach upon excitation at 485 nm the emission intensities of BODIPY-CD (λ_{em} = 540 nm) and Nd(tpOp)$_3$ (λ_{em} = 890, 1055, 1325 nm) in all three solutions was monitored in both visible and NIR region. Addition of the Nd(tpOp)$_3$ results to 74% decrease of the emission intensity of BOPIDY-CD in the visible region and in the same time appearing the characteristic emission signals of Nd(tpOp)$_3$ in NIR region indicates the excited state energy transfer to the $^4F_{3/2}$ of Nd(tpOp)$_3$ (Figure 6.10). The emission signals which appeared in NIR region are solely arising from energy transfer process as the Nd(tpOp)$_3$ solution in absence of BODIPY-CD in same concentration and conditions does not display any emission upon excitation at 485 nm. The excitation spectrum shows the λ_{max} of BODIPY-CD at 525 nm which confirms that the emission signals are purely caused by energy transfer process.
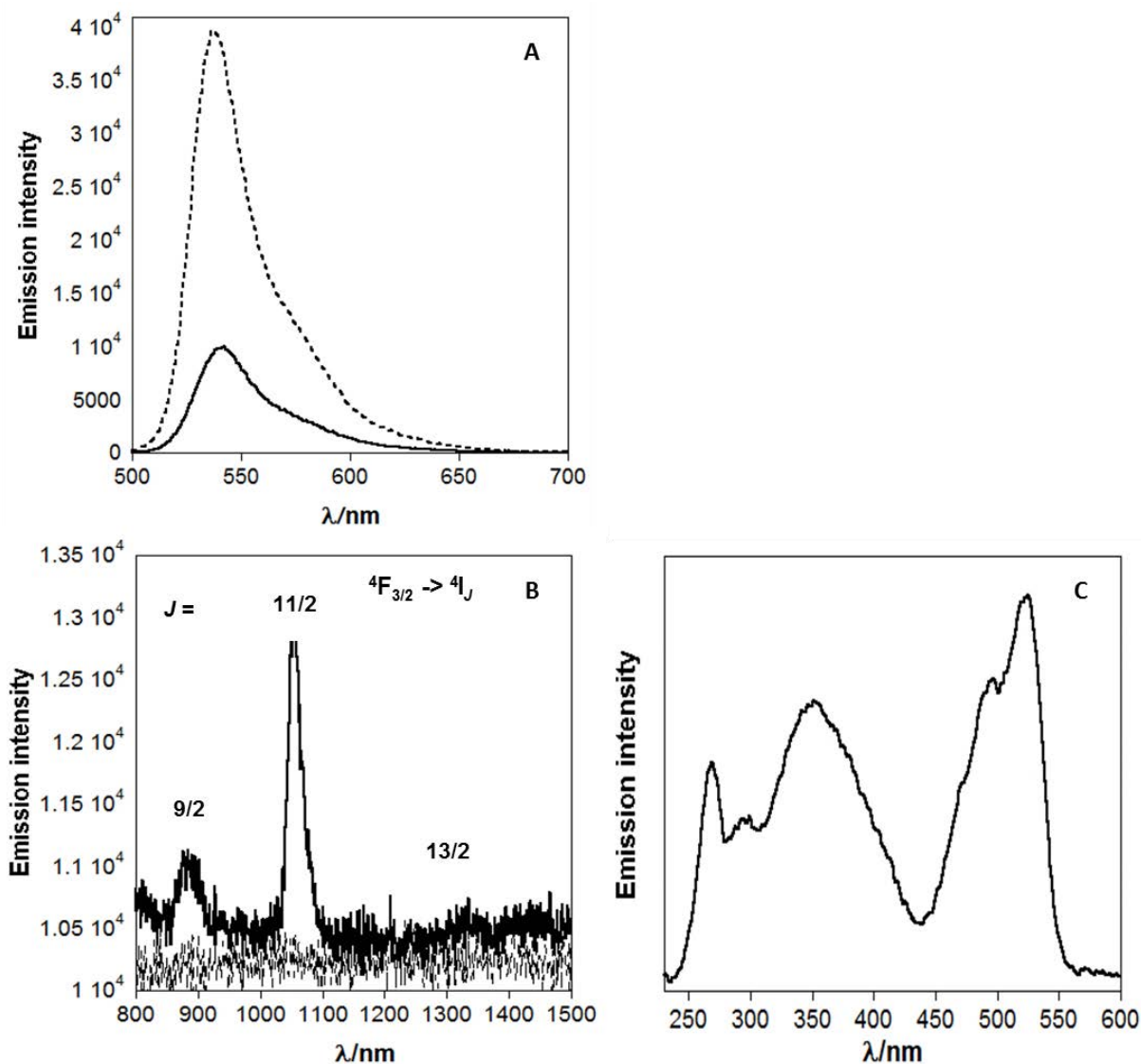
Figure 6.10 **A)** Visible region and **B)** NIR region of emission spectra of BODIPY-CD (C = 4 × 10^{-6} M, dotted line), Nd(tpOp)$_3$ (C = 32 × 10^{-6} M, dashed line) and solution of both components (C $_{BODIPY-CD}$ = 4 × 10^{-6} M, C $_{Nd(tpOp)3}$ = 32 × 10^{-6} M, solid line), λ_{ex} = 485 nm **C)** Excitation spectra of Nd(tpOp)$_3$ (dashed line) and solution of BODIPY-CD/ Nd(tpOp)$_3$ (solid line), λ_{em} = 1055 nm - All solutions are in MeCN/Water (10:90).

To examine the possible effect of energy transfer process to Nd(III) complexes not inserted into the cyclodextrin cavity, we used $Nd(F_6\text{-}acac)_3$, which doesn't carry any suitable hydrophobic guest moiety to insert to the cyclodextrin cavity. We observed no energy transfer between BODIPY-CD and $Nd(F_6\text{-}acac)_3$. The solution of the mixture of BODIPY-CD/ $Nd(F_6\text{-}acac)_3$ complex (4×10^{-6} M : 32×10^{-6} M) shows peaks at 300 nm attributed to the $F_6\text{-}acac$ absorption of the $Nd(F_6\text{-}acac)_3$ complex and 240, 518 nm and two shoulders at 400 and 490 nm attributed to the BODIPY chromophore (Figure 6.11).
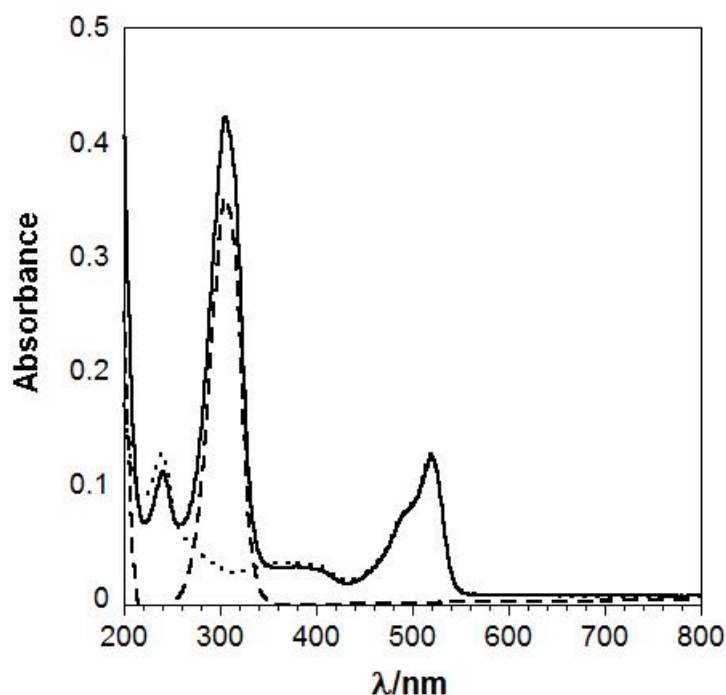
Figure 6.11 UV-Vis spectra of BODIPY-CD (C = 4×10^{-6} M, dotted line), $Nd(F_6\text{-}acac)_3$ (C = 32×10^{-6} M, dashed line) and solution of BODIPY-CD/ $Nd(F_6\text{-}acac)_3$ (C $_{BODIPY-CD}$ = 4×10^{-6} M, C $_{Nd(F6-acac)3}$ = 32×10^{-6} M, solid line), all solutions are in MeCN/Water (10:90).

The emission intensity of the BOPIDY-CD did not decrease when $Nd(F_6\text{-acac})_3$ was added, confirming that there is no energy transfer between BODIPY-CD and $Nd(F_6\text{-acac})_3$ (Figure 6.12).
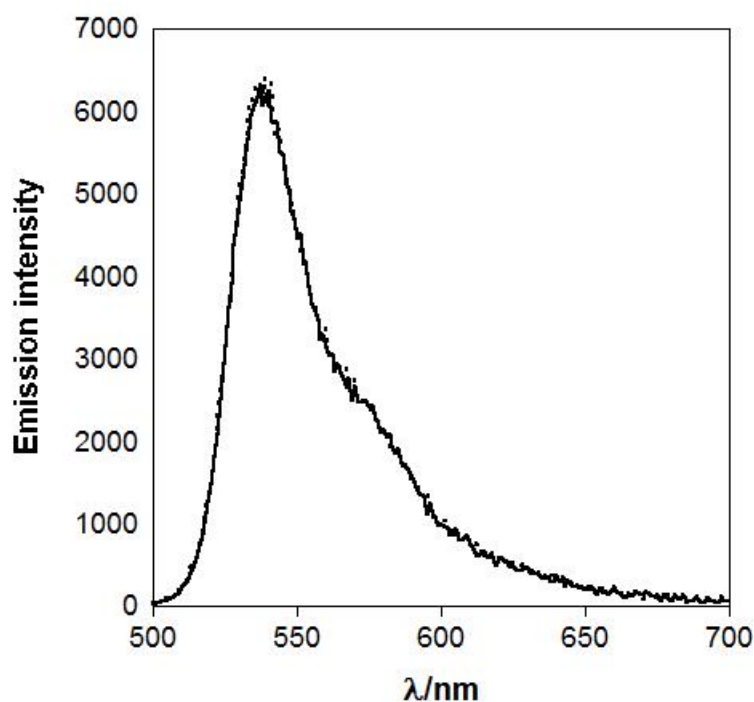
Figure 6.12 Emission spectra of BODIPY-CD (C = 4 × 10^{-6} M, dotted line) and solution of BODIPY-CD/ $Nd(F_6\text{-acac})_3$ (C $_{BODIPY\text{-}CD}$ = 4 × 10^{-6} M, C $_{Nd(F6\text{-}acac)3}$ = 32 × 10^{-6} M, solid line), all solutions are in MeCN/Water (10:90) - λ_{exc} = 485 nm.

The solution of the mixture of BODIPY-CD/ $Nd(F_6\text{-acac})_3$ complex (4× 10^{-6} M : 32 × 10^{-6} M) shows the characteristic emission bands in NIR region when excited at 300 nm (λ_{max} of $Nd(F_6\text{-acac})_3$), but there is no emission upon excitation of the λ_{max} of the BODIPY-CD at 485 nm which again indicates that there is no energy transfer process between BODIPY-CD and $Nd(F_6\text{-acac})_3$ (Figure 6.13).
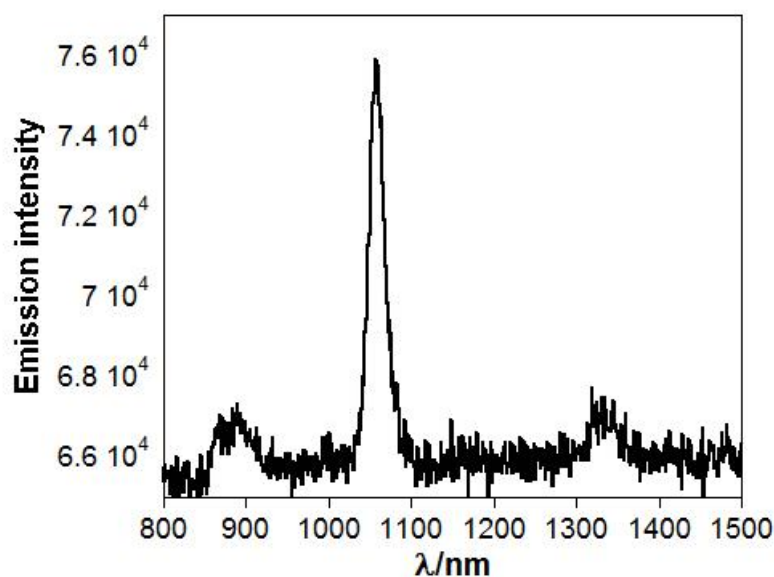
Figure 6.13 Emission spectra of Nd(F$_6$-acac)$_3$ (C = 32 × 10^{-6} M) in MeCN/Water (10:90),

λ_{exc} = 305 nm.

We also studied the effect of addition of 1-adamantylamine (adaNH$_2$) on the energy transfer process. The binding of the biphenyl guest was studied in our group[36,37] and determined to be 2.1 × 10^3 M^{-1} and adamantyl derivatives have been studied previously in the literature[38-40] to bind to cyclodextrin cavities in the order of ~ 10^5 M^{-1} which showed stronger binding constants in comparison with biphenyl and phenyl groups. It was expected that adaNH$_2$ would replace the biphenyl or phenyl groups and as the result break the non-covalent communication of the BODIPY dye and Nd(III) complexes and hence hinder the energy transfer process.

The emission spectra in the visible region show an increase in intensity upon addition of 50 μl of aqueous solution of adaNH$_2$ (1.4 × 10^{-2} M) to the solution of either the mixture of BODIPY-CD/ Nd(biphen)$_3$ complex or the solution of the mixture of BODIPY-CD/ Nd(tpOp)$_3$ complex (Figure 6.14 and 6.15), confirming the replacement

of the adaNH$_2$. However due to the low solubility of adaNH$_2$ in water, the full replacement was impossible. But even the partial replacement was enough to stop the sensitisation of Nd(III) complexes by BODIPY dye and resulting to no NIR emission of the Nd(biphen)$_3$ and Nd(tpOp)$_3$ complexes.
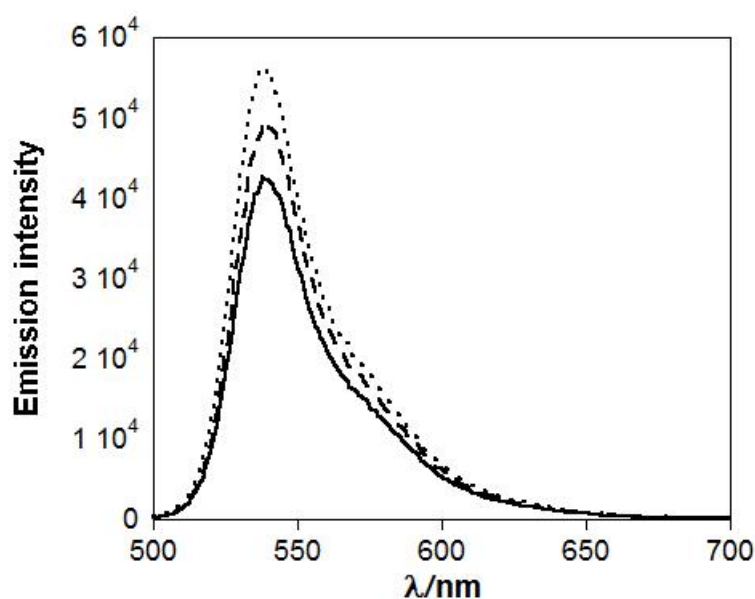
Figure 6.14 Emission spectra of BODIPY-CD (C = 4 × 10^{-6} M, dotted line), solution of BODIPY-CD/ Nd(biphen)$_3$ (C $_{BODIPY-CD}$ =4 × 10^{-6} M, C $_{Nd(biphen)3}$ = 32 × 10^{-6} M, solid line) and after addition of the adaNH$_2$ (C $_{BODIPY-CD}$ =4 × 10^{-6} M, C $_{Nd(biphen)3}$ = 32 × 10^{-6} M, C $_{adaNH2}$ = 7 × 10^{-4} M, dashed line) all solutions are in MeCN/Water (10:90) – λ$_{ex}$ = 485 nm.
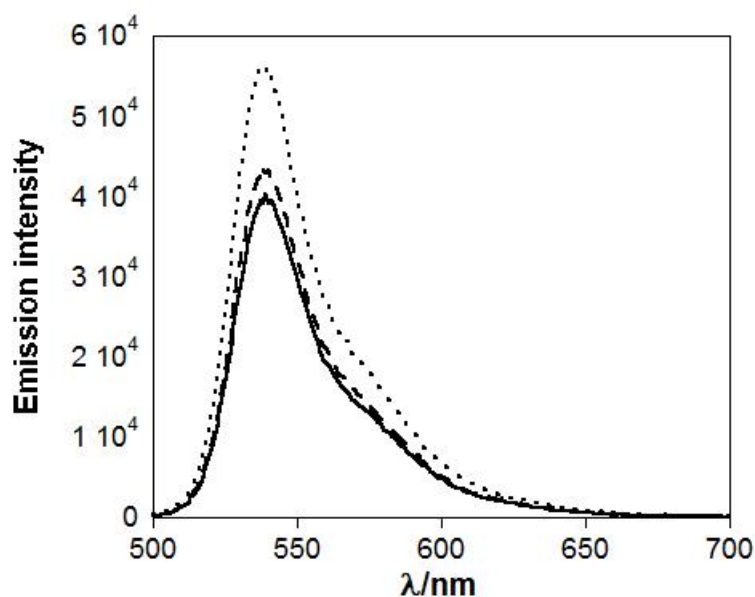
Figure 6.15 Emission spectra of BODIPY-CD (C = 4 × 10^{-6} M, dotted line), solution of BODIPY-CD/ Nd(tpop)$_3$ (C $_{BODIPY-CD}$ =4 × 10^{-6} M, C $_{Nd(tpOp)3}$ = 32 × 10^{-6} M, solid line) and after addition of the adaNH$_2$ (C $_{BODIPY-CD}$ =4 × 10^{-6} M, C $_{Nd(tpOp)3}$ = 32 × 10^{-6} M, C $_{adaNH2}$ = 7 × 10^{-4} M, dashed line) all solutions are in MeCN/Water (10:90) – λ_{ex} = 485 nm.

6.2.4. NMR spectroscopy studies of the metalloguests inclusion within cyclodextrins

The binding of the phenyl and biphenyl groups of the metalloguests with cyclodextrins was studied by NMR spectroscopy using permethylated-β-cyclodextrin (pm-β-CD). NMR spectroscopy is one of the most common techniques to study the inclusion, simply because of the availability of high frequency instruments.

Davis previously found out that among different lanthanides with the biphen ligand, Yb(biphen)$_3$ shows the most characteristic NMR spectrum[33], and so Yb(biphen)$_3$ was

used as a guest model for the inclusion studies. The ^{1}H NMR spectrum of the Yb(biphen)$_3$ in 50:50 CD$_3$CN/D$_2$O (C = 3.3 × 10^{-3} M) was first obtained. Due to the poor solubility of Yb(biphen)$_3$ we had to keep the acetonitrile up to 50% to have a reasonable solubility for running the NMR spectra. Another NMR sample containing same concentration of the Yb(biphen)$_3$ and a 12-fold excess of pm-β-CD (C = 4 × 10^{-2} M) in 50:50 CD$_3$CN/D$_2$O was also prepared and the ^{1}H NMR spectrum was obtained.

Comparison of the two NMR spectra shows that the signals for the biphenyl protons shift around 5 ppm down-field upon addition of pm-β-CD (Figure 6.16), giving a clear indication that inclusion in the cyclodextrin cavity has occurred. The peaks also show further splitting which can be the result of decreasing the rotational movement of the phenyl groups by insertion in the cyclodextrin cavity.
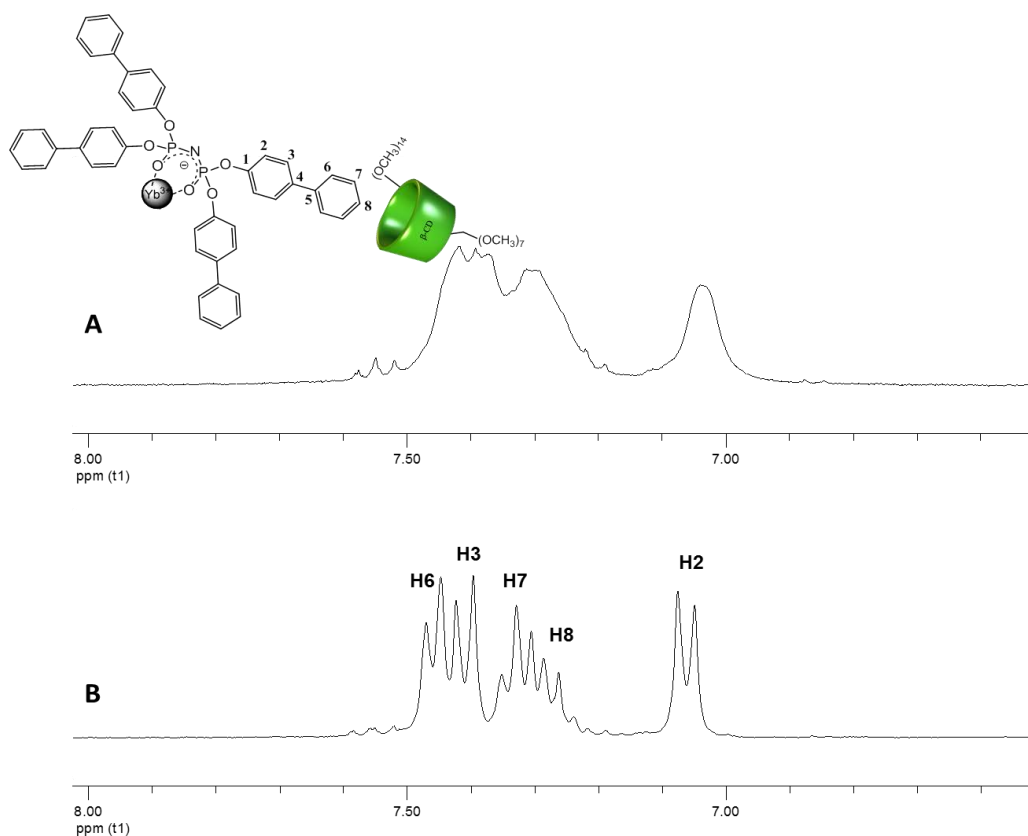
Figure 6.16 A) The 300 MHz ^{1}HNMR spectrum of Yb(biphen)$_3$ (C = 3.3 × 10^{-3} M) in 50:50 D$_2$O/CD$_3$CN B) The 300 MHz ^{1}HNMR spectrum of Yb(biphen)$_3$ (C = 3.3 × 10^{-3} M) and pm-β-CD (C = 4 × 10^{-2} M) in 50:50 D$_2$O/CD$_3$CN.

Among Ln(tpOp)$_3$ complexes, Eu(tpOp)$_3$ has the most characteristic NMR spectrum[33] and so was used as a guest model for the inclusion studies. Similarly two NMR samples was prepared, first Eu(tpOp)$_3$ in 50:50 CD$_3$CN/D$_2$O (C = 3.3 × 10^{-3} M) and the second containing the same concentration of the Eu(tpOp)$_3$ and a 12-fold excess of pm-β-CD (C = 4 × 10^{-2} M) in 50:50 CD$_3$CN/D$_2$O. The ^{1}H NMR spectra of both samples were obtained and showed around 5 ppm down-field shift upon addition of pm-β-CD (Figure 6.17) proving the inclusion of the phenyl unit in the cyclodextrin cavity.

The ^{31}P NMR and ^{13}C NMR spectra of all samples were also obtained and did not show any shift upon addition of the pm-β-CD (See figure A6.2 and A6.3).
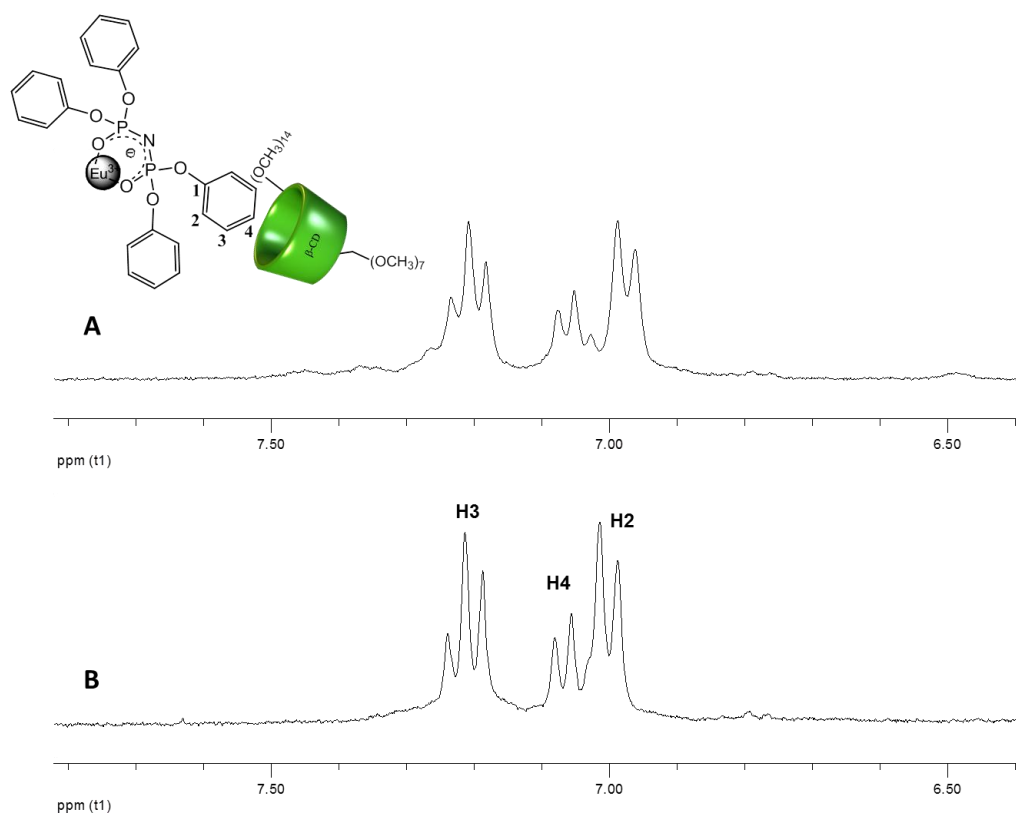
Figure 6.17 A) The 300 MHz ^{1}HNMR spectrum of Eu(tpOp)$_3$ (C = 3.3 × 10^{-3} M) in 50:50 D$_2$O/CD$_3$CN B) The 300 MHz ^{1}HNMR spectrum of Eu(tpOp)$_3$ (C = 3.3 × 10^{-3} M) and pm-β-CD (C = 40 × 10^{-3} M) in 50:50 D$_2$O/CD$_3$CN.

6.3. Conclusion

A new modified BODIPY dye (BODIPY-CD) carrying cyclodextrin cavity was synthesised and the photophysical properties of this new compound was demonstrated. The photo-induced energy transfer through a cyclodextrin cavity between the BODIPY centre and near infra-red emitting neodymium complexes bearing hydrophobic biphenyl and phenyl tails was examined.

The BODIPY-CD proved to be a good sensitizer for luminescence from the neodymium complexes. Also for the first time we showed a new way of sensitising the NIR lanthanides through non-covalent host-guest approach using cyclodextrin.

The inclusion of the hydrophobic biphenyl and phenyl tails in the cyclodextrin was proved by the NMR studies.

6.4. Experimental

6.4.1. Synthesis

propargyl-p.m.β-CD [32]
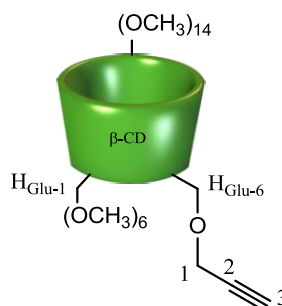
Monohydroxy-permethylated β-CD (250 mg, 0.17 mmol) was dissolved in dry DMF (5 ml) and the solution cooled to 0 °C. Sodium hydride (60 % in mineral oil, 26 mg, 0.63 mmol), was added and the mixture warmed at 50 °C for 45 mins. After this time the mixture was cooled to 0 °C and propargyl bromide (80 % in toluene, 140 mg, 0.93 mmol) and a catalytic amount of tetrabutyl ammonium iodide was added. The reaction mixture was stirred for 1 h at 0°C and for 20 h at room temperature. Methanol (3 ml) was added at 0 °C to quench the excess NaH and the solvents were evaporated. The residue was taken up in chloroform and washed with water. Purification by Biotage column chromatography (pre-packed silica gel column, 1 % methanol in ethyl acetate) yielded mono-6-O-propargyl permethylated β-cyclodextrin as a white solid (140 mg, 56 %).

^{1}H NMR (400 MHz, CDCl$_3$): $\delta = $ 5.12-5.09 (m, 7H, H$_{Glu-1}$), 4.19 (ABX, J = 2.3, 15.9, 21.2, 2H), 3.89 (dd, J = 3.7, 10.6, 1H), 3.84-3.15 (m, 101H), 2.42 (t, J = 2.3, 1H).

^{13}C NMR (100 MHz, CDCl$_3$): δ = 99.1-98.9, 82.0, 81.7, 80.3-80.0, 79.8, 74.5, 71.4-70.6, 68.8, 61.4, 59.0-58.3.

ESI MS(+): *m/z* 1476.5 [M+Na]$^+$

6.5. References

(1)   Klink, S. I.; Hebbink, G. A.; Grave, L.; Peters, F. G. A.; Veggel, F. C. J. M. V.; Reinhoudt, D. N.; Hofstraat, J. W. *Eur. J. Org. Chem.* **2000**, 1923–1931.

(2)   Hebbink, G. A.; Klink, S. I.; Alink, P. G. B. O.; Veggel, F. C. J. M. V. *Inorg. Chim. Acta* **2001**, *317*, 114–120.

(3)   Korovin, Y.; Rusakova, N. *Rev. Inorg. Chem.* **2001**, *21*, 299–329.

(4)   Wolbers, M. P. O.; Veggel, F. C. J. M. V.; Peters, F. G. A.; Beelen, E. S. E. V.; Hofstraat, J. W.; Geurts, F. A. J.; Reinhoudt, D. N. *Chem. Eur. J.* **1998**, *4*, 772-780.

(5)   Lenaerts, P.; Ryckebosch, E.; Driesen, K.; Deun, R. V.; Nockemann, P.; Görller-Walrand, C.; Binnemans, K. *J. Lumin.* **2005**, *114*, 77-84.

(6)   DiBari, L.; Pescitelli, G.; Sherry, A. D.; Woods, M. *Inorg. Chem.* **2005**, *44*, 8391-8398.

(7)   He, H.; Dubey, M.; Sykes, A. G.; May, P. S. *Dalton Trans.* **2010**, *39*, 6466-6474.

(8)   He, H.; May, P. S.; Galipeau, D. *Dalton Trans.* **2009**, 4766-4771.

(9)   Zhu, X.; W.-K.Wong; Guo, J.; W.-Y.Wong; Zhang, J.-P. *Eur. J. Inorg. Chem.* **2008**, 3515-3523.

(10)   Zhu, X.-J.; Jiang, F.-L.; Poon, C.-T.; Wong, W.-K.; Wong, W.-Y. *Eur. J. Inorg. Chem.* **2008**, 3151-3162.

(11)   Davies, D.; Hyde, G. J.; Ashford, A. E.; Cole, L. *J. Microsc.* **2000**, *197*, 239-248.

(12) Amati, M.; Belviso, S.; Cristinziano, P. L.; C.Minichino; Lelj, F.; Aiello, I.; LaDeda, M.; Ghedini, M. *J. Phys. Chem. A* **2007**, *111*, 13403-13414.

(13) Guminski, Y.; Grousseaud, M.; Cugnasse, S.; Brel, V.; Annereau, J. P.; Vispé, S.; Guilbaud, N.; Barret, J. M.; Bailly, C.; Imbert, T. *Bioorg. Med. Chem. Lett.* **2009**, *19*, 2474-2477.

(14) Rizzo, F.; Meinardi, F.; Tubino, R.; Pagliarin, R.; Dellepiane, G.; Papagni, A. *Synth. Met.* **2009**, *159*, 356-360.

(15) Shavaleev, N. M.; Scopelliti, R.; Gumy, F.; Bünzli, J.-C. G. *Inorg. Chem.* **2009**, *48*, 7937-7946.

(16) Shavaleev, N. M.; Scopelliti, R.; Gumy, F.; Bünzli, J.-C. G. *Inorg. Chem.* **2009**, *48*, 2908-2918.

(17) Zhang, J.; Petoud, S. *Chem. Eur. J.* **2008**, *14*, 1264-1272.

(18) Bassett, A. P.; Deun, R. V.; Nockemann, P.; Glover, P. B.; Kariuki, B. M.; Hecke, K.; Meervelt, L. V.; Pikramenou, Z. *Inorg. Chem.* **2005**, *44*, 6140-6142.

(19) Reeves, Z. R.; Mann, K. L. V.; Jeffery, J. C.; McCleverty, J. A.; Ward, M. D.; Barigelletti, F.; Armaroli, N. *J. Chem. Soc., Dalton Trans.* **1999**, 349-355.

(20) Muranaka, A.; Matsumoto, Y.; Uchiyama, M.; Jiang, J.; Bian, Y.; Ceulemans, A.; Kobayashi, N. *Inorg. Chem.* **2005**, *44*, 3818-3826.

(21) Chen, Z.-Q.; Ding, F.; Bian, Z.-Q.; Huang, C.-H. *Organic Electronics* **2010**, *11*, 369-376.

(22) López, M. V.; Eliseeva, S. V.; Blanco, J. M.; Rama, G.; Bermejo, M. R.; Vázquez, M. E.; Bünzli, J.-C. G. *Eur. J. Inorg. Chem.* **2010**, 4532-4545.

(23) Lu, X.; Bi, W.; Chai, W.; Song, J.; J.Meng; W.-Y.Wong; W.-K.Wong; Jones, R. A. *New J. Chem.* **2008**, *32*, 127-131.

(24)   Markus, A.; Olga, O.; Jean-Claude, G. B.; Frédéric, G.; Roland, F. *Chem. Eur. J.* **2009**, *15*, 8791-8799.

(25)   Nonat, A. M.; Allain, C. e.; Faulkner, S.; Gunnlaugsson, T. *Inorg. Chem.* **2010**, *49*, 8449–8456.

(26)   Nonat, A. M.; Quinn, S. J.; Gunnlaugsson, T. *Inorg. Chem.* **2009**, *48*, 4646-4648.

(27)   Treibs, A.; F.H.Kreuzer *Justus Liebigs Ann. Chem.* **1968**, *718*, 208.

(28)   Arroyo, I. J.; Hu, R.; Merino, G.; Tang, B. Z.; Pena-Cabrera, E. *J. Org. Chem.* **2009**, *74*, 5719–5722.

(29)   Schmitt, A. e.; Hinkeldey, B. t.; Wild, M. d.; Jung, G. *J. Fluoresc* **2009**, *19*, 755– 758.

(30)   Ziessel, R. F.; Ulrich, G.; Charbonniére, L.; Imbert, D.; Scopelliti, R.; Bünzli, J.-C. G. *Chem. Eur. J.* **2006**, *12*, 5060-5067.

(31)   Zhong, Y.; Si, L.; He, H.; Sykes, A. G. *Dalton Trans.* **2011**, *40*, 11389-11395.

(32)   Faiz, J. A.; Spencer, N.; Pikramenou, Z. *Org. Biomol. Chem.* **2005**, *3*, 4239-4245.

(33)   Davis, D. *PhD, University of Birmingham* **2010**.

(34)   Haider, J. M.; Pikramenou, Z. *Chem. Soc. Rev.* **2005**, *34*, 120-132.

(35)   Goeb, S.; Ziessel, R. *Tetrahedron Letters* **2008**, *49*, 2569–2574.

(36)   Haider, J. M.; Chavarot, M.; Weidner, S.; Sadler, I.; Williams, R. M.; Cola, L. D.; Pikramenou, Z. *Inorg. Chem.* **2001**, *40*, 3912-3921.

(37)   Kyllönen, L. E. P.; Chinuswamy, V.; Maffeo, D.; alas, E. T. K.; Haider, J. M.; Pikramenou, Z.; Mavridis, I. M.; Yannakopoulou, K.; Glezos, N. *J. Phys. Org. Chem.* **2012**, *25*, 198-206.

(38)   Corbellini, F.; Mulder, A.; Sartori, A.; Ludden, M. J. W.; Casnati, A.; Ungaro, R.; Huskens, J.; Crego-Calama, M.; Reinhoudt, D. N. *J. Am. Chem. Soc.* **2004**, *126*, 17050-17058.

(39)   Ivanov, P. M.; Salvatierra, D.; Jaime, C. *J. Org. Chem.* **1996**, *61*, 7012-7017.

(40)   McAlpine, S. R.; Garcia-Garibay, M. A. *J. Org. Chem.* **1996**, *61*, 8307-8309.

CHAPTER 7

General Conclusions and Future Works

A variety of ruthenium(II) and osmium(II) bipyridine complexes and a ruthenium(II) biquinoline-pyridine surface-active complex have been synthesised and fully characterised by several techniques such as NMR, MS, FTIR and elemental analysis. The X-ray crystal structures of some of the complexes have been also obtained to confirm the formation of the desired complexes. The photophysical properties of all complexes have been investigated in solution, as powder and in monolayers. The complexes exhibit relatively high quantum yields and lifetimes in all forms. The monolayers of such complexes show promising emission spectra. Although the emissions of the monolayers still suffer from some quenching by gold surface, the quenching is decreased significantly by introducing the long aliphatic chain as a spacer. Future work will focus on increasing the length of the spacer until the quenching is stopped completely.

The monolayer of the surface active Ru(II) biquinoline-pyridine complex has the advantage of bearing thioctic acid moieties which have two sulfurs to attach to the gold surface. This makes the monolayer of the complex very stable. More surface active complexes of biquinoline-pyridine with the thioctic acid moiety as well as their osmium(II) complexes will be developed in future.

We also present surface active ruthenium(II) and osmium(II) complexes which have β-cyclodextrin in their structure to act as a host on gold surfaces to afford supramolecular assemblies on surfaces. The complexes have been fully characterised and their photophysical properties in all forms have been studied. The acetonitrile solutions of the ruthenium complexes display luminescence from the ^{3}MLCT band, when excited at room temperature, with a red shift in emission spectrum with respect to [Ru(bpy)$_3$]Cl$_2$. The osmium complex displays weak emission at room temperature with a large red shift in emission spectrum with respect to [Os(bpy)$_3$]Cl$_2$.

New ruthenium(II) and iridium(III) biquinoline-pyridine metalloguests bearing biphenyl to bind β-cyclodextrin cavity have been developed. The energy transfer process between the multi-metal assemblies of Ru(II) – Ir(III) and Os(II) – Ru(II) have been built in both solution and on gold surface, using **16** and **17** as metallic guests, and the energy transfer between the metal centres have been investigated by luminescence studies. The photoinduced energy transfer between metal centres has been demonstrated via the supramolecular assembly of host-guest units in cyclodextrin cavities, in water and on the surface. XPS analysis of the assemblies on the gold substrates confirms the relative concentrations of both metals on the surface. Future work will be focused on developing molecular wires based on host-guest approach and include more metal centres to produce an efficient energy transfer to the gold surface.

We also propose a new and efficient method of sensitising Nd(III) NIR emission by non-covalent attachment of a BODIPY dye attached to β-cyclodextrin (BODIPY-CD). The BODIPY-CD has been proved to be a good sensitizer for the neodymium

complexes. This is the first time NIR lanthanides have been sensitised through non-covalent host-guest approach using cyclodextrin. The inclusion of the hydrophobic biphenyl and phenyl tails in the cyclodextrin has been proved by the NMR studies.

CHAPTER

8

Appendix
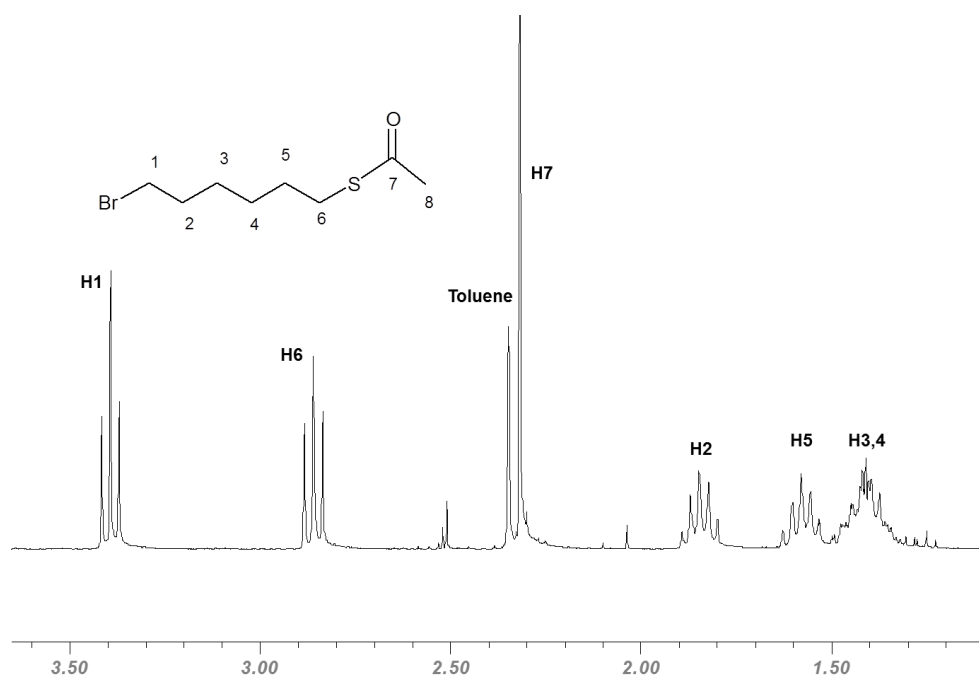
Figure A3.1. 300 MHz ¹H NMR spectrum (CDCl₃) of Br-SAc.
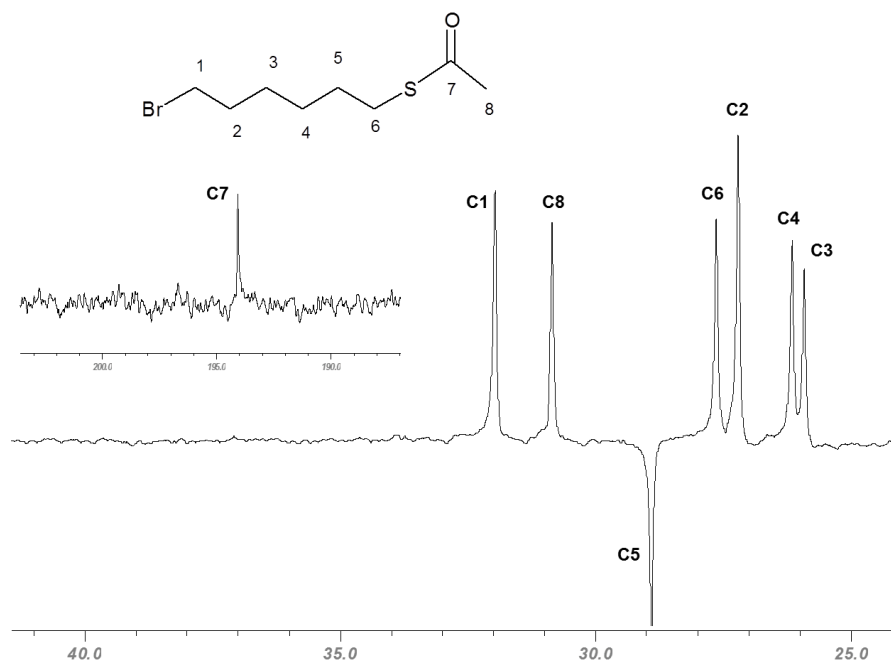
Figure A3.2. 100 MHz ^{13}C NMR spectrum (CDCl$_3$) of Br-SAc.
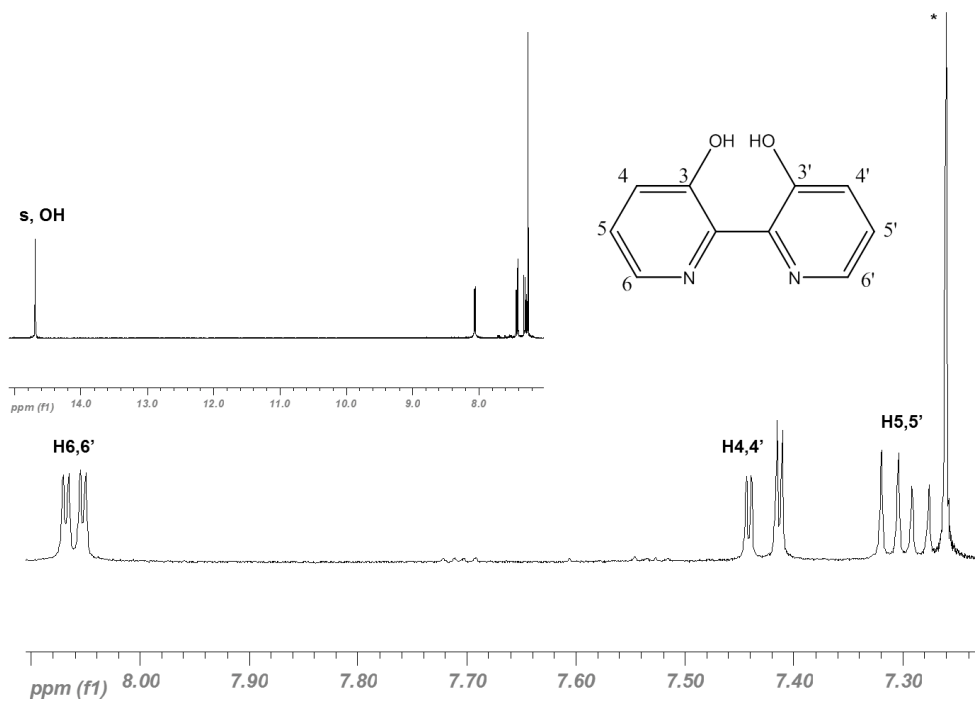
Figure A3.3. 300 MHz ^{1}H NMR spectrum (CDCl$_3$) of 3,3'-bpyOH.
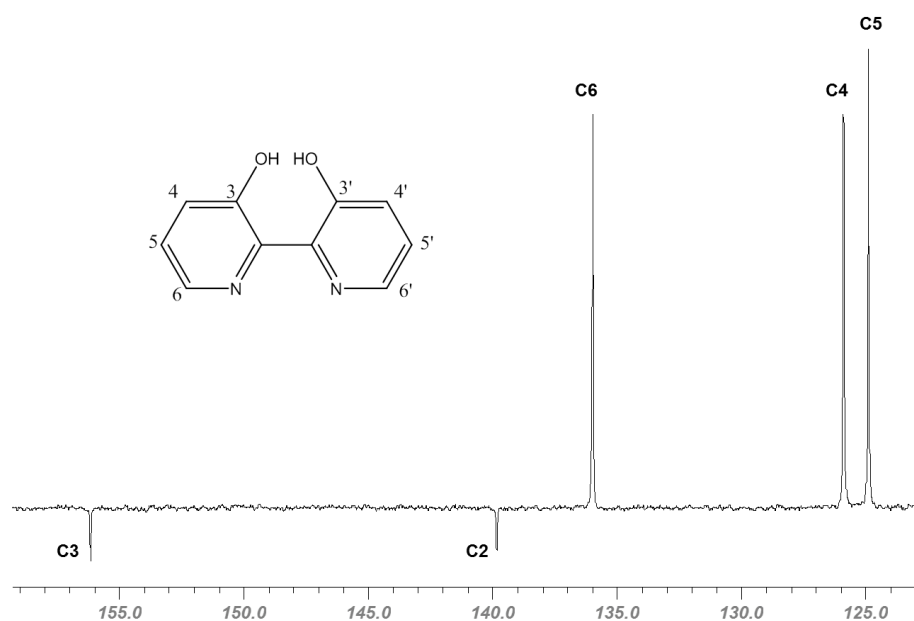
Figure A3.4. 100 MHz ^{13}C NMR spectrum (CDCl$_3$) of 3,3'-bpyOH.
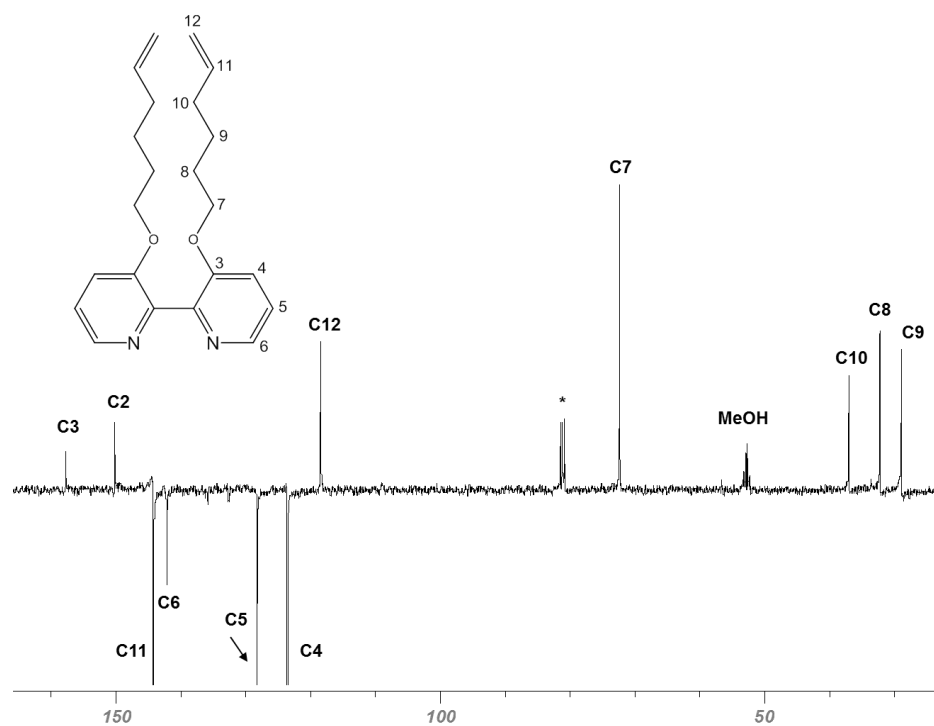
Figure A3.5. 100 MHz ^{13}C NMR spectrum (CDCl$_3$) of 3,3'-bpyhex.
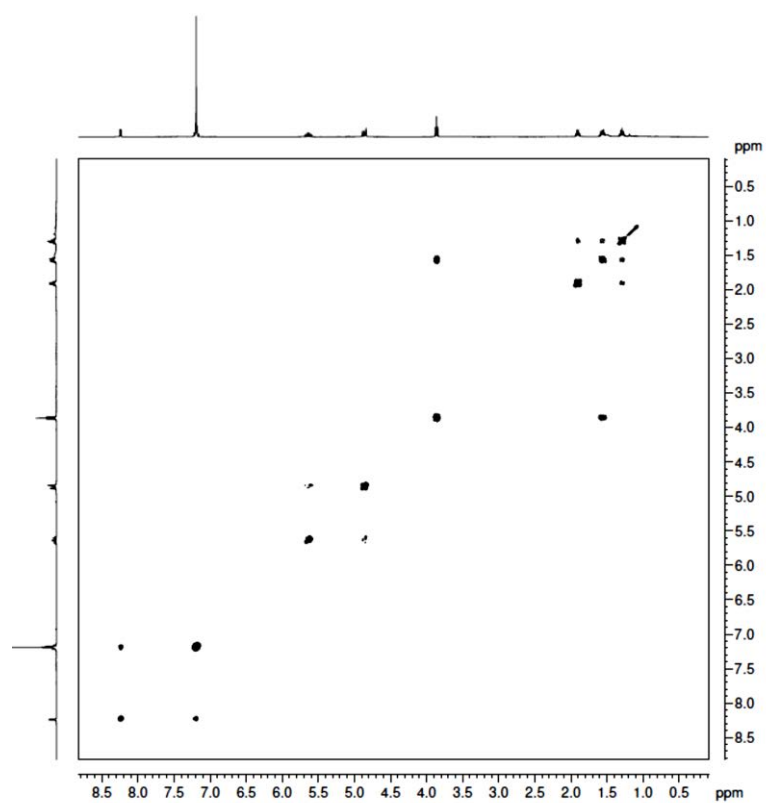
A3.6 COSY spectrum (CHCl₃) of 3,3'-bpyhex.
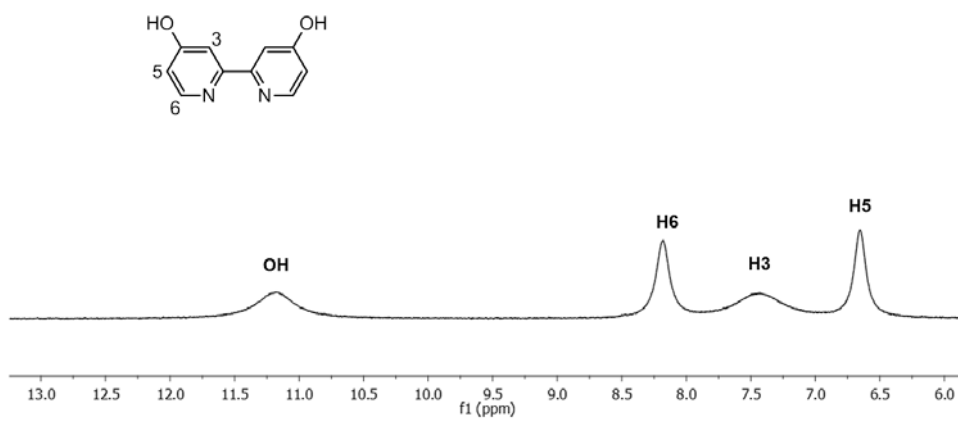
Figure A3.7. 300 MHz ^{13}H NMR spectrum (DMSO) of 4,4'-bpyOH.
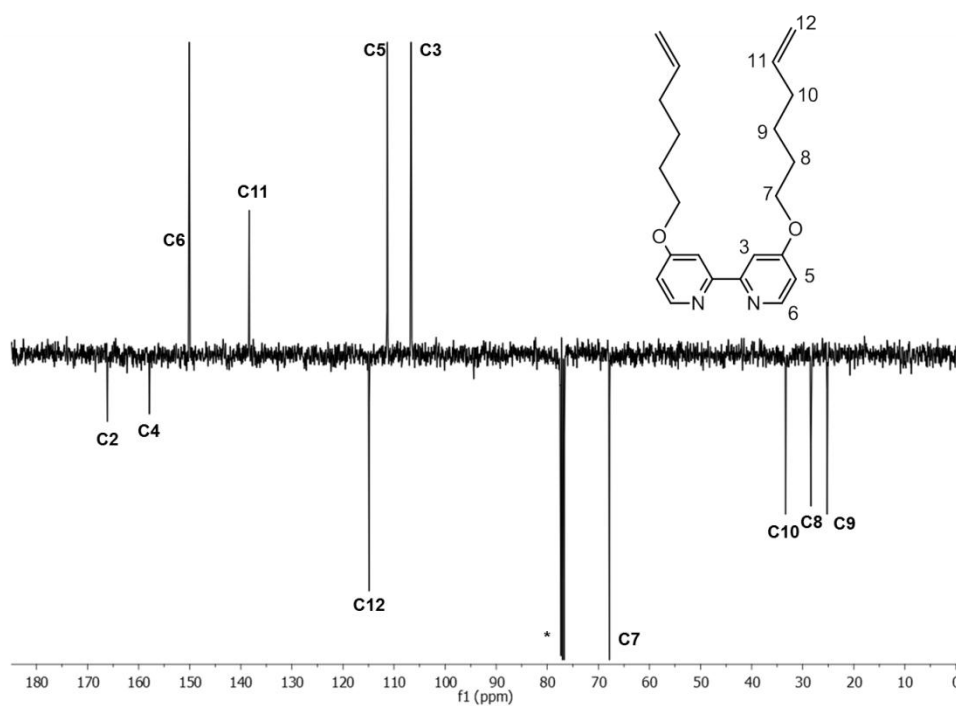
Figure A3.8. 100 MHz ^{13}C NMR spectrum (CDCl$_3$) of 4,4'-bpyhex.
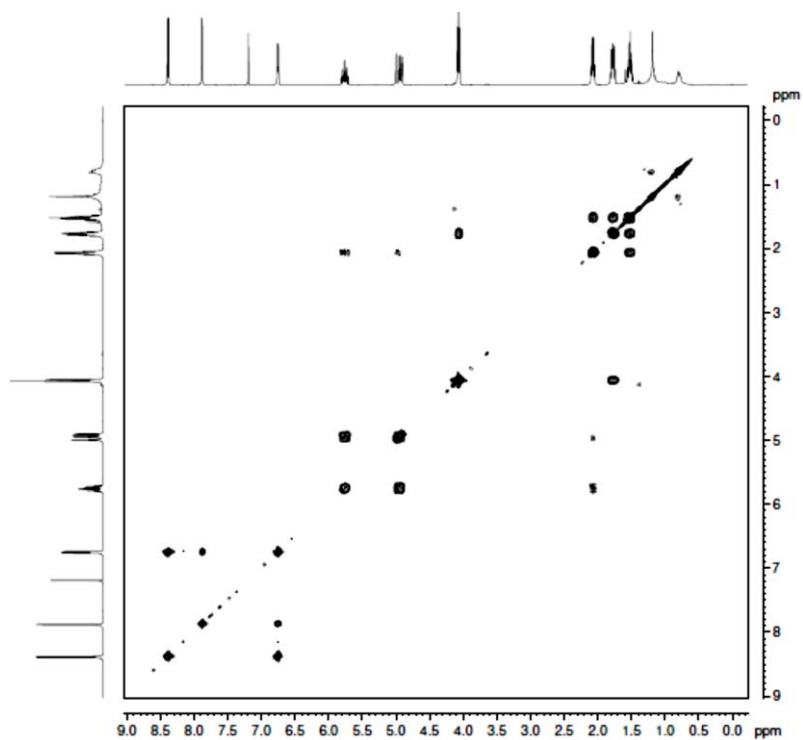
A3.9 COSY spectrum (CHCl$_3$) of 4,4'-bpyhex.
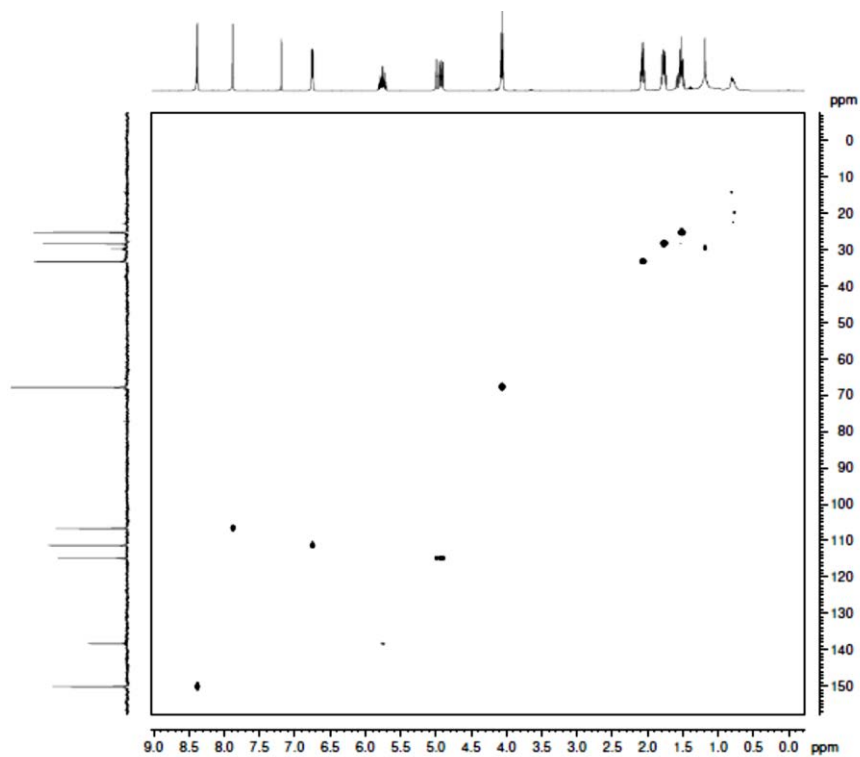
A3.10 HSQC spectrum (CHCl₃) of 4,4'-bpyhex.
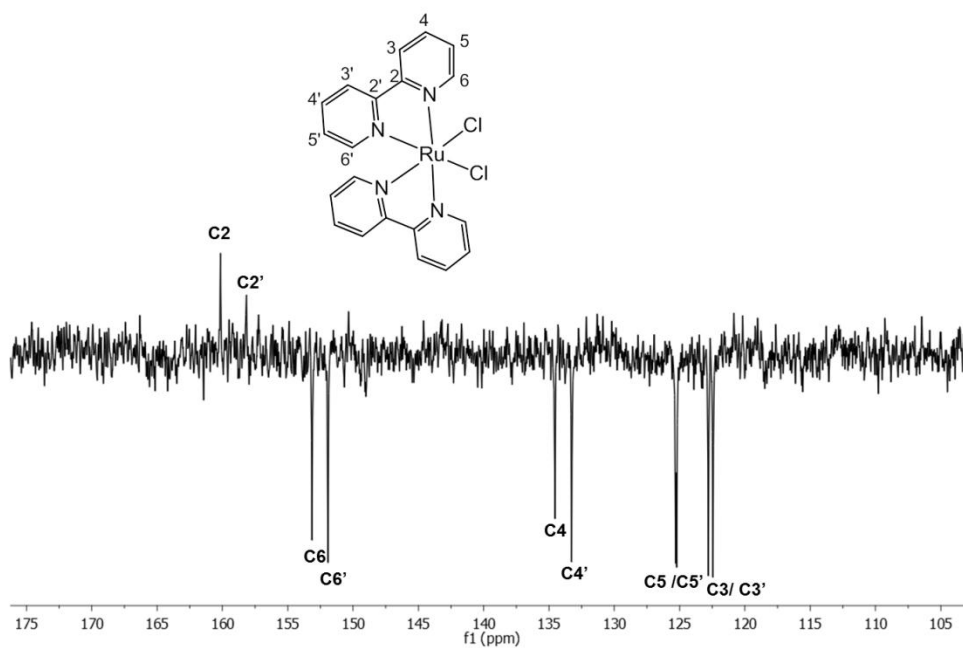
Figure A3.11. 100 MHz ¹³C NMR spectrum (DMSO) of Ru(bpy)₂Cl₂.
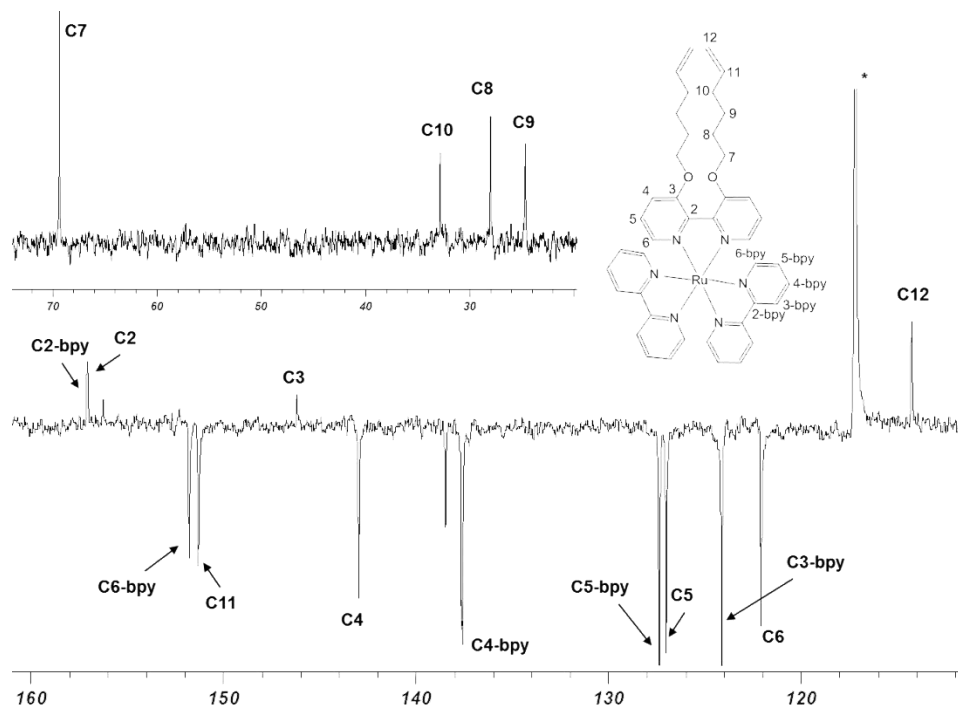
Figure A3.12. 100 MHz ^{13}C NMR spectrum (CD$_3$CN) of [Ru(bpy)$_2$(3,3'-bpyhex)](PF$_6$)$_2$.
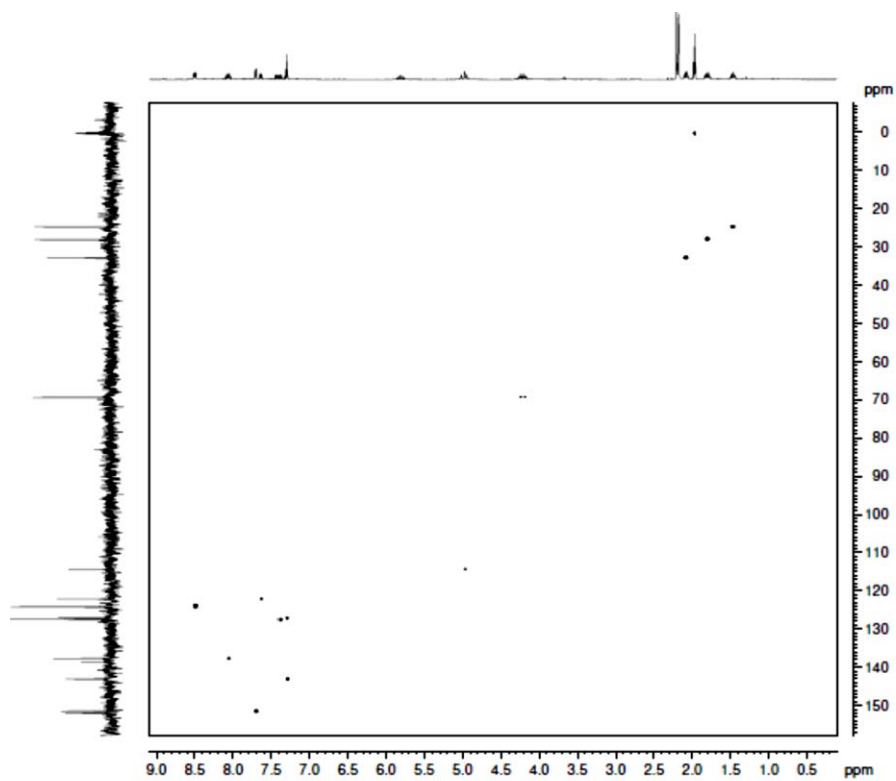
Figure A3.13. HSQC spectrum (CD$_3$CN) of [Ru(bpy)$_2$(3,3'-bpyhex)](PF$_6$)$_2$.
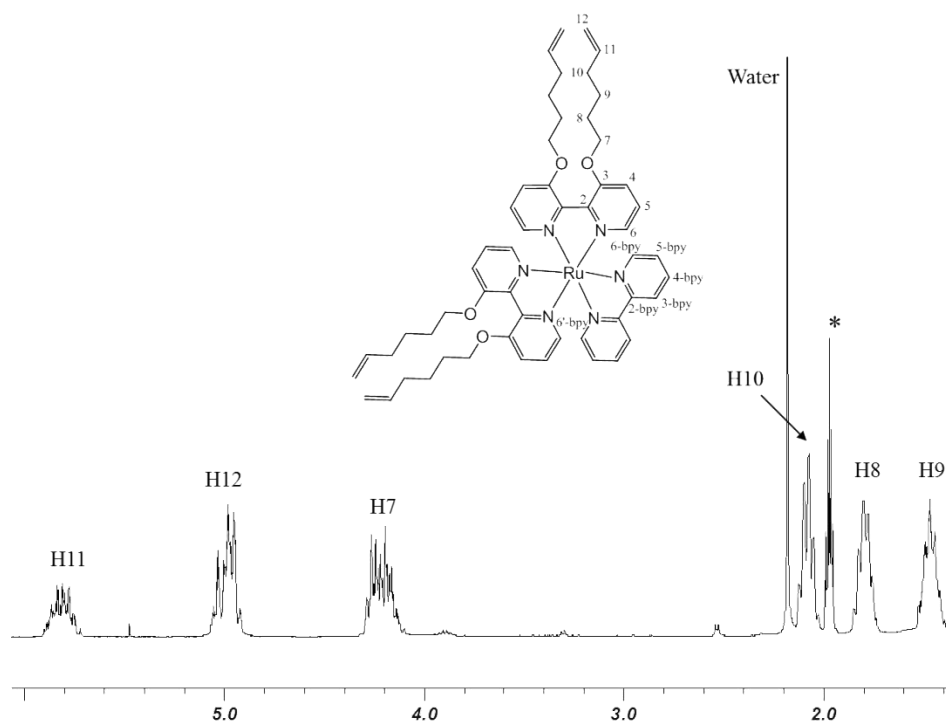
Figure A3.14. 400 MHz ^{1}H NMR spectrum (CD$_3$CN) of [Ru(bpy)(3,3'-bpyhex)$_2$](PF$_6$)$_2$, aliphatic region.
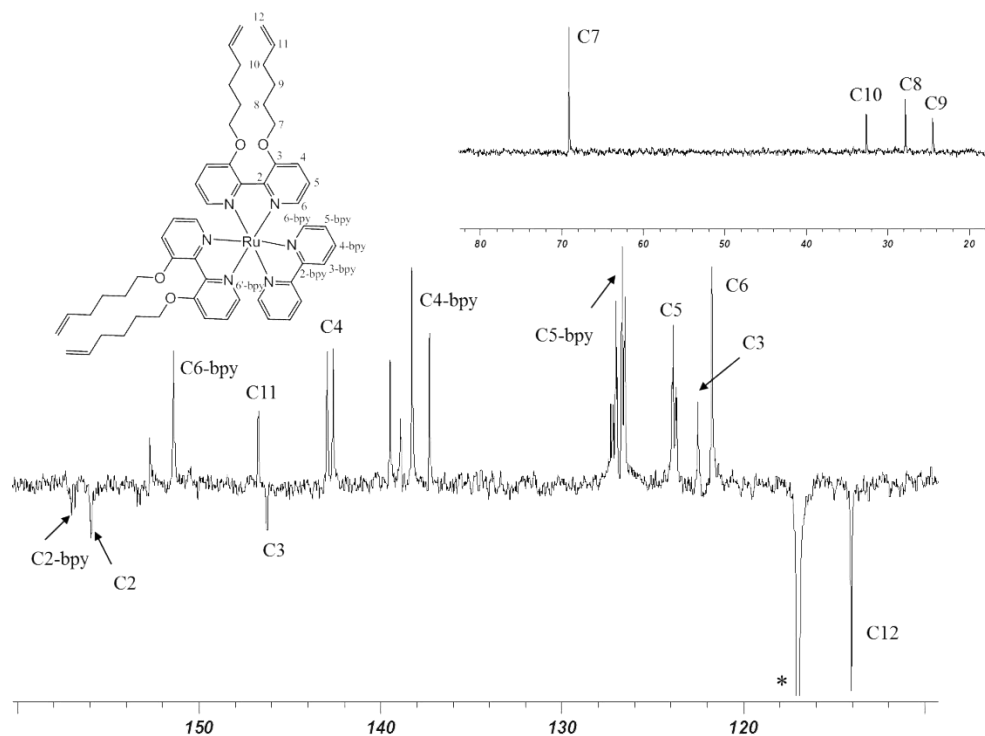
Figure A3.15. 100 MHz ^{13}C NMR spectrum (CD$_3$CN) of [Ru(bpy)(3,3'-bpyhex)$_2$](PF$_6$)$_2$.
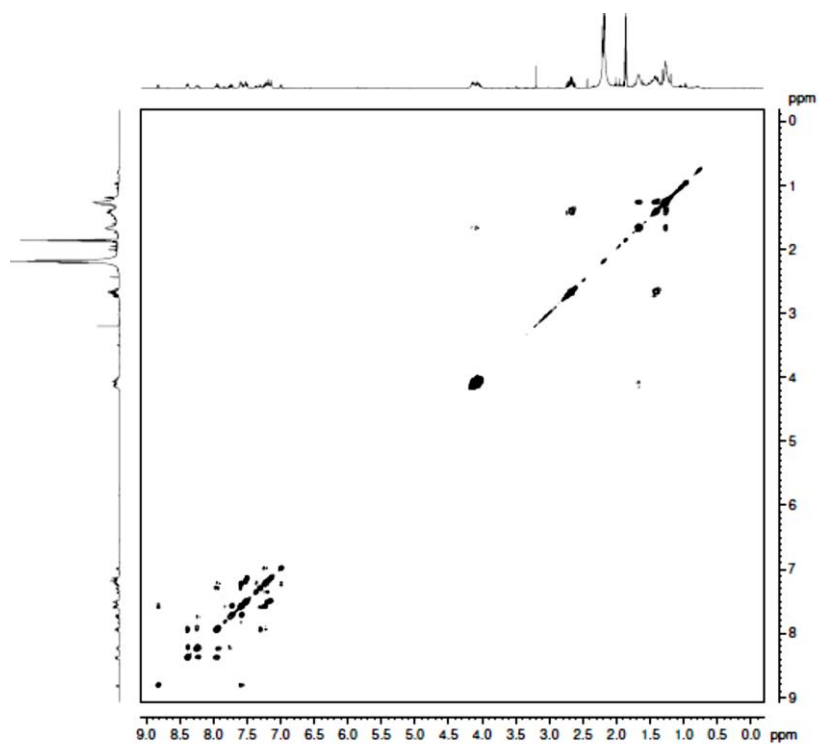
Figure A3.16. COSY spectrum (CD$_3$CN) of [Ru(bpy)(3,3'-bpyhex)$_2$](PF$_6$)$_2$.
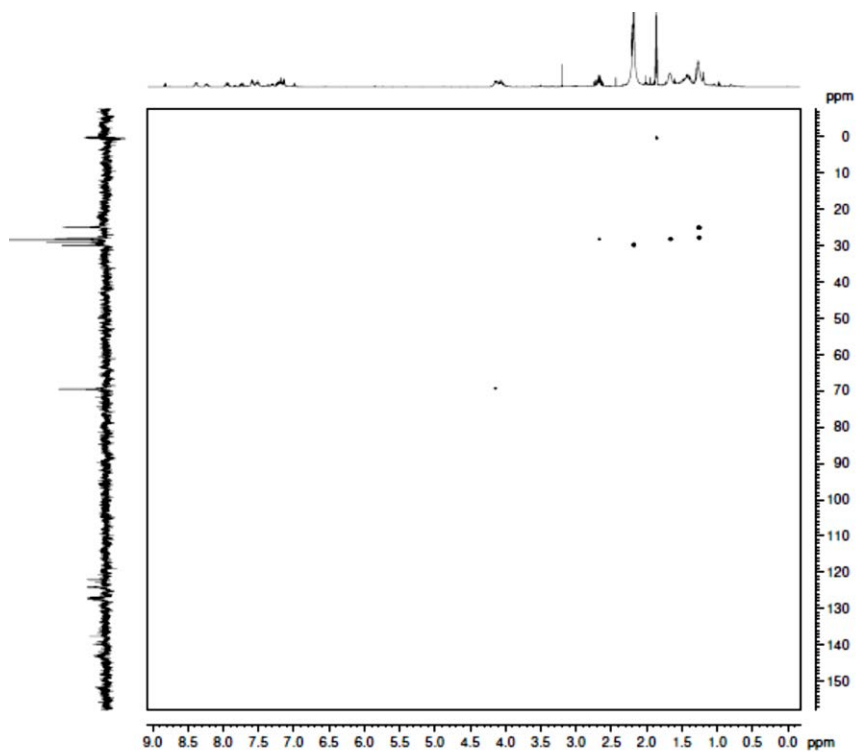
Figure A3.17. HSQC spectrum (CD$_3$CN) of [Ru(bpy)(3,3'-bpyhex)$_2$](PF$_6$)$_2$.
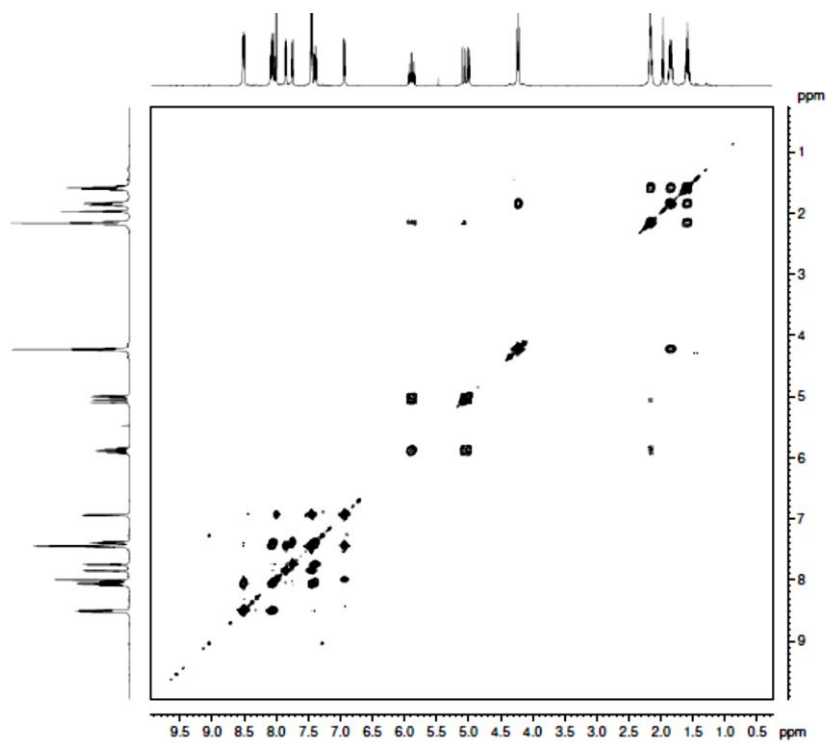
Figure A3.18. COSY spectrum (CD$_3$CN) of [Ru(bpy)$_2$(4,4'-bpyhex)](PF$_6$)$_2$.
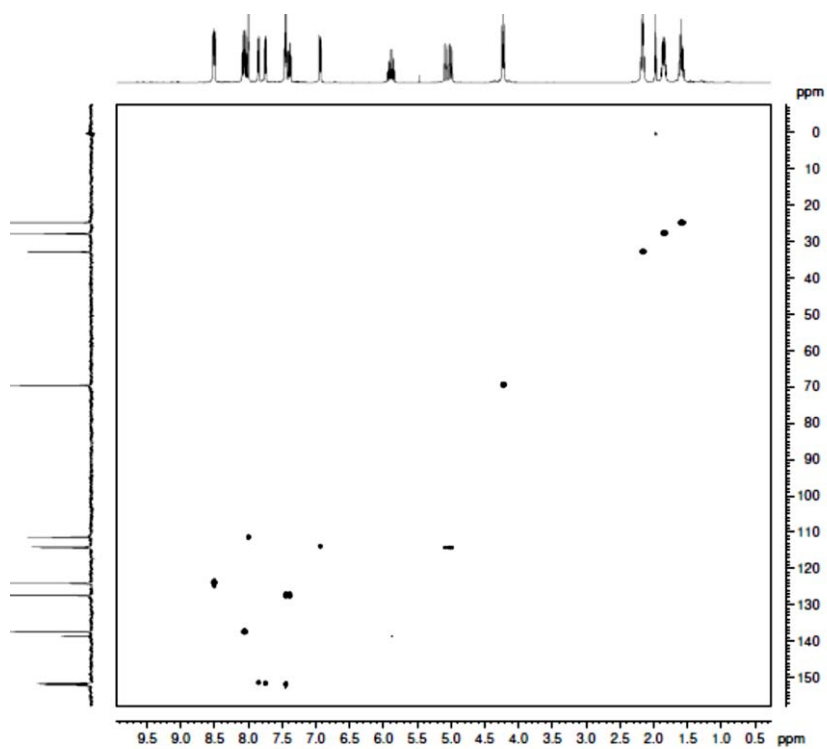
Figure A3.19. HSQC spectrum (CD$_3$CN) of [Ru(bpy)$_2$(4,4'-bpyhex)](PF$_6$)$_2$.
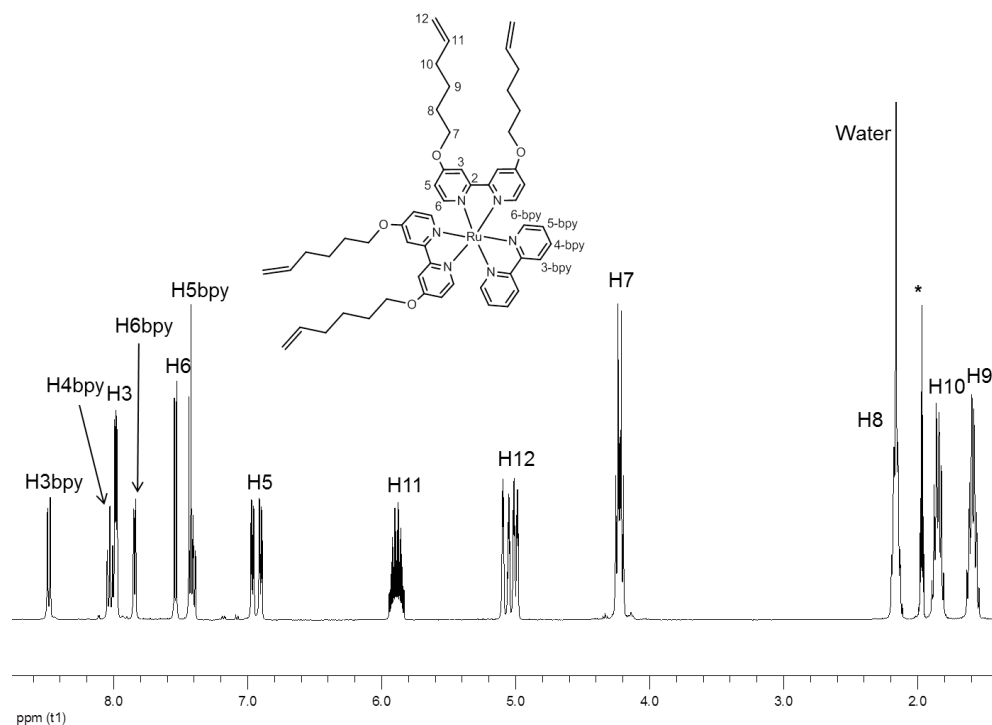
Figure A3.20. 400 MHz ^{1}H NMR spectrum (CD$_3$CN) of [Ru(bpy)(4,4'-bpyhex)$_2$](PF$_6$)$_2$.
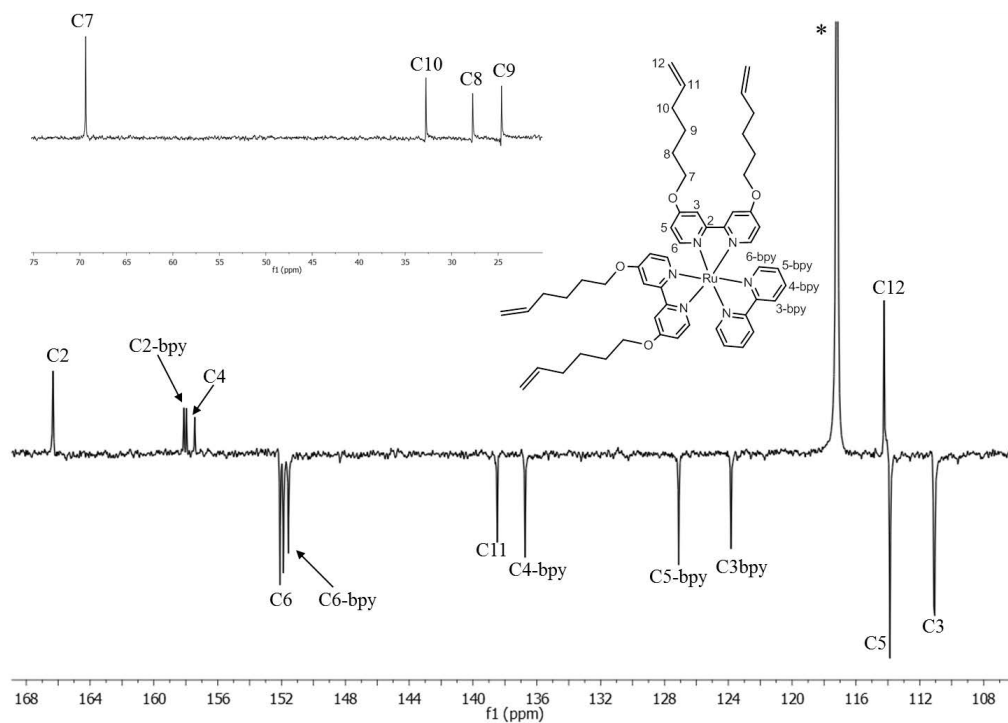
Figure A3.21. 100 MHz ^{13}C NMR spectrum (CD$_3$CN) of [Ru(bpy)(4,4'-bpyhex)$_2$](PF$_6$)$_2$.
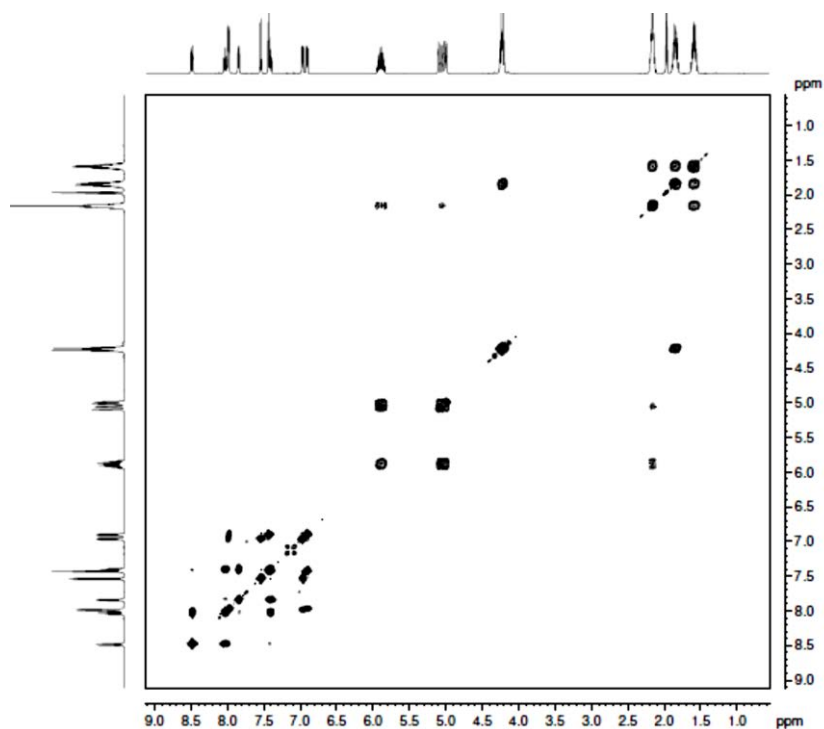
Figure A3.22. COSY spectrum (CD$_3$CN) of [Ru(bpy)(4,4'-bpyhex)$_2$](PF$_6$)$_2$.
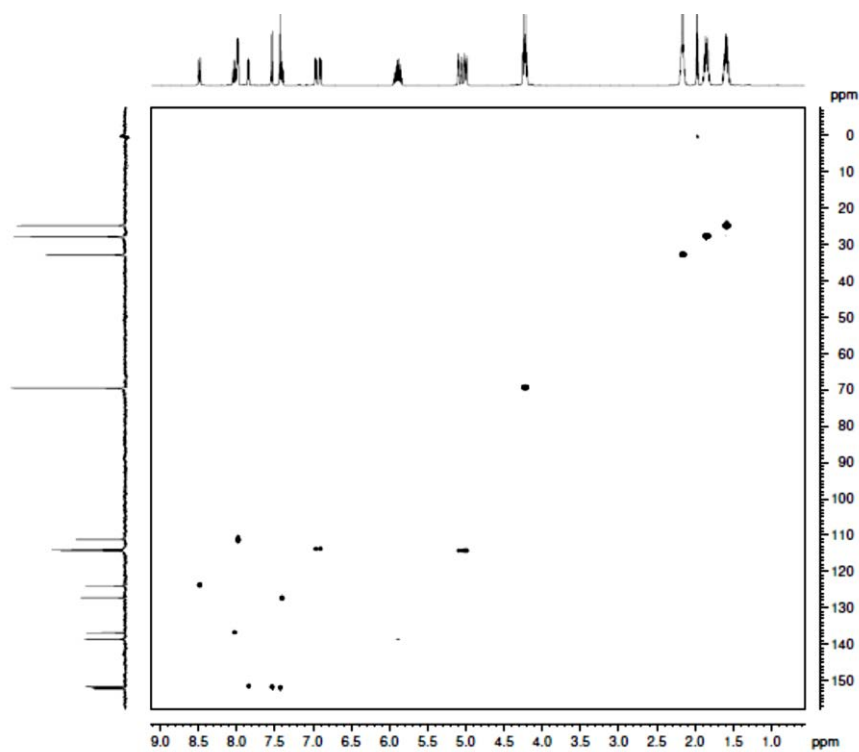
Figure A3.23. HSQC spectrum (CD$_3$CN) of [Ru(bpy)(4,4'-bpyhex)$_2$](PF$_6$)$_2$.
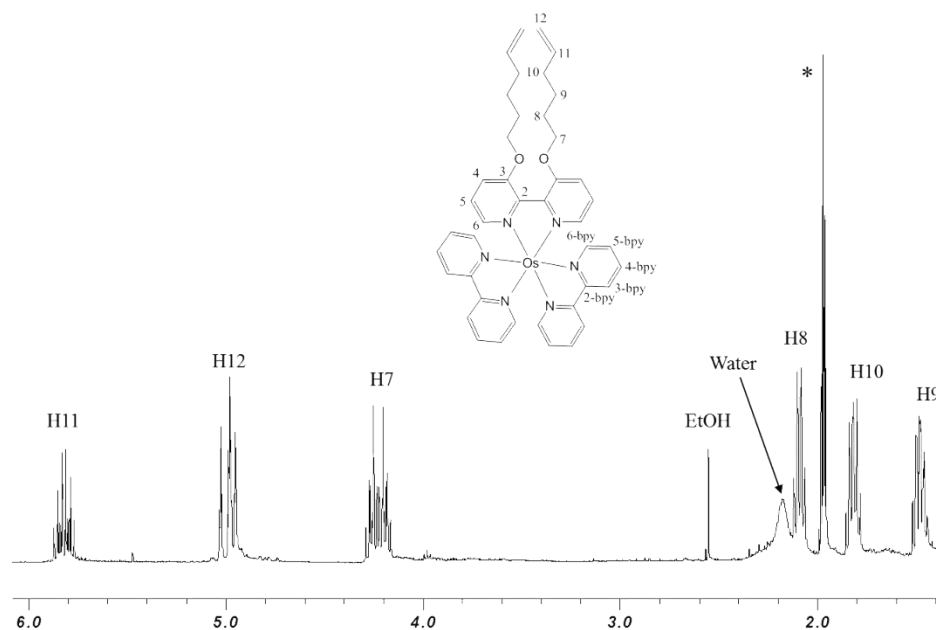
Figure A3.24. 400 MHz ^{1}H NMR spectrum (CD$_3$CN) of [Os(bpy)$_2$(3,3'-bpyhex)](PF$_6$)$_2$, aliphatic region.
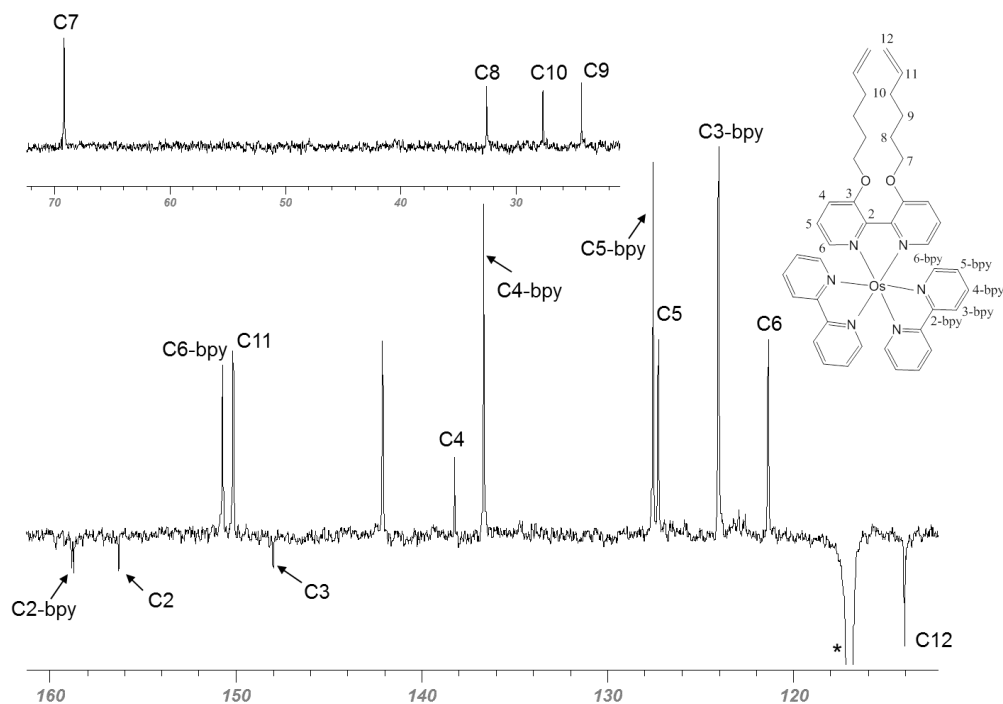
Figure A3.25. 100 MHz ^{13}C NMR spectrum (CD$_3$CN) of [Os(bpy)$_2$(3,3'-bpyhex)](PF$_6$)$_2$.
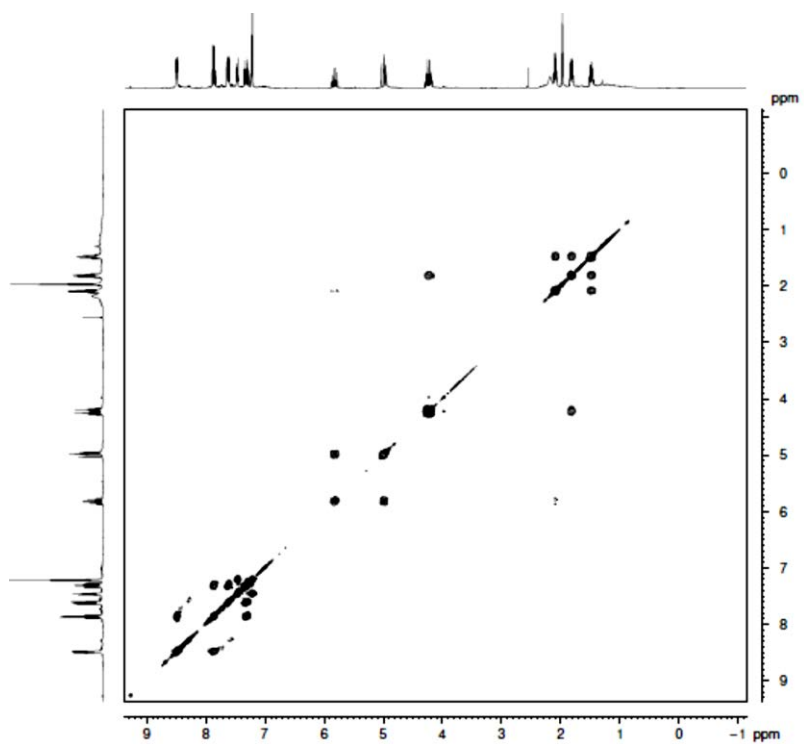
Figure A3.26. COSY spectrum (CD₃CN) of [Os(bpy)₂(3,3'-bpyhex)](PF₆)₂.
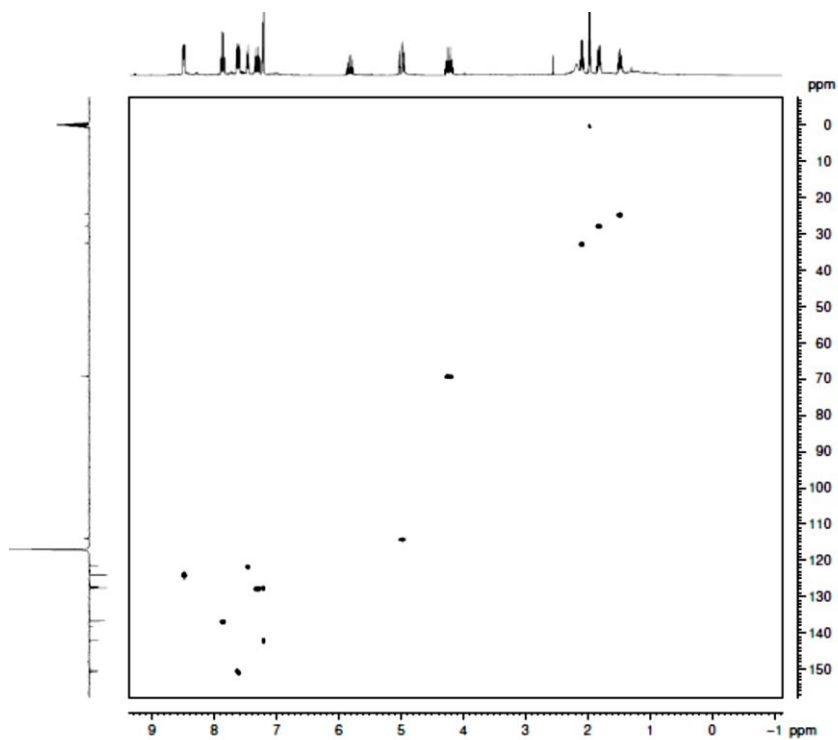
Figure A3.27. HSQC spectrum (CD₃CN) of [Os(bpy)₂(3,3'-bpyhex)](PF₆)₂.
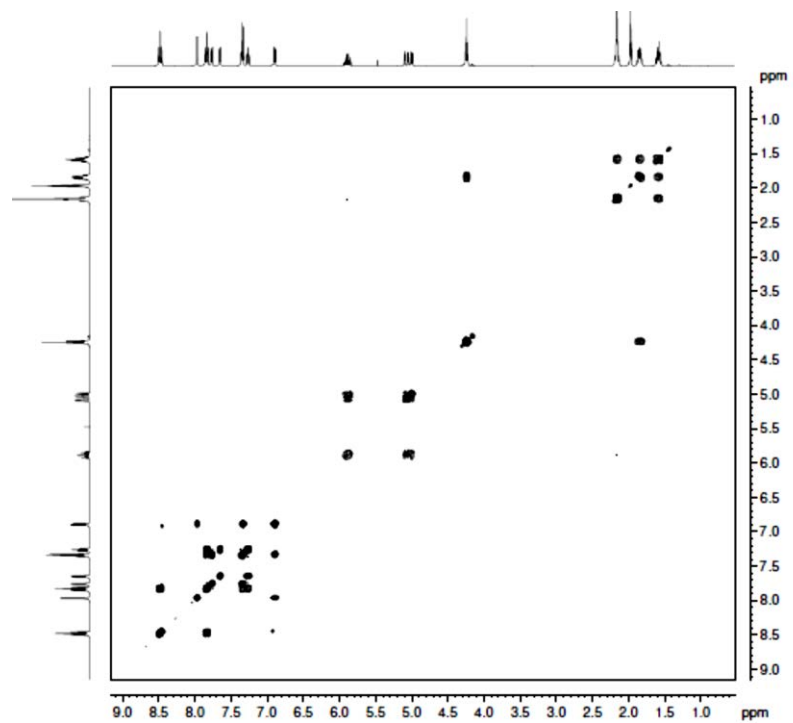
Figure A3.28. COSY spectrum (CD$_3$CN) of [Os(bpy)$_2$(4,4'-bpyhex)](PF$_6$)$_2$.
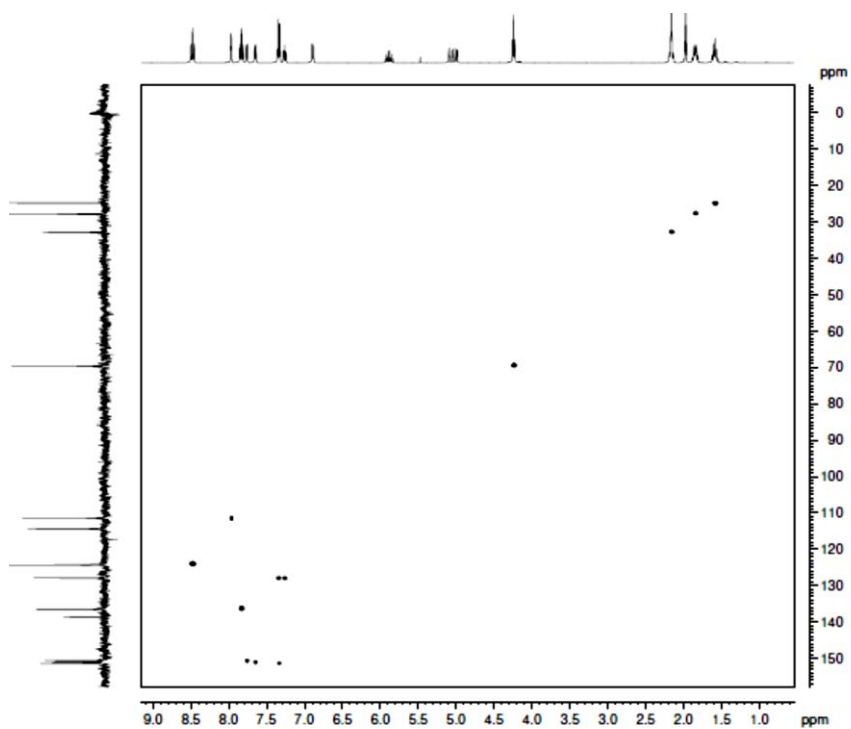
Figure A3.29. HSQC spectrum (CD$_3$CN) of [Os(bpy)$_2$(4,4'-bpyhex)](PF$_6$)$_2$.
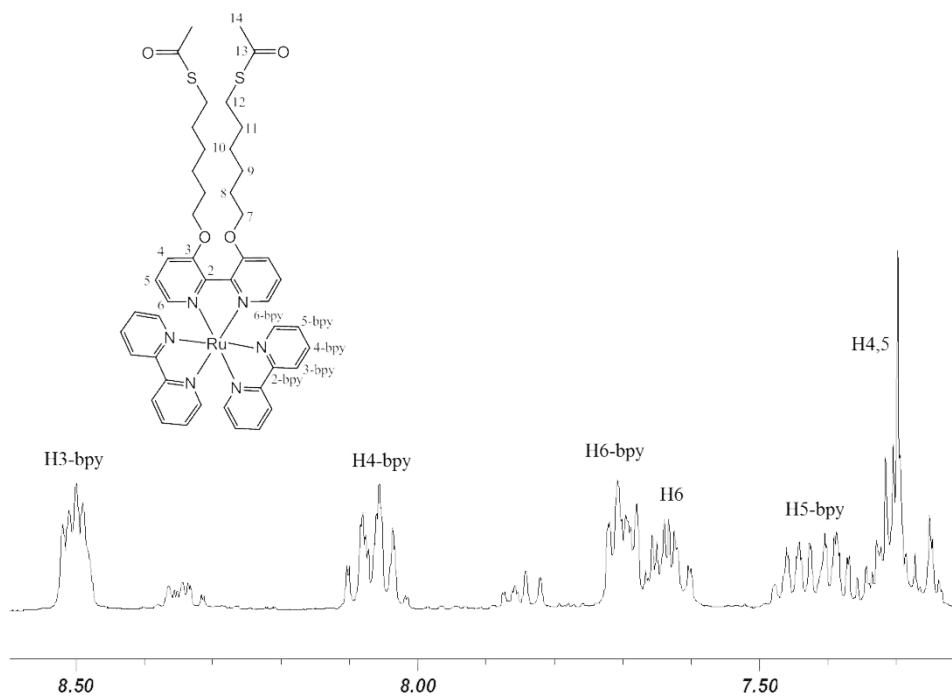
Figure A3.30. 400 MHz ^{1}H NMR spectrum (CD$_3$CN) of [Ru(bpy)$_2$(3,3'-bpysac)](PF$_6$)$_2$, aromatic region.
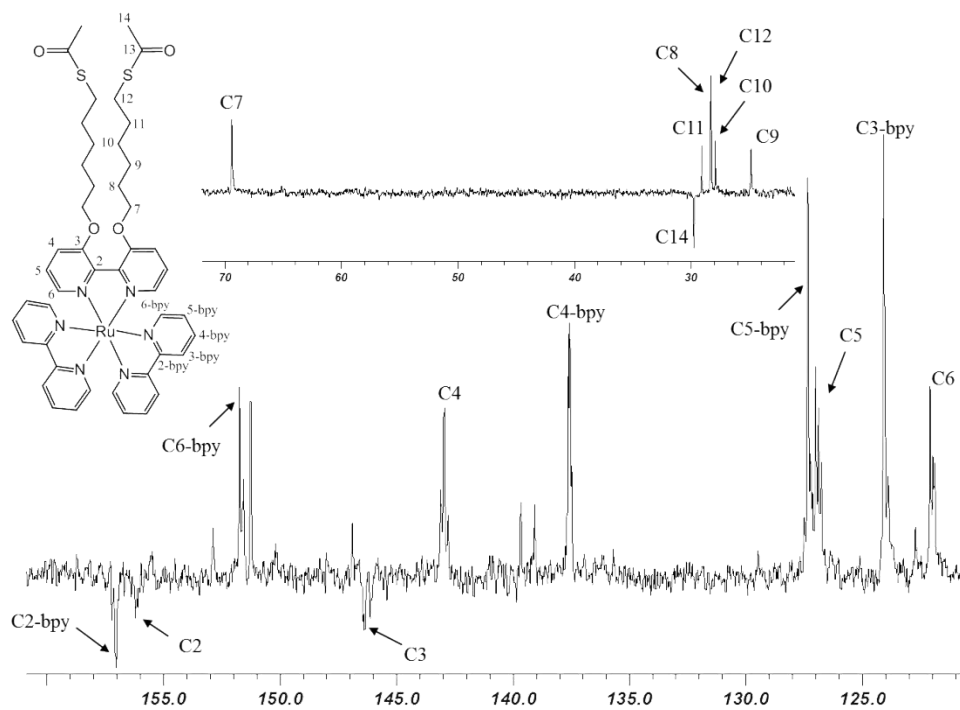
Figure A3.31. 100 MHz ^{13}C NMR spectrum (CD$_3$CN) of [Ru(bpy)$_2$(3,3'-bpysac)](PF$_6$)$_2$.
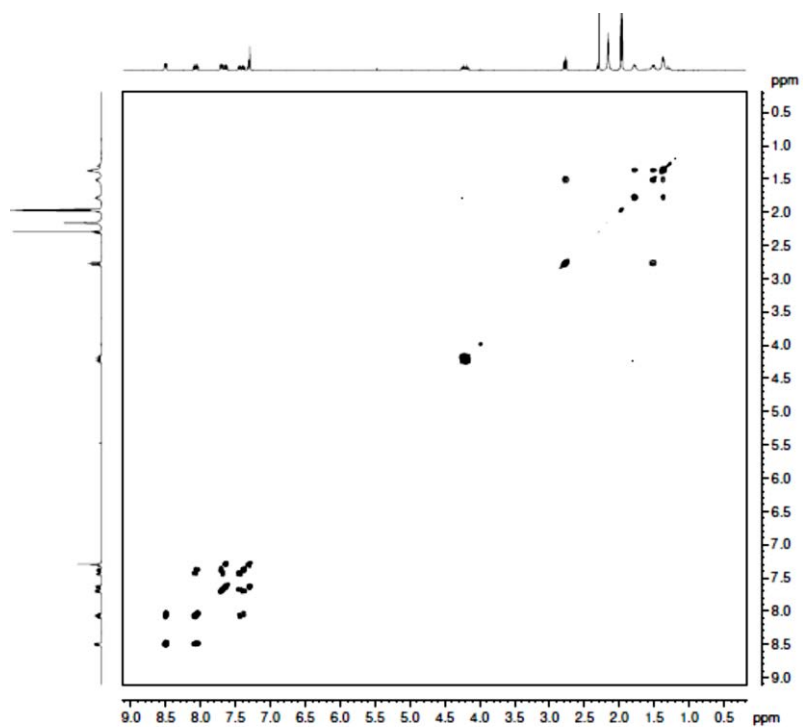
Figure A3.32. COSY spectrum (CD$_3$CN) of [Ru(bpy)$_2$(3,3'-bpysac)](PF$_6$)$_2$.
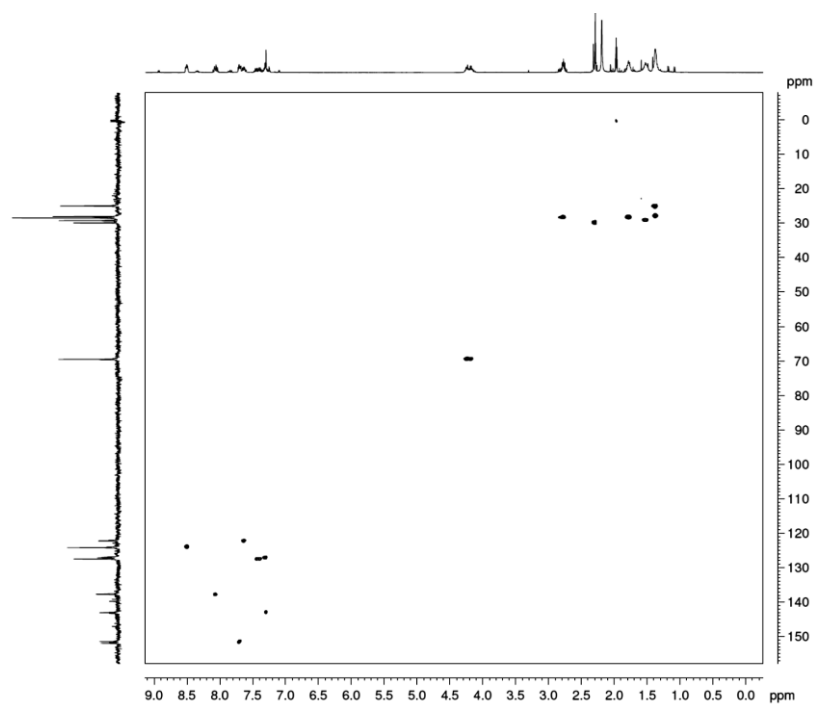
Figure A3.33. HSQC spectrum (CD$_3$CN) of [Ru(bpy)$_2$(3,3'-bpysac)](PF$_6$)$_2$.
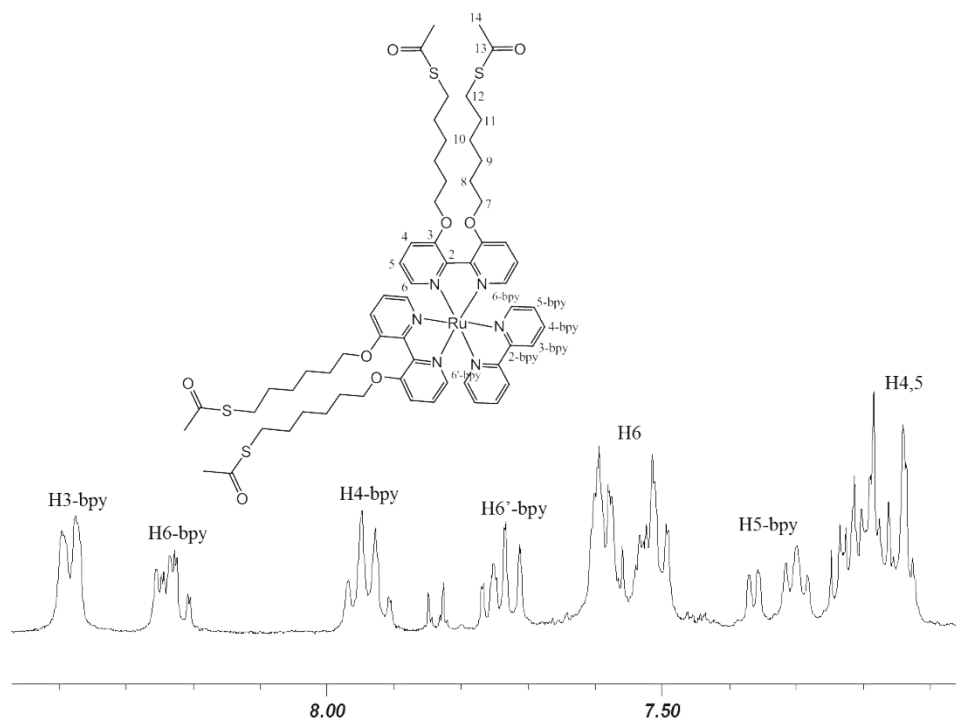
Figure A3.34. 400 MHz ^{1}H NMR spectrum (CD$_3$CN) of [Ru(bpy)(3,3'-bpysac)$_2$](PF$_6$)$_2$, aromatic region.
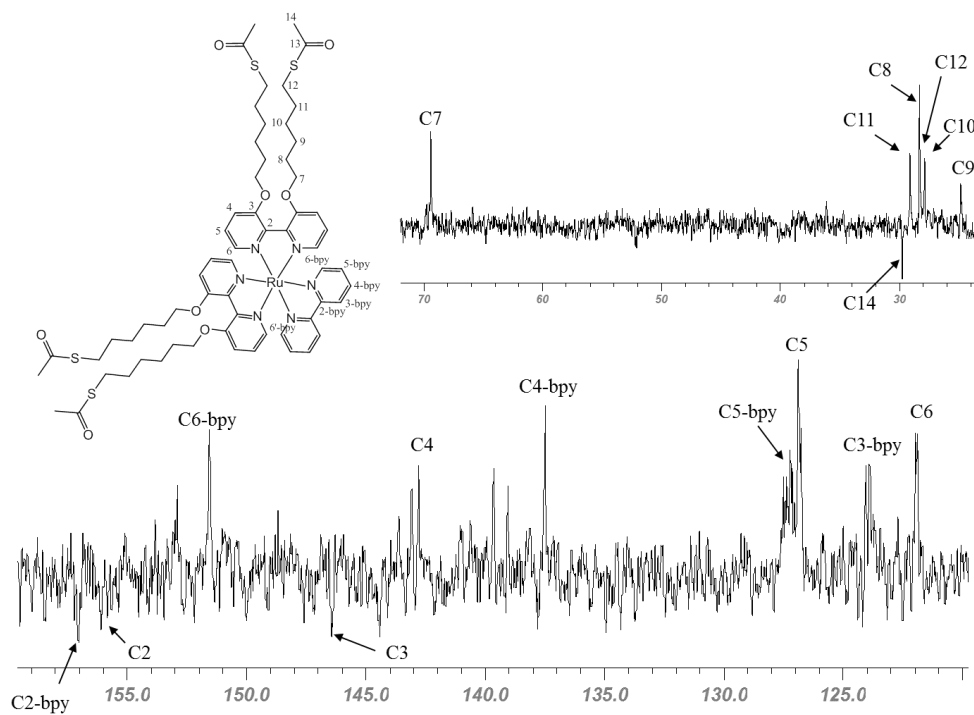
Figure A3.35. 100 MHz ^{13}C NMR spectrum (CD$_3$CN) of [Ru(bpy)(3,3'-bpysac)$_2$](PF$_6$)$_2$.
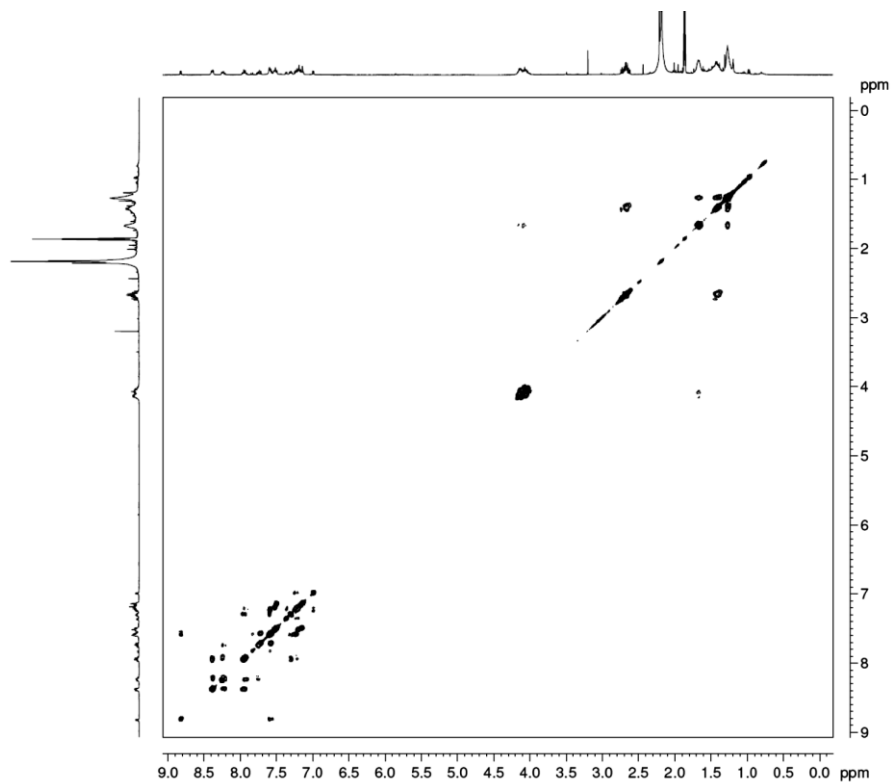
Figure A3.36. COSY spectrum (CD$_3$CN) of [Ru(bpy)(3,3'-bpysac)$_2$](PF$_6$)$_2$.
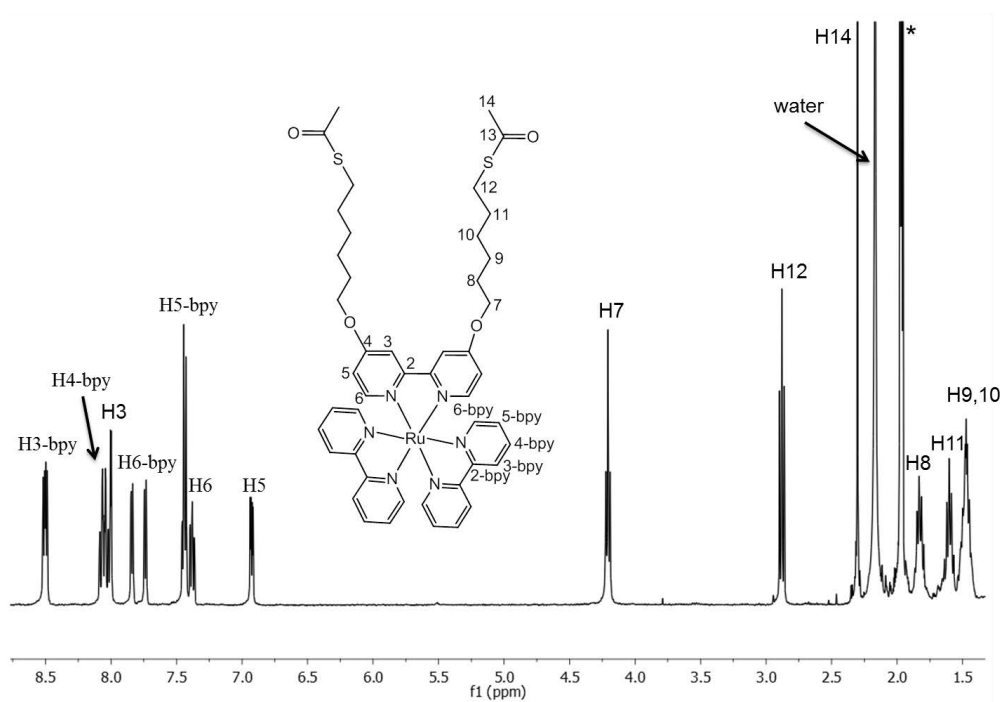
Figure A3.37. 400 MHz ^{1}H NMR spectrum (CD$_3$CN) of [Ru(bpy)$_2$(4,4'-bpysac)](PF$_6$)$_2$.
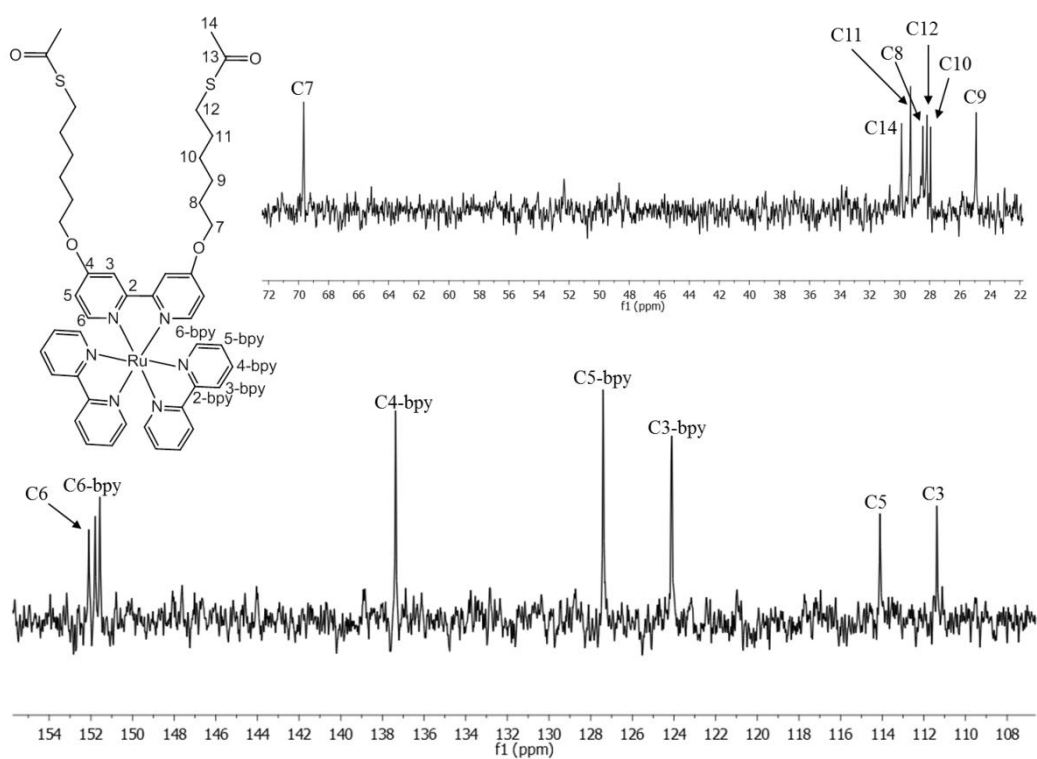
Figure A3.38. 100 MHz ^{13}C NMR spectrum (CD$_3$CN) of [Ru(bpy)$_2$(4,4'-bpysac)](PF$_6$)$_2$.
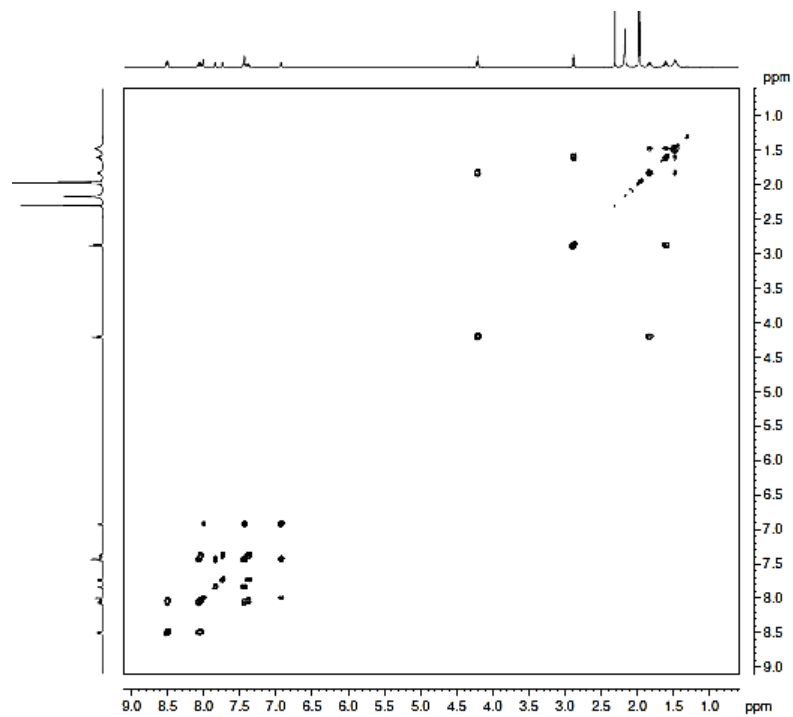
Figure A3.39. COSY spectrum (CD$_3$CN) of [Ru(bpy)$_2$(4,4'-bpysac)](PF$_6$)$_2$.
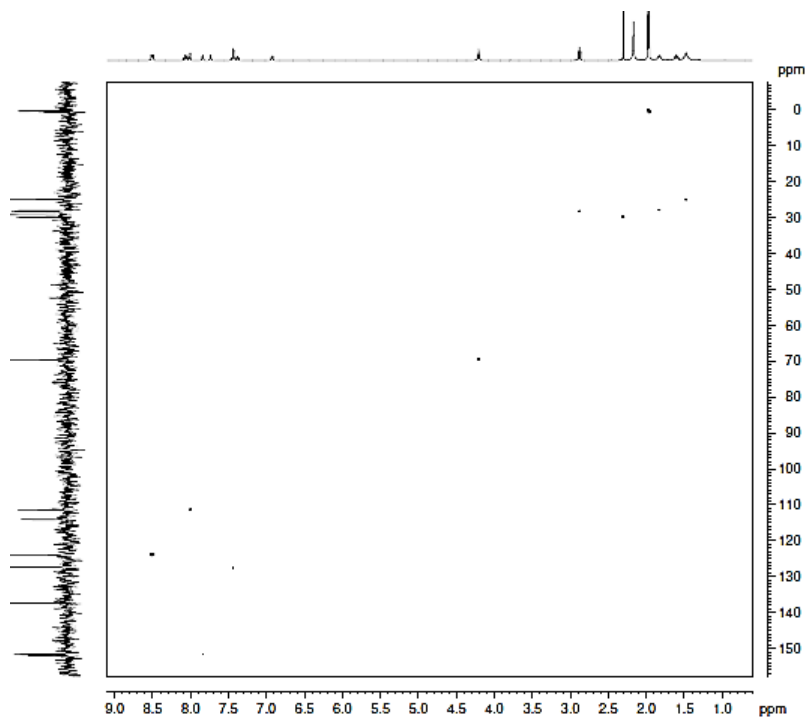
Figure A3.40. HSQC spectrum (CD₃CN) of [Ru(bpy)₂(4,4'-bpysac)](PF₆)₂.
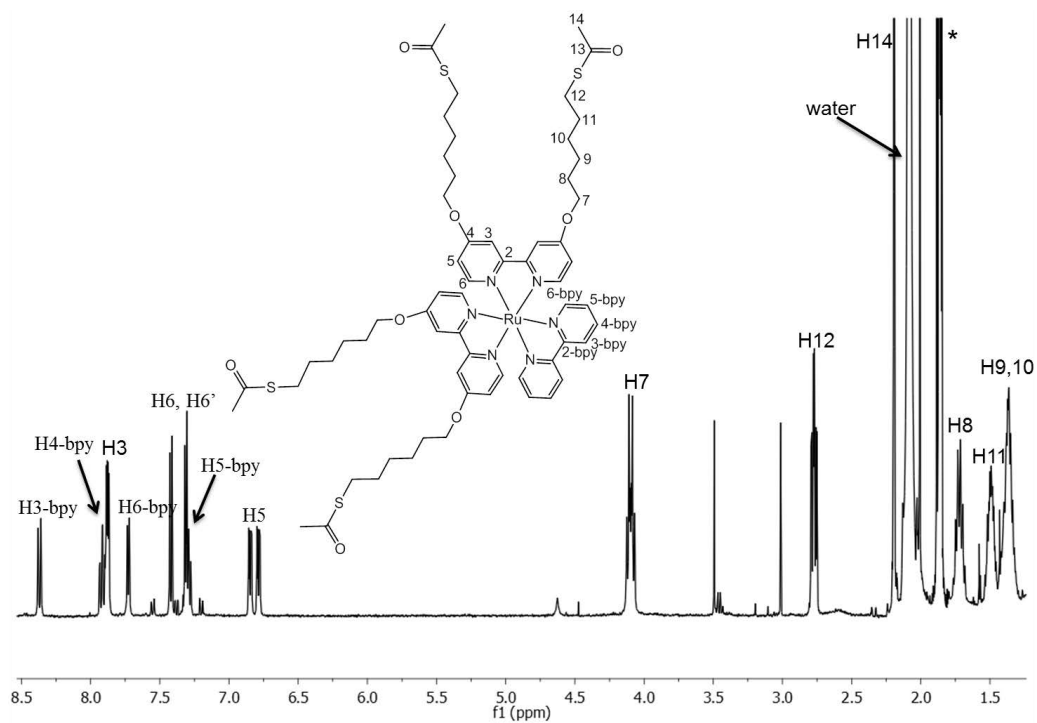
Figure A3.41. 400 MHz ¹H NMR spectrum (CD₃CN) of [Ru(bpy)(4,4'-bpysac)₂](PF₆)₂.
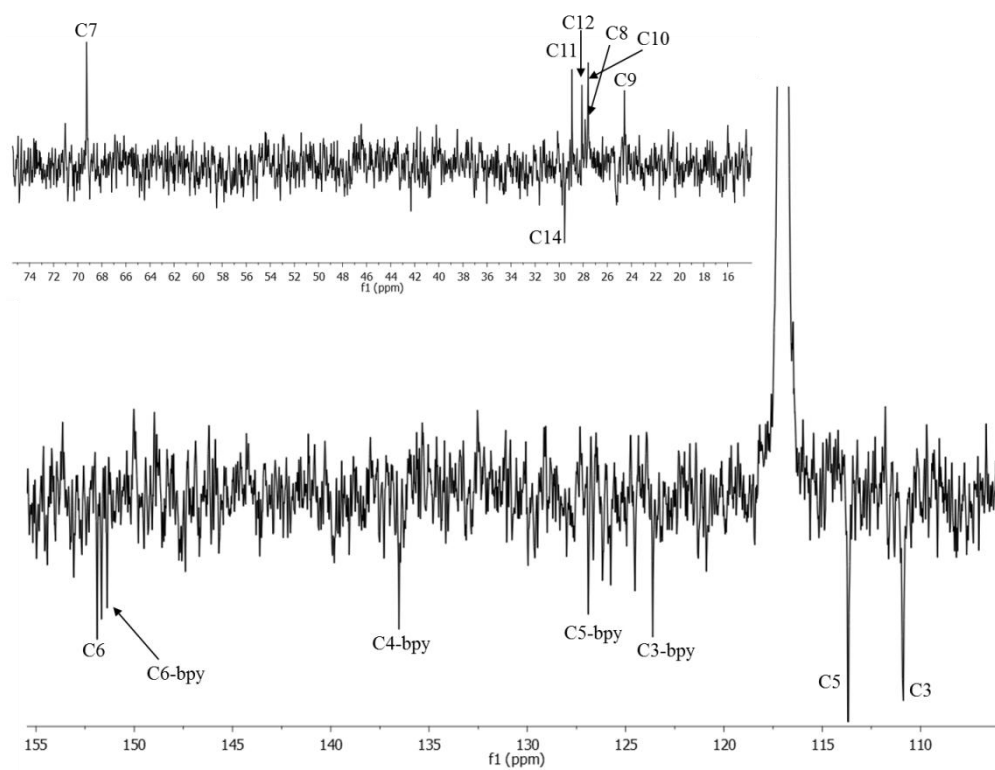
Figure A3.42. 100 MHz ^{13}C NMR spectrum (CD$_3$CN) of [Ru(bpy)(4,4'-bpysac)$_2$](PF$_6$)$_2$.
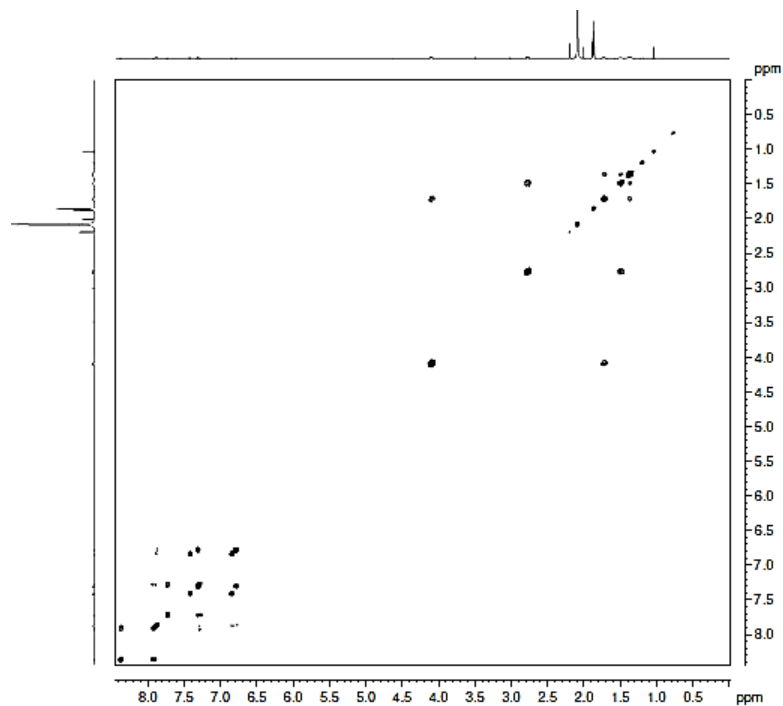
Figure A3.43. COSY spectrum (CD$_3$CN) of [Ru(bpy)(4,4'-bpysac)$_2$](PF$_6$)$_2$.
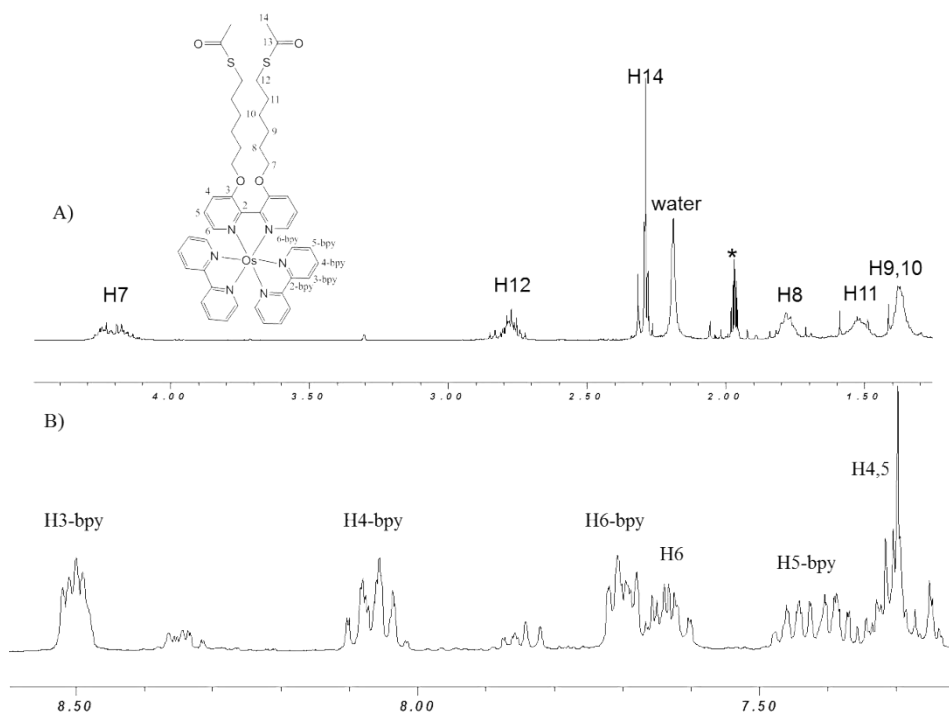
Figure A3.44. 400 MHz ^{1}H NMR spectrum (CD$_3$CN) of [Os(bpy)$_2$(3,3'-bpysac)](PF$_6$)$_2$.
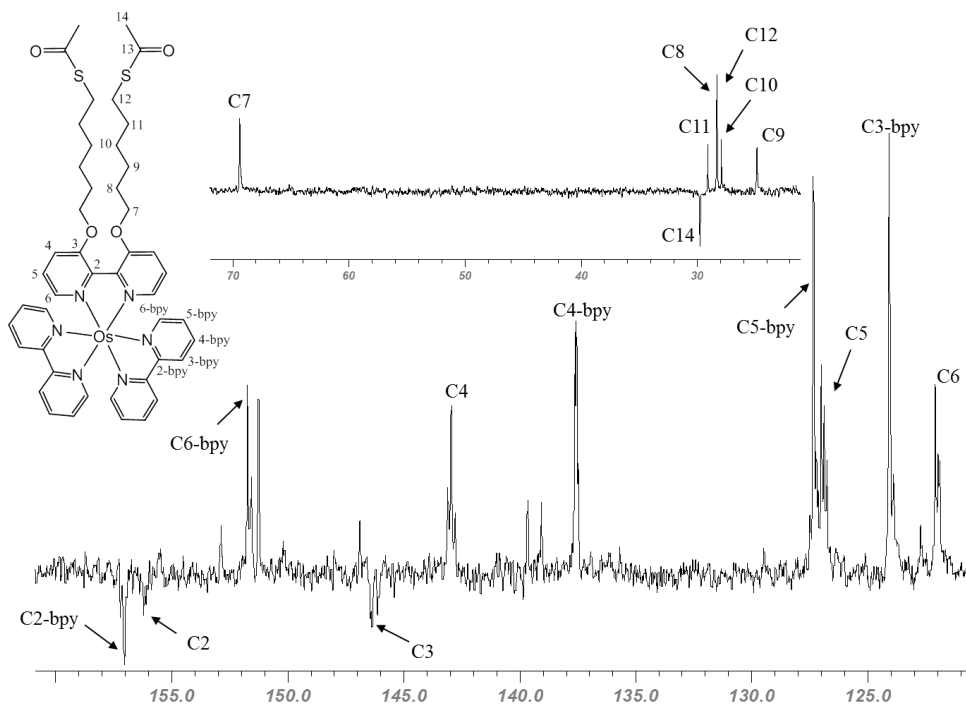
Figure A3.45. 100 MHz ^{13}C NMR spectrum (CD$_3$CN) of [Os(bpy)$_2$(3,3'-bpysac)](PF$_6$)$_2$.
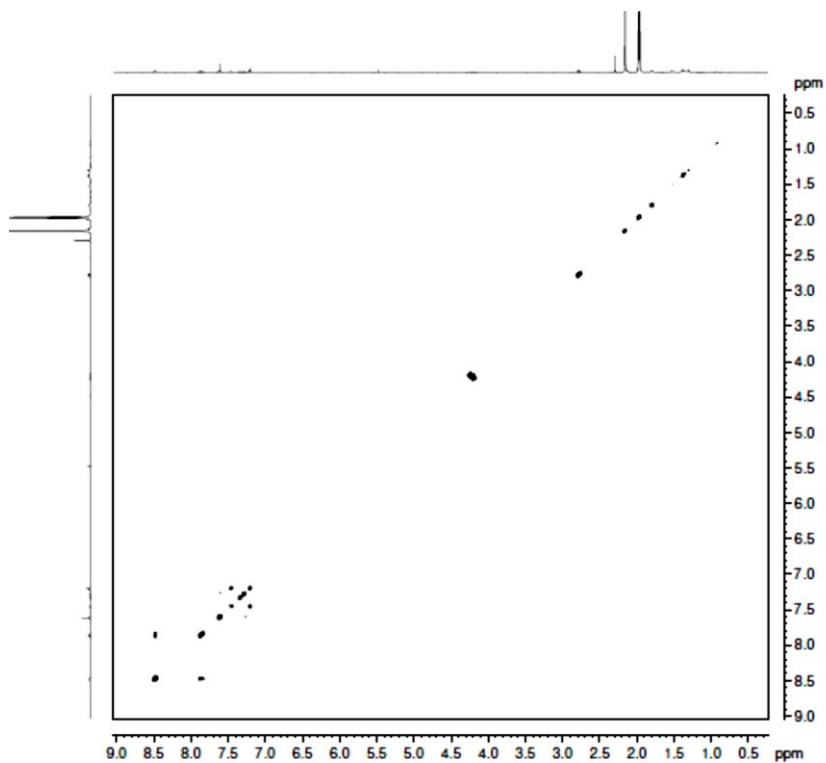
Figure A3.46. COSY spectrum (CD₃CN) of [Os(bpy)₂(3,3'-bpysac)](PF₆)₂.
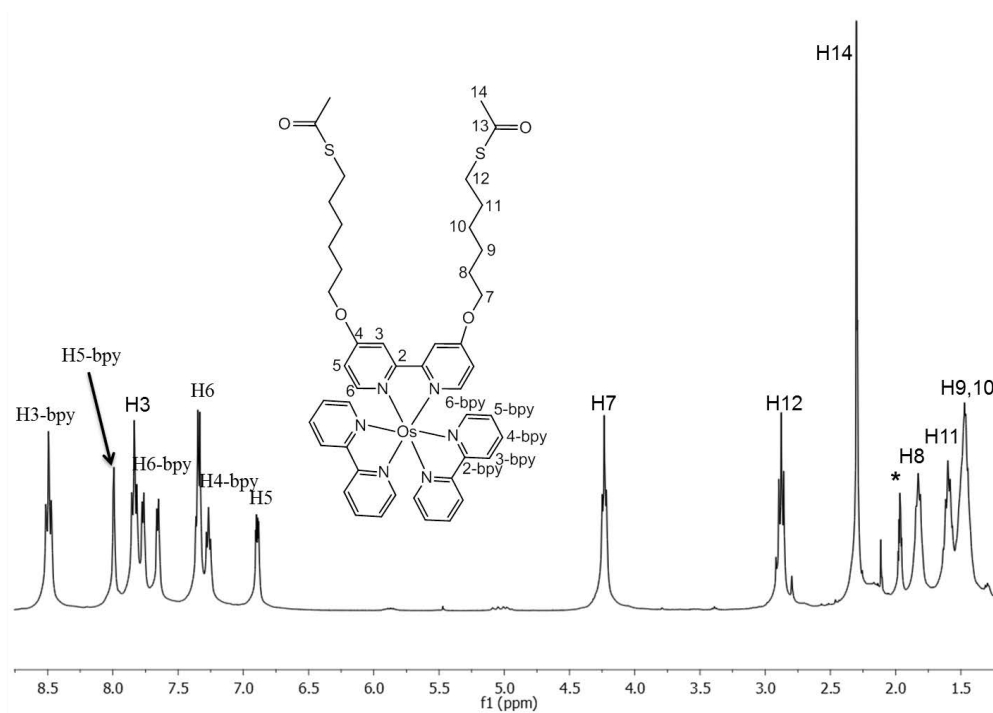
Figure A3.47. 400 MHz ¹H NMR spectrum (CD₃CN) of [Os(bpy)₂(4,4'-bpysac)](PF₆)₂.
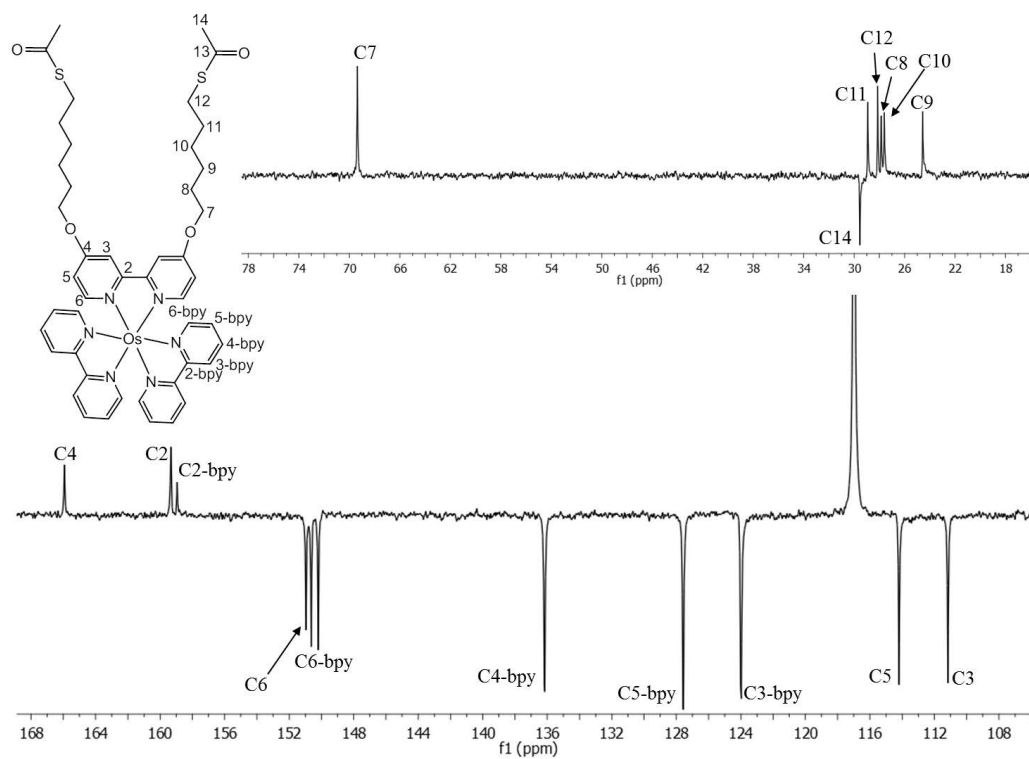
Figure A3.48. 100 MHz ^{13}C NMR spectrum (CD$_3$CN) of [Os(bpy)$_2$(4,4'-bpysac)](PF$_6$)$_2$.
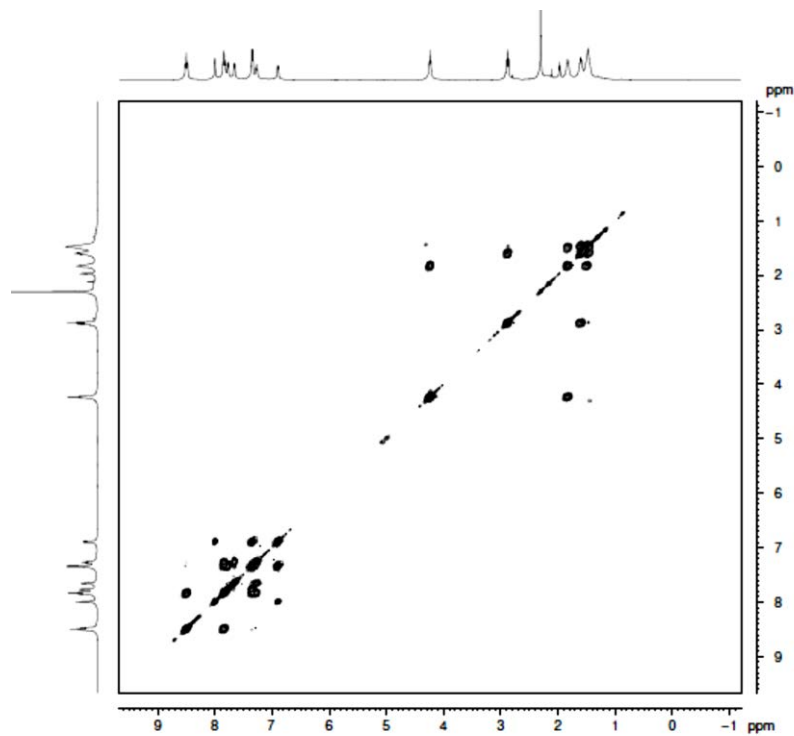
Figure A3.49. COSY spectrum (CD$_3$CN) of [Os(bpy)$_2$(4,4'-bpysac)](PF$_6$)$_2$.
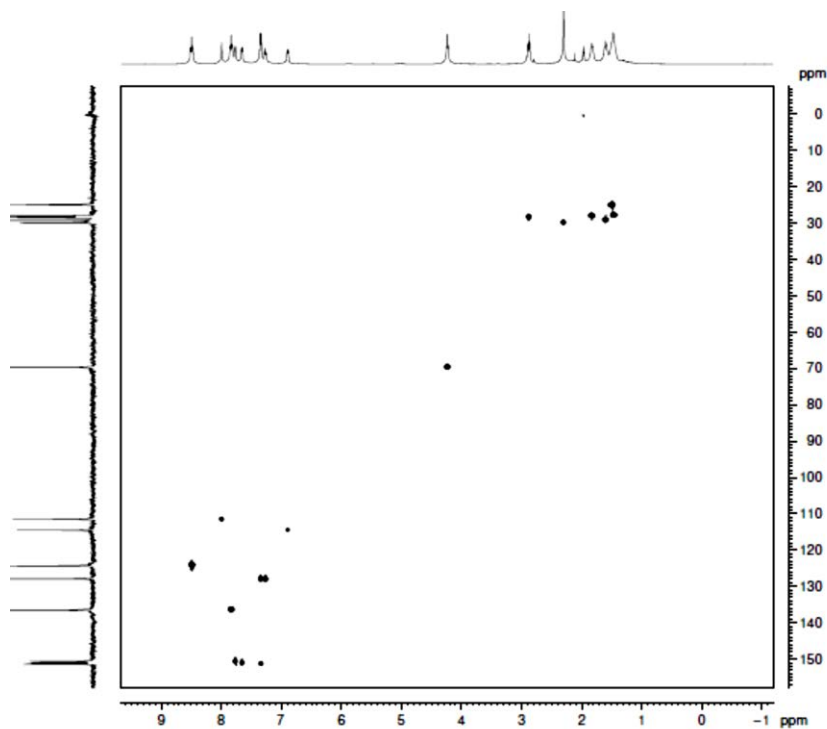
Figure A3.50. HSQC spectrum (CD$_3$CN) of [Os(bpy)$_2$(4,4'-bpysac)](PF$_6$)$_2$.
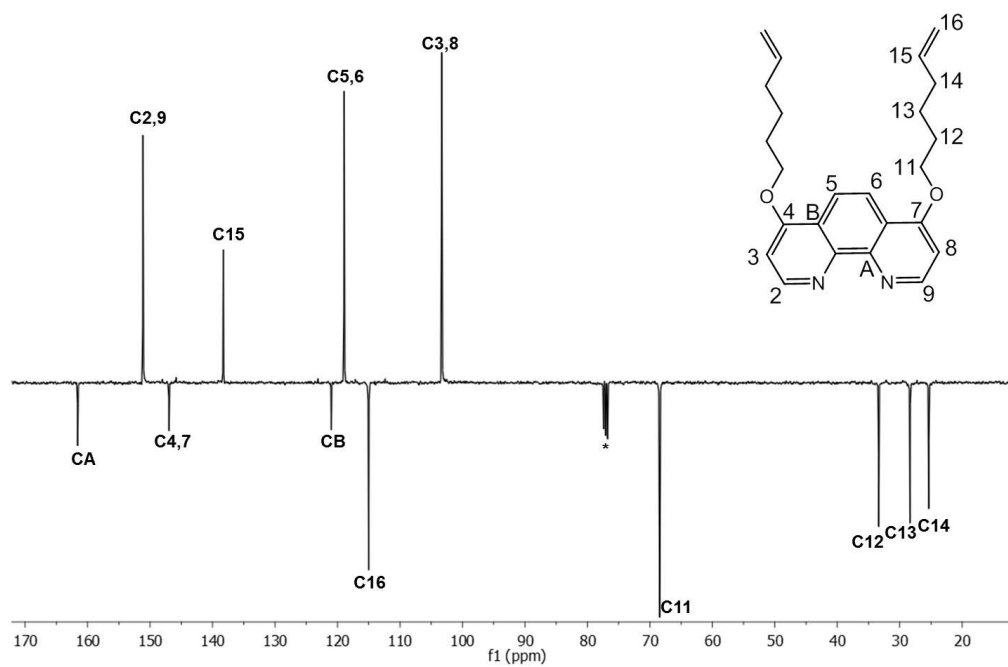
Figure A3.51. 100 MHz ^{13}C NMR spectrum (CDCl$_3$) of 4,7-phenhex.
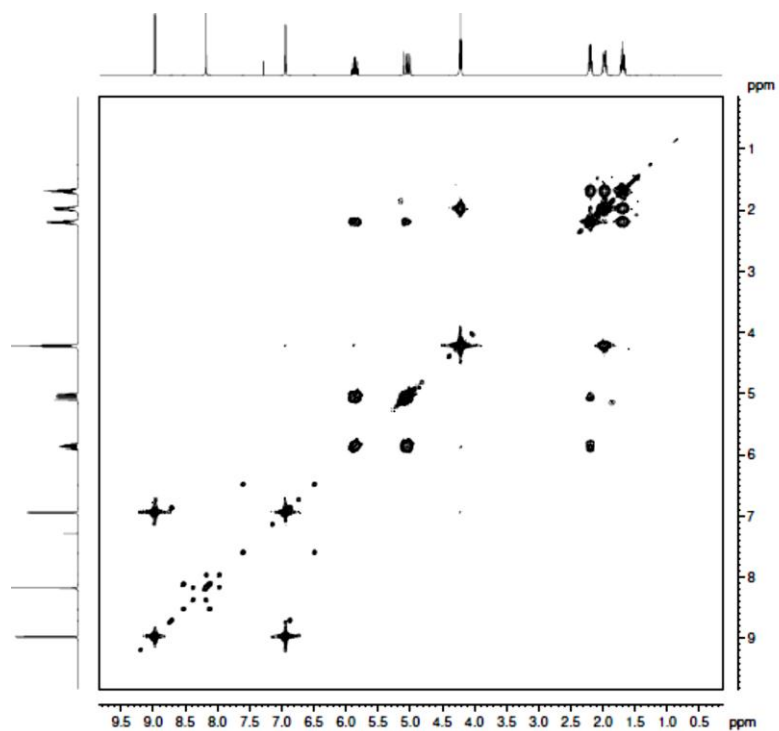
Figure A3.52. COSY spectrum (CDCl$_3$) of 4,7-phenhex.
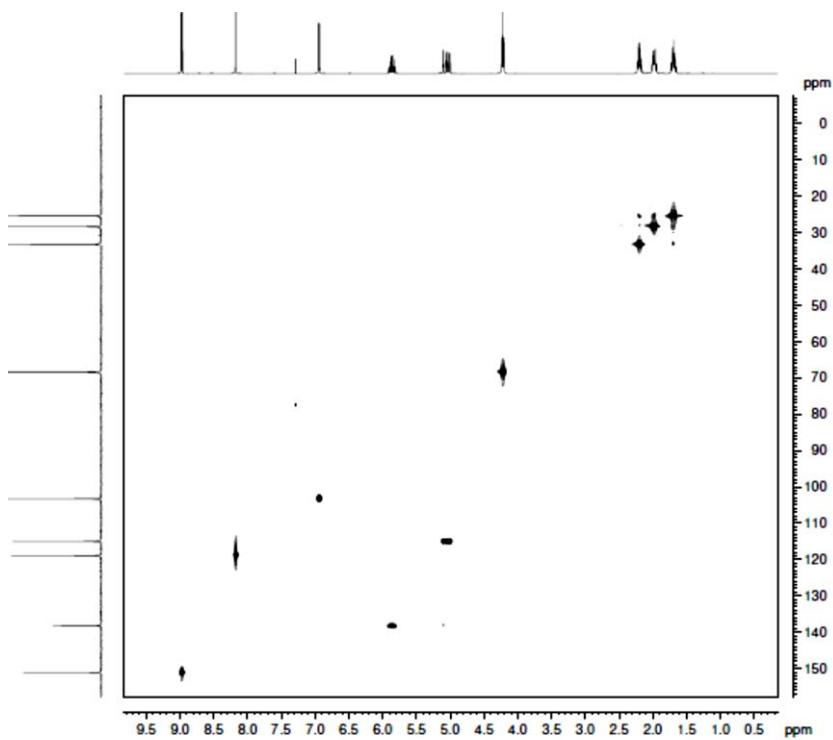
Figure A3.53. HSQC spectrum (CDCl$_3$) of 4,7-phenhex.
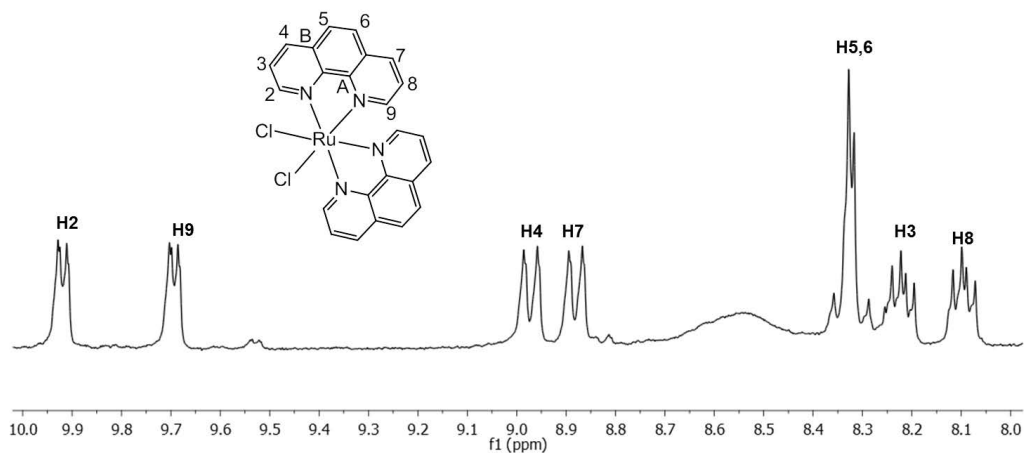
Figure A3.54. 300 MHz ^{1}H NMR spectrum (DMSO) of Ru(phen)$_2$Cl$_2$.
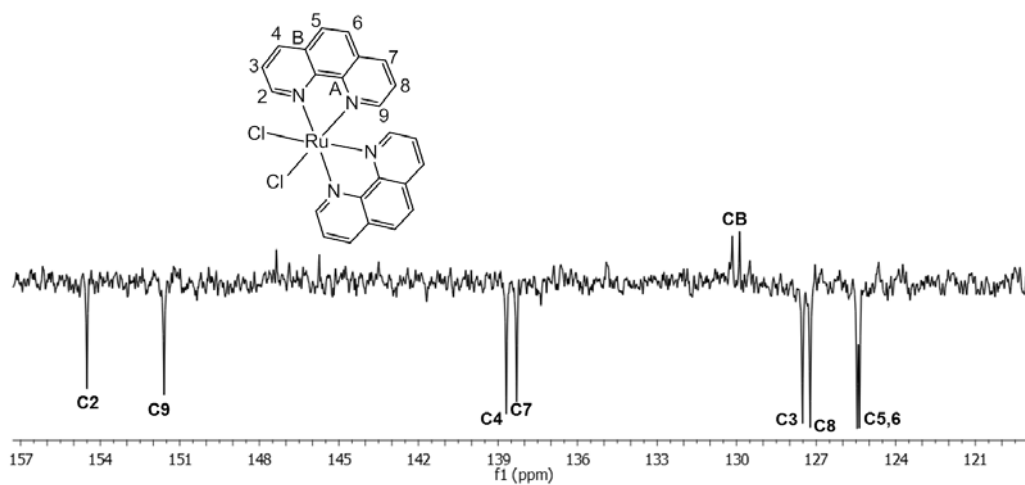
Figure A3.55. 100 MHz ^{13}C NMR spectrum (DMSO) of Ru(phen)$_2$Cl$_2$.
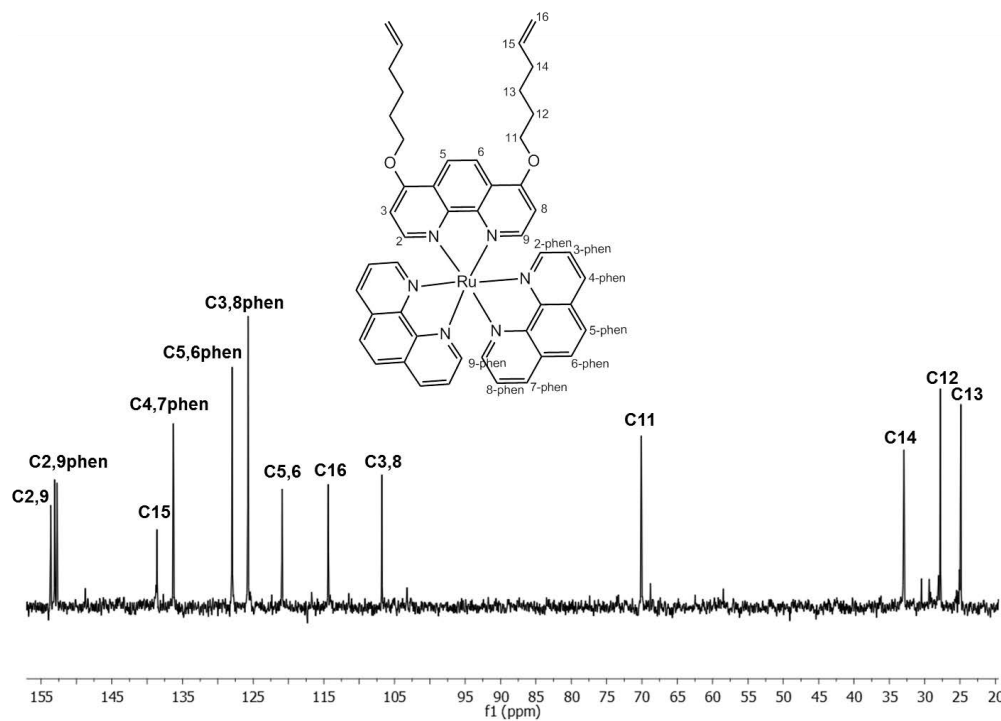
Figure A3.56. 100 MHz ^{13}C NMR spectrum (CDCN$_3$) of [Ru(phen)$_2$(4,7-phenhex)](PF$_6$)$_2$.
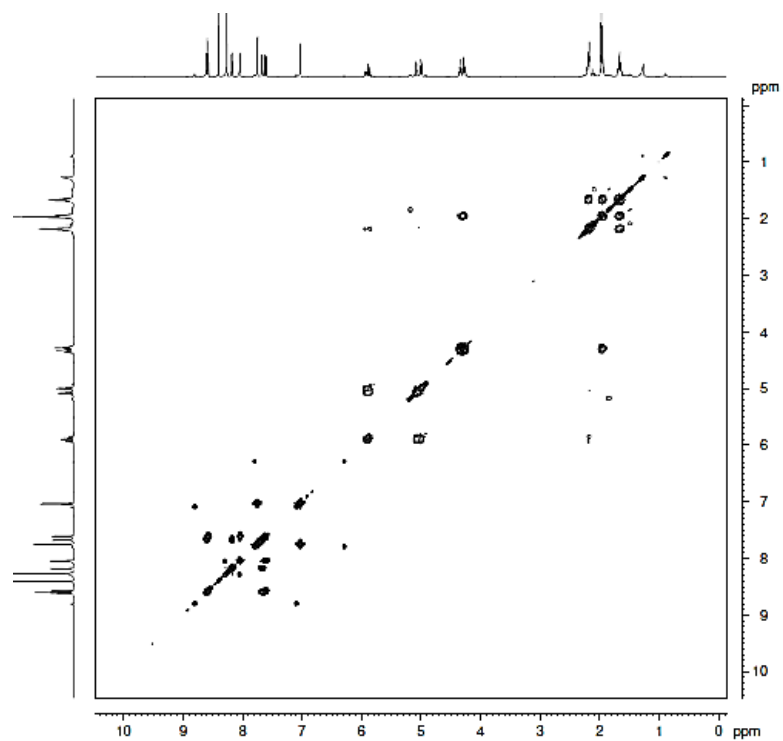
Figure A3.57. COSY spectrum (CDCN$_3$) of [Ru(phen)$_2$(4,7-phenhex)](PF$_6$)$_2$.
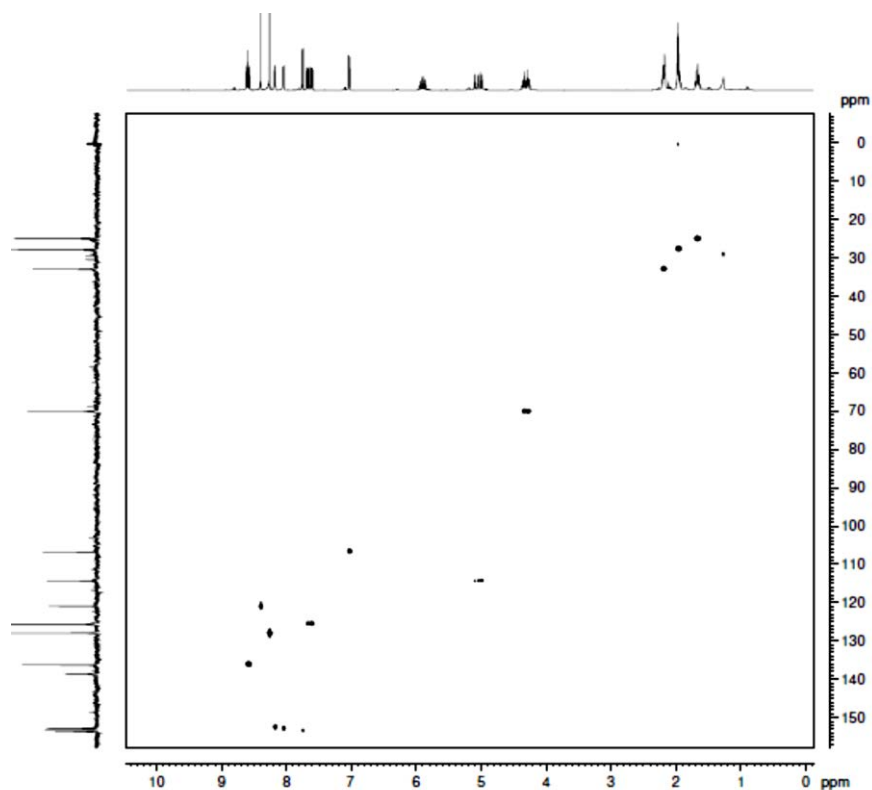
Figure A3.58. HSQC spectrum (CDCN$_3$) of [Ru(phen)$_2$(4,7-phenhex)](PF$_6$)$_2$.
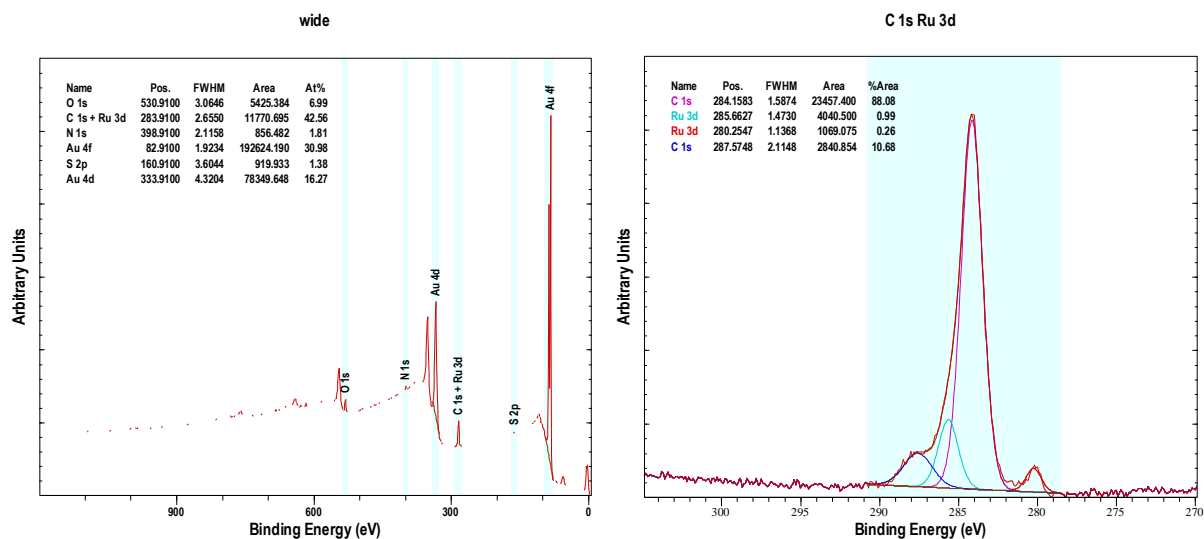
Figure A3.59 Full XPS spectrum of [Ru(bpy)$_2$(3,3'-bpysac)](PF$_6$)$_2$ monolayer on planar gold surface

(left), The narrow scan spectra of the C 1s, Ru 3d region (right).

wide

Name	Pos.	FWHM	Area	At%
O 1s	530.9100	3.0193	5826.829	7.54
C 1s + Ru 3d	283.9100	2.4223	16964.056	61.60
N 1s	398.9100	1.7440	276.081	0.58
Au 4f	82.9100	1.8405	65704.443	10.61
S 2p	162.9100	2.7280	9592.397	14.50
Au 4d	333.9100	4.4284	24751.196	5.16

C 1s Ru 3d

Name	Pos.	FWHM	Area	%Area
C 1s	283.9573	1.2712	30983.504	77.84
Ru 3d	284.9425	1.3498	9779.053	1.60
Ru 3d	279.9816	1.2063	1100.388	0.18
C 1s	286.4869	3.2365	8108.933	20.38
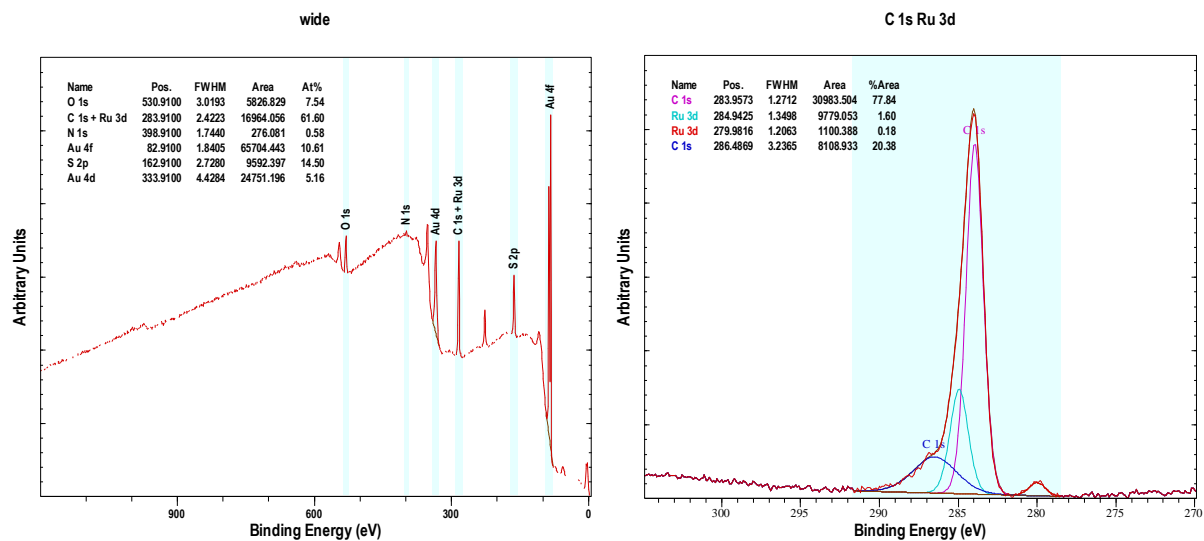
Figure A3.60 Full XPS spectrum of [Ru(bpy)(3,3'-bpysac)$_2$](PF$_6$)$_2$ monolayer on planar gold surface (left), The narrow scan spectra of the C 1s, Ru 3d region (right).

wide

Name	Pos.	FWHM	Area	At%
O 1s	530.9100	3.0696	4933.587	6.36
C 1s + Ru 3d	283.9100	2.2811	13897.859	50.30
N 1s	398.9100	3.0429	1187.572	2.51
Au 4f	82.9100	1.8597	161635.647	26.02
S 2p	161.9100	3.8736	924.639	1.39
Au 4d	333.9100	4.3444	64515.424	13.41

C 1s Ru 3d

Name	Pos.	FWHM	Area	% Area
C 1s	284.0812	1.2834	31568.943	92.23
C 1s	287.4770	1.5195	1298.951	3.80
C 1s	282.8596	1.5489	991.984	2.90
Ru 3d	280.2150	1.3893	1335.492	0.25
Ru 3d	285.5601	1.5539	4301.338	0.82
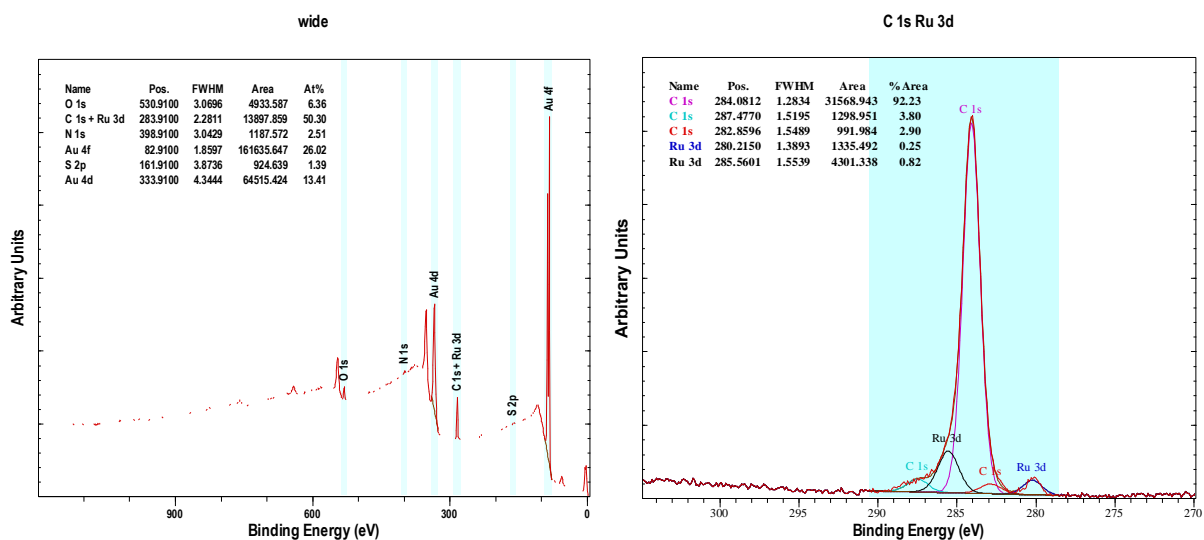
Figure A3.61 A) Full XPS spectrum of [Ru(bpy)$_2$(4,4'-bpysac)](PF$_6$)$_2$ monolayer on planar gold surface (left), The narrow scan spectra of the C 1s, Ru 3d region (right).

wide

Name	Pos.	FWHM	Area	At%
O 1s	529.9100	2.8975	12255.553	15.37
C 1s + Os 4d	283.9100	2.7575	15207.380	53.52
N 1s	398.9100	2.7974	1204.929	2.47
Na 1s	1070.9100	2.7780	1142.552	0.66
Au 4f	82.9100	2.1218	119134.962	18.65
S 2p	167.9100	2.1491	330.985	0.48
Au 4d	333.9100	3.9769	37410.140	7.56
Os 4f	55.9100	5.9221	5825.231	1.28

Os 4f

Name	Pos.	FWHM	Area	%Area
Os 4f	49.5386	1.5073	1278.787	50.60
Os 4f	47.4051	1.0686	502.636	19.88
Os 4f	52.4515	1.3835	745.850	29.52
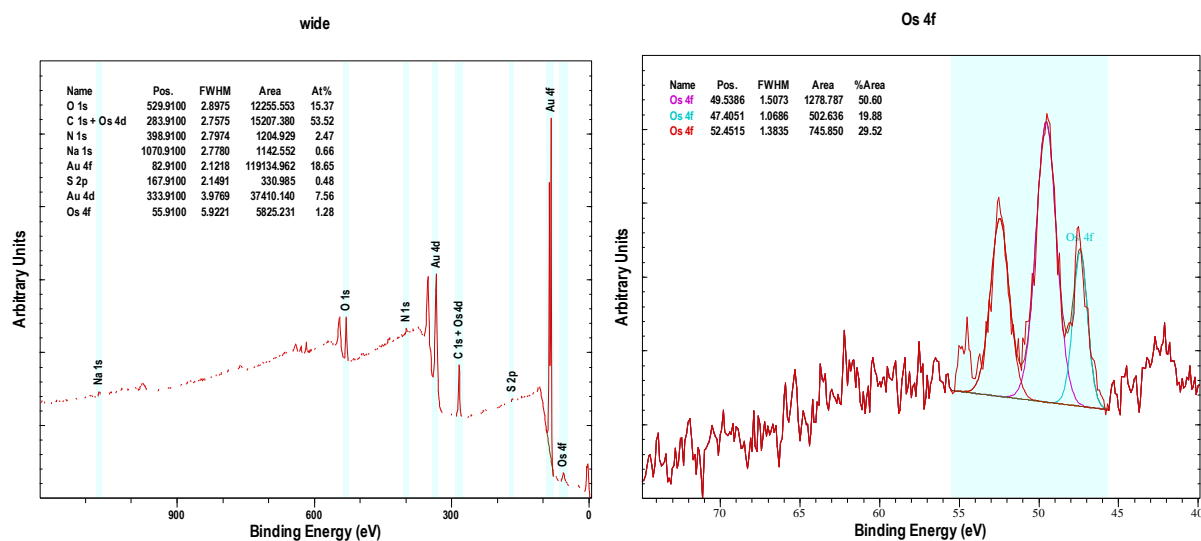
Figure A3.62 Full XPS spectrum of [Os(bpy)$_2$(3,3'-bpysac)](PF$_6$)$_2$ monolayer on planar gold surface (left), The narrow scan spectra of the Os 4f region (right).

S 2p

Name	Pos.	FWHM	Area	%Area
S 2p	167.4583	2.0968	1438.358	56.65
S 2p	161.5350	2.5629	661.575	26.11
S 2p	160.3363	1.5561	436.822	17.25

S 2p

Name	Pos.	FWHM	Area	%Area
S 2p	160.9331	1.6557	1378.113	30.00
S 2p	167.2579	2.2910	1928.210	41.88
S 2p	162.8954	2.6744	1292.822	28.12
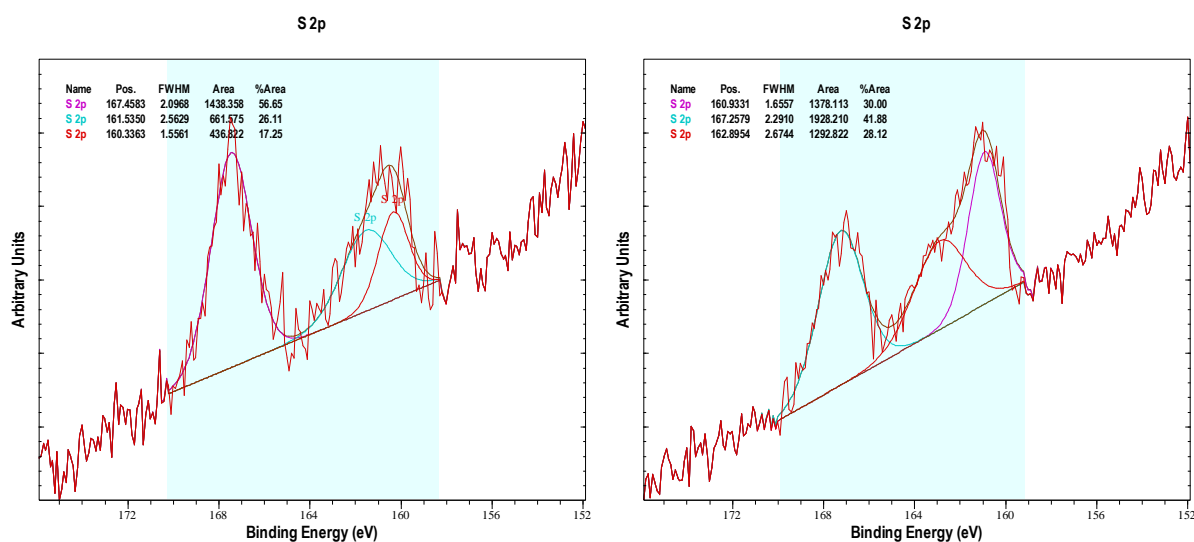
Figure A3.63 The narrow scan spectra of the S 2p region of [Os(bpy)$_2$(3,3'-bpysac)](PF$_6$)$_2$ (left) and [Os(bpy)$_2$(4,4'-bpysac)](PF$_6$)$_2$ (right).
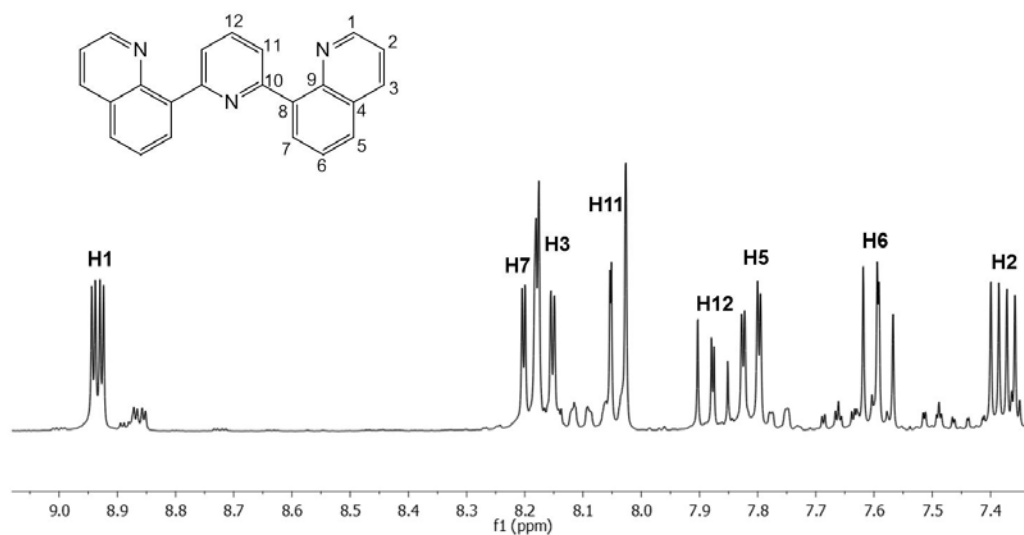
Figure A4.1 400 MHz ^{1}H NMR spectrum (CDCl$_3$) of 1.
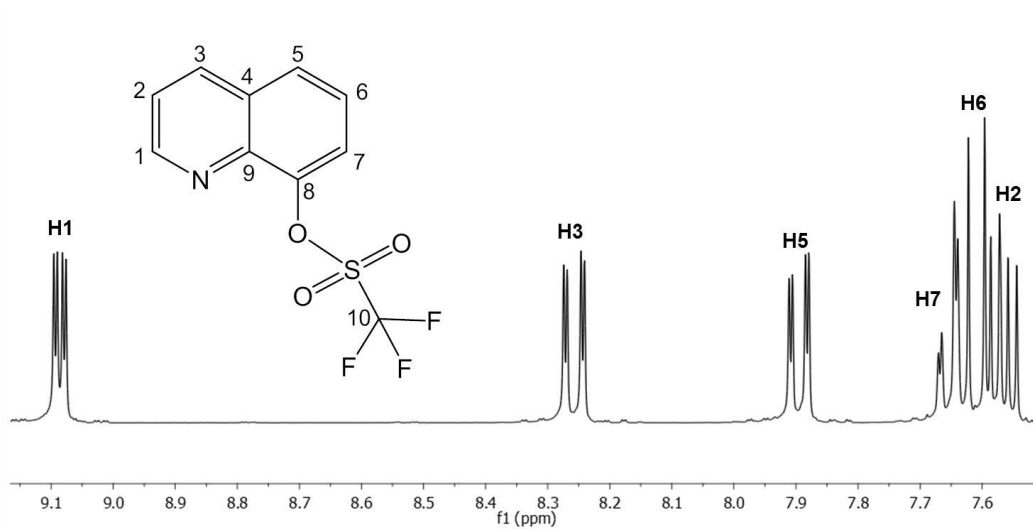
Figure A4.2 400 MHz ^{1}H NMR spectrum (CDCl$_3$) of Q-OTf.
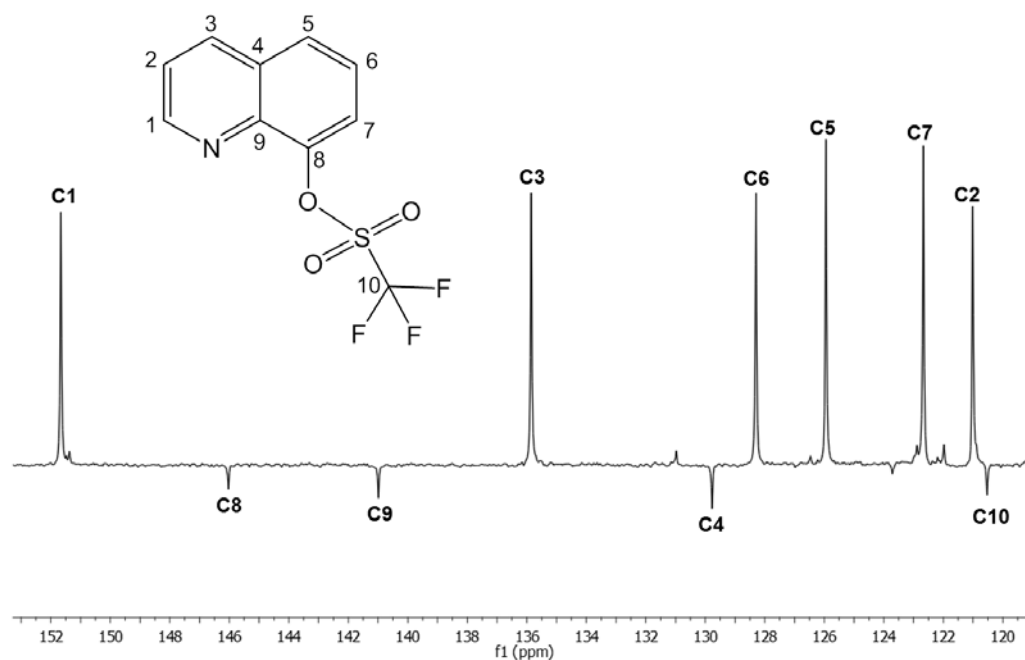
Figure A4.3 100 MHz ^{13}C NMR spectrum (CDCl$_3$) of Q-OTf.
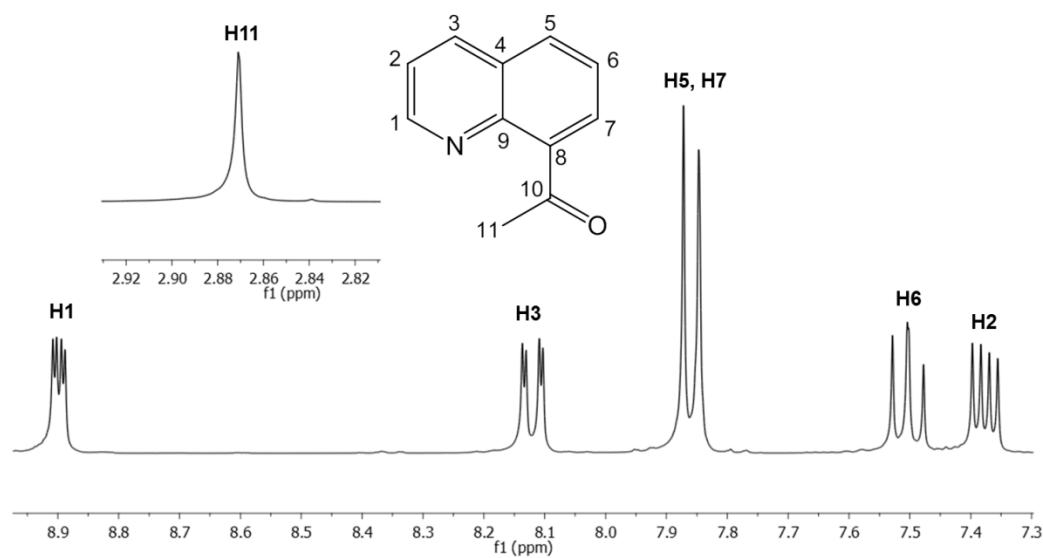
Figure A4.4 400 MHz ^{1}H NMR spectrum (CDCl$_3$) of Q-Ac.
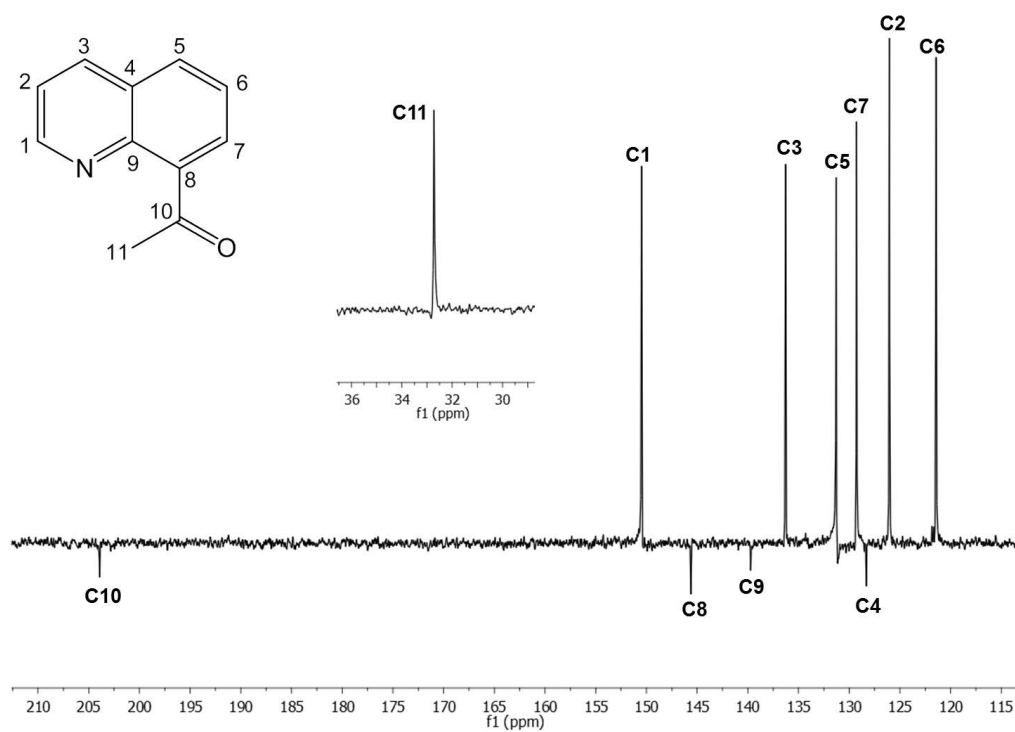
Figure A4.5 100 MHz ^{13}C NMR spectrum (CDCl$_3$) of Q-Ac.
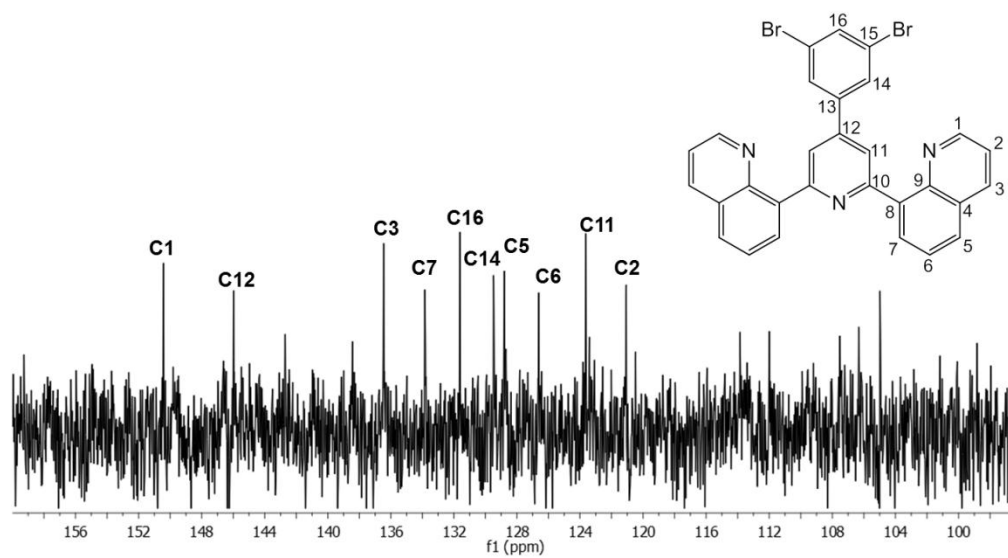
Figure A4.6 100 MHz ^{13}C NMR spectrum (CDCl$_3$) of 2.
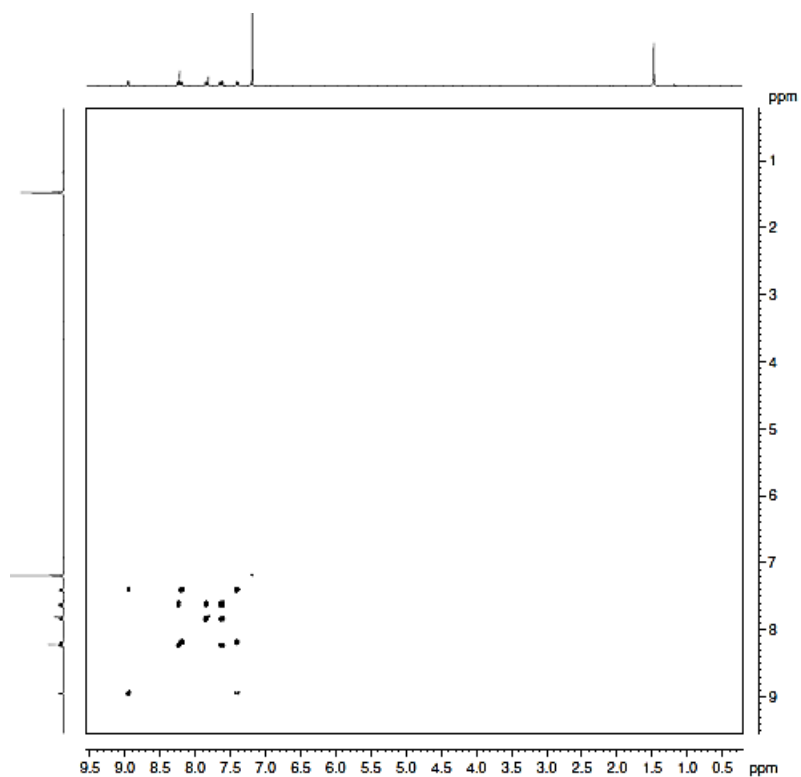
Figure A4.7 COSY NMR spectrum (CDCl$_3$) of 2.
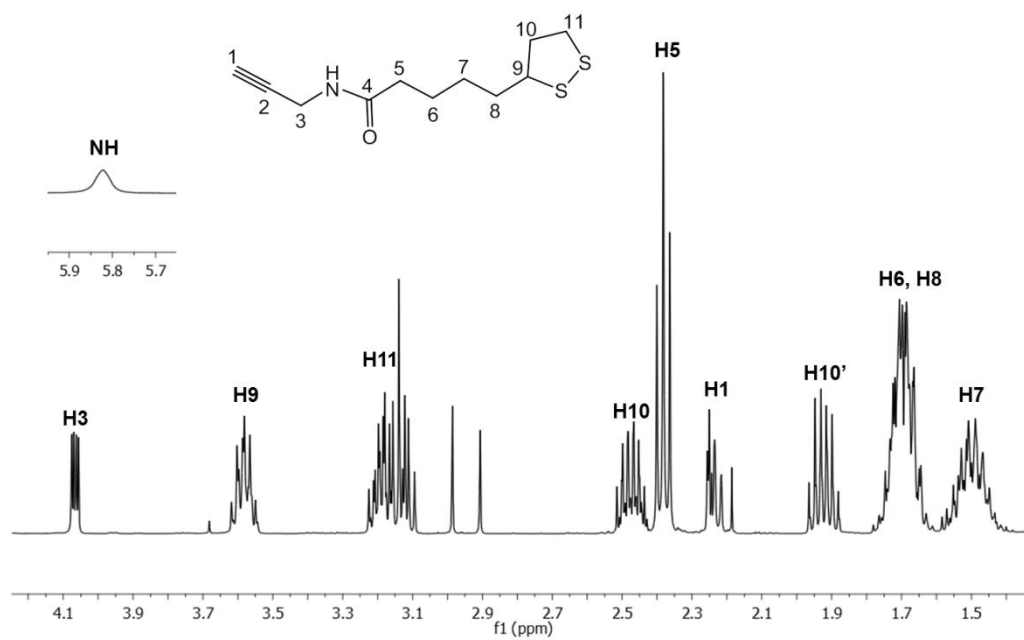
Figure A4.8 400 MHz ^{1}H NMR spectrum (CDCl$_3$) of 10.
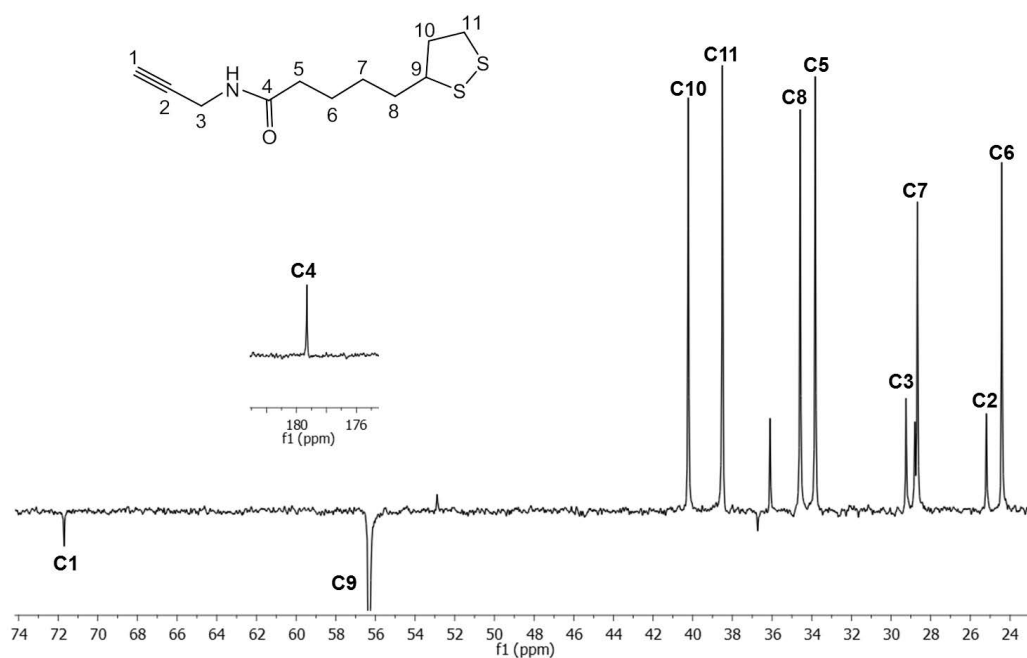
Figure A4.9 100 MHz ^{13}C NMR spectrum (CDCl$_3$) of 10.
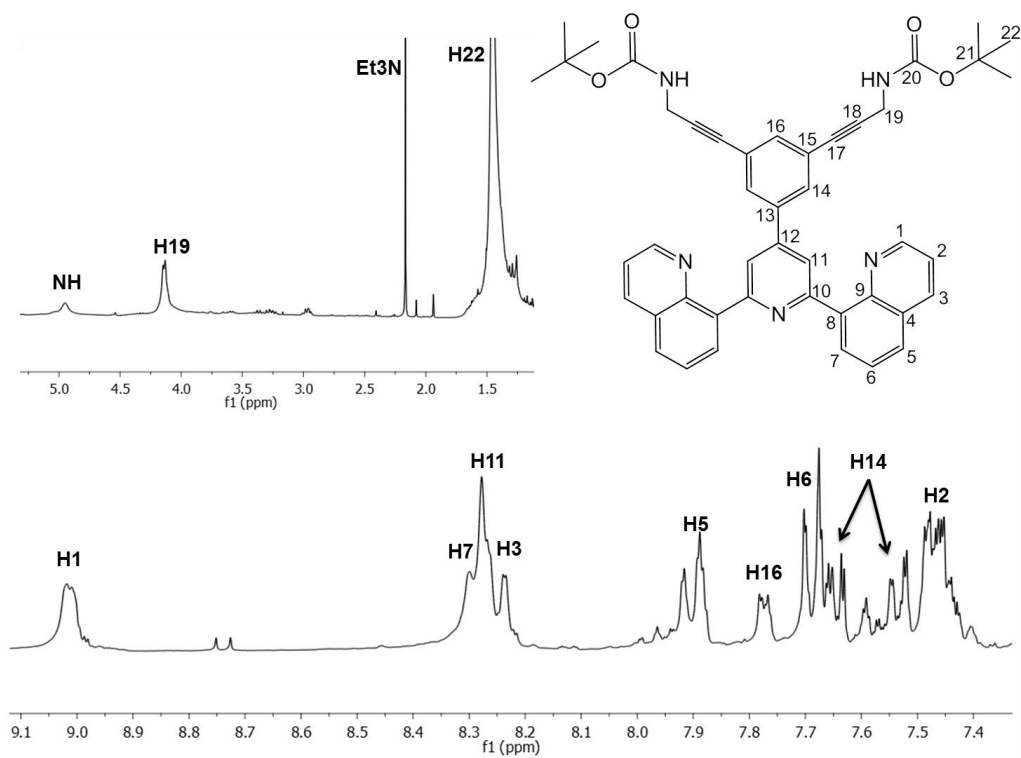
Figure A4.10 400 MHz ^{1}H NMR spectrum (CDCl$_3$) of 8.
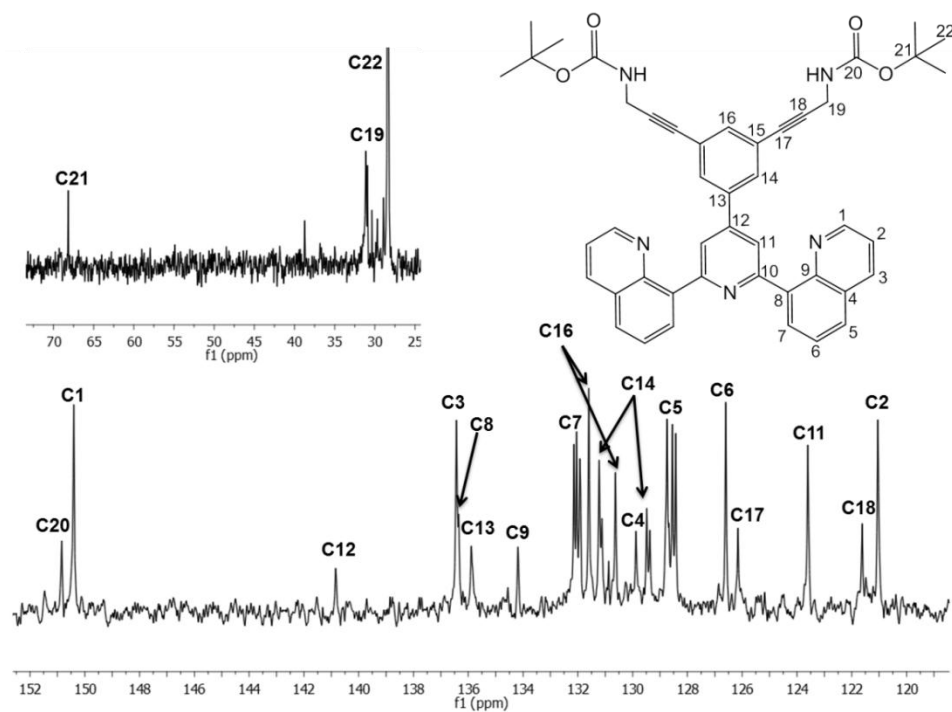
Figure A4.11 100 MHz ^{13}C NMR spectrum (CDCl$_3$) of 8.
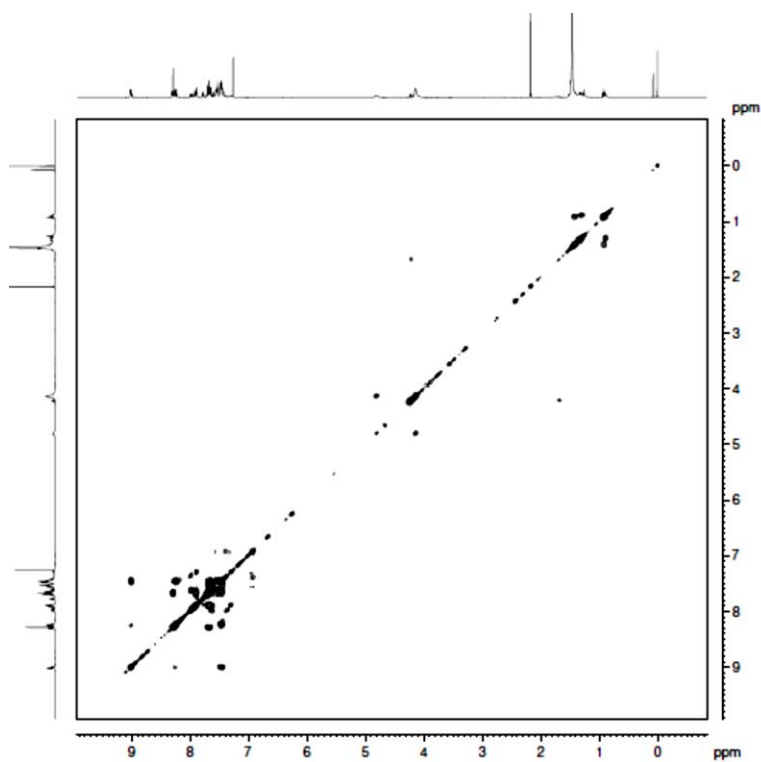
Figure A4.12 COSY NMR spectrum (CDCl$_3$) of 8.
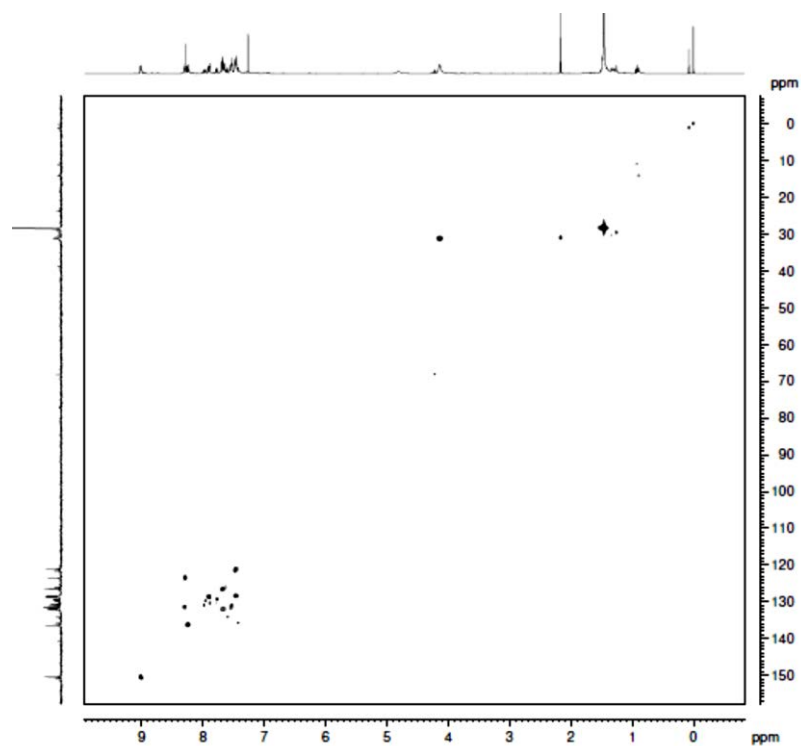
Figure A4.13 HSQC NMR spectrum (CDCl$_3$) of 8.
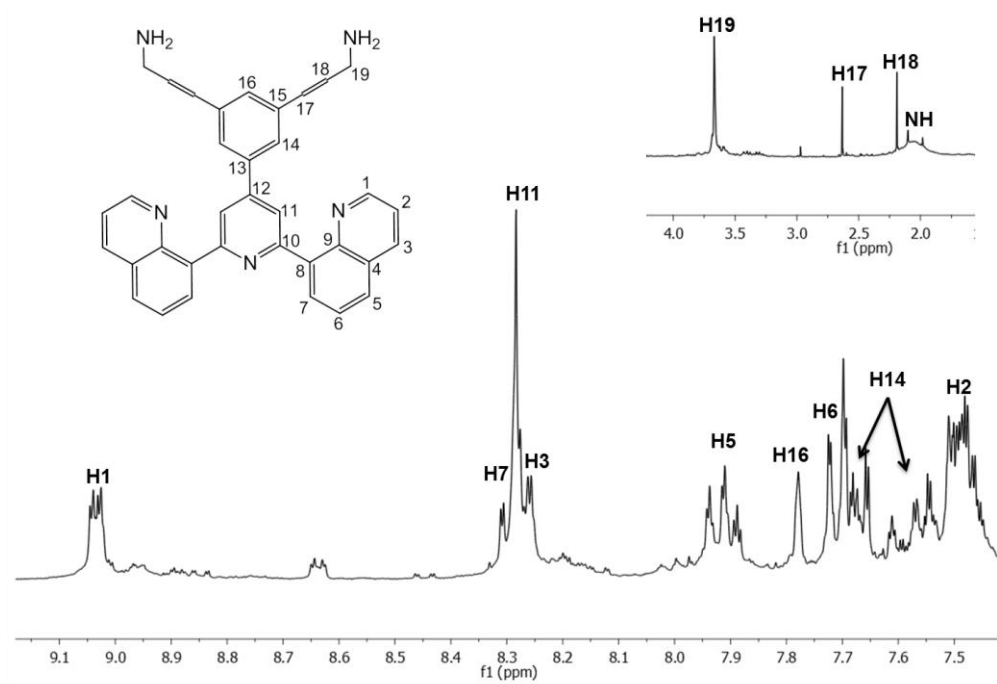
Figure A4.14 400 MHz ^{1}H NMR spectrum (CDCl$_3$) of 9.
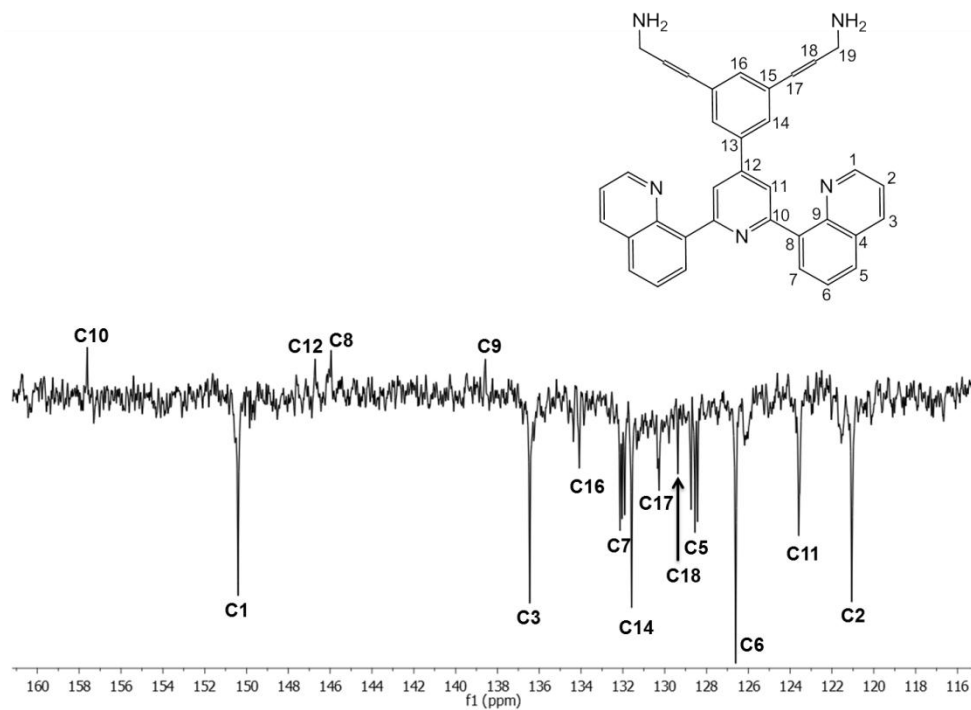
Figure A4.15 100 MHz ^{13}C NMR spectrum (CDCl$_3$) of 9.
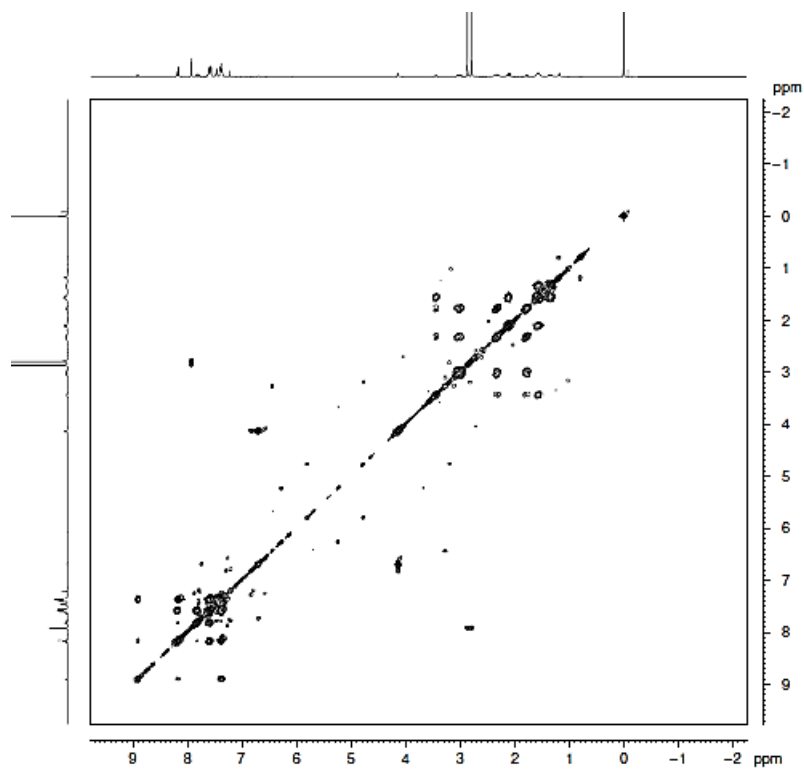
Figure A4.16 COSY NMR spectrum (CDCl$_3$) of 11.
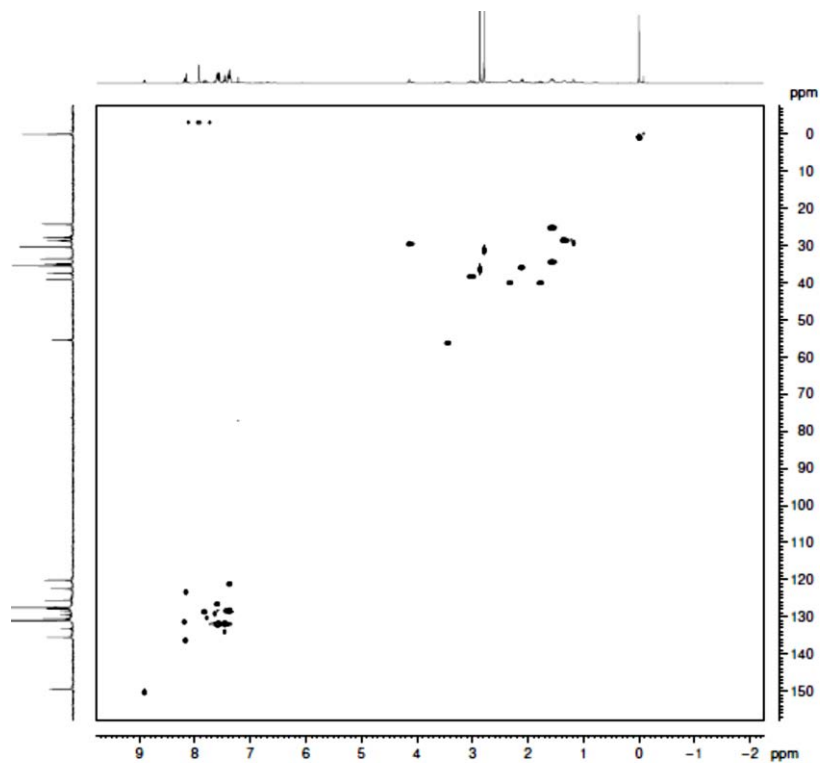
Figure A4.17 HSQC NMR spectrum (CDCl₃) of 11.
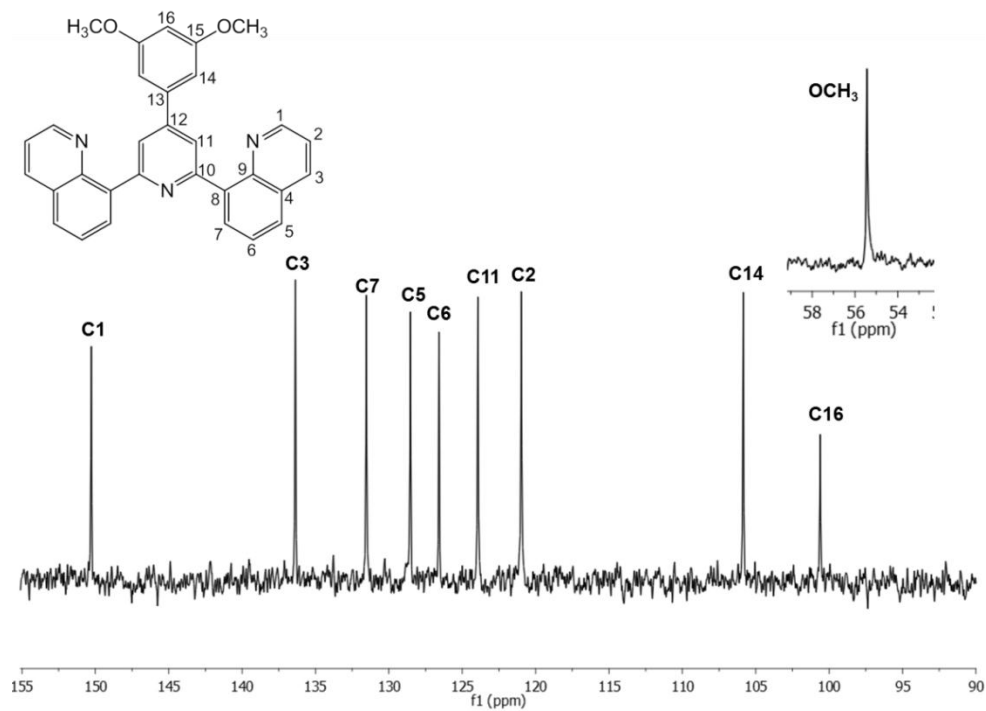
Figure A4.18 100 MHz ¹³C NMR spectrum (CDCl₃) of 3.
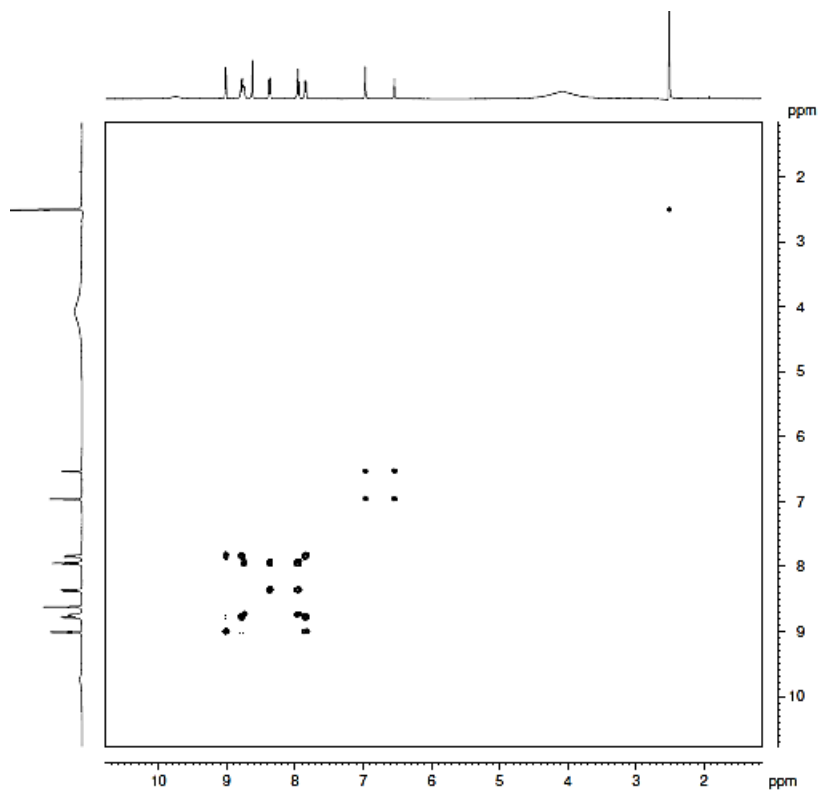
Figure A4.19 COSY NMR spectrum (CDCl$_3$) of 4.
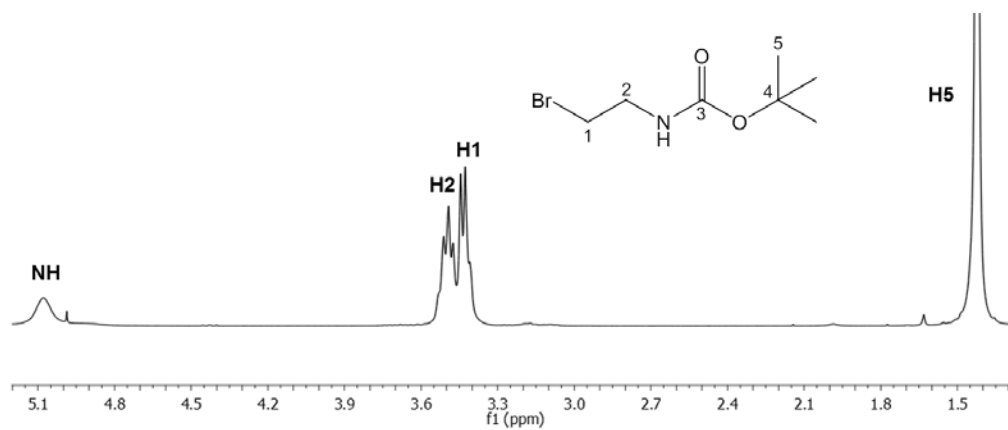
Figure A4.20 300 MHz ^{1}H NMR spectrum (CDCl$_3$) of Br(CH$_2$)$_2$NHBOc.
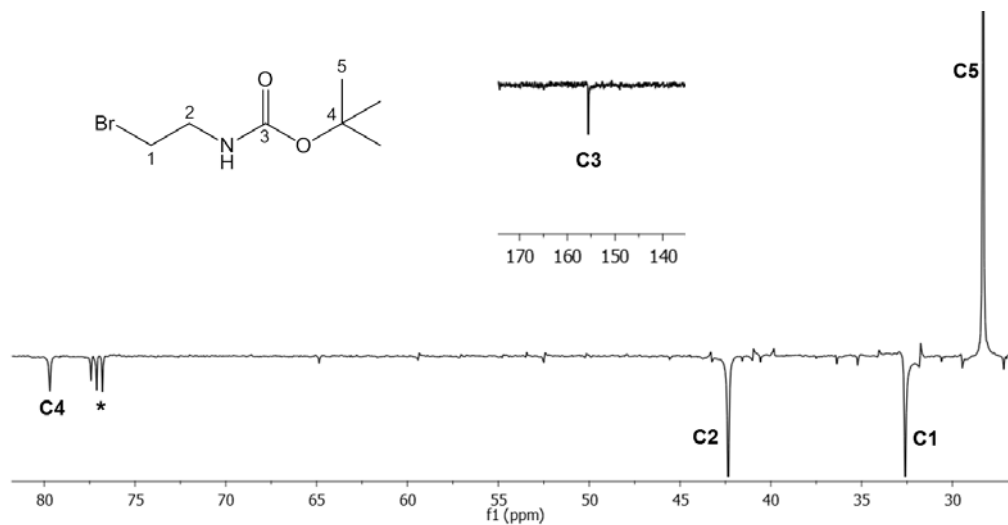
Figure A4.21 100 MHz ^{13}C NMR spectrum (CDCl$_3$) of Br(CH$_2$)$_2$NHBOc.
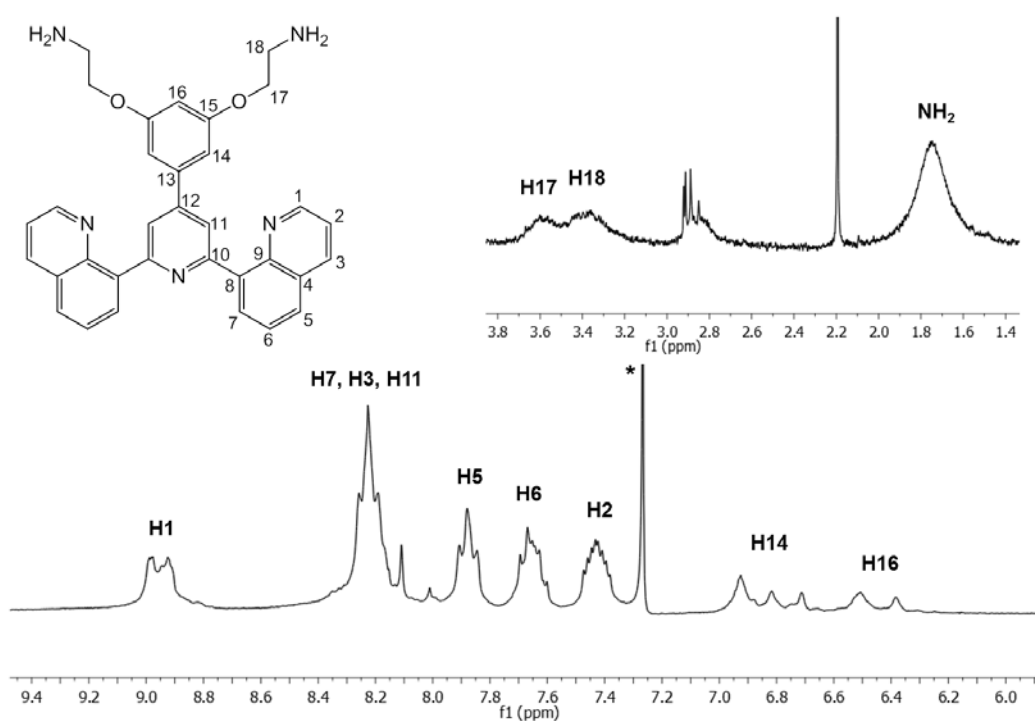
Figure A4.22 400 MHz ^{1}H NMR spectrum (CDCl$_3$) of 12.
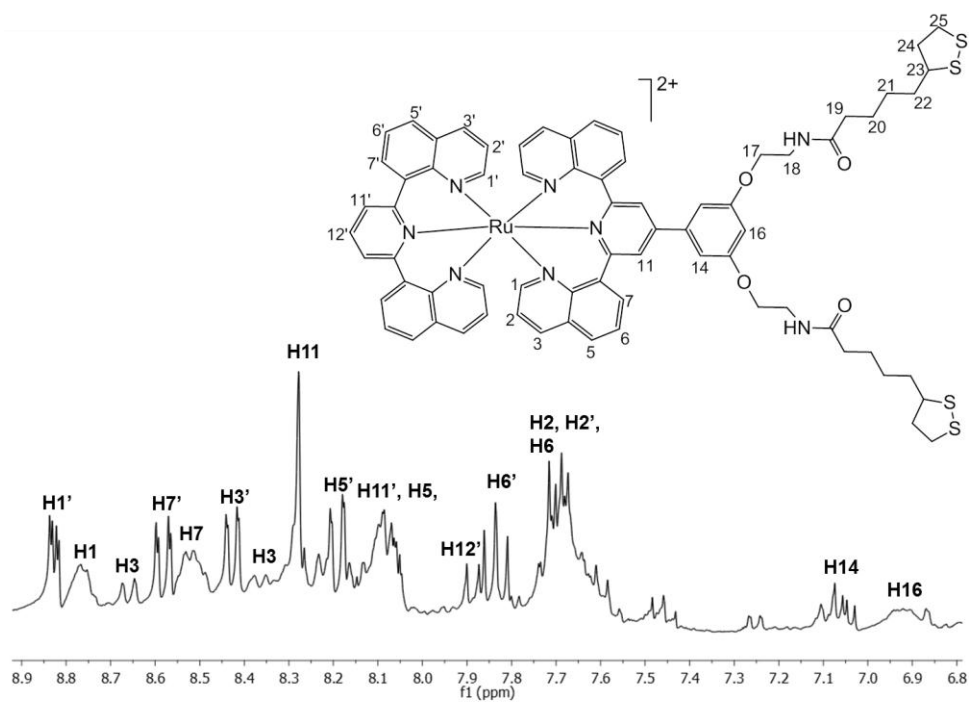
Figure A4.23 400 MHz ^{1}H NMR spectrum (CD$_3$CN) of [Ru(1)(13)](PF$_6$)$_2$.
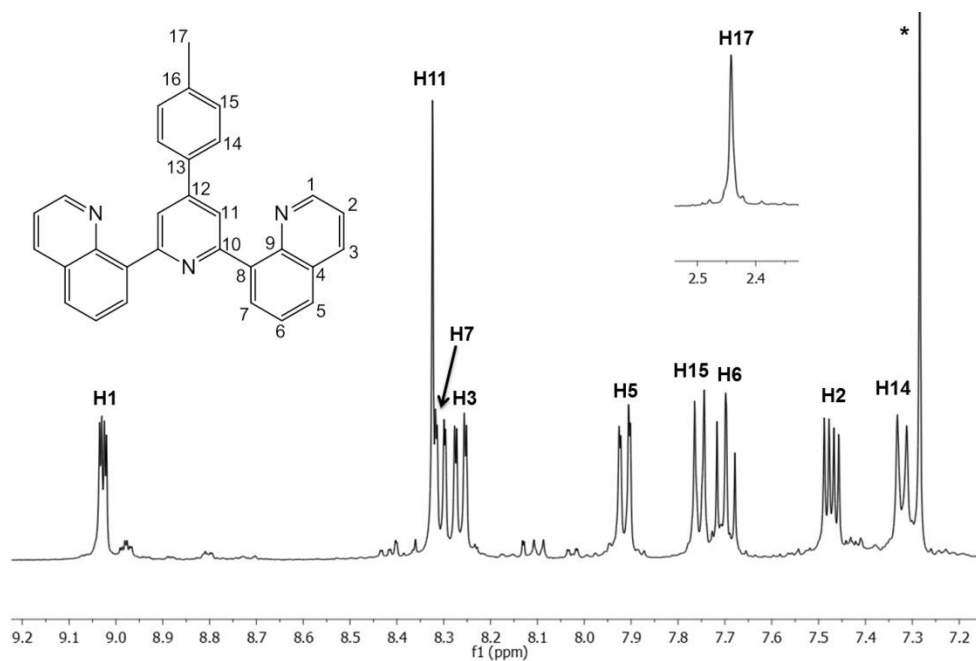
Figure A4.24 400 MHz ^{1}H NMR spectrum (CDCl$_3$) of 6.
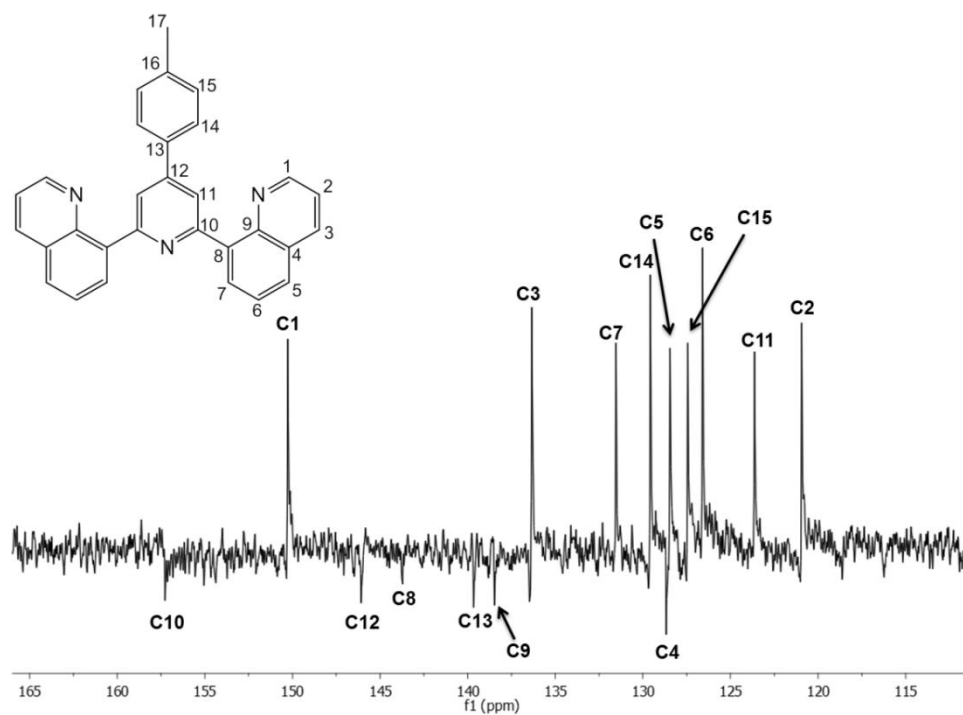
Figure A4.25 100 MHz ^{13}C NMR spectrum (CDCl$_3$) of 6.
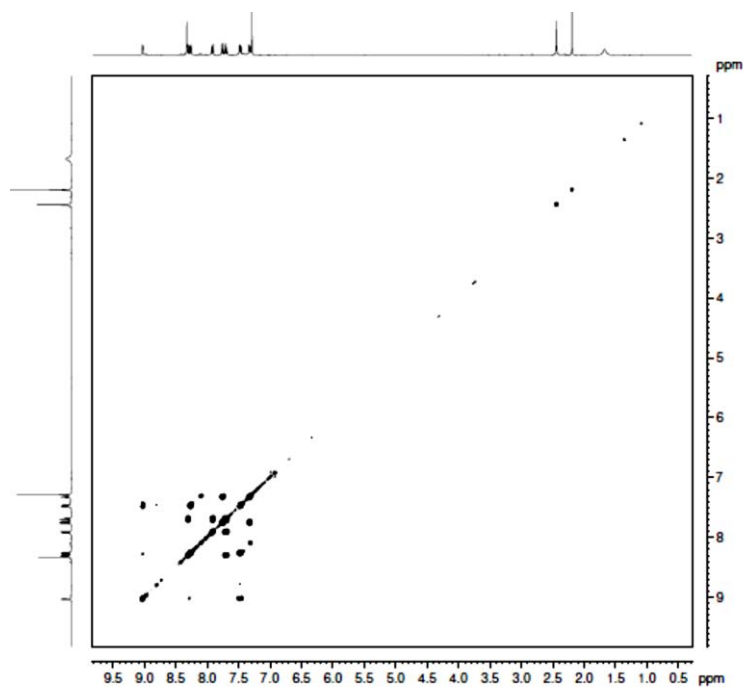
Figure A4.26 COSY NMR spectrum (CDCl$_3$) of 6.
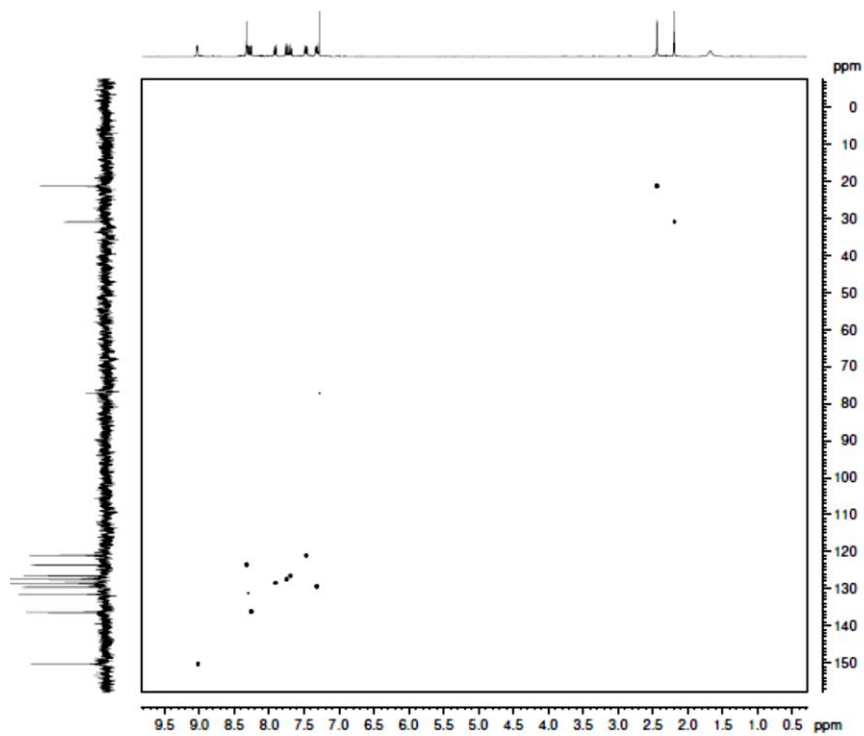
Figure A4.27 HSQC NMR spectrum (CDCl$_3$) of 6.
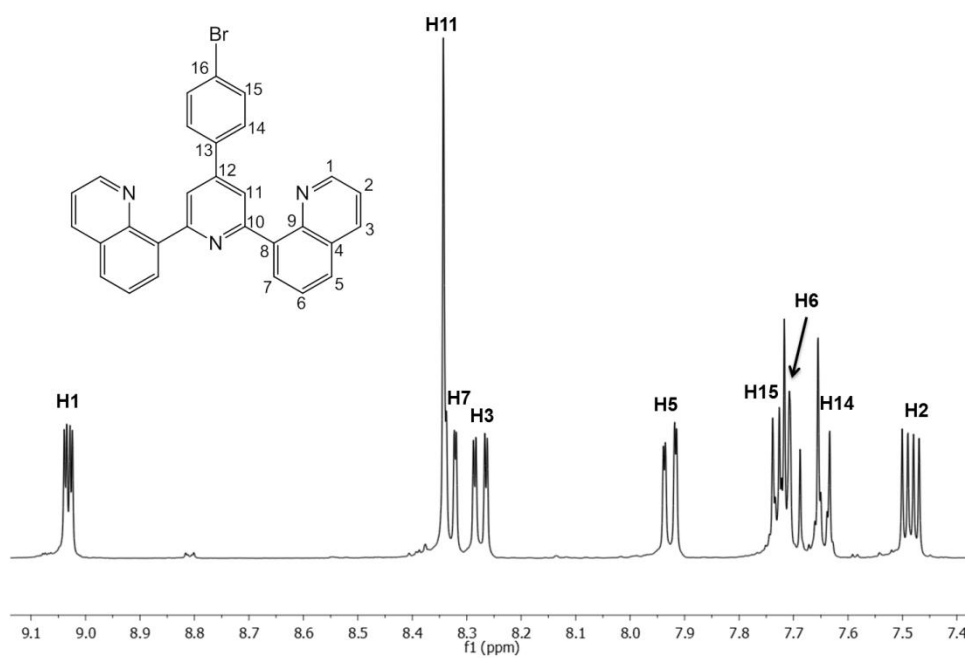
Figure A4.28 400 MHz ^{1}H NMR spectrum (CDCl$_3$) of 5.
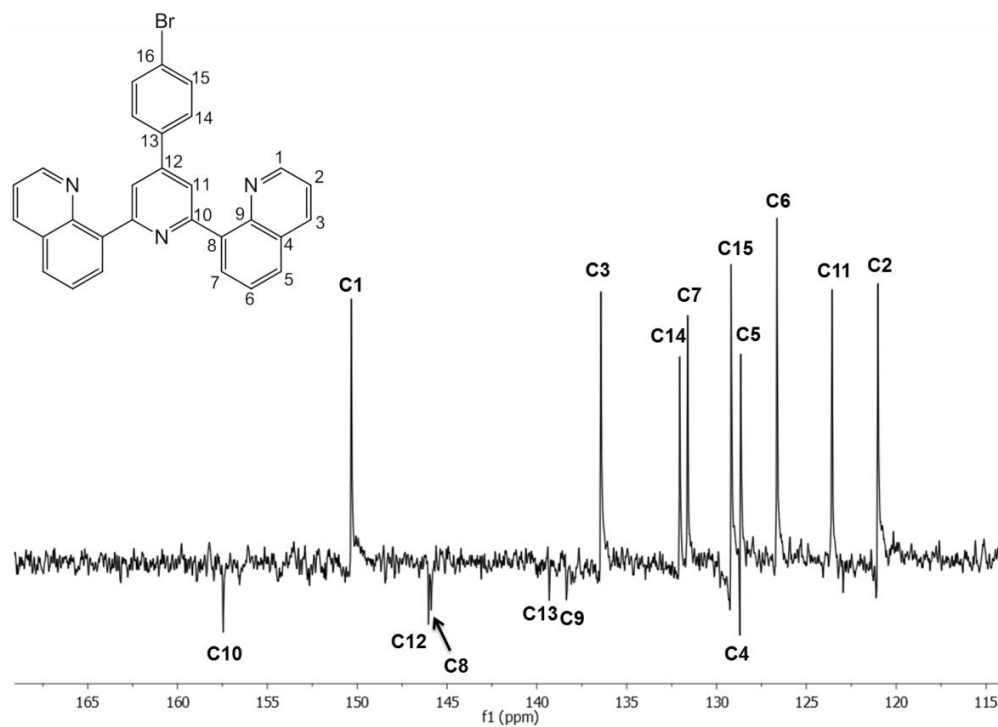
Figure A4.29 100 MHz ^{13}C NMR spectrum (CDCl$_3$) of 5.
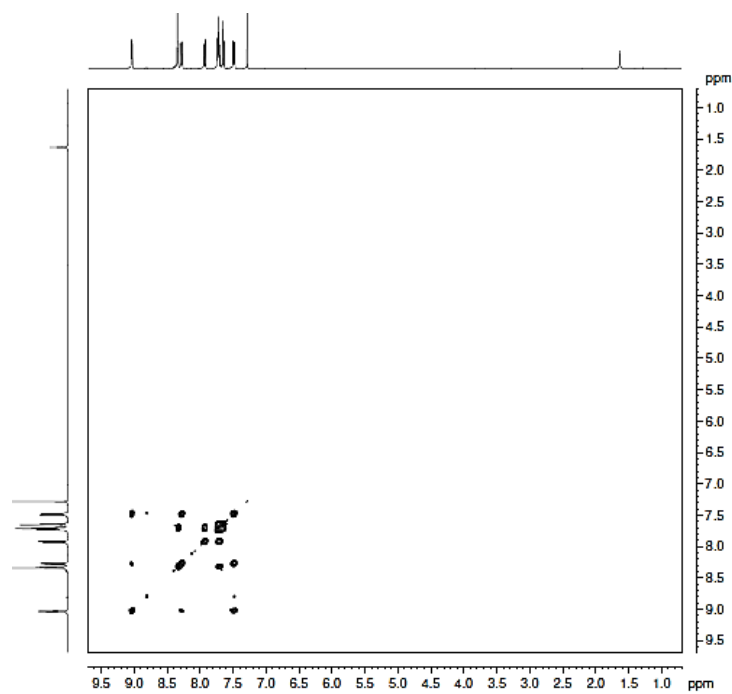
Figure A4.30 COSY NMR spectrum (CDCl$_3$) of 5.
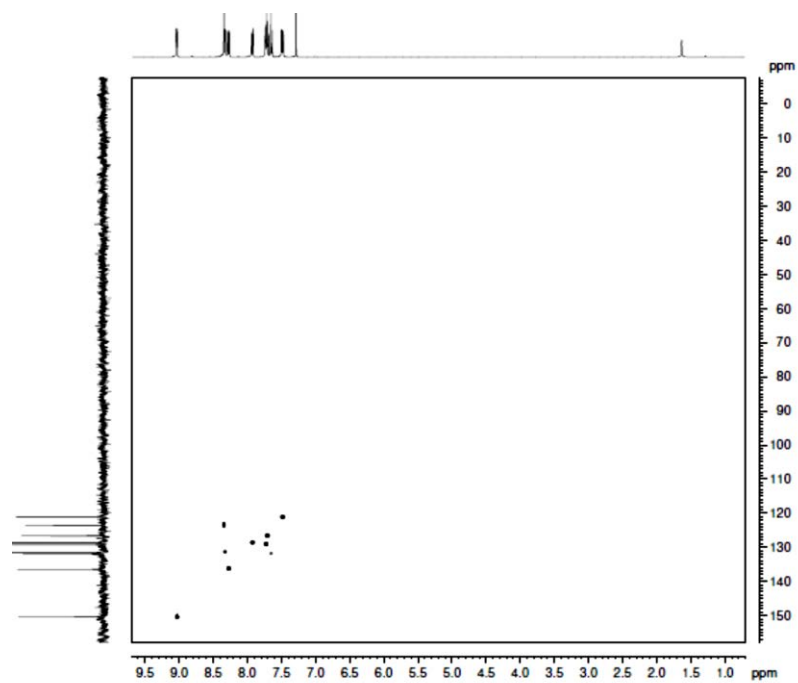
Figure A4.31 HSQC NMR spectrum (CDCl$_3$) of 5.
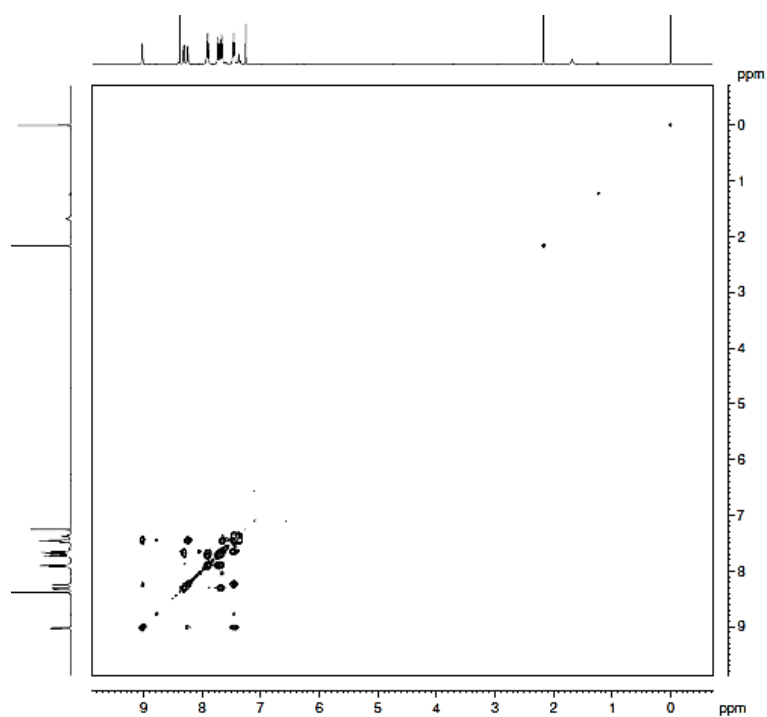
Figure A4.32 COSY NMR spectrum (CDCl$_3$) of 7.
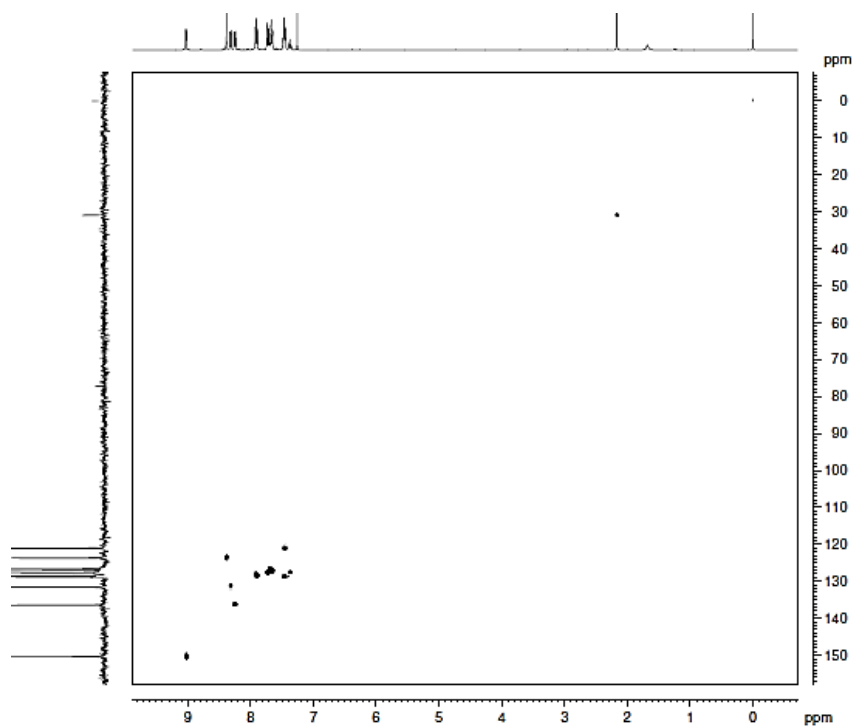
Figure A4.33 HSQC NMR spectrum (CDCl$_3$) of 7.
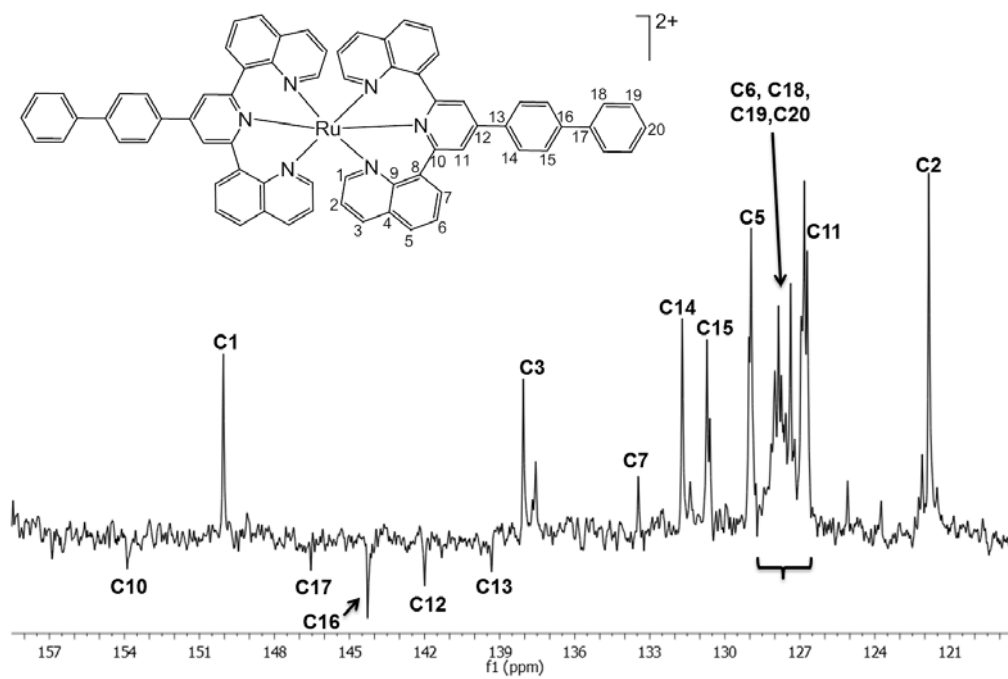
Figure A4.34 100 MHz ^{13}C NMR spectrum (CD$_3$CN) of [Ru(7)$_2$](PF$_6$)$_2$.
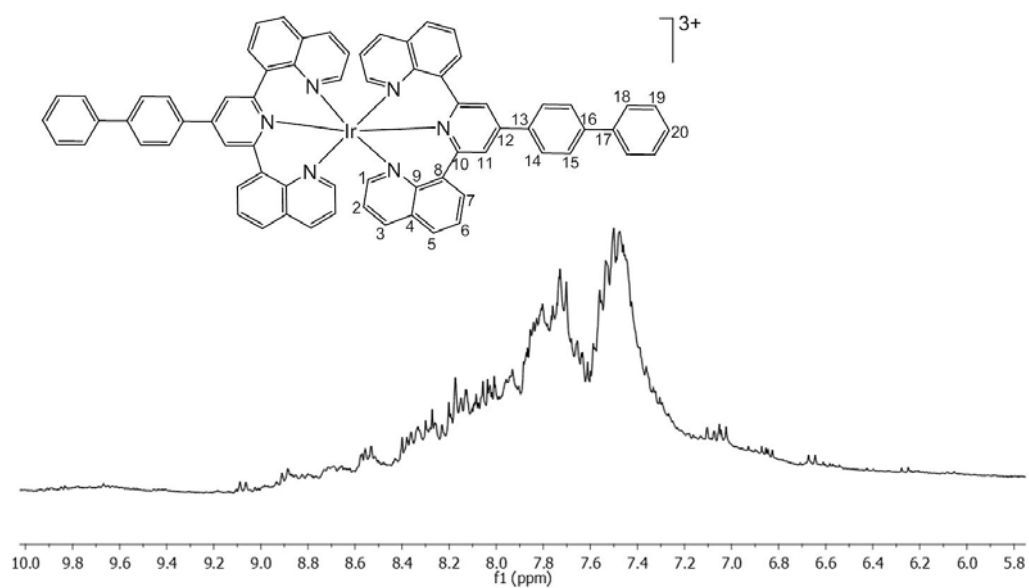
Figure A4.35. 400 MHz ^{1}H NMR spectrum (CD$_3$CN) of [Ir(7)$_2$](PF$_6$)$_3$.
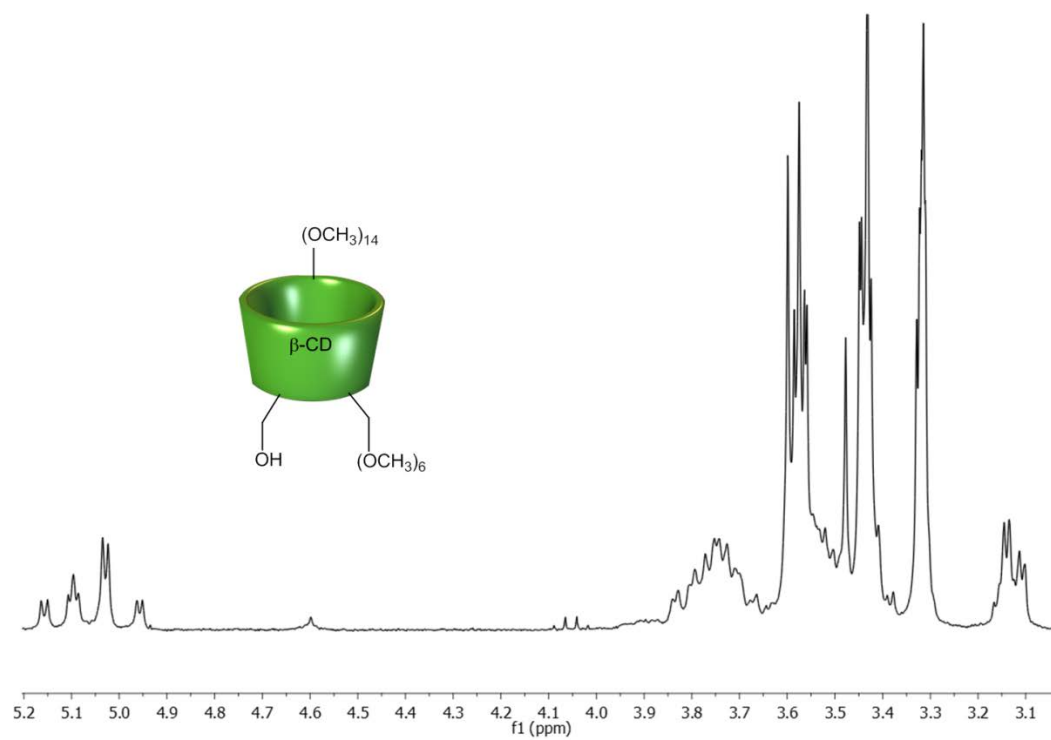
Figure A5.1. 400 MHz ^{1}H NMR spectrum (CDCl$_3$) of β-CD-OH.
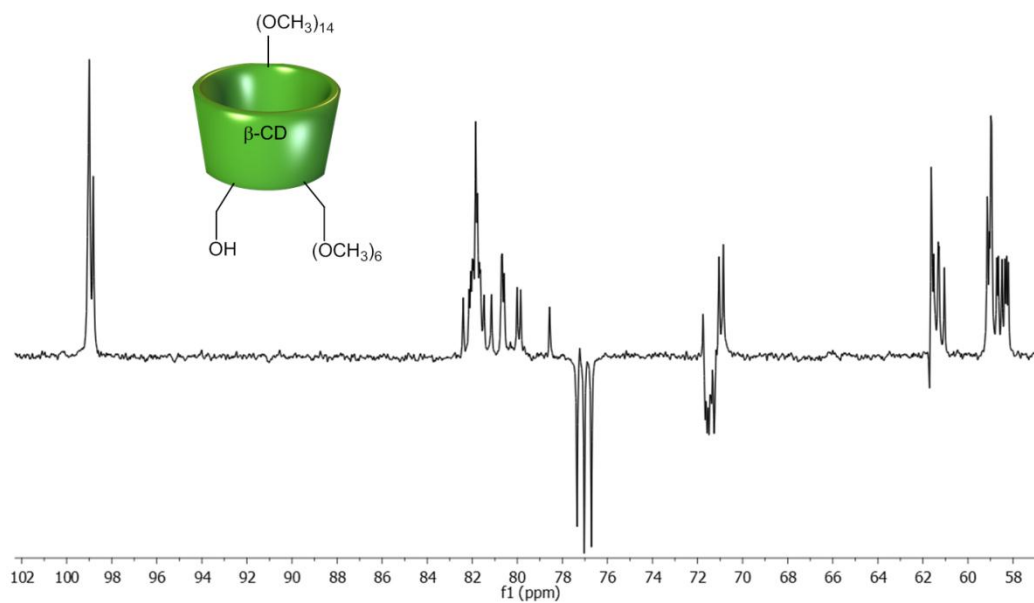
Figure A5.2. 100 MHz ^{13}C NMR spectrum (CDCl$_3$) of β-CD-OH.
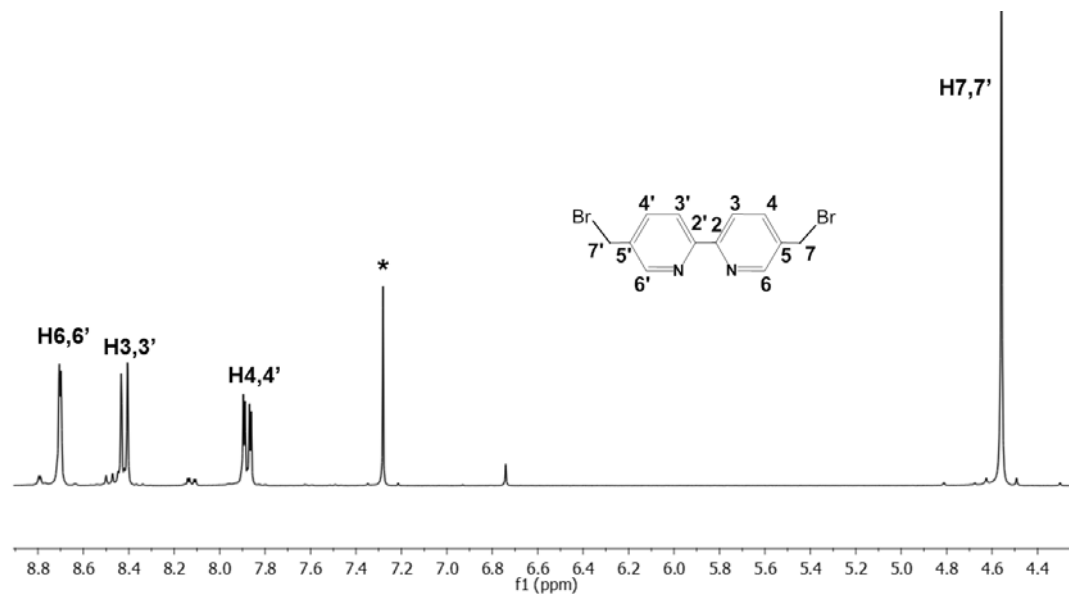
Figure A5.3. 400 MHz ^{1}H NMR spectrum (CDCl$_3$) of 5,5'-Brbpy.
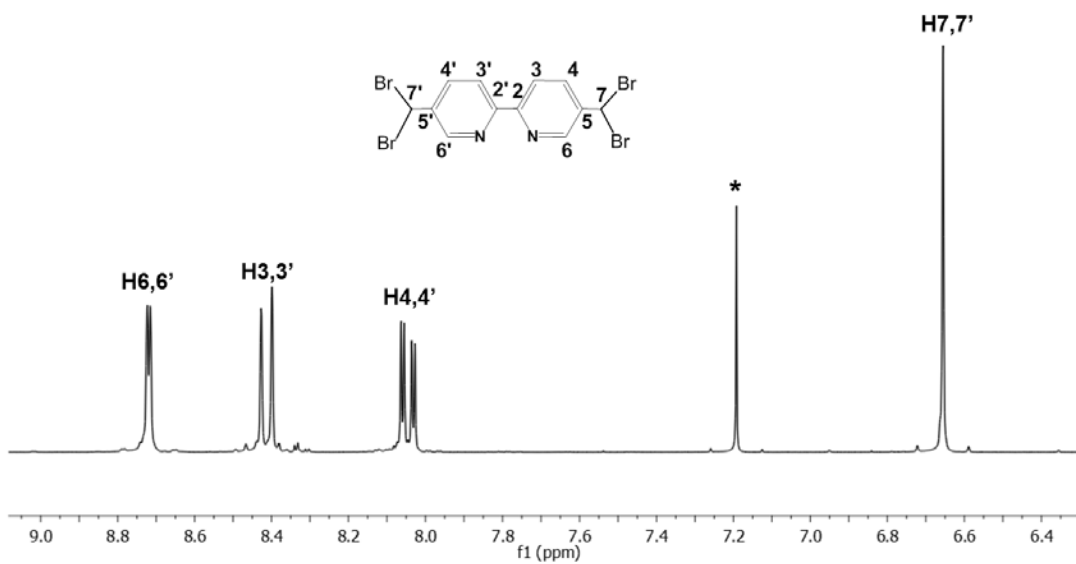
Figure A5.4. 400 MHz ^{1}H NMR spectrum (CDCl$_3$) of 5,5'-Br$_2$-bpy.
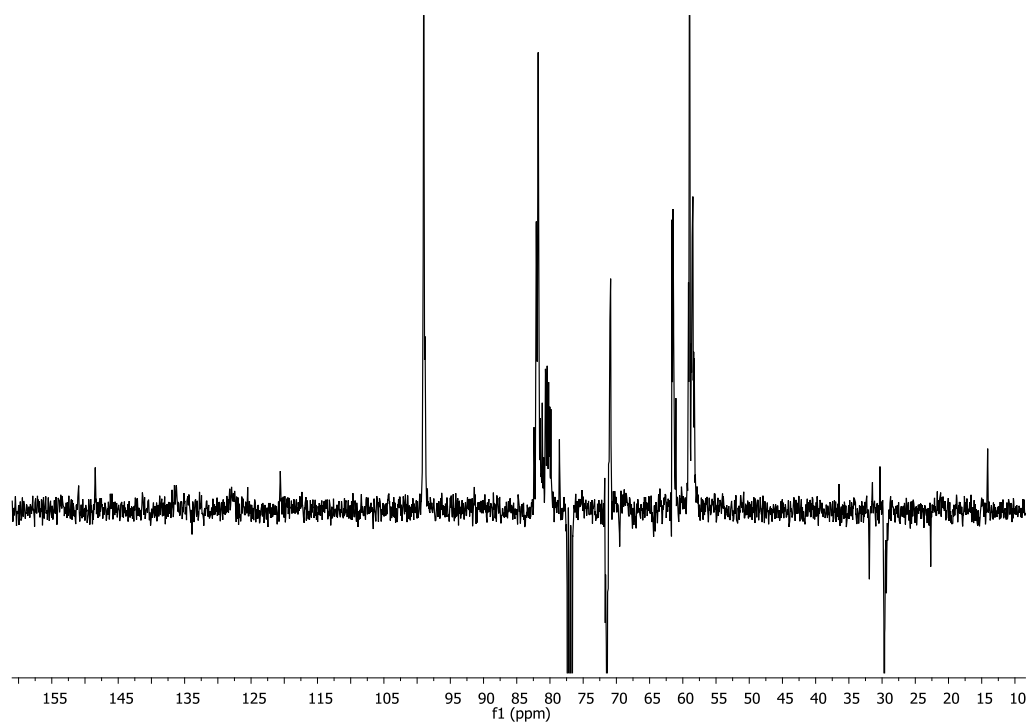
Figure A5.5. 100 MHz ^{13}C NMR spectrum (CDCl$_3$) of 5,5'-bpyCD.
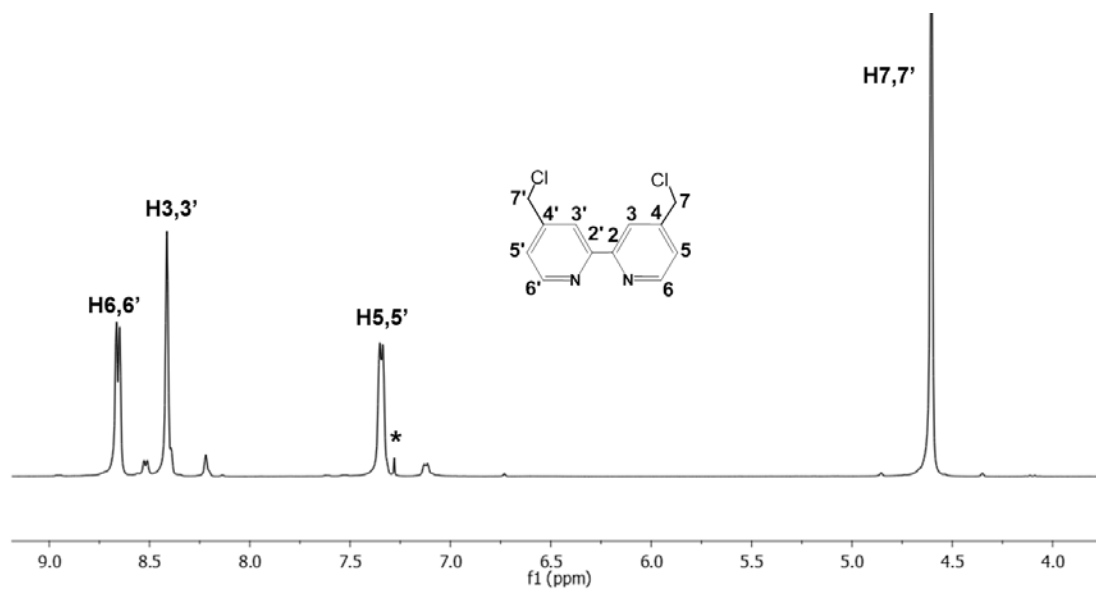
Figure A5.6. 300 MHz ^{1}H NMR spectrum (CDCl$_3$) of 4,4'-Cl-bpy.
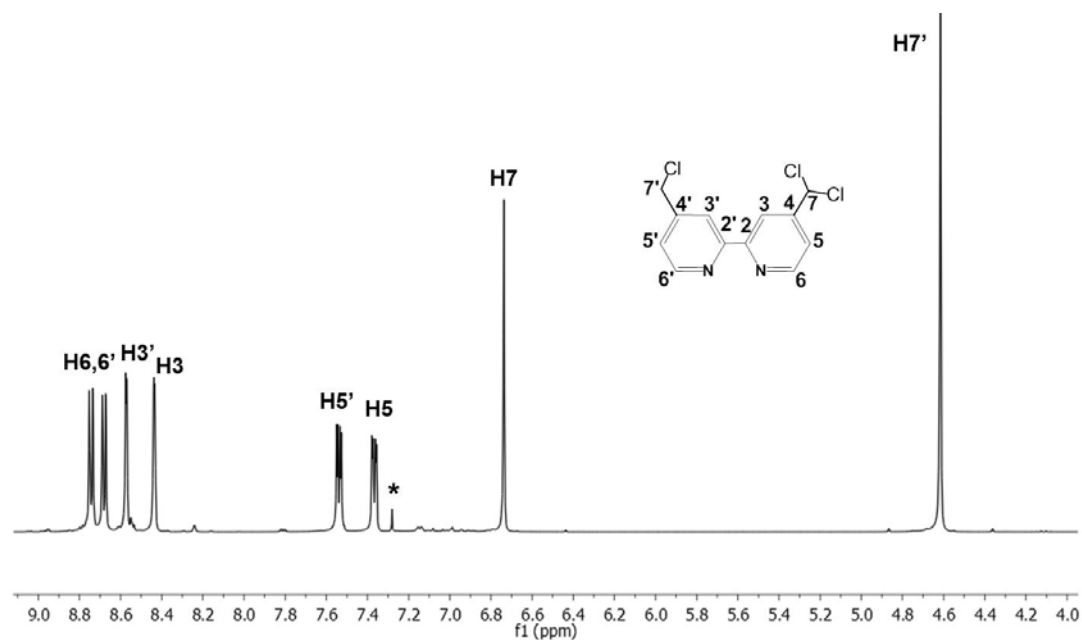
Figure A5.7. 300 MHz ^{1}H NMR spectrum (CDCl$_3$) of 4-Cl,4'-Cl$_2$-bpy.
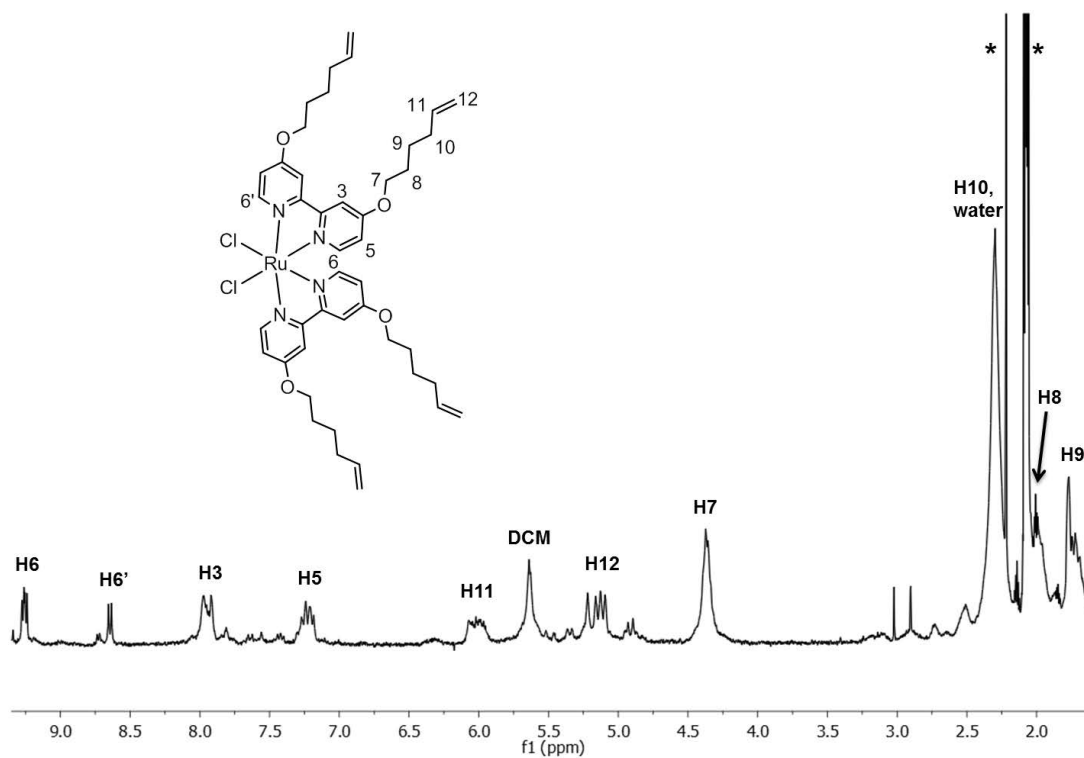
Figure A5.8. 300 MHz ^{1}H NMR spectrum (CD$_3$CN + Acetone) of Ru(4,4'-bpyhex)$_2$Cl$_2$.
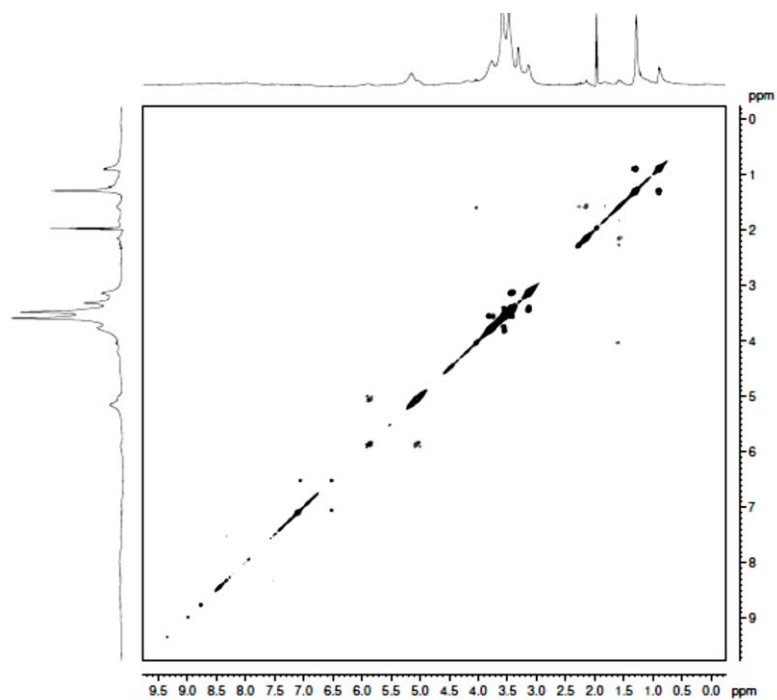
Figure A5.9. COSY NMR spectrum (CD$_3$CN) of [Ru(4,4'-bpyhex)$_2$(5,5'-bpyCD)](PF$_6$)$_2$.
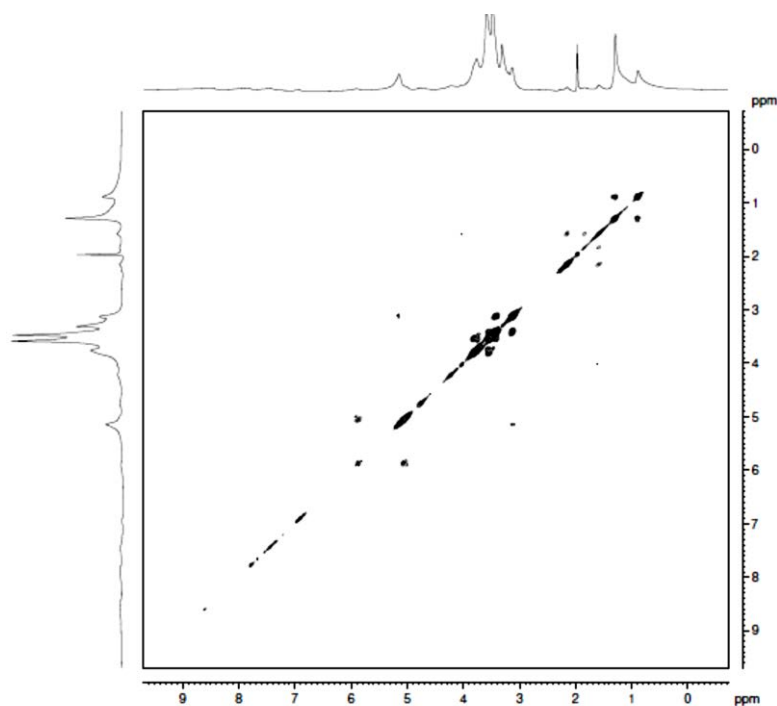
Figure A5.10. COSY NMR spectrum (CD$_3$CN) of [Ru(4,4'-bpyhex)$_2$(4,4'-bpyCD)](PF$_6$)$_2$.
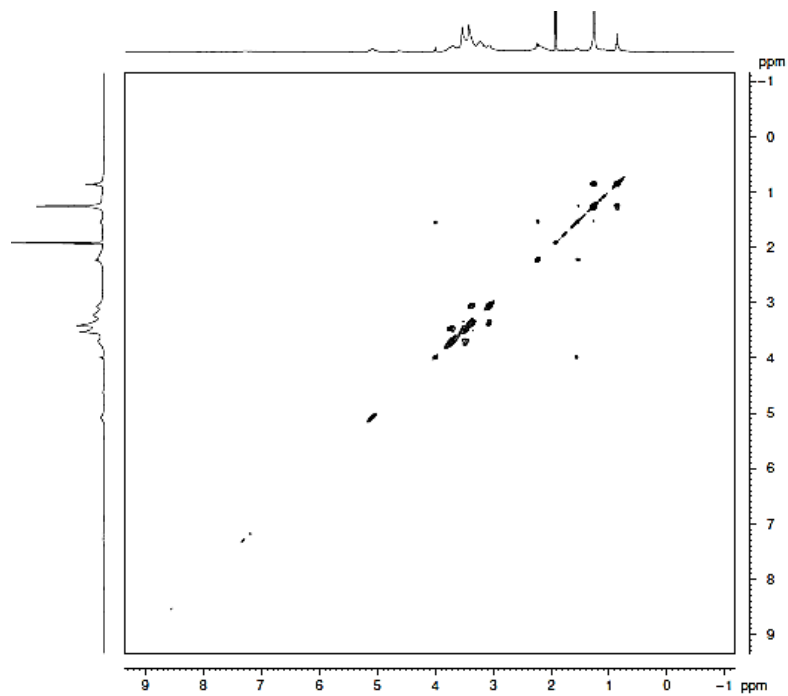
Figure A5.11. COSY NMR spectrum (CD$_3$CN) of [Os(4,4'-bpyhex)$_2$(4,4'-bpyCD)](PF$_6$)$_2$.
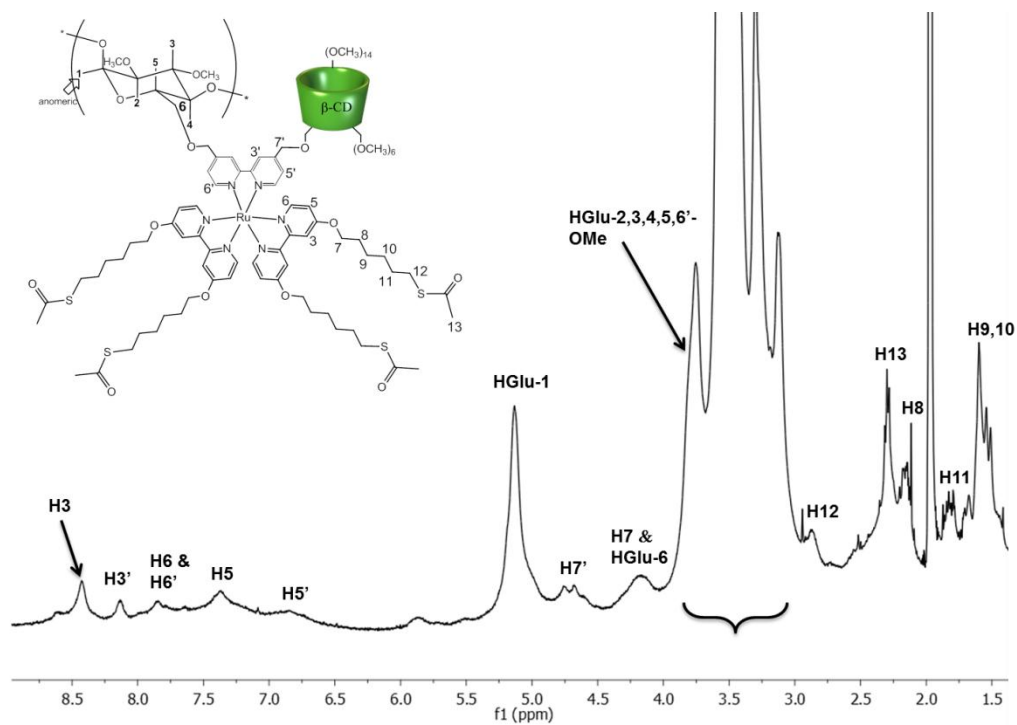
Figure A5.12. 400 MHz ^{1}H NMR spectrum (CD$_3$CN) of [Ru(4,4'-bpysac)$_2$(4,4'-bpyCD)](PF$_6$)$_2$.
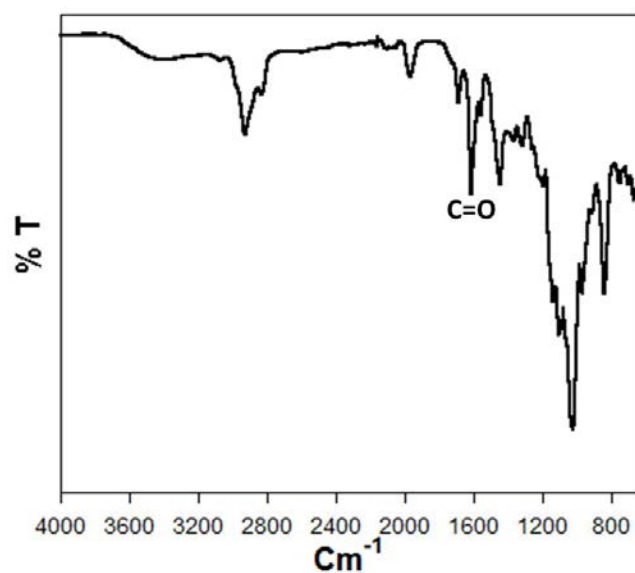
Figure A5.13. FTIR spectrum of [Ru(4,4'-bpysac)$_2$(4,4'-bpyCD)](PF$_6$)$_2$.
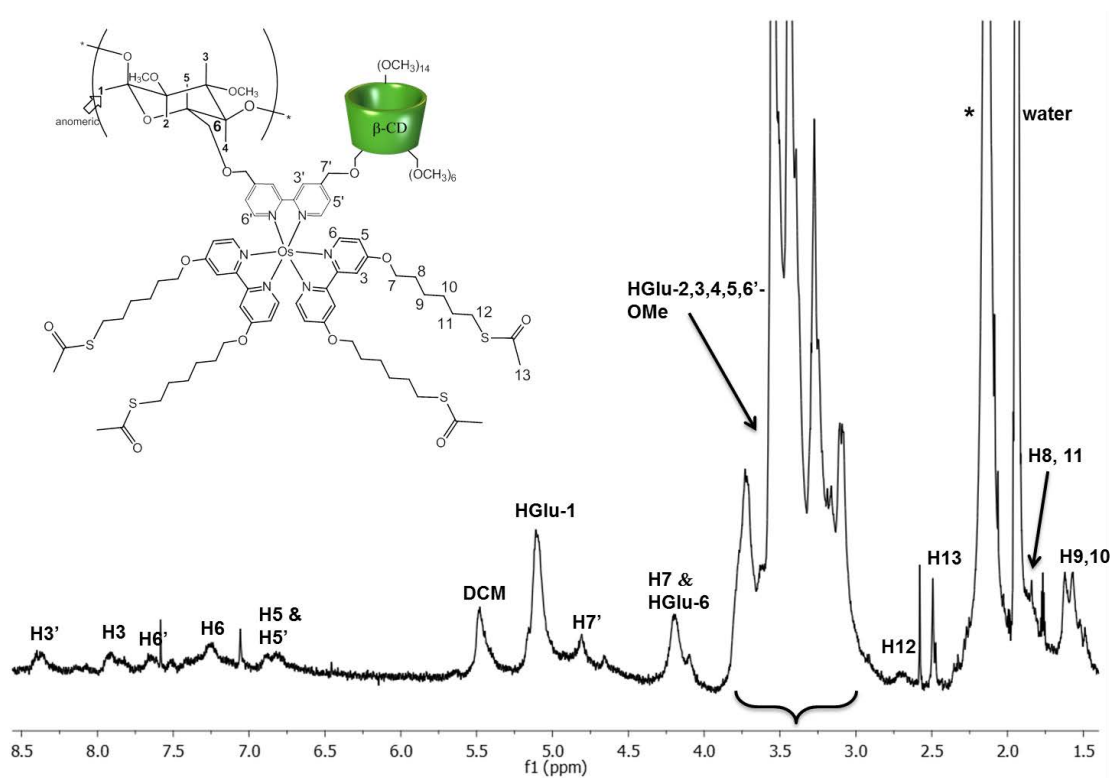
Figure A5.14. 400 MHz ^{1}H NMR spectrum (CD$_3$CN) of [Os(4,4'-bpysac)$_2$(4,4'-bpyCD)](PF$_6$)$_2$.
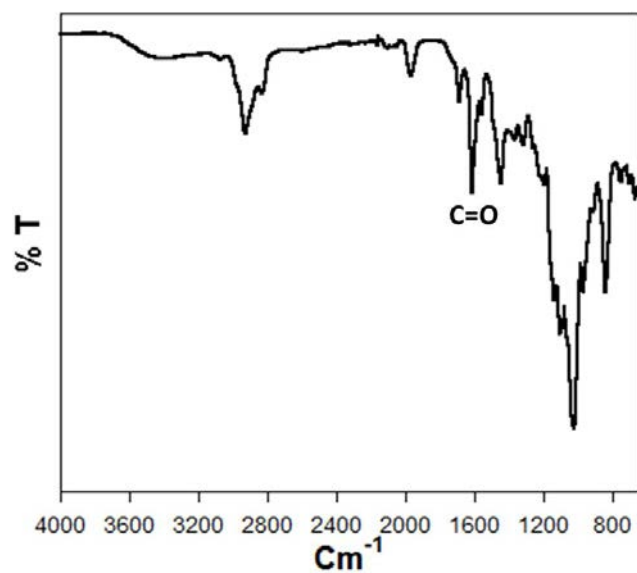
Figure A5.15. FTIR spectrum of [Os(4,4'-bpysac)$_2$(4,4'-bpyCD)](PF$_6$)$_2$.
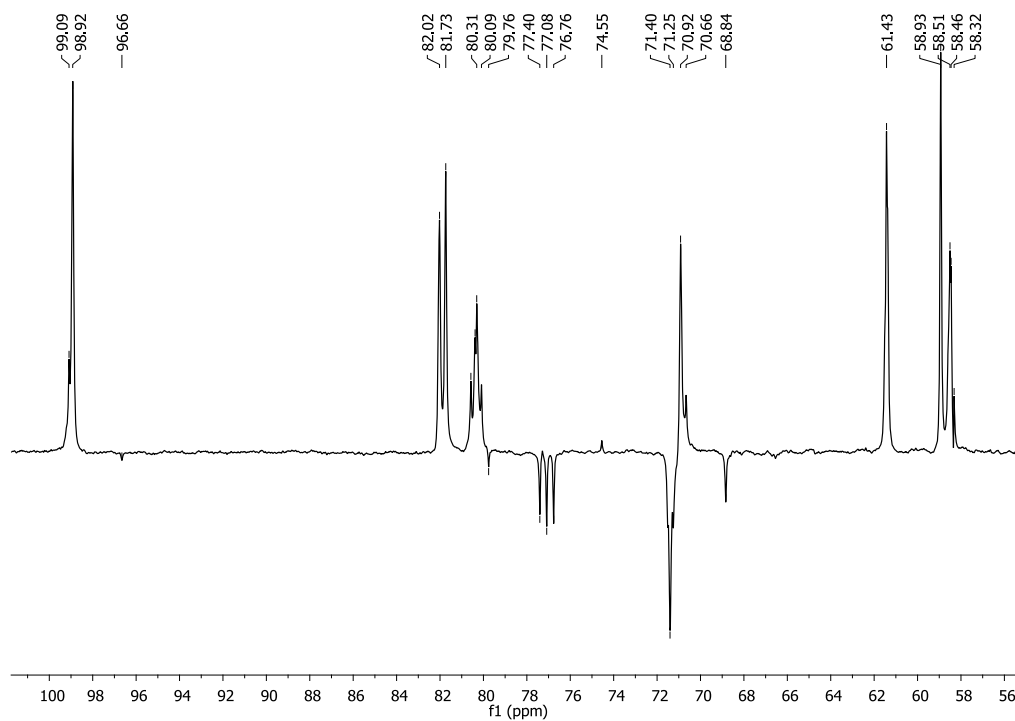
Figure A6.1. 100 MHz ^{13}C NMR spectrum (CDCl$_3$) of acetylene-CD.
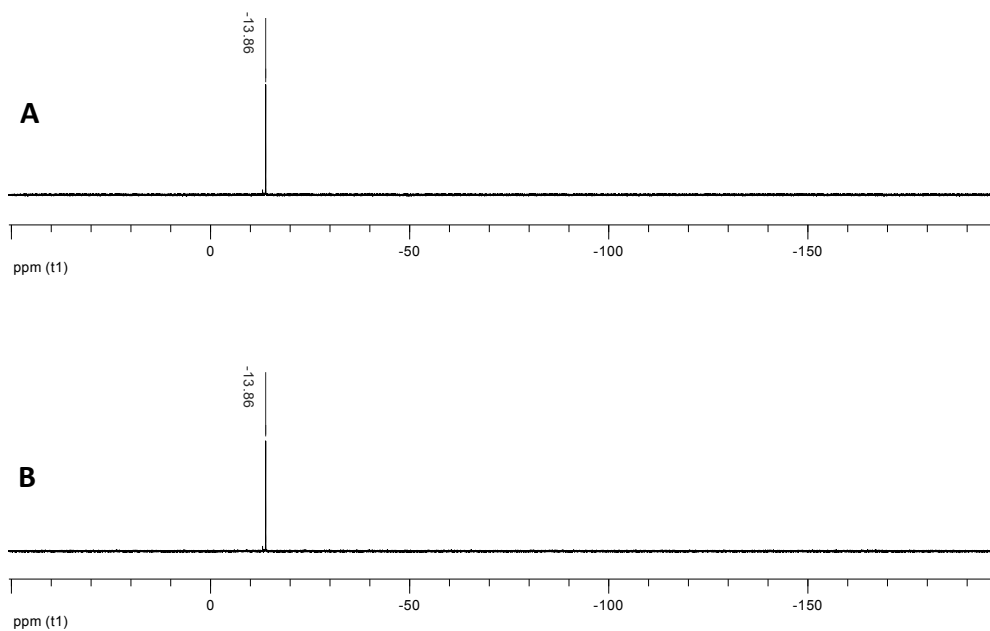
Figure A6.2 A) The 121 MHz ^{31}PNMR spectrum of Yb(biphen)$_3$ (C = 3.3 × 10^{-3} M) in 50:50 D$_2$O/CD$_3$CN B) The 121 MHz ^{31}PNMR spectrum of Yb(biphen)$_3$ (C = 3.3 × 10^{-3} M) and pm-β-CD (C = 40 × 10^{-3} M) in 50:50 D$_2$O/CD$_3$CN.
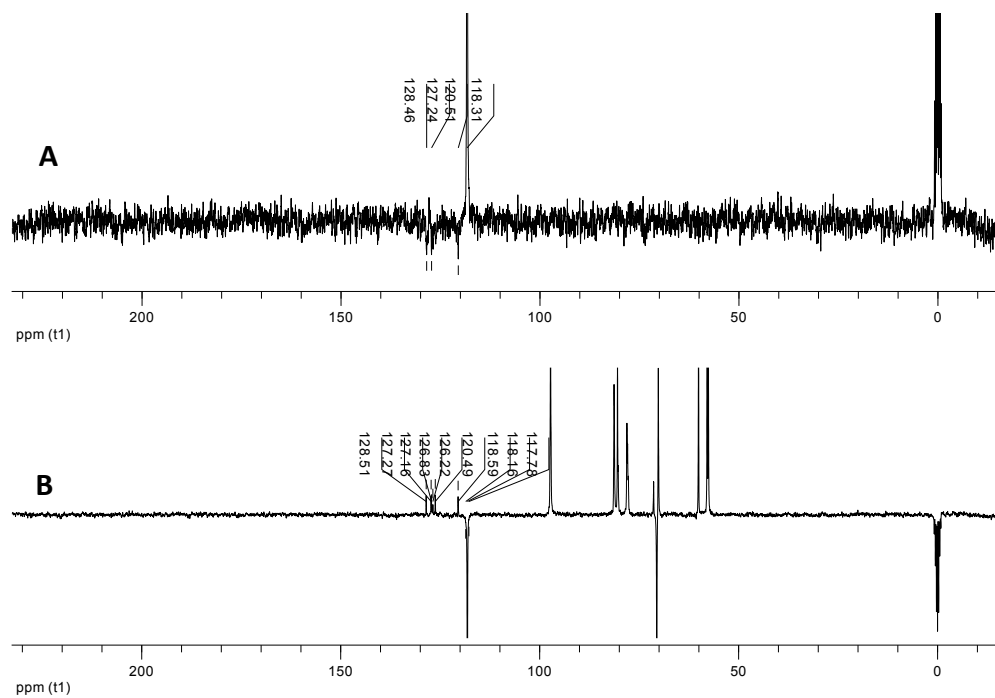
Figure A6.3 A) The 100 MHz ^{13}CNMR spectrum of Yb(biphen)$_3$ (C = 3.3 × 10^{-3} M) in 50:50 D$_2$O/CD$_3$CN

B) The 100 MHz ^{13}CNMR spectrum of Yb(biphen)$_3$ (C ≈ 3.3 × 10^{-3} M) and pm-β-CD (C = 40 × 10^{-3} M)

in 50:50 D$_2$O/CD$_3$CN.

Table A3.1. Atomic coordinates (x 10^4) and equivalent isotropic displacement parameters (Å^{2}x 10^3) for [Ru(bpy)$_2$(4,4'-bpyhex)](PF$_6$)$_2$. U(eq) is defined as one third of the trace of the orthogonalized U^{ij} tensor.

	x	y	z	U(eq)
C(1)	608(8)	1652(5)	1624(18)	70(4)
C(2)	1207(8)	1381(5)	2070(19)	76(4)
C(3)	1856(8)	1577(5)	1691(15)	70(3)
C(4)	1888(7)	2022(5)	975(14)	58(3)
C(5)	1312(6)	2287(4)	639(12)	46(2)
C(6)	1278(6)	2809(4)	-98(14)	52(3)
C(7)	1892(8)	3079(6)	-490(20)	89(5)
C(8)	1845(7)	3559(6)	-1100(20)	81(4)
C(9)	1190(7)	3739(5)	-1584(19)	69(4)
C(10)	610(7)	3449(5)	-1233(15)	57(3)
C(11)	192(8)	3002(6)	3402(17)	67(3)
C(12)	77(9)	3324(6)	4540(19)	80(4)
C(13)	-376(9)	3710(6)	4501(19)	81(4)
C(14)	-774(9)	3760(5)	3283(17)	71(3)
C(15)	-701(7)	3415(4)	1961(14)	56(3)
C(16)	-1080(6)	3446(4)	452(16)	57(2)
C(17)	-1546(6)	3841(4)	130(30)	70(3)
C(18)	-1882(7)	3859(6)	-1230(20)	77(4)
C(19)	-1720(7)	3454(5)	-2320(20)	71(3)
C(20)	-1265(7)	3076(5)	-1876(16)	58(3)
C(21)	-1243(7)	2000(5)	2215(15)	59(3)
C(22)	-1662(7)	1603(5)	2720(16)	64(3)
C(23)	-1791(6)	1218(6)	1734(14)	61(3)
C(24)	-1458(5)	1225(4)	359(17)	52(2)
C(25)	-1050(5)	1622(4)	-143(14)	49(2)
C(26)	-680(6)	1669(4)	-1569(16)	53(3)
C(27)	-770(8)	1343(5)	-2735(17)	70(4)
C(28)	-378(9)	1418(5)	-4095(16)	77(4)
C(29)	111(7)	1799(5)	-4177(15)	67(3)
C(30)	122(8)	2132(5)	-2963(18)	72(4)
C(31)	-2631(19)	783(19)	3390(30)	158(10)
C(32)	-3390(18)	865(18)	3210(60)	176(10)
C(33)	-3790(20)	576(19)	2020(60)	175(11)
C(34)	-3887(18)	14(17)	2150(70)	203(12)
C(35)	-4600(20)	-200(20)	2320(80)	235(15)
C(36)	-5203(16)	-128(16)	1660(50)	255(14)
C(31')	-2570(30)	840(20)	3540(40)	166(10)
C(32')	-3060(19)	388(18)	3490(60)	175(11)
C(33')	-3522(19)	500(20)	2100(60)	180(11)
C(34')	-4285(18)	460(20)	2560(70)	205(12)
C(35')	-4560(20)	30(30)	1540(80)	221(14)
C(36')	-5203(16)	-128(16)	1660(50)	255(14)

C(37)	-580(30)	576(12)	-5230(50)	143(9)
C(38)	-370(20)	311(13)	-6710(50)	149(10)
C(39)	-950(30)	-45(14)	-7250(60)	160(10)
C(40)	-910(30)	-538(15)	-6300(50)	169(10)
C(41)	-1230(20)	-982(14)	-7120(60)	151(12)
C(42)	-1730(30)	-951(16)	-8140(50)	146(14)
C(37')	-640(20)	596(10)	-5180(60)	142(9)
C(38')	-110(20)	172(12)	-5460(60)	170(10)
C(39')	-470(30)	-309(12)	-6000(60)	166(11)
C(40')	-950(30)	-214(17)	-7360(70)	174(11)
C(41')	-1440(30)	-650(20)	-7630(50)	165(12)
C(42')	-1600(20)	-875(19)	-8900(50)	141(14)
N(1)	649(5)	2110(3)	972(11)	47(2)
N(2)	670(5)	3005(4)	-500(13)	55(2)
N(3)	-239(6)	3045(4)	2139(12)	57(2)
N(4)	-938(5)	3060(4)	-527(13)	59(2)
N(5)	-937(5)	2006(4)	850(11)	54(2)
N(6)	-227(5)	2087(4)	-1686(12)	52(2)
O(1)	-2203(7)	823(6)	2064(15)	129(5)
O(2)	-300(8)	1085(5)	-5261(12)	123(5)
Ru(1)	-181(1)	2548(1)	239(2)	55(1)
F(101)	7550(9)	5217(4)	4298(18)	166(5)
F(102)	7303(7)	4733(4)	1094(17)	134(4)
F(103)	7211(6)	5522(3)	2180(16)	116(3)
F(104)	7585(6)	4405(3)	3413(17)	114(3)
F(105)	8209(6)	5043(4)	2390(20)	161(5)
F(106)	6618(6)	4880(5)	3210(20)	159(5)
P(101)	7417(3)	4972(1)	2739(8)	89(1)
F(201)	7821(9)	7664(6)	1977(18)	166(5)
F(202)	7954(7)	7199(5)	-1341(14)	126(4)
F(203)	8329(10)	7878(5)	-190(20)	214(7)
F(204)	7404(6)	6960(6)	948(12)	151(5)
F(205)	8571(5)	7146(5)	933(14)	120(3)
F(206)	7216(8)	7700(7)	-51(18)	200(6)
P(201)	7859(3)	7445(2)	345(12)	101(2)

_____

Table A3.2. Bond lengths [Å] and angles [°] for [Ru(bpy)₂(4,4'-bpyhex)](PF₆)₂.

C(1)-N(1)	1.319(15)	C(23)-C(24)	1.353(18)
C(1)-C(2)	1.392(19)	C(24)-C(25)	1.361(15)
C(1)-H(1)	0.9500	C(24)-H(24)	0.9500
C(2)-C(3)	1.37(2)	C(25)-N(5)	1.336(15)
C(2)-H(2)	0.9500	C(25)-C(26)	1.432(16)
C(3)-C(4)	1.313(18)	C(26)-C(27)	1.331(18)
C(3)-H(3)	0.9500	C(26)-N(6)	1.387(14)
C(4)-C(5)	1.324(16)	C(27)-C(28)	1.412(19)
C(4)-H(4)	0.9500	C(27)-H(27)	0.9500
C(5)-N(1)	1.371(14)	C(28)-O(2)	1.341(13)
C(5)-C(6)	1.500(15)	C(28)-C(29)	1.36(2)
C(6)-N(2)	1.310(15)	C(29)-C(30)	1.36(2)
C(6)-C(7)	1.401(17)	C(29)-H(29)	0.9500
C(7)-C(8)	1.358(19)	C(30)-N(6)	1.300(16)
C(7)-H(7)	0.9500	C(30)-H(30)	0.9500
C(8)-C(9)	1.393(19)	C(31)-O(1)	1.413(17)
C(8)-H(8)	0.9500	C(31)-C(32)	1.466(19)
C(9)-C(10)	1.367(17)	C(31)-H(31A)	0.9900
C(9)-H(9)	0.9500	C(31)-H(31B)	0.9900
C(10)-N(2)	1.322(15)	C(32)-C(33)	1.493(19)
C(10)-H(10)	0.9500	C(32)-H(32A)	0.9900
C(11)-C(12)	1.31(2)	C(32)-H(32B)	0.9900
C(11)-N(3)	1.375(18)	C(33)-C(34)	1.472(19)
C(11)-H(11)	0.9500	C(33)-H(33A)	0.9900
C(12)-C(13)	1.32(2)	C(33)-H(33B)	0.9900
C(12)-H(12)	0.9500	C(34)-C(35)	1.467(19)
C(13)-C(14)	1.31(2)	C(34)-H(34A)	0.9900
C(13)-H(13)	0.9500	C(34)-H(34B)	0.9900
C(14)-C(15)	1.464(18)	C(35)-C(36)	1.30(2)
C(14)-H(14)	0.9500	C(35)-H(35A)	0.9500
C(15)-N(3)	1.310(15)	C(36)-H(36A)	0.9500
C(15)-C(16)	1.500(14)	C(36)-H(36B)	0.9500
C(16)-N(4)	1.342(15)	C(31')-O(1)	1.460(18)
C(16)-C(17)	1.384(16)	C(31')-C(32')	1.504(19)
C(17)-C(18)	1.35(3)	C(31')-H(31C)	0.9900
C(17)-H(17)	0.9500	C(31')-H(31D)	0.9900
C(18)-C(19)	1.45(2)	C(32')-C(33')	1.52(2)
C(18)-H(18)	0.9500	C(32')-H(32C)	0.9900
C(19)-C(20)	1.362(18)	C(32')-H(32D)	0.9900
C(19)-H(19)	0.9500	C(33')-C(34')	1.506(19)
C(20)-N(4)	1.329(17)	C(33')-H(33C)	0.9900
C(20)-H(20)	0.9500	C(33')-H(33D)	0.9900
C(21)-N(5)	1.322(15)	C(34')-C(35')	1.52(2)
C(21)-C(22)	1.376(17)	C(34')-H(34C)	0.9900
C(21)-H(21)	0.9500	C(34')-H(34D)	0.9900
C(22)-C(23)	1.337(18)	C(35')-H(35B)	0.9500
C(22)-H(22)	0.9500	C(37)-O(2)	1.425(18)
C(23)-O(1)	1.322(15)	C(37)-C(38)	1.514(19)

C(37)-H(37A)	0.9900	C(40')-C(41')	1.471(19)
C(37)-H(37B)	0.9900	C(40')-H(40C)	0.9900
C(38)-C(39)	1.515(19)	C(40')-H(40D)	0.9900
C(38)-H(38A)	0.9900	C(41')-C(42')	1.290(19)
C(38)-H(38B)	0.9900	C(41')-H(41B)	0.9500
C(39)-C(40)	1.519(19)	C(42')-H(42C)	0.9500
C(39)-H(39A)	0.9900	C(42')-H(42D)	0.9500
C(39)-H(39B)	0.9900	N(1)-Ru(1)	2.046(9)
C(40)-C(41)	1.484(18)	N(2)-Ru(1)	2.106(9)
C(40)-H(40A)	0.9900	N(3)-Ru(1)	2.098(10)
C(40)-H(40B)	0.9900	N(4)-Ru(1)	2.068(10)
C(41)-C(42)	1.307(19)	N(5)-Ru(1)	2.079(10)
C(41)-H(41A)	0.9500	N(6)-Ru(1)	2.060(10)
C(42)-H(42A)	0.9500	F(101)-P(101)	1.519(15)
C(42)-H(42B)	0.9500	F(102)-P(101)	1.574(14)
C(37')-O(2)	1.427(18)	F(103)-P(101)	1.557(10)
C(37')-C(38')	1.52(2)	F(104)-P(101)	1.615(11)
C(37')-H(37C)	0.9900	F(105)-P(101)	1.547(12)
C(37')-H(37D)	0.9900	F(106)-P(101)	1.591(12)
C(38')-C(39')	1.496(19)	F(201)-P(201)	1.530(17)
C(38')-H(38C)	0.9900	F(202)-P(201)	1.610(15)
C(38')-H(38D)	0.9900	F(203)-P(201)	1.507(16)
C(39')-C(40')	1.524(19)	F(204)-P(201)	1.615(14)
C(39')-H(39C)	0.9900	F(205)-P(201)	1.642(12)
C(39')-H(39D)	0.9900	F(206)-P(201)	1.431(13)
N(1)-C(1)-C(2)	121.8(13)	N(2)-C(10)-H(10)	119.4
N(1)-C(1)-H(1)	119.1	C(9)-C(10)-H(10)	119.4
C(2)-C(1)-H(1)	119.1	C(12)-C(11)-N(3)	116.8(14)
C(3)-C(2)-C(1)	118.6(12)	C(12)-C(11)-H(11)	121.6
C(3)-C(2)-H(2)	120.7	N(3)-C(11)-H(11)	121.6
C(1)-C(2)-H(2)	120.7	C(11)-C(12)-C(13)	124.9(17)
C(4)-C(3)-C(2)	118.8(13)	C(11)-C(12)-H(12)	117.6
C(4)-C(3)-H(3)	120.6	C(13)-C(12)-H(12)	117.6
C(2)-C(3)-H(3)	120.6	C(14)-C(13)-C(12)	118.2(15)
C(3)-C(4)-C(5)	121.4(13)	C(14)-C(13)-H(13)	120.9
C(3)-C(4)-H(4)	119.3	C(12)-C(13)-H(13)	120.9
C(5)-C(4)-H(4)	119.3	C(13)-C(14)-C(15)	121.4(14)
C(4)-C(5)-N(1)	122.6(11)	C(13)-C(14)-H(14)	119.3
C(4)-C(5)-C(6)	126.7(11)	C(15)-C(14)-H(14)	119.3
N(1)-C(5)-C(6)	110.7(10)	N(3)-C(15)-C(14)	114.7(12)
N(2)-C(6)-C(7)	118.3(11)	N(3)-C(15)-C(16)	117.8(10)
N(2)-C(6)-C(5)	120.2(10)	C(14)-C(15)-C(16)	127.5(11)
C(7)-C(6)-C(5)	121.3(11)	N(4)-C(16)-C(17)	123.6(14)
C(8)-C(7)-C(6)	119.9(14)	N(4)-C(16)-C(15)	114.7(10)
C(8)-C(7)-H(7)	120.0	C(17)-C(16)-C(15)	121.7(13)
C(6)-C(7)-H(7)	120.0	C(18)-C(17)-C(16)	120.5(15)
C(7)-C(8)-C(9)	118.9(13)	C(18)-C(17)-H(17)	119.8
C(7)-C(8)-H(8)	120.5	C(16)-C(17)-H(17)	119.8
C(9)-C(8)-H(8)	120.5	C(17)-C(18)-C(19)	116.7(13)
C(10)-C(9)-C(8)	117.9(13)	C(17)-C(18)-H(18)	121.7
C(10)-C(9)-H(9)	121.0	C(19)-C(18)-H(18)	121.7
C(8)-C(9)-H(9)	121.0	C(20)-C(19)-C(18)	118.3(15)
N(2)-C(10)-C(9)	121.1(12)	C(20)-C(19)-H(19)	120.8

C(18)-C(19)-H(19)	120.8	C(33)-C(34)-H(34A)	107.5
N(4)-C(20)-C(19)	124.7(13)	C(35)-C(34)-H(34B)	107.5
N(4)-C(20)-H(20)	117.7	C(33)-C(34)-H(34B)	107.5
C(19)-C(20)-H(20)	117.7	H(34A)-C(34)-H(34B)	107.0
N(5)-C(21)-C(22)	123.3(13)	C(36)-C(35)-C(34)	136(4)
N(5)-C(21)-H(21)	118.3	C(36)-C(35)-H(35A)	112.0
C(22)-C(21)-H(21)	118.3	C(34)-C(35)-H(35A)	112.0
C(23)-C(22)-C(21)	117.4(13)	C(35)-C(36)-H(36A)	120.0
C(23)-C(22)-H(22)	121.3	C(35)-C(36)-H(36B)	120.0
C(21)-C(22)-H(22)	121.3	H(36A)-C(36)-H(36B)	120.0
O(1)-C(23)-C(22)	123.2(12)	O(1)-C(31')-C(32')	104(2)
O(1)-C(23)-C(24)	118.5(12)	O(1)-C(31')-H(31C)	110.9
C(22)-C(23)-C(24)	118.2(11)	C(32')-C(31')-H(31C)	110.9
C(23)-C(24)-C(25)	124.0(12)	O(1)-C(31')-H(31D)	110.9
C(23)-C(24)-H(24)	118.0	C(32')-C(31')-H(31D)	110.9
C(25)-C(24)-H(24)	118.0	H(31C)-C(31')-H(31D)	108.9
N(5)-C(25)-C(24)	116.7(11)	C(31')-C(32')-C(33')	103(2)
N(5)-C(25)-C(26)	114.7(9)	C(31')-C(32')-H(32C)	111.1
C(24)-C(25)-C(26)	128.5(11)	C(33')-C(32')-H(32C)	111.1
C(27)-C(26)-N(6)	121.4(11)	C(31')-C(32')-H(32D)	111.1
C(27)-C(26)-C(25)	122.8(11)	C(33')-C(32')-H(32D)	111.1
N(6)-C(26)-C(25)	115.8(11)	H(32C)-C(32')-H(32D)	109.1
C(26)-C(27)-C(28)	118.8(11)	C(34')-C(33')-C(32')	109(3)
C(26)-C(27)-H(27)	120.6	C(34')-C(33')-H(33C)	109.8
C(28)-C(27)-H(27)	120.6	C(32')-C(33')-H(33C)	109.8
O(2)-C(28)-C(29)	110.8(13)	C(34')-C(33')-H(33D)	109.8
O(2)-C(28)-C(27)	127.0(12)	C(32')-C(33')-H(33D)	109.8
C(29)-C(28)-C(27)	120.4(12)	H(33C)-C(33')-H(33D)	108.2
C(28)-C(29)-C(30)	115.5(12)	C(33')-C(34')-C(35')	103(2)
C(28)-C(29)-H(29)	122.3	C(33')-C(34')-H(34C)	111.1
C(30)-C(29)-H(29)	122.3	C(35')-C(34')-H(34C)	111.1
N(6)-C(30)-C(29)	126.6(12)	C(33')-C(34')-H(34D)	111.1
N(6)-C(30)-H(30)	116.7	C(35')-C(34')-H(34D)	111.1
C(29)-C(30)-H(30)	116.7	H(34C)-C(34')-H(34D)	109.1
O(1)-C(31)-C(32)	118(2)	C(34')-C(35')-H(35B)	119.7
O(1)-C(31)-H(31A)	107.8	O(2)-C(37)-C(38)	108(2)
C(32)-C(31)-H(31A)	107.8	O(2)-C(37)-H(37A)	110.2
O(1)-C(31)-H(31B)	107.8	C(38)-C(37)-H(37A)	110.2
C(32)-C(31)-H(31B)	107.8	O(2)-C(37)-H(37B)	110.2
H(31A)-C(31)-H(31B)	107.1	C(38)-C(37)-H(37B)	110.2
C(31)-C(32)-C(33)	120(3)	H(37A)-C(37)-H(37B)	108.5
C(31)-C(32)-H(32A)	107.2	C(37)-C(38)-C(39)	110(2)
C(33)-C(32)-H(32A)	107.2	C(37)-C(38)-H(38A)	109.6
C(31)-C(32)-H(32B)	107.2	C(39)-C(38)-H(38A)	109.6
C(33)-C(32)-H(32B)	107.2	C(37)-C(38)-H(38B)	109.6
H(32A)-C(32)-H(32B)	106.9	C(39)-C(38)-H(38B)	109.6
C(34)-C(33)-C(32)	120(2)	H(38A)-C(38)-H(38B)	108.1
C(34)-C(33)-H(33A)	107.2	C(38)-C(39)-C(40)	108(2)
C(32)-C(33)-H(33A)	107.2	C(38)-C(39)-H(39A)	110.1
C(34)-C(33)-H(33B)	107.2	C(40)-C(39)-H(39A)	110.1
C(32)-C(33)-H(33B)	107.2	C(38)-C(39)-H(39B)	110.1
H(33A)-C(33)-H(33B)	106.8	C(40)-C(39)-H(39B)	110.1
C(35)-C(34)-C(33)	119(2)	H(39A)-C(39)-H(39B)	108.4
C(35)-C(34)-H(34A)	107.5	C(41)-C(40)-C(39)	112(2)

C(41)-C(40)-H(40A)	109.2	C(21)-N(5)-Ru(1)	122.7(9)
C(39)-C(40)-H(40A)	109.2	C(25)-N(5)-Ru(1)	116.8(7)
C(41)-C(40)-H(40B)	109.2	C(30)-N(6)-C(26)	116.7(11)
C(39)-C(40)-H(40B)	109.2	C(30)-N(6)-Ru(1)	128.4(9)
H(40A)-C(40)-H(40B)	107.9	C(26)-N(6)-Ru(1)	114.9(8)
C(42)-C(41)-C(40)	125(3)	C(23)-O(1)-C(31)	125(2)
C(42)-C(41)-H(41A)	117.4	C(23)-O(1)-C(31')	116.4(18)
C(40)-C(41)-H(41A)	117.4	C(28)-O(2)-C(37)	122.7(16)
C(41)-C(42)-H(42A)	120.0	C(28)-O(2)-C(37')	119(2)
C(41)-C(42)-H(42B)	120.0	N(1)-Ru(1)-N(6)	87.9(4)
H(42A)-C(42)-H(42B)	120.0	N(1)-Ru(1)-N(4)	173.4(4)
O(2)-C(37')-C(38')	109(2)	N(6)-Ru(1)-N(4)	94.7(4)
O(2)-C(37')-H(37C)	109.8	N(1)-Ru(1)-N(5)	94.5(4)
C(38')-C(37')-H(37C)	109.8	N(6)-Ru(1)-N(5)	77.6(4)
O(2)-C(37')-H(37D)	109.8	N(4)-Ru(1)-N(5)	92.1(4)
C(38')-C(37')-H(37D)	109.8	N(1)-Ru(1)-N(3)	97.8(4)
H(37C)-C(37')-H(37D)	108.2	N(6)-Ru(1)-N(3)	174.0(4)
C(39')-C(38')-C(37')	111(2)	N(4)-Ru(1)-N(3)	79.8(4)
C(39')-C(38')-H(38C)	109.5	N(5)-Ru(1)-N(3)	100.2(4)
C(37')-C(38')-H(38C)	109.5	N(1)-Ru(1)-N(2)	79.4(3)
C(39')-C(38')-H(38D)	109.5	N(6)-Ru(1)-N(2)	96.4(4)
C(37')-C(38')-H(38D)	109.5	N(4)-Ru(1)-N(2)	94.3(4)
H(38C)-C(38')-H(38D)	108.1	N(5)-Ru(1)-N(2)	171.6(4)
C(38')-C(39')-C(40')	113(2)	N(3)-Ru(1)-N(2)	86.3(4)
C(38')-C(39')-H(39C)	109.1	F(101)-P(101)-F(105)	87.8(10)
C(40')-C(39')-H(39C)	109.1	F(101)-P(101)-F(103)	86.4(7)
C(38')-C(39')-H(39D)	109.1	F(105)-P(101)-F(103)	94.3(7)
C(40')-C(39')-H(39D)	109.1	F(101)-P(101)-F(102)	177.6(10)
H(39C)-C(39')-H(39D)	107.8	F(105)-P(101)-F(102)	90.3(9)
C(41')-C(40')-C(39')	112(3)	F(103)-P(101)-F(102)	92.4(7)
C(41')-C(40')-H(40C)	109.2	F(101)-P(101)-F(106)	89.4(10)
C(39')-C(40')-H(40C)	109.2	F(105)-P(101)-F(106)	175.6(12)
C(41')-C(40')-H(40D)	109.2	F(103)-P(101)-F(106)	88.8(7)
C(39')-C(40')-H(40D)	109.2	F(102)-P(101)-F(106)	92.7(9)
H(40C)-C(40')-H(40D)	107.9	F(101)-P(101)-F(104)	91.3(8)
C(42')-C(41')-C(40')	129(4)	F(105)-P(101)-F(104)	89.2(7)
C(42')-C(41')-H(41B)	115.5	F(103)-P(101)-F(104)	175.7(8)
C(40')-C(41')-H(41B)	115.5	F(102)-P(101)-F(104)	90.0(7)
C(41')-C(42')-H(42C)	120.0	F(106)-P(101)-F(104)	87.6(7)
C(41')-C(42')-H(42D)	120.0	F(206)-P(201)-F(203)	95.1(12)
H(42C)-C(42')-H(42D)	120.0	F(206)-P(201)-F(201)	90.7(8)
C(1)-N(1)-C(5)	116.5(10)	F(203)-P(201)-F(201)	92.2(11)
C(1)-N(1)-Ru(1)	126.1(9)	F(206)-P(201)-F(202)	93.4(9)
C(5)-N(1)-Ru(1)	117.2(7)	F(203)-P(201)-F(202)	87.0(10)
C(6)-N(2)-C(10)	122.9(10)	F(201)-P(201)-F(202)	175.9(8)
C(6)-N(2)-Ru(1)	112.1(8)	F(206)-P(201)-F(204)	89.0(11)
C(10)-N(2)-Ru(1)	124.9(9)	F(203)-P(201)-F(204)	176.0(9)
C(15)-N(3)-C(11)	123.6(11)	F(201)-P(201)-F(204)	87.8(11)
C(15)-N(3)-Ru(1)	113.0(9)	F(202)-P(201)-F(204)	92.7(6)
C(11)-N(3)-Ru(1)	123.3(9)	F(206)-P(201)-F(205)	175.6(11)
C(20)-N(4)-C(16)	116.2(11)	F(203)-P(201)-F(205)	87.7(8)
C(20)-N(4)-Ru(1)	129.1(9)	F(201)-P(201)-F(205)	85.7(7)
C(16)-N(4)-Ru(1)	114.5(8)	F(202)-P(201)-F(205)	90.2(8)
C(21)-N(5)-C(25)	120.1(10)	F(204)-P(201)-F(205)	88.3(7)

Table A3.3. Anisotropic displacement parameters (Å^2x 10^3)for [Ru(bpy)$_2$(4,4'-bpyhex)](PF$_6$)$_2$. The anisotropic displacement factor exponent takes the form: $-2\pi^2[h^2a^{*2}U^{11} + ... + 2\ h\ k\ a^*\ b^*\ U^{12}]$

	U^{11}	U^{22}	U^{33}	U^{23}	U^{13}	U^{12}
C(1)	80(7)	57(6)	74(9)	15(6)	53(7)	10(5)
C(2)	103(9)	50(6)	75(10)	9(6)	9(8)	14(6)
C(3)	94(7)	81(7)	35(7)	7(6)	20(7)	27(6)
C(4)	57(6)	78(7)	39(6)	3(5)	11(6)	13(5)
C(5)	53(4)	60(5)	24(6)	-3(4)	9(4)	1(4)
C(6)	56(5)	62(5)	37(7)	10(5)	9(5)	-1(4)
C(7)	52(6)	86(8)	128(14)	31(8)	-17(8)	-13(6)
C(8)	63(6)	76(8)	104(12)	22(8)	-14(8)	-25(6)
C(9)	71(7)	55(6)	81(10)	9(6)	-20(7)	-16(5)
C(10)	65(6)	59(6)	47(7)	3(5)	-4(6)	0(5)
C(11)	78(8)	76(8)	45(7)	-4(5)	4(5)	3(6)
C(12)	101(10)	82(9)	57(8)	-17(7)	1(7)	2(7)
C(13)	108(11)	72(8)	62(8)	-16(7)	-2(7)	0(7)
C(14)	106(10)	56(7)	52(7)	-9(6)	16(6)	8(6)
C(15)	78(8)	50(6)	41(5)	-4(5)	14(5)	1(5)
C(16)	56(6)	58(5)	57(6)	-5(5)	3(5)	-6(4)
C(17)	52(6)	65(6)	94(9)	-8(8)	3(7)	8(4)
C(18)	50(7)	68(7)	113(11)	2(7)	-21(7)	10(6)
C(19)	50(7)	79(8)	84(9)	6(6)	-10(7)	-7(5)
C(20)	58(7)	71(7)	45(6)	-8(5)	2(5)	-1(5)
C(21)	62(7)	77(7)	39(6)	-3(5)	12(6)	-7(5)
C(22)	62(7)	88(8)	43(7)	-5(5)	9(6)	-14(6)
C(23)	50(6)	97(8)	37(6)	-8(5)	6(5)	-17(5)
C(24)	54(6)	71(5)	32(5)	-9(6)	6(5)	-4(4)
C(25)	45(5)	53(5)	48(6)	5(4)	9(5)	-2(4)
C(26)	55(6)	48(5)	57(6)	1(4)	20(5)	1(4)
C(27)	82(9)	56(6)	71(8)	-12(6)	22(7)	-21(6)
C(28)	114(10)	69(7)	47(7)	-7(5)	21(7)	-4(6)
C(29)	81(9)	86(8)	34(6)	-3(5)	26(6)	-7(6)
C(30)	105(10)	54(7)	56(7)	4(5)	35(7)	-14(6)
C(31)	146(15)	200(20)	129(17)	-36(17)	84(13)	-85(16)
C(32)	156(14)	220(20)	160(20)	-2(19)	77(16)	-42(18)
C(33)	110(19)	240(20)	170(20)	-10(20)	79(17)	-40(20)
C(34)	156(18)	240(20)	210(20)	-40(20)	70(20)	-40(20)
C(35)	190(20)	270(30)	250(30)	-50(30)	70(30)	-90(20)
C(36)	165(19)	320(30)	280(30)	-80(30)	90(20)	-80(20)
C(31')	160(18)	210(20)	128(16)	-23(17)	93(13)	-76(16)
C(32')	147(18)	220(20)	160(20)	-10(20)	74(15)	-73(17)
C(33')	142(18)	220(20)	170(20)	-30(20)	67(16)	-39(18)
C(34')	144(18)	240(30)	230(30)	-30(20)	68(19)	-40(20)
C(35')	150(20)	260(30)	250(30)	-40(20)	50(20)	-60(20)
C(36')	165(19)	320(30)	280(30)	-80(30)	90(20)	-80(20)
C(37)	210(20)	122(13)	98(16)	-58(12)	76(16)	-35(15)
C(38)	220(20)	127(16)	98(18)	-70(14)	57(18)	-6(16)
C(39)	210(20)	135(18)	140(20)	-76(15)	40(19)	13(18)
C(40)	200(20)	150(18)	150(20)	-51(16)	58(19)	-15(18)

C(41)	180(30)	150(20)	130(20)	-60(20)	68(19)	10(20)
C(42)	280(40)	65(19)	90(30)	10(20)	30(20)	-20(20)
C(37')	200(20)	127(12)	96(17)	-60(13)	45(17)	-43(12)
C(38')	240(20)	135(12)	140(20)	-29(18)	46(18)	-8(15)
C(39')	200(20)	133(15)	160(20)	-41(19)	51(18)	9(17)
C(40')	200(20)	150(20)	170(20)	-40(20)	44(18)	9(19)
C(41')	200(30)	150(20)	140(20)	-40(20)	60(20)	-2(19)
C(42')	180(30)	120(30)	120(20)	-30(20)	100(20)	0(20)
N(1)	54(4)	58(4)	29(4)	1(4)	23(4)	2(3)
N(2)	51(4)	55(5)	61(6)	2(4)	0(4)	-6(3)
N(3)	82(7)	53(5)	36(5)	-1(4)	7(4)	5(4)
N(4)	58(5)	60(5)	58(6)	-13(4)	-3(4)	5(4)
N(5)	60(5)	66(5)	37(5)	-3(4)	17(4)	-4(4)
N(6)	44(5)	58(5)	54(5)	-14(4)	24(4)	-9(4)
O(1)	142(10)	153(10)	92(8)	-36(8)	51(7)	-79(8)
O(2)	177(12)	127(8)	65(7)	-47(6)	19(7)	-34(8)
Ru(1)	57(1)	50(1)	58(1)	-10(1)	11(1)	-2(1)
F(101)	284(13)	63(5)	151(8)	-46(6)	-45(9)	35(7)
F(102)	181(10)	79(6)	144(7)	-47(6)	-11(7)	18(6)
F(103)	152(8)	47(4)	149(9)	-17(5)	15(7)	18(4)
F(104)	136(7)	44(4)	161(9)	-19(5)	9(7)	13(4)
F(105)	93(5)	84(6)	305(17)	-4(9)	16(7)	-12(5)
F(106)	111(6)	114(8)	252(15)	11(9)	66(8)	20(5)
P(101)	100(3)	44(2)	124(3)	-29(2)	1(3)	13(2)
F(201)	219(13)	148(8)	131(7)	-87(7)	-112(8)	95(8)
F(202)	157(9)	140(9)	82(6)	-26(6)	32(6)	-54(8)
F(203)	307(16)	142(8)	192(12)	46(9)	-160(12)	-115(10)
F(204)	128(7)	261(11)	63(6)	0(7)	-34(6)	-104(8)
F(205)	78(5)	159(8)	124(9)	15(7)	17(5)	-5(5)
F(206)	208(10)	290(13)	101(12)	-69(11)	-101(10)	124(10)
P(201)	101(3)	93(3)	108(4)	-42(3)	-21(5)	-2(2)

Table A3.4. Hydrogen coordinates (x 10^4) and isotropic displacement parameters (Å^{2}x 10^3) for [Ru(bpy)$_2$(4,4'-bpyhex)](PF$_6$)$_2$.

_____

	x	y	z	U(eq)
H(1)	158	1503	1794	84
H(2)	1167	1066	2624	91
H(3)	2273	1394	1943	84
H(4)	2334	2157	691	69
H(7)	2340	2926	-326	106
H(8)	2252	3769	-1203	97
H(9)	1147	4053	-2138	83
H(10)	157	3570	-1521	68
H(11)	556	2751	3449	80
H(12)	338	3276	5460	96
H(13)	-412	3946	5334	97
H(14)	-1118	4025	3255	86
H(17)	-1630	4102	872	84

H(18)	-2208	4125	-1470	92
H(19)	-1926	3451	-3312	85
H(20)	-1175	2805	-2583	70
H(21)	-1169	2286	2881	71
H(22)	-1853	1601	3729	77
H(24)	-1513	935	-297	63
H(27)	-1093	1065	-2653	84
H(29)	425	1831	-5022	81
H(30)	415	2427	-3062	86
H(31A)	-2455	1035	4151	189
H(31B)	-2560	436	3831	189
H(32A)	-3463	1237	3013	211
H(32B)	-3611	789	4218	211
H(33A)	-4269	731	1968	210
H(33B)	-3564	644	1018	210
H(34A)	-3677	-144	1219	244
H(34B)	-3607	-104	3038	244
H(35A)	-4624	-447	3114	282
H(36A)	-5247	113	841	306
H(36B)	-5602	-319	1988	306
H(31C)	-2829	1168	3659	200
H(31D)	-2228	808	4402	200
H(32C)	-3344	368	4446	210
H(32D)	-2798	61	3360	210
H(33C)	-3422	852	1712	215
H(33D)	-3418	251	1273	215
H(34C)	-4538	787	2351	246
H(34D)	-4334	372	3660	246
H(35B)	-4252	-131	818	265
H(36C)	-5511	29	2379	306
H(36D)	-5370	-399	1018	306
H(37A)	-1101	588	-5144	171
H(37B)	-394	385	-4332	171
H(38A)	69	111	-6537	178
H(38B)	-272	574	-7507	178
H(39A)	-888	-125	-8351	192
H(39B)	-1413	121	-7103	192
H(40A)	-410	-616	-6073	203
H(40B)	-1156	-485	-5314	203
H(41A)	-1053	-1316	-6878	181
H(42A)	-1920	-625	-8409	175
H(42B)	-1907	-1255	-8609	175
H(37C)	-1021	578	-5958	170
H(37D)	-859	552	-4150	170
H(38C)	233	286	-6245	204
H(38D)	151	100	-4498	204
H(39C)	-747	-455	-5139	199
H(39D)	-107	-567	-6288	199
H(40C)	-1229	103	-7181	209
H(40D)	-664	-159	-8298	209
H(41B)	-1662	-780	-6733	199
H(42C)	-1389	-764	-9835	169
H(42D)	-1920	-1154	-8897	169

Table A3.5. Torsion angles [°] for [Ru(bpy)₂(4,4'-bpyhex)](PF₆)₂.

N(1)-C(1)-C(2)-C(3)	-6(2)
C(1)-C(2)-C(3)-C(4)	3(2)
C(2)-C(3)-C(4)-C(5)	1(2)
C(3)-C(4)-C(5)-N(1)	-1.9(19)
C(3)-C(4)-C(5)-C(6)	176.6(11)
C(4)-C(5)-C(6)-N(2)	173.4(13)
N(1)-C(5)-C(6)-N(2)	-7.9(13)
C(4)-C(5)-C(6)-C(7)	-1.2(17)
N(1)-C(5)-C(6)-C(7)	177.4(13)
N(2)-C(6)-C(7)-C(8)	8(2)
C(5)-C(6)-C(7)-C(8)	-177.5(14)
C(6)-C(7)-C(8)-C(9)	-11(3)
C(7)-C(8)-C(9)-C(10)	8(3)
C(8)-C(9)-C(10)-N(2)	-2(2)
N(3)-C(11)-C(12)-C(13)	-6(3)
C(11)-C(12)-C(13)-C(14)	5(3)
C(12)-C(13)-C(14)-C(15)	-3(3)
C(13)-C(14)-C(15)-N(3)	3(2)
C(13)-C(14)-C(15)-C(16)	-175.3(14)
N(3)-C(15)-C(16)-N(4)	4.8(17)
C(14)-C(15)-C(16)-N(4)	-176.5(12)
N(3)-C(15)-C(16)-C(17)	-176.2(12)
C(14)-C(15)-C(16)-C(17)	3(2)
N(4)-C(16)-C(17)-C(18)	-1(2)
C(15)-C(16)-C(17)-C(18)	-179.7(13)
C(16)-C(17)-C(18)-C(19)	-1(2)
C(17)-C(18)-C(19)-C(20)	2(2)
C(18)-C(19)-C(20)-N(4)	-2(2)
N(5)-C(21)-C(22)-C(23)	-4(2)
C(21)-C(22)-C(23)-O(1)	-177.8(15)
C(21)-C(22)-C(23)-C(24)	5(2)
O(1)-C(23)-C(24)-C(25)	176.6(14)
C(22)-C(23)-C(24)-C(25)	-6(2)
C(23)-C(24)-C(25)-N(5)	5.1(18)
C(23)-C(24)-C(25)-C(26)	-179.7(12)
N(5)-C(25)-C(26)-C(27)	-174.8(13)
C(24)-C(25)-C(26)-C(27)	10(2)
N(5)-C(25)-C(26)-N(6)	3.6(15)
C(24)-C(25)-C(26)-N(6)	-171.6(12)
N(6)-C(26)-C(27)-C(28)	2(2)
C(25)-C(26)-C(27)-C(28)	-179.6(13)
C(26)-C(27)-C(28)-O(2)	166.9(17)
C(26)-C(27)-C(28)-C(29)	4(2)
O(2)-C(28)-C(29)-C(30)	-174.0(15)
C(27)-C(28)-C(29)-C(30)	-8(2)
C(28)-C(29)-C(30)-N(6)	8(3)
O(1)-C(31)-C(32)-C(33)	52(5)
C(31)-C(32)-C(33)-C(34)	67(5)

C(32)-C(33)-C(34)-C(35)	117(5)
C(33)-C(34)-C(35)-C(36)	47(11)
O(1)-C(31')-C(32')-C(33')	-60(5)
C(31')-C(32')-C(33')-C(34')	-128(4)
C(32')-C(33')-C(34')-C(35')	-119(5)
O(2)-C(37)-C(38)-C(39)	-145(4)
C(37)-C(38)-C(39)-C(40)	-79(5)
C(38)-C(39)-C(40)-C(41)	-156(4)
C(39)-C(40)-C(41)-C(42)	-28(8)
O(2)-C(37')-C(38')-C(39')	-158(4)
C(37')-C(38')-C(39')-C(40')	52(6)
C(38')-C(39')-C(40')-C(41')	-165(5)
C(39')-C(40')-C(41')-C(42')	-134(6)
C(2)-C(1)-N(1)-C(5)	5(2)
C(2)-C(1)-N(1)-Ru(1)	179.3(11)
C(4)-C(5)-N(1)-C(1)	-1.4(17)
C(6)-C(5)-N(1)-C(1)	179.9(10)
C(4)-C(5)-N(1)-Ru(1)	-176.0(9)
C(6)-C(5)-N(1)-Ru(1)	5.3(10)
C(7)-C(6)-N(2)-C(10)	-1(2)
C(5)-C(6)-N(2)-C(10)	-176.0(11)
C(7)-C(6)-N(2)-Ru(1)	-178.8(12)
C(5)-C(6)-N(2)-Ru(1)	6.4(13)
C(9)-C(10)-N(2)-C(6)	-2(2)
C(9)-C(10)-N(2)-Ru(1)	175.6(11)
C(14)-C(15)-N(3)-C(11)	-5.4(18)
C(16)-C(15)-N(3)-C(11)	173.5(11)
C(14)-C(15)-N(3)-Ru(1)	178.1(9)
C(16)-C(15)-N(3)-Ru(1)	-3.0(14)
C(12)-C(11)-N(3)-C(15)	7(2)
C(12)-C(11)-N(3)-Ru(1)	-176.9(11)
C(19)-C(20)-N(4)-C(16)	0.5(19)
C(19)-C(20)-N(4)-Ru(1)	-174.8(10)
C(17)-C(16)-N(4)-C(20)	1.0(18)
C(15)-C(16)-N(4)-C(20)	-180.0(11)
C(17)-C(16)-N(4)-Ru(1)	177.0(10)
C(15)-C(16)-N(4)-Ru(1)	-4.0(13)
C(22)-C(21)-N(5)-C(25)	3(2)
C(22)-C(21)-N(5)-Ru(1)	-169.9(10)
C(24)-C(25)-N(5)-C(21)	-3.1(17)
C(26)-C(25)-N(5)-C(21)	-179.0(11)
C(24)-C(25)-N(5)-Ru(1)	169.8(8)
C(26)-C(25)-N(5)-Ru(1)	-6.1(13)
C(29)-C(30)-N(6)-C(26)	-3(2)
C(29)-C(30)-N(6)-Ru(1)	175.4(12)
C(27)-C(26)-N(6)-C(30)	-3(2)
C(25)-C(26)-N(6)-C(30)	178.9(12)
C(27)-C(26)-N(6)-Ru(1)	178.9(11)
C(25)-C(26)-N(6)-Ru(1)	0.5(14)
C(22)-C(23)-O(1)-C(31)	9(3)
C(24)-C(23)-O(1)-C(31)	-174(3)
C(22)-C(23)-O(1)-C(31')	5(4)
C(24)-C(23)-O(1)-C(31')	-178(3)
C(32)-C(31)-O(1)-C(23)	104(3)

C(32)-C(31)-O(1)-C(31')	128(29)
C(32')-C(31')-O(1)-C(23)	172(3)
C(32')-C(31')-O(1)-C(31)	14(24)
C(29)-C(28)-O(2)-C(37)	160(4)
C(27)-C(28)-O(2)-C(37)	-4(5)
C(29)-C(28)-O(2)-C(37')	165(3)
C(27)-C(28)-O(2)-C(37')	0(4)
C(38)-C(37)-O(2)-C(28)	-178(3)
C(38')-C(37')-O(2)-C(28)	-128(3)
C(1)-N(1)-Ru(1)-N(6)	-79.0(11)
C(5)-N(1)-Ru(1)-N(6)	95.0(8)
C(1)-N(1)-Ru(1)-N(5)	-1.6(11)
C(5)-N(1)-Ru(1)-N(5)	172.4(8)
C(1)-N(1)-Ru(1)-N(3)	99.4(11)
C(5)-N(1)-Ru(1)-N(3)	-86.6(8)
C(1)-N(1)-Ru(1)-N(2)	-175.9(11)
C(5)-N(1)-Ru(1)-N(2)	-1.9(8)
C(30)-N(6)-Ru(1)-N(1)	-85.9(12)
C(26)-N(6)-Ru(1)-N(1)	92.3(9)
C(30)-N(6)-Ru(1)-N(4)	87.9(13)
C(26)-N(6)-Ru(1)-N(4)	-93.8(9)
C(30)-N(6)-Ru(1)-N(5)	179.0(13)
C(26)-N(6)-Ru(1)-N(5)	-2.7(8)
C(30)-N(6)-Ru(1)-N(2)	-6.9(13)
C(26)-N(6)-Ru(1)-N(2)	171.3(9)
C(20)-N(4)-Ru(1)-N(6)	-4.9(12)
C(16)-N(4)-Ru(1)-N(6)	179.7(9)
C(20)-N(4)-Ru(1)-N(5)	-82.7(12)
C(16)-N(4)-Ru(1)-N(5)	102.0(9)
C(20)-N(4)-Ru(1)-N(3)	177.3(12)
C(16)-N(4)-Ru(1)-N(3)	1.9(9)
C(20)-N(4)-Ru(1)-N(2)	91.9(12)
C(16)-N(4)-Ru(1)-N(2)	-83.5(9)
C(21)-N(5)-Ru(1)-N(1)	90.7(10)
C(25)-N(5)-Ru(1)-N(1)	-82.0(9)
C(21)-N(5)-Ru(1)-N(6)	177.6(11)
C(25)-N(5)-Ru(1)-N(6)	4.9(9)
C(21)-N(5)-Ru(1)-N(4)	-88.1(11)
C(25)-N(5)-Ru(1)-N(4)	99.2(9)
C(21)-N(5)-Ru(1)-N(3)	-8.0(11)
C(25)-N(5)-Ru(1)-N(3)	179.2(8)
C(15)-N(3)-Ru(1)-N(1)	174.4(9)
C(11)-N(3)-Ru(1)-N(1)	-2.1(11)
C(15)-N(3)-Ru(1)-N(4)	0.7(9)
C(11)-N(3)-Ru(1)-N(4)	-175.9(11)
C(15)-N(3)-Ru(1)-N(5)	-89.6(9)
C(11)-N(3)-Ru(1)-N(5)	93.9(10)
C(15)-N(3)-Ru(1)-N(2)	95.7(9)
C(11)-N(3)-Ru(1)-N(2)	-80.9(10)
C(6)-N(2)-Ru(1)-N(1)	-2.5(9)
C(10)-N(2)-Ru(1)-N(1)	179.9(11)
C(6)-N(2)-Ru(1)-N(6)	-89.2(9)
C(10)-N(2)-Ru(1)-N(6)	93.3(11)
C(6)-N(2)-Ru(1)-N(4)	175.6(9)

C(10)-N(2)-Ru(1)-N(4)		-1.9(11)	
C(6)-N(2)-Ru(1)-N(3)		96.2(9)	
C(10)-N(2)-Ru(1)-N(3)		-81.4(11)	

_____

Table A3.6. Atomic coordinates (x 10^4) and equivalent isotropic displacement parameters (Å^2x 10^3) for [Ru(bpy)(4.4'-bpyhex)$_2$](PF$_6$)$_2$. U(eq) is defined as one third of the trace of the orthogonalized U^{ij} tensor.

	x	y	z	U(eq)
C(1)	2971(8)	45(6)	7828(4)	37(2)
C(2)	1945(10)	-451(7)	8168(4)	48(2)
C(3)	2119(11)	-981(7)	8807(5)	55(2)
C(4)	3276(10)	-977(6)	9088(4)	44(2)
C(5)	4278(8)	-453(5)	8734(4)	33(2)
C(6)	5565(9)	-421(5)	8991(4)	34(2)
C(7)	5969(10)	-906(6)	9621(4)	44(2)
C(8)	7197(10)	-827(6)	9817(4)	46(2)
C(9)	8020(9)	-262(6)	9383(4)	40(2)
C(10)	7584(8)	213(5)	8769(4)	32(2)
C(11)	3235(8)	2229(5)	8350(3)	31(2)
C(12)	2681(8)	2991(5)	8644(3)	31(2)
C(13)	3555(8)	3590(5)	8626(4)	33(2)
C(14)	4920(8)	3464(5)	8270(4)	35(2)
C(15)	5382(8)	2698(5)	7980(3)	27(1)
C(16)	6818(7)	2504(5)	7596(3)	24(1)
C(17)	7762(7)	3098(5)	7474(3)	29(2)
C(18)	9109(8)	2850(5)	7124(4)	30(2)
C(19)	9438(8)	2015(5)	6902(4)	33(2)
C(20)	8438(7)	1474(5)	7025(4)	31(2)
C(21)	3690(8)	2280(5)	6609(3)	31(2)
C(22)	3247(8)	2692(5)	5997(4)	35(2)
C(23)	3970(8)	2231(5)	5514(3)	28(2)
C(24)	5093(7)	1380(5)	5673(3)	26(1)
C(25)	5497(7)	1003(5)	6303(3)	26(1)
C(26)	6631(7)	69(5)	6538(3)	24(1)
C(27)	7487(8)	-505(5)	6145(4)	29(2)
C(28)	8502(8)	-1373(5)	6408(4)	34(2)
C(29)	8596(9)	-1655(6)	7073(4)	40(2)
C(30)	7714(8)	-1057(5)	7447(4)	32(2)
O(1)	3187(6)	4329(5)	8910(3)	53(2)
C(31)	1890(10)	4504(8)	9318(5)	49(3)
C(32)	2116(13)	5020(9)	9775(5)	58(3)
C(33)	3357(15)	4393(9)	10199(6)	72(3)
C(34)	3150(15)	3370(9)	10593(7)	82(4)
C(35)	1798(15)	3379(9)	11064(6)	73(3)
C(36)	757(16)	2945(10)	11085(7)	82(4)
O(1')	3187(6)	4329(5)	8910(3)	53(2)

C(31')	3950(30)	4340(30)	9410(16)	59(8)
C(32')	2790(50)	4700(60)	9900(20)	71(10)
C(33')	3350(50)	4510(60)	10553(19)	93(10)
C(34')	2180(60)	4340(60)	11121(19)	93(11)
C(35')	920(60)	4130(40)	10930(20)	74(11)
C(36')	120(60)	3570(40)	11290(30)	76(14)
C(37)	9780(8)	4251(5)	7201(4)	36(2)
C(38)	11149(9)	4629(6)	7019(5)	47(2)
C(39)	10919(9)	5581(7)	7200(5)	55(2)
C(40)	12380(16)	5849(14)	7174(8)	54(4)
C(41)	13182(16)	5902(14)	6514(8)	82(6)
C(42)	14350(20)	5242(19)	6402(14)	97(8)
C(39')	10919(9)	5581(7)	7200(5)	55(2)
C(40')	12170(20)	6068(19)	6898(19)	65(7)
C(41')	13622(13)	5380(20)	7082(16)	68(7)
C(42')	14640(50)	4950(40)	6730(20)	120(20)
C(43)	4237(9)	2319(6)	4372(4)	39(2)
C(44)	3530(9)	3054(6)	3784(4)	40(2)
C(45)	4321(10)	2830(8)	3167(4)	53(2)
C(46)	3745(11)	3604(10)	2563(4)	79(3)
C(47)	4712(17)	3621(14)	1948(7)	73(6)
C(48)	5852(19)	2946(13)	1868(9)	83(7)
C(46')	3745(11)	3604(10)	2563(4)	79(3)
C(47')	4280(40)	3200(20)	1984(8)	85(9)
C(48')	4990(50)	3570(30)	1468(17)	121(16)
C(49)	9548(10)	-1626(7)	5378(5)	60(2)
C(50)	11000(16)	-2157(14)	5067(11)	54(4)
C(51)	10769(17)	-3122(11)	5038(9)	52(4)
C(52)	12095(18)	-3724(12)	4710(9)	59(4)
C(53)	11940(20)	-4665(14)	4672(11)	76(6)
C(54)	10760(30)	-4954(17)	4810(16)	107(10)
C(49')	9548(10)	-1626(7)	5378(5)	60(2)
C(50')	10510(30)	-2559(12)	5178(8)	85(6)
C(51')	11600(30)	-2317(16)	4660(13)	109(7)
C(52')	12790(30)	-3145(16)	4466(12)	95(7)
C(53')	13220(40)	-4030(20)	4999(16)	152(10)
C(54')	13130(50)	-4860(20)	4940(20)	181(14)
N(1)	4121(7)	67(4)	8096(3)	28(1)
N(2)	6405(6)	138(4)	8563(3)	28(1)
N(3)	4579(6)	2061(4)	8030(3)	23(1)
N(4)	7130(6)	1692(4)	7370(3)	26(1)
N(5)	4812(6)	1468(4)	6767(3)	23(1)
N(6)	6767(6)	-185(4)	7185(3)	27(1)
O(2)	10131(6)	3354(4)	6993(3)	42(1)
O(3)	3441(6)	2676(4)	4923(2)	38(1)
O(4)	9421(6)	-1975(4)	6079(3)	47(1)
Ru(1)	5620(1)	859(1)	7665(1)	23(1)
F(101)	2631(5)	7094(4)	119(2)	52(1)
F(102)	323(6)	7599(4)	1290(2)	59(1)
F(103)	2233(7)	6293(4)	1176(3)	61(1)
F(104)	741(6)	8406(4)	237(2)	62(1)
F(105)	414(6)	6858(5)	507(3)	68(2)
F(106)	2559(6)	7835(4)	886(3)	55(1)
P(101)	1483(2)	7348(2)	702(1)	40(1)

F(201)	7654(6)	1479(4)	3748(3)	65(2)
F(202)	8049(6)	-826(4)	3942(3)	62(2)
F(203)	7004(6)	226(4)	4547(2)	60(1)
F(204)	8712(6)	413(5)	3138(3)	68(2)
F(205)	9369(5)	55(4)	4133(3)	57(1)
F(206)	6340(5)	590(4)	3546(3)	55(1)
P(201)	7845(2)	331(2)	3840(1)	40(1)

Table A3.7. Bond lengths [Å] and angles [°] for [Ru(bpy)(4.4'-bpyhex)$_2$](PF$_6$)$_2$.

C(1)-N(1)	1.349(9)	C(19)-H(19)	0.9500
C(1)-C(2)	1.378(11)	C(20)-N(4)	1.353(9)
C(1)-H(1)	0.9500	C(20)-H(20)	0.9500
C(2)-C(3)	1.380(13)	C(21)-N(5)	1.342(9)
C(2)-H(2)	0.9500	C(21)-C(22)	1.368(10)
C(3)-C(4)	1.362(12)	C(21)-H(21)	0.9500
C(3)-H(3)	0.9500	C(22)-C(23)	1.401(9)
C(4)-C(5)	1.393(10)	C(22)-H(22)	0.9500
C(4)-H(4)	0.9500	C(23)-O(3)	1.360(8)
C(5)-N(1)	1.374(9)	C(23)-C(24)	1.377(10)
C(5)-C(6)	1.462(11)	C(24)-C(25)	1.389(10)
C(6)-N(2)	1.365(9)	C(24)-H(24)	0.9500
C(6)-C(7)	1.399(11)	C(25)-N(5)	1.363(8)
C(7)-C(8)	1.370(12)	C(25)-C(26)	1.479(10)
C(7)-H(7)	0.9500	C(26)-N(6)	1.364(9)
C(8)-C(9)	1.364(12)	C(26)-C(27)	1.383(9)
C(8)-H(8)	0.9500	C(27)-C(28)	1.376(10)
C(9)-C(10)	1.377(10)	C(27)-H(27)	0.9500
C(9)-H(9)	0.9500	C(28)-O(4)	1.337(8)
C(10)-N(2)	1.334(9)	C(28)-C(29)	1.390(11)
C(10)-H(10)	0.9500	C(29)-C(30)	1.384(10)
C(11)-N(3)	1.350(9)	C(29)-H(29)	0.9500
C(11)-C(12)	1.387(10)	C(30)-N(6)	1.348(9)
C(11)-H(11)	0.9500	C(30)-H(30)	0.9500
C(12)-C(13)	1.376(10)	O(1)-C(31)	1.407(7)
C(12)-H(12)	0.9500	C(31)-C(32)	1.504(12)
C(13)-O(1)	1.342(8)	C(31)-H(31A)	0.9900
C(13)-C(14)	1.397(10)	C(31)-H(31B)	0.9900
C(14)-C(15)	1.381(9)	C(32)-C(33)	1.522(14)
C(14)-H(14)	0.9500	C(32)-H(32A)	0.9900
C(15)-N(3)	1.352(9)	C(32)-H(32B)	0.9900
C(15)-C(16)	1.483(9)	C(33)-C(34)	1.536(14)
C(16)-N(4)	1.363(8)	C(33)-H(33A)	0.9900
C(16)-C(17)	1.380(9)	C(33)-H(33B)	0.9900
C(17)-C(18)	1.393(9)	C(34)-C(35)	1.511(14)
C(17)-H(17)	0.9500	C(34)-H(34A)	0.9900
C(18)-O(2)	1.343(8)	C(34)-H(34B)	0.9900
C(18)-C(19)	1.386(10)	C(35)-C(36)	1.327(13)
C(19)-C(20)	1.367(10)	C(35)-H(35A)	0.9500

C(36)-H(36A)	0.9500	C(46)-H(46B)	0.9900
C(36)-H(36B)	0.9500	C(47)-C(48)	1.266(9)
C(31')-C(32')	1.507(19)	C(47)-H(47A)	0.9500
C(31')-H(31C)	0.9900	C(48)-H(48A)	0.9500
C(31')-H(31D)	0.9900	C(48)-H(48B)	0.9500
C(32')-C(33')	1.515(19)	C(47')-C(48')	1.270(10)
C(32')-H(32C)	0.9900	C(47')-H(47B)	0.9500
C(32')-H(32D)	0.9900	C(48')-H(48C)	0.9500
C(33')-C(34')	1.537(19)	C(48')-H(48D)	0.9500
C(33')-H(33C)	0.9900	C(49)-O(4)	1.450(11)
C(33')-H(33D)	0.9900	C(49)-C(50)	1.538(13)
C(34')-C(35')	1.494(19)	C(49)-H(49A)	0.9900
C(34')-H(34C)	0.9900	C(49)-H(49B)	0.9900
C(34')-H(34D)	0.9900	C(50)-C(51)	1.522(15)
C(35')-C(36')	1.291(19)	C(50)-H(50A)	0.9900
C(35')-H(35B)	0.9500	C(50)-H(50B)	0.9900
C(36')-H(36C)	0.9500	C(51)-C(52)	1.523(9)
C(36')-H(36D)	0.9500	C(51)-H(51A)	0.9900
C(37)-O(2)	1.453(8)	C(51)-H(51B)	0.9900
C(37)-C(38)	1.524(10)	C(52)-C(53)	1.464(16)
C(37)-H(37A)	0.9900	C(52)-H(52A)	0.9900
C(37)-H(37B)	0.9900	C(52)-H(52B)	0.9900
C(38)-C(39)	1.513(11)	C(53)-C(54)	1.282(17)
C(38)-H(38A)	0.9900	C(53)-H(53A)	0.9500
C(38)-H(38B)	0.9900	C(54)-H(54A)	0.9500
C(39)-C(40)	1.556(14)	C(54)-H(54B)	0.9500
C(39)-H(39A)	0.9900	C(50')-C(51')	1.438(16)
C(39)-H(39B)	0.9900	C(50')-H(50C)	0.9900
C(40)-C(41)	1.505(15)	C(50')-H(50D)	0.9900
C(40)-H(40A)	0.9900	C(51')-C(52')	1.510(16)
C(40)-H(40B)	0.9900	C(51')-H(51C)	0.9900
C(41)-C(42)	1.287(16)	C(51')-H(51D)	0.9900
C(41)-H(41A)	0.9500	C(52')-C(53')	1.458(18)
C(42)-H(42A)	0.9500	C(52')-H(52C)	0.9900
C(42)-H(42B)	0.9500	C(52')-H(52D)	0.9900
C(40')-C(41')	1.492(18)	C(53')-C(54')	1.287(19)
C(40')-H(40C)	0.9900	C(53')-H(53B)	0.9500
C(40')-H(40D)	0.9900	C(54')-H(54C)	0.9500
C(41')-C(42')	1.274(18)	C(54')-H(54D)	0.9500
C(41')-H(41B)	0.9500	N(1)-Ru(1)	2.044(6)
C(42')-H(42C)	0.9500	N(2)-Ru(1)	2.066(6)
C(42')-H(42D)	0.9500	N(3)-Ru(1)	2.072(5)
C(43)-O(3)	1.463(8)	N(4)-Ru(1)	2.068(6)
C(43)-C(44)	1.508(11)	N(5)-Ru(1)	2.065(6)
C(43)-H(43A)	0.9900	N(6)-Ru(1)	2.061(6)
C(43)-H(43B)	0.9900	F(101)-P(101)	1.594(5)
C(44)-C(45)	1.508(11)	F(102)-P(101)	1.606(5)
C(44)-H(44A)	0.9900	F(103)-P(101)	1.605(6)
C(44)-H(44B)	0.9900	F(104)-P(101)	1.598(6)
C(45)-C(46)	1.510(13)	F(105)-P(101)	1.593(5)
C(45)-H(45A)	0.9900	F(106)-P(101)	1.585(5)
C(45)-H(45B)	0.9900	F(201)-P(201)	1.593(5)
C(46)-C(47)	1.494(13)	F(202)-P(201)	1.599(5)
C(46)-H(46A)	0.9900	F(203)-P(201)	1.599(5)

F(204)-P(201)	1.602(5)	F(206)-P(201)	1.576(5)
F(205)-P(201)	1.588(5)		
N(1)-C(1)-C(2)	123.0(8)	O(2)-C(18)-C(19)	117.3(6)
N(1)-C(1)-H(1)	118.5	O(2)-C(18)-C(17)	124.6(6)
C(2)-C(1)-H(1)	118.5	C(19)-C(18)-C(17)	118.1(6)
C(1)-C(2)-C(3)	119.0(8)	C(20)-C(19)-C(18)	119.5(6)
C(1)-C(2)-H(2)	120.5	C(20)-C(19)-H(19)	120.2
C(3)-C(2)-H(2)	120.5	C(18)-C(19)-H(19)	120.2
C(4)-C(3)-C(2)	119.2(8)	N(4)-C(20)-C(19)	123.5(6)
C(4)-C(3)-H(3)	120.4	N(4)-C(20)-H(20)	118.3
C(2)-C(3)-H(3)	120.4	C(19)-C(20)-H(20)	118.3
C(3)-C(4)-C(5)	120.4(8)	N(5)-C(21)-C(22)	123.2(6)
C(3)-C(4)-H(4)	119.8	N(5)-C(21)-H(21)	118.4
C(5)-C(4)-H(4)	119.8	C(22)-C(21)-H(21)	118.4
N(1)-C(5)-C(4)	120.8(7)	C(21)-C(22)-C(23)	118.6(7)
N(1)-C(5)-C(6)	115.0(6)	C(21)-C(22)-H(22)	120.7
C(4)-C(5)-C(6)	124.2(7)	C(23)-C(22)-H(22)	120.7
N(2)-C(6)-C(7)	119.8(7)	O(3)-C(23)-C(24)	126.3(6)
N(2)-C(6)-C(5)	114.8(7)	O(3)-C(23)-C(22)	114.9(6)
C(7)-C(6)-C(5)	125.4(7)	C(24)-C(23)-C(22)	118.8(7)
C(8)-C(7)-C(6)	120.9(8)	C(23)-C(24)-C(25)	119.7(6)
C(8)-C(7)-H(7)	119.5	C(23)-C(24)-H(24)	120.1
C(6)-C(7)-H(7)	119.5	C(25)-C(24)-H(24)	120.1
C(9)-C(8)-C(7)	118.4(8)	N(5)-C(25)-C(24)	121.2(6)
C(9)-C(8)-H(8)	120.8	N(5)-C(25)-C(26)	114.3(6)
C(7)-C(8)-H(8)	120.8	C(24)-C(25)-C(26)	124.5(6)
C(8)-C(9)-C(10)	119.1(8)	N(6)-C(26)-C(27)	122.3(6)
C(8)-C(9)-H(9)	120.4	N(6)-C(26)-C(25)	113.9(6)
C(10)-C(9)-H(9)	120.4	C(27)-C(26)-C(25)	123.9(7)
N(2)-C(10)-C(9)	123.7(8)	C(28)-C(27)-C(26)	119.9(7)
N(2)-C(10)-H(10)	118.2	C(28)-C(27)-H(27)	120.1
C(9)-C(10)-H(10)	118.2	C(26)-C(27)-H(27)	120.1
N(3)-C(11)-C(12)	123.1(7)	O(4)-C(28)-C(27)	125.6(7)
N(3)-C(11)-H(11)	118.4	O(4)-C(28)-C(29)	116.5(7)
C(12)-C(11)-H(11)	118.4	C(27)-C(28)-C(29)	117.9(7)
C(13)-C(12)-C(11)	118.6(7)	C(30)-C(29)-C(28)	120.1(7)
C(13)-C(12)-H(12)	120.7	C(30)-C(29)-H(29)	119.9
C(11)-C(12)-H(12)	120.7	C(28)-C(29)-H(29)	119.9
O(1)-C(13)-C(12)	125.2(6)	N(6)-C(30)-C(29)	122.0(7)
O(1)-C(13)-C(14)	115.6(7)	N(6)-C(30)-H(30)	119.0
C(12)-C(13)-C(14)	119.2(6)	C(29)-C(30)-H(30)	119.0
C(15)-C(14)-C(13)	118.5(7)	C(13)-O(1)-C(31)	121.9(7)
C(15)-C(14)-H(14)	120.8	O(1)-C(31)-C(32)	108.0(8)
C(13)-C(14)-H(14)	120.8	O(1)-C(31)-H(31A)	110.1
N(3)-C(15)-C(14)	123.0(6)	C(32)-C(31)-H(31A)	110.1
N(3)-C(15)-C(16)	114.7(6)	O(1)-C(31)-H(31B)	110.1
C(14)-C(15)-C(16)	122.3(6)	C(32)-C(31)-H(31B)	110.1
N(4)-C(16)-C(17)	122.5(6)	H(31A)-C(31)-H(31B)	108.4
N(4)-C(16)-C(15)	114.6(6)	C(31)-C(32)-C(33)	112.3(10)
C(17)-C(16)-C(15)	122.9(6)	C(31)-C(32)-H(32A)	109.1
C(16)-C(17)-C(18)	119.4(6)	C(33)-C(32)-H(32A)	109.1
C(16)-C(17)-H(17)	120.3	C(31)-C(32)-H(32B)	109.1
C(18)-C(17)-H(17)	120.3	C(33)-C(32)-H(32B)	109.1

H(32A)-C(32)-H(32B)	107.9	C(37)-C(38)-H(38A)	109.3
C(32)-C(33)-C(34)	113.3(11)	C(39)-C(38)-H(38B)	109.3
C(32)-C(33)-H(33A)	108.9	C(37)-C(38)-H(38B)	109.3
C(34)-C(33)-H(33A)	108.9	H(38A)-C(38)-H(38B)	108.0
C(32)-C(33)-H(33B)	108.9	C(38)-C(39)-C(40)	112.6(9)
C(34)-C(33)-H(33B)	108.9	C(38)-C(39)-H(39A)	109.1
H(33A)-C(33)-H(33B)	107.7	C(40)-C(39)-H(39A)	109.1
C(35)-C(34)-C(33)	115.7(11)	C(38)-C(39)-H(39B)	109.1
C(35)-C(34)-H(34A)	108.4	C(40)-C(39)-H(39B)	109.1
C(33)-C(34)-H(34A)	108.4	H(39A)-C(39)-H(39B)	107.8
C(35)-C(34)-H(34B)	108.4	C(41)-C(40)-C(39)	109.5(11)
C(33)-C(34)-H(34B)	108.4	C(41)-C(40)-H(40A)	109.8
H(34A)-C(34)-H(34B)	107.4	C(39)-C(40)-H(40A)	109.8
C(36)-C(35)-C(34)	126.4(14)	C(41)-C(40)-H(40B)	109.8
C(36)-C(35)-H(35A)	116.8	C(39)-C(40)-H(40B)	109.8
C(34)-C(35)-H(35A)	116.8	H(40A)-C(40)-H(40B)	108.2
C(35)-C(36)-H(36A)	120.0	C(42)-C(41)-C(40)	123.2(19)
C(35)-C(36)-H(36B)	120.0	C(42)-C(41)-H(41A)	118.4
H(36A)-C(36)-H(36B)	120.0	C(40)-C(41)-H(41A)	118.4
C(32')-C(31')-H(31C)	110.5	C(41)-C(42)-H(42A)	120.0
C(32')-C(31')-H(31D)	110.5	C(41)-C(42)-H(42B)	120.0
H(31C)-C(31')-H(31D)	108.7	H(42A)-C(42)-H(42B)	120.0
C(31')-C(32')-C(33')	114(3)	C(41')-C(40')-H(40C)	109.3
C(31')-C(32')-H(32C)	108.7	C(41')-C(40')-H(40D)	109.3
C(33')-C(32')-H(32C)	108.7	H(40C)-C(40')-H(40D)	108.0
C(31')-C(32')-H(32D)	108.7	C(42')-C(41')-C(40')	128(3)
C(33')-C(32')-H(32D)	108.7	C(42')-C(41')-H(41B)	116.0
H(32C)-C(32')-H(32D)	107.6	C(40')-C(41')-H(41B)	116.0
C(32')-C(33')-C(34')	113(2)	C(41')-C(42')-H(42C)	120.0
C(32')-C(33')-H(33C)	109.0	C(41')-C(42')-H(42D)	120.0
C(34')-C(33')-H(33C)	109.0	H(42C)-C(42')-H(42D)	120.0
C(32')-C(33')-H(33D)	109.0	O(3)-C(43)-C(44)	105.6(6)
C(34')-C(33')-H(33D)	109.0	O(3)-C(43)-H(43A)	110.6
H(33C)-C(33')-H(33D)	107.8	C(44)-C(43)-H(43A)	110.6
C(35')-C(34')-C(33')	112(2)	O(3)-C(43)-H(43B)	110.6
C(35')-C(34')-H(34C)	109.3	C(44)-C(43)-H(43B)	110.6
C(33')-C(34')-H(34C)	109.3	H(43A)-C(43)-H(43B)	108.8
C(35')-C(34')-H(34D)	109.3	C(45)-C(44)-C(43)	111.7(7)
C(33')-C(34')-H(34D)	109.3	C(45)-C(44)-H(44A)	109.3
H(34C)-C(34')-H(34D)	108.0	C(43)-C(44)-H(44A)	109.3
C(36')-C(35')-C(34')	126(4)	C(45)-C(44)-H(44B)	109.3
C(36')-C(35')-H(35B)	116.9	C(43)-C(44)-H(44B)	109.3
C(34')-C(35')-H(35B)	116.9	H(44A)-C(44)-H(44B)	107.9
C(35')-C(36')-H(36C)	120.0	C(46)-C(45)-C(44)	113.6(8)
C(35')-C(36')-H(36D)	120.0	C(46)-C(45)-H(45A)	108.8
H(36C)-C(36')-H(36D)	120.0	C(44)-C(45)-H(45A)	108.8
O(2)-C(37)-C(38)	106.2(6)	C(46)-C(45)-H(45B)	108.8
O(2)-C(37)-H(37A)	110.5	C(44)-C(45)-H(45B)	108.8
C(38)-C(37)-H(37A)	110.5	H(45A)-C(45)-H(45B)	107.7
O(2)-C(37)-H(37B)	110.5	C(47)-C(46)-C(45)	117.3(10)
C(38)-C(37)-H(37B)	110.5	C(47)-C(46)-H(46A)	108.0
H(37A)-C(37)-H(37B)	108.7	C(45)-C(46)-H(46A)	108.0
C(39)-C(38)-C(37)	111.6(6)	C(47)-C(46)-H(46B)	108.0
C(39)-C(38)-H(38A)	109.3	C(45)-C(46)-H(46B)	108.0

H(46A)-C(46)-H(46B)	107.2	C(51')-C(52')-H(52D)	108.8
C(48)-C(47)-C(46)	125.2(16)	H(52C)-C(52')-H(52D)	107.7
C(48)-C(47)-H(47A)	117.4	C(54')-C(53')-C(52')	118(3)
C(46)-C(47)-H(47A)	117.4	C(54')-C(53')-H(53B)	121.2
C(47)-C(48)-H(48A)	120.0	C(52')-C(53')-H(53B)	121.2
C(47)-C(48)-H(48B)	120.0	C(53')-C(54')-H(54C)	120.0
H(48A)-C(48)-H(48B)	120.0	C(53')-C(54')-H(54D)	120.0
C(48')-C(47')-H(47B)	116.5	H(54C)-C(54')-H(54D)	120.0
C(47')-C(48')-H(48C)	120.0	C(1)-N(1)-C(5)	117.6(6)
C(47')-C(48')-H(48D)	120.0	C(1)-N(1)-Ru(1)	126.7(5)
H(48C)-C(48')-H(48D)	120.0	C(5)-N(1)-Ru(1)	115.6(5)
O(4)-C(49)-C(50)	113.2(11)	C(10)-N(2)-C(6)	118.0(7)
O(4)-C(49)-H(49A)	108.9	C(10)-N(2)-Ru(1)	126.5(5)
C(50)-C(49)-H(49A)	108.9	C(6)-N(2)-Ru(1)	115.4(5)
O(4)-C(49)-H(49B)	108.9	C(11)-N(3)-C(15)	117.3(6)
C(50)-C(49)-H(49B)	108.9	C(11)-N(3)-Ru(1)	126.7(5)
H(49A)-C(49)-H(49B)	107.8	C(15)-N(3)-Ru(1)	115.9(4)
C(51)-C(50)-C(49)	105.4(11)	C(20)-N(4)-C(16)	116.9(6)
C(51)-C(50)-H(50A)	110.7	C(20)-N(4)-Ru(1)	127.1(5)
C(49)-C(50)-H(50A)	110.7	C(16)-N(4)-Ru(1)	115.8(4)
C(51)-C(50)-H(50B)	110.7	C(21)-N(5)-C(25)	118.3(6)
C(49)-C(50)-H(50B)	110.7	C(21)-N(5)-Ru(1)	125.2(4)
H(50A)-C(50)-H(50B)	108.8	C(25)-N(5)-Ru(1)	116.4(5)
C(52)-C(51)-C(50)	112.3(13)	C(30)-N(6)-C(26)	117.7(6)
C(52)-C(51)-H(51A)	109.2	C(30)-N(6)-Ru(1)	125.5(5)
C(50)-C(51)-H(51A)	109.2	C(26)-N(6)-Ru(1)	116.6(4)
C(52)-C(51)-H(51B)	109.2	C(18)-O(2)-C(37)	117.9(5)
C(50)-C(51)-H(51B)	109.2	C(23)-O(3)-C(43)	118.6(6)
H(51A)-C(51)-H(51B)	107.9	C(28)-O(4)-C(49)	118.3(6)
C(53)-C(52)-C(51)	114.8(14)	N(1)-Ru(1)-N(6)	91.9(2)
C(53)-C(52)-H(52A)	108.6	N(1)-Ru(1)-N(5)	97.5(2)
C(51)-C(52)-H(52A)	108.6	N(6)-Ru(1)-N(5)	77.8(2)
C(53)-C(52)-H(52B)	108.6	N(1)-Ru(1)-N(2)	79.0(2)
C(51)-C(52)-H(52B)	108.6	N(6)-Ru(1)-N(2)	98.8(2)
H(52A)-C(52)-H(52B)	107.5	N(5)-Ru(1)-N(2)	175.2(2)
C(54)-C(53)-C(52)	126.2(18)	N(1)-Ru(1)-N(4)	171.0(2)
C(54)-C(53)-H(53A)	116.9	N(6)-Ru(1)-N(4)	94.7(2)
C(52)-C(53)-H(53A)	116.9	N(5)-Ru(1)-N(4)	89.9(2)
C(53)-C(54)-H(54A)	120.0	N(2)-Ru(1)-N(4)	93.9(2)
C(53)-C(54)-H(54B)	120.0	N(1)-Ru(1)-N(3)	95.6(2)
H(54A)-C(54)-H(54B)	120.0	N(6)-Ru(1)-N(3)	171.4(2)
C(51')-C(50')-H(50C)	109.3	N(5)-Ru(1)-N(3)	96.9(2)
C(51')-C(50')-H(50D)	109.3	N(2)-Ru(1)-N(3)	86.8(2)
H(50C)-C(50')-H(50D)	108.0	N(4)-Ru(1)-N(3)	78.4(2)
C(50')-C(51')-C(52')	119.3(17)	F(106)-P(101)-F(105)	179.2(3)
C(50')-C(51')-H(51C)	107.5	F(106)-P(101)-F(101)	89.9(3)
C(52')-C(51')-H(51C)	107.5	F(105)-P(101)-F(101)	89.3(3)
C(50')-C(51')-H(51D)	107.5	F(106)-P(101)-F(104)	89.1(3)
C(52')-C(51')-H(51D)	107.5	F(105)-P(101)-F(104)	90.7(4)
H(51C)-C(51')-H(51D)	107.0	F(101)-P(101)-F(104)	90.3(3)
C(53')-C(52')-C(51')	114.0(19)	F(106)-P(101)-F(103)	90.1(3)
C(53')-C(52')-H(52C)	108.8	F(105)-P(101)-F(103)	90.1(3)
C(51')-C(52')-H(52C)	108.8	F(101)-P(101)-F(103)	90.2(3)
C(53')-C(52')-H(52D)	108.8	F(104)-P(101)-F(103)	179.1(3)

F(106)-P(101)-F(102)	90.3(3)
F(105)-P(101)-F(102)	90.5(3)
F(101)-P(101)-F(102)	179.7(3)
F(104)-P(101)-F(102)	89.9(3)
F(103)-P(101)-F(102)	89.7(3)
F(206)-P(201)-F(205)	179.2(3)
F(206)-P(201)-F(201)	90.3(3)
F(205)-P(201)-F(201)	90.5(3)
F(206)-P(201)-F(203)	89.7(3)
F(205)-P(201)-F(203)	90.6(3)
F(201)-P(201)-F(203)	90.6(3)
F(206)-P(201)-F(202)	90.5(3)
F(205)-P(201)-F(202)	88.8(3)
F(201)-P(201)-F(202)	179.1(4)
F(203)-P(201)-F(202)	88.9(3)
F(206)-P(201)-F(204)	91.0(3)
F(205)-P(201)-F(204)	88.6(3)
F(201)-P(201)-F(204)	90.4(3)
F(203)-P(201)-F(204)	178.8(4)
F(202)-P(201)-F(204)	90.1(3)

Table A3.8. Anisotropic displacement parameters (Å^2 x 10^3)for [Ru(bpy)(4.4'-bpyhex)$_2$](PF$_6$)$_2$. The anisotropic displacement factor exponent takes the form: $-2\pi^2[\,h^2a^{*2}U^{11} + ... + 2\,h\,k\,a^*\,b^*\,U^{12}\,]$

	U^{11}	U^{22}	U^{33}	U^{23}	U^{13}	U^{12}
C(1)	35(4)	44(4)	41(4)	-17(3)	0(3)	-18(3)
C(2)	48(5)	54(5)	50(5)	-11(4)	-2(4)	-31(4)
C(3)	53(5)	64(6)	54(5)	-8(4)	3(4)	-36(5)
C(4)	55(5)	48(5)	37(4)	-9(4)	5(4)	-30(4)
C(5)	38(4)	28(4)	34(4)	-10(3)	2(3)	-12(3)
C(6)	37(4)	30(4)	33(3)	-12(3)	6(3)	-10(3)
C(7)	54(5)	38(4)	31(4)	-2(3)	0(3)	-11(4)
C(8)	56(5)	42(5)	35(4)	-6(4)	-11(4)	-6(4)
C(9)	43(5)	36(4)	39(4)	-10(3)	-16(3)	-2(3)
C(10)	36(4)	27(4)	36(4)	-9(3)	-11(3)	-6(3)
C(11)	29(4)	30(4)	34(4)	-13(3)	4(3)	-9(3)
C(12)	25(4)	35(4)	33(4)	-15(3)	8(3)	-7(3)
C(13)	30(4)	30(4)	39(4)	-19(3)	8(3)	-4(3)
C(14)	29(4)	27(4)	50(5)	-19(3)	7(3)	-7(3)
C(15)	27(3)	24(3)	32(4)	-12(3)	-2(3)	-4(3)
C(16)	19(3)	20(3)	34(4)	-10(3)	3(3)	-5(2)
C(17)	25(3)	23(3)	39(4)	-17(3)	2(3)	-1(3)
C(18)	20(3)	28(4)	43(4)	-16(3)	7(3)	-7(3)
C(19)	19(3)	33(4)	47(4)	-21(3)	8(3)	-2(3)
C(20)	21(3)	28(4)	42(4)	-20(3)	1(3)	6(3)
C(21)	28(4)	29(4)	28(3)	-11(3)	6(3)	2(3)
C(22)	38(4)	27(4)	35(4)	-13(3)	-2(3)	2(3)
C(23)	27(4)	29(4)	29(3)	-13(3)	-3(3)	-4(3)
C(24)	21(3)	30(4)	27(3)	-16(3)	4(3)	-5(3)
C(25)	25(3)	21(3)	34(3)	-14(3)	3(3)	-5(3)
C(26)	18(3)	25(3)	36(3)	-15(3)	3(3)	-9(2)
C(27)	27(4)	27(3)	37(4)	-18(3)	2(3)	-6(3)
C(28)	28(4)	32(4)	53(4)	-29(3)	-1(3)	-7(3)
C(29)	40(4)	22(4)	60(4)	-16(3)	-15(4)	2(3)
C(30)	32(4)	25(3)	39(4)	-8(3)	-5(3)	-5(3)
O(1)	51(4)	53(4)	63(4)	-40(3)	12(3)	-13(3)
C(31)	38(6)	57(7)	60(6)	-38(5)	18(4)	-14(5)
C(32)	61(8)	60(7)	62(7)	-39(5)	25(5)	-25(6)
C(33)	80(9)	79(8)	77(9)	-59(7)	4(6)	-21(6)
C(34)	93(9)	67(7)	94(10)	-37(6)	-28(7)	-6(7)
C(35)	94(9)	53(7)	73(8)	-11(6)	-35(6)	-13(6)
C(36)	99(10)	49(8)	95(11)	-6(7)	-51(8)	-5(7)
O(1')	51(4)	53(4)	63(4)	-40(3)	12(3)	-13(3)
C(31')	64(18)	55(18)	80(16)	-44(14)	3(12)	-28(16)
C(32')	80(20)	74(19)	81(14)	-56(15)	-4(15)	-18(18)
C(33')	92(19)	110(20)	79(16)	-50(20)	-10(16)	-10(19)
C(34')	90(20)	100(20)	79(15)	-20(20)	-17(16)	-8(18)
C(35')	86(16)	62(17)	65(17)	-25(13)	-11(13)	5(13)
C(36')	70(30)	50(30)	70(30)	0(20)	-30(20)	17(18)
C(37)	32(4)	27(4)	51(5)	-18(3)	7(4)	-9(3)
C(38)	41(5)	38(4)	68(6)	-25(4)	14(4)	-18(4)
C(39)	42(5)	42(5)	88(7)	-33(5)	14(5)	-19(4)

C(40)	59(8)	47(8)	71(10)	-23(7)	-5(7)	-29(7)
C(41)	61(9)	91(12)	89(11)	-13(10)	13(8)	-34(8)
C(42)	56(11)	119(19)	130(20)	-50(17)	31(12)	-46(10)
C(39')	42(5)	42(5)	88(7)	-33(5)	14(5)	-19(4)
C(40')	51(10)	57(12)	100(17)	-33(13)	18(12)	-33(8)
C(41')	54(8)	62(14)	94(17)	-25(12)	13(12)	-31(10)
C(42')	80(20)	110(30)	100(30)	10(20)	50(20)	5(19)
C(43)	43(5)	47(5)	35(4)	-22(3)	-1(3)	-16(4)
C(44)	42(5)	48(5)	33(3)	-14(3)	-8(3)	-13(4)
C(45)	40(5)	78(6)	44(4)	-23(4)	-3(4)	-13(5)
C(46)	51(6)	126(9)	39(4)	-18(5)	-6(4)	2(6)
C(47)	54(10)	110(13)	45(7)	-19(8)	-1(7)	-11(8)
C(48)	107(14)	78(13)	47(10)	-27(9)	-11(9)	14(10)
C(46')	51(6)	126(9)	39(4)	-18(5)	-6(4)	2(6)
C(47')	73(17)	128(19)	44(8)	-18(11)	6(11)	-25(15)
C(48')	140(30)	120(30)	77(19)	-40(20)	60(20)	-30(20)
C(49)	45(4)	72(5)	63(4)	-46(4)	5(4)	7(4)
C(50)	30(8)	78(10)	77(10)	-56(9)	18(7)	-24(7)
C(51)	53(10)	47(8)	58(10)	-34(8)	-15(8)	10(7)
C(52)	57(10)	56(9)	51(10)	-17(8)	-18(8)	14(8)
C(53)	82(13)	63(11)	75(13)	-45(11)	-40(12)	36(9)
C(54)	130(20)	38(12)	160(30)	-45(16)	-40(20)	7(14)
C(49')	45(4)	72(5)	63(4)	-46(4)	5(4)	7(4)
C(50')	84(11)	67(10)	97(10)	-49(8)	27(8)	-3(9)
C(51')	85(11)	105(11)	119(12)	-44(9)	43(9)	-13(9)
C(52')	76(11)	98(11)	102(12)	-40(9)	32(10)	-17(9)
C(53')	149(16)	122(12)	146(15)	-22(11)	5(14)	-7(12)
C(54')	210(30)	111(14)	180(30)	-24(17)	50(20)	-30(20)
N(1)	33(3)	22(3)	31(3)	-10(2)	3(2)	-9(3)
N(2)	27(3)	20(3)	35(3)	-11(2)	-1(2)	-2(2)
N(3)	22(3)	22(3)	24(3)	-9(2)	2(2)	-2(2)
N(4)	24(3)	25(3)	32(3)	-15(2)	-1(2)	-4(2)
N(5)	22(3)	25(3)	24(3)	-11(2)	8(2)	-9(2)
N(6)	24(3)	23(3)	37(3)	-14(2)	-2(2)	-5(2)
O(2)	29(3)	30(3)	71(4)	-26(3)	16(3)	-12(2)
O(3)	36(3)	46(3)	27(3)	-14(2)	-4(2)	1(2)
O(4)	33(3)	37(3)	72(4)	-37(3)	-2(3)	11(2)
Ru(1)	23(1)	22(1)	26(1)	-11(1)	2(1)	-5(1)
F(101)	36(3)	57(3)	58(3)	-16(2)	13(2)	-17(2)
F(102)	66(3)	75(4)	52(3)	-38(3)	10(3)	-28(3)
F(103)	89(4)	37(3)	55(3)	-9(2)	0(3)	-19(3)
F(104)	46(3)	68(3)	55(3)	-15(3)	-11(2)	9(3)
F(105)	45(3)	121(5)	73(4)	-67(4)	26(3)	-47(3)
F(106)	57(3)	38(3)	77(4)	-10(2)	-26(3)	-16(2)
P(101)	36(1)	46(1)	43(1)	-14(1)	2(1)	-18(1)
F(201)	56(3)	48(3)	105(5)	-36(3)	-5(3)	-22(3)
F(202)	46(3)	52(3)	101(4)	-50(3)	23(3)	-18(2)
F(203)	47(3)	79(4)	54(3)	-42(3)	14(2)	-1(3)
F(204)	52(3)	101(4)	55(3)	-37(3)	21(3)	-27(3)
F(205)	37(3)	66(3)	74(4)	-24(3)	-2(2)	-18(2)
F(206)	37(3)	78(4)	67(3)	-42(3)	8(2)	-25(2)
P(201)	29(1)	47(1)	54(1)	-34(1)	12(1)	-13(1)

Table A3.9. Hydrogen coordinates (x 10⁴) and isotropic displacement parameters (Å²x 10³) for [Ru(bpy)(4.4'-bpyhex)₂](PF₆)₂.

	x	y	z	U(eq)
H(1)	2863	387	7384	45
H(2)	1130	-428	7966	58
H(3)	1440	-1343	9047	66
H(4)	3399	-1335	9529	53
H(7)	5383	-1296	9918	52
H(8)	7470	-1158	10245	56
H(9)	8883	-197	9503	48
H(10)	8154	617	8475	39
H(11)	2640	1804	8375	37
H(12)	1717	3099	8854	37
H(14)	5516	3895	8227	42
H(17)	7494	3671	7626	34
H(19)	10352	1822	6665	40
H(20)	8673	915	6859	37
H(21)	3179	2583	6938	37
H(22)	2465	3278	5901	42
H(24)	5590	1052	5354	31
H(27)	7375	-301	5695	35
H(29)	9268	-2258	7270	48
H(30)	7778	-1268	7901	39
H(31A)	1664	3868	9564	59
H(31B)	1060	4925	9058	59
H(32A)	1199	5174	10054	69
H(32B)	2337	5655	9522	69
H(33A)	3434	4756	10500	86
H(33B)	4291	4300	9922	86
H(34A)	3115	3002	10288	98
H(34B)	4021	2997	10837	98
H(35A)	1682	3732	11376	87
H(36A)	823	2583	10784	98
H(36B)	-54	2995	11402	98
H(31C)	4598	4787	9236	70
H(31D)	4552	3662	9606	70
H(32C)	1997	4373	9970	85
H(32D)	2369	5424	9729	85
H(33C)	3680	5092	10550	111
H(33D)	4202	3926	10618	111
H(34C)	2622	3778	11478	111
H(34D)	1816	4940	11282	111
H(35B)	675	4444	10492	89
H(36C)	322	3241	11728	91
H(36D)	-659	3479	11122	91
H(37A)	9521	4103	7674	43
H(37B)	8941	4754	6980	43
H(38A)	11975	4117	7244	57

H(38B)	11412	4748	6548	57
H(39A)	10424	5512	7643	66
H(39B)	10267	6131	6901	66
H(40A)	12172	6497	7268	65
H(40B)	12998	5339	7506	65
H(41A)	12807	6449	6162	99
H(42A)	14747	4688	6746	116
H(42B)	14817	5309	5976	116
H(39C)	10859	5436	7677	66
H(39D)	9980	6048	7051	66
H(40C)	12165	6276	6421	78
H(40D)	12011	6670	7042	78
H(41B)	13814	5237	7519	82
H(42C)	14509	5062	6284	144
H(42D)	15519	4523	6901	144
H(43A)	4153	1646	4416	46
H(43B)	5288	2294	4342	46
H(44A)	2498	3037	3812	47
H(44B)	3530	3731	3776	47
H(45A)	5375	2775	3165	64
H(45B)	4235	2179	3160	64
H(46A)	2808	3509	2500	94
H(46B)	3522	4265	2639	94
H(47A)	4451	4184	1588	87
H(48A)	6151	2371	2216	100
H(48B)	6410	3013	1461	100
H(46C)	4087	4202	2497	94
H(46D)	2661	3799	2612	94
H(47B)	4054	2599	2009	102
H(48C)	5243	4165	1417	145
H(48D)	5271	3246	1133	145
H(49A)	9462	-905	5246	72
H(49B)	8724	-1727	5213	72
H(50A)	11227	-1746	4628	65
H(50B)	11817	-2293	5332	65
H(51A)	10565	-3525	5483	62
H(51B)	9903	-2968	4798	62
H(52A)	12291	-3314	4266	71
H(52B)	12959	-3863	4948	71
H(53A)	12798	-5105	4531	91
H(54A)	9882	-4540	4953	129
H(54B)	10775	-5581	4770	129
H(49C)	10027	-1077	5224	72
H(49D)	8575	-1399	5207	72
H(50C)	11003	-3047	5556	101
H(50D)	9881	-2869	5040	101
H(51C)	12085	-1896	4777	131
H(51D)	11078	-1903	4272	131
H(52C)	12442	-3327	4130	114
H(52D)	13660	-2898	4271	114
H(53B)	13555	-4002	5375	182
H(54C)	12790	-4874	4564	218
H(54D)	13399	-5452	5281	218

Table A3.10. Torsion angles [°] for [Ru(bpy)(4.4'-bpyhex)₂](PF₆)₂.

N(1)-C(1)-C(2)-C(3)	-2.4(14)
C(1)-C(2)-C(3)-C(4)	1.8(15)
C(2)-C(3)-C(4)-C(5)	-0.6(14)
C(3)-C(4)-C(5)-N(1)	-0.1(12)
C(3)-C(4)-C(5)-C(6)	-178.9(8)
N(1)-C(5)-C(6)-N(2)	1.2(9)
C(4)-C(5)-C(6)-N(2)	-179.9(7)
N(1)-C(5)-C(6)-C(7)	-178.8(7)
C(4)-C(5)-C(6)-C(7)	0.0(12)
N(2)-C(6)-C(7)-C(8)	0.1(12)
C(5)-C(6)-C(7)-C(8)	-179.8(8)
C(6)-C(7)-C(8)-C(9)	0.1(13)
C(7)-C(8)-C(9)-C(10)	0.5(12)
C(8)-C(9)-C(10)-N(2)	-1.5(12)
N(3)-C(11)-C(12)-C(13)	-2.0(12)
C(11)-C(12)-C(13)-O(1)	-177.3(7)
C(11)-C(12)-C(13)-C(14)	5.2(12)
O(1)-C(13)-C(14)-C(15)	178.2(7)
C(12)-C(13)-C(14)-C(15)	-4.1(12)
C(13)-C(14)-C(15)-N(3)	-0.4(12)
C(13)-C(14)-C(15)-C(16)	-179.6(7)
N(3)-C(15)-C(16)-N(4)	-2.1(9)
C(14)-C(15)-C(16)-N(4)	177.1(7)
N(3)-C(15)-C(16)-C(17)	177.6(7)
C(14)-C(15)-C(16)-C(17)	-3.3(11)
N(4)-C(16)-C(17)-C(18)	-2.2(11)
C(15)-C(16)-C(17)-C(18)	178.2(7)
C(16)-C(17)-C(18)-O(2)	-177.8(7)
C(16)-C(17)-C(18)-C(19)	1.1(11)
O(2)-C(18)-C(19)-C(20)	179.6(7)
C(17)-C(18)-C(19)-C(20)	0.7(12)
C(18)-C(19)-C(20)-N(4)	-1.6(12)
N(5)-C(21)-C(22)-C(23)	1.8(12)
C(21)-C(22)-C(23)-O(3)	178.6(7)
C(21)-C(22)-C(23)-C(24)	0.3(11)
O(3)-C(23)-C(24)-C(25)	-178.9(7)
C(22)-C(23)-C(24)-C(25)	-0.7(11)
C(23)-C(24)-C(25)-N(5)	-0.8(10)
C(23)-C(24)-C(25)-C(26)	176.7(6)
N(5)-C(25)-C(26)-N(6)	2.0(8)
C(24)-C(25)-C(26)-N(6)	-175.7(6)
N(5)-C(25)-C(26)-C(27)	-178.0(6)
C(24)-C(25)-C(26)-C(27)	4.3(11)
N(6)-C(26)-C(27)-C(28)	1.0(10)
C(25)-C(26)-C(27)-C(28)	-179.0(6)
C(26)-C(27)-C(28)-O(4)	-177.9(7)
C(26)-C(27)-C(28)-C(29)	1.8(11)
O(4)-C(28)-C(29)-C(30)	178.1(7)
C(27)-C(28)-C(29)-C(30)	-1.7(11)
C(28)-C(29)-C(30)-N(6)	-1.4(12)
C(12)-C(13)-O(1)-C(31)	6.5(13)

C(14)-C(13)-O(1)-C(31)	-175.9(8)
C(13)-O(1)-C(31)-C(32)	154.6(9)
O(1)-C(31)-C(32)-C(33)	-61.2(12)
C(31)-C(32)-C(33)-C(34)	-56.6(13)
C(32)-C(33)-C(34)-C(35)	-61.0(15)
C(33)-C(34)-C(35)-C(36)	123.9(15)
C(31')-C(32')-C(33')-C(34')	-149(6)
C(32')-C(33')-C(34')-C(35')	15(9)
C(33')-C(34')-C(35')-C(36')	148(7)
O(2)-C(37)-C(38)-C(39)	179.0(8)
C(37)-C(38)-C(39)-C(40)	166.3(9)
C(38)-C(39)-C(40)-C(41)	55.7(17)
C(39)-C(40)-C(41)-C(42)	-108(2)
O(3)-C(43)-C(44)-C(45)	175.2(7)
C(43)-C(44)-C(45)-C(46)	-174.2(8)
C(44)-C(45)-C(46)-C(47)	161.9(13)
C(45)-C(46)-C(47)-C(48)	13(3)
O(4)-C(49)-C(50)-C(51)	82.6(16)
C(49)-C(50)-C(51)-C(52)	177.3(15)
C(50)-C(51)-C(52)-C(53)	179.6(18)
C(51)-C(52)-C(53)-C(54)	9(4)
C(50')-C(51')-C(52')-C(53')	-32(4)
C(51')-C(52')-C(53')-C(54')	123(4)
C(2)-C(1)-N(1)-C(5)	1.6(11)
C(2)-C(1)-N(1)-Ru(1)	-174.9(6)
C(4)-C(5)-N(1)-C(1)	-0.4(10)
C(6)-C(5)-N(1)-C(1)	178.5(6)
C(4)-C(5)-N(1)-Ru(1)	176.6(6)
C(6)-C(5)-N(1)-Ru(1)	-4.6(8)
C(9)-C(10)-N(2)-C(6)	1.8(11)
C(9)-C(10)-N(2)-Ru(1)	177.6(6)
C(7)-C(6)-N(2)-C(10)	-1.1(10)
C(5)-C(6)-N(2)-C(10)	178.9(6)
C(7)-C(6)-N(2)-Ru(1)	-177.3(6)
C(5)-C(6)-N(2)-Ru(1)	2.6(8)
C(12)-C(11)-N(3)-C(15)	-2.4(11)
C(12)-C(11)-N(3)-Ru(1)	172.4(6)
C(14)-C(15)-N(3)-C(11)	3.6(11)
C(16)-C(15)-N(3)-C(11)	-177.2(6)
C(14)-C(15)-N(3)-Ru(1)	-171.7(6)
C(16)-C(15)-N(3)-Ru(1)	7.5(8)
C(19)-C(20)-N(4)-C(16)	0.6(11)
C(19)-C(20)-N(4)-Ru(1)	-173.5(6)
C(17)-C(16)-N(4)-C(20)	1.3(10)
C(15)-C(16)-N(4)-C(20)	-179.1(6)
C(17)-C(16)-N(4)-Ru(1)	176.1(5)
C(15)-C(16)-N(4)-Ru(1)	-4.3(8)
C(22)-C(21)-N(5)-C(25)	-3.3(11)
C(22)-C(21)-N(5)-Ru(1)	175.9(6)
C(24)-C(25)-N(5)-C(21)	2.8(10)
C(26)-C(25)-N(5)-C(21)	-175.0(6)
C(24)-C(25)-N(5)-Ru(1)	-176.5(5)
C(26)-C(25)-N(5)-Ru(1)	5.7(7)
C(29)-C(30)-N(6)-C(26)	4.1(10)

C(29)-C(30)-N(6)-Ru(1)	-170.6(6)
C(27)-C(26)-N(6)-C(30)	-4.0(10)
C(25)-C(26)-N(6)-C(30)	176.0(6)
C(27)-C(26)-N(6)-Ru(1)	171.2(5)
C(25)-C(26)-N(6)-Ru(1)	-8.8(7)
C(19)-C(18)-O(2)-C(37)	177.7(7)
C(17)-C(18)-O(2)-C(37)	-3.5(12)
C(38)-C(37)-O(2)-C(18)	177.4(7)
C(24)-C(23)-O(3)-C(43)	-9.1(11)
C(22)-C(23)-O(3)-C(43)	172.7(7)
C(44)-C(43)-O(3)-C(23)	-171.2(6)
C(27)-C(28)-O(4)-C(49)	10.6(11)
C(29)-C(28)-O(4)-C(49)	-169.1(7)
C(50)-C(49)-O(4)-C(28)	157.2(9)
C(1)-N(1)-Ru(1)-N(6)	-80.2(6)
C(5)-N(1)-Ru(1)-N(6)	103.2(5)
C(1)-N(1)-Ru(1)-N(5)	-2.2(6)
C(5)-N(1)-Ru(1)-N(5)	-178.8(5)
C(1)-N(1)-Ru(1)-N(2)	-178.8(6)
C(5)-N(1)-Ru(1)-N(2)	4.6(5)
C(1)-N(1)-Ru(1)-N(3)	95.6(6)
C(5)-N(1)-Ru(1)-N(3)	-81.1(5)
C(30)-N(6)-Ru(1)-N(1)	-78.9(6)
C(26)-N(6)-Ru(1)-N(1)	106.4(5)
C(30)-N(6)-Ru(1)-N(5)	-176.1(6)
C(26)-N(6)-Ru(1)-N(5)	9.1(5)
C(30)-N(6)-Ru(1)-N(2)	0.3(6)
C(26)-N(6)-Ru(1)-N(2)	-174.5(5)
C(30)-N(6)-Ru(1)-N(4)	95.0(6)
C(26)-N(6)-Ru(1)-N(4)	-79.8(5)
C(21)-N(5)-Ru(1)-N(1)	82.5(6)
C(25)-N(5)-Ru(1)-N(1)	-98.2(5)
C(21)-N(5)-Ru(1)-N(6)	172.8(6)
C(25)-N(5)-Ru(1)-N(6)	-7.9(5)
C(21)-N(5)-Ru(1)-N(4)	-92.4(6)
C(25)-N(5)-Ru(1)-N(4)	86.9(5)
C(21)-N(5)-Ru(1)-N(3)	-14.1(6)
C(25)-N(5)-Ru(1)-N(3)	165.2(5)
C(10)-N(2)-Ru(1)-N(1)	-179.8(6)
C(6)-N(2)-Ru(1)-N(1)	-3.9(5)
C(10)-N(2)-Ru(1)-N(6)	90.0(6)
C(6)-N(2)-Ru(1)-N(6)	-94.1(5)
C(10)-N(2)-Ru(1)-N(4)	-5.3(6)
C(6)-N(2)-Ru(1)-N(4)	170.6(5)
C(10)-N(2)-Ru(1)-N(3)	-83.4(6)
C(6)-N(2)-Ru(1)-N(3)	92.5(5)
C(20)-N(4)-Ru(1)-N(6)	-4.7(6)
C(16)-N(4)-Ru(1)-N(6)	-178.8(5)
C(20)-N(4)-Ru(1)-N(5)	-82.5(6)
C(16)-N(4)-Ru(1)-N(5)	103.4(5)
C(20)-N(4)-Ru(1)-N(2)	94.5(6)
C(16)-N(4)-Ru(1)-N(2)	-79.6(5)
C(20)-N(4)-Ru(1)-N(3)	-179.6(6)
C(16)-N(4)-Ru(1)-N(3)	6.3(5)

C(11)-N(3)-Ru(1)-N(1)	-9.1(6)
C(15)-N(3)-Ru(1)-N(1)	165.7(5)
C(11)-N(3)-Ru(1)-N(5)	89.1(6)
C(15)-N(3)-Ru(1)-N(5)	-96.0(5)
C(11)-N(3)-Ru(1)-N(2)	-87.8(6)
C(15)-N(3)-Ru(1)-N(2)	87.1(5)
C(11)-N(3)-Ru(1)-N(4)	177.6(6)
C(15)-N(3)-Ru(1)-N(4)	-7.5(5)

Table A3.11. Atomic coordinates (x 10^4) and equivalent isotropic displacement parameters (Å^2x 10^3) for [Os(bpy)$_2$(4,4'-bpyhex)](PF$_6$)$_2$. U(eq) is defined as one third of the trace of the orthogonalized U^{ij} tensor.

	x	y	z	U(eq)
C(1)	4374(13)	3311(9)	8200(30)	42(4)
C(2)	3791(13)	3568(9)	8710(30)	43(4)
C(3)	3131(13)	3400(9)	8200(30)	46(5)
C(4)	3090(12)	2928(8)	7570(30)	34(4)
C(5)	3684(11)	2670(8)	7173(19)	28(3)
C(6)	3690(11)	2164(8)	6440(20)	34(4)
C(7)	3120(13)	1863(9)	6090(30)	38(4)
C(8)	3175(13)	1392(9)	5320(30)	41(4)
C(9)	3802(12)	1199(9)	5040(30)	38(4)
C(10)	4387(12)	1505(8)	5410(30)	31(3)
C(11)	6270(12)	1892(7)	4730(30)	32(4)
C(12)	6736(13)	1506(8)	4320(30)	38(4)
C(13)	6900(12)	1129(8)	5280(30)	35(4)
C(14)	6572(10)	1130(7)	6700(50)	43(4)
C(15)	6082(11)	1543(7)	7140(30)	33(3)
C(16)	5703(13)	1555(8)	8600(30)	34(3)
C(17)	5824(15)	1209(10)	9870(30)	47(5)
C(18)	5409(16)	1242(11)	11090(30)	62(5)
C(19)	4904(15)	1630(10)	11090(30)	53(5)
C(20)	4814(13)	1964(9)	9930(30)	38(4)
C(21)	6229(12)	2960(9)	8770(30)	36(4)
C(22)	6648(12)	3366(10)	9260(30)	45(4)
C(23)	6769(13)	3743(11)	8200(30)	48(4)
C(24)	6438(9)	3748(7)	6890(40)	34(3)
C(25)	6018(11)	3357(8)	6440(20)	29(3)
C(26)	5654(11)	3288(8)	4990(30)	30(3)
C(27)	5689(13)	3645(9)	3770(30)	38(4)
C(28)	5303(15)	3543(11)	2420(30)	47(4)
C(29)	4898(13)	3150(9)	2300(20)	40(4)
C(30)	4853(13)	2812(10)	3610(20)	38(4)
C(31)	7602(17)	4149(14)	9960(40)	88(6)
C(32)	8116(17)	4572(14)	9890(40)	86(7)
C(33)	8633(18)	4530(15)	8680(40)	95(7)
C(34)	9066(18)	5008(15)	8430(40)	106(8)

C(35)	9669(16)	4904(17)	7440(40)	109(8)
C(36)	10315(17)	4985(17)	7720(40)	108(10)
C(37)	5618(17)	4368(11)	1330(30)	70(6)
C(38)	5400(20)	4642(15)	-210(40)	95(7)
C(39)	5910(20)	5025(14)	-820(40)	108(8)
C(40)	5750(20)	5498(14)	70(50)	121(9)
C(41)	6210(20)	5913(16)	-550(50)	117(9)
C(42)	6540(20)	5977(16)	-1830(40)	108(10)
N(1)	4334(9)	2855(7)	7500(20)	32(3)
N(2)	4335(9)	1958(6)	6080(20)	27(2)
N(3)	5931(10)	1915(6)	6050(20)	31(3)
N(4)	5232(10)	1925(7)	8690(20)	34(3)
N(5)	5896(9)	2954(7)	7365(19)	30(3)
N(6)	5201(10)	2873(7)	4930(20)	30(3)
O(1)	7188(10)	4161(9)	8570(20)	68(5)
O(2)	5254(10)	3872(8)	1276(18)	62(5)
Os(1)	5169(1)	2406(1)	6781(2)	33(1)
F(101)	2436(8)	1904(7)	2447(16)	63(3)
F(102)	3296(11)	2870(7)	1430(20)	100(5)
F(103)	3572(8)	2129(7)	2580(20)	72(4)
F(104)	2157(9)	2659(7)	1470(20)	82(4)
F(105)	2737(10)	2622(7)	3678(19)	75(4)
F(106)	2971(9)	2168(7)	317(19)	69(4)
P(101)	2844(4)	2407(3)	2001(11)	56(2)
F(201)	1874(10)	5049(6)	-1150(30)	80(4)
F(202)	3501(10)	4832(7)	-440(20)	82(4)
F(203)	2487(9)	4401(5)	-110(20)	68(4)
F(204)	2888(9)	5497(6)	-1380(20)	66(3)
F(205)	2771(10)	4706(6)	-2380(20)	74(4)
F(206)	2618(11)	5191(6)	920(20)	81(4)
P(201)	2681(5)	4951(2)	-747(11)	56(2)

_____

Table A3.12. Bond lengths [Å] and angles [°] for [Os(bpy)₂(4,4'-bpyhex)](PF₆)₂.

C(1)-N(1)	1.34(3)	C(25)-N(5)	1.34(2)
C(1)-C(2)	1.37(3)	C(25)-C(26)	1.46(3)
C(1)-H(1)	0.9500	C(26)-N(6)	1.39(3)
C(2)-C(3)	1.41(3)	C(26)-C(27)	1.41(3)
C(2)-H(2)	0.9500	C(27)-C(28)	1.42(3)
C(3)-C(4)	1.35(3)	C(27)-H(27)	0.9500
C(3)-H(3)	0.9500	C(28)-C(29)	1.29(3)
C(4)-C(5)	1.37(3)	C(28)-O(2)	1.31(3)
C(4)-H(4)	0.9500	C(29)-C(30)	1.45(3)
C(5)-N(1)	1.37(3)	C(29)-H(29)	0.9500
C(5)-C(6)	1.46(3)	C(30)-N(6)	1.34(3)
C(6)-C(7)	1.38(3)	C(30)-H(30)	0.9500
C(6)-N(2)	1.38(3)	C(31)-O(1)	1.45(3)
C(7)-C(8)	1.40(3)	C(31)-C(32)	1.479(18)
C(7)-H(7)	0.9500	C(31)-H(31A)	0.9900
C(8)-C(9)	1.33(3)	C(31)-H(31B)	0.9900
C(8)-H(8)	0.9500	C(32)-C(33)	1.45(5)
C(9)-C(10)	1.41(3)	C(32)-H(32A)	0.9900
C(9)-H(9)	0.9500	C(32)-H(32B)	0.9900
C(10)-N(2)	1.32(3)	C(33)-C(34)	1.512(19)
C(10)-H(10)	0.9500	C(33)-H(33A)	0.9900
C(11)-N(3)	1.33(3)	C(33)-H(33B)	0.9900
C(11)-C(12)	1.39(3)	C(34)-C(35)	1.468(19)
C(11)-H(11)	0.9500	C(34)-H(34A)	0.9900
C(12)-C(13)	1.33(3)	C(34)-H(34B)	0.9900
C(12)-H(12)	0.9500	C(35)-C(36)	1.279(18)
C(13)-C(14)	1.39(4)	C(35)-H(35)	0.9500
C(13)-H(13)	0.9500	C(36)-H(36A)	0.9500
C(14)-C(15)	1.48(3)	C(36)-H(36B)	0.9500
C(14)-H(14)	0.9500	C(37)-O(2)	1.47(3)
C(15)-N(3)	1.38(3)	C(37)-C(38)	1.57(3)
C(15)-C(16)	1.47(3)	C(37)-H(37A)	0.9900
C(16)-N(4)	1.32(3)	C(37)-H(37B)	0.9900
C(16)-C(17)	1.45(3)	C(38)-C(39)	1.50(5)
C(17)-C(18)	1.33(4)	C(38)-H(38A)	0.9900
C(17)-H(17)	0.9500	C(38)-H(38B)	0.9900
C(18)-C(19)	1.40(4)	C(39)-C(40)	1.491(19)
C(18)-H(18)	0.9500	C(39)-H(39A)	0.9900
C(19)-C(20)	1.34(3)	C(39)-H(39B)	0.9900
C(19)-H(19)	0.9500	C(40)-C(41)	1.500(19)
C(20)-N(4)	1.35(3)	C(40)-H(40A)	0.9900
C(20)-H(20)	0.9500	C(40)-H(40B)	0.9900
C(21)-N(5)	1.38(3)	C(41)-C(42)	1.294(19)
C(21)-C(22)	1.39(3)	C(41)-H(41)	0.9500
C(21)-H(21)	0.9500	C(42)-H(42A)	0.9500
C(22)-C(23)	1.36(4)	C(42)-H(42B)	0.9500
C(22)-H(22)	0.9500	N(1)-Os(1)	2.079(18)
C(23)-C(24)	1.31(4)	N(2)-Os(1)	2.071(17)
C(23)-O(1)	1.39(3)	N(3)-Os(1)	2.044(18)
C(24)-C(25)	1.36(3)	N(4)-Os(1)	2.087(18)
C(24)-H(24)	0.9500	N(5)-Os(1)	2.059(17)

N(6)-Os(1)	2.022(17)	F(201)-P(201)	1.61(2)
F(101)-P(101)	1.573(16)	F(202)-P(201)	1.62(2)
F(102)-P(101)	1.566(18)	F(203)-P(201)	1.580(17)
F(103)-P(101)	1.652(18)	F(204)-P(201)	1.577(17)
F(104)-P(101)	1.543(17)	F(205)-P(201)	1.572(18)
F(105)-P(101)	1.579(19)	F(206)-P(201)	1.589(18)
F(106)-P(101)	1.613(19)		
N(1)-C(1)-C(2)	122(2)	N(4)-C(16)-C(15)	113.9(19)
N(1)-C(1)-H(1)	119.0	C(17)-C(16)-C(15)	125(2)
C(2)-C(1)-H(1)	119.0	C(18)-C(17)-C(16)	118(3)
C(1)-C(2)-C(3)	119(2)	C(18)-C(17)-H(17)	120.8
C(1)-C(2)-H(2)	120.6	C(16)-C(17)-H(17)	120.8
C(3)-C(2)-H(2)	120.6	C(17)-C(18)-C(19)	118(3)
C(4)-C(3)-C(2)	117(2)	C(17)-C(18)-H(18)	121.2
C(4)-C(3)-H(3)	121.3	C(19)-C(18)-H(18)	121.2
C(2)-C(3)-H(3)	121.3	C(20)-C(19)-C(18)	124(3)
C(3)-C(4)-C(5)	120(2)	C(20)-C(19)-H(19)	118.2
C(3)-C(4)-H(4)	119.9	C(18)-C(19)-H(19)	118.2
C(5)-C(4)-H(4)	119.9	C(19)-C(20)-N(4)	119(2)
C(4)-C(5)-N(1)	122.2(18)	C(19)-C(20)-H(20)	120.7
C(4)-C(5)-C(6)	124(2)	N(4)-C(20)-H(20)	120.7
N(1)-C(5)-C(6)	113.7(19)	N(5)-C(21)-C(22)	123(2)
C(7)-C(6)-N(2)	116.0(19)	N(5)-C(21)-H(21)	118.5
C(7)-C(6)-C(5)	127(2)	C(22)-C(21)-H(21)	118.5
N(2)-C(6)-C(5)	117.0(18)	C(23)-C(22)-C(21)	116(2)
C(6)-C(7)-C(8)	123(2)	C(23)-C(22)-H(22)	122.0
C(6)-C(7)-H(7)	118.5	C(21)-C(22)-H(22)	122.0
C(8)-C(7)-H(7)	118.5	C(24)-C(23)-C(22)	121(2)
C(9)-C(8)-C(7)	119(2)	C(24)-C(23)-O(1)	118(2)
C(9)-C(8)-H(8)	120.4	C(22)-C(23)-O(1)	120(2)
C(7)-C(8)-H(8)	120.4	C(23)-C(24)-C(25)	122(2)
C(8)-C(9)-C(10)	118(2)	C(23)-C(24)-H(24)	118.9
C(8)-C(9)-H(9)	121.2	C(25)-C(24)-H(24)	118.9
C(10)-C(9)-H(9)	121.2	N(5)-C(25)-C(24)	121(2)
N(2)-C(10)-C(9)	123(2)	N(5)-C(25)-C(26)	110.0(17)
N(2)-C(10)-H(10)	118.5	C(24)-C(25)-C(26)	129(2)
C(9)-C(10)-H(10)	118.5	N(6)-C(26)-C(27)	121(2)
N(3)-C(11)-C(12)	125(2)	N(6)-C(26)-C(25)	115.3(18)
N(3)-C(11)-H(11)	117.7	C(27)-C(26)-C(25)	123(2)
C(12)-C(11)-H(11)	117.7	C(26)-C(27)-C(28)	119(2)
C(13)-C(12)-C(11)	122(2)	C(26)-C(27)-H(27)	120.7
C(13)-C(12)-H(12)	119.1	C(28)-C(27)-H(27)	120.7
C(11)-C(12)-H(12)	119.1	C(29)-C(28)-O(2)	114(2)
C(12)-C(13)-C(14)	117(2)	C(29)-C(28)-C(27)	122(2)
C(12)-C(13)-H(13)	121.6	O(2)-C(28)-C(27)	123(2)
C(14)-C(13)-H(13)	121.6	C(28)-C(29)-C(30)	117(2)
C(13)-C(14)-C(15)	121(2)	C(28)-C(29)-H(29)	121.4
C(13)-C(14)-H(14)	119.3	C(30)-C(29)-H(29)	121.4
C(15)-C(14)-H(14)	119.3	N(6)-C(30)-C(29)	125(2)
N(3)-C(15)-C(16)	118.4(18)	N(6)-C(30)-H(30)	117.4
N(3)-C(15)-C(14)	118(2)	C(29)-C(30)-H(30)	117.4
C(16)-C(15)-C(14)	124(2)	O(1)-C(31)-C(32)	108(2)
N(4)-C(16)-C(17)	121(2)	O(1)-C(31)-H(31A)	110.0

C(32)-C(31)-H(31A)	110.0	C(40)-C(41)-H(41)	113.1
O(1)-C(31)-H(31B)	110.0	C(41)-C(42)-H(42A)	120.0
C(32)-C(31)-H(31B)	110.0	C(41)-C(42)-H(42B)	120.0
H(31A)-C(31)-H(31B)	108.4	H(42A)-C(42)-H(42B)	120.0
C(33)-C(32)-C(31)	115(3)	C(1)-N(1)-C(5)	117.5(19)
C(33)-C(32)-H(32A)	108.4	C(1)-N(1)-Os(1)	126.4(16)
C(31)-C(32)-H(32A)	108.4	C(5)-N(1)-Os(1)	116.1(13)
C(33)-C(32)-H(32B)	108.4	C(10)-N(2)-C(6)	120.8(18)
C(31)-C(32)-H(32B)	108.4	C(10)-N(2)-Os(1)	125.1(15)
H(32A)-C(32)-H(32B)	107.5	C(6)-N(2)-Os(1)	114.0(13)
C(32)-C(33)-C(34)	115(3)	C(11)-N(3)-C(15)	117.5(18)
C(32)-C(33)-H(33A)	108.6	C(11)-N(3)-Os(1)	130.5(15)
C(34)-C(33)-H(33A)	108.6	C(15)-N(3)-Os(1)	112.0(14)
C(32)-C(33)-H(33B)	108.6	C(16)-N(4)-C(20)	120(2)
C(34)-C(33)-H(33B)	108.6	C(16)-N(4)-Os(1)	115.4(15)
H(33A)-C(33)-H(33B)	107.5	C(20)-N(4)-Os(1)	124.1(16)
C(35)-C(34)-C(33)	111(3)	C(25)-N(5)-C(21)	116.4(18)
C(35)-C(34)-H(34A)	109.3	C(25)-N(5)-Os(1)	120.6(13)
C(33)-C(34)-H(34A)	109.3	C(21)-N(5)-Os(1)	122.7(15)
C(35)-C(34)-H(34B)	109.3	C(30)-N(6)-C(26)	115.9(18)
C(33)-C(34)-H(34B)	109.3	C(30)-N(6)-Os(1)	126.7(15)
H(34A)-C(34)-H(34B)	108.0	C(26)-N(6)-Os(1)	117.3(14)
C(36)-C(35)-C(34)	128(4)	C(23)-O(1)-C(31)	119(2)
C(36)-C(35)-H(35)	115.9	C(28)-O(2)-C(37)	121.0(19)
C(34)-C(35)-H(35)	115.9	N(6)-Os(1)-N(3)	96.2(7)
C(35)-C(36)-H(36A)	120.0	N(6)-Os(1)-N(5)	76.1(7)
C(35)-C(36)-H(36B)	120.0	N(3)-Os(1)-N(5)	91.5(7)
H(36A)-C(36)-H(36B)	120.0	N(6)-Os(1)-N(2)	97.3(7)
O(2)-C(37)-C(38)	104(2)	N(3)-Os(1)-N(2)	96.2(7)
O(2)-C(37)-H(37A)	110.9	N(5)-Os(1)-N(2)	170.4(6)
C(38)-C(37)-H(37A)	110.9	N(6)-Os(1)-N(1)	85.8(7)
O(2)-C(37)-H(37B)	110.9	N(3)-Os(1)-N(1)	175.1(7)
C(38)-C(37)-H(37B)	110.9	N(5)-Os(1)-N(1)	93.3(7)
H(37A)-C(37)-H(37B)	109.0	N(2)-Os(1)-N(1)	79.1(6)
C(39)-C(38)-C(37)	115(3)	N(6)-Os(1)-N(4)	174.9(7)
C(39)-C(38)-H(38A)	108.5	N(3)-Os(1)-N(4)	80.2(7)
C(37)-C(38)-H(38A)	108.5	N(5)-Os(1)-N(4)	100.3(7)
C(39)-C(38)-H(38B)	108.5	N(2)-Os(1)-N(4)	86.7(7)
C(37)-C(38)-H(38B)	108.5	N(1)-Os(1)-N(4)	98.0(7)
H(38A)-C(38)-H(38B)	107.5	F(104)-P(101)-F(102)	92.9(11)
C(40)-C(39)-C(38)	103(3)	F(104)-P(101)-F(101)	90.2(10)
C(40)-C(39)-H(39A)	111.1	F(102)-P(101)-F(101)	173.7(13)
C(38)-C(39)-H(39A)	111.1	F(104)-P(101)-F(105)	90.9(10)
C(40)-C(39)-H(39B)	111.1	F(102)-P(101)-F(105)	95.3(11)
C(38)-C(39)-H(39B)	111.1	F(101)-P(101)-F(105)	90.1(10)
H(39A)-C(39)-H(39B)	109.1	F(104)-P(101)-F(106)	91.1(11)
C(39)-C(40)-C(41)	106(4)	F(102)-P(101)-F(106)	85.7(11)
C(39)-C(40)-H(40A)	110.4	F(101)-P(101)-F(106)	88.8(9)
C(41)-C(40)-H(40A)	110.4	F(105)-P(101)-F(106)	177.7(12)
C(39)-C(40)-H(40B)	110.4	F(104)-P(101)-F(103)	179.1(11)
C(41)-C(40)-H(40B)	110.4	F(102)-P(101)-F(103)	88.1(10)
H(40A)-C(40)-H(40B)	108.6	F(101)-P(101)-F(103)	88.8(9)
C(42)-C(41)-C(40)	134(5)	F(105)-P(101)-F(103)	88.9(10)
C(42)-C(41)-H(41)	113.1	F(106)-P(101)-F(103)	89.0(10)

F(205)-P(201)-F(204)	91.1(10)
F(205)-P(201)-F(203)	88.8(9)
F(204)-P(201)-F(203)	179.1(11)
F(205)-P(201)-F(206)	177.9(13)
F(204)-P(201)-F(206)	89.2(9)
F(203)-P(201)-F(206)	90.9(10)
F(205)-P(201)-F(201)	88.4(11)
F(204)-P(201)-F(201)	91.3(10)
F(203)-P(201)-F(201)	89.6(10)
F(206)-P(201)-F(201)	93.6(12)
F(205)-P(201)-F(202)	87.9(11)
F(204)-P(201)-F(202)	89.1(10)
F(203)-P(201)-F(202)	89.9(10)
F(206)-P(201)-F(202)	90.0(12)
F(201)-P(201)-F(202)	176.3(12)

Table A3.13 Anisotropic displacement parameters ($Å^2$ x 10^3)for [Os(bpy)$_2$(4,4'-bpyhex)](PF$_6$)$_2$. The anisotropic displacement factor exponent takes the form: $-2\pi^2[\ h^2 a^{*2} U^{11} + ... + 2\ h\ k\ a^*\ b^*\ U^{12}\ ]$

	U^{11}	U^{22}	U^{33}	U^{23}	U^{13}	U^{12}
C(1)	42(7)	41(8)	43(11)	-13(8)	-14(9)	-6(6)
C(2)	45(9)	29(9)	55(12)	-11(8)	-20(9)	0(6)
C(3)	44(7)	31(8)	64(12)	-12(8)	-26(9)	8(7)
C(4)	34(5)	29(8)	40(10)	-3(7)	-21(8)	4(6)
C(5)	35(4)	37(7)	14(8)	-9(6)	3(6)	-6(5)
C(6)	34(4)	38(7)	30(10)	-9(6)	0(7)	-6(5)
C(7)	38(5)	38(8)	37(9)	-6(7)	0(8)	-10(6)
C(8)	38(7)	44(9)	42(10)	-13(8)	-7(9)	-9(7)
C(9)	43(8)	35(8)	35(10)	-4(7)	0(9)	-8(6)
C(10)	36(7)	18(6)	40(9)	12(6)	-2(7)	0(5)
C(11)	49(9)	11(7)	37(7)	6(6)	4(6)	-5(6)
C(12)	45(9)	13(7)	58(9)	3(6)	8(7)	-6(6)
C(13)	39(9)	11(7)	54(8)	-2(6)	3(7)	-2(6)
C(14)	46(9)	23(7)	59(9)	8(8)	8(9)	-2(5)
C(15)	38(8)	21(7)	38(7)	8(5)	4(6)	-7(5)
C(16)	53(9)	25(8)	25(6)	4(5)	-6(6)	-1(6)
C(17)	64(11)	46(10)	33(8)	16(7)	-5(8)	2(8)
C(18)	82(13)	61(12)	42(9)	22(9)	9(9)	6(9)
C(19)	56(11)	58(12)	46(9)	24(8)	11(8)	-8(8)
C(20)	49(10)	36(10)	30(7)	4(6)	4(7)	-12(7)
C(21)	36(9)	48(9)	23(7)	1(6)	-3(6)	1(7)
C(22)	35(10)	72(11)	27(8)	2(7)	-6(7)	-17(8)
C(23)	33(9)	75(10)	37(8)	8(7)	-8(7)	-22(7)
C(24)	30(8)	45(7)	27(8)	1(7)	4(7)	-13(6)
C(25)	37(8)	31(7)	20(6)	-3(5)	3(6)	-6(5)
C(26)	34(8)	32(8)	24(6)	7(5)	-2(6)	-9(6)
C(27)	46(10)	41(9)	26(7)	11(6)	0(7)	-13(7)
C(28)	62(10)	54(9)	25(7)	12(6)	-7(7)	-9(8)
C(29)	57(11)	53(9)	11(6)	-3(5)	-4(7)	-6(8)
C(30)	46(10)	47(9)	20(6)	-2(5)	-2(7)	-12(7)
C(31)	72(12)	136(15)	57(11)	0(11)	-35(8)	-39(10)
C(32)	66(11)	138(15)	53(11)	-15(12)	-28(8)	-37(10)
C(33)	67(13)	159(18)	58(13)	-6(14)	-23(10)	-26(12)
C(34)	83(14)	166(19)	69(15)	9(15)	-10(11)	-29(13)
C(35)	83(14)	170(20)	72(15)	17(15)	-9(11)	-23(15)
C(36)	83(13)	170(30)	67(18)	16(18)	-13(14)	-21(19)
C(37)	90(14)	77(11)	42(12)	33(8)	-21(10)	-24(10)
C(38)	122(17)	105(13)	59(13)	58(10)	-20(13)	-17(13)
C(39)	134(18)	106(13)	85(16)	67(11)	-22(14)	-22(14)
C(40)	140(20)	112(14)	107(17)	47(13)	-46(16)	-22(15)
C(41)	130(20)	112(15)	107(19)	47(15)	-50(17)	-20(14)
C(42)	120(20)	99(19)	100(20)	51(17)	-56(17)	-9(17)
N(1)	34(4)	33(6)	30(7)	-2(5)	-4(5)	-5(4)
N(2)	36(4)	12(5)	32(7)	14(4)	-2(5)	0(3)
N(3)	36(5)	22(5)	35(6)	10(4)	1(5)	-8(4)
N(4)	47(8)	30(6)	24(5)	3(4)	-3(4)	-3(4)
N(5)	33(5)	33(5)	24(6)	1(4)	-3(5)	-1(5)
N(6)	36(8)	26(6)	26(5)	6(4)	-6(4)	-7(4)

O(1)	52(9)	100(11)	52(9)	18(8)	-23(7)	-44(8)
O(2)	75(10)	77(9)	35(8)	27(6)	-11(7)	-20(9)
Os(1)	33(1)	32(1)	35(1)	14(1)	-5(1)	-5(1)
F(101)	59(7)	89(7)	40(6)	13(6)	-26(6)	-34(6)
F(102)	127(9)	90(8)	83(11)	18(7)	-36(9)	-62(7)
F(103)	42(5)	99(9)	74(9)	-1(7)	-5(6)	-11(5)
F(104)	90(7)	90(8)	65(11)	-15(7)	-38(7)	17(6)
F(105)	83(10)	83(9)	58(6)	-15(6)	-30(6)	13(8)
F(106)	75(9)	79(9)	54(6)	0(6)	4(6)	-23(7)
P(101)	61(4)	59(3)	49(5)	6(4)	-19(4)	-16(3)
F(201)	73(5)	39(8)	129(12)	-13(8)	-6(7)	2(5)
F(202)	77(5)	58(9)	113(11)	0(8)	-19(7)	-6(6)
F(203)	92(9)	20(4)	93(9)	-18(5)	-3(8)	-7(5)
F(204)	90(9)	28(5)	80(8)	-11(5)	5(8)	-7(5)
F(205)	99(10)	45(7)	79(6)	-30(6)	0(7)	-4(8)
F(206)	136(11)	29(7)	77(6)	-25(5)	12(7)	-32(8)
P(201)	77(4)	17(3)	75(4)	-19(3)	-10(4)	-7(3)

Table A3.14. Hydrogen coordinates (x 10^4) and isotropic displacement parameters (Å^{2}x 10^3) for [Os(bpy)$_2$(4,4'-bpyhex)](PF$_6$)$_2$.

	x	y	z	U(eq)
H(1)	4819	3463	8359	51
H(2)	3832	3853	9379	52
H(3)	2729	3611	8302	55
H(4)	2648	2774	7397	41
H(7)	2670	1980	6377	45
H(8)	2768	1214	5003	50
H(9)	3857	866	4613	45
H(10)	4838	1380	5159	38
H(11)	6190	2159	4006	39
H(12)	6942	1512	3333	46
H(13)	7227	870	5014	42
H(14)	6664	860	7406	51
H(17)	6191	964	9835	57
H(18)	5454	1011	11926	74
H(19)	4609	1660	11966	64
H(20)	4463	2221	9987	46
H(21)	6170	2675	9438	43
H(22)	6839	3380	10264	54
H(24)	6495	4035	6224	41
H(27)	5964	3946	3857	45
H(29)	4639	3085	1391	48
H(30)	4552	2523	3534	45
H(31A)	7845	3815	10046	106
H(31B)	7297	4192	10865	106
H(32A)	7861	4899	9758	103
H(32B)	8361	4589	10888	103
H(33A)	8391	4445	7709	114

H(33B)	8949	4242	8925	114
H(34A)	8773	5277	7952	127
H(34B)	9231	5139	9433	127
H(35)	9567	4757	6470	130
H(36A)	10451	5132	8674	129
H(36B)	10657	4900	6978	129
H(37A)	6129	4318	1365	84
H(37B)	5471	4571	2230	84
H(38A)	5317	4375	-1001	114
H(38B)	4945	4818	-35	114
H(39A)	6393	4910	-647	130
H(39B)	5837	5083	-1935	130
H(40A)	5844	5441	1178	145
H(40B)	5253	5594	-48	145
H(41)	6281	6187	155	141
H(42A)	6506	5725	-2615	129
H(42B)	6812	6277	-1990	129

Table A3.15. Torsion angles [°] for [Os(bpy)$_2$(4,4'-bpyhex)](PF$_6$)$_2$.

N(1)-C(1)-C(2)-C(3)	-13(4)
C(1)-C(2)-C(3)-C(4)	16(4)
C(2)-C(3)-C(4)-C(5)	-12(4)
C(3)-C(4)-C(5)-N(1)	5(3)
C(3)-C(4)-C(5)-C(6)	-178(2)
C(4)-C(5)-C(6)-C(7)	-3(3)
N(1)-C(5)-C(6)-C(7)	174(2)
C(4)-C(5)-C(6)-N(2)	179(2)
N(1)-C(5)-C(6)-N(2)	-4(2)
N(2)-C(6)-C(7)-C(8)	-4(3)
C(5)-C(6)-C(7)-C(8)	177(2)
C(6)-C(7)-C(8)-C(9)	7(4)
C(7)-C(8)-C(9)-C(10)	-6(4)
C(8)-C(9)-C(10)-N(2)	4(4)
N(3)-C(11)-C(12)-C(13)	-3(4)
C(11)-C(12)-C(13)-C(14)	2(3)
C(12)-C(13)-C(14)-C(15)	-2(3)
C(13)-C(14)-C(15)-N(3)	4(3)
C(13)-C(14)-C(15)-C(16)	178(2)
N(3)-C(15)-C(16)-N(4)	2(3)
C(14)-C(15)-C(16)-N(4)	-173(2)
N(3)-C(15)-C(16)-C(17)	-177(2)
C(14)-C(15)-C(16)-C(17)	9(4)
N(4)-C(16)-C(17)-C(18)	6(4)
C(15)-C(16)-C(17)-C(18)	-176(2)
C(16)-C(17)-C(18)-C(19)	-3(4)
C(17)-C(18)-C(19)-C(20)	1(5)
C(18)-C(19)-C(20)-N(4)	0(4)
N(5)-C(21)-C(22)-C(23)	-6(4)

C(21)-C(22)-C(23)-C(24)	8(4)
C(21)-C(22)-C(23)-O(1)	-179(2)
C(22)-C(23)-C(24)-C(25)	-7(4)
O(1)-C(23)-C(24)-C(25)	-180(2)
C(23)-C(24)-C(25)-N(5)	3(3)
C(23)-C(24)-C(25)-C(26)	-176(2)
N(5)-C(25)-C(26)-N(6)	8(3)
C(24)-C(25)-C(26)-N(6)	-173(2)
N(5)-C(25)-C(26)-C(27)	-179(2)
C(24)-C(25)-C(26)-C(27)	0(4)
N(6)-C(26)-C(27)-C(28)	-6(4)
C(25)-C(26)-C(27)-C(28)	-179(2)
C(26)-C(27)-C(28)-C(29)	4(4)
C(26)-C(27)-C(28)-O(2)	174(2)
O(2)-C(28)-C(29)-C(30)	-171(2)
C(27)-C(28)-C(29)-C(30)	0(4)
C(28)-C(29)-C(30)-N(6)	0(4)
O(1)-C(31)-C(32)-C(33)	-65(4)
C(31)-C(32)-C(33)-C(34)	169(3)
C(32)-C(33)-C(34)-C(35)	168(3)
C(33)-C(34)-C(35)-C(36)	-125(5)
O(2)-C(37)-C(38)-C(39)	-153(3)
C(37)-C(38)-C(39)-C(40)	-83(4)
C(38)-C(39)-C(40)-C(41)	-176(3)
C(39)-C(40)-C(41)-C(42)	22(7)
C(2)-C(1)-N(1)-C(5)	6(4)
C(2)-C(1)-N(1)-Os(1)	-176.8(19)
C(4)-C(5)-N(1)-C(1)	-2(3)
C(6)-C(5)-N(1)-C(1)	-178.7(19)
C(4)-C(5)-N(1)-Os(1)	-179.4(16)
C(6)-C(5)-N(1)-Os(1)	4(2)
C(9)-C(10)-N(2)-C(6)	-1(3)
C(9)-C(10)-N(2)-Os(1)	175.7(17)
C(7)-C(6)-N(2)-C(10)	2(3)
C(5)-C(6)-N(2)-C(10)	-179.5(18)
C(7)-C(6)-N(2)-Os(1)	-175.9(16)
C(5)-C(6)-N(2)-Os(1)	3(2)
C(12)-C(11)-N(3)-C(15)	4(3)
C(12)-C(11)-N(3)-Os(1)	-173.7(17)
C(16)-C(15)-N(3)-C(11)	-179(2)
C(14)-C(15)-N(3)-C(11)	-4(3)
C(16)-C(15)-N(3)-Os(1)	-1(2)
C(14)-C(15)-N(3)-Os(1)	173.8(15)
C(17)-C(16)-N(4)-C(20)	-5(3)
C(15)-C(16)-N(4)-C(20)	176.0(19)
C(17)-C(16)-N(4)-Os(1)	177.1(18)
C(15)-C(16)-N(4)-Os(1)	-2(2)
C(19)-C(20)-N(4)-C(16)	3(3)
C(19)-C(20)-N(4)-Os(1)	179.9(19)
C(24)-C(25)-N(5)-C(21)	-1(3)
C(26)-C(25)-N(5)-C(21)	178.0(19)
C(24)-C(25)-N(5)-Os(1)	172.7(16)
C(26)-C(25)-N(5)-Os(1)	-8(2)
C(22)-C(21)-N(5)-C(25)	3(3)

C(22)-C(21)-N(5)-Os(1)	-171.0(18)
C(29)-C(30)-N(6)-C(26)	-2(3)
C(29)-C(30)-N(6)-Os(1)	-178.9(18)
C(27)-C(26)-N(6)-C(30)	6(3)
C(25)-C(26)-N(6)-C(30)	179(2)
C(27)-C(26)-N(6)-Os(1)	-177.4(18)
C(25)-C(26)-N(6)-Os(1)	-4(3)
C(24)-C(23)-O(1)-C(31)	-175(3)
C(22)-C(23)-O(1)-C(31)	12(4)
C(32)-C(31)-O(1)-C(23)	167(3)
C(29)-C(28)-O(2)-C(37)	173(3)
C(27)-C(28)-O(2)-C(37)	2(4)
C(38)-C(37)-O(2)-C(28)	-178(3)
C(30)-N(6)-Os(1)-N(3)	86(2)
C(26)-N(6)-Os(1)-N(3)	-90.0(17)
C(30)-N(6)-Os(1)-N(5)	177(2)
C(26)-N(6)-Os(1)-N(5)	0.0(16)
C(30)-N(6)-Os(1)-N(2)	-11(2)
C(26)-N(6)-Os(1)-N(2)	172.9(16)
C(30)-N(6)-Os(1)-N(1)	-89(2)
C(26)-N(6)-Os(1)-N(1)	94.5(17)
C(11)-N(3)-Os(1)-N(6)	-6(2)
C(15)-N(3)-Os(1)-N(6)	176.4(14)
C(11)-N(3)-Os(1)-N(5)	-82(2)
C(15)-N(3)-Os(1)-N(5)	100.2(14)
C(11)-N(3)-Os(1)-N(2)	92.1(19)
C(15)-N(3)-Os(1)-N(2)	-85.6(14)
C(11)-N(3)-Os(1)-N(4)	178(2)
C(15)-N(3)-Os(1)-N(4)	0.0(14)
C(25)-N(5)-Os(1)-N(6)	4.9(15)
C(21)-N(5)-Os(1)-N(6)	178.3(18)
C(25)-N(5)-Os(1)-N(3)	100.9(15)
C(21)-N(5)-Os(1)-N(3)	-85.7(17)
C(25)-N(5)-Os(1)-N(1)	-79.9(16)
C(21)-N(5)-Os(1)-N(1)	93.4(17)
C(25)-N(5)-Os(1)-N(4)	-178.7(15)
C(21)-N(5)-Os(1)-N(4)	-5.4(18)
C(10)-N(2)-Os(1)-N(6)	97.6(17)
C(6)-N(2)-Os(1)-N(6)	-85.1(15)
C(10)-N(2)-Os(1)-N(3)	0.5(18)
C(6)-N(2)-Os(1)-N(3)	177.8(14)
C(10)-N(2)-Os(1)-N(1)	-178.1(17)
C(6)-N(2)-Os(1)-N(1)	-0.8(15)
C(10)-N(2)-Os(1)-N(4)	-79.3(17)
C(6)-N(2)-Os(1)-N(4)	98.0(15)
C(1)-N(1)-Os(1)-N(6)	-81(2)
C(5)-N(1)-Os(1)-N(6)	96.6(15)
C(1)-N(1)-Os(1)-N(5)	-5(2)
C(5)-N(1)-Os(1)-N(5)	172.4(15)
C(1)-N(1)-Os(1)-N(2)	-179(2)
C(5)-N(1)-Os(1)-N(2)	-1.7(15)
C(1)-N(1)-Os(1)-N(4)	96(2)
C(5)-N(1)-Os(1)-N(4)	-86.7(15)
C(16)-N(4)-Os(1)-N(3)	0.9(16)

C(20)-N(4)-Os(1)-N(3)	-176.5(19)
C(16)-N(4)-Os(1)-N(5)	-88.9(17)
C(20)-N(4)-Os(1)-N(5)	93.7(18)
C(16)-N(4)-Os(1)-N(2)	97.8(17)
C(20)-N(4)-Os(1)-N(2)	-79.6(18)
C(16)-N(4)-Os(1)-N(1)	176.3(16)
C(20)-N(4)-Os(1)-N(1)	-1.2(18)

Table A3.16 Atomic coordinates (x 10^4) and equivalent isotropic displacement parameters ($Å^2$x 10^3) for [Os(bpy)$_2$(4,4'-bpysac)](PF$_6$)$_2$. U(eq) is defined as one third of the trace of the orthogonalized U^{ij} tensor.

	x	y	z	U(eq)
C(1)	322(14)	9378(10)	7390(5)	45(3)
C(2)	-1139(13)	8797(10)	7411(5)	43(3)
C(3)	-1438(13)	8238(10)	7881(6)	49(3)
C(4)	-255(14)	8223(9)	8314(5)	44(3)
C(5)	1230(13)	8782(9)	8268(4)	36(3)
C(6)	2591(15)	8794(9)	8689(4)	41(3)
C(7)	2590(16)	8238(10)	9192(5)	51(3)
C(8)	3931(17)	8310(11)	9551(5)	56(4)
C(9)	5256(18)	8908(10)	9417(5)	55(4)
C(10)	5229(15)	9443(10)	8906(5)	51(3)
C(11)	2387(15)	11625(8)	8725(5)	42(3)
C(12)	2441(16)	12471(10)	9169(5)	51(3)
C(13)	3775(17)	13238(10)	9373(5)	51(3)
C(14)	5054(16)	13131(9)	9147(5)	47(3)
C(15)	4973(13)	12287(8)	8710(4)	37(3)
C(16)	6247(13)	12130(9)	8425(5)	40(3)
C(17)	7714(14)	12792(9)	8572(5)	47(3)
C(18)	8814(15)	12628(10)	8256(6)	53(3)
C(19)	8454(13)	11817(10)	7783(5)	46(3)
C(20)	6969(12)	11153(9)	7669(5)	42(3)
C(21)	4309(11)	8298(8)	7230(4)	28(2)
C(22)	4450(12)	7627(9)	6756(4)	35(3)
C(23)	4153(12)	7915(9)	6186(5)	36(3)
C(24)	3709(11)	8897(9)	6114(5)	33(2)
C(25)	3612(11)	9550(8)	6609(4)	28(2)
C(26)	3216(11)	10635(8)	6586(4)	27(2)
C(27)	2867(12)	11107(9)	6072(5)	33(2)
C(28)	2497(11)	12116(8)	6110(4)	29(2)
C(29)	2543(13)	12659(9)	6665(5)	39(3)
C(30)	2877(12)	12154(8)	7147(5)	35(2)
C(31)	3899(14)	7412(9)	5140(4)	41(3)
C(32)	4042(15)	6419(10)	4752(5)	49(3)
C(33)	3631(14)	6540(10)	4098(5)	45(3)
C(34)	3958(15)	5605(10)	3709(5)	46(3)

C(35)	3458(14)	5686(9)	3048(4)	42(3)
C(36)	3874(15)	4791(10)	2668(5)	48(3)
C(37)	4031(14)	3879(10)	1576(5)	42(3)
C(38)	3706(16)	3697(10)	926(5)	56(3)
C(39)	1935(16)	12087(10)	5068(5)	51(3)
C(40)	1597(17)	12906(12)	4633(6)	66(4)
C(41)	143(18)	13132(13)	4671(6)	70(4)
C(42)	-202(19)	14019(12)	4267(6)	68(4)
C(43)	-297(15)	13653(11)	3621(5)	54(3)
C(44)	-926(15)	14434(11)	3219(5)	49(3)
C(45)	-1789(14)	14877(10)	2091(5)	47(3)
C(46)	-2006(17)	14635(10)	1437(5)	60(4)
N(1)	1487(10)	9423(7)	7815(4)	33(2)
N(2)	3921(11)	9399(7)	8546(4)	35(2)
N(3)	3622(10)	11544(7)	8486(3)	31(2)
N(4)	5878(10)	11272(6)	7979(4)	30(2)
N(5)	3894(9)	9257(6)	7158(3)	27(2)
N(6)	3209(10)	11156(7)	7124(3)	30(2)
O(1)	4271(9)	7178(6)	5748(3)	41(2)
O(2)	4796(10)	3352(7)	1865(4)	52(2)
O(3)	2173(9)	12672(6)	5647(3)	45(2)
O(4)	-2181(12)	15610(8)	2344(4)	70(3)
S(1)	3208(4)	4849(3)	1900(1)	52(1)
S(2)	-975(4)	13932(3)	2465(1)	58(1)
Os(1)	3689(1)	10338(1)	7850(1)	29(1)
F(101)	7272(8)	-710(6)	6040(3)	62(2)
F(102)	8689(8)	1780(6)	5797(3)	58(2)
F(103)	7119(9)	259(7)	5261(3)	74(2)
F(104)	8854(11)	824(7)	6577(3)	80(3)
F(105)	9398(8)	157(7)	5727(4)	73(2)
F(106)	6566(9)	920(6)	6120(4)	73(2)
P(101)	7981(4)	547(3)	5921(1)	43(1)
F(201)	9565(12)	5987(8)	338(4)	100(3)
F(202)	10637(10)	4679(8)	615(3)	86(3)
F(203)	11635(11)	5748(9)	-30(4)	109(4)
P(201)	10000	5000	0	53(1)
F(301)	-706(11)	8756(6)	-280(4)	86(3)
F(302)	1362(10)	10089(6)	-353(4)	76(2)
F(303)	895(10)	9587(8)	527(4)	93(3)
P(301)	0	10000	0	58(1)

Table A3.17. Bond lengths [Å] and angles [°] for [Os(bpy)$_2$(4,4'-bpysac)](PF$_6$)$_2$.

C(1)-N(1)	1.335(14)	C(3)-H(3)	0.9500
C(1)-C(2)	1.374(16)	C(4)-C(5)	1.398(16)
C(1)-H(1)	0.9500	C(4)-H(4)	0.9500
C(2)-C(3)	1.356(16)	C(5)-N(1)	1.374(13)
C(2)-H(2)	0.9500	C(5)-C(6)	1.469(16)
C(3)-C(4)	1.374(16)	C(6)-N(2)	1.370(14)

C(6)-C(7)	1.393(15)	C(31)-H(31B)	0.9900
C(7)-C(8)	1.365(17)	C(32)-C(33)	1.530(15)
C(7)-H(7)	0.9500	C(32)-H(32A)	0.9900
C(8)-C(9)	1.356(18)	C(32)-H(32B)	0.9900
C(8)-H(8)	0.9500	C(33)-C(34)	1.532(15)
C(9)-C(10)	1.395(16)	C(33)-H(33A)	0.9900
C(9)-H(9)	0.9500	C(33)-H(33B)	0.9900
C(10)-N(2)	1.349(14)	C(34)-C(35)	1.548(15)
C(10)-H(10)	0.9500	C(34)-H(34A)	0.9900
C(11)-N(3)	1.349(14)	C(34)-H(34B)	0.9900
C(11)-C(12)	1.405(15)	C(35)-C(36)	1.521(14)
C(11)-H(11)	0.9500	C(35)-H(35A)	0.9900
C(12)-C(13)	1.363(18)	C(35)-H(35B)	0.9900
C(12)-H(12)	0.9500	C(36)-S(1)	1.806(12)
C(13)-C(14)	1.379(17)	C(36)-H(36A)	0.9900
C(13)-H(13)	0.9500	C(36)-H(36B)	0.9900
C(14)-C(15)	1.386(14)	C(37)-O(2)	1.232(13)
C(14)-H(14)	0.9500	C(37)-C(38)	1.477(15)
C(15)-N(3)	1.369(13)	C(37)-S(1)	1.748(12)
C(15)-C(16)	1.464(16)	C(38)-H(38A)	0.9800
C(16)-N(4)	1.376(13)	C(38)-H(38B)	0.9800
C(16)-C(17)	1.384(16)	C(38)-H(38C)	0.9800
C(17)-C(18)	1.370(17)	C(39)-O(3)	1.439(13)
C(17)-H(17)	0.9500	C(39)-C(40)	1.535(16)
C(18)-C(19)	1.381(16)	C(39)-H(39A)	0.9900
C(18)-H(18)	0.9500	C(39)-H(39B)	0.9900
C(19)-C(20)	1.395(15)	C(40)-C(41)	1.441(19)
C(19)-H(19)	0.9500	C(40)-H(40A)	0.9900
C(20)-N(4)	1.339(13)	C(40)-H(40B)	0.9900
C(20)-H(20)	0.9500	C(41)-C(42)	1.558(18)
C(21)-N(5)	1.352(12)	C(41)-H(41A)	0.9900
C(21)-C(22)	1.369(13)	C(41)-H(41B)	0.9900
C(21)-H(21)	0.9500	C(42)-C(43)	1.513(17)
C(22)-C(23)	1.396(14)	C(42)-H(42A)	0.9900
C(22)-H(22)	0.9500	C(42)-H(42B)	0.9900
C(23)-O(1)	1.351(12)	C(43)-C(44)	1.544(16)
C(23)-C(24)	1.392(14)	C(43)-H(43A)	0.9900
C(24)-C(25)	1.380(13)	C(43)-H(43B)	0.9900
C(24)-H(24)	0.9500	C(44)-S(2)	1.799(11)
C(25)-N(5)	1.352(12)	C(44)-H(44A)	0.9900
C(25)-C(26)	1.483(13)	C(44)-H(44B)	0.9900
C(26)-N(6)	1.362(12)	C(45)-O(4)	1.202(14)
C(26)-C(27)	1.392(13)	C(45)-C(46)	1.494(16)
C(27)-C(28)	1.378(14)	C(45)-S(2)	1.753(13)
C(27)-H(27)	0.9500	C(46)-H(46A)	0.9800
C(28)-O(3)	1.351(11)	C(46)-H(46B)	0.9800
C(28)-C(29)	1.396(14)	C(46)-H(46C)	0.9800
C(29)-C(30)	1.350(14)	N(1)-Os(1)	2.059(9)
C(29)-H(29)	0.9500	N(2)-Os(1)	2.072(9)
C(30)-N(6)	1.348(12)	N(3)-Os(1)	2.042(8)
C(30)-H(30)	0.9500	N(4)-Os(1)	2.039(8)
C(31)-O(1)	1.464(12)	N(5)-Os(1)	2.074(8)
C(31)-C(32)	1.519(14)	N(6)-Os(1)	2.071(8)
C(31)-H(31A)	0.9900	F(101)-P(101)	1.607(7)

F(102)-P(101)	1.584(7)	P(201)-F(202)#1	1.574(8)
F(103)-P(101)	1.590(7)	P(201)-F(203)#1	1.582(9)
F(104)-P(101)	1.585(7)	F(301)-P(301)	1.583(8)
F(105)-P(101)	1.601(8)	F(302)-P(301)	1.572(7)
F(106)-P(101)	1.592(8)	F(303)-P(301)	1.560(9)
F(201)-P(201)	1.570(8)	P(301)-F(303)#2	1.560(9)
F(202)-P(201)	1.574(8)	P(301)-F(302)#2	1.572(7)
F(203)-P(201)	1.582(9)	P(301)-F(301)#2	1.583(8)
P(201)-F(201)#1	1.570(8)		
N(1)-C(1)-C(2)	123.0(11)	C(14)-C(15)-C(16)	125.0(11)
N(1)-C(1)-H(1)	118.5	N(4)-C(16)-C(17)	121.1(11)
C(2)-C(1)-H(1)	118.5	N(4)-C(16)-C(15)	114.7(10)
C(3)-C(2)-C(1)	119.7(11)	C(17)-C(16)-C(15)	124.1(10)
C(3)-C(2)-H(2)	120.2	C(18)-C(17)-C(16)	120.0(11)
C(1)-C(2)-H(2)	120.2	C(18)-C(17)-H(17)	120.0
C(2)-C(3)-C(4)	119.0(11)	C(16)-C(17)-H(17)	120.0
C(2)-C(3)-H(3)	120.5	C(17)-C(18)-C(19)	120.0(12)
C(4)-C(3)-H(3)	120.5	C(17)-C(18)-H(18)	120.0
C(3)-C(4)-C(5)	120.1(11)	C(19)-C(18)-H(18)	120.0
C(3)-C(4)-H(4)	120.0	C(18)-C(19)-C(20)	117.2(12)
C(5)-C(4)-H(4)	120.0	C(18)-C(19)-H(19)	121.4
N(1)-C(5)-C(4)	119.8(10)	C(20)-C(19)-H(19)	121.4
N(1)-C(5)-C(6)	114.9(10)	N(4)-C(20)-C(19)	124.2(11)
C(4)-C(5)-C(6)	125.2(10)	N(4)-C(20)-H(20)	117.9
N(2)-C(6)-C(7)	121.0(11)	C(19)-C(20)-H(20)	117.9
N(2)-C(6)-C(5)	114.3(9)	N(5)-C(21)-C(22)	120.9(9)
C(7)-C(6)-C(5)	124.7(12)	N(5)-C(21)-H(21)	119.5
C(8)-C(7)-C(6)	119.4(13)	C(22)-C(21)-H(21)	119.5
C(8)-C(7)-H(7)	120.3	C(21)-C(22)-C(23)	120.6(10)
C(6)-C(7)-H(7)	120.3	C(21)-C(22)-H(22)	119.7
C(9)-C(8)-C(7)	120.3(12)	C(23)-C(22)-H(22)	119.7
C(9)-C(8)-H(8)	119.9	O(1)-C(23)-C(24)	125.8(10)
C(7)-C(8)-H(8)	119.9	O(1)-C(23)-C(22)	115.9(9)
C(8)-C(9)-C(10)	119.2(13)	C(24)-C(23)-C(22)	118.3(9)
C(8)-C(9)-H(9)	120.4	C(25)-C(24)-C(23)	118.7(10)
C(10)-C(9)-H(9)	120.4	C(25)-C(24)-H(24)	120.7
N(2)-C(10)-C(9)	121.9(13)	C(23)-C(24)-H(24)	120.7
N(2)-C(10)-H(10)	119.1	N(5)-C(25)-C(24)	122.4(9)
C(9)-C(10)-H(10)	119.1	N(5)-C(25)-C(26)	114.4(8)
N(3)-C(11)-C(12)	122.1(12)	C(24)-C(25)-C(26)	123.2(9)
N(3)-C(11)-H(11)	118.9	N(6)-C(26)-C(27)	121.2(9)
C(12)-C(11)-H(11)	118.9	N(6)-C(26)-C(25)	113.9(8)
C(13)-C(12)-C(11)	119.8(12)	C(27)-C(26)-C(25)	124.9(9)
C(13)-C(12)-H(12)	120.1	C(28)-C(27)-C(26)	119.3(10)
C(11)-C(12)-H(12)	120.1	C(28)-C(27)-H(27)	120.3
C(12)-C(13)-C(14)	118.3(11)	C(26)-C(27)-H(27)	120.3
C(12)-C(13)-H(13)	120.9	O(3)-C(28)-C(27)	125.1(9)
C(14)-C(13)-H(13)	120.9	O(3)-C(28)-C(29)	115.8(9)
C(13)-C(14)-C(15)	120.9(12)	C(27)-C(28)-C(29)	119.0(9)
C(13)-C(14)-H(14)	119.6	C(30)-C(29)-C(28)	118.9(10)
C(15)-C(14)-H(14)	119.6	C(30)-C(29)-H(29)	120.6
N(3)-C(15)-C(14)	121.0(11)	C(28)-C(29)-H(29)	120.6
N(3)-C(15)-C(16)	113.9(9)	N(6)-C(30)-C(29)	123.6(10)

N(6)-C(30)-H(30)	118.2	C(41)-C(40)-H(40A)	109.5
C(29)-C(30)-H(30)	118.2	C(39)-C(40)-H(40A)	109.5
O(1)-C(31)-C(32)	106.2(9)	C(41)-C(40)-H(40B)	109.5
O(1)-C(31)-H(31A)	110.5	C(39)-C(40)-H(40B)	109.5
C(32)-C(31)-H(31A)	110.5	H(40A)-C(40)-H(40B)	108.1
O(1)-C(31)-H(31B)	110.5	C(40)-C(41)-C(42)	112.7(12)
C(32)-C(31)-H(31B)	110.5	C(40)-C(41)-H(41A)	109.1
H(31A)-C(31)-H(31B)	108.7	C(42)-C(41)-H(41A)	109.1
C(31)-C(32)-C(33)	111.7(10)	C(40)-C(41)-H(41B)	109.1
C(31)-C(32)-H(32A)	109.3	C(42)-C(41)-H(41B)	109.1
C(33)-C(32)-H(32A)	109.3	H(41A)-C(41)-H(41B)	107.8
C(31)-C(32)-H(32B)	109.3	C(43)-C(42)-C(41)	112.9(11)
C(33)-C(32)-H(32B)	109.3	C(43)-C(42)-H(42A)	109.0
H(32A)-C(32)-H(32B)	107.9	C(41)-C(42)-H(42A)	109.0
C(32)-C(33)-C(34)	111.3(10)	C(43)-C(42)-H(42B)	109.0
C(32)-C(33)-H(33A)	109.4	C(41)-C(42)-H(42B)	109.0
C(34)-C(33)-H(33A)	109.4	H(42A)-C(42)-H(42B)	107.8
C(32)-C(33)-H(33B)	109.4	C(42)-C(43)-C(44)	112.4(10)
C(34)-C(33)-H(33B)	109.4	C(42)-C(43)-H(43A)	109.1
H(33A)-C(33)-H(33B)	108.0	C(44)-C(43)-H(43A)	109.1
C(33)-C(34)-C(35)	111.5(10)	C(42)-C(43)-H(43B)	109.1
C(33)-C(34)-H(34A)	109.3	C(44)-C(43)-H(43B)	109.1
C(35)-C(34)-H(34A)	109.3	H(43A)-C(43)-H(43B)	107.9
C(33)-C(34)-H(34B)	109.3	C(43)-C(44)-S(2)	108.7(8)
C(35)-C(34)-H(34B)	109.3	C(43)-C(44)-H(44A)	110.0
H(34A)-C(34)-H(34B)	108.0	S(2)-C(44)-H(44A)	110.0
C(36)-C(35)-C(34)	110.6(9)	C(43)-C(44)-H(44B)	110.0
C(36)-C(35)-H(35A)	109.5	S(2)-C(44)-H(44B)	110.0
C(34)-C(35)-H(35A)	109.5	H(44A)-C(44)-H(44B)	108.3
C(36)-C(35)-H(35B)	109.5	O(4)-C(45)-C(46)	124.6(12)
C(34)-C(35)-H(35B)	109.5	O(4)-C(45)-S(2)	122.3(10)
H(35A)-C(35)-H(35B)	108.1	C(46)-C(45)-S(2)	113.1(9)
C(35)-C(36)-S(1)	110.4(8)	C(45)-C(46)-H(46A)	109.5
C(35)-C(36)-H(36A)	109.6	C(45)-C(46)-H(46B)	109.5
S(1)-C(36)-H(36A)	109.6	H(46A)-C(46)-H(46B)	109.5
C(35)-C(36)-H(36B)	109.6	C(45)-C(46)-H(46C)	109.5
S(1)-C(36)-H(36B)	109.6	H(46A)-C(46)-H(46C)	109.5
H(36A)-C(36)-H(36B)	108.1	H(46B)-C(46)-H(46C)	109.5
O(2)-C(37)-C(38)	121.6(11)	C(1)-N(1)-C(5)	118.1(10)
O(2)-C(37)-S(1)	122.8(9)	C(1)-N(1)-Os(1)	126.1(8)
C(38)-C(37)-S(1)	115.5(9)	C(5)-N(1)-Os(1)	115.8(7)
C(37)-C(38)-H(38A)	109.5	C(10)-N(2)-C(6)	118.2(10)
C(37)-C(38)-H(38B)	109.5	C(10)-N(2)-Os(1)	125.5(9)
H(38A)-C(38)-H(38B)	109.5	C(6)-N(2)-Os(1)	115.7(7)
C(37)-C(38)-H(38C)	109.5	C(11)-N(3)-C(15)	117.8(9)
H(38A)-C(38)-H(38C)	109.5	C(11)-N(3)-Os(1)	125.6(7)
H(38B)-C(38)-H(38C)	109.5	C(15)-N(3)-Os(1)	116.5(7)
O(3)-C(39)-C(40)	106.4(10)	C(20)-N(4)-C(16)	117.2(9)
O(3)-C(39)-H(39A)	110.5	C(20)-N(4)-Os(1)	127.0(7)
C(40)-C(39)-H(39A)	110.5	C(16)-N(4)-Os(1)	115.8(7)
O(3)-C(39)-H(39B)	110.5	C(25)-N(5)-C(21)	119.2(8)
C(40)-C(39)-H(39B)	110.5	C(25)-N(5)-Os(1)	117.2(6)
H(39A)-C(39)-H(39B)	108.7	C(21)-N(5)-Os(1)	123.6(6)
C(41)-C(40)-C(39)	110.8(12)	C(30)-N(6)-C(26)	118.0(8)

C(30)-N(6)-Os(1)	124.8(7)
C(26)-N(6)-Os(1)	117.1(6)
C(23)-O(1)-C(31)	118.2(8)
C(28)-O(3)-C(39)	117.4(8)
C(37)-S(1)-C(36)	100.3(5)
C(45)-S(2)-C(44)	101.4(6)
N(4)-Os(1)-N(3)	78.9(3)
N(4)-Os(1)-N(1)	173.9(3)
N(3)-Os(1)-N(1)	96.4(3)
N(4)-Os(1)-N(6)	89.4(3)
N(3)-Os(1)-N(6)	97.9(3)
N(1)-Os(1)-N(6)	95.1(3)
N(4)-Os(1)-N(2)	97.2(4)
N(3)-Os(1)-N(2)	84.4(3)
N(1)-Os(1)-N(2)	78.5(4)
N(6)-Os(1)-N(2)	173.4(4)
N(4)-Os(1)-N(5)	96.5(3)
N(3)-Os(1)-N(5)	173.5(3)
N(1)-Os(1)-N(5)	88.6(3)
N(6)-Os(1)-N(5)	77.4(3)
N(2)-Os(1)-N(5)	100.8(3)
F(102)-P(101)-F(104)	89.8(4)
F(102)-P(101)-F(103)	90.5(4)
F(104)-P(101)-F(103)	179.2(5)
F(102)-P(101)-F(106)	89.9(4)
F(104)-P(101)-F(106)	90.1(5)
F(103)-P(101)-F(106)	90.6(5)
F(102)-P(101)-F(105)	90.9(4)
F(104)-P(101)-F(105)	89.6(5)
F(103)-P(101)-F(105)	89.7(5)
F(106)-P(101)-F(105)	179.2(5)
F(102)-P(101)-F(101)	179.3(4)
F(104)-P(101)-F(101)	90.6(4)
F(103)-P(101)-F(101)	89.1(4)
F(106)-P(101)-F(101)	90.7(4)
F(105)-P(101)-F(101)	88.5(4)
F(201)#1-P(201)-F(201)	180.0(6)
F(201)#1-P(201)-F(202)#1	88.0(5)
F(201)-P(201)-F(202)#1	92.0(5)
F(201)#1-P(201)-F(202)	92.0(5)
F(201)-P(201)-F(202)	88.0(5)
F(202)#1-P(201)-F(202)	180.0(7)
F(201)#1-P(201)-F(203)#1	91.6(6)
F(201)-P(201)-F(203)#1	88.4(6)
F(202)#1-P(201)-F(203)#1	89.3(5)
F(202)-P(201)-F(203)#1	90.7(5)
F(201)#1-P(201)-F(203)	88.4(6)
F(201)-P(201)-F(203)	91.6(6)
F(202)#1-P(201)-F(203)	90.7(5)
F(202)-P(201)-F(203)	89.3(5)
F(203)#1-P(201)-F(203)	180.0(10)
F(303)#2-P(301)-F(303)	180.0(7)
F(303)#2-P(301)-F(302)	88.8(5)
F(303)-P(301)-F(302)	91.2(5)

F(303)#2-P(301)-F(302)#2	91.2(5)
F(303)-P(301)-F(302)#2	88.8(5)
F(302)-P(301)-F(302)#2	180.000(1)
F(303)#2-P(301)-F(301)	90.0(5)
F(303)-P(301)-F(301)	90.0(5)
F(302)-P(301)-F(301)	90.6(4)
F(302)#2-P(301)-F(301)	89.4(4)
F(303)#2-P(301)-F(301)#2	90.0(5)
F(303)-P(301)-F(301)#2	90.0(5)
F(302)-P(301)-F(301)#2	89.4(4)
F(302)#2-P(301)-F(301)#2	90.6(4)
F(301)-P(301)-F(301)#2	180.0(6)

Table A3.18 Anisotropic displacement parameters (Å^{2}x 10^3)for [Os(bpy)$_2$(4,4'-bpysac)](PF$_6$)2. The anisotropic displacement factor exponent takes the form: -2π^2[h^{2}a*^{2}U^{11} + ... + 2 h k a* b* U^{12}]

	U^{11}	U^{22}	U^{33}	U^{23}	U^{13}	U^{12}
C(1)	57(8)	53(7)	27(6)	-2(5)	5(6)	22(6)
C(2)	32(7)	53(7)	45(7)	5(6)	1(6)	13(6)
C(3)	28(7)	56(8)	58(8)	-4(6)	4(6)	7(6)
C(4)	59(8)	42(7)	37(7)	8(5)	12(6)	18(6)
C(5)	49(7)	39(6)	24(5)	1(5)	7(5)	18(5)
C(6)	64(8)	45(7)	23(6)	1(5)	11(6)	28(6)
C(7)	77(10)	41(7)	40(7)	6(6)	15(7)	20(7)
C(8)	79(10)	62(9)	32(7)	4(6)	-7(7)	36(8)
C(9)	84(11)	52(8)	31(7)	9(6)	-11(7)	32(8)
C(10)	59(8)	46(7)	47(7)	-11(6)	-8(6)	29(6)
C(11)	76(9)	24(6)	33(6)	2(5)	9(6)	24(6)
C(12)	75(10)	49(8)	40(7)	14(6)	12(7)	34(7)
C(13)	97(11)	35(7)	26(6)	-1(5)	3(7)	31(7)
C(14)	79(9)	31(6)	26(6)	-4(5)	-7(6)	16(6)
C(15)	50(7)	32(6)	26(6)	-4(5)	-11(5)	16(5)
C(16)	50(7)	33(6)	34(6)	1(5)	-4(5)	10(5)
C(17)	54(8)	33(6)	50(7)	1(5)	-12(6)	15(6)
C(18)	49(8)	42(7)	55(8)	-8(6)	-15(7)	1(6)
C(19)	40(7)	53(8)	46(7)	2(6)	6(6)	13(6)
C(20)	33(7)	44(7)	42(7)	-1(5)	-11(5)	7(5)
C(21)	42(6)	24(5)	17(5)	0(4)	-9(4)	15(5)
C(22)	43(7)	34(6)	27(6)	-4(5)	-2(5)	14(5)
C(23)	42(7)	38(6)	29(6)	-4(5)	5(5)	12(5)
C(24)	25(6)	42(6)	31(6)	-1(5)	-2(5)	13(5)
C(25)	22(5)	28(5)	35(6)	0(4)	0(4)	11(4)
C(26)	22(5)	25(5)	29(6)	4(4)	-4(4)	-1(4)
C(27)	33(6)	37(6)	31(6)	9(5)	6(5)	11(5)
C(28)	31(6)	31(6)	28(5)	7(4)	1(5)	14(5)
C(29)	48(7)	28(6)	45(7)	12(5)	1(6)	18(5)
C(30)	38(6)	33(6)	30(6)	3(5)	0(5)	7(5)
C(31)	58(8)	38(6)	28(6)	4(5)	9(5)	14(6)
C(32)	58(8)	44(7)	43(7)	-6(6)	14(6)	6(6)
C(33)	55(8)	49(7)	34(6)	6(5)	9(6)	18(6)
C(34)	60(8)	44(7)	33(6)	2(5)	7(6)	13(6)
C(35)	56(8)	43(7)	27(6)	0(5)	3(5)	16(6)
C(36)	63(9)	43(7)	41(7)	0(6)	6(6)	24(6)
C(37)	49(7)	46(7)	33(6)	2(5)	3(5)	19(6)
C(38)	84(10)	51(8)	40(7)	2(6)	5(7)	33(7)
C(39)	72(9)	56(8)	27(6)	0(5)	1(6)	24(7)
C(40)	73(10)	72(10)	58(9)	17(7)	0(8)	32(8)
C(41)	95(12)	81(11)	42(8)	7(7)	8(8)	38(9)
C(42)	102(12)	61(9)	49(8)	8(7)	10(8)	39(9)
C(43)	56(8)	56(8)	55(8)	14(6)	5(7)	25(7)
C(44)	56(8)	60(8)	37(7)	8(6)	5(6)	28(7)
C(45)	56(8)	42(7)	42(7)	4(6)	19(6)	6(6)
C(46)	93(11)	47(8)	43(7)	10(6)	6(7)	25(7)
N(1)	42(6)	36(5)	21(4)	3(4)	0(4)	13(4)

N(2)	45(6)	42(5)	21(5)	-5(4)	-4(4)	23(5)
N(3)	42(6)	39(5)	18(4)	-2(4)	2(4)	25(4)
N(4)	33(5)	25(5)	28(5)	-2(4)	-7(4)	7(4)
N(5)	29(5)	28(5)	23(4)	0(4)	0(4)	9(4)
N(6)	38(5)	29(5)	24(4)	2(4)	-3(4)	15(4)
O(1)	59(5)	39(4)	27(4)	-5(3)	2(4)	21(4)
O(2)	65(6)	49(5)	49(5)	8(4)	7(4)	27(5)
O(3)	57(5)	49(5)	36(4)	13(4)	5(4)	23(4)
O(4)	104(8)	58(6)	59(6)	8(5)	12(6)	39(6)
S(1)	81(2)	53(2)	34(2)	6(1)	11(2)	37(2)
S(2)	75(2)	65(2)	42(2)	6(2)	7(2)	38(2)
Os(1)	36(1)	29(1)	22(1)	0(1)	-2(1)	13(1)
F(101)	67(5)	54(4)	73(5)	22(4)	21(4)	22(4)
F(102)	51(4)	64(5)	54(4)	18(4)	4(4)	2(4)
F(103)	87(6)	82(6)	45(4)	-2(4)	-20(4)	22(5)
F(104)	124(7)	78(6)	34(4)	-3(4)	-20(4)	39(5)
F(105)	42(4)	79(6)	97(6)	-5(5)	16(4)	13(4)
F(106)	62(5)	66(5)	106(7)	21(5)	44(5)	22(4)
P(101)	42(2)	57(2)	28(2)	8(1)	2(1)	10(2)
F(201)	132(8)	103(7)	77(6)	-30(5)	0(6)	72(6)
F(202)	85(6)	123(8)	58(5)	3(5)	-5(5)	55(6)
F(203)	74(6)	150(10)	76(6)	-8(6)	-5(5)	-10(6)
P(201)	47(3)	68(3)	41(3)	-18(2)	-7(2)	27(3)
F(301)	112(7)	54(5)	90(6)	-9(4)	56(6)	2(5)
F(302)	92(6)	63(5)	80(6)	-2(4)	48(5)	16(4)
F(303)	82(6)	99(7)	91(7)	23(6)	-4(5)	14(5)
P(301)	71(4)	43(3)	61(3)	-4(2)	28(3)	10(3)

Table A3.19.   Hydrogen coordinates (x 10^4) and isotropic displacement parameters (Å^{2}x 10^3) for [Os(bpy)$_2$(4,4'-bpysac)](PF$_6$)$_2$.

	x	y	z	U(eq)
H(1)	510	9766	7057	54
H(2)	-1935	8788	7098	52
H(3)	-2450	7862	7910	58
H(4)	-445	7832	8645	53
H(7)	1663	7812	9283	61
H(8)	3937	7940	9897	68
H(9)	6190	8963	9667	66
H(10)	6160	9849	8808	61
H(11)	1451	11092	8588	51
H(12)	1549	12508	9327	61
H(13)	3824	13831	9663	61
H(14)	6002	13642	9293	56
H(17)	7958	13360	8892	56
H(18)	9826	13073	8362	64
H(19)	9187	11715	7545	56
H(20)	6716	10580	7351	50
H(21)	4504	8086	7615	34

H(22)	4754	6960	6815	42
H(24)	3478	9113	5733	39
H(27)	2884	10737	5700	39
H(29)	2342	13372	6703	47
H(30)	2879	12522	7522	41
H(31A)	4611	8099	5064	49
H(31B)	2851	7508	5063	49
H(32A)	3363	5736	4849	59
H(32B)	5099	6342	4831	59
H(33A)	4225	7265	4010	54
H(33B)	2539	6525	4008	54
H(34A)	3412	4879	3813	55
H(34B)	5060	5647	3783	55
H(35A)	2346	5599	2968	51
H(35B)	3961	6427	2947	51
H(36A)	3411	4051	2782	57
H(36B)	4991	4899	2734	57
H(38A)	4664	3853	769	84
H(38B)	3091	4194	778	84
H(38C)	3148	2924	801	84
H(39A)	1069	11424	5024	61
H(39B)	2854	11845	4998	61
H(40A)	2403	13608	4721	79
H(40B)	1601	12589	4228	79
H(41A)	120	13395	5084	84
H(41B)	-663	12434	4560	84
H(42A)	-1177	14178	4332	81
H(42B)	605	14716	4378	81
H(43A)	-962	12892	3525	65
H(43B)	728	13632	3541	65
H(44A)	-268	15199	3309	58
H(44B)	-1962	14450	3288	58
H(46A)	-2531	15153	1252	90
H(46B)	-2616	13872	1320	90
H(46C)	-1014	14721	1310	90

_____

Table A3.20. Torsion angles [°] for [Os(bpy)₂(4,4'-bpysac)](PF₆)₂.

N(1)-C(1)-C(2)-C(3)	0.0(18)
C(1)-C(2)-C(3)-C(4)	-3.0(18)
C(2)-C(3)-C(4)-C(5)	0.3(18)
C(3)-C(4)-C(5)-N(1)	5.5(16)
C(3)-C(4)-C(5)-C(6)	-177.6(10)
N(1)-C(5)-C(6)-N(2)	-3.3(13)
C(4)-C(5)-C(6)-N(2)	179.7(10)
N(1)-C(5)-C(6)-C(7)	177.7(10)
C(4)-C(5)-C(6)-C(7)	0.6(17)
N(2)-C(6)-C(7)-C(8)	0.9(17)
C(5)-C(6)-C(7)-C(8)	180.0(11)
C(6)-C(7)-C(8)-C(9)	-0.7(18)
C(7)-C(8)-C(9)-C(10)	-0.3(19)
C(8)-C(9)-C(10)-N(2)	1.2(18)
N(3)-C(11)-C(12)-C(13)	-0.4(17)
C(11)-C(12)-C(13)-C(14)	-2.3(17)
C(12)-C(13)-C(14)-C(15)	2.1(17)
C(13)-C(14)-C(15)-N(3)	0.7(16)
C(13)-C(14)-C(15)-C(16)	177.3(10)
N(3)-C(15)-C(16)-N(4)	0.4(13)
C(14)-C(15)-C(16)-N(4)	-176.4(10)
N(3)-C(15)-C(16)-C(17)	179.0(10)
C(14)-C(15)-C(16)-C(17)	2.2(18)
N(4)-C(16)-C(17)-C(18)	2.7(17)
C(15)-C(16)-C(17)-C(18)	-175.8(11)
C(16)-C(17)-C(18)-C(19)	1.3(18)
C(17)-C(18)-C(19)-C(20)	-3.3(18)
C(18)-C(19)-C(20)-N(4)	1.6(18)
N(5)-C(21)-C(22)-C(23)	-0.7(16)
C(21)-C(22)-C(23)-O(1)	-177.6(10)
C(21)-C(22)-C(23)-C(24)	-0.1(16)
O(1)-C(23)-C(24)-C(25)	178.5(10)
C(22)-C(23)-C(24)-C(25)	1.2(15)
C(23)-C(24)-C(25)-N(5)	-1.7(15)
C(23)-C(24)-C(25)-C(26)	177.3(9)
N(5)-C(25)-C(26)-N(6)	0.2(12)
C(24)-C(25)-C(26)-N(6)	-178.8(9)
N(5)-C(25)-C(26)-C(27)	-179.4(9)
C(24)-C(25)-C(26)-C(27)	1.5(16)
N(6)-C(26)-C(27)-C(28)	-0.5(15)
C(25)-C(26)-C(27)-C(28)	179.1(9)
C(26)-C(27)-C(28)-O(3)	178.3(9)
C(26)-C(27)-C(28)-C(29)	2.6(15)
O(3)-C(28)-C(29)-C(30)	-179.3(10)
C(27)-C(28)-C(29)-C(30)	-3.1(16)
C(28)-C(29)-C(30)-N(6)	1.6(17)
O(1)-C(31)-C(32)-C(33)	178.2(9)
C(31)-C(32)-C(33)-C(34)	173.3(10)
C(32)-C(33)-C(34)-C(35)	176.7(10)
C(33)-C(34)-C(35)-C(36)	176.8(10)
C(34)-C(35)-C(36)-S(1)	177.3(9)
O(3)-C(39)-C(40)-C(41)	-68.9(15)

C(39)-C(40)-C(41)-C(42)	176.2(11)
C(40)-C(41)-C(42)-C(43)	62.6(18)
C(41)-C(42)-C(43)-C(44)	169.4(12)
C(42)-C(43)-C(44)-S(2)	179.5(10)
C(2)-C(1)-N(1)-C(5)	5.7(16)
C(2)-C(1)-N(1)-Os(1)	-176.2(8)
C(4)-C(5)-N(1)-C(1)	-8.3(14)
C(6)-C(5)-N(1)-C(1)	174.5(9)
C(4)-C(5)-N(1)-Os(1)	173.4(8)
C(6)-C(5)-N(1)-Os(1)	-3.8(11)
C(9)-C(10)-N(2)-C(6)	-1.0(15)
C(9)-C(10)-N(2)-Os(1)	170.2(8)
C(7)-C(6)-N(2)-C(10)	-0.1(15)
C(5)-C(6)-N(2)-C(10)	-179.2(9)
C(7)-C(6)-N(2)-Os(1)	-172.1(8)
C(5)-C(6)-N(2)-Os(1)	8.7(11)
C(12)-C(11)-N(3)-C(15)	3.2(15)
C(12)-C(11)-N(3)-Os(1)	178.9(8)
C(14)-C(15)-N(3)-C(11)	-3.3(15)
C(16)-C(15)-N(3)-C(11)	179.7(9)
C(14)-C(15)-N(3)-Os(1)	-179.4(8)
C(16)-C(15)-N(3)-Os(1)	3.6(11)
C(19)-C(20)-N(4)-C(16)	2.2(16)
C(19)-C(20)-N(4)-Os(1)	-179.5(8)
C(17)-C(16)-N(4)-C(20)	-4.4(15)
C(15)-C(16)-N(4)-C(20)	174.3(9)
C(17)-C(16)-N(4)-Os(1)	177.1(8)
C(15)-C(16)-N(4)-Os(1)	-4.2(12)
C(24)-C(25)-N(5)-C(21)	1.0(15)
C(26)-C(25)-N(5)-C(21)	-178.1(8)
C(24)-C(25)-N(5)-Os(1)	-179.9(7)
C(26)-C(25)-N(5)-Os(1)	1.0(11)
C(22)-C(21)-N(5)-C(25)	0.2(15)
C(22)-C(21)-N(5)-Os(1)	-178.8(8)
C(29)-C(30)-N(6)-C(26)	0.5(16)
C(29)-C(30)-N(6)-Os(1)	-178.8(8)
C(27)-C(26)-N(6)-C(30)	-1.0(14)
C(25)-C(26)-N(6)-C(30)	179.3(9)
C(27)-C(26)-N(6)-Os(1)	178.3(7)
C(25)-C(26)-N(6)-Os(1)	-1.4(11)
C(24)-C(23)-O(1)-C(31)	-0.3(16)
C(22)-C(23)-O(1)-C(31)	177.1(10)
C(32)-C(31)-O(1)-C(23)	-176.6(9)
C(27)-C(28)-O(3)-C(39)	11.4(16)
C(29)-C(28)-O(3)-C(39)	-172.7(10)
C(40)-C(39)-O(3)-C(28)	-179.8(10)
O(2)-C(37)-S(1)-C(36)	1.6(12)
C(38)-C(37)-S(1)-C(36)	179.5(10)
C(35)-C(36)-S(1)-C(37)	173.0(9)
O(4)-C(45)-S(2)-C(44)	-1.5(13)
C(46)-C(45)-S(2)-C(44)	-178.6(10)
C(43)-C(44)-S(2)-C(45)	177.4(9)
C(20)-N(4)-Os(1)-N(3)	-173.6(9)
C(16)-N(4)-Os(1)-N(3)	4.7(7)
C(20)-N(4)-Os(1)-N(1)	147(3)

C(16)-N(4)-Os(1)-N(1)	-34(4)
C(20)-N(4)-Os(1)-N(6)	-75.4(9)
C(16)-N(4)-Os(1)-N(6)	102.9(7)
C(20)-N(4)-Os(1)-N(2)	103.6(9)
C(16)-N(4)-Os(1)-N(2)	-78.1(7)
C(20)-N(4)-Os(1)-N(5)	1.8(9)
C(16)-N(4)-Os(1)-N(5)	-179.8(7)
C(11)-N(3)-Os(1)-N(4)	179.7(9)
C(15)-N(3)-Os(1)-N(4)	-4.5(7)
C(11)-N(3)-Os(1)-N(1)	-4.2(9)
C(15)-N(3)-Os(1)-N(1)	171.6(7)
C(11)-N(3)-Os(1)-N(6)	91.9(8)
C(15)-N(3)-Os(1)-N(6)	-92.3(7)
C(11)-N(3)-Os(1)-N(2)	-81.9(8)
C(15)-N(3)-Os(1)-N(2)	93.9(7)
C(11)-N(3)-Os(1)-N(5)	135(3)
C(15)-N(3)-Os(1)-N(5)	-49(3)
C(1)-N(1)-Os(1)-N(4)	144(3)
C(5)-N(1)-Os(1)-N(4)	-38(4)
C(1)-N(1)-Os(1)-N(3)	105.4(9)
C(5)-N(1)-Os(1)-N(3)	-76.5(7)
C(1)-N(1)-Os(1)-N(6)	6.8(9)
C(5)-N(1)-Os(1)-N(6)	-175.0(7)
C(1)-N(1)-Os(1)-N(2)	-171.7(9)
C(5)-N(1)-Os(1)-N(2)	6.4(7)
C(1)-N(1)-Os(1)-N(5)	-70.4(9)
C(5)-N(1)-Os(1)-N(5)	107.7(7)
C(30)-N(6)-Os(1)-N(4)	-82.5(9)
C(26)-N(6)-Os(1)-N(4)	98.3(7)
C(30)-N(6)-Os(1)-N(3)	-3.8(9)
C(26)-N(6)-Os(1)-N(3)	177.0(7)
C(30)-N(6)-Os(1)-N(1)	93.4(8)
C(26)-N(6)-Os(1)-N(1)	-85.9(7)
C(30)-N(6)-Os(1)-N(2)	106(3)
C(26)-N(6)-Os(1)-N(2)	-73(3)
C(30)-N(6)-Os(1)-N(5)	-179.3(9)
C(26)-N(6)-Os(1)-N(5)	1.5(7)
C(10)-N(2)-Os(1)-N(4)	-4.0(9)
C(6)-N(2)-Os(1)-N(4)	167.4(7)
C(10)-N(2)-Os(1)-N(3)	-82.0(9)
C(6)-N(2)-Os(1)-N(3)	89.4(7)
C(10)-N(2)-Os(1)-N(1)	-179.7(9)
C(6)-N(2)-Os(1)-N(1)	-8.3(7)
C(10)-N(2)-Os(1)-N(6)	167(3)
C(6)-N(2)-Os(1)-N(6)	-21(3)
C(10)-N(2)-Os(1)-N(5)	94.0(8)
C(6)-N(2)-Os(1)-N(5)	-94.6(7)
C(25)-N(5)-Os(1)-N(4)	-89.3(7)
C(21)-N(5)-Os(1)-N(4)	89.8(8)
C(25)-N(5)-Os(1)-N(3)	-46(3)
C(21)-N(5)-Os(1)-N(3)	134(3)
C(25)-N(5)-Os(1)-N(1)	94.2(7)
C(21)-N(5)-Os(1)-N(1)	-86.7(8)
C(25)-N(5)-Os(1)-N(6)	-1.4(7)
C(21)-N(5)-Os(1)-N(6)	177.7(8)

C(25)-N(5)-Os(1)-N(2)   172.1(7)
C(21)-N(5)-Os(1)-N(2)   -8.8(8)

_____

Symmetry transformations used to generate equivalent atoms:

#1 -x+2,-y+1,-z   #2 -x,-y+2,-z